1993

Response Statistics Of Shell Structures With Geometrical And Material Nonlinearities

Meilan Liu

RESPONSE STATISTICS OF SHELL STRUCTURES WITH GEOMETRICAL AND MATERIAL NONLINEARITIES

Volume I

by

Meilan Liu

Department of Mechanical Engineering
Faculty of Engineering Science

Submitted in partial fulfilment of
the requirement for the degree of
Doctor of Philosophy

Faculty of Graduate Studies
The University of Western Ontario
London, Ontario, Canada
July, 1993

National Library
of Canada

Acquisitions and
Bibliographic Services Branch

395 Wellington Street
Ottawa, Ontario
K1A 0N4

Bibliothèque nationale
du Canada

Direction des acquisitions et
des services bibliographiques

395, rue Wellington
Ottawa (Ontario)
K1A 0N4

Your file Votre référence

Our file Notre référence

ISBN 0-315-84006-4

Canada

ABSTRACT

The investigation in this thesis is concerned with response statistics of shell structures with geometrical and material nonlinearities under stationary and non-stationary Gaussian random excitations.

A series of hybrid strain based three node flat triangular shell elements is developed for linear and nonlinear shell structural analyses. In the former the Hellinger-Reissner variational principle is employed. The elements are obtained by combining a triangular bending element and a plane stress element, and incorporating the drilling degrees-of-freedom. For the nonlinear analysis the updated Lagrangian formulation and the incremental Hellinger-Reissner variational principle are applied, with incremental displacements and strains being the independently assumed fields. Accordingly, the incremental second Piola-Kirchhoff stress and the incremental Washizu strain are selected as the incremental stress and strain measures. Schemes to transform the second Piola-Kirchhoff stresses to Cauchy stresses are included. The director and simplified versions of the stiffness and consistent mass matrices are derived. Material nonlinearity is of elasto-plastic type with isotropic hardening which is formulated by the J_2 flow theory with Ilyushin's yield criterion. In all cases, explicit expressions for the stiffness and consistent mass matrices are obtained. Various shell structures studied in this thesis show that the element formulations are accurate, effective, flexible, and applicable to thin to moderately thick shells with geometrical and material nonlinearities.

In parallel, the stochastic central difference (SCD) method and its associated computational strategies are applied to determine response statistics of general structures. The strategies include the time co-ordinate transformation (TCT) and adaptive time schemes (ATS). The SCD method with the strategies has excellent accuracy and effectiveness, and does not cause computational instability.

The SCD method is subsequently extended to include a relatively general non-stationary random excitation that consists of a deterministic and stochastic components. In conjunction with the TCT and ATS, it is applied to compute the random responses of general nonlinear shell structures that are discretized by the derived shell elements. Numerical results employing the proposed methodologies are presented and the effectiveness of the methodologies addressed.

The thesis concludes with recommendations for further investigations.

ACKNOWLEDGEMENTS

The author wishes to express her sincere and deep gratitude to her supervisor, Professor C.W.S. To, for his invaluable guidance, constructive instruction and continuous encouragement throughout the course of this work.

Thanks are extended to those fellow graduate students and computing facility managing staff who have offered their valuable suggestions, kind assistance and friendly co-operations.

The following fellowship and scholarships are gratefully acknowledged: The Zonta International's Amelia Earhart Fellowship, The Ministry of Colleges and Universities of Ontario's Ontario Graduate scholarship and The University of Western Ontario's Special University Scholarship. The financial assistance received from the Department of Mechanical Engineering and Faculty of Graduate Studies, and the financial support received by her supervisor from the Natural Science and Engineering Research Council of Canada are also gratefully acknowledged.

Finally, the author would like to express her deep appreciation to all her family members, her husband Dawen in particular. Without their understanding, support and sacrifice this work would not have been attempted and completed.

TABLE OF CONTENTS

Volume I

TABLE OF CONTENTS
(cont'd)

TABLE OF CONTENTS
(cont'd)

TABLE OF CONTENTS
(cont'd)

TABLE OF CONTENTS
(cont'd)

TABLE OF CONTENTS
(cont'd)

LIST OF TABLES

LIST OF TABLES
(cont'd)

LIST OF TABLES
(cont'd)

LIST OF TABLES
(cont'd)

LIST OF TABLES
(cont'd)

LIST OF FIGURES

LIST OF FIGURES
(cont'd)

LIST OF FIGURES
(cont'd)

LIST OF FIGURES
(cont'd)

LIST OF FIGURES
(cont'd)

LIST OF FIGURES
(cont'd)

LIST OF FIGURES
(cont'd)

LIST OF FIGURES
(cont'd)

LIST OF FIGURES
(cont'd)

LIST OF FIGURES
(cont'd)

LIST OF FIGURES
(cont'd)

LIST OF APPENDICES

NOMENCLATURE

Following is a list of the principal symblos and notations used in this thesis. The symbols and notations less frequently used and those have different meanings in different contexts are defined where they are used.

Roman Letters

a_{ij}	geometrical parameters of a triangle.
A	the area of an element.
b_{ij}	geometrical parameters of a triangle.
B	strain-displacement matrix.
B_b, B_d, B_s	component strain-displacement matrices associated with bending, drilling degrees-of-freedom (DDOF) and transversal shear, respectively.
B_m, $(B_m)'$	component strain-displacement matrices associated with membrane.
B_L, B_{NL}	linear and nonlinear strain-displacement matrices, respectively.
$B(s)$	matrix used in the stochastic central difference method.
C	assembled damping matrix.
C_τ	assembled damping matrix in the dimensionless time co-ordinate.
C_{ijkl}	the consitutive tensor for homogeneous, isotropic and linear elastic materials.
C_{ijkl}^{ep}	the consitutive tensor for elasto-plastic materials with isotropic strain hardening.

NOMENCLATURE
(cont'd)

$\mathbf{D}$	elastic matrix of a material.
$\mathbf{D(s)}$	matrix used in the stochastic central difference method.
$\mathbf{e(t)}$	an element of the vector $\bar{e}(t)$.
$\bar{e}(t)$	vector of deterministic amplitude modulating fuction.
$\Delta\mathbf{e}$	vector of assumed incremental Green strain.
$\Delta\bar{e}$	vector of incremental Washizu strain calculated from assumed incremental displacements.
$\mathbf{E}$	Young's modulus.
E_τ	a constant used to normalize e(t).
E_T	tangent modulus.
$\mathbf{f}$	body force vector.
$\mathbf{f(t)}$	vector of general excitation.
$f_\tau(\tau)$	vector of general excitation in the dimensionless time co-ordinate.
f_c	consistent load vector.
F_I	pseudo-force vector at time "t".
$F(t+\Delta t)$	consistent nodal force vector at time "t+Δt".
$F_t^{t+\Delta t}$	relative deformation gradient from time "t" to "t+Δt".
$\mathbf{G}$	shear modulus.
G_e	matrix defined by equation (3.8b).

NOMENCLATURE
(cont'd)

$(G_e)_b$	component matrix of G_e associated with bending.
$(G_e)_d$	component matrix of G_e associated with DDOF.
$(G_e)_m$, $(G_e)'_m$	component matrices of G_e associated with membrane.
$(G_e)_s$	component matrix of G_e associated with transversal shear.
G_{dyn}	weak form of momentum balance.
G_{sta}	the static part of G_{dyn}.
G_{vel}	the part of G_{dyn} associated with the linear and angular velocities and accelerations.
G_{rot}	the part of G_{vel} associated with angular velocities and accelerations.
G_{tra}	the part of G_{vel} associated with linear velocities and accelerations.
h, h^t	thickness of a shell at time "t".
H	matrix defined by equation (3.8a).
H_5	H matrix for the 5 degrees-of-freedom (DOF) per node version.
$\tilde{H}$	H matrix that accounts for the DDOF.
H_i	matrix containing derivatives of displacements.
J_2	the second invariant of stresses.
k	element stiffness matrix.
k_b, k_d, k_s	component element stiffness matrices associated with bending, the DDOF and transversal shear, respectively.
k_m, $(k_m)'$	component element stiffness matrices associated with membrane.

NOMENCLATURE
(cont'd)

k_t	component element stiffness matrix associted with the DDOF.
k_t^i	k_t matrix based on the constant strain triangle and using i-point integration.
$(k_t^i)'$	k_t matrix based on the Allman's triangle and using i-point integration.
k_L, k_{NL}	element linear and initial stress stiffness matrices, respectively.
K	assembled stiffness matrix.
K_τ	assembled stiffness matrix in the dimensionless time co-ordinate.
L	linear operator to calculate strains from displacements.
m_{rot}	rotational part of element consistent mass matrix associated with the bending rotational DOF.
m_{tra}	translational part of element consistent mass matrix.
M	assembled consistent mass matrix.
M_τ	assembled consistent mass matrix in the dimensionless time co-ordinate.
N	matrix of displacement interpolation functions.
N_1, N_2, N_3	matrices in the stochastic central difference method.
N_5	matrix of displacement interpolation functions for the 5 DOF per node version.
N_m	interpolation function matrix for the mid-surface displacements.
N_r	interpolation function matrix for bending rotations.
N_t	matrix of displacement interpolation functions for the DDOF.
p	linear momentum.

NOMENCLATURE
(cont'd)

$p(t)$	the deterministic component of a random excitation.
$\bar{p}_i$	geometrical parameters of a triangle.
P	matrix of strain interpolation functions.
P_5	matrix of strain interpolation functions for the 5 DOF per node version.
$\bar{P}$	P matrix that accounts for the DDOF.
q	nodal displacement vector.
Δq	vector of incremental displacements.
$\bar{q}_i$	geometrical parameters of a triangle.
Q	global displacemenet vector.
Q_t, Q_m, Q_{tm}	quantities used in Ilyushin's yield conditions.
$r(t)$	stochastic excitation vector.
$r_\tau(\tau)$	stochastic excitation vector in the dimensionless time co-ordinate.
r_2, r_3, s_3	geometrical parameters of a triangle.
$R(s)$	cross-correlation matrix.
s	time step index for the stochastic central difference method.
S, S_0	spectral intensity of a Gaussian white noise.
ΔS	vector of incremental second Piola-Kirchhoff stress.
t	time co-ordinate.
$\bar{t}$	vector of prescribed surface traction.

NOMENCLATURE
(cont'd)

Δt	time step size.
$(\Delta t)_{cr}$	critical time step size.
T	transformation matrix between the global and local co-ordinates.
T_c, T_{c4}	transformation matrices.
T_v	matrix used to update directors.
u, v, w	local displacements in the r,s and t axes, respectively.
U, V, W	global displacements in the X, Y, and Z axes, respectively (for boundary conditions only).
V, V_e	the volume of an element.
V_b	the volume of a body.
V^t	the volume of a body at time "t"; or the second summation on the right hand side (RHS) of equation (6.13).
V_i^t	the director of node i at time "t".
ΔV_i^t	the increment of director of node i from time "t" to "t+Δt".
V(s)	covariance matrix.
w(t)	stationary Gaussian white niose process with zero mean.
$W^{t+\Delta t}$	work done by prescribed body force and surface traction at time "t+Δt".
x	displacement vector in the dimensionless time co-ordinate.
X	displacement vector.
$\bar{Y}$	a row matrix used to calculate k_t.

NOMENCLATURE
(cont'd)

Greek Letters

α	a parameter indicating whether the material is undergoing plastic deformation.
α_1, α_2	time constants for the amplitude modulating function.
α_{r1}, α_{r2}	time constants for the vector of amplitude modulating function.
$\Delta\alpha$	virtual rotation of the director field.
β	vector of strain parameters.
$\Delta\beta$	vector of incremental strain parameters.
Γ_i^t	an orthogonal matrix associated with finite rotations.
δ	time step size.
$\delta(0)$, δ_{mn}	the Kronecker delta.
ε	vector of strains.
ε_r, ε_s	normal strains.
ε_{rs}, ε_{st}, ε_{tr}	shear strains.
ε_{rs}^s	the skew-symmetric part of the strain tensor.
$\Delta\varepsilon$, $\Delta\eta$	the linear and quadratic parts of $\Delta\bar{e}$, respectively.
ζ_i	modal damping ratio.
Λ_i^t	a matrix constructed from Ω_i^t and Γ_i^t.
η^t	local co-ordinate along the director direction.
θ_r, θ_s, θ_t	local rotations about the r, s and t axes, respectively.

NOMENCLATURE
(cont'd)

$(\Delta\theta_i)'$	incremental rotational vector of node i from time "t" to "t+Δt" relative to the director orthogonal frame.
$\Delta\theta_i$	incremental rotational vector of node i from time "t" to "t+Δt" relative to the local r, s and t axes.
Θ_x, Θ_y, Θ_z	global rotations about the X, Y, and X axes, respectively (for boundary conditions only).
κ_s	form factor of shear.
λ_k, λ_m	Rayleigh damping coefficients associated with stiffness and mass matrices, respectively.
ν	Poisson's ratio.
ξ_1, ξ_2, ξ_3	the natural (area) co-ordinates of a triangle.
ρ, ρ'	density (per unit volume) at time "t".
π_{HR}	functional for the Hellinger-Reissner variational principle.
π_t	functional associated with the DDOF.
$\Delta\pi_{HR}$	functional for the incremental Hellinger-Reissner variational principle.
σ	vector of (Cauchy) stress.
σ_r, σ_s	normal stresses.
σ_{rs}, σ_{st}, σ_{tr}	shear stresses.
σ_{rs}^s	the skew-symmetric part of the stress tensor.
σ_y	yield stress of a material in simple tension.

NOMENCLATURE
(cont'd)

σ^D	stress diviator.
$\bar{\sigma}$	matrix constructed from σ.
τ	dimensionless time co-ordinate.
$\Delta\tau$	time step size in the dimensionless time co-ordinate.
$(\Delta\tau)_{cr}$	critical time step size in the dimensionless time co-ordinate.
ϕ	the first summation on the RHS of equation (6.13).
$_{\cdot}\phi$	virtual mid-surface displacement.
$_i\phi$	the i-th mode shape vector that is orthonormal relative to mass matrix.
χ	angular momentum.
ω_i	the i-th natural frequency of a discretized system.
Ω	the highest natural frequency of a discretized system.
Ω_i^t	skew-symmetric matrix constructed from V_i^t.

CHAPTER 1

INTRODUCTION

Shell structures have a wide range of applications in practice. A large amount of industrial equipment contains parts of shells. For example, shell components are used in missiles and space vehicles, submarines and tankers, nuclear reactor vessels, refinery equipment and so on. Consequently, shell structures have long been the focus of studies in mechanical, civil and aerospace engineering.

1.1 General

Analytical tools for shell structural analysis were first developed a century or so ago. Lamé and Clapeyron [1.1] established the fundamental theory for shell membrane stress in 1826. Aron [1.2] considered bending behaviours in 1874, but the first general theory was not advanced until 1888, by Love [1.3]. Subsequent theoretical efforts have been directed towards improvements of Love's formulations and solutions of the associated differential equations. Such solutions are of course hard to obtain such that available analytical solutions to shell structural problems are limited in scope and in general do not apply to arbitrary shapes, load conditions, irregular stiffening and support conditions, cut-outs and many other aspects of practical design. The finite element method (FEM) has thus come to the fore as an approach to shell structural analysis because of its capability to deal with these complications.

The 1950's are believed to be the formative years of the finite element method for shell analysis when planar elements were used to form finite element idealizations. Later during the early 1960's curved shell elements became appealing. One of the first developments of singly curved thin shell element, a circular cylindrical element, was undertaken by Gallagher in 1966 [1.4]. The early attempt to develop a doubly curved triangular shell element was due to Utku [1.5] in 1967. By 1970 a large number of curved shell elements had appeared in the literature. Around the late 1960's and early 1970's the so-called degenerate shell elements started to draw attention [1.6]. The elements are deduced from three-dimensional (3D) elements to accommodate the need of thick, moderately thick, even thin shell structure modelling.

Meanwhile the first attempts of applying the finite element technique to nonlinear analysis of shells date back to the late 1960's. Most of these early efforts were limited to studies of shells of particular geometrical shape, such as axisymmetric shells and cylindrical shells. These early efforts were also mainly focused on large deformation (that is, large displacement and rotation) problems. It was not until the further development in nonlinear finite element technology and in computer hardware and software that the more advanced nonlinear analysis, such as large strain problems, combinations of geometrical and material nonlinearities and so on, had been dealt with. Now, nonlinear structural analysis for general shells including the effects of both geometrical (for example, large deformation and finite strain) and material (for example, plasticity) nonlinearities has generated a considerable number of publications over the years, and especially in recent years. One of the outcomes of these efforts, together with the advancements of finite

element analysis for other structural components (such as beam, truss and frame, etc.), is large-scale computer programs for solutions of nonlinear structural and solid mechanics problems.

Surveys conducted in 1980 to 1981 of such general purpose computer programs reviewed up to 36 computer programs [1.7-9]. For brevity, details of the surveys will not be included in this thesis. However, some of the concerned statistics are in order:

11 programs are capable of performing nonlinear transient response analysis;

7 programs are equipped with dynamic response analysis for large strain plasticity applications;

4 programs are available if random loading is to be brought into the scope. Note that with random loading the programs conduct Fourier analysis which implies that only the stationary responses are taken into consideration.

Later surveys in the mid-1980 [1.10-11] on major commercially available general purpose finite element analysis programs revealed similar information. Linear elasticity analysis, which serves as the basis of nonlinear analysis and has its own importance in applications, is on the menu of every program. However, only a few programs are provided with geometrically and materially nonlinear analysis, static and dynamic, deterministic and stochastic, in which large strain is considered. Such an analysis is believed to be the most general and challenging case of nonlinear structural and mechanical analysis. More effort to conduct such research is indeed needed.

Nonlinear shell structural analysis is no doubt challenged by many conceptual, theoretical and computational difficulties involved in such an analysis. The difficulties that

researchers face when carrying out the nonlinear analysis arise from many aspects. As pointed out in reference [1.7], an effective development (even an effective use) of a nonlinear finite element program requires detailed knowledge about:

(1) finite element discretization and formulating;

(2) continuum mechanics basis and formulation aspects (this is particularly important when solving large strain problems);

(3) constitutive relations and material modelling;

(4) solution techniques for nonlinear static problems;

(5) temporal integration and solution techniques for nonlinear dynamic problems; and

(6) considerations for the design of software systems for nonlinear analysis.

The above list, however, is mainly concerned with deterministic analysis. With regard to stochastic dynamic responses of shell structures, a review article by To [1.12] examined and identified some techniques that might be applicable to the computation of responses of complex structures with geometrical and material nonlinearities subjected to non-stationary excitations. It was found that techniques suitable to be applied with the finite element method for the evaluation of response statistics of generally nonlinear structures were far from satisfactory. Consequently, the stochastic version of the Newmark family of algorithms and the stochastic central difference (SCD) method in particular were introduced [1.13-15]. Compared with other techniques, such as the state-space formulation [1.16-17] and the auto-regressive-moving-average (ARMA) models [1.18-19], the SCD method has the advantages of, for example, low computational cost, no restriction on the type of damping, being applicable to finite element analysis, no

modal analysis required, and having the potential to deal with discretized structures incorporating geometrical and material nonlinearities which are frequently not defined explicitly [1.14-15]. However, the potential of the SCD method has not yet been fully demonstrated in the literature, and some strategies to make more effective the application of the SCD method remain to be verified.

1.2 Objectives and Methodologies

The investigation in this thesis is aimed at determining the random responses of general shell structures with geometrical and material nonlinearities subjected to stationary and non-stationary Gaussian random excitations. To this end, the following investigation strategies are considered. Firstly, some accurate, effective and versatile shell elements that are applicable to thin to moderately thick shell structures are developed and examined. At the same time, strategies to effectively apply the SCD method to shell structures represented by finite elements are to be investigated. Theses strategies include the time co-ordinate transformation (TCT) technique and the adaptive time schemes (ATS). In the final phase of the investigation, the shell elements developed in the first phase and their extension to nonlinear analysis considered in the second phase are used in conjunction with the SCD method and the TCT and ATS techniques to determine the stationary and non-stationary random responses of thin to moderately thick shell structures undergoing large strain elasto-plastic deformations subjected to stationary and non-stationary Gaussian random excitations.

The main objectives of the investigation are therefore,

(1) identifications of advantages and problems of existing theories and various finite element methods and stochastic analysis methods;

(2) solutions to existing problems by exploiting theoretical formulations and computational strategies;

(3) implementations of developed theories and computational strategies, and evaluations of responses, static and dynamic, deterministic and stochastic, of representative shell structures; and

(4) better and more detailed understanding of behaviours of shell structures under various loading conditions.

In the investigation, the FEM is one of the main computational tools. The development of shell finite elements is concentrated on some elements with hybrid strain formulation and very simple geometry, three node flat triangle. The nodal degrees-of-freedom are displacements and rotations and no higher order derivatives of the displacements are required. In parallel, the SCD method in conjunction with the TCT and ATS techniques is applied to nonlinear systems subjected to stationary and non-stationary Gaussian random excitations.

The investigation consists of three phases. The first phase is concerned with the development of hybrid strain based three node flat triangular shell elements that are accurate, effective, and versatile, and applicable to thin to moderately thick shell structures. This phase is also involved with, at the same time, the study of computational aspects of the SCD method and its application to dynamic systems having many DOF and nonlinear stiffness subjected to stationary and nonstationary Gaussian random excitations.

The second phase consists of the extension of the shell elements developed in the first phase to general nonlinear problems with a focus on elasto-plastic deformations of finite strains. In the final phase, the developed elements and the SCD method are applied to several practical shell structures with random loadings.

1.3 Organization of the Thesis

This thesis consists of nine chapters and three appendices.

Chapter 1, as already brought forth, deals with the introduction.

Chapter 2 is concerned with the SCD method and its applications to linear systems with many DOF (Section 2.1) and to nonlinear systems with explicitly defined nonlinearities (Sections 2.2 and 2.3). Strategies to effectively apply the SCD method, mainly, the TCT and ATS are also included (Sections 2.1 and 2.3).

Following Chapter 2, Chapters 3 through 7 present the parts of investigation associated with the finite element method. Theories and results related to the linear analysis are included in Chapters 3 through 5 while those for the nonlinear analysis in Chapters 6 and 7. These are detailed as follows.

Chapter 3 contains the theoretical development of the hybrid strain based three node flat triangular shell elements for linear applications. Variational principle, displacement and strain assumptions, and element stiffness matrices are discussed. The explicit expressions for the element stiffness matrices are obtained.

Chapter 4 deals with the numerical studies of the derived shell elements in the static cases. More than ten examples are considered which include the so-called obstacle

course [1.20]. These examples are grouped into plate problems and shell problems and presented by two sections, Sections 4.1 and 4.2.

Subsequently, Chapter 5 presents the results of vibration analysis using the proposed shell elements. The consistent element mass matrices corresponding to the displacement assumption of Chapter 3 are derived. Convergence characteristic of the natural frequencies are established through numerical examples.

Chapter 6 first gives an overview of nonlinear FEM analysis covering aspects such as incremental formulations and variational principles, linearization of the incremental principle, stress and strain measures large rotations and so on. It continues to present the incremental principle and the derivation of stiffness matrices, linear and nonlinear, and consistent mass matrices. Constitutive relations and updating schemes for configuration and stress are also presented.

Chapter 7 is concerned with the application of the theory and formulation of Chapter 6. It contains numerical results of static analysis of geometrically, and geometrically and materially nonlinear problems, and dynamic analysis of general nonlinear shell structures.

Upon the completion of finite element modeling of general shell structures, in Chapter 8 the finite element representations are used in conjunction with the SCD method, TCT and ATS to determine response statistics of shell structures with geometrical and material nonlinearities subjected random excitations. An extension of the SCD formulation of Chapter 2 to Gaussian stationary and nonstationary random

excitations treated as a combination of deterministic and stochastic components of excitations is also presented together with a brief review of the TCT and ATS.

Finally, Chapter 9 concludes the thesis and introduces recommendations for further studies.

The thesis will be divided into two volumes. The first volume contains Chapter 1 through Chapter 9. Figures, appendices and references are included in Volume 2.

CHAPTER 2

THE STOCHASTIC CENTRAL DIFFERENCE METHOD

As mentioned in Chapter 1, the stochastic central difference (SCD) method has distinctive features and is used as the tool to determine the random statistics of shell structures with geometric and material nonlinearities. Therefore, in this chapter, it is intended to (a) apply the SCD to structures discretized by finite elements which are usually associated with many degree-of-freedom (DOF) and a wide range of natural frequency; and (b) investigate several adaptive time schemes that can be used in conjunction with the SCD. The studies will not only demonstrate the potential of the SCD, but also establish a theoretical and computational basis for the investigation of Chapter 8.

This chapter consists of four sections. Section 2.1 deals with the application of the SCD to linear systems and introduces the time co-ordinate transformation (TCT) technique. Section 2.2 presents the recursive expressions for time-dependent means and mean squares of responses of a two DOF non-symmetric nonlinear system. In Section 2.3 several adaptive time schemes are proposed to be incorporated into the SCD with TCT. Finally, Section 2.4 is concluding remarks.

2.1 Random Responses of Discretized Beams and Plates by the Stochastic Central Difference Method with Time Co-ordinate Transformation

2.1.1 Introduction

In the computation of responses of complex structures under stationary and non-stationary random excitations, many techniques have been proposed. Among them the stochastic central difference (SCD) method is particularly appealing [2.1-3]. Its main advantages include: low computational cost, excellent accuracy, no normal mode analysis, no restriction on the type of damping, and being capable of handling geometrical and material non-linearities. The SCD method has originally been developed for application in the finite element analysis of complex structures and to-date no demonstration of such application has been reported in the literature. The focus of this section is, therefore, to present the methodology of applying the SCD method to structures idealized by the finite element method, which are usually concerned with large sizes of system matrices and a wide range of natural frequencies. The methodology developed here will be later (see Chapter 8) used to calculate random responses of complex structures with large geometrical and material nonlinearities under intensive transient forces modelled as stationary and non-stationary random excitations.

The organization of the section is as follows. Sub-section 2.1.2 briefly outlines the SCD method. Sub-section 2.1.3 considers the time co-ordinate transformation for the SCD method so that large size finite element representations of structural systems can be solved. Two cases concerning discretized linear beam and plate structures are considered,

and their computed results are presented in Sub-section 2.1.4. Sub-section 2.1.5 includes discussion on the determination of time step size of the SCD method for application to structures discretized by the finite element method. The final section, Sub-section 2.1.6 contains concluding remarks.

2.1.2 Brief outline of the SCD method

The formulation of SCD has been clearly presented in [2.1-2] and is outlined in the following for completeness. Consider a multi-degree-of-freedom (MDOF) system with the following matrix governing equation of motion

$$M\ddot{X} + C\dot{X} + KX = r(t) = \bar{e}(t)w(t) \tag{2.1}$$

where M , C and K are the assembled mass, damping and stiffness matrices, respectively; $\ddot{X}$, $\dot{X}$ and X are the stochastic acceleration, velocity and displacement vectors; and r(t) is the stochastic excitation vector which is expressed as a product of the time-dependent deterministic vector $\bar{e}(t)$ and the stationary random process w(t). The latter is assumed to be a zero-mean Gaussian white noise process with spectral density S_0.

Equation (2.1) is valid for any given time instant t_s and therefore after applying the central difference method one can easily show that

$$X_{s+1} = (\Delta t)^2 N_1 r_s + N_2 X_s + N_3 X_{s-1} \tag{2.2}$$

where

$$N_1 = \left[M + \frac{1}{2}(\Delta t)\,C\right]^{-1}, \quad N_2 = N_1\left[2M - (\Delta t)^2 K\right],$$

$$N_3 = N_1\left[\frac{1}{2}(\Delta t)\,C - M\right].$$

Equation (2.2) expresses the displacement vector at the next time step in terms of the displacement vectors at the current and last time steps.

After taking the transpose of X_{s+1} , multiplying X_{s+1} by X^T_{s+1} , taking ensemble averages and re-arranging, one has

$$\begin{aligned} R(s+1) = {} & N_2 R(s) N_2^T + N_3 R(s-1) N_3^T \\ & + (\Delta t)^4 N_1 B(s) N_1^T + N_2 D(s) N_3^T \\ & + N_3 D^T(s) N_2^T \end{aligned} \tag{2.3a}$$

where

$$D(s) = N_2 R(s-1) + N_3 D^T(s-1) .$$

note that since the stationary random process w(t) has been assumed to be of zero mean, the mean squares or cross-correlations of displacements calculated from equation (2.3a) are equal to the variances or covariances of the displacements. That is

$$V(s) = R(s) , \quad \langle X_s \rangle = 0 \tag{2.3b}$$

The cases in which the means of displacements are not zero will be considered in Chapter 8.

Equations (2.3a) and (2.3b) are the recursive expression for the variances and covariances of displacement responses of MDOF systems under random excitations. Note that in equation (2.3a)

$$R(s) = \langle X(t_s)\, X^T(t_s) \rangle \ , \quad D(s) = \langle X(t_s)\, X^T(t_{s-1}) \rangle \ ,$$

$$B(s) = 2\pi S_0\, \bar{e}(t_s)\, \bar{e}^T(t_s)$$

in which the angular brackets denote "ensemble average" of the enclosed quantity.

Similar to its deterministic counterpart, the SCD method is conditionally stable. A parametric study on the SCD algorithm was performed and presented in [2.4], which revealed the dependence of the actually used time step size on the natural frequency of the system. Although the parametric study is about a single-degree-of-freedom (SDOF) system, the conclusions are applicable to MDOF systems. For stiff structures or systems with high-valued natural frequencies, the actual time-step size Δt will be very small and computational instability can therefore occur.

2.1.3 Time co-ordinate transformation

A strategy for dealing with the computational instability and increasing the efficiency of the SCD algorithm has first been suggested by To in reference [2.5]. In this strategy a time co-ordinate transformation is performed on equation (2.1). It is assumed that the stiff system governed by equation (2.1) has its highest natural frequency Ω.

Dividing both sides of equation (2.1) by the square of Ω and transforming the resulting equation of motion from the time co-ordinate t to the dimensionless time co-ordinate τ such that

$$Mx'' + \frac{1}{\Omega}Cx' + \frac{1}{\Omega^2}Kx = \frac{1}{\Omega^2}r(\tau) \tag{2.4}$$

where the prime and double prime designate the first and second derivatives with respect to the dimensionless time τ ; the response vector x and the forcing vector r are functions of τ which is being chosen as

$$\tau = \Omega t \, . \tag{2.5}$$

The variances and covariances of responses for the system described by equation (2.4) can then be evaluated with equation (2.3) in which the assembled mass matrix M is identical to that in equation (2.1), the damping matrix C is equal to the original damping matrix C in equation (2.1) divided by Ω , the stiffness matrix K is equal to the original stiffness matrix K in equation (2.1) divided by Ω^2 , and the excitation vector r is equal to the original forcing vector in equation (2.1) divided by Ω^2 . In other words, if we write the equation in the τ co-ordinate

$$M_\tau \frac{d^2x}{d\tau^2} + C_\tau \frac{dx}{d\tau} + K_\tau x = r_\tau \, , \tag{2.6}$$

then

$$M_\tau = M \ , \ C_\tau = \frac{1}{\Omega} C \ , \ K_\tau = \frac{1}{\Omega^2} K \ , \ r_\tau = \frac{1}{\Omega^2} r \ ,$$

where M , C , K , and r are defined in the original equation, equation (2.1), so that equation (2.3) can be applied to evaluate the variances and covariances of responses in τ . In applying equation (2.3) to obtain the variances and covariances of responses in the dimensionless time co-ordinate τ , M , C , K , and r_s in equation (2.3) have to be replaced respectively with M_τ , C_τ , K_τ , and $r_{\tau s}$. Note that $r_{\tau s}$ is r_τ at the dimensionless time step τ_s while Δt in equation (2.3) is now replaced by $\Delta \tau$.

Once the variances and covariances of responses in τ are determined by using equation (2.3) they are converted back to the t co-ordinate. They are related by the following expressions,

$$R_t(s) = \Omega R(s) \ , \quad t = \frac{\tau}{\Omega} \tag{2.7}$$

where the subscript t denotes the t domain solution while R(s) is understood to be in the dimensionless τ domain. Equation (2.7) can be easily verified if one considers the stationary variance of displacement for a SDOF linear system excited by a zero mean Gaussian white noise.

2.1.4 Beam and plate structures under random excitations

In this sub-section discretized beam and plate structures under random excitations are considered. Random responses are evaluated by applying the SCD method in

conjunction with the time co-ordinate transformation strategy outlined in the last sub-section. The results are compared with those obtained by using the exact expressions in [2.6] and associated digital computer program.

(i) *Cantilever Beam Under Base Excitation*

As shown in Figure 2.1 the cantilever beam is discretized by 2-node elements, N-1 of which are of length ℓ_1 and the other 2 at the clamped end are of length ℓ_2. Thus, there are N+1 elements and N+2 nodes. Every node has three DOF, namely, axial displacement u, flexural displacement v and rotation about z-axis θ. The 2-node element is considered as a combination of a 2-node bar element and 2-node beam element [2.7]. It is applied here because of its simplicity and ready availability. The consistent element mass matrix is

$$[m] = \frac{\rho A \ell}{420}\begin{bmatrix} 140 & 0 & 0 & 70 & 0 & 0 \\ 0 & 156 & 22\ell & 0 & 54 & -13\ell \\ 0 & 22\ell & 4\ell^2 & 0 & 13\ell & -3\ell^2 \\ 70 & 0 & 0 & 140 & 0 & 0 \\ 0 & 54 & 13\ell & 0 & 156 & -22\ell \\ 0 & -13\ell & -3\ell^2 & 0 & -22\ell & 4\ell^2 \end{bmatrix} \qquad (2.8)$$

where ρ is the mass density per unit volume, A the cross sectional area, and ℓ the length of the element. The consistent element stiffness matrix can easily be obtained as

$$[k] = \begin{bmatrix} a & 0 & 0 & -a & 0 & 0 \\ 0 & 12b & 6\ell b & 0 & -12b & 6\ell b \\ 0 & 6\ell b & 4\ell^2 b & 0 & -6\ell b & 2\ell^2 b \\ -a & 0 & 0 & a & 0 & 0 \\ 0 & -12b & -6\ell b & 0 & 12b & -6\ell b \\ 0 & 6\ell b & 2\ell^2 b & 0 & -6\ell b & 4\ell^2 b \end{bmatrix} \qquad (2.9)$$

where a and b are defined as

$$a = \frac{EA}{\ell} , \qquad b = \frac{EI}{\ell^3}$$

with E being the Young's modulus and I the moment of inertia of the cross-section of the beam.

The nodal displacement vector accompanying equations (2.8) and (2.9) is

$$\{q\} = [\, u_i , v_i , \theta_i , u_{i+1} , v_{i+1} , \theta_{i+1} \,]^T$$

Based on [m] and [k] the assembled mass and stiffness matrices can be obtained as

$$[M] = \sum_{i=1}^{N+1} [M]_i , \qquad [K] = \sum_{i=1}^{N+1} [K]_i , \qquad (2.10)$$

where the subscript i denotes the element number, $[M]_i$ and $[K]_i$ have the same order as the assembled mass matrix [M] and stiffness matrix [K], respectively. The non-zero elements in the latter matrices are only those in rows and columns that correspond to element degrees of freedom.

For comparison to results obtained by the exact expressions in [2.6], which apply to Rayleigh damping cases only, we define the proportional damping matrix

$$[C] = [M] \sum_{p} \lambda_p [M^{-1}K]^p \tag{2.11}$$

where λ_p are constants to be determined and p = 0, 1, 2, ... The upper limit of the summation is not defined as it varies from one system to another.

The governing matrix equation of motion in terms of the global nodal displacement, velocity, and acceleration vectors is

$$[M]\{\ddot{Q}\} + [C]\{\dot{Q}\} + [K]\{Q\} = \{P\} \tag{2.12}$$

where {P} is the vector of consistent nodal forces due to the external random excitations and {Q} the global nodal displacement vector.

Partitioning {Q} into two parts

$$\begin{aligned} \{Q\} &= \begin{Bmatrix} Y \\ X \end{Bmatrix}, \\ Y &= [\, u_1 \quad v_1 \quad \theta_1 \,], \\ X &= [\, u_2 \quad v_2 \quad \theta_2 \quad \ldots\ldots \quad \theta_{N+2} \,]^T, \end{aligned} \tag{2.13}$$

equation (2.12) can further be written as

$$\begin{bmatrix} M_{YY} & M_{YX} \\ M_{XY} & M_{XX} \end{bmatrix} \begin{Bmatrix} \ddot{Y} \\ \ddot{X} \end{Bmatrix} + \begin{bmatrix} C_{YY} & C_{YX} \\ C_{XY} & C_{XX} \end{bmatrix} \begin{Bmatrix} \dot{Y} \\ \dot{X} \end{Bmatrix} + \begin{bmatrix} K_{YY} & K_{YX} \\ K_{XY} & K_{XX} \end{bmatrix} \begin{Bmatrix} Y \\ X \end{Bmatrix} = \begin{Bmatrix} F_Y \\ 0 \end{Bmatrix} \tag{2.14}$$

Considering the second equation of (2.14), one has

$$[M_{XX}]\{\ddot{X}\} + [C_{XX}]\{\dot{X}\} + [K_{XX}]\{X\} = \{F_X\} \tag{2.15}$$

where

$$\{F_X\} = -[M_{XY}]\{\ddot{Y}\} - [C_{XY}]\{\dot{Y}\} - [K_{XY}]\{Y\} \approx -[K_{XY}]\{Y\}$$

since the elements of [K_{XY}] are generally several orders of magnitude greater than those of [M_{XY}] and [C_{XY}]. Equation (2.15) is now the governing matrix equation of motion for the cantilever beam with transversal base displacement.

To define the elements of the excitation vector on the right hand side (RHS) of equation (2.15) one can start with the transversal base displacement

$$\{Y\} = \begin{Bmatrix} 0 \\ \hat{Y}(t) \\ 0 \end{Bmatrix} = \begin{Bmatrix} 0 \\ -e(t)\,w(t) \\ 0 \end{Bmatrix}$$

where e(t) in this example is a scalar deterministic modulating function which is defined as

$$e(t) = E_r(e^{-\alpha_1 t} - e^{-\alpha_2 t}) \tag{2.16}$$

in which α_1 and α_2 are positive constants satisfying $\alpha_1 < \alpha_2$, and E_r is a constant used to normalize e(t) such that *max* {e(t)} = 1.0 .

One then arrives at the following excitation vector for equation (2.15)

$$\{F_X\} = e(t)[K_{42}, K_{52}, K_{62}, 0, \ldots\ldots, 0]^T w(t)$$

where K_{ij} denotes the ij-th element of matrix [K] and $K_{42} = 0$.

With the definition of [C] in equation (2.11) the following algebraic equations can be written to determine constants λ_p

$$2\zeta_i \omega_i = \sum_p \lambda_p \omega_i^{2p} \tag{2.17}$$

or in matrix notation

$$[\lambda_0 \ \lambda_1 \ \lambda_2 \ \ldots]^T$$
$$= 2\Xi^{-1}[\zeta_1 \ \zeta_2 \ \zeta_3 \ \ldots]^T$$

where Ξ is a square matrix with components $\Xi_{ij} = \omega_i^{2j-3}$, ω_i and ζ_i are the i-th natural frequency and modal damping ratio, respectively. As many equations of (2.17) must be included as there are specified modal damping ratios.

This line of forming [C] seems to be straightforward. However, with more modes included equation (2.17) yields a damping matrix that is not diagonal after normal mode transformation. The consequence of this is that computational difficulty is likely to occur.

Another way to construct [C] based on specified modal damping ratios is to apply the following formula [2.8]

$$[C] = [M]\left(\sum_i 2\zeta_i \omega_i [{}_i\phi][{}_i\phi]^T\right)[M] \tag{2.18}$$

where ${}_i\phi$ is the i-th mode shape vector which is orthonormal relative to [M] and the summation may be performed over several modes the modal damping ratios of which are specified. Those unspecified modes are in fact undamped modes. The undamped modes may manifest in the solution to the extent that they may introduce computational difficulty. Another drawback of the damping matrix defined by equation (2.18) is that mode shapes have to be evaluated beforehand, which may be time-consuming when the size of the matrices is large and many modes are included. One of the main purposes of applying direct integration algorithms for the solution of the governing equation of motion is to eliminate the normal mode analysis. Therefore, application of equation (2.18) would destroy this purpose.

Warburton [2.9] gave an example in which the Rayleigh damping matrix was constructed from two damping ratios. This is the case defined in equation (2.17) when $p = 0, 1$. Of course, this definition of proportional damping has its simplicity and the damping ratios associated with the higher modes are functions of the first two damping ratios. It has the advantage of simplicity and the assurance of accurate response computation for systems under deterministic excitations For the beam structure investigated in this sub-section, $p = 0, 1$ are adopted to construct [C]. The results obtained by the SCD method with the time co-ordinate transformation described in Sub-section 2.1.3 above, to be simply referred to as the SCD method henceforth, are compared with those evaluated by the digital computer program based on the exact expressions of [2.6]. For convenience of reference, the latter computer program is

designated as EQ75. It may be appropriate to note that the computer program applies to any number of modes.

In the present investigation, the beam structure has the following properties: ρ = 7860.0 kg/m^3 , E = 2.07 $\times$ 10^{11} N/m^2 , A = 6.25 $\times$ 10^{-4} m^2 , I = 3.26 $\times$ 10^{-8} m^4 , and L = 1 m . Four finite element representations are considered for the cantilevered beam structure. Data required in the four representations are presented in Table 2.1. Table 2.2 includes natural frequencies obtained for the computation.

The modulating function e(t) is chosen as

$$e(t) = 9.4815\,(e^{-45t} - e^{-60t})$$

such that at t = t_p = 0.15 second the excitation can be considered insignificantly small, $e(t_p)$ = 0.01 , where t_p is the duration of the non-stationary random excitation. Note that the fundamental period ($T_1 = 2\pi / \omega_1$) equals 0.04819 second and therefore the duration of excitation chosen above is slightly more than 3 times the fundamental period. The first two modal damping ratios are: $\zeta_1 = \zeta_2 = 0.05$. Additional data required for the computation are included in Tables 2.3 through 2.6, while Table 2.7 contains computed typical maximum variances. The time step sizes, execution times for the SCD program, and discrepancies between variances of displacements and rotations at the free end of the beam structure are presented in Table 2.8. Of course, the computer program based on the SCD method provides all the variances and covariances of the covariance matrix. This is why the execution time increases rapidly as the number of effective DOF of the system is increased. For brevity, only the variances of displacement and rotation at the free end

of the beam structure are presented in Figures 2.2 through 2.11 while the execution times are summarized in Table 2.8. Note that Figures 2.2 and 2.3 are for the 2 element model with no damping considered.

Table 2.1 Finite element discretizations (beam)

Number of elements	ℓ_1	ℓ_2	Total DOF	Effective DOF
2	-	0.5	9	6
11	0.1	0.05	36	33
15	0.07	0.045	48	45
21	0.05	0.025	66	63

Table 2.2 Natural frequencies in rad/sec (beam)

DOF	6	33	45	63
ω_1	130.3777	130.3138	130.3147	130.3147
ω_2	823.5985	816.6954	816.6749	816.6701
ω_3	2785.5606	2287.2760	2286.8373	2286.7325
ω_4	8084.8891	4485.2487	4482.0623	4481.2894
ω_5	8269.5425	7425.7774	7412.0839	7408.6839
These natural frequencies are not required in the analysis.				
Ω	28888.7357	404056.5917	543912.8794	1616226.3648

Table 2.3 Modal damping ratios (beam)

DOF	6	33	45	63
ζ_1	0.05	0.05	0.05	0.05
ζ_2	0.05	0.05	0.05	0.05
ζ_3	0.1413	0.1231	0.1231	0.1232
ζ_4	0.4049	0.2381	0.2379	0.2379
ζ_5	0.4142	0.3928	0.3921	0.3919

Table 2.4 λ_m and λ_k for the Rayleigh damping matrix (beam)

DOF	6	33	45	63
λ_m	11.3379	11.3333	11.2382	11.2382
λ_k	0.0001			

Table 2.5 Data for computation of variances by EQ75 (beam)

DOF	K_{52}	K_{62}
6	-0.64783×10^{6}	0.16196×10^{6}
33	-0.64783×10^{9}	0.16196×10^{8}
45	-0.88865×10^{9}	0.19995×10^{8}
63	-0.51826×10^{10}	0.64783×10^{8}

Table 2.6 Data for computation of variances by EQ75 (beam)

2 element discretization				
j	2	3	5	6
$_1\Phi_j$	-0.3067	-0.1051×10	-0.9032	-0.1243×10
$_2\Phi_j$	-0.6578	0.3959	0.9112	0.4387×10
$_3\Phi_j$	0.1031	-0.7750×10	0.1014×10	0.9774×10
$_4\Phi_j$	0.4309	0.8857×10	0.1702×10	0.3390×10^{2}
$_5\Phi_j$	-0.7823×10^{-16}	-0.1850×10^{-14}	-0.4154×10^{-15}	-0.2144×10^{-14}

Table 2.6 Data for computation of variances by EQ75 (beam)
(continued from 2 element discretization)

11 element discretization				
j	2	3	32	33
$_1\phi_j$	-0.3875×10^{-2}	-0.1532	-0.9024	-0.1242×10
$_2\phi_j$	-0.2288×10^{-1}	-0.8754	0.9024	0.4314×10
$_3\phi_j$	-0.6052×10^{-1}	-0.2239×10	-0.9028	-0.7086×10
$_4\phi_j$	-0.11163	-0.3967×10	0.9040	0.9942×10
$_5\phi_j$	-0.17338	-0.5877×10	-0.9066	-0.1282×10
15 element discretization				
j	2	3	44	45
$_1\phi_j$	-0.3146×10^{-2}	0.1384	0.9024	0.1242×10
$_2\phi_j$	-0.1869×10^{-1}	-0.7985	0.9024	0.4314×10
$_3\phi_j$	0.4974×10^{-1}	0.2063×10	0.9025	0.7083×10
$_4\phi_j$	-0.9230×10^{-1}	-0.3699×10	0.9028	0.9927×10
$_5\phi_j$	0.1441	0.5551×10	0.9035	0.1277×10^{2}
21 element discretization				
j	2	3	62	63
$_1\phi_j$	0.9801×10^{-3}	0.7795×10^{-1}	0.9024	0.1242×10
$_2\phi_j$	0.5966×10^{-2}	0.4674	-0.9024	-0.4314×10
$_3\phi_j$	0.1626×10^{-1}	0.1255×10	0.9024	0.7083×10
$_4\phi_j$	-0.3097×10^{-1}	-0.2353×10	0.9025	0.9924×10
$_5\phi_j$	-0.4974×10^{-1}	-0.3714×10	-0.9027	-0.1276×10^{2}

Table 2.7 Maximum variances by EQ75 (beam)

Only the first 3 modes were considered		
DOF	maximum variance of tip displacement ($\times S_0$)	maximum variance of tip rotation ($\times S_0$)
6	0.11015×10^{5} @ 0.031	0.26096×10^{6} @ 0.028
33	0.23545×10^{5} @ 0.028	0.74965×10^{6} @ 0.024
45	0.23521×10^{5} @ 0.028	0.74922×10^{6} @ 0.024
63	0.23548×10^{5} @ 0.028	0.75038×10^{6} @ 0.024
Only the first 5 modes were considered		
DOF	maximum variance of tip displacement ($\times S_0$)	maximum variance of tip rotation ($\times S_0$)
6	0.11003×10^{5} @ 0.031	0.26187×10^{6} @ 0.028
33	0.24873×10^{5} @ 0.028	0.10395×10^{7} @ 0.024
45	0.24844×10^{5} @ 0.028	0.10375×10^{7} @ 0.024
63	0.24883×10^{5} @ 0.028	0.10414×10^{7} @ 0.024

It can be observed that the results obtained by the SCD method and EQ75 by including the first three modes and first five modes of vibration are in excellent agreement. The agreement for the two element model in which no damping was considered and presented in Figures 2.2 and 2.3 is also excellent except for the case when only the first three modes were included in applying EQ75. The explanation is that for the undamped case higher modes have to be included in EQ75 since the influence of every mode on the response is important. This is in contrast to the cases in which higher modes are attenuated by the present of damping.

In addition to the comparison with the exact expressions of [2.6], the SCD results are also compared with those from Monte Carlo simulation. Some representative results are shown in Figures 2.12 and 2.13 for the 2 element model. Again excellent agreement is observed.

Before leaving this example it may be appropriate to note that since the above results are based on linear random vibration theory, the following condition should be satisfied:

$$\max\{<X_L^2(t)>\} \leq \left(\frac{5L}{100}\right)^2$$

where $<X^2_L>$ is the variance of tip displacement. That is,

$$0.25 \times 10^5 S_0 \leq 0.05^2$$

or

$$S_0 \leq 0.9804 \times 10^{-7}\ m^2/rad\ .$$

Table 2.8 Time step sizes and execution times by SCD method (beam)

DOF	time step size $\Delta\tau$	execution time (in hours)	error in % with respect to EQ75 result	
			tip displacement	tip rotation
6	0.95	0.15*	4.02	2.22
33	1.00	11.5*	2.43	-6.67
45	1.00	50.0*	2.62	-6.51
63	1.00	89.5**	2.57	-7.12

* Denotes computation by SUN4.0 workstation
** Denotes computation by Silicon Graphics workstation

(ii) *Square Plate with Random Excitation Concentrated at Nodes*

A square plate with geometrical dimensions $1.0 \times 1.0 \times 0.005$ m^3 and material properties $E = 2 \times 10^{11}$ N/m^2, $\rho = 7830$ kg/m^3 and Poisson's ratio $\nu = 0.3$ is considered. The plate is discretized by triangular bending elements th. ormulation of which is reported in [2.10]. The two finite element idealizations considered are summarized in Table 2.9 and Figures 2.14 and 2.15 while the natural frequencies required in the computation of the responses are listed in Table 2.10 together with their corresponding modal damping ratios.

The governing equation of motion for the plate structure can be expressed as equation (2.1) in which [C] is formed according to equation (2.18). The excitation for each case is a nodal force acting in the transversal direction. The nodal force is modeled as a product of modulating function e(t) and the Gaussian white noise w(t) the spectral intensity S_0 of which is unity (that is, $S_0 = 1.0$). The modulating function e(t) considered in this example is

$$e(t) = 9.4815\,(e^{-45t} - e^{-60t})$$

As pointed out earlier, application of equation (2.18) for the construction of [C] would destroy the purpose of applying the SCD method. However, for comparison to results available in [2.10], which were evaluated by EQ75 with the first five damping ratios, ζ_1 through ζ_5, being set equal to 0.05, equation (2.18) is employed here. Of course, the damping matrix so constructed have little, if any, reflection of the physical damping in the discretized plate structure. This, indeed, indicates the difficulty of defining

the damping matrix in the finite element analysis of structural and MDOF mechanical systems. In structural systems the meaning of modai damping ratio is difficult to clarify and has been an area of investigation by Ma [2.11].

Additional data for the computation are given in Table 2.11. In the latter w_j is the j-th nodal displacement. Typical results of maximum variances are included in Table 2.12. In the SCD method the time step sizes employed in the computation are included in Table 2.13. For brevity and comparison between results determined by the SCD method and EQ75, representative cases are given in Table 2.13 and Figures 2.16-2.18.

Table 2.9 Finite element representations (plate)

elements	boundary condition	total DOF	effective DOF
8	CF3*	54	27
32	C4**	150	66

* Designates cantilever plate
** Designates all 4 sides are clamped

Table 2.10 Natural frequencies and damping ratios (plate)

mode number i	CF3, 27 DOF		C4, 66 DOF	
	ω_i (rad/sec)	ζ_i	ω_i (rad/sec)	ζ_i
1	26.7193	0.05	275.2883	0.05
2	67.5943		562.0487	
3	164.0702		562.9375	
4	213.2028		833.8993	
5	244.4920		1011.3255	
6	425.9661		1018.6845	
7	These data are not required for computation		1277.8441	
8			1290.5347	
These data are not required for computation				
Ω	4959.0863		21641.7317	

Table 2.11 Data for calculation of variances by EQ75 (plate)

model	CF3 plate		C4 plate
w_j	w_8	w_5	w_{13}
${}_1\Phi_j$	0.3230	0.1100	-0.3935
${}_2\Phi_j$	0.1590×10^{-2}	0.2120×10^{-2}	0.1496×10^{-13}
${}_3\Phi_j$	0.3844	-0.1718	0.1705×10^{-13}
${}_4\Phi_j$	-0.2533	-0.2326	-0.2281×10^{-2}
${}_5\Phi_j$	0.7412×10^{-2}	0.1059×10^{-1}	0.1204×10^{-12}
${}_6\Phi_j$	0.4643	-0.2652	0.4873
${}_7\Phi_j$	These data are not required for computation		-0.4910×10^{-14}
${}_8\Phi_j$			0.9097×10^{-14}

Table 2.12 Maximum variances by EQ75 (plate)

plate	modes considered	excitation, applied at node	maximum variance of displacement
CF3	6	8, transversal	0.32592×10^{-6}, for w_5
			0.24617×10^{-5}, for w_8
C4	8	13, transversal	0.18708×10^{-7}, for w_{13}

Table 2.13 Time step sizes and results by SCD (plate)

plate	time step size $\Delta\tau$	execution time (in hours*)	error in % with respect to EQ75
CF3	0.96	0.2	-4.27 for w_5
			-3.82 for w_8
C4	0.94	13.5	-3.15 for w_{13}

* Denotes computation by SUN 4.0 workstation

2.1.5 Determination of time step size for the SCD method

The objective in this sub-section is to investigate the relation between time step size and natural frequencies of a MDOF system, so that the actual time step size can be predicted before performing the SCD scheme. Note that for MDOF systems the time co-ordinate transformation described in Sub-section 2.1.3 leads to that the highest natural frequency for every system equals to unity. Applying the procedure in [2.4], which considered SDOF linear and nonlinear systems under zero-mean Gaussian white noise excitations, time step sizes for SDOF linear oscillators with natural frequencies less than unity are evaluated and presented in Table 2.14. It is interesting to observe that the time step size approaches 1.0 as the natural frequency tends to zero.

Table 2.14 Influence of natural frequency on time step size

ω (rad/sec)	time step size	ω (rad/sec)	time step size
0.1	0.9975	0.6	0.9232
0.2	0.9902	0.7	0.9006
0.3	0.9785	0.8	0.8770
0.4	0.9630	0.9	0.8525
0.5	0.9443	1.0	0.8300

On the other hand, the time step sizes for the discretized beam and plate structures investigated in the last section and summarized in Table 2.15 suggest that:

(1) the actual time step sizes fall between $\Delta\tau_1$ and $\Delta\tau_m$ (where $\Delta\tau_1$ is the time step size associated with the lowest natural frequency and $\Delta\tau_m$ the time step size associated with the highest natural frequency);

(2) the actual time step size is reduced as the lowest natural frequency is increased; and

(3) the actual time step sizes can be expressed as a function of log (ω_1), see Figure 2.19.

With reference to the results in Tables 2.14 and 2.15, and Table 1 of [2.4], and making use of the following two pairs of data: (ω_1 = 0.0127, $\Delta\tau$ = 0.945) and (ω_1 = 0.806×10^{-4}, $\Delta\tau$ = 0.995) one can deduce a relation between the actual time step size

in the dimensionless time co-ordinate τ and the lowest dimensionless natural frequency ω_1, for discretized structures whose dimensionless highest natural frequency is unity, as

$$\Delta\tau = 0.9 - 0.023 \log(\omega_1) \tag{2.19}$$

equation (2.19) is valid for structures idealized by the finite element method as MDOF systems and whose physical time co-ordinate is transformed into dimensionless time co-ordinate in accordance with equation (2.5).

Table 2.15 Time step sizes of the finite element systems*

system description	actual $\Delta\tau$	lowest mode		highest mode	
		ω_1	$\Delta\tau_1$	ω_{max}	$\Delta\tau_m$
C4 plate	0.94	0.127×10^{-1}	1.0	1.0	0.83
CF3 plate	0.96	0.539×10^{-2}			
6 DOF beam	0.95	0.451×10^{-2}			
33 DOF beam	1.00	0.323×10^{-3}			
45 DOF beam	1.00	0.240×10^{-3}			
63 DOF beam	1.00	0.806×10^{-4}			

* All natural frequencies are with respect to the τ domain; $\Delta\tau_1$ and $\Delta\tau_m$ are the time step sizes corresponding to ω_1 and ω_{max}, respectively.

2.1.6 Concluding remarks

In this sub-section the SCD method in conjunction with the TCT is proposed as an effective method for the determination of variances and covariances of responses of structures idealized by the FEM. Two structural systems, a cantilever beam under a non-stationary random base excitation, and a square plate subjected to a concentrated non-stationary random transversal excitation, have been studied. These two relatively very stiff systems are chosen to demonstrate the usefulness and capability of the proposed method, which eliminates the computational instability problem associated with the small time step size required by the stability criterion. Results obtained show that the accuracy and effectiveness of the proposed method are excellent. A formula, equation (2.19) has also been obtained which can be applied to predict the time step size in the dimensionless τ co-ordinate based upon the lowest dimensionless natural frequency of the transformed system. Issues concerning the construction of the damping matrix [C] have also been discussed.

The dynamic systems studied in this section are confined to linear ones. However, the proposed method can be easily extended to include nonlinearities, provided that the time-dependent system matrices, such as [K], [C] and [M], are updated and the time step size $\Delta\tau$ is determined by equation (2.19) at every time step. This will be demonstrated in Section 2.3 which studies the Duffing's oscillator and a 2 DOF non-symmetric nonlinear system using several adaptive time step schemes. The latter is associated with explicit nonlinearities and therefore the stochastic linearization (SL) technique can be applied. This will be dealt with in the coming section, Section 2.2.

2.2 Recursive Expressions for Time Dependent Means and Mean Squares of Responses of a Multi-Degree-of-Freedom Nonlinear System

2.2.1 Introduction

The stochastic central difference (SCD) method, when used for the computation of the responses of complex structures with geometric and material nonlinearities subjected to stationary and non-stationary random excitations, is able to deal with systems incorporating nonlinearities which are defined explicitly and implicitly. The latter cases will be discussed in Chapter 8. On the other hand, reference [2.3] demonstrated, with results for a Duffing's oscillator having hardening behaviour under non-stationary random excitation, that the SCD in conjunction with the statistical linearization (SL) technique, simply referred to as the SCD-SL technique, can be applied to single-degree-of-freedom (SDOF) nonlinear systems whose nonlinearities are explicitly defined. As another demonstration of the application of the SCD-SL technique and an attempt to further examine the usefulness of the technique for multi-degree-of-freedom (MDOF) nonlinear systems with explicit nonlinearities, in this section we present recursive expressions for time-dependent or non-stationary means and time-dependent or non-stationary mean squares (henceforth, will be referred to as means and mean squares for simplicity) of responses of a MDOF system under stationary and non-stationary random excitations. The system includes non-symmetric nonlinear stiffness terms and exhibits non-zero time-dependent means even when the excitation is Gaussian white noise with zero mean. Thus, steps have to be taken in the derivation of various recursive schemes by applying the

SCD-SL technique. The accuracy and effectiveness of the derived recursive schemes will be studied and discussed accordingly.

In the following sub-section the recursive expressions for the non-symmetric nonlinear two degree-of-freedom (2DOF) system, previously studied by Kimura and Sakata [2.12], will be presented. Computed results and discussions are included in Sub-section 2.2.3. The final sub-section is concerned with concluding remarks.

2.2.2 Recursive expressions

(i) *Equation of motion*

Consider the 2DOF system shown in Figure 2.20. The system is subjected to non-stationary excitation at its base and the restoring force of the spring connecting the two masses M_1 and M_2 has quadratic and cubic nonlinearity terms associated with, respectively, parameters η' and ϵ'. This 2DOF system under a modulated white noise excitation was considered in reference [2.12] by Kimura and Sakata. However, no verification of the results for this 2DOF system was presented by them. Practical examples that can be modeled by the system in Figure 2.20 are soil-structure coupled system and a primary building structure with secondary system representing installed equipment under an earthquake excitation.

Applying relative displacements $X_1 = x_1 - x_0$ and $X_2 = x_2 - x_1$, where x_0, x_1 and x_2 are, respectively, the absolute displacements at the base, M_1 and M_2 (the relative displacements are called inter-storey drifts in the field of earthquake engineering), the matrix equation of motion can be expressed as

$$\begin{bmatrix}1 & 0\\ 0 & 1\end{bmatrix}\begin{Bmatrix}\ddot{X}_1\\ \ddot{X}_2\end{Bmatrix} + \begin{bmatrix}2\zeta_1 W & -2\mu\zeta_2\\ -2\zeta_1 W & 2(1+\mu)\zeta_2\end{bmatrix}\begin{Bmatrix}\dot{X}_1\\ \dot{X}_2\end{Bmatrix}$$

$$+ \begin{bmatrix}W^2 & -\mu\\ -W^2 & 1+\mu\end{bmatrix}\begin{Bmatrix}X_1\\ X_2\end{Bmatrix} \qquad (2.20)$$

$$+ \begin{Bmatrix}\mu\eta X_2^2 - \mu\epsilon X_2^3\\ (1-\mu)\eta X_2^2 + (1+\mu)\epsilon X_2^3\end{Bmatrix}$$

$$= \begin{Bmatrix}-\ddot{x}_0\\ 0\end{Bmatrix} = \begin{Bmatrix}e(\tau)w(\tau)\\ 0\end{Bmatrix}$$

or in a more compact form

$$M\,\ddot{X} + C\,\dot{X} + K_0\,X + g(X) = r(\tau) \qquad (2.21)$$

where

$$M = \begin{bmatrix}1 & 0\\ 0 & 1\end{bmatrix},\quad C = \begin{bmatrix}2\zeta_1 W & -2\mu\zeta_2\\ -2\zeta_1 W & 2(1+\mu)\zeta_2\end{bmatrix},$$

$$K_0 = \begin{bmatrix}W^2 & -\mu\\ -W^2 & 1+\mu\end{bmatrix},\quad g(X) = \begin{Bmatrix}\mu\eta X_2^2 - \mu\epsilon X_2^3\\ (1-\mu)\eta X_2^2 + (1+\mu)\epsilon X_2^3\end{Bmatrix},$$

$$X = \begin{Bmatrix}X_1\\ X_2\end{Bmatrix},\quad r(\tau) = \begin{Bmatrix}e(\tau)w(\tau)\\ 0\end{Bmatrix},$$

the over-dot and double over-dot denote, respectively, the first and second derivatives with respect to τ. In equation (2.20) the non-stationary random excitation is represented as a product of a deterministic amplitude modulating function $e(\tau)$ and a zero mean

Gaussian white noise process $w(\tau)$ whose spectral density is S_0. Note that the following definitions have been applied in equations (2.20) and (2.21)

$$\begin{aligned} \omega_1^2 &= K_1/M_1 , \quad \omega_2^2 = K_2/M_2 , \\ 2\zeta_1\omega_1 &= C_1/M_1 , \quad 2\zeta_2\omega_2 = C_2/M_2 , \\ \eta &= \eta'/M_2\omega_2^2 , \quad \varepsilon = \varepsilon'/M_2\omega_2^2 , \\ \mu &= M_2/M_1 , \quad W = \omega_1/\omega_2 , \quad \tau = \omega_2 t . \end{aligned} \tag{2.22}$$

such that eqqationns (2.20) and (2.21) are dimensionless. For easy reference we employ in equation (2.22) the notations identical to those in [2.12]. Therefore, the τ in this section should not be confused with the τ used for time co-ordinate transformation in the previous and coming sections.

The discretization of equation (2.21) in the τ domain leads to

$$M \ddot{X}_s + C \dot{X}_s + K_0 X_s + g(X_s) = r_s \tag{2.23}$$

where the subscript s is a positive integer denoting the time step τ_s such that $\Delta\tau = \tau_{s+1} - \tau_s$ and $\tau_0 = 0$.

(ii) *Recursive expressions by the SCD-SL technique*

For the above system four recursive algorithms or schemes have been derived by applying the SCD-SL technique. As pointed out in Sub-section 2.2.1, this system has non-zero time dependent means even when the excitation is a Gaussian white noise with zero mean. Therefore, steps have to be taken in the derivation of various recursive schemes.

One assumption common to all schemes is that the responses at every time step are Gaussian. For brevity, the lengthy derivation is not included here. Instead, the recursive schemes will be briefly outlined and presented in what follows.

SCHEME I

In this scheme the nonlinear system defined by equation (2.23) is approximated by a linearized equation

$$M \ddot{X}_s + C \dot{X}_s + K_{el} X_s = r_s + a_e(s) \qquad s = 1, 2, \ldots, m \tag{2.24}$$

in which K_{el} is the equivalent stiffness matrix and $a_e(s)$ is an equivalent forcing vector at time step s to account for the effect of quadratic nonlinearity while m is the total number of time steps for the duration of the non-stationary random excitation. If matrices K_{el} and $a_e(s)$ or simply a_e are independent of time τ, equation (2.24) is a time-invariant system. In the analysis of non-stationary random responses an equivalent linear system whose coefficient matrices are functions of time τ is expected to provide more accurate approximate solutions of the nonlinear system. Consequently, in this first scheme we are interested in obtaining the time dependent coefficient matrices (Strictly speaking, the coefficient matrices are dependent of the time step $\Delta\tau$ which is assumed to be constant.). To this end, K_{el} and a_e are determined through minimizing the mean square error $\langle E(s)E(s)^T \rangle$, in which the angular brackets designate the ensemble averaging or

mathematical expectation of the enclosing quantity whereas the superscript T denotes the "transpose of". Note that the SL technique is applied at time step τ_s. That is,

$$\frac{\partial \langle E(s)\, E(s)^T \rangle}{\partial K_{el_{ij}}} = 0$$

$$\frac{\partial \langle E(s)\, E(s)^T \rangle}{\partial a_{e_i}} = 0 \qquad (2.25)$$

$$i, j = 1, 2$$

in which the error vector E(s) is defined as the difference between equations (2.21) and (2.24) at time step τ_s. Operating equation (2.6) gives the following relations

$$K_{el}(s) = K_0 + \begin{bmatrix} 0 & 2\mu\eta\langle X_2(s)\rangle + 3\mu\varepsilon\langle X_2^2(s)\rangle \\ 0 & 2(1-\mu)\eta\langle X_2(s)\rangle + 3(1+\mu)\varepsilon\langle X_2^2(s)\rangle \end{bmatrix},$$

(2.26)

$$a_e(s) = \begin{Bmatrix} \mu\eta[\, 2\langle X_2(s)\rangle^2 - \langle X_2^2(s)\rangle] - 2\mu\varepsilon\langle X_2(s)\rangle^3 \\ (1-\mu)\eta[\, 2\langle X_2(s)\rangle^2 - \langle X_2^2(s)\rangle\,] + 2(1+\mu)\varepsilon\langle X_2(s)\rangle^3 \end{Bmatrix}.$$

Note that the results in equation (2.26) were also reported in [2.12].

Following the steps presented in Sub-section 2.1.2 the recursive relation for the means and mean squares can be found, respectively, as

$$\bar{\mu}(s+1) = N_2(s)\,\bar{\mu}(s) + N_3\,\bar{\mu}(s-1) + (\Delta\tau)^2 N_1\, a_e(s) \qquad (2.27)$$

and

$$
\begin{aligned}
R(s+1) &= (\Delta\tau)^4 N_1[\,B(s) + A_e(s)]N_1^T \\
&+ N_2(s)\,R(s)\,N_2(s)^T + N_3\,R(s-1)N_3^T \\
&+ N_2(s)\,D(s)\,N_3^T + N_3\,D(s)^T\,N_2(s)^T \\
&+ (\Delta\tau)^2 N_2(s)\,A_m(s)\,N_1^T + (\Delta\tau)^2 N_1\,A_m(s)^T\,N_2(s)^T \\
&+ (\Delta\tau)^2 N_3\,A_{m-1}(s)\,N_1^T + (\Delta\tau)^2 N_1\,A_{m-1}(s)^T\,N_3^T
\end{aligned}
\tag{2.28}
$$

$$
D(s) = N_2(s)\,R(s-1) + N_3\,D(s-1)^T + (\Delta\tau)^2 N_1\,A_m(s-1)^T
$$

where

$$
\bar{\mu}(s) = \langle X_s \rangle = \langle X(s) \rangle = \begin{Bmatrix} \langle X_1(s) \rangle \\ \langle X_2(s) \rangle \end{Bmatrix}
$$

$$
R(s) = \begin{bmatrix} \langle X_1(s)^2 \rangle & \langle X_1(s)\,X_2(s) \rangle \\ \langle X_2(s)\,X_1(s) \rangle & \langle X_2(s)^2 \rangle \end{bmatrix}
$$

$$
D(s) = \begin{bmatrix} \langle X_1(s)\,X_1(s-1) \rangle & \langle X_1(s)\,X_2(s-1) \rangle \\ \langle X_2(s)\,X_1(s-1) \rangle & \langle X_2(s)\,X_2(s-1) \rangle \end{bmatrix}
$$

$$
B(s) = \langle r_s\,r_s^T \rangle = \langle r(s)\,r(s)^T \rangle = 2\pi S_0 \begin{bmatrix} e(s)^2 & 0 \\ 0 & 0 \end{bmatrix}
\tag{2.29}
$$

$$
N_1 = [\,M + 0.5(\Delta\tau)C\,]^{-1}
$$

$$
N_2(s) = N_1[\,2M - (\Delta\tau)^2 K_{el}(s)\,]
$$

$$
N_3 = N_1[\,0.5(\Delta\tau)C - M\,]
$$

$$
A_e(s) = a_e(s)\;a_e(s)^T
$$

$$
A_m(s) = \bar{\mu}(s)\,a_e(s)^T
$$

$$
A_{m-1}(s) = \bar{\mu}(s-1)\,a_e(s)^T
$$

The starting conditions for equations (2.27) and (2.28) are

$$\bar{\mu}(0) = \bar{\mu}(1) = \begin{Bmatrix} 0 \\ 0 \end{Bmatrix},$$

$$R(0) = R(1) = \begin{bmatrix} 0 & 0 \\ 0 & 0 \end{bmatrix}, \tag{2.30}$$

$$D(0) = \begin{bmatrix} 0 & 0 \\ 0 & 0 \end{bmatrix}.$$

SCHEME II and III

The system described by equation (2.23) is represented by the following linearized equation

$$M \ddot{X}_s + C \dot{X}_s + K_{eII} X_s = f_s \tag{2.31}$$

where there is no equivalent forcing term and the effect of the quadratic nonlinearity has been incorporated into the equivalent stiffness matrix K_{eII} , which can be shown to be

$$\begin{aligned} K_{eII}(s) &= K_{eI}(s) + K^a{}_{eII}(s) \\ K^a{}_{eII}(s) &= K_0^a(s)\, K_1^a(s)\, a_e(s)^T \end{aligned} \tag{2.32}$$

where

$$K_0^a(s) = \frac{1}{\langle X_1(s)^2 \rangle \langle X_2(s)^2 \rangle - \langle X_1(s)\, X_2(s) \rangle^2},$$

$$K_1^a(s) = \begin{Bmatrix} \langle X_1(s) \rangle \langle X_2(s)^2 \rangle - \langle X_2(s) \rangle \langle X_1(s)\, X_2(s) \rangle \\ \langle X_2(s) \rangle \langle X_1(s)^2 \rangle - \langle X_1(s) \rangle \langle X_1(s)\, X_2(s) \rangle \end{Bmatrix},$$

and the matrices K_{eI} and a_e have been defined by equation (2.26) in Scheme I. Again, following the steps in Sub-section 2.1.2 one can obtain the recursive expression for the mean squares as

$$\begin{aligned} R(s+1) &= (\Delta\tau)^4 N_1 B(s) N_1^T \\ &\quad + N_2(s) R(s) N_2(s)^T + N_3 R(s-1) N_3^T \\ &\quad + N_2(s) D(s) N_3^T + N_3 D(s)^T N_2(s)^T , \\ D(s) &= N_2(s) R(s-1) + N_3 D(s-1)^T , \end{aligned} \tag{2.33}$$

where the symbols are defined in equation (2.29). Note that K_{eI} in $N_2(s)$ is now replaced by K_{eII} .

The starting conditions for equation (2.33) are given by equation (2.29). For the recursive relation of the mean responses two different approaches can be considered. These two approaches give rise to two distinct schemes. We shall consider these two cases in the following and they will be referred to as Scheme II and Scheme III.

Case (i) Scheme II

From Sub-section 2.1.2 one has the recursive relation for the displacement vector as

$$X(s+1) = N_2(s) X(s) + N_3 X(s-1) + (\Delta\tau)^2 N_1 r(s) . \tag{2.34}$$

Taking the ensemble average of equation (2.34) yields

$$\bar{\mu}(s+1) = N_2(s)\,\bar{\mu}(s) + N_3\,\bar{\mu}(s-1) \ . \tag{2.35}$$

Clearly, if the starting conditions in equation (2.30) were applied to equation (2.35) one would obtain zero means. To preserve the non-zero means one requires non-zero starting conditions for equation (2.35). To this end we rearrange equation (2.21) at time step τ_s as

$$M\,\ddot{X}(s) + C\,\dot{X}(s) + K_0\,X(s) = r(s) - g(X(s)) \ , \tag{2.36}$$

substitute for the velocity and acceleration terms the following central difference approximation

$$\begin{aligned} \dot{X}(s) &= \frac{[\,X(s+1) - X(s-1)\,]}{2\,\Delta\tau} \ , \\ \ddot{X}(s) &= \frac{[\,X(s+1) - 2\,X(s) + X(s-1)\,]}{(\Delta\tau)^2} \ , \end{aligned} \tag{2.37}$$

into equation (2.36) to give

$$\begin{aligned} X(s+1) = \bar{N}_2\,X(s) + N_3\,X(s-1) + (\Delta\tau)^2\,N_1\,r(s) \\ - (\Delta\tau)^2\,N_1\,g(X(s)) \ , \end{aligned} \tag{2.38}$$

in which

$$\bar{N}_2 = N_1\,[\,2M - (\Delta\tau)^2 K_0\,] \ . \tag{2.39}$$

Taking the ensemble average of equation (2.38) one obtains

$$\bar{\mu}(s+1) = \bar{N}_2\,\bar{\mu}(s) + N_3\,\bar{\mu}(s-1) - (\Delta\tau)^2 N_1 \langle g(X(s))\rangle ,$$

$$\langle g(X(s))\rangle = \begin{Bmatrix} \mu\eta\langle X_2(s)^2\rangle - \\ \quad \mu\varepsilon[3\langle X_2(s)\rangle\langle X_2(s)^2\rangle - 2\langle X_2(s)\rangle^3] \\ \\ (1-\mu)\eta\langle X_2(s)^2\rangle + \\ \quad (1+\mu)\varepsilon[3\langle X_2(s)\rangle\langle X_2(s)^2\rangle - 2\langle X_2(s)\rangle^3] \end{Bmatrix} . \qquad (2.40)$$

Substituting equation (2.30) into equations (2.33), (2.35) and (2.40) one then has

$$R(2) = (\Delta\tau)^4 N_1 B(1) N_1^T ,$$

$$\bar{\mu}(2) = \begin{Bmatrix} 0 \\ 0 \end{Bmatrix} , \qquad (2.41)$$

$$\bar{\mu}(3) = -(\Delta\tau)^2 \eta \langle X_2(s)^2\rangle N_1 \begin{Bmatrix} \mu \\ 1-\mu \end{Bmatrix} .$$

as soon as the above non-zero means are found, one can go back to equation (2.35). For $s > 3$, equation (2.35) can be applied to obtain the non-zero means. Of course, the recursive mean squares are given by equation (2.33).

Case (ii) Scheme III

In this scheme equation (2.40) is applied to provide the mean responses instead of equation (2.35) while equation (2.33) is employed to give the mean squares. Here the starting conditions are those given by equation (2.30).

SCHEME IV

The linearized matrix equation for the system is similar to that in equation (2.31), that is,

$$M\,\ddot{X}_s + C\,\dot{X}_s + K_{eIV}\,X_s = r_s \tag{2.42}$$

except that in this scheme K_{eIV} is determined by the following equation

$$K_{eIV_{ij}} = (K_{eIV})_{ij} = \left\langle \frac{\partial g_i(X(s))}{\partial X_j(s)} \right\rangle, \qquad i,j = 1,2. \tag{2.43}$$

Operating on equation (2.43) gives

$$K_{eIV} = K_{eI} \tag{2.44}$$

where K_{eI} is given by equation (2.26) whose derivation is based on an approach different from that for equation (2.43). Recall that the assumption common to both approaches is that the responses are Gaussian at every time step.

Thus, the recursive expression for the mean squares in this scheme is similar to that given by equation (2.28) in which the equivalent forcing vector $a_e(s)$ is now zero. The recursive relation for means of Scheme III, that is, equation (2.40), is selected for the present scheme.

(iii) *Remarks*

Firstly, Schemes I through III were obtained strictly following equation (2.25). In their derivations a substantial amount of algebraic manipulation was required. On the other hand, application of equation (2.43) in the derivation of Scheme IV resulted in a very significant reduction of algebraic manipulations.

Secondly, equation (2.32) shows that the equivalent stiffness matrices K_{eII} and K_{eI} (and therefore K_{eIV}) become identical when both the relative displacements, X_1 and X_2, have zero means. This implies that K_{eI} and K_{eIV} alone are not able to account for the quadratic nonlinearity. Therefore, the equivalent forcing vector $a_e(s)$ is introduced to account for the effect of quadratic nonlinearity in Scheme I, while in Scheme IV equation (2.40) is applied for similar reason. Equation (2.40) is based on the assumption that the responses are Gaussian at every time step.

2.2.3 Results and discussions

The objectives of the following numerical study are: (a) to verify the correctness and the accuracy of the proposed schemes in Sub-section 2.2.2; (b) to investigate the effect of nonlinearities on time step size; and (c) to make comparisons among the schemes. In order to accomplish these goals both stationary and non-stationary excitations are considered. For the latter case the amplitude modulating function $e(\tau)$ is

$$e(\tau) = 4(e^{-0.125\tau} - e^{-0.25\tau}) \tag{2.45}$$

and the other parameters chosen are

$$W = \mu = 1.0\ , \quad \zeta_1 = \zeta_2 = 0.1\ , \quad S_0 = 0.0012\ . \tag{2.46}$$

In addition, Monte Carlo simulation (MCS) results based on equation (2.20) are obtained for comparison. The simulated means and mean squares are evaluated by taking an ensemble average of 150 realizations, each of which is represented by 25,600 points. Thus, the total number of points used for determining the simulated results is $150 \times 25{,}600 = 3{,}840{,}000$. The Gaussian white noise realizations are generated numerically by a pseudo-random number subroutine, and the simulated responses are computed by applying the technique in [2.13]. The simulations are performed with a time step size of $\Delta\tau = 2\pi/256$ and a correction factor (that is, β in [2.13]) of 0.136.

Before evaluating and examining the results for stationary and non-stationary random responses, a comparison of the presented schemes in Sub-section 2.2.2 is in order.

(i) *Comparison of various schemes*

To compare the four different schemes in Section 2 two sets of nonlinearity strengths η and ε are considered. The system is subjected to stationary random excitations. That is, the RHS of equation (2.45) is equal to 1. The results are included in Table 2.16. For the means Scheme II yields much smaller results than the simulated data, while for the mean squares Schemes I and IV seem to be more accurate, especially for larger nonlinearities. Recall that Scheme IV requires the least amount of algebraic

manipulations and is therefore the most efficient algorithm. In what follows SCD-SL results are obtained by applying Scheme IV unless otherwise stated.

(ii) *Non-stationary random responses*

The non-stationary mean squares obtained by applying Scheme IV and their corresponding MCS data are presented in Figures 2.21 through 2.26 for various nonlinearity strengths η and ε. The time step sizes are included in Table 2.17. It should be noted that similar results for other nonlinearity strengths can be obtained by the same approach so that the relationship between time step sizes and strengths of nonlinearities may be established.

With reference to Figures 2.21 through 2.26 it can be seen that the SCD-SL results are in good agreement with the simulation data. Note that the SCD-SL computation for each set of η and ε took approximately 1 minute of execution time on a SUN 4.1 workstation compared with 3 hours for the digital simulation data. This means that the SCD-SL technique is approximately 299 times faster than the MCS method. The accuracy and efficiency of the SCD-SL technique are excellent.

Table 2.16 Comparison of the four schemes
(S_0 = 0.0012)

MEANS OF RESPONSES (/√S_0)					
(η,ε) and $\Delta\tau$	SCHEME	$<X_1>$		$<X_2>$	
		SCD-SL	simulation	SCD-SL	simulation
(-0.02, 0.03) 0.945	I	0.0317	0.0393	0.0158	0.0198
	II	$10^{-16\sim17}$		$10^{-16\sim17}$	
	III	0.0319		0.0160	
	IV	0.0319		0.0160	
(-1.0, 1.5) 0.995	I	1.461	1.436	0.657	0.640
	II	$10^{-21\sim22}$		$10^{-21\sim22}$	
	III	1.959		1.101	
	IV	1.919		1.077	
MEAN SQUARES OF RESPONSES (/S_0)					
(η , ε) and $\Delta\tau$	SCHEME	$<X_1^2>$		$<X_2^2>$	
		SCD-SL	simulation	SCD-SL	simulation
(-0.02, 0.03) 0.945	I	58.979	58.971	22.913	22.367
	II	58.977		22.913	
	III	58.980		22.913	
	IV	58.978		22.913	
(-1.0, 1.5) 0.995	I	70.195	69.707	21.089	20.598
	II	65.479		20.443	
	III	72.241		21.257	
	IV	69.791		20.933	

Table 2.17 $\Delta\tau$ for variance computations

S_0	η	ε	$\Delta\tau$
0.0012	0.	0.	0.91
	-0.02	0.03	0.945
	-0.2	0.3	0.95
	-0.6	0.9	0.975
	-1.0	1.5	0.99
	-1.5	2.25	1.1

During the computations it was observed that when the spectral density S_0 was increased to 1.0 numerical instability occurred (except for the linear case where η and ε are both zero). A pausible explanation is as follows. For the nonlinear system under consideration its responses are excitation dependent. Therefore, the same η and ε in equation (2.20) may correspond to different levels of strength of nonlinearities if the system is subjected to excitations of various levels of spectral density. One may use the so-called normalized nonlinearity parameter to measure the strength of nonlinearity. For the present system one may define the normalized nonlinearity parameters as

$$\hat{\eta} = \frac{\sqrt{\langle X_1^2 \rangle_{max}}}{\omega_{n2}} \eta \ , \qquad \hat{\varepsilon} = \frac{\langle X_1^2 \rangle_{max}}{\omega_{n2}} \varepsilon \ , \tag{2.47}$$

where $\langle X_1^2 \rangle_{max}$ is the maximum mean square value of X_1 for the linear system (that is, η and ε are both zero) under a non-stationary random excitation identical to that

applied to the nonlinear system being investigated; and ω_{n2} is the higher natural frequency of the linear system. For the system considered above one can show that

$$\langle X_1^2 \rangle_{max} = 24.7728 S_0 , \quad \omega_{n2} = 1.61804 . \tag{2.48}$$

By making use of equations (2.47) and (2.48), one can obtain the normalized nonlinearities and compare them with those before the normalization. These data are included in Table 2.18. Note that the normalized ε's for $S_0 = 1.0$ are equal to 0.46 and 4.59, which are approximately 835 times larger than those for $S_0 = 0.0012$. Note also that the minus sign in front of the term $\mu\varepsilon X_2^3$ in equation (2.20) indicates that the system has a softening stiffness. Thus, the relatively large excitation strength of $S_0 = 1.0$ and the softening stiffness are highly likely to cause unstable solutions. Under these circumstances numerical overflow is most certain.

Table 2.18 Normalization of η and ε

S_0	η , ε before normalization		η , ε after normalization	
0.0012	-0.02	0.03	-0.0021	0.00055
	-0.2	0.3	0.021	0.0055
1.0	-0.02	0.03	-0.062	0.46
	-0.2	0.3	-0.62	4.59

(iii) *Stationary random responses*

Results for the cases with stationary excitation and responses by applying Scheme IV are listed in Table 2.19. As expected the time step sizes, time step sizes $\Delta\tau$ are the same as those included in Table 2.17. For the case with $\eta = -1.5$ and $\varepsilon = 2.25$ numerical instability was observed when $\Delta\tau$ was equal to or larger than 1.10. Based on the simulation results of this case the stationary mean responses and mean squares are:

$$\langle X_1 \rangle = 2.2127\sqrt{S_0} - 0.0767 , \quad \langle X_2 \rangle = 0.9377\sqrt{S_0} - 0.0325 ,$$

$$\langle X_1^2 \rangle = 82.2252\, S_0 - 0.0987 , \quad \langle X_2^2 \rangle = 21.2552\, S_0 - 0.0255 .$$

Substituting these values into the equivalent stiffness matrix K_{el} defined by equation (2.26) and solving for the eigenvalue problem of the equivalent linear system, one can find that the two natural frequencies are 0.6 and 1.7. The corresponding critical time step size $(\Delta\tau)_{cr}$, by applying equation (27) of [2.14], is

$$(\Delta\tau)_{cr} = \frac{\sqrt{2}}{\omega_{n2}} = 0.81865 . \tag{2.49}$$

clearly, the critical time step size was well exceeded and therefore numerical instability occurred.

Table 2.19 Results for stationary responses
(S_0 = 0.0012)

MEANS OF RESPONSES (/$\sqrt{S_0}$)						
η	ε	$<X_1>$		$<X_2>$		$\Delta\tau$
		simulation	SCD-SL	simulation	SCD-SL	
-0.02	0.03	0.0393	0.0319	0.0198	0.0160	0.945
-0.2	0.3	0.309	0.324	0.151	0.166	0.95
-0.6	0.9	0.878	1.045	0.408	0.561	0.975
-1.0	1.5	1.436	1.919	0.640	1.077	0.995
MEAN SQUARES OF RESPONSES (/S_0)						
η	ε	$<X_1^2>$		$<X_2^2>$		$\Delta\tau$
		simulation	SCD-SL	simulation	SCD-SL	
-0.02	0.03	58.97	58.98	22,37	22.91	0.945
-0.2	0.3	59.98	60.02	21.68	22.22	0.95
-0.6	0.9	64.13	64.16	20.93	21.42	0.975
-1.0	1.5	69.71	69.70	20.60	20.93	0.995

2.2.4 Concluding remarks

In this section we present recursive expressions of means and mean squares of a MDOF system with non-symmetric nonlinearities in its stiffness terms. The system is explored by four different schemes derived by applying the SCD-SL method. It has been shown that it is critical to derive the recursive relations of the means of responses right from the original nonlinear matrix equation so that the effects of quadratic displacement terms are accurately represented.

The various schemes developed are applicable to both stationary and non-stationary random excitations. From the point of view of less algebraic manipulation in the derivation, accuracy, and less computational effort, Scheme IV presented in Sub-section 2.2.2 seems to be the most appropriate algorithm to employ.

Computed results by using the presented recursive expressions and in particular Scheme IV indicate that (a) the recursive expressions are easy to be implemented in a digital computer, (b) the computed response statistics are accurate, and (c) that they are far more economical to employ than the MCS.

The results of this section by using the SCD-SL will also be compared with those from the adaptive time schemes in the next section.

2.3 Adaptive Time Schemes for Responses of Nonlinear Multi-Degree-of-Freedom Systems Under Random Excitation

2.3.1 Introduction

The previous section and the parametric study in reference [2.4] of the SCD method for a nonlinear single-degree-of-freedom (SDOF) system under stationary Gaussian white noise have been shown that the time step size used in the computation is reduced with increased natural frequency. This suggests that for nonlinear systems the time step size at every time step has to be changed. Consequently, many direct integration schemes may be derived by using a combination of the SCD and some time step size up-dating strategies. In what follows three representative schemes are proposed. These are the stochastic central difference and adaptive time scheme (SCD-ATS), the stochastic central difference and adaptive time scheme with time co-ordinate transformation (SCD-ATST), and the stochastic central difference and time co-ordinate transformation with adaptive time scheme (SCD-TATS). For simplicity, these three schemes shall be collectively called SCD-MATS. In the SCD-ATS the lowest natural frequency of the nonlinear or linearized system at every time step is evaluated so that the time step size for application of the SCD can be determined in accordance with the procedure given in [2.4]. In the SCD-ATST the nonlinear or linearized system at every time step is first transformed into its corresponding dimensionless time co-ordinate and then the adaptive time scheme (ATS) is performed. The response is evaluated in the dimensionless time co-ordinate and subsequently converted back to the original time co-ordinate. This scheme

may prove to be relatively much more expensive than the SCD-TATS for nonlinear systems with a large number of DOF as it requires time co-ordinate transformation (TCT) at every time step. The SCD-TATS involves the TCT being performed once at the beginning of the computation before the application of the ATS. It may be appropriate to note that the technique of employing the SCD with TCT, first proposed in reference [2.5], eliminates the computational instability inherent in the SCD method and therefore reduces very significantly the computational costs for stiff systems. This has clearly been demonstrated in Section 2.1 in which discretized beam and plate structures were considered.

The orginization of this section is: the following sub-section includes outline and implementation of the SCD-MATS. Sub-section 2.3.3 is concerned with results of a series of numerical studies of the SCD-MATS for two nonlinear systems. The first system is a Duffing oscillator under non-stationary random excitation, and the second one is a 2DOF system with non-symmetric nonlinearities excited by a non-stationary random process representating an earthquake excitation. The first system has been studied in [2.3] while the second one has been investigated by Kimura and Sakata [2.12], and in Section 2.3.3. A summary and concluding remarks are given in Sub-section 2.3.4.

2.3.2 Stochastic central difference with adaptive time schemes and implementation

The SCD-ATS, SCD-ATST, and SCD-TATS or collectively called the SCD-MATS proposed here are simple and easy to be implemented in a digital computer program. The crucial steps in their implementation are (a) the selection of the time step

size , and (b) TCT when the systems have relatively high natural frequencies. These two steps are considered in this sub-section.

(i) *Time Step Size and Natural Frequency*

Determining the relation between the time step size Δt and the natural frequency ω of a SDOF system is the first step in implementing the SCD-MATS. The parametric study in [2.4] provides a methodology of constructing such a relation and many pertinent data. Results for the range of natural frequencies that are less than 1.0 were presented in Sub-section 2.1.5. Table 2.20 summarizes the data taken from [2.4] and Sub-section 2.1.5. The dependence of Δt on ω is shown in Figure 2.27. It is observed that as the natural frequency reduces to a small value the time step size Δt approaches 1.0. From Figure 2.27 the relation between Δt and ω may be written as

$$\begin{aligned} \Delta t &= 0.83 - 0.72 \log_{10} \omega \qquad 1.0 \le \omega < 5.0 \\ \Delta t &= 1.0 - 0.053\,\omega - 0.12\,\omega^2 \qquad \omega \le 1.0 \end{aligned} \tag{2.50}$$

where ω is in rad/sec. In arriving at equation (2.50), the following pairs of (ω , Δt) data have been used: (0.0 , 1.0), (0.5 , 0.9443), (1.0 , 0.83) and (5.0 , 0.33).

Note that equation (2.50) does not include a formula for $\omega \ge 5.0$ rad/sec. This is because if a natural frequency is higher than the latter the time step size becomes too small to be computationally effective. In case that natural frequency of the system is higher than 5.0 rad/sec the TCT technique should be used. If necessary, formula for the

relation between Δt and ω that is not included in equation (2.50) can be similarly constructed. Such construction can be performed by applying the finding in [2.4].

Though equation (2.50) is constructed from data of a SDOF system, it can be applied to MDOF systems. For such systems, the ω of equation (2.50) should be understood as the fundamental frequency or the dimensionless fundamental frequency. For example, the results obtained by using the SCD method with TCT for MDOF linear systems (Section 2.1) were based on the dimensionless time step sizes associated with the dimensionless fundamental natural frequencies. The rationale behind this was to better represent response caused by the fundamental mode. This reasoning has also been adopted by Bathe and Wilson in [2.15] for deterministic responses. The pitfall with this approach in the deterministic response computation is that the time step size may well exceed the critical time step size, if the fundamental and the highest natural frequencies are far apart from each other. Indeed, wide separation of the fundamental and highest natural frequencies occurs in many structural systems represented by finite elements. The SCD with TCT scheme has eliminated this pitfall because the dimensionless time step size associated with the dimensionless fundamental natural frequency reaches 1.0 as the dimensionless fundamental natural frequency approaches zero. This dimensionless time step size of 1.0 is well below the dimensionless critical time step, $(\Delta\tau)_{cr} = 2^{1/2}$ according to equation (27) of [2.14], if the highest dimensionless natural frequency is 1.

It should then be mentioned that equations (2.19) and (2.50) both express the relation between the time step size and the fundamental frequency. Recalling that equation (2.19) is based on MDOF systems represented by finite elements whose dimensionless

fundamental frequency is well below 1.0. Therefore a dimensionless time step size of 1.0 is recommended for such systems.

Table 2.20 Time step size and natural frequency

ω	Δt	ω	Δt
0.1	0.9975	2.0	0.61
0.2	0.9902	2.3	0.57
0.3	0.9785	2.6	0.53
0.4	0.9630	3.0	0.48
0.5	0.9443	3.3	0.45
0.6	0.9232	3.6	0.42
0.7	0.9006	4.0	0.39
0.8	0.877	4.3	0.37
0.9	0.8525	4.6	0.35
1.0	0.83	5.0	0.33
1.2	0.78	10.0	0.1812
1.4	0.74	40.0	0.04876
1.6	0.69	70.0	0.02816
1.8	0.65	100.0	0.0198

(ii) *Time Co-ordinate Transformation*

The TCT technique has been discussed in detail in Sub-section 2.1.3 and will therefore not be repeated here for conciseness.

2.3.3 Numerical studies

In this section a Duffing's oscillator under a non-stationary random excitation, and a two DOF nonlinear system excited by an earthquake are studied. These two systems have been studied and Monte Carlo simulation results have been presented in [2.3] and Section 2.2. Therefore, comparison can be made and effectiveness of the presently proposed algorithms can be assessed.

(i) *Duffing's oscillator*

The Duffing's oscillator considered here has the following equation of motion [2.3]

$$\ddot{x} + 2\zeta\omega\dot{x} + \omega^2\left[1 + \varepsilon\left(\frac{x}{\sigma}\right)^2\right] = r(t) \tag{2.51}$$

where x , $\dot{x}$ and $\ddot{x}$ are displacement, velocity and acceleration of the oscillator; ζ is the damping ratio, ε the strength of nonlinearity, and ω the natural frequency of the corresponding linear oscillator (that is, when $\varepsilon = 0$). If the excitation r(t) is stationary random, σ^2 is defined as $\sigma^2 = \pi S/(2\zeta\omega^3)$. If the excitation is non-stationary random, σ^2

is the maximum value of the variance response of the corresponding linear system. The excitation is defined as r(t) = e(t)w(t), where e(t) is a deterministic envelope function and w(t) the zero-mean Gaussian white noise. For this example, e(t) is defined as

$$e(t) = 4.0(e^{-0.05t} - e^{-0.10t}) \tag{2.52}$$

Applying the SCD-SL technique, the recursive expression for equation (2.51) is given as [2.3]

$$\begin{aligned} R(s+1) &= a^2R(s) + b^2R(s-1) + 2abD(s) + z^2B(s)\ , \\ D(s) &= aR(s-1) + bD(s-1)\ , \end{aligned} \tag{2.53}$$

where

$$a = \frac{\left[2-(\omega_e \Delta t)^2\right]}{(1+\zeta\omega\Delta t)}\ ,\quad b = -\frac{(1-\zeta\omega\Delta t)}{(1+\zeta\omega\Delta t)}\ ,\quad z = \frac{(\Delta t)^2}{(1+\zeta\omega\Delta t)}\ .$$

without ambiguity the responses and excitation in equation (2.53) are understood to be in the t domain. The equivalent natural frequency at time instant t_s is [2.3]

$$\omega_e(s) = \omega\sqrt{1+\frac{3eR(s)}{\sigma^2}} \tag{2.54}$$

note that the above equations also hold true in the τ domain provided that one substitutes $\Delta\tau$ for Δt, and recognizes that all the other quantities are with respect to the τ domain.

The variance of response for the system of equation (2.51) is evaluated here using the proposed SCD-MATS. Note that the SCD-TATS is identical to the SCD-ATS numerically in this particular example. In the SCD-ATS, equation (2.54) is used to determine the time-dependent natural frequency at time t_s which is substituted into equation (2.50) to obtain Δt_s , the time step size at time instant t_s . Δt_s is then applied to determine the terms a, b and z, and the variance of response at the next time instant R(s+1). Therefore, in the entire computational process the time step sizes are computed automatically. In the SCD-ATST the $\omega_e(s)$ of equation (2.54) is applied to perform the TCT. Consequently, in this particular example the dimensionless natural frequency of the transformed oscillator in the τ domain is always 1.0 and the dimensionless time step size in the τ domain is always 0.83. Of course, for MDOF nonlinear systems, the time step size in the τ domain, in general, varies from one time step to another.

Table 2.21 lists the results applying the SCD-ATS and SCD-ATST, and compares them with those from [2.3] using SCD-SL. Note that the SCD-SL results have been found to compare very well with the digital simulation data [2.3]. Table 2.21 indicates that results obtained by employing the SCD-ATS and SCD-ATST agree very well with those using the SCD-SL. This is particularly true for the cases with damping ratios higher than 0.05.

Table 2.21 Variance of response of the Duffing's oscillator*

S	ζ	ε	maximum variance		
			SCD-SL	SCD-ATS	SCD-ATST
10^{-10}	0.01	0.0	51.659×10^{-10}	51.659×10^{-10}	51.659×10^{-10}
		0.1	43.358	44.756	47.969
		0.3	36.358	37.209	42.259
		0.5	31.918	32.782	38.206
		1.0	26.242	26.575	31.813
		5.0	14.861	14.344	17.784
1.0	0.05	0.0	23.53	23.533	23.533
		0.1	19.97	19.634	20.366
		0.3	16.02	15.789	16.738
		0.5	14.20	13.716	14.610
		1.0	11.15	10.933	11.712
		5.0	6.35	5.783	6.227
1.0	0.5	0.0	3.1	3.137	3.137
		0.1	2.48	2.507	2.533
		0.3	2.0	1.969	2.001
		0.5	1.76	1.695	1.726
		1.0	1.41	1.340	1.366
		5.0	0.71	0.707	0.714

* SCD-SL results are from, [2.3] for $S=10^{-10}$ and [2.4] for $S=1.0$.

(ii) *A two degree-of-freedom system with non-symmetric nonlinear stiffness*

This two DOF nonlinear system, shown in Figure 2.20, has previously been investigated by Kimura and Sakata [2.12], and in Section 2.2. The governing equation of motion of the system has been presented by equations (2.20) through (2.23) and will not be repeated here. Two routes can be followed in applying the SCD-MATS. The first route is to apply the SCD-MATS introduced in Sub-section 2.3.2 directly to equation (2.21), while the second route is to linearize equation (2.21) and then apply the SCD-MATS to the linearized system. The latter route is followed here in this study as Section 2.2 has obtained the recursive expressions for the system by using the SCD-SL technique. In Section 2.2 it was found that the SCD-SL scheme IV gave excellent results compared with those by digital simulation. Therefore, the SCD-SL scheme IV is adopted here. The system is assumed to have the following modulating function

$$e(\tau) = 4(e^{-0.125\tau} - e^{-0.25\tau}) \tag{2.55}$$

and parameters

$$W = \mu = 1.0\ ,\quad \zeta_1 = \zeta_2 = 0.1\ ,\quad S_0 = 0.0012\ . \tag{2.56}$$

The ranges of nonlinearities studied were: - 0.02 to - 1.5 for η, and 0.03 to 2.25 for ε. Digital simulation results were also obtained for smaller η and larger ε in addition to the above two ranges of nonlinearities. The smaller η and larger ε were: η = - 2.0 and ε = 3.0. However, it was found that numerical instability could occur for certain

combinations of η and ε when using the SCD-SL (see Section 2.2). On the other hand, the presently proposed SCD-ATS, SCD-ATST, and SCD-TATS do not have numerical instability. Note that when η and ε both equal to zero it is a linear system. In this special case, the two natural frequencies are 0.61804 and 1.61804.

Results obtained by employing the three SCD-MATS are presented in Table 2.22 and compared with those evaluated by the SCD-SL and Monte Carlo simulation (MCS) in Figures 2.28 through 2.33. From Table 2.22 and Figures 2.28 through 2.33 it can observed that the computed maximum variances are slightly smaller than those obtained by the SCD-SL. Of course, The discrepancy increases with increasing intensities of nonlinearities. For small intensities of nonlinearities the three SCD-MATS give very close results. As the intensities of nonlinearities are increased the SCD-TATS results have the best agreement with those using the SCD-SL and MCS. Therefore the SCD-TATS seems to be the best alogarithm to employ in terms of accuracy and computing cost over wide ranges of nonlinearities.

Table 2.22 Maximum variance of responses of the 2 DOF system

(η,ε)	scheme	$<X_1^2>$	$<X_1X_2>$	$<X_2^2>$
(-0.02, 0.03)	SCD-SL	25.6397	15.1325	10.3236
	SCD-ATS	24.8217	14.7068	9.9657
	SCD-ATST	24.6697	14.7959	9.6327
	SCD-TATS	24.6744	14.7810	9.6202
(-0.2, 0.3)	SCD-SL	25.9606	15.1362	10.2092
	SCD-ATS	24.9091	14.6228	9.7952
	SCD-ATST	24.8343	14.7372	9.4858
	SCD-TATS	24.9065	14.6663	9.3600
(-0.6, 0.9)	SCD-SL	26.8154	15.2945	9.9782
	SCD-ATS	25.3070	14.4733	9.4364
	SCD-ATST	25.2358	14.6338	9.1733
	SCD-TATS	25.6460	14.5125	8.8307
(-1.0, 1.5)	SCD-SL	28.3533	15.5543	9.9993
	SCD-ATS	25.7276	14.3781	9.1117
	SCD-ATST	25.7343	14.5750	8.8888
	SCD-TATS	26.8538	14.6206	8.4911
(-1.5, 2.25)	SCD-SL	33.7253	16.7801	11.4832
	SCD-ATS	26.4225	14.3400	8.7908
	SCD-ATST	26.5014	14.5749	8.6116
	SCD-TATS	29.5495	15.3829	8.4428
(-2.0, 3.0)	SCD-SL	overflow		
	SCD-ATS	27.2930	19.3983	8.5630
	SCD-ATST	27.4225	14.7002	8.4111
	SCD-TATS	34.5062	17.0326	8.7753

2.3.4 Summary and concluding remarks

To recapitulate, in this section three adaptive time schemes are incorporated into the stochastic central difference method with time co-ordinate transformation for the determination of variances and covariances of responses of multi-degrees-of-freedom nonlinear systems. The resulting procedures are called the SCD-ATS, SCD-ATST, and SCD-TATS. A SDOF Duffing's oscillator disturbed by a non-stationary random excitation, and a two DOF nonlinear system under a non-stationary random process have been studied. A relation, equation (2.50), has also been presented for the evaluation of time step size required in the implementation of the aforementioned procedures.

It has been found that computational times required by the above three procedures for obtaining the results of the two nonlinear systems have insignificant differences. However, it is expected that the SCD-ATST is more expensive to employ for nonlinear systems with many DOF (see Chapter 8).

The three procedures are very efficient to apply compared with digital simulation. Furthermore, they are free from computational instability and give very accurate results for highly nonlinear systems.

2.4 Concluding Remarks

In this chapter the stochastic central difference (SCD) method and strategies to effectively apply the SCD method, that is, SCD-ATS, SCD-TATS and SCD-ATST, are introduced and their implementation presented. In particular, Section 2.1 is concerned with the SCD method with the TCT which is applied to two linear structures discretized

by the finite element method and having relatively very high natural frequencies. The SCD-SL technique is employed in Section 2.2 to a 2 DOF system with non-symmetric nonlinear stiffness. Section 2.3 presents the several adaptive time schemes and applies them to a SDOF Duffing's oscillator and a 2 DOF nonlinear system, both under non-stationary random excitations.

In addition, relations have also been proposed for the evaluation of time step size required in the implementation of the strategies.

It has been found that the schemes are equally satisfactory in terms of accuracy. The computational times required by the above schemes to obtain the results of the two nonlinear systems studied in Section 2.3 have insignificant differences. However, it is expected that the SCD-TATS is more effective to employ for nonlinear systems with many DOF. This will be verified in Chapter 8.

CHAPTER 3

HYBRID STRAIN BASED THREE NODE FLAT TRIANGULAR SHELL ELEMENTS

To accomplish the objective of determining the random responses of complex shell structures with geometric and material nonlinearities, the development of shell finite elements that are accurate, effective, versatile and applicable to thin to moderately thick shells is essential. This chapter and the coming four chapters are aimed at the development and application of the elements. Following the common approach, we shall start with the linear analysis. Therefore, this chapter is to derive hybrid strain based three node flat triangular shell elements. This solution strategy is justified in Section 3.1 which is an introduction. Subsequently, Section 3.2 is concerned with the derivation of the 5 DOF per node version of the element stiffness matrices while Section 3.3 deals with the problematic drilling degree-of-freedom (DDOF), and completes the 6 DOF per node version. In the final section, Section 3.4, discussions and concluding remarks are presented. The explicit expressions for the element stiffness matrices are included in Appendices A and B.

3.1 Introduction

The development of low-order (C^0) flat triangular elements with 3 nodes, 15 or 18 degrees-of-freedom (DOF) dates back to the early 1960s and has attracted considerable attention since then. Such flat elements model shells by superposition of stretching behaviour (membrane element) and bending behaviour (plate bending element). The major attractive features of this shell modelling, among others, are: (1) it is simple to formulate; (2) it is easy to input data to describe the shell geometry; (3) it can be mixed with other types of elements; (4) it is capable of representing rigid body motions; (5) general shell geometry can be treated; and (6) the requirement of using a relatively large number of elements provides the advantages of convenience in incorporating complex loading and boundary conditions. Some notable early formulations of 3-node flat triangular shell elements include those by Zienkiewicz *at el.* [3.1], and Clough and Johnson [3.2], both of which were with 5 DOF (two in-plane displacements, transversal displacement and its two first derivatives with respect to the two axes perpendicular to the transversal displacement) per node. Argyris *et al.* [3.3] chose the mixed second-order derivative of the lateral displacement, together with the 5 DOF mentioned above, as nodal DOF and thus had 18 DOF per element. In these three elements the in-plane displacements were linear and the lateral one was cubic. Later in the 1980s discrete Kirchhoff theory (DKT) elements appeared [3.4-5]. Some 3-node shell elements were developed [3.6-7] by combining the 3-node DKT triangular elements and the constant strain triangle (CST).

Other shell elements that have also attracted considerable attention are the so-called degenerate shell elements. This is due to, partly the need for analysis of

moderately-thick to thick shells, and partly their advantages. The latter include mathematical consistency, easy extendability to non-linear analysis and simplicity in formulation. Degenerate shell elements are also capable of representing the coupled effects between membrane and bending actions, if the elements are of high enough order. For a 3-node degenerate element, such coupling is unfortunately missed, since the element can only describe "flat" geometry. While the degenerate elements perform satisfactorily with thick shells, they become less accurate in the "thin" limit. This stems from the excessive transversal shear strain involved in the formulation and is known as the shear-locking phenomenon. Some techniques have been proposed to reduce or even circumvent shear-locking. For a summary, the readers are referred to reference [3.8]. One such technique commonly adopted is the reduced or selective integration [3.9]. However, it may lead to matrices that are rank-deficient and possess spurious or hourglass or zero-energy modes. Consequently, stabilization matrices are required to remove these spurious modes.

Another scheme for dealing with the shear-locking problem is the hybrid/mixed formulation. In terms of handling shear-locking, it has been shown that the hybrid/mixed approach is equivalent to the displacement-based formulation with reduced integration [3.8, 3.10]. Furthermore, in term of providing continuity for both the displacement and strain or stress fields, hybrid/mixed formulation is unique.

Degenerate shell elements may also exhibit membrane-locking when low-order in-plane displacement functions are used in the formulation of curved elements [3.11-12]. The physical interpretation of membrane-locking is the inability of an element to bend

without stretching which causes a bending-dominated deformation to be replaced by a membrane-dominated deformation. Techniques to handle membrane-locking include, among others, utilization of enhanced membrane strain interpolations [3.13] and sufficiently high order in-plane displacement field [3.11]. It is also found that [3.14] the reduced integration for shear strain also reduces the effects of membrane-locking. However, such reduction is accompanied by a deterioration of membrane-bending coupling. In passing, it may be noted that membrane-locking does not exist if the degenerate element is flat.

In addition to the shear-locking and membrane-locking, another problem found in low-order shell elements is that due to rotations about the normal to the shell surface, also known as drilling degrees-of-freedom (DDOF). In a general-purpose finite element computer program if the DDOF are present among structural DOF while they are not included in the shell elements that are coplanar at a certain node, the global stiffness matrix becomes singular. Moreover, simply omitting the rotations interferes with rigid body motion and thus destroys an important convergence criterion: correct representation of general rigid body motion. The finite element literature to date has not resolved the problem caused by the DDOF. A common approach in dealing with the latter problem is to add fictitious normal rotational stiffness. For instance, reference [3.15] included the normal rotation by employing curved membrane component element. The shell element so-formed was later found to be identical to Allman's triangle [3.16-18]. In the same reference a scheme was proposed to eliminate the normal rotations while incorporating full rigid body motions. In regard to accuracy, reference [3.19] argued that better

accuracy could be achieved by adding fictitious normal rotational stiffness than by simply omitting the rotations. Reference [3.20] observed that the scheme that it introduced did not recover the performance of the 6 DOF per node version, although it reduced the deficiency of the 5 DOF per node version. The conclusion at this stage is that the number of DOF per node and mesh topology are important considerations in the performance of triangular elements.

In short, low-order, 3-node flat triangular shell elements based on displacement formulation possess several important and advantageous features while they have shear-locking and problem caused by the DDOF. Consequently, in the present investigation, several 3-node, 18 DOF, low-order flat triangular shell elements are developed. These elements have several improved features over existing 3-node, 18 DOF, low-order flat triangular shell elements. The first feature is the hybrid strain as well as degenerate formulation that can provide continuity of displacements and strains, and circumvent the shear-locking problem. The degenerate nature allows the elements for application to thin and thick shells, and further extension to non-linear analysis. In this formulation a discrete Kirchhoff type transversal shear strain is assumed. The choice of strain field rather than displacement or stress field in this hybrid formulation is based on mathematical and practical reasons. Mathematically, strain energy in the shell element is to be minimized in the variational principle applied and variations of strain in the element converge more rapidly. Furthermore, the generalized strains of a shell element can be varied independently whereas the generalized displacements of the same shell element cannot. Practically, straightforward integration can be performed on the strain-

displacement relationships to give the corresponding displacement functions which are subsequently applied to calculate the element stiffness matrix. The second feature is the shell element stiffness matrix which is explicitly expressed by a combination of manual and computer-assisted derivations. The explicit expressions eliminate the need for numerical integration and thereby improve significantly the computational time. The third feature is the re-examination of various formulations of the DDOF and their replacement with one that has a more satisfactory physical basis so that the resulting elements are capable of reflecting true normal rotations as well as desirable bending and membrane behaviours. As shown in the next Chapter such replacement results in improved performance of the proposed shell elements. In the following section (Section 3.2) the formulation and explicit expressions for the element stiffness matrices of several shell elements without DDOF (the 5 DOF per node version) are presented. Section 3.3 addresses the DDOF and combines the results in Sections 3.2 and 3.3 to form six shell elements each of which has three nodes with six DOF per node. The final section, Section 3.4 includes discussion and concluding remarks. Numerical studies that include the obstacle course [3.22] are presented in the next chapter.

3.2 Formulation and Element Stiffness Matrices

This section is to derive the 5 DOF per node version of element stiffness matrices that possess the several features discussed in the previous section (Section 3.1). It starts with the Hellinger-Reissner variational principle (Sub-sections 3.2.1 and 3.2.2). After introducing element geometry (Sub-section 3.2.3) and displacement and strain assumptions (Sub-section 3.2.4), the element stiffness matrices are developed in Sub-section 3.2.5.

3.2.1 Variational principle

Four major variational principles are acknowledged as the starting point of finite element formulations. These are: the principle of minimum potential energy, the principle of minimum complementary energy, the Hu-Washizu principle, and the Hellinger-Reissner principle. The last one assumes displacements and stresses, or displacements and strains as independent variables, is adopted in the present formulation for the reasons mentioned in the foregoing section. The functional for the Hellinger-Reissner principle can be written as:

$$\pi_{HR}(u,\sigma) = \int_{V_b} \left[-\frac{1}{2}\sigma^T C\sigma + \sigma^T(Lu) - u^T f \right] dv - \int_{S_t} u^T \bar{t}\, ds - \int_{S_u} (u-\bar{u})^T(\Gamma\sigma)\, ds \tag{3.1}$$

or

$$\pi_{HR}(u,\varepsilon) = \int_{V_b}\left[-\frac{1}{2}\varepsilon^T D\varepsilon + \varepsilon^T D(Lu) - u^T f\right]dv - \int_{S_t} u^T \bar{t}\, ds - \int_{S_u} (u-\bar{u})^T[\Gamma(D\varepsilon)]ds \tag{3.2}$$

where

u is the displacement vector;

σ is the stress vector;

ε is the strain vector;

f is the body force vector;

D is the elastic matrix of the material, such that $\sigma = D\varepsilon$;

C is the compliance matrix of the material, such that $\varepsilon = C\sigma$;

L is the linear operator to calculate strain from displacement;

Γ is the linear operator to evaluate surface traction from stress;

$\bar{u}$ is the vector of prescribed displacement on boundary;

$\bar{t}$ is the vector of prescribed surface traction;

V_b is the volume of the body;

S_t is the portion of the surface of the body where $\bar{t}$ is applied;

S_u is the portion of the surface of the body where $\bar{u}$ is applied;

and the superscript "T" denotes transpose.

Since in hybrid strain formulation the final unknowns are nodal displacements, the satisfaction of displacement boundary condition, $u = \bar{u}$, is easily met and the term with $(u - \bar{u})$ can thus be disregarded. Equation (3.2) then becomes

$$\pi_{HR}(u,\varepsilon) = \int_{V_e} \left[-\frac{1}{2} \varepsilon^T D \varepsilon + \varepsilon^T D(Lu) - u^T f \right] dv - \int_{S_t} u^T \bar{t}\, ds \qquad (3.3)$$

Equation (3.3) is the foundation of the present hybrid-strain triangular shell finite element formulation. The physical interpretation of equation (3.3) is that it represents the total potential energy in which strain vector and its transpose are directly included. In taking the variation of equation (3.3) the strain energy is minimized. As pointed out in reference [3.23], in shell analysis displacements and strains are coupled in such a way that some strains are functions of more than one displacement. Therefore, the strains will not be independent, if only displacements are made independent of one another, as in displacement-based finite element formulation. Reference [3.23] argued that, by independently assuming displacement and strain fields within an element, the independence of strains is at least partially true, since the strains can be varied by changing the thickness of the shell and its elastic material properties. Changing the thickness of the shell will alter the relationship between membrane and bending strains. Changing the elastic material properties of an anisotropic shell will vary the strains in different directions with some degree of independence.

3.2.2 Stationarity of the functional

Assuming that in the element level

$$u = Nq \,, \qquad \varepsilon = P\beta \,, \tag{3.4a,b}$$

where q and β are vectors of nodal displacement, and strain parameter, respectively, while N and P are the corresponding interpolation matrices.

Substituting equation (3.4) into (3.3) gives

$$\begin{aligned} \pi_{HR}(u,\varepsilon) &= \sum \pi_{HR}(q,\beta) \\ &= \sum \left\{ \int_V \left[-\frac{1}{2}\beta^T P^T D P \beta + \beta^T P^T D (LNq) \right] dV \right\} \\ &\quad - \sum \left[\int_V (q^T N^T f)\, dV - \int_A (q^T N^T \bar{t})\, dA \right] \end{aligned} \tag{3.5}$$

where V and A are the volume and area of an element, respectively, and the summation is performed over all the elements.

Minimizing the total potential energy in equation (3.5) with respect to β leads to

$$\frac{\partial \pi_{HR}(u,\beta)}{\partial \beta} = -\sum \left[\int_V P^T D P \, dV \right] \beta + \sum \left[\int_V P^T D B \, dV \right] q = 0 \tag{3.6}$$

or

$$-\left[\int_V P^T D P \, dV \right] \beta + \left[\int_V P^T D B \, dV \right] q = 0 \tag{3.7}$$

in which B = LN is the strain-displacement matrix. Now defining

$$H = \int_V P^T D P \, dV \,, \quad G_e = \int_V P^T D B \, dV \tag{3.8a,b}$$

such that equation (3.7) can be written as

$$- H\beta + G_e q = 0$$

or

$$\beta = H^{-1} G_e q \ , \tag{3.9}$$

Substituting equation (3.9) into (3.5) results in

$$\begin{aligned} \pi_{HR}(u,\varepsilon) &= \sum \pi_{HR}(q) \\ &= \sum \left[\frac{1}{2} q^T G_e^T H^{-1} G_e q \right] - \sum q^T \left[\int_V (N^T f) dV \right] \\ &\quad - \sum q^T \left[\int_A (N^T \bar{t}\,) dA \right] \end{aligned} \tag{3.10}$$

Minimizing equation (3.10) with respect to q gives

$$G_e^T H^{-1} G_e q - \int_V N^T f dV - \int_A N^T \bar{t}\, dA = 0 \ . \tag{3.11}$$

Defining

$$\begin{aligned} k &= G_e^T H^{-1} G_e \\ f_c &= \int_V N^T f dV + \int_A N^T \bar{t}\, dA \end{aligned} \tag{3.12a,b}$$

where k is the element stiffness matrix, and f_c the consistent load vector due to body force and surface traction, equation (3.11) can then be written as

$$k q = f_c \ .$$

Assembling all elements yields the equilibrium equation

$$KQ = F_c \,, \tag{3.13}$$

with K, Q and F_c being the assembled stiffness matrix, assembled nodal displacement and consistent load vectors, respectively. The unknowns of equation (3.13) are vector Q which, after being solved, is applied to recover the strain or stress vector by the following relations

$$\begin{aligned} \varepsilon &= P\beta = PH^{-1}G_e q \,, \\ \sigma &= D\varepsilon = DPH^{-1}G_e q \,. \end{aligned} \tag{3.14}$$

3.2.3 Element geometry

Elements considered in the present investigation are 3-node flat triangles. A representative element is shown in Figure 3.1. The three nodes are allocated at the three corners of the mid-surface of the triangular shell element. A local rectangular co-ordinate system is attached to node 1, with its r-axis coinciding with the side 1-2, its t-axis being parallel to the normal of the element and its s-axis perpendicular to the r-t plane. With such co-ordinate system, the r and s co-ordinates of nodes 1, 2, and 3 are: (0,0), $(r_2,0)$ and (r_3,s_3), respectively. There are 6 local degrees-of-freedom DOF at each node, which are

u displacement in the r-axis,

v displacement in the s-axis,

w displacement in the t-axis,

θ_r rotation about r-axis,

θ_s rotation about s-axis, and

θ_t drilling degree-of-freedom (DDOF).

They are considered positive if along the positive directions of r, s, and t-axes. For the rotations the right-hand screw rule is adopted.

The triangular element can be easily described by the natural (area) co-ordinate system. If ξ_i (i=1, 2 and 3) are the natural co-ordinates, they satisfy the condition

$$\xi_1 + \xi_2 + \xi_3 = 1 .$$

The relation between the natural and the r-s co-ordinates is

$$\begin{Bmatrix} \xi_1 \\ \xi_2 \\ \xi_3 \end{Bmatrix} = \frac{1}{r_2 s_3} \begin{bmatrix} r_2 s_3 & -s_3 & r_3 - r_2 \\ 0 & s_3 & -r_3 \\ 0 & 0 & r_2 \end{bmatrix} \begin{Bmatrix} 1 \\ r \\ s \end{Bmatrix} . \tag{3.15}$$

The first-order partial derivatives of ξ_i with respect to r and s are

$$\begin{aligned} \xi_{1,r} &= -\frac{1}{r_2} \qquad \xi_{1,s} = \frac{r_3 - r_2}{r_2 s_3} , \\ \xi_{2,r} &= \frac{1}{r_2} \qquad \xi_{2,s} = -\frac{r_3}{r_2 s_3} , \\ \xi_{3,r} &= 0 , \qquad \xi_{3,s} = \frac{1}{s_3} . \end{aligned} \tag{3.16}$$

In the computation the three quantities r_2, r_3 and s_3 need be determined from known global position vectors of the three nodes: $P_i = (X_i, Y_i, Z_i)$, where i runs from 1 to 3. With reference to Figure 3.2,

$$r_2 = l_{12}\ ,\quad r_3 = l_{31}\cos\theta_{23}\ ,\quad s_3 = l_{31}\sin\theta_{23}\ ,$$

where

$$l_{ij} = |\,P_j - P_i\,|\ ,\quad \cos\theta_{ij} = \frac{(P_i - P_k)\bullet(P_j - P_k)}{|\,P_i - P_k\,|\,|\,P_j - P_k\,|}\ ,$$

and • indicates dot product of two vectors, while $|.|$ denotes the magnitude of a vector. The index k ranges from 1 to 3 and takes values other than i and j. For instance, when i=2 and j=3, k is 1.

Finally, the transformation matrix T is defined as

$$T = \begin{bmatrix} T_3 & & & & & \\ & T_3 & & & & \\ & & T_3 & & & \\ & & & T_3 & & \\ & & & & T_3 & \\ & & & & & T_3 \end{bmatrix}_{18\times 18} \tag{3.17}$$

where the 3 by 3 sub-matrix T_3 is

$$T_3 = \begin{bmatrix} l_1 & m_1 & n_1 \\ l_2 & m_2 & n_2 \\ l_3 & m_3 & n_3 \end{bmatrix} \tag{3.18}$$

with (l_i, m_i, n_i) being the directional cosines of the i-th local axis (referring to Figure 2, i = 1 corresponds to r axis; i = 2 corresponds to s axis; and i = 3 corresponds to t axis) with respect to the global X-Y-Z axes. The calculation of the directional cosines can be found, for example, in pages 110 through 114 of reference [3.24]. Both T and T_3 are orthogonal matrices and therefore their inverses equal to their corresponding transposes.

3.2.4 Displacement and strain assumptions

The DDOF in flat shell finite elements seem to be problematic. In practice, their contributions in the form of fictitious stiffness, see for instances references [3.6, 3.19, 3.24-25], are added separately to the bending element stiffness matrix which has 5 DOF per node. In the present investigation the 5 DOF per node shell element stiffness matrix is derived first. Subsequently, the contributions of the DDOF to the element stiffness matrix are studied in detail and they are added to the 5 DOF per node component to form the 6 DOF per node shell element stiffness matrix. The detailed study about the DDOF is presented in Section 3.3 while the rest of this section is concerned with the development of various versions of the 5 DOF per node element.

With 3 nodal variables available for the interpolation of u, v, w, θ_r and θ_s , the following linear interpolation relation can be written in terms of triangular natural co-ordinates:

$$\begin{aligned} &\left[\, u \;\; v \;\; w \;\; \theta_r \;\; \theta_s \;\; \theta_t \,\right]^T = \\ &N_5 \left[\, u_1 \;\; v_1 \;\; w_1 \;\; \theta_{r1} \;\; \theta_{s1} \;\; \theta_{t1} \;\; u_2 \;\; \ldots \;\; \theta_{s3} \;\; \theta_{t3} \,\right]^T \end{aligned} \tag{3.19}$$

where the second subscript in the rotation denotes the nodal number, and

$$N_5 = \left[[N_1]_{6\times5} \;\; [0]_{6\times1} \;\; [N_2]_{6\times5} \;\; [0]_{6\times1} \;\; [N_3]_{6\times5} \;\; [0]_{6\times1} \right]_{6\times18} \tag{3.20a}$$

with

$$[N_i] = \begin{bmatrix} \xi_i & 0 & 0 & 0 & 0 \\ 0 & \xi_i & 0 & 0 & 0 \\ 0 & 0 & \xi_i & 0 & 0 \\ 0 & 0 & 0 & \xi_i & 0 \\ 0 & 0 & 0 & 0 & \xi_i \\ 0 & 0 & 0 & 0 & 0 \end{bmatrix}_{6\times5} \qquad i=1,2,3 \tag{3.20b}$$

and $[0]_{6\times1}$ being null matrix of dimension 6×1.

The assumed strain field is

$$\left[\varepsilon_r \;\; \varepsilon_s \;\; \varepsilon_{rs} \;\; \varepsilon_{st} \;\; \varepsilon_{tr} \right]^T = P_5 \left[\beta_1 \;\; \beta_2 \;\; \beta_3 \;\; \cdots \;\; \beta_8 \;\; \beta_9 \right]^T \tag{3.21}$$

where

$$P_5 = \begin{bmatrix} 1 & 0 & 0 & t & 0 & 0 & 0 & 0 & 0 \\ 0 & 1 & 0 & 0 & t & 0 & 0 & 0 & 0 \\ 0 & 0 & 1 & 0 & 0 & t & 0 & 0 & 0 \\ 0 & 0 & 0 & 0 & 0 & 0 & -s_3(1-2\xi_2) & s_3(2\xi_2+2\xi_3-1) & 0 \\ 0 & 0 & 0 & 0 & 0 & 0 & -r_3(1-2\xi_2) & (r_3-r_2)(2\xi_2+2\xi_3-1) & r_2(1-2\xi_3) \end{bmatrix}_{5\times9} \tag{3.22}$$

in which t is the thickness co-ordinate ranging from - h/2 to h/2. h is the thickness of the shell element.

As pointed out in references [3.25-26], the selection of assumed strain field should: (1) enable stresses calculated from the assumed strain functions to satisfy the point-wise equilibrium condition; (2) suppress all kinematic deformation modes; (3) keep the element properties invariant; and (4) possess favourable constraint index counting. Equations (3.21) and (3.22) completely satisfies the first three conditions, while the constraint index count is configuration dependent. In fact P_5 in equation (3.22) was employed in reference [3.25] for a hybrid stress formulation. Reference [3.25] argued that, since transversal shear strains ε_{st} and ε_{tr} are written in terms of natural co-ordinates ξ_2 and ξ_3 only, the resulting shear constraints, when shear strains diminishes to zero for large length/thickness ratio, will all be of discrete-Kirchhoff type. This effectively prevents shear-locking from occurring. It should also be noted that the 9 strain parameters are evenly distributed over membrane, bending and transverse strain fields. Specifically, β_1 through β_3 describe a constant membrane strain field, β_4 through β_6 correspond to a constant bending curvature distribution, and β_7 through β_9 represent a constant (over thickness) transverse shear strain field.

3.2.5 Derivation of stiffness matrices

Based on the definition of engineering strains, the strain-displacement relation for membrane strains is,

$$\varepsilon_r = u_{s,r} \quad , \quad \varepsilon_s = v_{s,s} \quad , \quad \varepsilon_{rs} = u_{s,s} + v_{s,r} \quad . \tag{3.23}$$

Similarly, for the bending strains the strain-displacement relation is

$$\varepsilon_r = t\theta_{s,r} \quad , \qquad \varepsilon_s = -t\theta_{r,s} \quad , \qquad \varepsilon_{rs} = t(\theta_{s,s} - \theta_{r,r}) \quad . \tag{3.24}$$

Finally, for the transverse shear strain the strain-displacement relation is

$$\varepsilon_{st} = w_{,s} - \theta_r \quad , \qquad \varepsilon_{tr} = w_{,r} + \theta_s \quad . \tag{3.25}$$

In equations (3.23) through (3.25) the subscripts ,s and ,r denote $\partial/\partial s$ and $\partial/\partial r$, respectively. Then the strain-displacement matrix B can be obtained as

$$\begin{aligned} B_m &= \left[\, [B_{m1}]_{5\times6} \; [B_{m2}]_{5\times6} \; [B_{m3}]_{5\times6} \, \right]_{5\times18} \\ B_b &= \left[\, [B_{b1}]_{5\times6} \; [B_{b2}]_{5\times6} \; [B_{b3}]_{5\times6} \, \right]_{5\times18} \\ B_s &= \left[\, [B_{s1}]_{5\times6} \; [B_{s2}]_{5\times6} \; [B_{s3}]_{5\times6} \, \right]_{5\times18} \end{aligned} \tag{3.26}$$

with

$$B_{mi} = \begin{bmatrix} \xi_{i,r} & 0 & 0 & 0 & 0 & 0 \\ 0 & \xi_{i,s} & 0 & 0 & 0 & 0 \\ \xi_{i,s} & \xi_{i,r} & 0 & 0 & 0 & 0 \\ 0 & 0 & 0 & 0 & 0 & 0 \\ 0 & 0 & 0 & 0 & 0 & 0 \end{bmatrix}_{5\times6} \qquad i=1,2,3$$

$$B_{bi} = \begin{bmatrix} 0 & 0 & 0 & 0 & t\xi_{i,r} & 0 \\ 0 & 0 & 0 & -t\xi_{i,s} & 0 & 0 \\ 0 & 0 & 0 & -t\xi_{i,r} & t\xi_{i,s} & 0 \\ 0 & 0 & 0 & 0 & 0 & 0 \\ 0 & 0 & 0 & 0 & 0 & 0 \end{bmatrix}_{5\times6} \qquad i=1,2,3 \tag{3.27a,b}$$

and

$$B_{si} = \begin{bmatrix} 0 & 0 & 0 & 0 & 0 & 0 \\ 0 & 0 & 0 & 0 & 0 & 0 \\ 0 & 0 & 0 & 0 & 0 & 0 \\ 0 & 0 & \xi_{i,s} & -\xi_i & 0 & 0 \\ 0 & 0 & \xi_{i,r} & 0 & \xi_i & 0 \end{bmatrix}_{5\times 6} \qquad i=1,2,3 \tag{3.27c}$$

where the subscripts m, b, and s indicate membrane, bending and transverse shear components, respectively.

Considering an isotropic, homogeneous and linear elastic material the constitutive law, $\sigma = D\varepsilon$, becomes

$$\begin{Bmatrix} \sigma_r \\ \sigma_s \\ \sigma_{rs} \\ \sigma_{st} \\ \sigma_{tr} \end{Bmatrix} = \begin{bmatrix} \frac{E}{1-\nu^2} & \frac{\nu E}{1-\nu^2} & 0 & 0 & 0 \\ \frac{\nu E}{1-\nu^2} & \frac{E}{1-\nu^2} & 0 & 0 & 0 \\ 0 & 0 & G & 0 & 0 \\ 0 & 0 & 0 & \kappa_s G & 0 \\ 0 & 0 & 0 & 0 & \kappa_s G \end{bmatrix}_{5\times 5} \begin{Bmatrix} \varepsilon_r \\ \varepsilon_s \\ \varepsilon_{rs} \\ \varepsilon_{st} \\ \varepsilon_{tr} \end{Bmatrix} \tag{3.28}$$

where E is the Young's modulus, G the shear modulus, ν Poisson's ratio and κ_s the form factor of shear which is equal to 5/6.

Substituting equations (3.22), (3.27) and (3.28) into (3.8) gives

$$
\begin{aligned}
H_5 &= \int_V P_5^T D P_5 \, dV \\
(G_e)_m &= \int_V P_5^T D B_m \, dV \\
(G_e)_b &= \int_V P_5^T D B_b \, dV \\
(G_e)_s &= \int_V P_5^T D B_s \, dV
\end{aligned}
\qquad (3.29a,b,c,d)
$$

By making use of equations (3.29) and (3.12a), one has

$$
\begin{aligned}
k_m &= (G_e)_m^T H_5^{-1} (G_e)_m \\
k_b &= (G_e)_b^T H_5^{-1} (G_e)_b \\
k_s &= (G_e)_s^T H_5^{-1} (G_e)_s \\
k &= k_m + k_b + k_s \ .
\end{aligned}
\qquad (3.30a,b,c,d)
$$

Note that the arrangement of the non-zero elements in matrices B_m, B_b and B_s leads to decoupling between k_m and k_b. This is a consequence of the fact that the element is flat. However, k_b and k_s are still coupled.

Equations (3.29) and (3.30) indicate that, to obtain the element stiffness matrix k, four integrals have to be evaluated. These integrations can be performed numerically. However, as the triangular natural co-ordinates are employed it is possible to perform the integrations analytically by making use of the following formula:

$$
\int_A \xi_1^k \, \xi_2^l \, \xi_3^m \, dA = 2A \, \frac{k!\, l!\, m!}{(2 + k + l + m)!} \qquad (3.31)
$$

The integrations are performed by the symbolic manipulation package, MAPLE [3.27]. For the derivation of H_5 the steps are

(1) establishing D and P_5 matrices,

(2) performing matrix multiplication $P_5^T D P_5$,

(3) performing integration along the thickness direction, $H_h = \int_{-\frac{h}{2}}^{\frac{h}{2}} P_5^T D P_5 \, dt$,

(4) performing integration over the area, $H_5 = \int_A H_h dA$, and

(5) obtaining the inverse of H_5.

For the evaluations of matrices $(G_e)_m$, $(G_e)_b$, and $(G_e)_s$ the procedures are

(1) writing matrices N_5, D and P_5,

(2) forming corresponding B matrix based on equations (23) through (25),

(3) performing matrix multiplication $P_5^T DB$,

(4) performing integration along the thickness direction, $(G_e)_h = \int_{-\frac{h}{2}}^{\frac{h}{2}} P_5^T D B \, dt$, and

(5) performing integration over the area, $(G_e) = \int_A (G_e)_h dA$.

The elements of these matrices are listed in Appendix A.

3.3 DDOF and Element Stiffness Matrices

As mentioned in Section 3.2, the DDOF is problematic. Omitting these DOF interferes with rigid body motion and therefore destroys an important convergence criterion: being capable of representing adequate rigid body motion. On the other hand, in a general-purpose finite element computer program if the DDOF are present among structural DOF while they are not included in the shell elements that are coplanar at a certain node, the global stiffness matrix becomes singular. This is due to the fact that the DDOF in the structural DOF at that node is not resisted.

3.3.1 Previous attempts in dealing with DDOF

Some schemes have been proposed in an attempt to solve the aforementioned problem. One of such schemes is to add fictitious diagonal stiffness components to the element stiffness matrix. Symbolically, the element stiffness matrix with the fictitious diagonal stiffness components can be written as

$$[\,k\,]_{18\times 18} = \begin{bmatrix} [G_e^{\,T} H^{-1} G_e]_{15\times 15} & [0]_{3\times 15} \\ [0]_{15\times 3} & [k_{\theta_t}]_{3\times 3} \end{bmatrix}_{18\times 18}$$

where $[0]_{15\times 3}$ and $[0]_{3\times 15}$ are null matrices with dimensions 15×3 and 3×15, and the 3×3 matrix $[k_{\theta t}]$ is diagonal and contains three equally valued entries $k_{\theta t}$. In references [3.6, 3.25] it was suggested to set $k_{\theta t} = 10^{-4}$, and $k_{\theta t} = 10^{-3}$ to 10^{-6} times of the smallest bending stiffness, respectively. References [3.19] and [3.24] proposed the following matrix $[k_{\theta t}]$,

$$[\, k_{\theta\alpha} \,] = \alpha E V \begin{bmatrix} 1.0 & -0.5 & -0.5 \\ -0.5 & 1.0 & -0.5 \\ -0.5 & -0.5 & 1.0 \end{bmatrix}$$

in which E is the Young's modulus, V the element volume and α a "small number" defined in the range $10^{-6} < \alpha < 10^{-2}$. This $[k_{\theta\alpha}]$ provides each DDOF a fictitious stiffness but offers no resistance to the deformation mode $\theta_{t1} = \theta_{t2} = \theta_{t3} = 0.0$. Note that the values 10^{-4}, or 10^{-6} to 10^{-2}, and α are determined from numerical experiments and are thus artificial.

As the flat triangular shell element is a combination of a triangular plane stress element and a triangular bending element, Allman's proposal of incorporating the DDOF into a triangular or quadrilateral plane stress/strain element [3.16-18] provides a starting point. It should be noted that Allman's scheme was motivated by the desire of improving the performance of constant strain triangle (CST) without invoking the complexity of linear strain triangle (LST). It also found applications in shell analysis [3.17]. By making use of the formulation of reference [3.16], the entire matrix of displacement interpolation function is

$$[\, u \; v \; w \; \theta_r \; \theta_s \; \theta_t \,]^T = N [\, u_1 \; v_1 \; w_1 \; \theta_{r1} \; \theta_{s1} \; \theta_{t1} \; u_2 \; \ldots \; \theta_{s3} \; \theta_{t3} \,]^T \qquad (3.32a)$$

where

$$N = N_5 + N_6 \tag{3.32b}$$

in which N_5 is as defined in equation (3.20), and

$$N_6 = \begin{bmatrix} [0]_{5\times5} & [p_1]_{5\times1} & [0]_{5\times5} & [p_2]_{5\times1} & [0]_{5\times5} & [p_3]_{5\times1} \\ [d_1]_{1\times5} & c_1 & [d_2]_{1\times5} & c_2 & [d_3]_{1\times5} & c_3 \end{bmatrix}_{6\times18} . \tag{3.33}$$

In equation (3.33), $[0]_{5\times5}$ is a null matrix with dimension 5×5. The matrices $[p_i]$ and $[q_i]$, and constants c_i, where $i=1$, 2 and 3 are defined as

$$\begin{aligned} [p_i] &= [\, \bar{p}_i,\ \bar{q}_i,\ 0,\ 0,\ 0\,]^T \\ [d_1] &= \left[\, \frac{r_2-r_3}{4A},\ -\frac{s_3}{4A},\ 0,\ 0,\ 0 \,\right] \\ [d_2] &= \left[\, \frac{r_3}{4A},\ \frac{s_3}{4A},\ 0,\ 0,\ 0 \,\right] \\ [d_3] &= \left[\, -\frac{r_2}{4A},\ 0,\ 0,\ 0,\ 0 \,\right] \\ c_i &= \frac{3\xi_i - 1}{4} \end{aligned} \tag{3.34}$$

where $\bar{p}_i$ and $\bar{q}_i$ defined as

$$\begin{aligned} \bar{p}_1 &= (a_{31}\xi_3 - a_{12}\xi_2)\xi_1 \\ \bar{p}_2 &= (a_{12}\xi_1 - a_{23}\xi_3)\xi_2 \\ \bar{p}_3 &= (a_{23}\xi_2 - a_{31}\xi_1)\xi_3 \end{aligned} \tag{3.35a}$$

$$\begin{aligned} \bar{q}_1 &= (b_{31}\xi_3 - b_{12}\xi_2)\xi_1 \\ \bar{q}_2 &= (b_{12}\xi_1 - b_{23}\xi_3)\xi_2 \\ \bar{q}_3 &= (b_{23}\xi_2 - b_{31}\xi_1)\xi_3 \end{aligned} \tag{3.35b}$$

and with reference to Figure 3.3,

$$a_{12} = \frac{1}{2}\ell_{12}\cos\gamma_{12} \quad , \quad b_{12} = \frac{1}{2}\ell_{12}\sin\gamma_{12}$$

$$a_{23} = \frac{1}{2}\ell_{23}\cos\gamma_{23} \quad , \quad b_{23} = \frac{1}{2}\ell_{23}\sin\gamma_{23}$$

$$a_{31} = \frac{1}{2}\ell_{31}\cos\gamma_{31} \quad , \quad b_{31} = \frac{1}{2}\ell_{31}\sin\gamma_{31} \ .$$

The in-plane displacements u and v are now coupled with the DDOF through quantities such as $\bar{p}_i$ and $\bar{q}_i$ in equations (3.35a) and (3.35b). The consequence of this coupling is to replace B_{mi} (i=1,2 and 3) in equation (3.27) with the following new bending part of the strain-displacement matrix as, $(B_{mi})'$. The latter is defined as

$$(B_{mi})' = \begin{bmatrix} \xi_{i,r} & 0 & 0 & 0 & 0 & \bar{p}_{i,r} \\ 0 & \xi_{i,s} & 0 & 0 & 0 & \bar{q}_{i,s} \\ \xi_{i,s} & \xi_{i,r} & 0 & 0 & 0 & \bar{p}_{i,s} + \bar{q}_{i,r} \\ 0 & 0 & 0 & 0 & 0 & 0 \\ 0 & 0 & 0 & 0 & 0 & 0 \end{bmatrix}_{5\times 6} \qquad i = 1,2,3 \tag{3.36}$$

and B_m in equation (3.26), $(G_e)_m$ in equation (3.29b) and k_m in equation (3.30a) are changed to $(B_m)'$, $(G_e)_m'$ and $(k_m)'$, accordingly. Note that the coupling between the in-plane displacements and the DDOF does not alter the two remaining parts, namely, k_b

and k_s of the element stifffness matrix k. Furthermore, the interpolation function for θ_t itself, that is the last row of matrix N defined in equation (3.32a), does not enter into $(B_{mi})'$. Thus, it has no contribution to k.

Following the steps in Section 3.2, the matrix $(G_e)_m'$ may be integrated analytically. It is found that $(G_e)_m'$ is the sum of $(G_e)_m$ and some other non-zero elements located in the 6th, 12th and 18th columns of the matrix. This is given in Appendix A. Note that this approach has two pitfalls, both resulting in rank deficiency of the stiffness matrix at the element and hence at the global level. One of them is the existence of an unusual type of zero energy mode in addition to rigid body modes [3.16-18]. A procedure to eliminate the unusual zero energy mode by adding a stabilized matrix has been outlined in reference [3.28]. The other pitfall is the occurrence of zero, or even negative, diagonal components in the element matrix and therefore in the global or assembled stiffness matrix. This occurrence is due to, partly the involvement of $\bar{p}_t$ and $\bar{q}_t$ terms, and partly the negative components in matrix H^{-1}. This phenomenon is in agreement with the observation made by Noor and Hartley [3.29] that hybrid/mixed models may lead to non-positive definite global stiffness matrix.

Another notable attempt in dealing with the DDOF is that due to Kanok-Nukulchai [3.30]. In this attempt he introduced to the strain energy functional a penalty function

$$\pi_t = \kappa_t G h \sum \left\{ \int_A \left[\theta_t - \frac{1}{2}(v_{,r} - u_{,s}) \right]^2 dA \right\} \tag{3.37}$$

where κ_t is a parameter that is greater than 0.1. Clearly, if $\kappa_t = 1/2$, π_t in equation (3.37) becomes the strain energy due to torsional deformation. Since $\frac{1}{2}(v_{,r} - u_{,s})$ is the (averaged) normal rotation from elasticity theory, equation (3.37) therefore force θ_t to approach the "true" normal rotation and result in the desired constraint:

$$\theta_t \approx \frac{1}{2}(v_{,r} - u_{,s}) \ . \tag{3.38}$$

In reference [3.30] it was suggested to use 1-point quadrature to evaluate equation (3.35) so as to avoid an over-constrained situation similar to shear-locking.

3.3.2 Present representations of the DDOF

Introducing the following complete interpolation function matrix N

$$N = N_5 + N_t \tag{3.39}$$

where N_5 is defined in equation (3.20), and

$$N_t = \begin{bmatrix} [0]_{5\times5} & [0]_{5\times1} & [0]_{5\times5} & [0]_{5\times1} & [0]_{5\times5} & [0]_{5\times1} \\ [0]_{1\times5} & \xi_1 & [0]_{1\times5} & \xi_2 & [0]_{1\times5} & \xi_3 \end{bmatrix}_{6\times18} \tag{3.40}$$

such that π_t of equation (3.37) may be expressed as a function of q, that is,

$$\pi_t(q) = \frac{1}{2} Gh \sum \left(\int_A q^T \bar{Y}^T \bar{Y} q \, dA \right) \tag{3.41}$$

in which κ_t has been set to 1/2 and the row matrix $\bar{Y}$ is

$$\bar{Y} = \frac{1}{2}\left[\frac{r_3 - r_2}{r_2 s_3}, \frac{1}{r_2}, 0,0,0,2\xi_1, -\frac{r_3}{r_2 s_3}, -\frac{1}{r_2}, 0, \right. \\ \left. 0,0,2\xi_2, \frac{1}{s_3}, 0,0,0,0,2\xi_3 \right]_{1\times18} . \tag{3.42}$$

Note that the last row of equation (3.40) represents a linear variation of θ_t over an element. That is,

$$\theta_t = \xi_1 \theta_{t1} + \xi_2 \theta_{t2} + \xi_3 \theta_{t3} . \tag{3.43}$$

Applying equations (3.2) and (3.41) one has the following functional

$$\pi(q,\beta) = \pi_{HR}(q,\beta) + \pi_t(q) . \tag{3.44}$$

In repeating the steps in Sub-section 3.2.2 for the stationarity of equation (3.44) with respect to β, and then with respect to q it leads to the element stiffness matrix

$$k = k_m + k_b + k_s + k_t \tag{3.45}$$

where k_m, k_b and k_s are defined as in equation (3.30) and

$$k_t = \frac{1}{2} Gh \int_A \bar{Y}^T \bar{Y} dA \ . \tag{3.46}$$

Since the integrands in the last equation are polynomials up to degree 2, the exact integration of k_t requires 3-point quadrature. Such integration results are denoted by k_t^3 the non-zero entries of which are listed in Appendix B.

Following the suggestion given in reference [3.30] to use 1-point integration for k_t, that is, replacing the integral in equation (3.46) with

$$A \bar{Y}^T(\xi_1 - \xi_2 - \xi_3 - \frac{1}{3}) \bar{Y}(\xi_1 - \xi_2 - \xi_3 - \frac{1}{3})$$

the resulting k_t from equation (3.46), denoted as k_t^1, differs from k_t^3 only in those components located at the 6th, 12th and 18th rows and columns of the matrix. These elements of k_t^1 are included in Appendix B. In fact it can be shown that, k_t^1 can be obtained by replacing θ_t with

$$\theta_t = \frac{1}{3} (\theta_{t1} + \theta_{t2} + \theta_{t3}) \tag{3.47}$$

and then replacing $\bar{Y}$ with

$$\bar{Y} = \frac{1}{2}\left[\frac{r_3 - r_2}{r_2 s_3}, \frac{1}{r_2}, 0, 0, 0, \frac{2}{3}, -\frac{r_3}{r_2 s_3}, -\frac{1}{r_2}, 0, \right.$$
$$\left. 0, 0, \frac{2}{3}, \frac{1}{s_3}, 0, 0, 0, 0, \frac{2}{3}\right]_{1\times 18} . \tag{3.48}$$

This indicates that using 1-point integration for k_t whose $\bar{Y}$ is defined by equation (3.43) is equivalent to full integration for k_t whose $\bar{Y}$ is defined by equation (3.47). As u and v both vary linearly over an element, the resulting "true" normal rotation $\frac{1}{2}(v_{,r} - u_{,s})$ is thus a constant over the element. Selecting equation (3.47) as the θ_t interpolation function instead of the linear one, equation (3.43), ensures consistency in both the physical sense and mathematical sense. This is because physically there is no over constraining and mathematically θ_t and the "true" rotation employ polynomials of the same order. It may be appropriate to note that application of equation (3.47) will not change the element to superparametric or subparametric, since the interpolation of co-ordinates of any point within the element depends on the first five nodal DOF only. This, in turn, means that the characteristics of isoparametric elements, such as C^0 continuity and completeness of linear polynomials, will be preserved when employing equation (3.39). However, one should be aware of the possibility of rank deficiency when using reduced integration. In the present study no such problem was detected, because it is equivalent to full integration of a constant θ_t field and because full integration ensures rank sufficiency.

In the preceding derivations k_m corresponds to the CST in the hybrid sense, and it is identical to the CST in the displacement-based formulation. This membrane component can be replaced by the Allman's triangle (AT). Denoting this new membrane component stiffness matrix as $(k_m)'$ which is defined as $(k_m)' = (G_e)'_m{}^T H_5^{-1} (G_e)'_m$, in which the elements of $(G_e)'_m$ is given in Appendix A. Associated with this stiffness matrix, $(k_m)'$, the row matrix $\bar{Y}$ in the torsional component, by applying equation (3.43) as the θ_t interpolation function, becomes

$$\bar{Y} = \frac{1}{2}\left[\frac{r_3 - r_2}{r_2 s_3}, \frac{1}{r_2}, 0, 0, 0, 2\xi_1 - \bar{p}_{1,s} + \bar{q}_{1,r},\right.$$

$$-\frac{r_3}{r_2 s_3}, -\frac{1}{r_2}, 0, 0, 0, 2\xi_2 - \bar{q}_{2,s} + \bar{p}_{2,r}, \qquad (3.49)$$

$$\left.\frac{1}{s_3}, 0, 0, 0, 0, 2\xi_3 - \bar{q}_{3,s} + \bar{p}_{3,r}\right]_{1\times 18}$$

or if equation (3.47) is employed so that

$$\bar{Y} = \frac{1}{2}\left[\frac{r_3 - r_2}{r_2 s_3}, \frac{1}{r_2}, 0, 0, 0, \frac{2}{3} - \bar{p}_{1,s} + \bar{q}_{1,r},\right.$$

$$-\frac{r_3}{r_2 s_3}, -\frac{1}{r_2}, 0, 0, 0, \frac{2}{3} - \bar{q}_{2,s} + \bar{p}_{2,r}, \qquad (3.50)$$

$$\left.\frac{1}{s_3}, 0, 0, 0, 0, \frac{2}{3} - \bar{q}_{3,s} + \bar{p}_{3,r}\right]_{1\times 18}.$$

Substituting equation (3.49) or (3.50) into (3.46) and performing the integration leads to the desired stiffness matrices. Note that the exact integration needs 3-point quadrature for either employing equation (3.49) or (3.50). Only two options are studied here. The result by exact integration upon equation (3.49) shall be designated as $(k_t^3)'$, and that with 1-point integration upon equation (3.50) as $(k_t^1)'$. It should also be pointed out that 1-point integration upon (3.49) also gives $(k_t^1)'$. The explicit expressions for $(k_t^3)'$ and $(k_t^1)'$ are presented in Appendix B.

The foregoing approaches lead to matrices, k_t^1 and k_t^3, or $(k_t^1)'$ and $(k_t^3)'$. These are, in fact, not different from the corresponding stiffness matrices derived by the displacement formulation. As the remaining components, k_m or $(k_m)'$, k_b and k_s, of the element stiffness matrix, k are obtained through hybrid formulation, it is desired to derive k_t by applying the hybrid formulation for consistency. The latter matrix shall be called k_d. To begin with this derivation of k_d, it is noted that $\theta_t = \frac{1}{2}(v_{,r} - u_{,s})$ is the shear

strain related to the so-called "skew symmetric" component of shear stress occurring on the r-s plane [3.31-33]. This enables one to add, on top of the membrane, bending and

transverse shear strains defined by equations (3.23) through (3.25), the following "normal rotational" shear strain

$$\varepsilon^{s}_{rs} = \theta_{t} - \frac{1}{2}(v_{,r} - u_{,s}) \tag{3.51}$$

such that the total r-s plane shear strains are

$$\varepsilon^{t}_{rs} = \varepsilon_{rs} + \varepsilon^{s}_{rs} \quad , \qquad \varepsilon^{t}_{sr} = \varepsilon_{rs} - \varepsilon^{s}_{rs} \tag{3.52a,b}$$

and are related to r-s plane shear stresses, respectively, by

$$\sigma^{t}_{rs} = \sigma_{rs} + \sigma^{s}_{rs} \quad , \qquad \sigma^{t}_{sr} = \sigma_{rs} - \sigma^{s}_{rs} \tag{3.53a,b}$$

in which

$$\sigma_{rs} = G\varepsilon_{rs} \quad , \qquad \sigma^{s}_{rs} = G\varepsilon^{s}_{rs} \quad . \tag{3.54a,b}$$

In equations (3.51) through (3.54), the superscript "s" denotes the "skew symmetric" part of, "t" indicates the "total" and G is the shear modulus as already defined above.

To proceed further, one may now introduce the following constitutive law

$$\begin{Bmatrix} \sigma_r \\ \sigma_s \\ \sigma_{rs} \\ \sigma_{st} \\ \sigma_{tr} \\ \sigma^s{}_{rs} \end{Bmatrix} = \begin{bmatrix} [D]_{5\times5} & [0]_{5\times1} \\ [0]_{1\times5} & G \end{bmatrix}_{6\times6} \begin{Bmatrix} \varepsilon_r \\ \varepsilon_s \\ \varepsilon_{rs} \\ \varepsilon_{st} \\ \varepsilon_{tr} \\ \varepsilon^s{}_{rs} \end{Bmatrix} \tag{3.55}$$

and assumed strain field

$$\begin{Bmatrix} \varepsilon_r \\ \varepsilon_s \\ \varepsilon_{rs} \\ \varepsilon_{st} \\ \varepsilon_{tr} \\ \varepsilon^s{}_{rs} \end{Bmatrix} = \begin{bmatrix} [P_5]_{5\times9} & [0]_{5\times1} \\ [0]_{1\times9} & 1 \end{bmatrix}_{6\times10} \begin{Bmatrix} \beta_1 \\ \beta_2 \\ . \\ . \\ \beta_9 \\ \beta_{10} \end{Bmatrix} . \tag{3.56}$$

Note that $\varepsilon^s{}_{rs}$ is independently assumed to be constant over an element and represented by the parameter β_{10}. The latter, β_{10} is added to the other β's in a single expression so that the skew-symmetrical part of the strain tensor can be related to the displacement field in the same manner as the remaining components of the tensor. The interpolation function for θ_t can be either that defined by equation (3.43) for linear distribution or (3.47) for a constant one.

One may then make use of the strain-displacement relation, equation (3.51), and arrive at the following strain-displacement matrix B_d, which relates the "skew symmetric" component of strain to the displacements,

$$B_d = \left[\left[B_{d1}\right]_{1\times 6} \ \left[B_{d2}\right]_{1\times 6} \ \left[B_{d3}\right]_{1\times 6} \right]_{1\times 18} \tag{3.57}$$

where

$$B_{di} = \left[\frac{1}{2}\xi_{i,s} \ -\frac{1}{2}\xi_{i,r} \ 0 \ 0 \ 0 \ \xi_i \right] \qquad i=1,2,3 \tag{3.58a}$$

for linear distribution of θ_t, or

$$B_{di} = \left[\frac{1}{2}\xi_{i,s} \ -\frac{1}{2}\xi_{i,r} \ 0 \ 0 \ 0 \ \frac{1}{3} \right] \qquad i=1,2,3 \tag{3.58b}$$

for constant distribution.

Note that in equation (3.55) the shear modulus G and the elastic matrix D which is defined in equation (3.28) are uncoupled, so are 1 and $[P_S]$ of (3.56). This enables one to separate the derivation of k_d from the remaining components. Following the steps illustrated in Section 3.2 one can obtain

$$\begin{aligned} (G_d)_e &= \int_V \tilde{P}^T G B_d \, dV \\ k_d &= (G_d)_e{}^T \tilde{H}^{-1} (G_d)_e \\ k &= k_m + k_b + k_s + k_d \end{aligned} \tag{3.59}$$

where

$$\tilde{P} = [0\ 0\ 0\ 0\ 0\ 0\ 0\ 0\ 0\ 1]_{1\times 10}$$

$$\tilde{H} = \begin{bmatrix} [H_5]_{9\times 9} & [0]_{9\times 1} \\ [0]_{1\times 9} & GhA \end{bmatrix}_{10\times 10} . \tag{3.60}$$

In equation (3.59) k_m , based on the CST, can be replaced by $(k_m)'$ which makes use of the AT.

Similar to the other component matrices of G_e , G_d can also be integrated analytically. The results are included in Appendix A. Note that whether the interpolation function for θ_t defined by equation (3.43) or (3.47) is used there is no difference between the final results of G_d. This is because all the integrands of equation (3.57) are either polynomials of degree 1 in terms of ξ_i (i=1, 2 and 3), if equation (3.43) is employed for interpolating θ_t, or constants if equation (3.47) is applied instead. In the former case exact integration requires 1 point quadrature; that is, evaluating the integrands at the centroid of the element ($\xi_1 = \xi_2 = \xi_3 = 1/3$) before multiplying by the element area. Clearly, the evaluation of the integrands at the centroid of the element is equivalent to setting all ξ_i (i=1, 2 and 3) to 1/3. This, on the other hand, demonstrates the capability of hybrid formulation of relaxing over-constrained displacement fields so as to avoid problems such as shear-locking. In fact, reference [3.10] strongly argued for the equivalence between hybrid formulation and reduced integration techniques, from the viewpoint of variational principle.

3.4 Concluding Remarks

Combining the results in Sections 3.2 and 3.3 a series of flat triangular shell elements with three corner nodes and six DOF per node is obtained. The elements have a simple geometry and contain only basic nodal DOF. Each of these elements can be considered as a combination of a triangular bending element and a plane stress element. The bending component element is degenerate and isoparametric in nature and adopts the specially designed strain distribution, equation (3.22), to suppress shear-locking in the "thin" limit. Thus, it is generally applicable to thin and thick problems. The plane stress component element is built on the basis of CST or AT, while much effort has been directed to include the DDOF and couple them with in-plane displacements u and v. In the present study such attempts have led to six variations of the element stiffness matrix k, depending on how the DDOF are treated and whether CST or AT is employed. These variations are identified as CST+k_t^1, CST+k_t^3, CST+k_d, AT+$(k_t^1)'$, AT+$(k_t^3)'$ and AT+k_d, and numerical results obtained with these different element stiffness matrices will be presented in the next chapter.

For identification purpose and easy reference the characteristics of the six variations of the shell element are summarized as follows.

CST+k_t^1 is $k = k_m+k_b+k_s+k_t^1$. Stiffness associated with DDOF enters k via the displacement-based k_t^1. The interpolation function for θ_t is constant over the shell element.

$CST+k_t^3$ is $k = k_m+k_b+k_s+k_t^3$. The inclusion of DDOF is through matrix k_t^3 which is derived by displacement-based method and makes use of linearly varied interpolation function for θ_t.

$CST+k_d$ is $k = k_m+k_b+k_s+k_d$. Strain associated with shear caused by DDOF and the "true" normal rotations is accounted for by forming k_d based the hybrid formulation. θ_t can be constant or linear over the element.

$AT+(k_t^1)'$ is $k = (k_m)'+k_b+k_s+(k_t^1)'$. Similar to $CST+k_t^1$ except that Allman's formulation is incorporated such that $(k_m)'$ replaces k_m and k_t^1 is substituted by $(k_t^1)'$.

$AT+(k_t^3)'$ is $k = (k_m)'+k_b+k_s+(k_t^3)'$. Similar to $AT+(k_t^1)'$ except that θ_t is varied linearly over an element.

$AT+k_d$ is $k = (k_m)'+k_b+k_s+k_d$. Similar to $CST+k_d$ except that the AT is employed instead of CST.

Before leaving this section several remarks are in order. Firstly, to the author's best knowledge, no similar detailed study of DDOF incorporating the hybrid formulation has been reported in the literature. In reference [3.31] a variational formulation is suggested, which included the "normal rotational" shear strain and its corresponding "skew symmetrical" stress component. Subsequently, in reference [3.32] the formulation is changed to suit the need of finite element applications. Among the very few implementations of the variational formulation, reference [3.34] derived a displacement-

based element including the DDOF while reference [3.33] presented a mixed-type quadrilateral element which combined the Allman-type formulation with an independently interpolated rotation field.

Secondly, there are two main distinctions between the present study and that in reference [3.33] in addition to the difference in element geometrical configuration. The first main distinction is that in reference [3.33] the skew-symmetrical part of the stress tensor is introduced as a Lagrangian multiplier so as to enforce the equality between independently assumed normal rotations and the skew-symmetrical part of the displacement gradient. However, in the present study it assumes, independent of the remaining displacements and strains, a normal rotation field as well as an interpolation function for the skew-symmetrical part of the strain, and applies all of them through the corresponding strain-displacement relation and constitutive law. The second main distinction is that in reference [3.33] the skew-symmetrical part of the stress is eliminated at the element level by applying static condensation, while in the present study the skew-symmetrical part of the strain, together with the remaining symmetrical strain components, are eliminated due to a relation between strains and displacements derived from the stationarity requirement of the variational principle. Furthermore, in the present study all the strain components, symmetrical or skew-symmetrical, can be recovered from known displacements through equation (3.14). However, reference [3.33] requires to obtain strains by differentiating displacements. This indicates that the formulation in the present study asssures better the continuity of the strain (stress) field.

Finally, explicit expressions of flat triangular shell element stiffness matrices are obtained by making use of a combination of manual and computer assisted derivations. These explicit expressions eliminate the need for numerical integration and thereby improve significantly the computational time.

CHAPTER 4

STATIC ANALYSIS OF SHELL STRUCTURES

A series of six hybrid strain based flat triangular shell elements with three corner nodes and six degrees-of-freedom (DOF) per node has been proposed in Chapter 3. In this chapter, results of numerical studies applying the proposed six elements are presented. The numerical studies contain more than ten examples, including those of the obstacle course [4.1]. These examples are grouped into plate and shell problems. The plate problems include the plane stress beam, patch test, straight cantilever beam, curved beam, rectangular plate, and circular plate. The shell problems studied are the twisted beam, pinched cylinder, Scordelis-Lo Roof, spherical ring loaded with its own weight, spherical shell with point load at the pole, and hemispherical shell with alternating point loads at equator.

The organization of this chapter is as follows. In Section 4.1 results of the plate problems are presented while Section 4.2 considers the shell problems. The final section, Section 4.3 is concerned with the concluding remarks.

4.1 Plate Problems

In this section results of numerical studies to assess the performance of the triangular flat shell elements introduced in the previous chapter are presented. The focus

of the numerical studies included in this section was on plate bending problems. The studies of shell problems are considered in Section 4.2 below. The plate problems in this section include a plane stress beam, examples in the so-called obstacle course proposed by MacNeal and Harder [4.1], and a circular plate. The plane stress beam has been used extensively in the finite element literature to test plane stress elements in bending applications [4.3-5]. Performances of the hybrid formulation elements identified as CST+k_t^1, CST+k_t^3, CST+k_d, AT+$(k_t^1)'$, AT+$(k_t^3)'$ and AT+k_d are also compared with each other. For plate bending elements the obstacle course consists of: (1) the patch test, (2) a straight cantilever beam, (3) a curved beam, and (4) a rectangular plate. The patch test of reference [4.1] was performed by prescribing boundary displacements, zero or non-zero, to a patch of elements. The objective of the test is to achieve the states of constant bending moment. Some other patch tests are also suggested in the literature which, instead of defining zero and non-zero boundary displacements, apply certain lateral forces and bending moments to the boundary nodes. The objective of theses tests is to obtain correct nodal displacements. In the present investigation the latter approach of the patch test is adopted, the given data of which are from reference [4.3]. The four examples of the obstacle course follow the description in reference [4.1]. Finally, the circular plate was studied by varying its thickness so as to evaluate the relation between the aspect ratio (radius/thickness) and the performance of the finite element. Note that the normalized values presented in the following are with respect to their corresponding exact

solutions. For boundary conditions, capital alphabets indicate displacements (rotations) in the global co-ordinates, unless it is stated otherwise.

4.1.1 Plane stress beam

The plane stress cantilever was subjected to a vertical parabolic shear end load. This is illustrated in Figure 4.1 in which its geometrical and material properties are given. The exact values of the vertical displacement and rotation at the end of the cantilever were quoted as 9.07542 mm (0.3573 in) and 0.0106 radians [4.4, 4.7]. Note that the vertical tip displacement of 9.07542 mm (0.3573 in) includes the portion of displacement due to transverse shear deformation, which is 0.4064 mm (0.016 in). However, the tip rotation is derived from Euler beam theory and therefore does not account for the rotation due to transverse shear. Six finite element discretizations, 4×1B, 4×1D, 8×2B, 8×2D, 16×4B and 16×4D (the two integers indicating the numbers of node spaces along the length and height directions of the beam, respectively, and the alphabet denoting the mesh type as portrayed in Figure 4.2) are used. Their consistent end loads are shown in Figure 4.3. In all six discretizations every bending DOF, that is, W or Θ_x or Θ_y, was constrained while U, V, and Θ_z were set to zero at the fixed end only. Finite element results are given in Tables 4.1 and 4.2. For comparison, the present elements were reduced to the CST based on the hybrid formulation (henceforth, shall be simply denoted as CST unless stated otherwise) by disregarding matrix k_t^1 or k_t^3 of equation (3.45) or k_d of equation (3.59),

and at the same time all the Θ_z's in the finite element meshes were constrained. These CST results are also listed in Table 4.1. Note that the attempt of forming an AT without the DDOF by the hybrid approach, that is, by employing Allman's in-plane displacement interpolation function [4.4] led to rank deficiency, as mentioned in Section 3.3, and therefore comparisons can only be made among results obtained from the three elements based on the AT with DDOF and hybrid formulation (henceforth, are referred to as AT-based elements). The following remarks for the beam structure in this sub-section are in order.

(1) The results using the CST are identical to those of reference [4.3] which were obtained by applying the displacement-based CST. This serves as a proof that the CST coincides with its displacement-based counterpart. Reference [4.3] reported 6.84784 mm (0.2696 in) and 8.81634 mm (0.3471 in) for meshes 4×1B and 16×4D, respectively, by using the displacement-based AT. Note that the value of 6.84784 mm (0.2696 in) falls between the present results using AT+$(k_t^1)'$ and AT+k_d while that of 8.81634 mm (0.3471 in) is smaller than the present results with the same mesh. Overall, the present AT-based elements seem to be less stiff than the displacement-based counterpart.

(2) Applying CST+k_d and CST+k_t^1 produced same results which were closer to the exact ones than CST+k_t^3 did. The improvement of results by CST+k_d and CST+k_t^1 over CST+k_t^3 was more significant for tip rotation than for tip displacement. This improvement was reduced as meshes became finer.

(3) For the three AT-based elements, AT+$(k_t^1)'$ seems to be superior to the other two. However, differences among results from the these three elements reduced as meshes were refined.

(4) Applying the CST itself and CST+k_d or CST+k_t^1 gave the same displacements. The implication is that the incorporation of the DDOF, as discussed in Section 3.3, had no contribution to accuracy and convergence. The incorporation of the DDOF seems to only force the DDOF to approach the "true" normal rotation. The task of improving accuracy and convergence was therefore borne by the AT-based elements since the latter produced substantial improvements over the CST-based elements, especially for coarse mesh cases.

(5) Note that the difference between k_t^1 and $(k_t^1)'$, or k_t^3 and $(k_t^3)'$ lies in the form of $\bar{Y}$

in equations (3.42) and (3.48) through (3.50). Consequently, $(k_t^1)'$ and $(k_t^3)'$ are capable of representing the coupling effects between the two in-plane displacements and the DDOF (which do not exist in k_t^1, k_t^3 and k_d). This coupling plays considerably important role in improving the accuracy and convergence of the displacement based CST element, as observed by Allman [4.4-6]. Therefore, it may be concluded that $(k_t^1)'$ and $(k_t^3)'$ enforce the DDOF to approach the "true" normal rotation as well as improve the performance of the AT elements. This remark is in agreement with the following observation of the present results: among the three AT-based elements, AT+$(k_t^1)'$ and AT+$(k_t^3)'$ yielded better results than AT+k_d did. It should be noted that in AT+k_d only the AT includes

the coupling effects between the two in-plane displacements and the DDOF. This fact explains why AT+k_d is not as accurate as AT+$(k_t^1)'$ or AT+$(k_t^3)'$.

(6) The convergence rates for tip displacement and rotation are comparable with each other for the CST-based elements. When using AT-based elements, however, tip rotation converged faster than tip displacement. Monotonic convergence, that is, approaching the exact value from below, prevailed except for the case of tip rotation using AT+$(k_t^1)'$. Note that these elements will be extended to nonlinear analyses of finite strains and rotations (see Chapters 6 through 8) which need rotations about all axes to update deformed configurations, therefore the correct and accurate representation of DDOF is necessary and essential. The slightly larger than 1.0 normalized tip rotations associated with mesh 16×4D are due to the fact that the "exact" solution, 0.0106 radians, does not represent the portion of the rotation caused by transverse shear deformation.

Table 4.1 Normalized tip displacement of the plane stress beam

mesh	neq.*	CST	CST +		
			k_t^1	k_t^3	k_d
4×1B	24	0.254	0.254	0.247	0.254
4×1D	36	0.576	0.576	0.555	0.576
8×2B	72	0.556	0.556	0.547	0.556
8×2D	120	0.835	0.835	0.823	0.835
16×4B	240	0.823	0.823	0.817	0.823
16×4D	432	0.949	0.949	0.945	0.949
mesh	neq.	AT	AT +		
			$(k_t^1)'$	$(k_t^3)'$	k_d
4×1B	24	not available	0.755	0.746	0.723
4×1D	36		0.943	0.939	0.935
8×2B	72		0.895	0.893	0.887
8×2D	120		0.976	0.975	0.973
16×4B	240		0.963	0.963	0.961
16×4D	432		0.990	0.990	0.989

* neq. denotes the total number of the unknown displacements or the number of final algebraic equations.

Table 4.2 Normalized tip rotation of the plane stress beam

mesh	neq.	CST +		
		k_t^1	k_t^3	k_d
4×1B	24	0.265	0.236	0.265
4×1D	36	0.628	0.562	0.628
8×2B	72	0.565	0.549	0.565
8×2D	120	0.906	0.842	0.906
16×4B	240	0.846	0.836	0.846
16×4D	432	1.028	0.970	1.028
mesh	neq.	AT +		
		$(k_t^1)'$	$(k_t^3)'$	k_d
4×1B	24	0.948	0.898	0.848
4×1D	36	0.994	0.990	0.982
8×2B	72	0.896	0.903	0.891
8×2D	120	0.992	0.991	0.992
16×4B	240	0.998	0.995	0.992
16×4D	432	1.013	1.012	1.013

4.1.2 Patch test

The patch test performed here is described in Appendix B of reference [4.3] together with its analytical solutions (see Figure 4.4 and Tables 4.3 through 4.5). It involves a rectangular plate which is divided into four triangular elements. The geometrical dimension of the plate is $1 \times 2 \times 0.001$ m^3, and its material properties are: Young's modulus $E = 10^8$ N/m^2, and Poisson's ratio $\nu = 0.25$. The fifth node has coordinates $X_5 = 0.7$ m and $Y_5 = 0.9$ m. By prescribing boundary conditions and bending moments in accordance with Tables 4.3 through 4.5, states of constant bending curvature and constant twist can be reached. The analytical solutions and the finite element results are included in Table 4.6. It is evident that the triangular element passes the patch test. In fact, other thicknesses such as 0.0001 m and 0.1 m were also tried and the same degree of agreement with the analytical solutions as in Table 4.7 was observed. Note that nodal DOF associated with displacements in X and Y directions and rotations about Z axis were all constrained. In this case the six presently proposed elements became identical. In passing, m_1 and m_2 in Tables 4.3 through 4.5 are applied end moments.

4.1.3 Straight cantilever beam

In this test tip loads were applied in various directions such that extension, in-plane shear, out-of-plane shear and twist were modeled (Figure 4.5). The dimensions of the beam are, length = 0.1524 m (6.0 in), width = 5.08 mm (0.2 in) and depth = 2.54 mm (0.1 in). The material properties of the beam are: $E = 6.985 \times 10^{10}$ (10^7 psi) and $\nu = 0.30$. The theoretical solutions, under unit tip loads, can be seen in Table 4.7.

Table 4.3 Patch test of constant curvature bending (X-direction)

description of boundary conditions and applied loads						
node	boundary conditions			applied loads		
	W	θ_x	θ_y	f_z	m_x	m_y
1	fixed	fixed	free	0	0	$-m_2$
2	fixed	fixed	free	0	0	m_2
3	fixed	fixed	free	0	0	$-m_2$
4	fixed	fixed	free	0	0	m_2
5	free	fixed	free	0	0	0

analytical solution for displacement				
node	W	θ_x	θ_y	$\theta = \frac{m_2 L_1}{D L_2}$ $a = x_5\left(1 - \frac{x_5}{L_1}\right)$ $b = \frac{2x_5}{L_1} - 1$ $D = \frac{Eh^3}{12(1-\nu^2)}$
1	0	0	$-\theta$	
2	0	0	θ	
3	0	0	$-\theta$	
4	0	0	θ	
5	$a\theta$	0	$b\theta$	

Table 4.4 Patch test of constant curvature bending (Y-direction)

description of boundary conditions and applied loads						
node	boundary conditions			applied loads		
	W	Θ_x	Θ_y	f_z	m_x	m_y
1	fixed	free	fixed	0	m_1	0
2	fixed	free	fixed	0	m_1	0
3	fixed	free	fixed	0	$-m_1$	0
4	fixed	free	fixed	0	$-m_1$	0
5	free	free	fixed	0	0	0
analytical solution for displacement						
node	W	Θ_x	Θ_y			
1	0	θ	0			
2	0	θ	0			
3	0	$-\theta$	0			
4	0	$-\theta$	0			
5	$a\theta$	$b\theta$	0			

$$\theta = \frac{m_1 L_2}{D L_1}$$

$$a = y_5\left(1 - \frac{y_5}{L_2}\right)$$

$$b = 1 - \frac{2y_5}{L_2}$$

$$D = \frac{Eh^3}{12(1-\nu^2)}$$

Table 4.5 Patch test of constant twist

description of boundary conditions and applied loads						
node	boundary conditions			applied loads		
	W	Θ_x	Θ_y	f_z	m_x	m_y^*
1	fixed	free	free	0	$-m_1$	m_2
2	fixed	free	free	0	m_1	m_2
3	fixed	free	free	0	$-m_1$	$-m_2$
4	free	free	free	0	m_1	$-m_2$
5	free	free	free	0	0	0
analytical solution for displacement						
node	W	Θ_x	Θ_y			
1	0	0	0			
2	0	κL_1	0			
3	0	0	$-\kappa L_2$			
4	$\kappa L_1 L_2$	κL_1	$-\kappa L_2$			
5	$\kappa x_5 y_5$	κx_5	$-\kappa y_5$			

$$m = \frac{2m_1}{L_2}$$

$$\kappa = \frac{m}{D(1-\nu)}$$

$$D = \frac{Eh^3}{12(1-\nu^2)}$$

* $m_2 = m_1 L_1 / L_2$.

Table 4.6 Finite element results of the patch test for bending

constant bending curvature in X-direction, $m_2=1.0$						
node	analytical			triangular element		
	W	Θ_x	Θ_y	W	Θ_x	Θ_y
1	0	0	-56.25	0	0	-56.25
2	0	0	56.25	0	0	56.25
3	0	0	-56.25	0	0	-56.25
4	0	0	56.25	0	0	56.25
5	11.8125	0	22.50	11.81	0	22.50
constant bending curvature in Y-direction, $m_1=1.0$						
node	analytical			triangular element		
	W	Θ_x	Θ_y	W	Θ_x	Θ_y
1	0	225.0	0	0	225.0	0
2	0	225.0	0	0	225.0	0
3	0	-225.0	0	0	-225.0	0
4	0	-225.0	0	0	-225.0	0
5	111.375	22.50	0	111.4	22.50	0
constant twist, $m_1=1.0$, $m_2=0.5$						
node	analytical			triangular element		
	W	Θ_x	Θ_y	W	Θ_x	Θ_y
1	0	0	0	0	$-\alpha^*$	β^*
2	0	150.0	0	0	150.0	$-\beta^*$
3	0	0	-300.0	0	α^*	-300.0
4	300.0	150.0	-300.0	300.0	150.0	-300.0
5	94.50	105.0	135.0	94.50	105.0	135.0

* $\alpha = 0.2687\times10^{-8}$, $\beta = 0.1045\times10^{-8}$.

Table 4.7 Theoretical solutions of the straight cantilever beam

tip load direction	displacement in direction of load mm (in)
extension	7.62×10^{-4} (3.0×10^{-5})
in-plane shear	2.74574 (0.1081)
out-of-plane shear	10.97534 (0.4321)
twist	0.814832 (0.03208)

In the finite element representation, the following five meshes were considered, 6×1A, 6×1B, 6×1D, 12×1A and 14×1A, with the first integer indicating the number of node spacings on the edge along the length direction and the second integer the number of node spacings along the width direction, and the alphabet following the second integer denoting mesh types in Figure 4.2. The first four meshes are of uniform spacing along the length direction of the beam. While the last one is formed from the mesh 12×1A by sub-dividing into two the element adjacent to the fixed end. This discretization is able to more accurately represent the stress concentration effect near the fixed end of the beam. The unit tip load was equally shared by the two tip nodes. For the cases of extension, out-of-plane shear and twist, the tip loads, each having the value of 2.2295 N (0.5 lb), were applied along the directions of X, Z and Θ_x, respectively. In order to model the in-plane shear beam by bending elements instead of the CST or AT, the width and the depth of the beam were inter-exchanged. The original in-plane beam was then transferred into an out-of-plane beam with width 2.54 mm (0.1 in) and depth 5.08 mm (0.2 in). To this

transferred out-of-plane beam, two tip loads each valued at 2.2295 N (0.5 lb) were also applied along the Z direction. In this way all four cases became beams lying on the X-Y plane, the corresponding boundary conditions were the X- and Y-direction displacements and DDOF were set to zero. At the fixed end, W, Θ_x and Θ_y were also set to zero. For the case of extension W, Θ_x, Θ_y and Θ_z all were constrained. The intent was to model the extension case by the CST itself. If the latter were able to provide sufficiently accurate results, the presently proposed elements will no doubt give better results. Note that, with such arrangements, the six proposed elements are identical.

Two remarks can be made in regard to the finite element results in Tables 4.8 and 4.9. Firstly, it is noticed that, mesh types A and B yield no difference in this example (which is not true for other cases as will be seen later), and although meshes 6×1D and 12×1A have the same numbers of elements, the results suggest that the latter is more accurate. Secondly, for the most coarse meshes used, 6×1A, or 6×1B, the normalized displacements for the four loading cases are, 0.992, 0.972, 0.972 and 0.927, respectively. All of these are being larger than 0.9. Reference [4.1] cited an assessing criterion that requires that the relative error be less than 10%. Judged by the cited criterion, the present elements do pass the test of the straight cantilever beam. Furthermore, reference [4.1] suggested a less than 2% error for the extension case and designated the extension test as a throwaway test in the sense that any elements that can not pass it should not be used for finite element modelling. In this regard, the results in Table 4.8 clearly indicate that the presently proposed elements are acceptable.

Table 4.8 Normalized dis[' -cements of the straight cantilever beam

mesh	neq.	extension
6×1A	24	0.992
6×1B	24	0.992
6×1D	36	0.995
12×1A	48	0.996
14×1A	52	0.998

Table 4.9 Normalized displacements of the straight cantilever beam

mesh	neq.	in-plane shear	out-of-plane shear	twist
6×1A	36	0.972	0.972	0.927
6×1B	36	0.972	0.972	0.927
6×1D	54	0.978	0.978	0.937
12×1A	72	0.987	0.987	0.939
14×1A	78	0.993	0.993	0.943

4.1.4 Curved beam

The curved beam was tested with unit in-plane and out-of-plane loads applied at the tip, as shown in Figure 4.6. The theoretical solutions for the two loading cases are -2.218436 mm (- 0.08734 in) and 12.75588 mm (0.5022 in), respectively, when its geometrical and material properties are: inner radius = 104.648 mm (4.12 in), outer radius = 109.728 mm (4.32 in), arc = 90° (from fixed end to tip), thickness = 2.54 mm (0.1 in), E = 6.985×10^{10} (10^7 psi), and $\nu = 0.25$. The curved beam is slim. Its ratio of mean radius 168.37 mm (6.629 in) over height 5.08 mm (0.2 in) was 33.144. Five meshes were employed, 6×1B, 12×1B, 14×1B, 20×1B and 32×1B. Note that all meshes except 14×1B were obtained by equally dividing the arc into 6, 12, 20 and 32 segments. Mesh 14×1B came as a result of sub-dividing the first element from the fixed end of mesh 12×1B into two. Mesh 14×1B was designed to consider the stress concentration effect near the fixed end of the curved beam. Similar to the cantilever beam, the unit tip loads here were again equally shared by the two tip nodes and applied in Z direction for the case of out-of-plane shear and in -Y direction for the in-plane shear. The constraints to the beam were only present at the fixed end where all the 6 DOF of each of the nodes were set to zero.

The results reported in Tables 4.10 through 4.12 show that, for the case of out-of-plane shear, the agreement between the theoretical solution and the finite element result is such that the averaged (over the inner and outer radii) normalized tip displacement exceeds 90% even with the most coarse mesh 6×1B. Thus, the elements passed this test. Furthermore, results of all the six elements show no difference, since it is again a plate

bending problem, though the in-plane displacements U and V, and the DDOF are free except at the fixed end. However, for the aforementioned five meshes the elements failed to capture the case of in-plane shear. Note that in this case the CST-based and the AT-based elements were applied to model bending behaviours of the beam. When the bending behaviours were modelled by CST-based elements the normalized tip displacement reached only 0.226 even with a 32×1B mesh. The same normalized displacement was increased by 2.08 times and became 0.696 if modelled by the AT-based elements. This indicates that finer meshes are required to achieve better accuracy. One way of improving the accuracy was to sub-divide into two the element next to the fixed end. For example, mesh 14×1B increased the tip displacement of the in-plane shear case by 20.73% using CST+k_d and 10.64% using AT+k_d, with respect to 12×1B. A better way seemed to be employing mesh type D. For instance, using a 20×1D mesh with the AT+k_d element, the normalized tip displacements became 0.965 and 0.937 for the cases of out-of-plane shear and in-plane shear, respectively. The total number of unknown displacement of the 20×1D mesh is 360. Finally, one may notice that, when modelling the in-plane shear case, the six proposed elements give different results. This is due to the fact that in-plane displacements and DDOF are involved.

Comparisons were also made between mesh type A and B and the results are included in Table 4.13. It seems that type B works better for the out-of-plane shear case. As to the in-plane shear, differences between mesh type A and B are negligible with both the CST-based, and AT-based elements.

Table 4.10 Normalized tip displacement of the curved beam (out-of-plane shear, for all six elements)

mesh	neq.	inner radius	outer radius
6×1B	72	0.899	0.925
12×1B	144	0.930	0.956
14×1B	156	0.938	0.964
20×1B	240	0.939	0.965
32×1B	384	0.943	0.969

Table 4.11 Normalized tip displacement of the curved beam* (in-plane shear)

mesh	neq.	CST+k_d or k_t^1	CST+k_t^3
6×1B	72	0.025	0.023
12×1B	144	0.082	0.077
14×1B	156	0.099	0.094
20×1B	240	0.156	0.150
32×1B	384	0.226	0.221

* averaged over inner and outer radii.

**Table 4.12 Normalized tip displacement of the curved beam*
(in-plane shear)**

mesh	neq.	AT+$(k_t^1)'$	AT+$(k_t^3)'$	AT+k_d
6×1B	72	0.179	0.171	0.162
12×1B	144	0.459	0.445	0.423
14×1B	156	0.507	0.492	0.468
20×1B	240	0.654	0.642	0.615
32×1B	384	0.724	0.717	0.696

* averaged over inner and outer radii.

**Table 4.13 Normalized tip displacement of the curved beam*
(out-of-plane shear, for all six elements)**

mesh size	neq.	mesh type A	mesh type B
12×1	144	0.940	0.943
14×1	156	0.949	0.951
20×1	240	0.950	0.952

* averaged over inner and outer radii.

4.1.5 Rectangular plate

This test, which was performed on a rectangular plate with dimensions a = 2.0, b = 2.0 or 10.0 , thickness h = 0.0001 Figure 4.7), Young's modulus E = 1.7472 $\times 10^7$ and Poisson's ratio ν = 0.3, considers factors such as aspect ratio b/a and boundary support. The applied loading can be either uniform pressure of intensity q = 10^{-4}, or a central concentrated load P = 4×10^{-4}, acting perpendicular to the plane of the plate along the -Z direction (that is, directing towards the plane of the plate as shown in Figure 4.7). The theoretical solutions can be seen in Table 4.14. Note that the plate is very thin since its length/thickness ratio is 2.0/0.0001 = 20000.

In the finite element discretization only a quarter of the plate was considered due to symmetry of geometry, boundary conditions and loading. The quarter plate was then represented by elements equally spaced along both the X and Y directions, and by mesh types A, B, C or D (see Figure 4.2). Since it is a plate problem, displacements in X and Y directions and rotations about Z axis were all constrained. In addition, the boundary conditions of the symmetrical sides were, Θ_x = 0.0 for the side parallel to X axis and Θ_y = 0.0 for the one parallel to Y axis. The central point then has constraints $\Theta_x = \Theta_y = 0.0$. Note that these conditions of symmetry applied to cases of fully clamped (C4) as well as simply supported at four sides (SS4). If the plate is fully clamped, the boundary conditions for the two clamped sides (X = 0.0 and Y = 0.0, see Figure 4.7) are W = Θ_x = Θ_y = 0.0. If the plate is simply supported at four sides, boundary conditions of W = Θ_x = 0.0 need be imposed on the side X = 0.0, and W = Θ_y = 0.0 on the side Y = 0.0.

Table 4.14 Displacement at center of the plate

boundary condition	aspect ratio b/a	uniform pressure over the plate	concentrated force at center
simply supported	1.0	4.062	11.60
simply supported	5.0	12.97	16.96
clamped	1.0	1.26	5.60
clamped	5.0	2.56	7.23

Table 4.15 Normalized central displacements of the rectangular plate

mesh	neq.	SS4, uniform pressure	
		b/a = 1.0	b/a = 5.0
1×1A	3	0.321	0.371
2×2A	12	0.681	0.789
4×4A	48	0.771	0.894
8×8A	192	0.794	0.920
8×8B	192	0.215×10^{-2}	0.869×10^{-2}
2×2C	12	0.721	0.835
4×4C	48	0.928	1.043
8×8C	192	0.982	1.027
1×1D	6	0.641	0.743
2×2D	24	0.912	1.043
4×4D	96	0.978	1.048

Table 4.16 Normalized central displacements of the rectangular plate

mesh	neq.	C4, concentrated load	
		b/a = 1.0	b/a = 5.0
2×2A	8	0.211×10^{-5}	0.384×10^{-5}
4×4A	40	0.517×10^{-4}	0.103×10^{-3}
8×8A	176	0.953×10^{-2}	0.191×10^{-2}
8×8B	176	0.953×10^{-2}	0.191×10^{-2}
2×2C	8	0.765×10^{-6}	0.154×10^{-5}
4×4C	40	0.728	0.355
8×8C	176	0.924	0.570
1×1D	4	0.127×10^{-6}	0.531×10^{-7}
2×2D	20	0.698	0.280
4×4D	88	0.904	0.501

Table 4.17 Normalized central displacements of the C4 plate (with different thickness)

mesh	neq.	h=0.0001 a/h=20000	h=0.01 a/h=200
2×2A	8	0.211×10^{-5}	0.209
4×4A	40	0.517×10^{-4}	0.318
8×8A	176	0.953×10^{-2}	0.853
2×2C	8	0.765×10^{-6}	0.758×10^{-1}
4×4C	40	0.728	0.742
8×8C	176	0.924	0.939
1×1D	4	0.127×10^{-6}	0.128×10^{-1}
2×2D	20	0.698	0.700
4×4D	88	0.904	0.904

Tables 4.15 and 4.16 list the finite element results for the plate, from which the following remarks may be made.

(1) The convergence study with aspect ratio b/a=1.0 is illustrated in Figures 4.8 and 4.9 which show that the finite element results approach the exact ones from below, or, the finite element results serve as lower bounds.

(2) Figures 4.8 and 4.9 also reveal that mesh type D seems to be more accurate than types A and C. Note that the comparison is made in terms of total element numbers.

(3) For the SS4 plate under loading of uniform pressure, mesh types A and B lead to substantially different results (comparing 8×8A with 8×8B). This means that mesh configurations are a crucial factor to the accuracy of finite element results. In reference [4.10] it was suggested that mesh type B did not possess favourable constraint index, and therefore, is not free of shear-locking. Table 4.15 seems to agree with the suggestion of reference [4.10]. However, it should be pointed out that type B gives good results in other problems investigated in the present study in which the plates are not very thin (see Sub-sections 4.1.3 and 4.1.4).

(4) Comparing results for mesh types A and C (also see Figure 4.8), the latter has a better performance, which is particularly true for the C4 plate. Note that mesh types A, B and C have the same numbers of nodes, elements and effective DOF. In reference [4.3] C4 thin plates discretized by mesh types A or B were analyzed and it was concluded that a new type of "shear-locking", the so-called reverse curvature bending, existed. The authors of reference [4.3] suggested to use a shear

scaling factor to account for the effects of this type of shear-locking. Our study here seems to suggest that by changing mesh configuration, for example, using mesh type C instead of A or B, the shear-locking can be avoided.

(5) It is also found that the shear-locking-like phenomenon associated with C4 plate becomes less severe if the thickness of the plate is increased. Table 4.17 compares normalized displacements for thicknesses 0.0001 and 0.01 m. In the latter case the normalized displacements with mesh type A are improved substantially.

(6) Another way to improve the performance of the elements under fully clamped boundary conditions is to employ finer meshes in areas near the clamped sides, as discussed in Sub-sections 4.1.3 and 4.1.4. For example, consider meshes that are originally of type A all over the plate. Then all the elements that are adjacent to the clamped sides are sub-divided into four triangles to form mesh type D along the clamped sides. Results for such meshes (identified by *) are compared with those consisting of entirely type A or D (Table 4.18). It can be seen that the refined (along the clamped sides) meshes improve the performance of type A meshes substantially, but do not outperform type D meshes, as expected. This certainly indicates that the refined meshes work effectively for problems with clamped boundary conditions. However, one may notice that 4×4A* does not perform better than 2×2A*, nor does 8×8A* than 4×4A*. This somewhat contradicts the general perception about finite element methods that the more elements are used, the closer the results are to the exact solution. Based on this and some of the examples in Section 4.2, the present study observes that the

above perception is correct, given that the convergence study is conducted on a series of meshes that are of the same pattern. Otherwise results may be misleading. This is particularly critical for complex stress distributions such as plates, shells and other three-dimensional structures (see Sub-section 4.2.3 for further discussion).

(7) To substantiate the point made in remark (6), a 4×4A** mesh is formed. This mesh covers 75% of the area of the quarter plate with type D, while the remaining 25% area around the central point of the plate is still of type A. The normalized central displacement of mesh 4×4A** is then found to be 0.836. This value is larger than the 0.698 from mesh 2×2A*. Note that 2×2A* also covers 75% of the plate with type D. Therefore, 2×2A* and 4×4A** possess the same discretization features. The comparison between these two meshes shows the trend that as element number is increased, finite element results become closer to the exact solutions.

(8) When the aspect ratio b/a is 5.0, the finite element results seem less satisfactory than those with aspect ratio 1.0. For the C4 plate, the normalized displacements are small compared to those of b/a=1.0; yet for the SS4 plate some of the normalized displacements exceed 1.0. This contradicts the observations we have had from all the foregoing examples: the finite element results approach the exact ones from below. Therefore, elements with large aspect ratio should not be used routinely.

(9) A 20×8C mesh for the plate with aspect ratio b/a = 5.0 gives normalized central displacements 0.995 for SS4 plate and 0.897 for C4 plate. The total numbers of unknown displacement are 481 and 452, respectively.

Table 4.18 Normalized central displacements of the C4 plate (b/a = 1.0, h = 0.0001)

mesh	neq.	normalized displacement
2×2A	8	0.211×10^{-5}
2×2A*	17	0.698
2×2D	20	0.698
4×4A	40	0.517×10^{-4}
4×4A*	61	0.681
4×4A**	76	0.836
4×4D	88	0.902
8×8A	176	0.953×10^{-2}
8×8A*	221	0.597

4.1.6 Circular plate (Study of effect of aspect ratios)

Although degenerate shell elements are capable of dealing with thin to thick shell problems, their performance deteriorates as the shells become "thin". On the other hand, the degenerate elements assume that the transverse normal stress is zero or negligible. This assumption is not true when the shells are sufficiently "thick". Therefore, it is of practical interest to find out the range of aspect ratios where the finite element results are accurate and reliable. The circular plate was chosen because it has analytical solution

[4.11] and has been studied by other researchers for the similar purpose [4.3, 4.12]. It was intended to investigate how the present elements perform for different radius/thickness ratios. According to reference [4.11], a circular plate of radius a and thickness h , and under uniform transverse loading q , has the following central deflections

$$\delta = \frac{qa^4}{64D}\left(1+\frac{16}{5(1-\nu)}\frac{h^2}{a^2}\right)$$

if it is fully clamped, and

$$\delta = \frac{qa^4}{64D}\left(\frac{5+\nu}{1-\nu}+\frac{16}{5(1-\nu)}\frac{h^2}{a^2}\right)$$

if it is simply supported. In the above formulas D is the flexural rigidity.

In the finite element representation only a quadrant of the plate was discretized and 54A, 54C and 81A (the integer indicating the number of elements) models were used (see Figures 4.10 and 4.11 for meshes 54C and 81A, all quadrilaterals are sub-divided into two triangles like those shown). Since it is a plate problem, all the displacements along the X and Y directions and the DDOF were constrained. The sides of X = 0.0 and Y = 0.0 were sides of symmetry (see Figures 4.10 and 4.11). Their boundary conditions were: $\Theta_y = 0.0$ for the side X = 0.0 and $\Theta_x = 0.0$ for the side Y = 0.0. For the arc the boundary conditions were $W = \Theta_x = \Theta_y = 0.0$ for fully clamped case, and W = 0.0 for simply supported case.

The radius of the plate is a = 1.0 m and its material properties are $E = 10^8$ N/m^2 and $\nu = 0.25$. The intensity of uniform loading is $q = 1.0$ N/m^2. For various thicknesses the normalized central displacements are listed in Table 4.19 and illustrated in Figure 4.12.

For the simply supported circular plate, the three meshes show less differences in the "thick" range (that is, small radius/thickness ratio) than in the "thin" regime. Considering mesh 81A, for thickness ranging from 0.001 to 0.25 m, or radius/thickness ratio 1000 to 4, the calculated normalized central displacements fall between $\pm 10\%$ of 1.0. As meshes become finer, for example, using mesh type D, the thickness range can be expected to further expand.

In general, for fully clamped plates, mesh configurations play a crucial role. However, in the present example, the change of mesh types does not greatly affect the results as does to the C4 rectangular plate (Sub-section 4.1.5), but the increase of element number clearly improves the performance of the elements. For instance, when employing mesh 54A, results with relative error less than $\pm 10\%$ can only be obtained for radius/thickness ratio ranging from 10 to 20 approximately. This range is expanded to 10-50 by increasing element numbers to 81. Better results can be expected by further increasing element numbers and changing mesh types, or more effectively, employing refined meshes in area that is near the clamped arc. Figure 4.13 compares meshes 54A and 54A* which is different from 54A in that the quadrilaterals adjacent to the clamped edge are sub-divided using mesh type D instead of A. The total number of unknown displacements of the mesh 54A* is 95 while that of the mesh 54A is 77. It can be seen

that the range of radius/thickness ratio where finite elements yield error of less than $\pm 10\%$ is now expanded to 10-200. With the refined mesh (around the clamped edge), the performance of the elements is improved substantially in the "thin" range. However, when the clamped plate is sufficiently thick, employing refined meshes may not be necessary.

Table 4.19 Normalized central displacement of the circular plate

fully clamped				
h	a/h	54A (77)*	54C (77)	81A (113)
0.0001	10000	2.2×10^{-4}	4.5×10^{-4}	1.2×10^{-3}
0.001	1000	2.1×10^{-2}	0.04	0.11
0.0015	667	4.6×10^{-2}	0.07	0.21
0.005	200	0.33	0.35	0.70
0.01	100	0.62	0.62	0.87
0.02	50	0.83	0.84	0.94
0.05	20	0.95	0.95	0.98
0.1	10	1.01	1.00	1.03
0.25	4	1.25	1.24	1.23
0.5	2	1.79	1.74	1.69
fully simply supported				
h	a/h	54A (89)	54C (89)	81A (131)
0.0001	10000	0.79	0.74	0.83
0.001	1000	0.88	0.83	0.92
0.0015	667	0.90	0.87	0.93
0.005	200	0.91	0.95	0.95
0.01	100	0.93	0.96	0.96
0.02	50	0.95	0.97	0.97
0.05	20	0.97	0.97	0.98
0.1	10	0.98	0.98	0.98
0.25	4	1.03	1.02	1.03
0.5	2	1.12	1.14	1.12

* The integer inside the parentheses indicates the total number of equations solved.

4.2 Shell Problems

As a continuing effort of the numerical studies and assessments of the performances of the shell elements presented in the previous chapter, in this section various shell problems are investigated. The chosen problems include a twisted beam, two singly-curved shells (the pinched cylinder, and the Scordelis-Lo roof), and three doubly-curved shells (a spherical ring loaded with its own weight, a sphere loaded at poles, and a hemisphere with alternating point loads at the equator). The twisted beam, the Scordelis-Lo roof and the hemisphere are from MacNeal and Harder's obstacle course [4.1] while the remaining problems are selected to enrich the obstacle course so as to further demonstrate the accuracy, reliability and versatility of the presented elements.

4.2.1 Twisted beam

The twisted beam, as shown in Figure 4.14, is subjected to unit force at the tip along the Y and Z directions to represent respectively, the in-plane and out-of-plane shears. The geometrical properties of the beam are: length = 304.8 mm (12.0 in), width = 27.94 mm (1.1 in), depth = 8.13 mm (0.32 in), twist angle = 90° (root to tip). The material properties are $E = 20.0 \times 10^{10}$ N/m^2 (29.0×106 psi) and $\nu = 0.22$. The theoretical solutions of the tip displacement were given in reference [4.1] as 0.0446 mm (0.001754 in) for in-plane shear and 0.138 mm (0.005424 in) for out-of-plane shear. This example tests the ability for an element to represent spatial bending actions as well as the effects of warping.

In the finite element representation three discretizations were considered: 6×2, 12×2, and 24×2. For example, Figure 4.14 gives the 6×2 mesh. In all meshes the six DOF of the nodes associated with the fixed end were constrained while the remaining DOF were unconstrained. The finite element results are included in Table 4.20.

Similar to the plane stress beam problem, CST+k_d and CST+k_t^1 have the same performance: with the mesh 6×2 they give normalized tip displacements that are well above 0.9 for the in-plane shear case while the accuracy of the out-of-plane shear case is less than satisfactory. Comparing CST+k_d (or k_t^1) with CST+k_t^3, it can be observed that improvements of the former over the latter are noticeable only when coarse mesh was used. For the AT-based elements, AT+$(k_t^1)'$ is no longer identical to AT+k_d, yet the differences of computed results between them were not substantial. Moreover the normalized tip displacements of the out-of-plane case became higher than 0.9 when the AT-based elements were employed. One may observe that the convergence behaviour of the finite element results is consistently approaching the exact value from below.

4.2.2 Pinched cylinder

This example is not part of the obstacle course but has been studied by a number of authors, for example, [4.10, 4.13-16]. It is one of the most severe tests available to determine the ability of shell elements to describe both inextensional bending modes and very complex membrane stress states. There is also significant coupling between membrane and bending actions in this problem.

Table 4.20 Normalized tip displacement of the twisted beam

in-plane shear							
mesh	neq.	AT +			CST +		
		$(k_t^1)'$	$(k_t^3)'$	k_d	k_t^1	k_t^3	k_d
6×2	108	0.950	0.945	0.944	0.967	0.875	0.967
12×2	216	0.982	0.981	0.981	0.983	0.977	0.983
24×2	432	0.991	0.991	0.991	0.989	0.989	0.989
out-of-plane shear							
mesh	neq.	AT +			CST +		
		$(k_t^1)'$	$(k_t^3)'$	k_d	k_t^1	k_t^3	k_d
6×2	108	0.933	0.925	0.920	0.744	0.684	0.744
12×2	216	0.993	0.991	0.986	0.835	0.827	0.835
24×2	432	0.996	0.995	0.993	0.889	0.884	0.889

The cylinder is with rigid end diaphragms and subjected to point loads as shown in Figure 4.15. The exact deflection at the loading points is 0.463×10^{-3} mm (0.18248×10^{-4} in) as quoted from [4.10, 4.13-16]. Only one-eighth of the cylinder was considered due to symmetry. The boundary conditions were therefore, U = V = Θ_z = 0 for arc AD, V = Θ_x = Θ_z = 0 for side DC, U = Θ_y = Θ_z = 0 for side AB and W = Θ_x = Θ_y = 0 arc BC. The geometrical and material properties are: R = 0.762 m (300 in), L = 1.524 m (600 in), thickness = 76.2 mm (3 in), E = 20.7×10^{10} N/m^2 (3.0×106 psi) and ν = 0.3. The point load was F = 4.459 N (1.0 lb) for the problem, or 1.115 N (0.25 lb) for the finite element models.

The finite element meshes used and results acquired are given in Table 4.21. For this problem CST+k_t^1 performs better than CST+k_t^3 and CST+k_d. However, the difference between CST+k_t^1 and CST+k_d is not significant. The same observation can be made on AT+$(k_t^1)'$, AT+$(k_t^3)'$ and AT+k_d. Note that meshes 4×4C, 8×8C and 20×20C are added to study the effect of mesh configuration, which indicates that mesh type C, having the same numbers of nodes and unknown displacements as type A, seems to have mixed behaviours: out-performing type A for mesh sizes 4×4 and 8×8, yet falling behind for mesh size 12×12. This may suggest that improvements of type C over A are mesh-dependent and are weakened as meshes become finer. It should be noted that results from different mesh types are problem-dependent, which again demonstrate the importance of element configuration to the performance of triangular elements.

Figures 4.16 and 4.17 contain results of the present elements and that from refe ence [4.10], which show normalized displacement at point C against, respectively, total number of nodes and elements. It can be observed that the present elements have almost the same rate of convergence as the element of reference [4.10]. Note that the element reported in the latter was based on hybrid stress formulation with its assumed stresses given by equation (3.22). In applications for linear problems the present hybrid strain elements and the hybrid stress element of reference [10] yielded no distinction. The only differences are that in reference [4.10] the DDOF were of fictitious stiffnesses and that it used "macro-elements" each of which consisted of four non-planar triangles. The interior (fifth) node of the macro-element was determined by a scheme explained in reference [4.10] and did not necessarily lie on the surface of the cylinder, while in the

present study all nodes were situated exactly on the surface. Results from reference [4.10] were compared with the present ones because the features of its element seemed to be closer to the present study than some others, such as those in references [4.14-15]. The latter two references reported faster convergence. However, reference [4.14] considered the discrete Kirchhoff theory (DKT) together with a 3-node curved membrane element which employed the Margurre membrane strains. The element in reference [4.14], denoted as DKT+CST* there, however, did not exhibit monotonically convergent pattern. That is, the finite element results of reference [4.14] may approach the exact value from below, or from above, or both. On the other hand, reference [4.15] added a "rapidly converged stability matrix" to the DKT and AT elements. Consequently, while the convergence rate in reference [4.15] was improved, lower or upper bound feature of the convergence could not be assured. In this regard, the elements currently being presented are more reliable in the sense that their convergent pattern is consistent (approaching the exact value from below), and that their results are, in general, lower bound to the exact solution. The relatively slow convergence rate reflects the absence of coupling between membrane and bending actions in the present elements as they are flat. Therefore, for this particular problem the finite element used for the approximation should have the coupling between membrane and bending.

As indicated in the discussions in Section 4.1, mesh type D has superior performance in terms of both accuracy and convergence in most of the cases tested. For the pinched cylinder, mesh type D was employed to form meshes 4×4D, 5×5D, 6×6D and 8×8D. The results of these meshes are given in Table 4.22. It is interesting to note

that, when using CST+k_d and CST+k_t^1, the results from type D meshes were smaller than those from the corresponding type A meshes. For instance, with the element CST+k_d, 4×4D gave a displacement 0.5530 mm (0.02177 in) while 4×4A yielded 0.7087 mm (0.02790 in). Results from reference [4.14] showed similar trend, that is, mesh type A out-performed type D meshes. In addition to the pinched cylinder, similar trends were also observed for the Scordelis-Lo roof and the hemisphere in reference [4.14]. For the present elements, this trend does not apply to results obtained with the AT-based elements, nor does it to problems of the Scordelis-Lo roof and the hemispherical shell except for mesh 4×4A* and D* (see Tables 4.23 and 4.28). Note that the results from type D meshes exhibit monotonic convergence on their own. Given that all the convergence requirements are met, which is the case for the present elements, the above discussion again suggests that, convergence studies should be conducted on the same type of meshes, or on meshes having same pattern (see Sub-section 4.1.5). Simple comparisons that are made in terms of element numbers, node numbers or total unknowns may be misleading.

Table 4.22 also shows that mesh type D with the elements AT+k_d and AT+$(k_t^1)'$ out-performs mesh type A with the AT-based elements. The convergence rate of mesh type D is, however, comparable with that of type A as indicated in Figure 4.16.

Table 4.21 Normalized displacement of the pinched cylinder (at point of load)

mesh	neq.	CST +		
		k_d	k_t^1	k_t^3
4×4A	96	0.153	0.154	0.150
4×4C	96	0.171	0.173	0.156
5×5A	150	0.247	0.249	0.245
6×6A	216	0.346	0.347	0.343
8×8A	384	0.518	0.519	0.516
8×8C	384	0.569	0.570	0.562
10×10A	600	0.643	0.643	0.641
12×12A	864	0.730	0.730	0.728
12×12C	864	0.699	0.700	0.693
15×10A	900	0.768	0.769	0.767
16×10A	960	0.784	0.785	0.783
mesh	neq.	AT +		
		k_d	$(k_t^1)'$	$(k_t^3)'$
4×4A	96	0.181	0.183	0.183
4×4C	96	0.182	0.187	0.186
5×5A	150	0.283	0.285	0.285
6×6A	216	0.384	0.386	0.386
8×8A	384	0.555	0.557	0.556
8×8C	384	0.592	0.593	0.593
10×10A	600	0.675	0.676	0.676
12×12A	864	0.758	0.758	0.758
12×12C	864	0.729	0.731	0.730
15×10A	900	0.789	0.789	0.789
16×10A	960	0.803	0.803	0.803

Table 4.22 Normalized displacement of the pinched cylinder (at point of load application)

mesh	neq.	AT +		CST +	
		k_d	$(k_t^1)'$	k_d	k_t^1
4×4D	192	0.297	0.299	0.119	0.120
5×5D	300	0.430	0.432	0.181	0.182
6×6D	432	0.542	0.544	0.254	0.255
8×8D	768	0.695	0.697	0.411	0.412

4.2.3 The Scordelis-Lo roof

The cylindrical roof shown in Figure 4.18 was loaded vertically by its uniform dead weight 620.55 × 10^3 N/m^2 (90 lb/in2) and supported by rigid diaphragms at both ends. Note that in this roof a substantial part of the strain energy is due to membrane. The coupling of membrane and bending actions is significant. This problem was included in reference [4.1] as one of the tests in the obstacle course. The pertinent data of the roof are: R = 635 mm (25 in), L = 1.27 m (50 in), thickness h = 6.35 mm (0.25 in), arc BAB=80°, E = 29.79 × 10^{11} N/m^2 (4.32×108 psi) and ν = 0. The exact value of vertical displacement at point C is - 7.838 mm (- 0.3086 in). By making use of geometrical and loading symmetry, and imposing the following boundary conditions, U = W = Θ_y = 0 at arc AB, free at side BC, V = Θ_x = Θ_z = 0 at arc DC, and U = Θ_y = Θ_z = 0 at side AD, only one quarter of the roof was solved. It should be pointed out that the uniform dead weight was given in units of surface pressure. It was cast into its corresponding consistent nodal loads, the process being that: (1) within each element the

vertically loaded dead weight was first transformed into surface pressures along the local r-s-t directions; (2) such surface pressures together with the displacement interpolation matrix N in equation (3.34) constituted the integrands which upon integration over the element area yielded the consistent loads, see the second integral of equation (3.12b); and (3) the consistent loads were then transformed back to the global co-ordinate systems prior to assembling. The finite element results are presented in Tables 4.23 and 4.24, and Figure 4.19.

With reference to Tables 4.23 and 4.24, accuracy and convergence were substantially improved by modelling membrane behaviours of the roof with the AT instead of the CST. Results from the present study and references [4.10, 4.14] are plotted in Figure 4.19. It can be observed that the convergence rate of CST+k_d is slightly lower than those of references [4.10] and [4.14], yet the AT+k_d performs very well that it reaches 97.1% of the exact solution even with a 4×4D mesh. When the total element number is larger than 200, approximately, mesh type A seems to perform better than type D. Note that the element of reference [4.14] is a 3-node curved triangular one which does not yield as satisfactory results as the present 3-node flat triangular elements. Furthermore, reference [4.17] used quadrilateral shell elements to investigate the same problem and reported - 7.506 mm (- 0.2955 in) for the displacement at point C for a 8×8 mesh. In the present study, results that were less than - 7.506 mm (0.2955 in) were obtained with meshes 10×10A, for example, or 4×4D and finer meshes. An interesting point from Figure 4.19 is that element AT+k_d with type D mesh is almost independent of mesh sizes, except for the 2×2D case.

Table 4.23 Normalized displacement of the Scordelis-Lo roof

mesh	neq.	CST +		
		k_d	k_t^1	k_t^3
2×2A	33	0.190	0.192	0.172
4×4A	111	0.451	0.452	0.445
5×5A	168	0.586	0.587	0.578
6×6A	237	0.684	0.685	0.677
8×8A	411	0.802	0.803	0.796
8×10A	513	0.838	0.839	0.834
8×12A	618	0.863	0.863	0.860
10×10A	633	0.885	0.886	0.880
10×14A	885	0.902	0.902	0.899
2×2D	57	0.513	0.526	0.456
4×4D	207	0.773	0.774	0.754
5×5D	318	0.837	0.837	0.824
6×6D	453	0.876	0.876	0.866
8×8D	795	0.918	0 918	0.912
8×10D	993	0.936	0.936	0.932
8×12D	1194	0.951	0.951	0.947

Table 4.24 Normalized displacement of the Scordelis-Lo roof

mesh	neq.	AT +		
		k_d	$(k_t^1)'$	$(k_t^3)'$
2×2A	33	0.309	0.318	0.313
4×4A	111	0.600	0.603	0.603
5×5A	168	0.739	0.744	0.742
6×6A	237	0.827	0.831	0.830
8×8A	411	0.909	0.912	0.911
8×10A	513	0.927	0.929	0.928
8×12A	618	0.940	0.941	0.941
10×10A	633	0.981	0.984	0.983
10×14A	885	0.998	0.999	0.999
2×2D	57	0.910	0.934	0.922
4×4D	207	0.971	0.974	0.972
5×5D	318	0.976	0.977	0.976
6×6D	453	0.977	0.978	0.977
8×8D	795	0.977	0.978	0.977
8×10D	993	0.977	0.978	0.978
8×12D	1194	0.980	0.980	0.980

To study the effect of thickness on the displacement, meshes 4×4A and 8×10D were chosen (the former being considered as coarse and the latter as fine) for calculations of 13 different thicknesses. Results are included in Figure 7.20. For both meshes and aspect ratio (R/h) from 5 to 1000 the AT+k_d and CST+k_d elements exhibited the same behaviours, though the AT+k_d element out-performed the CST+k_d element as expected. For small R/h ratio, or for "thick" shells, mesh 4×4A yielded little difference from mesh 8×10D, while in the "thin" region, mesh size played a crucial role, so did the element formulation which was mesh-dependent (mesh 8×10D displayed less discrepancy between the AT+k_d and the CST+k_d elements than 4×4A did for "thin" shells). One possible explanation is that for thin shells a correct representation of the true stress distribution is important and therefore is sensitive to the mesh types. The conclusion for this problem is that in order to provide good results for "thin" problems, a large number of AT+k_d elements is preferred, while for "thick" problems relatively coarse meshes with the AT+k_d or CST+k_d elements are recommended.

Note that no exact solutions are available for thickness other than h = 6.35 mm (0.25 in). In reference [4.17] a finite element result of - 0.655 mm (- 0.02577 in) was reported for thickness h = 63.5 mm (2.5 in), which was based on the quadrilateral element derived there. The mesh size used was 6×6. This result implies that the displacement at point C is approximately proportional to h^{-1}, or, the roof is membrane-dominant. Loosely speaking, the present elements lead to results that are proportional to h^{-2}. Since the roof exhibits significant coupling between the membrane and bending

actions, the present results make more sense because they indicate that the roof is not membrane-dominant, nor is it governed by bending action to a large extent.

4.2.4 Spherical ring loaded with its own weight

The spherical ring, the meridian of which is shown in Figure 4.21, is clamped at its lower edge and free at the upper one. The material properties of the ring are: $E = 30.0\times10^9$ N/m^2, $\nu = 1/6$ and the weight is along the vertical direction and measured at 3×10^3 N/m^2. With a thickness of 60.0 mm, the radial displacement of the free edge, quoted from reference [4.18], is - 238.0 mm, or the vertical displacement of that edge is - 220.2 mm. By making use of symmetry, only a quadrant of the ring was modeled by finite elements. The boundary conditions are, $U = V = W = \Theta_x = \Theta_y = \Theta_z = 0.0$ along the clamped edge, $U = \Theta_y = \Theta_z = 0.0$ for nodes with $X = 0.0$, and $V = \Theta_x = \Theta_z = 0.0$ for nodes with $Y = 0.0$. Four meshes were formed, 4×4A, 4×4C, 6×6A and 6×6C. The finite element results in Table 4.25 show that using the AT-based elements the problem can be adequately represented with relatively coarse meshes such as 4×4 and 6×6. One possible explanation for the excellent results with these coarse meshes is that the stress distribution is relatively even in this example.

Table 4.25 Normalized vertical displacement of the spherical ring

mesh	neq.	AT +		CST +	
		k_d	$(k_t^1)'$	k_d	k_t^1
4×4A	96	0.901	0.919	0.759	0.762
6×6A	216	0.956	0.967	0.815	0.817
4×4C	96	0.935	0.953	0.790	0.795
6×6C	216	0.980	0.991	0.837	0.840

4.2.5 Spherical shell with point load at the pole

This point loaded sphere as shown in Figure 4.22 is a severe test for finite elements because it contains regions of large bending stresses, regions where membrane stresses predominate and a region of stress concentration. Note that, in the present finite element study, only one quadrant of half of the sphere was discretized due to the axi-symmetry of the problem. The meshes were formed by uniformly dividing the longitude and simultaneously spacing the colatitude in ratio 1:2:3...:N approximately so as to adequately account for the effect due to stress concentration around the pole. Therefore, for the meshes used, the latitudinal spacing from the equator to the pole was as follows:

4×4A	36°, 27°, 18° and 9°;
6×6A	25.714°, 21.429°, 17.143°, 12.857°, 8.571° and 4.286°;
8×8A	20°, 17.5°, 15°, 12.5°, 10°, 7.5°, 5° and 2.5°; and
9×9A,10×9A	18°, 16°, 14°, 12°, 10°, 8°, 6°, 4° and 2°.

Note that the sum of the latitudinal spacing of each mesh is 90°.

The boundary conditions were: $W = \Theta_x = \Theta_y = 0$ for nodes on the X-Y plane, $V = \Theta_x = \Theta_z = 0$ for nodes on the X-Z plane, and $U = \Theta_y = \Theta_z = 0$ for nodes on the Y-Z plane. The mesh labelling is that, the first number corresponds to the spacing of the longitudinal direction, and the second indicates the spacing of the latitudinal direction.

The radial displacement of the pole is 0.262×10^{-2} mm (0.1033×10^{-3} in) which is obtained based on shallow shell theory [4.11]. The corresponding geometrical and material properties of the shell were, radius = 254 mm (10.0 in), thickness = 5.08 mm (0.2 in), $E = 6.985 \times 10^9$ N/m^2 (10^6 psi) and $\nu = 0.3$. The point load at the pole was set to 4.459 N (1 lb) for the problem. That is, it was set to 1.115 N (0.25 lb) for the finite element models. The normalized pole radial displacements are then listed in Table 4.26. Figure 4.23 presents the distribution of radial displacements along the colatitude where the finite element results using the 9×9A mesh with element AT+k_d are compared with those from the shallow shell theory [4.11]. Note that the shallow shell theory was calculated and compared with up to 30° only. The finite element results agree very well with the theoretical ones except at the pole where the theoretical displacement solution is not valid. Finally, it should be pointed out that the radial displacement at the equator is predicted as -0.26×10^{-2} mm (-1.0235×10^{-3} in) by the AT+k_d element with the 9×9A mesh, which is very close to -0.263×10^{-2} mm (-1.035×10^{-3} in). The latter is the solution from membrane theory of shell [4.19].

Compared with reference [4.19], which used cubic interpolation functions for the two in-plane displacements and is therefore softer than the present elements, the present elements produce more accurate results with coarse meshes. For example, the normalized

radial displacement at the pole was 0.379 from reference [4.19] and the present study gave 0.413 to 0.432. As meshes were refined results from reference [4.19] became larger than the theoretical solution by 5% with a 12×12 mesh, while the present results were smaller than the theoretical one by less than 5% with meshes 9×9A and 10×9A. Considering the invalidity of the theoretical solution at the pole and the comparisons made above, it may be concluded that, except for the singular area near the pole, the present elements can provide results with good accuracy.

Table 4.26 Normalized radial displacement at the pole

mesh	neq.	AT +		CST +	
		k_d	$(k_t^1)'$	k_d	k_t^1
4×4A	84	0.430	0.432	0.413	0.414
6×6A	198	0.769	0.770	0.760	0.760
8×8A	360	0.913	0.913	0.911	0.911
9×9A	461	0.958	0.958	0.957	0.957
10×9A	512	0.959	0.960	0.958	0.958
6×6A*	198	0.741	0.741	0.716	0.717
8×8A*	360	0.861	0.861	0.870	0.870
9×9A*	461	0.877	0.878	0.881	0.881
10×9A*	512	0.879	0.879	0.882	0.882

Since there is stress concentration around the pole, the choice of mesh configuration in the area near the pole is important. Results with meshes 6×6A, 8×8A, 9×9A and 10×9A with meshes 6×6A*, 8×8A*, 9×9A* and 10×9A* are included in Table 4.25 for comparison. Note that the latitudinal spacing of the latter four meshes was:

6×6A*	25°, 20°, 18°, 12°, 10° and 5°;
8×8A*	20°, 17.5°, 15°, 12.5°, 5°, 5° and 5°; and
9×9A*, 10×9A*	20°, 15°, 12.5°, 10°, 10°, 7.5°, 5°, 5° and 5°.

In this example the spacing around the pole was kept at 5°.

Results in Table 4.26 clearly demonstrates the better accuracy gained due to finer discretizations around the pole. It is also interesting to note that the meshes 8×8A* to 10×9A* with the CST-based elements gave slightly larger results than with the AT-based elements. This phenomenon was also observed in the study of the hemispherical shell to be considered in the following sub-section. It contradicts previously made remark that the AT-based elements out-performed the CST-based ones. One possible explanation is that it may indicate that meshes 6×6A through 10×9A are more appropriate to the problem than their counterparts 6×6A* through 10×9A*.

4.2.6 Hemispherical shell with alternating point loads at equator

The hemisphere shown in Figure 4.24 was included as one of the tests of the obstacle course and is a challenging test for an element's ability to represent inextensional modes since it exhibits almost no membrane strains. In addition, this problem is useful

in checking the ability to handle rigid body rotations about normal to the shell surface because large sections of the shell rotate almost as a rigid body under the given loads.

The description of the problem is: radius = 254 mm (10.0 in), thickness = 1.016 mm (0.04 in), E = 4.706×10^{11} N/m^2 (6.825×107 psi) and $\nu = 0.3$. By making use of symmetry of geometry, only one quadrant of the hemisphere was analyzed and each of the two alternating point loads on the quadrant was F = 8.91 N (2.0 lb). With such geometry and loading, reference [4.1] found that the solution for the displacements of the point under the load was 2.347 mm (0.0924 in). Note that this value is a theoretical lower bound [4.1].

The boundary conditions in this case were: free for nodes on the X-Y plane, V = $\Theta_x = \Theta_z = 0$ for nodes on the X-Z plane and U = $\Theta_y = \Theta_z = 0$ for nodes on the Y-Z plane. Finally, the pole was fixed, that is, all of its six DOF were set to zero.

In the finite element representation, mesh type A was first employed. Regular A, regular A*, irregular A, and irregular A* meshes were considered. Regular A meshes were formed by equally dividing longitude, and dividing colatitude according to the ratio 1:2:3...:N. Except for the triangles that were generated near the pole, each of all the quadrilaterals was sub-divided into two triangles as shown in Figure 4.24. Regular A* meshes, on the other hand, were designed to have a 5° latitudinal spacing around the pole. Irregular meshes differ from regular meshes in the way in which the areas around the two loading points were discretized. Such meshes were generated by adding one more node to each of the two quadrilaterals near the loading points and sub-dividing each of the quadrilaterals into four triangles. Clearly, irregular meshes express better the stress

concentrations near the loading points. For both the regular and irregular meshes, the spacing of the latitude was:

4×4A	36°, 27°, 18° and 9°;
6×6A	25.714°, 21.429°, 17.143°, 12.857°, 8.571° and 4.286°;
6×6A*	25°, 20°, 18°, 12°, 10° and 5°;
8×8A	20°, 17.5°, 15°, 12.5°, 10°, 7.5°, 5° and 2.5°;
8×8A*	20°, 17.5°, 15°, 12.5°, 10°, 5°, 5° and 5°;
9×9A, 10×9A	18°, 16°, 14°, 12°, 10°, 8°, 6°, 4° and 2°;
9×9A*, 10×9A*	20°, 15°, 12.5°, 10°, 10°, 7.5°, 5°, 5° and 5°;
10×10A	16.364°, 14.727°, 13.091°, 11.455°, 9.818°, 8.182°, 6.545°, 4.909°, 3.273° and 1.636°;
10×10A*	15°, 13°, 12°, 11°, 10°, 8°, 6°, 5°, 5° and 5°;
12×12A	13.846`, 12.692°, 11.538°, 10.385°, 9.231°, 8.077°, 6.923°, 5.729°, 4.615°, 3.462°, 2.308° and 1.154°;
12×12A*	12°, 11°, 10°, 9°, 8°, 7°, 6°, 6°, 6°, 5°, 5° and 5°; and
13×13A	13°, 12°, 11°, 10°, 9°, 8°, 7°, 6°, 5°, 4°, 2.5°, 1.5° and 1°.

Mesh type D was then included. It also made use of the foregoing latitude spacing.

In the study of the spherical shell of Sub-section 4.2.5, meshes with 5° latitudinal spacing around the pole were also employed, but they seemed to be less satisfactory than those strictly followed 1:2: ...:N ratio. The difference is that, in this example there was no stress concentration effect around the pole, while stress concentrations were present

in the spherical shell considered in Sub-section 4.2.5. Results for meshes A, A* and D, regular and irregular, are presented in Tables 4.27 through 4.29.

In passing, the following remarks are to be included.

(1) Comparing meshes that strictly followed the 1:2:3...:N ratio of colatitudinal spacing with those whose latitudinal spacing around the pole was kept at 5° (see Table 4.27), the latter ones clearly demonstrate a faster convergence. One possible explanation is that, since there was no stress concentration around the pole, the 5° latitudinal spacing was adequate to represent the stress state around the pole. At the same time, the latitudinal spacing near the equator was allowed to become finer (than those following the 1:2:3...:N ratio), resulting in the better convergence rate.

(2) Irregular meshes improved results over regular meshes to a larger extent. The improvement was more substantial with coarse meshes. For example, by applying the AT+k_d element the 4×4A irregular mesh led to results that were 1.83 times of that from the 4×4A regular mesh. When the mesh size was increased to 9×9, the improvement of 9×9A irregular mesh fell to 1.43 times of that of 9×9A regular.

(3) It is interesting to note that, for all irregular meshes the AT-based elements out-performed their CST-based counterparts while for some regular meshes the CST-based elements gave higher normalized displacements than the AT-based ones. For instance, this observation occurred in regular meshes 4×4A through 10×9A and 6×6A* through 10×9A*. Sub-section 4.2.5 encountered the same phenomenon

and it was explained that those meshes were not fine enough to capture the complex state of stress of the problem at hand. In this regard, irregular meshes seem to be better than the regular ones due to their capability to express the effect of stress concentration near the loading points.

(4) The performance of the four groups of meshes, regular A and A*, irregular A* and D* in conjunction with the AT+k_d element, are compared in Figure 4.25. It can be seen that with irregular A mesh it was possible to use fewer elements than meshes A, A* and D*, if the same normalized displacement was to be achieved. The explanation is again that irregular A mesh was able to capture the stress concentration effect around the points of loading. In terms of convergence rate, the performances of the four mesh groups have no difference.

(5) Among various publications that had studied the present shell problem, references [4.14] and [4.15] reported more accurate results. The results in reference [4.14], which employed a curve shell element, show monotonic convergence. In reference [4.15], a stabilization matrix was added to circumvent rank deficiency of the stiffness matrix and to accelerate the convergence. While these two goals, of providing accurate results and circumventing rank deficiency, seemed to have been achieved in reference [4.15], its formulation failed to establish a monotonically convergence pattern.

(6) It is interesting to point out that, in many cases (for examples, see Tables 4.1, 4.2, 4.20 and 4.24), the AT-based elements in conjunction with mesh type D, AT+$(k_t^3)'$ gives results that lie between AT+k_d and AT+$(k_t^1)'$. This is also true

for the hemispherical shell studied in this sub-section, as demonstrated in Table 4.29. In fact, element AT+$(\bar{k}_t^3)'$ with D* mesh seemed to be the "best choice" for modelling the hemisphere in that it yielded fast convergence and satisfactory accuracy while it did not produce higher than 1.0 normalized displacements (see Figure 4.26).

Table 4.27 Normalized displacement at points of loading

regular mesh	neq.	AT +		CST +	
		k_d	$(k_t^1)'$	k_d	k_t^1
4×4A	96	0.102	0.112	0.108	0.115
6×6A	216	0.199	0.209	0.205	0.211
8×8A	384	0.375	0.387	0.377	0.385
9×9A	486	0.491	0.503	0.491	0.498
10×9A	540	0.558	0.570	0.566	0.573
10×10A	600	0.620	0.632	0.618	0.625
12×12A	864	0.892	0.904	0.886	0.893
13×13A	1014	1.014	1.024	1.007	1.013
6×6A*	216	0.219	0.230	0.221	0.228
8×8A*	384	0.375	0.387	0.377	0.385
9×9A*	486	0.531	0.544	0.525	0.533
10×9A*	540	0.600	0.613	0.601	0.609
10×10A*	600	0.713	0.726	0.700	0.708
12×12A*	864	1.029	1.040	1.012	1.018

Table 4.28 Normalized displacement at points of loading

irregular mesh	neq.	AT +		CST +	
		k_d	$(k_t^1)'$	k_d	k_t^1
4×4A*	108	0.187	0.227	0.134	0.155
6×6A*	228	0.425	0.473	0.308	0.332
8×8A*	396	0.598	0.631	0.430	0.445
9×9A*	498	0.720	0.751	0.509	0.522
10×9A*	552	0.745	0.771	0.505	0.516
10×10A*	612	0.771	0.799	0.712	0.727
12×12A*	876	1.180	1.194	1.101	1.109

Table 4.29 Normalized displacement at point of loading

mesh	neq.	AT +		
		k_d	$(k_t^1)'$	$(k_t^3)'$
4×4D*	168	0.133	0.191	0.172
6×6D*	396	0.466	0.619	0.574
8×8D*	720	0.810	0.973	0.923
10×9D*	1020	0.886	1.031	0.972

4.2.7 Discussions

One may notice that some of the meshes investigated in Section 4.2.6 reported normalized displacements higher than 1.0. Since in most of the cases studied so far, including all the plate problems, the twisted beam, all the singly curved shells, and the spherical ring loaded with its own weight, the present finite element results provide lower bounds to the exact solutions, this sub-section is intended to discuss some of the causes of higher than 1.0 normalized displacements associated with deep spherical shells. In fact, when the 13×13A regular mesh used for the hemispherical shell of Sub-section 4.2.6 was applied to the spherical shell of Sub-section 4.2.5 with the corresponding boundary conditions, the normalized radial displacement at the pole became 1.062, which was also higher than 1.0. The possible causes are elaborated in the followings.

(1) One of the possible causes is concerned with the element aspect ratio. In Sub-section 4.1.5 it was observed that normalized displacements exceeded 1.0 with elements having aspect ratio of 5.0 for the SS4 plate. It was suggested that such aspect ratio should be avoided. The regular and irregular meshes generated for the problem of Section 3.6, however, included elements with high element aspect ratio, especially around the pole. For example, in the 13×13A regular mesh the element aspect ratio of the row having 13 elements connected to the pole was 8.7. Elements with such aspect ratio can be avoided by gradually reducing the number of elements in each row in the area around the pole, see for instance Figure 4.8 of reference [4.10]. Three such finite element discretizations and their corresponding results for the hemispherical shell of Sub-section 4.2.6 are listed

in Table 4.30. Note that in mesh size labelling, the two integers indicate numbers of rows (latitudinal) and columns (longitudinal) of the meshes. The number of elements of each of the last five rows, counting from the equator, was reduced by 2, leaving two elements connected to the pole. In this case the element aspect ratio was close to 1.0. Results are presented in Table 4.30 which show that the problem of higher than 1.0 displacement still exists.

Table 4.30 Normalized displacement at points of loading

mesh size	neq.	AT +		CST +	
		k_d	$(k_t^1)'$	k_d	k_t^1
14×10A	720	0.856	0.870	0.837	0.844
15×10A	780	0.911	0.923	0.889	0.896
18×10A	960	1.076	1.088	1.053	1.060

(2) It should be mentioned that in the present study, all nodes were allocated exactly on the mid-surface of the shell. Therefore, the area of the mid-surface, thus the volume of the shell, were under-estimated. In turn, the element stiffness matrix was under-estimated. Similarly, the consistent load vector was under-estimated. However, for the problems of Sub-sections 4.2.5 and 4.2.6, only concentrated loads were present, hence the right hand side (RHS) of equation (3.13) was considered "exact". Consequently, the displacement will be over-estimated. This over-estimate is with respect to the displacement from a finite element solution in which the area of the mid-surface of the shell was evaluated exactly. Numerical

results showed that when meshes were sufficiently fine, the area of the mid-surface represented by a large number of flat triangles was very close to the exact mid-surface area. For example, for the regular meshes 12×12A and 13×13A of Section 3.6, the finite element approximations to the mid-surface area were 99.356% and 99.436%, respectively, of the exact value 0.1013 m^2 (157.0796 in^2). However one question remains how the small difference in area will be manifested in the displacement solutions ?

(3) To answer the above question, the following study was performed. Firstly, the ratio of the exact mid-surface area to the area of mid-surface represented by flat triangular shell elements was determined. Then, the finite element solution was obtained by multiplying each of the mid-surface area from the flat triangular finite element representation with the ratio evaluated in the first step. The results proved the argument of remark (2) above, that the displacement solution from the presently proposed flat triangular finite elements was indeed over-estimated. However, after using the "modified area of mid-surface", displacements were reduced slightly, and the normalized displacements approached even closer to unity though it was still larger than 1.0 (see Table 4.31).

(4) The absence of coupling between membrane and bending actions in the present elements may also be one of the causes.

(5) Since the present elements have a flat geometry, they are more accurate when used for shallow shell problems. This proved to be the case in the present study. For example, the elements exhibited excellent performance in the Scordelis-Lo

roof and the spherical ring with its own weight. In the several deep shells studied, the elements show relatively slow convergence in the case of pinched cylinder, and normalized displacements higher than 1.0 were obtained for the spherical shells of Sub-sections 4.2.5 and 4.2.6.

(6) It is known that mesh topology is an important consideration when applying triangular shell elements to model shell structures. This may be even more crucial if the shell structures are deep and complicated. Sub-section 4.2.6 observed the good performance by D* mesh with the AT+$(k_t^3)'$ element, see remark (6) of Sub-section 4.2.6.

(7) Finally, the above remarks should not be confused as stating that the present finite elements lead to over-estimates of the exact results. The fact is that the presently proposed elements give results that approach monotonically the exact solutions from below. This remains true for all the problems investigated in the present study. If the problems at hand are shallow shells, lower bounds to the exact solutions can, in general, be established. For deep shell structures, one should carefully choose meshes and formulations employed, and simultaneously be aware of the possibility of over-estimating the solutions.

Table 4.31 Normalized displacement at points of loading

mesh	AT + k_d	
	flat triangle	modified
4×4A	0.102	0.097
6×6A	0.199	0.195
8×8A	0.375	0.370
9×9A	0.491	0.485
10×9A	0.558	0.552
10×10A	0.620	0.614
12×12A	0.892	0.886
13×13A	1.014	1.008

4.3 Concluding Remarks

In this chapter results of numerical studies for various plate and shell problems, including those in the obstacle course [4.1], are presented. These results were obtained with the six hybrid strain based flat triangular shell finite elements developed in Chapter 3. The following concluding remarks may be drawn from the numerical studies presented in Sections 4.1 and 4.2.

(1) The present investigation consider more than ten numerical examples, covering plane stress, plate and shell problems. The proposed elements give excellent results for plane stress, plate and shallow shell applications. When the shells are deep, the present elements seem to either converge relatively slowly, or lead to results that are slightly larger than the desired ones. For all the examples, the six proposed elements exhibit a consistent convergence pattern: approaching the exact solutions from below. The finite element results also serve as lower bounds to the exact solutions when used in shallow shell analysis.

(2) The six proposed elements have been tested in both thin and thick problems. In the thin limit, the assumed strain field offers discrete Kirchhoff type shear constraints. Thus, it effectively circumvents shear-locking. Mesh topology, too, has much to do with reducing shear-locking, and over-stiff phenomenon associated with clamped boundary conditions. In this regard, cross-diagonal mesh and refined mesh along the clamped boundaries appear to be better choices.

(3) Mesh topology is a crucial consideration of finite element modelling by triangular elements. Four representative types of meshes have been examined. Type D mesh

seems to be superior to the others in plane stress and plate problems. However, in shell applications, shallow or deep, this may not be true. Overall, for plane stress, plate and shell problems type A mesh appears to be favourable in terms of accuracy, convergence and cost effectiveness. It may be appropriate to note that when stress state of the problem at hand is complex, such as in the cases of plates and shells, comparison of convergence should be based on meshes having the same pattern. Otherwise, misleading conclusions may be drawn.

(4) It is found that the incorporation of matrix k_d, k_t^1 or k_t^3 with the other component element stiffness matrices has no contribution to accuracy and convergence of the final (displacement) results. However, the incorporation secures rank sufficiency of the element and global stiffness matrices, even when several elements connected to a node are coplanar. It has been shown in Chapter 3 that the drilling degrees-of-freedom (DDOF) can be included in a mathematically rigorous manner without leading to rank deficiency. In the present numerical studies it has been observed that the DDOF can be included without interfering with remaining component element stiffness matrices.

(5) It is also found that when $(k_m)'$, and/or $(k_t^1)'$ or $(k_t^3)'$ are employed instead of k_m, k_t^1 or k_t^3, the accuracy and convergence of the corresponding elements are improved to a very large extent. For instance, matrices $(k_m)'$, $(k_t^1)'$ and $(k_t^3)'$ are capable of representing the coupling effects between the two in-plane displacements and the DDOF. The conclusion is that the DDOF should not and

can not be disregarded. In fact, they play a crucial role in achieving satisfactory accuracy and convergence of shell elements.

(6) Comparing the performance of the six elements, $AT+(k_t^1)'$ generally out-performs the others. In terms of mathematical and formulation consistency, accuracy and computational effectiveness, $AT+k_d$ is, however, the best.

CHAPTER 5

VIBRATION ANALYSIS OF SHELL STRUCTURES

Following the derivations (Chapter 3) and applications (Chapter 4) of the hybrid strain based three node flat triangular shell elements for linear static cases, we continue the studies which are now extended to consider the dynamic aspects. In this chapter, vibration analysis of shell structures using the derived shell elements are emphasized. The derivation and explicit expressions of the element stiffness matrices have been obtained earlier in Chapter 3. Consequently, the derivation and explicit expressions of the corresponding consistent element mass matrices are dealt with in this chapter (Section 5.2). Section 5.3 includes computed results of several problems that were considered in the obstacle course in the static analysis (see, Chapter 4). The final section, Section 5.4 is concluding remarks.

5.1 Introduction

The literature on free vibration of plates and shells is vast. Vibration of plates alone generated monographs and a series of survey papers [5.1-7]. Leissa [5.6] pointed out that, for the period up to 1985, over 600 references studying the basic aspects of plate vibration problem had appeared in two major abstract journals: The Shock and Vibration Digest, and Applied Mechanics Reviews. According to Leissa [5.7], contributions

involving with complicating effects of plate vibrations amounted to over 200 for the period 1981-1985. Apparently, the first survey paper on shallow shell vibration by Qatu [5.8] appeared in 1992 while earlier researches on shell vibration were summarized by Leissa in reference [5.9]. All these contributions reflect the continuous interests, and importance of free vibration analysis of plate and shell structures.

The above survey papers cover various solution techniques, from analytical to numerical. The two major categories of techniques are those based on the Rayleigh-Ritz method and finite element method. With particular reference to the application of the finite element method for free vibration analysis of plates and shells, reference [5.10], for example, employed NASTRAN's high precision conforming triangular and quadrilateral elements to calculate natural frequencies and mode shapes of thin, uniform circular plates with partially free, and partially clamped edges. In reference [5.11] a method was proposed to separate the deflection configuration into linear combinations of rigid body, doubly symmetric, doubly antisymmetric and symmetric-antisymmetric deflection modes. This method is limited to rectangular plates. The three-dimensional isoparametric, eight node brick element with three degrees-of-freedom (DOF) per node was applied in reference [5.12] for free vibration analysis of annular sectorial plates with various inner to outer radius ratios. It is to be noted that the outer radius-to-thickness ratio of the annular sectorial plates was 50 in reference [5.12] while other formulations tried to incorporate effects of transverse shear and rotary inertia. Among them is, for instance, reference [5.13]. For more complex geometry, reference [5.5] summarized studies of

twisted cantilevered plates, or more precisely, right helicoidal shells, which often find applications in the design of propellers, windmills, and turbine blades, to mention but a few. The finite element analyses of free vibration of twisted plates applied two- or three-dimensional elements. The two-dimensional representations involved either flat plate or shell elements, and were characterized completely by a single surface of mesh points lying in the mid-surface of the twisted plate or shell. Three-dimensional models, on the other hand, had more than a single surface of mesh points, with two or more nodes in the thickness direction. References [5.14-15] were concerned with free vibration analysis of cones and cylinders using the finite element method. Free vibration analysis of deep spherical shells employing axisymmetrical elements was reported in reference [5.16]. Other free vibration analyses of plates and shells can be found in references [5.1-8, 5.17-23].

Of special interest in the present investigation is reference [5.24]. In the latter a set of explicit expressions for the mass and stiffness matrices of a triangular element was presented. The element is flat and of hybrid stress nature, consisting of 3 corner nodes and 6 DOF for each node. A feature in the derivation of this element is that, the two in-plane displacements were defined along the edges of the triangle and assumed to be polynomials having different order. The displacement normal to the edge was a cubic polynomial while the displacement along the edge a linear one. For the bending part, lateral displacement was assumed cubic along the edges whereas the rotation along and about each edge was linear. In the derivation of the element mass matrix, reference [5.24]

made use of the concept of dividing the triangle into "beam elements" that were parallel to one of the three edges so as to establish a relation between edge displacements and displacements within the triangle, since the assumed displacements were defined edge-wise. It appears that the setup of assumed displacements (defined on the edges) increased the complexity of formulation. Moreover, to eliminate the discrepancy due to forming "beam elements" parallel to one side or others, reference [5.24] repeated the procedure on each of the sides and took the mean as the final element mass matrix. As a result the amount of computation involved was also increased.

The aim of the present study is therefore to develop finite elements that are capable of representing vibration behaviours of general plate and shell structures. The formulations and derivation of the explicit stiffness matrices of the elements have already been obtained (Chapter 3) and adopted for static analysis (Chapter 4). These 3-node 18-DOF flat triangular shell elements have been proven to be accurate and reliable for general shell structures (see Chapter 4). These shell elements are of hybrid strain type and degenerate in nature. The degenerate nature allows for applications to thin as well as thick shells and makes extension to non-linear analysis simple. The hybrid strain feature, however, provides continuity of displacements and strains. Efforts are also directed towards the handling of normal rotation so that the resulting elements are capable of reflecting true normal rotation as well as desirable membrane and bending behaviours. The formulations for and derivation of the corresponding explicit consistent element mass matrices, based on the same displacement interpolation functions used for the stiffness

matrices will be presented in Section 5.2. The explicit element matrices are determined by a combination of manual and computer assisted algebraic manipulations. The computer assisted algebraic manipulation is achieved with the symbolic computer package, MAPLE [5.27]. The presently proposed consistent element mass matrices include effects of rotary inertia due to bending and torsion. It may be appropriate to note that a common practice at the present time is to ignore the effects of rotary inertia due to bending. For instance, the finite element packages NASTRAN and NISA adopt this practice. However, when the shell structure is relatively thick the rotary inertia effect due to bending is not negligible. Moreover, it has been found that the drilling degrees-of-freedom (DDOF) play a crucial role in the accuracy and convergence of the elements (see Chapter 4). Therefore, it is natural and necessary to bring in the effects due to torsional deformation associated with the DDOF. Our present formulations are therefore different from that of referernce [5.24]. In reference [5.24], though the DDOF were included in the formulation because of the use of "beam elements" concept, physical interpretation of its element mass matrix was not apparent. The same can be said about the terms associated with its two bending DOF. On the other hand, our results have ample physical interpretation.

The layout of this chapter is as follows: Section 5.2 includes a brief outline of the displacement interpolation functions formulations employed in Chapter 3, and the derivation of consistent element mass matrices; Section 5.3 is concerned with applications of the derived explicit expressions to a variety of problems most of which were studied in Chapter 4; and Section 5.4 presents concluding remarks.

5.2 Formulation and Element Matrices

The formulation of Chapter 3 is adopted in this part of the investigation. In the following, Sub-section 5.2.1 outlines the displacement interpolation functions developed in Chapter 3 while Sub-section 5.2.2 deals with the corresponding consistent element mass matrices. Improvement for bending action is considered in Sub-section 5.2.3.

5.2.1 Displacement interpolation functions

Elements considered in the present investigation are 3-node flat triangles. A representative element is shown in Figure 5.1. The three nodes are allocated at the three corners of the mid-surface of the triangular shell element. A local rectangular co-ordinate system is attached to node 1, with its r-axis coinciding with the side 1-2, its t-axis being parallel to the normal of the element and its s-axis perpendicular to the r-t plane. With such co-ordinate system, the r and s co-ordinates of nodes 1, 2, and 3 are: (0,0), $(r_2,0)$ and (r_3,s_3), respectively. There are 6 local DOF at each node, which are

- u the displacement in the r-direction,
- v the displacement in the s-direction,
- w the displacement in the t-direction,
- θ_r the rotation about r-axis,
- θ_s the rotation about s-axis, and
- θ_t the drilling degree-of-freedom (DDOF).

and they are considered positive if along the positive directions of r, s, and t-axes. For the rotations the right-hand screw rule is adopted.

The assumed displacement interpolation functions in matrix form are

$$\begin{aligned} &[\, u \;\; v \;\; w \;\; \theta_r \;\; \theta_s \;\; \theta_t \,]^T \\ &= N\,[\, u_1 \;\; v_1 \;\; w_1 \;\; \theta_{r1} \;\; \theta_{s1} \;\; \theta_{t1} \;\; u_2 \;\; \cdots \;\; \theta_{s3} \;\; \theta_{t3} \,]^T \end{aligned} \tag{5.1}$$

where

$$N = N_5 + N_t \tag{5.2}$$

with

$$N_5 = \left[\, [N_1]_{6\times5} \;\; [0]_{6\times1} \;\; [N_2]_{6\times5} \;\; [0]_{6\times1} \;\; [N_3]_{6\times5} \;\; [0]_{6\times1} \,\right]_{6\times18} \tag{5.3}$$

and

$$N_t = \begin{bmatrix} [0]_{5\times5} & [0]_{5\times1} & [0]_{5\times5} & [0]_{5\times1} & [0]_{5\times5} & [0]_{5\times1} \\ [0]_{1\times5} & \xi_1 & [0]_{1\times5} & \xi_2 & [0]_{1\times5} & \xi_3 \end{bmatrix}_{6\times18} \tag{5.4}$$

or

$$N_t = \begin{bmatrix} [0]_{5\times5} & [0]_{5\times1} & [0]_{5\times5} & [0]_{5\times1} & [0]_{5\times5} & [0]_{5\times1} \\ [0]_{1\times5} & \frac{1}{3} & [0]_{1\times5} & \frac{1}{3} & [0]_{1\times5} & \frac{1}{3} \end{bmatrix}_{6\times18} \tag{5.5}$$

Note that equation (5.4) corresponds to linearly varied normal rotation θ_t while equation (5.5) represents a constant θ_t over an element. The $[N_i]$ (i=1, 2, and 3) matrices of equation (5.3) are

$$[N_i] = \begin{bmatrix} \xi_i & 0 & 0 & 0 & 0 \\ 0 & \xi_i & 0 & 0 & 0 \\ 0 & 0 & \xi_i & 0 & 0 \\ 0 & 0 & 0 & \xi_i & 0 \\ 0 & 0 & 0 & 0 & \xi_i \\ 0 & 0 & 0 & 0 & 0 \end{bmatrix}_{6\times5} \qquad i=1,2,3 \tag{5.6}$$

while $[0]_{6\times1}$, $[0]_{5\times5}$, $[0]_{5\times1}$ and $[0]_{1\times5}$ are null matrices of dimension 6×1, 5×5, 5×1 and 1×5, respectively.

The linear interpolation relation of equation (5.3) can be replaced by the following matrix so as to form the so-called Allman's triangle (AT):

$$N_5 = \left[[N_1]_{6\times5} \; [p_1]_{6\times1} \; [N_2]_{6\times5} \; [p_2]_{6\times1} \; [N_3]_{6\times5} \; [p_3]_{6\times1} \right]_{6\times18} \tag{5.7}$$

where $[N_i]_{6\times5}$ has been defined in equation (5.6) and the matrices $[p_i]$ (i=1, 2 and 3) are defined as

$$[p_i] = [\, \bar{p}_i, \bar{q}_i, 0, 0, 0, 0 \,]^T \tag{5.8}$$

in which the terms $\bar{p}_i$ and $\bar{q}_i$ are

$$\begin{aligned} \bar{p}_1 &= (a_{31}\xi_3 - a_{12}\xi_2)\xi_1 \\ \bar{p}_2 &= (a_{12}\xi_1 - a_{23}\xi_3)\xi_2 \\ \bar{p}_3 &= (a_{23}\xi_2 - a_{31}\xi_1)\xi_3 \end{aligned} \tag{5.9}$$

$$\begin{aligned} \bar{q}_1 &= (b_{31}\xi_3 - b_{12}\xi_2)\xi_1 \\ \bar{q}_2 &= (b_{12}\xi_1 - b_{23}\xi_3)\xi_2 \\ \bar{q}_3 &= (b_{23}\xi_2 - b_{31}\xi_1)\xi_3 \end{aligned} \tag{5.10}$$

and with reference to Figure 5.2

$$a_{12} = \frac{1}{2}\ell_{12}\cos\gamma_{12} \qquad b_{12} = \frac{1}{2}\ell_{12}\sin\gamma_{12}$$

$$a_{23} = \frac{1}{2}\ell_{23}\cos\gamma_{23} \qquad b_{23} = \frac{1}{2}\ell_{23}\sin\gamma_{23}$$

$$a_{31} = \frac{1}{2}\ell_{31}\cos\gamma_{31} \qquad b_{31} = \frac{1}{2}\ell_{31}\sin\gamma_{31} \ .$$

5.2.2 Consistent element mass matrices

The usual definition of consistent element mass matrix is

$$m = \int_V \rho N^T N dV \tag{5.11}$$

where ρ is the mass density of the material. This definition, however, is only applicable to translational DOF. For rotational DOF, equation (5.11) leads to results that have no physical meaning. This may be one of the reasons that rotational DOF are disregarded in free vibration analysis by the finite element method [5.28-29]. In reference [5.23] it was suggested to replace ρ by a diagonal matrix $[\rho]$ whose elements are, ρ for translational DOF, and $\rho h^2/12$, moment of inertia per unit cross-sectional width, for rotational DOF that are related to bending. Note that no details of elements of the mass matrix associated with DDOF were given in reference [5.23]. Therefore, they are considered here. Similar to the reasoning in the translational and rotational DOF, the elements of $[\rho]$ that are associated with the DDOF are the polar moment of inertia of the

triangle (per unit area of the triangle) about its centroid. That is, each of the elements of [ρ] associated with the DDOF is

$$J_d = \rho \frac{\frac{r_2 s_3}{36}\left[r_2^2 + s_3^2 + r_3(r_3 - r_2)\right]}{\frac{r_2 s_3}{2}} = \rho \frac{\left[r_2^2 + s_3^2 + r_3(r_3 - r_2)\right]}{18} . \tag{5.12}$$

Now, the definition of consistent element mass matrix becomes

$$m = \int_V N^T [\rho] N \, dV \tag{5.13}$$

where

$$[\rho] = \begin{bmatrix} [\bar{\rho}] & & \\ & [\bar{\rho}] & \\ & & [\bar{\rho}] \end{bmatrix}_{18\times 18} \tag{5.14}$$

and the diagonal sub-matrix $[\bar{\rho}]$ is defined as

$$[\bar{\rho}] = \begin{bmatrix} \rho & & & & & \\ & \rho & & & & \\ & & \rho & & & \\ & & & \frac{\rho h^2}{12} & & \\ & & & & \frac{\rho h^2}{12} & \\ & & & & & J_d \end{bmatrix}_{6\times 6} . \qquad (5.15)$$

Finally, the consistent element mass matrix is obtained by substituting the displacement interpolation function matrix N of equation (5.2) into (5.13) and performing the required integration. It should be emphasized that, in the present study, the integration is performed analytically by the symbolic algebraic manipulation package, MAPLE [5.27] and it is "exact" in the sense that no numerical integration is used. It should also be mentioned that, since the interpolation function matrix N_s can be either equation (5.3) or (5.7) and N_t either (5.4) or (5.5), there are a number of variations of the element mass matrix defined by eqaution (5.13). They will be summarized in the following sub-section.

5.2.3 Improvement of bending action

A strategy of improving the insufficiency of bending action due to the use of low order interpolation proposed in reference [5.30] is adopted in the present investigation.

The strategy includes quadratic lateral displacement and linear rotations. Expressed mathematically, the strategy is to replace $[N_i]$ of equation (5.6) by

$$[N_i] = \begin{bmatrix} \xi_i & 0 & 0 & 0 & 0 \\ 0 & \xi_i & 0 & 0 & 0 \\ 0 & 0 & \xi_i & -\bar{p}_i & -\bar{q}_i \\ 0 & 0 & 0 & \xi_i & 0 \\ 0 & 0 & 0 & 0 & \xi_i \\ 0 & 0 & 0 & 0 & 0 \end{bmatrix}_{6\times5} \qquad i=1,2,3 \tag{5.16}$$

and B_{si} (i=1, 2 and 3) of equation (3.27c) becomes, accordingly,

$$B_{si} = \begin{bmatrix} 0 & 0 & 0 & 0 & 0 & 0 \\ 0 & 0 & 0 & 0 & 0 & 0 \\ 0 & 0 & 0 & 0 & 0 & 0 \\ 0 & 0 & \xi_{i,s} & -\xi_i\bar{p}_{i,s} & -\bar{q}_{i,s} & 0 \\ 0 & 0 & \xi_{i,r} & -\bar{p}_{i,r} & \xi_i\bar{q}_{i,s} & 0 \end{bmatrix}_{5\times6} \qquad i=1,2,3\ . \tag{5.17}$$

Therefore, the change in matrix $[N_i]$ (i=1, 2 and 3) leads to changes in B_s as well as consistent element mass matrix m. However, it has been found during the derivation that k_s actually remains unchanged. This conclusion implies that the bending element (that is, k_b and k_s) of Chapter 3 is in fact with quadratic lateral displacement. Consequently, the element is softer than the C^0 bending element. Because of the hybrid strain feature,

better performance of the bending element is achieved without invoking relatively complicated formulation.

Returning to the consistent element mass matrix, application of equation (5.16) results in better performance. This is substantiated by the numerical results to be presented in Section 5.3. There are also a number of variations of the consistent element mass matrix. Such variations depend upon the form of N_s and N_t. Table 5.1 is a summary of 16 such variations. Each of such variations is identified by NFORMU which takes the value of 1 to 16.

The explicit expressions for the consistent element mass matrices derived in this section are included in Appendix C.

Table 5.1 Summary of formulations

NFORMU	stiffness matrix k	consistent mass matrix m		
		u,v	w	θ_t
1	CST+k_d	linear	linear	constant
2	CST+k_d			linear
3	CST+k_t^1			constant
4	CST+k_t^3			linear
5	AT+k_d	quadratic		constant
6	AT+k_d			linear
7	AT+$(k_t^1)'$			constant
8	AT+$(k_t^3)'$			linear
9	CST+k_d	linear	quadratic	constant
10	CST+k_d			linear
11	CST+k_t^1			constant
12	CST+k_k^3			linear
13	AT+k_d	quadratic		constant
14	AT+k_d			linear
15	AT+$(k_t^1)'$			constant
16	AT+$(k_t^3)'$			linear

5.3 Numerical Studies

In this section several numerical examples are investigated. These are: a square plate with various boundary conditions, a skew plate, a plane stress cantilever beam, a curved beam, a twisted beam, a pinched cylinder, the Scordelis-Lo roof and a hemisphere. Note that all the examples have been employed in the static analysis of Chapter 4, except for the square plate and the skew plate. The square plate is chosen because "exact" solutions are available [5.2]. Therefore, comparisons can be made so as to examine the present elements in issues of accuracy and convergence. The focus in this section is to establish the convergence features of the currently proposed elements under various boundary conditions. All examples, except for the skew plate, employ the same meshes and boundary conditions as those in Chapter 4. Thus, when symmetry of the structure is exploited for computational efficiency only natural frequencies and mode shapes associated with the specific boundary conditions are included in this section. Of course, in order to determine all the natural frequencies and mode shapes (anti-symmetric and symmetric) other boundary conditions have to be considered. However, in order to maintain a reasonable length of the present chapter they are not included here since they can be obtained by applying the steps outlined in the following sub-sections. In the following, the natural frequencies are all measured in Hz.

Before we present the several selected examples, it may be appropriate to mention the results of unconstrained single element test. This test is designed to detect spurious modes. It is found that, among the 16 variations of the shell element formulation, elements identified as NFORMU=4, 8, 12 and 16 do not possess the spurious modes.

which are associated with in-plane displacements and the DDOF only. The remaining variations have either two or three spurious modes. Therefore, when using these elements to represent rigid body motions, one should be aware of the aforementioned fact.

5.3.1 Square plate with various boundary conditions

The geometrical dimension of the square plate is $1 \times 1 \times 0.005$ m^3, and its material properties are, Young's modulus $E=2\times10^{11}$ N/m^2, Poisson's ratio $\nu=0.3$ and mass per unit volume $\rho=7830$ N/m^3.

In the finite element representation, various mesh types are considered and they are included in Figure 5.3. Figure 5.4 shows the entire plate. Because of the nature of the problem, the two in-plane displacements U and V and the normal rotation about Z-axis are constrained to zero. Consequently, the 16 variations of the element are reduced to two. That is, NFORMU=1 through 8 reduce to one single formulation and NFORMU=9 through 16 reduce to another.

(i) *Rigid body modes*

For this case, no constraints are applied to the lateral displacement and rotations about X- and Y-axes. Therefore, three zero natural frequencies exist. This is confirmed by the present finite element results in which the first three natural frequencies are technically zero. The first three non-zero natural frequencies are listed in Tables 5.2 and 5.3. Exact solutions from reference [5.2] are also included for comparison. Note that the rigid body modes here are not associated with in-plane displacements and the DDOF and no spurious modes are detected.

(ii) *Simply-supported at four corners*

The boundary conditions are, $W=0$ for the four corner points. Although Θ_x and Θ_y are not constrained, no zero natural frequencies are found. The first three natural frequencies are given in Tables 5.4 and 5.5.

(iii) *Simply-supported at four sides*

Constraints are, $W=\Theta_y=0$ for sides parallel to X-axis, and $W=\Theta_x=0$ for sides parallel to Y-axis. Therefore, at the four corner points, $W=\Theta_x=\Theta_y=0$. The finite element results are presented in Tables 5.6 and 5.7.

(iv) *Clamped at one side and free at other three sides*

For the clamped side, boundary conditions are $W=\Theta_x=\Theta_y=0$. The finite element results are listed in Tables 5.8 and 5.9.

(v) *Clamped at four sides*

In this case, W, Θ_x and Θ_y of nodes at the four sides are constrained to zero. Finite element results are given in Tables 5.10 and 5.11.

Various observations from the foregoing results can be summarized in the following.

(1) Mesh types A and B show no difference in natural frequencies. Therefore, only results of mesh type A are listed. Note that in Chapter 4, mesh types A and B may lead to substantial difference because in the static analysis applied forces are included.

(2) Mesh type A is not as capable as types C and D of representing repetitive natural frequencies.

(3) Considering convergence pattern of the present finite element results as shown in Figures 5.5-5.7, all cases except for the rigid body modes and clamped at one side with linear lateral displacement field (NFORMU = 1 through 8) show consistency: approaching the exact solutions from above. The cases of rigid body modes and clamped at one side with NFORMU = 1 through 8, however, exhibit the above convergence pattern when the mesh used is relatively fine. For examples, 8×8C or 4×4D and finer meshes for the rigid body modes, and 2×2A and finer meshes for the cantilevered plate. This phenomenon may be due to the low order interpolation function employed for the lateral displacement, since consistent convergence holds true even with coarse meshes when the order of the lateral displacement interpolation function is increased to 2 (NFORMU = 9 through 16). Therefore, the present finite element results indicate upper bounds to the exact solutions.

(4) Comparing the two lateral displacement fields, the higher order one gives, in general, lower, thus more accurate, natural frequencies. This is particularly true for coarse meshes and for higher modes. The cantilevered plate is an exception. For this case, the linear lateral displacement field leads to lower natural frequencies of the first and second modes. Nevertheless, the quadratic lateral displacement field gives better natural frequencies than the linear one for the third and higher modes.

Table 5.2 First three non-zero natural frequencies of the square plate

NFORMU = 1 through 8				
mesh	neq.*	f_4	f_5	f_6
1×1A	12	12.2187	2443.84	3330.40
2×2A	27	16.7320	28.2138	38.4450
4×4A	75	16.9940	25.4531	32.8110
2×2C	27	14.1084	28.2138	38.4450
4×4C	75	16.8045	25.4242	32.6750
8×8C	243	16.8127	24.3304	30.4750
16×16C	867	16.4532	23.9697	29.8658
1×1D	15	14.1089	33.2986	2443.84
2×2D	39	16.9550	28.2104	36.9310
4×4D	123	16.9749	24.9946	31.7765
8×8D	435	16.5130	24.1609	30.1402
solution from [5.2]		16.3972	23.8497	29.5384

* neq. denotes the total number of the unknown displacements or the number of final algebraic equations.

Table 5.3 First three non-zero natural frequencies of the square plate

NFORMU = 9 through 16				
mesh	neq.	f_4	f_5	f_6
1×1A	12	17.2794	27.3213	37.2306
2×2A	27	17.0009	27.3173	36.6497
4×4A	75	16.9246	24.4869	30.8171
2×2C	27	17.2791	27.3179	37.2276
4×4C	75	16.7859	24.4870	30.8172
8×8C	243	16.7779	24.0506	29.9279
16×16C	867	16.4360	23.9008	29.6354
1×1D	15	17.2794	27.3213	37.2285
2×2D	39	16.7881	27.3120	35.9087
4×4D	123	16.6598	24.4843	30.8117
8×8D	435	16.4770	24.0243	29.8819
solution from [5.2]		16.3972	23.8497	29.5384

Table 5.4 First three natural frequencies of the square plate (simply supported at four corners)

NFORMU = 1 thorugh 8				
mesh	neq.	f_1	f_2	f_3
1×1A	8	2443.84	3330.40	4130.49
2×2A	23	14.2424	24.7489	28.2138
4×4A	71	10.3387	21.4112	25.4531
8×8A	239	9.4379	20.2642	24.3304
2×2C	23	14.5290	28.2138	42.3119
4×4C	71	9.9518	23.0529	23.0529
8×8C	239	9.0056	20.1508	20.1508
1×1D	11	19.2256	2443.84	4130.14
2×2D	35	12.2140	27.4196	27.4196
4×4D	119	9.5388	21.1198	21.1198
solution from [5.2]		8.6655	19.1931	19.1931

Table 5.5 First three natural frequencies of the square plate (simply supported at four corners)

NFORMU = 9 through 16				
mesh	neq.	f_1	f_2	f_3
1×1A	8	11.2265	26.6640	27.3213
2×2A	23	11.1078	23.4723	27.3173
4×4A	71	9.8437	21.2146	24.4869
8×8A	239	9.3346	20.2273	24.0506
2×2C	23	11.2233	26.5370	26.5370
4×4C	71	9.5339	21.8113	21.8113
8×8C	239	8.9197	19.8852	19.8852
1×1D	11	11.2263	26.6622	26.6622
2×2D	35	10.9680	23.4637	23.4637
4×4D	119	9.3437	20.5031	20.5031
solution from [5.2]		8.6655	19.1931	19.1931

Table 5.6 First three natural frequencies of the square plate (simply supported at four sides)

NFORMU = 1 through 8				
mesh	neq.	f_1	f_2	f_3
2×2A	7	744.466	7154.84	182212.
4×4A	39	60.5822	94.5421	388.452
8×8A	175	32.5724	69.6235	113.458
2×2C	7	911.172	150317.	150317.
4×4C	39	29.7802	104.290	104.290
8×8C	175	25.2938	67.7518	67.7518
1×1D	3	1288.02	223117.	223117.
2×2D	19	33.7182	164.814	164.814
4×4D	87	25.9892	75.8620	75.8620
solution from [5.2]		24.0239	60.0596	60.0596

Table 5.7 First three natural frequencies of the square plate (simply supported at four sides)

NFORMU = 9 through 16				
mesh	neq.	f_1	f_2	f_3
2×2A	7	75.4123	512.941	2586.47
4×4A	39	53.8731	74.7847	258.694
8×8A	175	31.7669	65.9834	105.412
2×2C	7	746.259	1683.06	1683.06
4×4C	39	26.6515	75.3323	75.3323
8×8C	175	24.6414	63.3625	63.3625
1×1D	3	1288.02	3527.35	3527.35
2×2D	19	26.6590	75.3875	75.3875
4×4D	87	24.6470	65.9516	65.9516
solution from [5.2]		24.0239	60.0596	60.0596

Table 5.8 First three natural frequencies of the square plate (cantilevered plate)

NFORMU = 1 through 8				
mesh	neq.	f_1	f_2	f_3
1×1A	6	4.1116	16.4100	96180.2
2×2A	18	4.3451	20.9461	48.9385
4×4A	60	4.2971	18.7287	31.1244
2×2C	18	4.3482	13.9889	43.7942
4×4C	60	4.2777	12.0455	30.4386
8×8C	216	4.2454	10.8134	27.0538
1×1D	9	4.6302	12.6921	52.3512
2×2D	30	4.3975	12.2364	43.3922
4×4D	108	4.2839	10.9315	29.2389
solution from [5.2]		4.2410	10.3755	26.0817

Table 5.9 First three natural frequencies of the square plate (cantilevered plate)

NFORMU = 9 through 16				
mesh	neq.	f_1	f_2	f_3
1×1A	6	5.2067	23.8712	1248.07
2×2A	18	4.4716	21.7218	45.0816
4×4A	60	4.3194	18.7536	29.2389
2×2C	18	4.4402	17.8309	40.4871
4×4C	60	4.2945	12.0407	28.8273
8×8C	216	4.2492	10.7974	26.6823
1×1D	9	4.9821	18.1491	44.2683
2×2D	30	4.4399	12.1713	40.3947
4×4D	108	4.2920	10.8941	28.5493
solution from [5.2]		4.2410	10.3755	26.0817

Table 5.10 First three natural frequencies of the square plate (clamped at four sides)

NFORMU = 1 through 8				
mesh	neq.	f_1	f_2	f_3
2×2A	3	1662.82	182206.	257626.
4×4A	27	306.293	796.505	1265.79
8×8A	147	74.8277	153.574	209.323
2×2C	3	1577.49	223117.	223117.
4×4C	27	539.372	1031.93	1031.93
8×8C	147	51.9350	118.618	118.618
1×1D	3	1288.02	223117.	223117.
2×2D	15	1272.99	2351.88	2351.88
4×4D	75	54.7119	152.388	152.388
solution from [5.2]		43.8021	89.3446	89.3446

Table 5.11 First three natural frequencies of the square plate (clamped at four sides)

NFORMU = 9 through 16				
mesh	neq.	f_1	f_2	f_3
2×2A	3	1662.82	3643.02	4461.77
4×4A	27	269.728	593.520	874.679
8×8A	147	72.5492	144.107	191.763
2×2C	3	1577.49	3527.35	3527.35
4×4C	27	482.042	719.039	719.039
8×8C	147	50.1722	108.709	108.709
1×1D	3	1288.02	3527.35	3527.35
2×2D	15	1189.69	1936.27	1936.27
4×4D	75	50.9270	123.741	123.741
solution from [5.2]		43.8021	89.3446	89.3446

5.3.2 Skew plate

The skew plate shown in Figure 5.8 has a skewed angle of 30°. The two sides are of 1.0 m in length. The thickness is 0.005 m. The material properties are: $E=2\times10^{11}$ N/m^2, $\nu=0.3$ and $\rho=7830$ kg/m^3. Similar to the square plate in Sub-section 5.3.1, the two in-plane displacements and the normal rotation about the Z-axis are constrained. At the clamped side where Y=0.0, constraints $W=\Theta_x=\Theta_y=0.0$ are also imposed. The finite element results are presented in Table 5.12 and the first three mode shapes in Figures 5.9 through 5.11. Note that the mode shapes are with mesh 16×8B. The mesh notations are that the first integer indicates number of spacing along the X-direction and the second integer denotes number of spacing along the Y-direction.

Reference [5.2] gave results of the plate as: $f_1 = 4.8208$ Hz, and $f_2 = 12.4019$ Hz. (See Table 5.12, page 170 of reference [5.2]). Results for higher modes, however, were not presented in reference [5.2]. These results were obtained by using the Rayleigh-Ritz method with 18 terms of the deflection function which are products of characteristic beam functions. The first natural frequency f_1 in reference [5.2] is therefore an upper bound solution. The present results are slightly higher than those in reference [5.2]. For example, the fundamental frequency of the present elements with mesh 16×8B is 3.94%, with respect to that of reference [5.2], higher than that of reference [5.2].

Finally, one may notice that f_1 and f_2 using NFORMU = 9 through 16 are, in general, higher than those from NFORMU = 1 through 8. This agrees with the observation of the cantilevered square plate in Sub-section 5.3.1.

Table 5.12 First three natural frequencies of the skew plate (clamped at one side)

NFORMU = 1 through 8				
mesh	neq.	f_1	f_2	f_3
4×2B	30	5.5234	33.8336	62.7879
6×3B	63	5.6836	25.5351	45.8341
8×4B	108	5.5280	19.0033	40.3372
16×8B	408	5.0043	12.5964	33.1078
NFORMU = 9 - 16				
mesh	neq.	f_1	f_2	f_3
4×2B	30	5.6875	35.7054	58.7392
6×3B	63	5.7432	25.8492	41.7741
8×4B	108	5.5604	19.0324	38.1498
16×8B	408	5.0107	12.5906	32.8107

5.3.3 Plane stress beam

The plane stress beam shown in Figure 5.12 involves with no bending DOF. That is, W, Θ_x and Θ_y are all constrained to zero. In this case, whether the lateral displacement field is of order 1 or 2 does not make any difference. However, the formulations concerning the in-plane displacements and the DDOF lead to different natural frequencies. To compare such formulations, meshes 4×1B and 4×1D are chosen for calculating the natural frequencies which are included in Table 5.13. These calculations are repeated with NFORMU=1 through 8.

With reference to Table 5.13 it can be seen that selecting NFORMU=7 results in the lowest natural frequencies for both meshes and for f_1 through f_3. This indicates that using the $AT+(k_t^1)'$ as the element stiffness matrix and a consistent element mass matrix that corresponds to quadratic in-plane displacements, constant normal rotation and linear or quadratic lateral displacement (no distinction for the linear and quadratic lateral displacements exists for the present example). For general shell vibration problems, Sub-section 5.3.6 will show that the quadratic one is a better choice in the sense that it leads to the best performance among all formulations. In other words, best results are obtained from a displacement field in which, the in-plane displacements are coupled with the DDOF, the normal rotation is constant over the element, the rotations θ_r and θ_s are linearly interpolated, and the lateral displacement is quadratic and coupled with θ_r and θ_s.

Comparing results from NFORMU=6 with those from NFORMU=7, the difference is only 2.2% for the 4×1B mesh and 0.4% for the 4×1D mesh. The percentage differences are with respect to the results applying NFORMU=7. Note that the features of the formulation NFORMU=6 are the same as those of NFORMU=7 except that the normal rotation θ_t is linearly interpolated. From the viewpoint of mathematical consistency, NFORMU=6 is superior to NFORMU=7 because $AT+k_d$ is used in the element stiffness matrix rather than $AT+(k_t^1)'$. This has been discussed in Chapter 4.

Having compared the features of the present formulations, calculations were carried out for four other meshes by selecting NFORMU=6 or 7. Results are given in Table 5.14. The following points are to be noted.

(1) Consistent convergence is preserved for f_1 and f_3 with mesh types B and D, and f_2 with mesh type D. This holds true for both values of NFORMU. When mesh type B is used, mesh 4×1B leads to f_2 that is smaller than that of the meshes 8×2B and 16×4B.

(2) The difference between NFORMU=6 and 7 reduces as meshes are refined. For example, the difference is 0.05% for the mesh 16×4D, compared with 2.2% for the mesh 4×1B.

(3) The first three natural frequencies, based on Euler's thin beam theory, are 8.7088, 54.5774 and 152.8178 Hz., respectively. Therefore, the percentage reductions of natural frequencies due to transverse shear deformation, using the present results from mesh 16×4D and NFORMU=6, are 3.84%, 21.57% and 64.64% with respect to the corresponding Euler beam solution, respectively. Clearly, the percentage reduction is increased drastically as the mode number is increased. It may be appropriate to mention that reference [5.31] studied effects of rotary inertia and transverse shear on the natural frequencies of uniform beams, and reported similar trend. The numerical results of reference [5.31] were concerned with a thin cantilever beam. The ratio of cross-sectional area to length of the beam is 0.0694 in reference [5.31], while the ratio of the presently studied plane stress beam is 0.25. Hence, the reductions of natural frequencies are expected to be more substantial.

Table 5.13 First three natural frequencies of the plane stress beam

4×1B mesh, neq.=24			
NFORMU	f_1	f_2	f_3
1	15.8965	54.4924	66.3323
2	15.8927	51.0321	54.4846
3	15.8958	54.4899	66.0582
4	16.1407	54.5251	67.5240
5	9.6137	40.9883	54.6608
6	9.6118	40.6818	54.6350
7	9.4049	39.4187	54.5538
8	9.4508	39.5369	54.4900
4×1D mesh, neq.=36			
NFORMU	f_1	f_2	f_3
9	10.8524	54.3742	54.7101
10	10.8519	46.3618	54.3557
11	10.8523	54.3742	54.6659
12	11.0563	54.3923	55.7116
13	8.5741	43.5771	54.4272
14	8.5737	43.5247	54.4272
15	8.5405	43.3306	54.3958
16	8.5585	43.3996	54.3958

Table 5.14 First three natural frequencies of the plane stress beam

NFORMU = 6				
mesh	neq.	f_1	f_2	f_3
4×1B	24	9.6118	40.6818	54.6350
8×2B	72	8.8164	43.7394	54.2408
16×4B	240	8.4895	43.1219	54.0885
4×1D	36	8.5737	43.5247	54.4270
8×2D	120	8.4394	43.2239	54.1572
16×4D	432	8.3745	42.8041	54.0624
NFORMU = 7				
mesh	neq.	f_1	f_2	f_3
4×1B	24	9.4049	39.4187	54.5539
8×2B	72	8.7766	43.4452	54.2309
16×4B	240	8.4783	43.0427	54.0856
4×1D	36	8.5405	43.3306	54.3958
8×2D	120	8.4255	43.0742	54.1477
16×4D	432	8.3704	42.7544	54.0595

5.3.4 Curved beam

The curved beam shown in Figure 5.13 is represented by five meshes of the same type, mesh type B. The first three natural frequencies are given in Table 5.15. The results show the previously observed convergence pattern: consistently approaching the exact solutions from above. These results, therefore, are upper bounds to the exact values. Note that the calculation is based on NFORMU=14. This is because the formulation has all the features of NFORMU=6. The only difference between NFORMU=6 and 14 is that the latter employs quadratic interpolation function for the lateral displacement field, which makes the formulation better than NFORMU=6 in general applications. Sub-section 5.3.6 makes comparisons among NFORMU=6, 7, 14 and 15 and confirms the above observation.

Table 5.15 First three natural frequencies of the curved beam

NFORMU = 14				
mesh	neq.	f_1	f_2	f_3
6×1B	72	2.4524	11.5686	11.8657
12×1B	144	2.3929	7.1719	11.5078
14×1B	156	2.3823	6.5948	11.4748
20×1B	240	2.3770	5.9392	11.4196
32×1B	384	2.3706	5.5733	11.3828

5.3.5 Twisted beam

Finite element results of the twisted beam, shown in Figure 5.14, using NFORMU=14 are presented in Table 5.16. They exhibit convergence features similar to those observed above.

Table 5.16 First three natural frequencies of the twisted beam

NFORMU = 14				
mesh	neq.	f_1	f_2	f_3
6×2	108	3.8163	11.0652	34.1765
12×2	216	3.7574	10.0630	31.5143
24×2	432	3.7472	9.8283	30.8461
48×2	864	3.7453	9.7891	30.7465

5.3.6 Scordelis-Lo roof

The first objective of studying the roof shown in Figure 5.15 is to examine the differences among various formulations. For meshes 2×2A and 4×4A, the first three natural frequencies are obtained by repeatedly setting NFORMU equal to 6, 7, 14 and 15. The results are included in Table 5.17. It can be seen that NFORMU=15 seems to give the best results. This is different from that in Sub-section 5.3.3 where it was found that NFORMU=7 gave the best results. The explanation is that, in that particular case, lateral displacements were constrained, therefore NFORMU=7 and 15 became identical.

However, in the Scordelis-Lo roof lateral displacements are active DOF. Consequently, NFORMU=15 and NFORMU=7 are different. Results obtained indicate that NFORMU=15 out-performs NFORMU=7. It should also be noted that the difference between NFORMU=14 and 15 is not significant. Moreover, such difference reduces as meshes become finer (see Table 5.17). With the most coarse mesh 2×2A considered here the difference between f_1 obtained from NFORMU=14 and 15 is 1.7% with respect to that from NFORMU=15. The difference is reduced to 0.15% when the 4×4D mesh is employed. Recalling that Sub-section 5.3.3 also suggested the use of NFORMU=6 due to its mathematical consistency. This implies that NFORMU=14 should be chosen for general applications where lateral displacements are not all constrained.

The second objective is to determine the influence of mesh types on the natural frequencies. Two meshes, types A and D are considered and their results are presented in Tables 5.18 and 5.19. In all the computations NFORMU has been set equal to 14. The results demonstrate a rapid convergence. It is especially true for mesh type D. In fact, the first natural frequencies from 4×4D and finer mesh cases differ slightly from each other. This seems to agree with the observation of Chapter 4 that the element AT+k_d with type D meshes is almost independent of mesh sizes except for the 2×2D case.

The the first three modes are illustrated in Figures 5.16 through 5.18. They are obtained from mesh 10×14A.

Table 5.17 First three natural frequencies of the Scordelis-Lo roof

mesh	neq.	NFORMU	f_1	f_2	f_3
2×2A	33	6	20.8289	48.6420	161.089
		7	20.5047	47.8108	159.749
		14	17.8850	46.9440	121.335
		15	17.5876	46.1436	117.967
4×4A	111	6	14.6002	45.2501	65.9806
		7	14.5529	45.1405	65.8821
		14	14.2169	44.5005	59.4277
		15	14.1707	44.3941	59.3349
2×2D	57	14	12.1083	43.2182	47.3347
		15	11.9470	42.9007	47.1336
4×4D	207	14	11.3746	43.3444	46.7688
		15	11.3575	43.2940	46.6687

Table 5.18 First three natural frequencies the Scordelis-Lo roof

NFORMU = 14				
mesh	neq.	f_1	f_2	f_3
2×2A	33	17.8850	46.9440	121.335
4×4A	111	14.2169	44.5005	59.4277
5×5A	168	12.8311	44.0643	53.5314
6×6A	237	12.1528	43.8106	50.9315
8×8A	411	11.6145	43.5034	48.6511
8×10A	513	11.5286	43.4501	47.6790
8×12A	618	11.4679	43.3976	46.8651
10×10A	633	11.4325	43.3607	46.8802
10×14A	885	11.3741	43.3164	45.6746

Table 5.19 First three natural frequencies of the Scordelis-Lo roof

NFORMU = 14				
mesh	neq.	f_1	f_2	f_3
2×2D	57	12.1083	43.2182	47.3347
4×4D	207	11.3746	43.3444	46.7686
5×5D	318	11.3099	43.2930	46.0095
6×6D	453	11.2810	43.2558	45.5018
8×8D	795	11.2583	43.2110	44.9280

5.3.7 Pinched cylinder

The first three natural frequencies and the corresponding mode shapes of the pinched cylinder, shown in Figure 5.19, are given in Table 5.20 and Figures 5.20 through 5.22. The convergence of the fundamental frequency appears to be relatively slow, compared with the Scordelis-Lo roof. Note that the static study of the pinched cylinder revealed the same trend (see Chapter 4). In fact, it will be seen in the following sub-section that the convergence rate of static analysis and free vibration analysis seem to be in close pace.

Figure 5.12 in page 63 of reference [5.9] contains curves of the fundamental frequency of a cylinder with end diaphragms. Using the geometrical and material properties of the present problem, the fundamental frequency is found to be 0.2162 Hz. This frequency corresponds to axial wave number of 1 and circumferential wave number larger than 2. Note that this result is based on reading from the figure of reference [5.9]. Taking 0.2162 Hz as reference, the results in Table 5.20 are clearly upper bound solutions.

5.3.8 Hemispherical shell

The hemispherical shell with fixed pole, shown in Figure 5.23, is studied using meshes 4×4A through 13×13A. Computed results are presented in Table 5.21 and Figures 5.24 through 5.26. The mode shapes are from the case with mesh 13×13A.

Table 5.20 First three natural frequencies of the pinched cylinder

NFORMU = 14				
mesh	neq.	f_1	f_2	f_3
4×4A	96	0.3193	0.5845	0.5940
5×5A	150	0.2759	0.4057	0.5946
6×6A	216	0.2592	0.3240	0.5834
8×8A	384	0.2478	0.2617	0.4422
10×10A	600	0.2414	0.2443	0.3945
12×12A	864	0.2332	0.2429	0.3745

Table 5.21 First three natural frequencies of the hemispherical shell

NFORMU = 14				
mesh	neq.	f_1	f_2	f_3
4×4A	96	5.3186	32.6766	35.9891
6×6A	216	3.9549	16.8620	29.3665
8×8A	384	2.9209	12.5473	23.4131
9×9A	486	2.5630	11.8372	20.9623
10×10A	600	2.2866	11.3766	18.8576
12×12A	864	1.9114	10.8038	15.5564
13×13A	1014	1.7950	10.5927	14.3537

5.4 Concluding Remarks

Finite elements that are capable of representing vibration behaviours of general plate and shell structures have been developed and presented in this chapter. The formulations and derivation of the explicit stiffness matrices of the elements have already been proposed and obtained earlier in Chapter 4. In the present chapter explicit expressions for corresponding consistent mass matrices are presented. Results of several problems that were considered in the obstacle course of the static analysis are computed. These results indicated that the shell elements have good convergence rates, and since explicit expressions for the element matrices were employed no numerical integration is required. Consequently, the presented elements are attractive to be employed for vibration analysis of general plate and shell structures.

CHAPTER 6

THEORIES AND FORMULATIONS FOR NONLINEAR ANALYSIS OF SHELL STRUCTURES

Chapters 3 through 5 were aimed at the derivations and applications of the hybrid strain based three node flat triangular shell elements within the framework of linear (static and dynamic) analysis. Our next objective is the general nonlinear analysis of shell structures. The nonlinearities considered can be geometrical, material and both geometrical and material. In this thesis, the nonlinear analysis of shell structures are presented by two chapters. This chapter includes the theoretical and computational aspects of the analysis while Chapter 7 is concerned with numerical studies.

The organization of Chapter 6 is as follows. Section 6.1 is an introduction and overview; Section 6.2 presents the incremental variational principle whereas Sections 6.3 and 6.4 include the derivation of element stiffness matrices and consistent mass matrices, respectively. Constitutive relations for elastic and elasto-plastic materials are considered in Section 6.5. Schemes for updating configurations and stresses are introduced in Section 6.6. The final section, Section 6.7 is concluding remarks.

6.1 Introduction and Overview

The first attempts of applying the finite element technique to nonlinear analysis of shells may date back to the late 1960's. Most of these early efforts were limited to the scope of geometrical nonlinearity and to studies of shells of particular geometrical shape,

such as axisymmetric shells [6.1-2] and cylindrical shells [6.3]. A considerable literature existed on the application of finite elements to the large deflection analysis of shallow shells (see references [6.4-5], for example). Later the efforts were extended to deep, free form shells [6.6-7]. It was then found that the conventional, displacement-based finite element approach proved difficult in pursuing the goal of simple and accurate element formulation, which severely limits the scope of displacement-based finite elements. Consequently, mixed, or hybrid finite element formulations began to gain popularity. For instances, Tahiani and Lachance [6.8] employed 3 and 6 node triangular shell elements to study geometrically nonlinear thin shallow shells, while Noor and Hartley [6.9] developed a 6-node triangular and a 8-node quadrilateral shell element using the mixed, isoparametric approach. Tahiani and Lachance [6.8] also pointed out that the nonlinear stiffness matrices can be explicitly integrated when the triangular element is with straight sides. Note that references [6.8] and [6.9] both in fact applied the total Lagrangian incremental formulation. The applications of the updated Lagrangian formulation can be found in references [6.10-13], among many others. References [6.10] and [6.11] were based on the hybrid stress approach. The elements in references [6.12] and [6.13], on the other hand, adopted the discrete Kirchhoff theory (DKT) as the bending component element and the constant strain triangle (CST) as the membrane component element, and were displacement-based.

Meanwhile, more general nonlinear shell analysis which includes material (such as plasticity) and geometric (such as large displacements and rotations, and finite strains) nonlinearities has over the years generated many publications in the literature, among

them are, for instance, references [6.14-22] * . In references [6.14-15] both the total and updated Lagrangian formulations were employed in conjunction with some displacement-based isoparametric elements. Reference [6.16] considered effects of large strain and large rotation and rate-type constitutive law, and the elements used were displacement-based and isoparametric. Reference [6.17], on the other hand, studied large membrane strains and Mooney-Rivlin material. While reference [6.18] combined the total Lagrangian formulation with semi-Loof elements to investigate small strain elasto-plastic problems. Similar approaches can be found in reference [6.19]. Using 4-node degenerate elements and the total or updated Lagrangian formulations, Parisch [6.20] employed a layer model for the treatment of plastic behaviours of material. For mixed/hybrid formulations, Pinsky and Jang [6.21] considered small strain elasto-plastic deformation by employing curved 9-node quadrilateral C^0 shell elements which were based on assumed co-variant strains referred to the element natural co-ordinate system. Note that in curvilinear co-ordinate system the co-variant strains are non-physical. But they have physical meanings under Cartesian co-ordinates. Adopting the updated Lagrangian approach, Saleeb and co-workers [6.22] also developed a quadrilateral C^0 element with independently assumed

---

* It should be pointed out that for large strain rate problems, Atluri derived a Hu-Washizu type funtional in which displacement and rotation fields are independent (*J. Structural Mechanics*, **8**, 61-92, 1980). Based on the linear form of this functional Atluri *et al.* constructed 4-node plane stress elements with drilling DOF (*Computational Mechanics*, **9**, 417-428, 1992 and **11**, 229-251, 1993).

strains. In addition, it accounted for effects such as large rotations, finite strains and used rate-type material model.

It is well known that general nonlinear shell analysis is challenged by many conceptual, theoretical, as well as computational difficulties. As Saleeb and co-workers [6.22] pointed out, these difficulties may include, even when confining the scope to static and quasi-static analysis: (1) **consistent linearization** of the underlying variational form of the governing equations; (2) use of **objective measures** of stress and strain, and their rate, that are suitable for the particular form of the constitutive relation used; (3) treatment of **large rotations**, in both stiffness derivation and configuratio.. updating; and (4) the proper representation of **nonlinear material behaviours**. On the computational side, efficient algorithmic developments, for both the element level calculation and the global level incremental, iterative solution strategies, are crucial considerations. For dynamic problems, the construction of mass matrix has to be carefully dealt with, especially when encountering large angular velocity and acceleration. These issues will be elaborated as follows.

(1) *Incremental formulations and variational principles*

For structural problems with both geometric and material non-linearities, the total Lagrangian and updated Lagrangian formulations come as two natural choices. The total Lagrangian formulation has found wide application in problems involving geometrical non-linearity and elastic stability. The updated Lagrangian approach is believed to be better suited for problems with materials having rate form constitutive relations.

References [6.10-13] argued that the updated Lagrangian formulation may be particularly useful for slender structures such as beams, plates and shells, and may be more effective for shell elements that use interpolation functions of different order for the bending and membrane displacements. From the viewpoint of computational effectiveness, Bathe and Bolourchi [6.12] pointed out that the updated Lagrangian approach may be better. However, the issue has no black-and-white answers. As Bathe [6.23] indicated, the only theoretical difference between the two formulations lies in the choice of reference configurations for the kinematic and static variables. Therefore, the choice of using either the total Lagrangian or the updated Lagrangian formulation in a finite element solution depends [6.23], in practice, on their relative numerical effectiveness. A general observation is that the total Lagrangian formulation is involved with a more complex strain-displacement relation. This complexity enables one to include the so-called "initial displacement effects", and to have more control over the accuracy of total displacements. On the other hand, the updated Lagrangian formulation needs to update all the kinematic and static variables at every time step. Although the updated formulation itself does not have device to consider the "initial displacement effects", references [6.11, 6.22] were able to do so by adding a corresponding strain energy term to the variational principle so as to enforce the compatibility of the total displacements.

Concerning the updated Lagrangian formulation combined with mixed or hybrid elements, references [6.10-11, 6.22] offered detailed discussions. The incremental variational principle of Horrigmoe [6.10] chose incremental displacements and stresses as independently assumed variables, and was based on a modified incremental form of

Hellinger-Reissner's principle [6.24]. The modifications [6.10, 6.24] here included the introduction of element boundary displacement field and the corresponding stress resultants at the element boundary as the Lagrangian multipliers. It can be shown that, if the state of stresses is in equilibrium within the element and at the element boundary, the modified Hellinger-Reissner's principle in references [6.10, 6.24] reduces to the incremental complimentary energy functional. It should then be mentioned that both references [6.10] and [6.24] assumed that the equilibrium at the reference configuration is satisfied. On the other hand, references [6.11, 6.22] derived their incremental variational principles without invoking such an assumption. In fact, a similar development can be traced back to reference [6.25]. Since the reference configuration is not completely in equilibrium, correction terms are brought in. These correction terms should represent the imbalance of stresses in the reference configuration, and are therefore expected to reduce, even vanish, when the equilibrium state of the reference configuration is achieved with greater numerical accuracy. The functional presented in references [6.11, 6.22, 6.25] was capable of reflecting such an imbalance. In addition, Boland and Pian [6.11] employed the convected, updated Lagrangian formulation. In this formulation, the Cauchy stresses were chosen as the initial stresses and were referred to the convected co-ordinate system. Another feature of the formulation by Boland and Pian [6.11] is that it brought in a correction term to check for the compatibility mismatch between the total strains accumulated from the independently assumed incremental strains and the strains calculated from the total displacements. The same correction term was included in reference [6.22]. Its independently assumed strains, and thus the corresponding stresses, were defined with

respect to the lamina co-ordinate. Such a definition simplifies the numerical integration required in forming the element stiffness matrix. References [6.11, 6.22] argued that for an incremental analysis using hybrid or mixed formulation it is desirable to ensure the compatibility between the total strains and displacements. In the total Lagrangian formulation, the compatibility of the total strains and displacements is accounted for through the part of its linear stiffness matrix that contains the initial displacement effects. As a result, the total Lagrangian formulation usually does not require the compatibility mismatch correction term. For the updated Lagrangian formulation, Saleeb and co-workers [6.22] found that the correction term was only necessary for the first iteration of every load increment. However, completely disregarding the correction term resulted in convergence difficulties. Another concern of the correction term is that, direct summation of incremental strains has little physical ground, since the incremental strains obtained at every time step are measured with respect to different configurations. Saleeb and co-workers [6.22] outlined an approximate scheme to sum up such incremental strains.

(2) *Linearization of the incremental principle*

As Gadala and co-workers [6.26-27] pointed out, the most general approach for Lagrangian formulation is to consider fully nonlinear kinematic relations within a linear increment. Starting from the energy balance equation in the rate form, Gadala and co-workers [6.26] derived an incremental equilibrium equation whose left hand side (LHS) consists of four stiffness matrices: the usual small displacement (or incremental) stiffness

matrix, the initial stress (or the geometric) stiffness matrix, the initial displacement (or the initial rotation) stiffness matrix, and the initial load matrix; and whose right hand side (RHS) includes the incremental load vector. In fact, Oden [6.28] arrived at the same four component stiffness matrices. Comparing the formulations in references [6.26, 6.28] with some other total or updated Lagrangian formulations, for example, references [6.8-25], one may find that the difference is that, in references [6.26, 6.28] the initial displacement (or rotation) stiffness matrix exists for both the total and the updated Lagrangian formulations, while in references [6.8-25] it is associated with the total Lagrangian formulation only. Two factors may contribute to the difference. Firstly, references [6.8-25] began with virtual work principle rather than the energy balance equation in the rate form. The latter is believed to be more appropriate. Secondly, the linearization process is invoked during the derivations in references [6.8-25]. This seems to suggest that, for the updated Lagrangian approach, the initial displacement (or rotation) matrix is somehow missed during the linearization process. Note that if the development in reference [6.26] is followed, the updated Lagrangian formulation would lose its attractiveness: being simpler in terms of formulating. Furthermore, the formulation developed in reference [6.26], when employed for dynamic analysis, would be extremely expensive , if not computationally infeasible.

Therefore, confining our attention to the updated Lagrangian formulation, linearizing the incremental variational principle would be a more practical approach. A closer look of the formulation of Gadala and co-workers [6.26] reveals that, the small displacement and the initial stress stiffness matrices contain the second-order "product"

of the first-order derivatives of displacement. For the initial displacement (or rotation) stiffness matrix the order of the "product" is either three or four. If the third and fourth order terms are disregarded as in references [6.8-26], it indicates that the linearization is second-order accurate. As to the initial load matrix, it is associated with non-conservative loads and will not be further discussed since it is beyond the scope of the present study.

A remark here is that, as observed in Section 3.3, owing to the existence of drilling degrees-of-freedom (DDOF), the stress tensor has its symmetric and skew-symmetric components. Consequently, the initial stress (or the geometric) stiffness matrix becomes non-symmetric (see further discussion in Section 6.3 below). In the present study, the skew-symmetric part of the stiffness matrix will be disregarded so as to provide a basis for comparison to the case in which the skew-symmetric part of the stiffness matrix is incorporated in the derivation. The incorporation of the skew-symmetric part of the stiffness matrix and the comparison to results of the present study remain part of the author's interests of ongoing investigation. Results of such investigation will be reported in due course.

(3) *Stress and strain measures*

The most commonly used stress measures are [6.23, 6.30]: the Cauchy stress tensor, the second Piola-Kirchhoff stress tensor and the Jaumann stress rate tensor. The Cauchy stresses represent the true state of stress of a deformed body and yield simpler equations of motion compared with the second Piola-Kirchhoff stresses. The Cauchy stresses should be used when determining the occurrence of yielding. The second Piola-

Kirchhoff stress tensor, on the other hand, measures the state of stress with respect to the undeformed configuration and therefore has little physical meaning. However, its components are invariant under a rigid body rotation of the material, that is, the second Piola-Kirchhoff stress tensor is **objective**. The Jaumann stress rate tensor also preserves invariance under rigid body rotations of the material.

The three most frequently used strain measures are [6.23, 6.30]: the Green or the Green-Lagrange strain tensor, the Almansi strain tensor and the velocity strain or the rate of strain tensor. Both the Green strain tensor and the velocity strain tensor are objective tensors and they are energetically conjugate to their corresponding stress tensor, the second Piola-Kirchhoff stress tensor and the Jaumann stress rate tensor, respectively. The Almansi strain tensor, however, in contrast to the Green strain tensor, is not invariant under rigid body rotations [6.23]. Another strain measure is the so-called co-rotational or convected strain [6.30-32]. Belytschko [6.30] compared the accuracy of the four aforementioned strain measures (for the velocity strain tensor, its accumulative or integrated result was applied, which is the so-called logarithmic strain) and showed that for large strain problems, there is a large difference among different strain measures. In general, the Almansi strain tensor performs relatively poorly. The co-rotational strain seems to be the most accurate measure, followed by the Green strain tensor. The co-rotational strain tensor has little physical meaning (except for specific cases such as uniaxial deformation) and should be transformed to the Green, or Almansi strain tensor [6.30].

When pairing stress and strain measures, two factors must be taken into account: (1) the stress and strain measures should be energetically conjugate; and (2) they should be in accordance with the constitutive law used to model material behaviours. Between the two conjugate pairs of stress and strain measures mentioned in the previous paragraph, the second Piola-Kirchhoff stress tensor and the Green strain tensor are suited for elastic and hyper-elastic materials whose behaviours are determined from the total current strains; and the Jaumann stress rate tensor and the velocity strain tensor are more effective for analysis of rate form constitutive relations, or path-dependent materials.

In addition, there are incremental stress and strain measures. Such incremental measures are necessary since incremental formulation is used in numerical computation. The incremental stress is usually the incremental second Piola-Kirchhoff stress tensor, and the incremental strain the incremental Green strain tensor. Note that the actual form of the incremental Green strain tensor may be different depending on whether the total or the updated Lagrangian formulation is used. The incremental Green strain tensor is generally separated into "linear" and "quadratic" parts. The "quadratic" part remains the same while the "linear" part differs in whether the initial displacement is included. Detailed formulation of these incremental strain measures can be found in, for example, equations (2.54) and (2.56) of reference [6.33]. Chiou and co-workers [6.34] used the term "incremental Green strain" when it is applied with the total Lagrangian formulation, and the term "incremental Washizu strain" with the updated Lagrangian formulation. Other alternative stress and strain measures were introduced by Atluri [6.35].

Regarding constitutive law for elasto-plastic deformation, the classical small deformation elasto-plasticity theory decomposes the total infinitesimal strain as the sum of the "elastic" and "plastic" parts. Such a theory establishes [6.23, 6.33] a relation between the rate of the second Piola-Kirchhoff stress tensor and the rate of the Green strain tensor, or in its incremental form, a relation between the incremental second Piola-Kirchhoff stress tensor and the incremental Green strain tensor or the incremental Washizu strain tensor depending on whether the total or the updated Lagrangian formulation is used.

The additive decomposition which is usually accredited to Green and Naghdi finds physical ground and can be deduced mathematically only when the strain considered is infinitesimally small. In finite elasto-plastic deformation problems, the decomposition of strain measures is not clearly distinguished. At the present time, two major approaches appear in the literature, which are the Nemat-Nasser's additive decomposition of total strain rate into its "elastic" and "plastic" parts [6.36-38] and Lee's multiplicative decomposition of total deformation gradient into products of "elastic" and "plastic" deformation gradient [6.39-44]. Green and Naghdi [6.45] stated that the "elastic strain" in their formulation is not the ordinary elastic strain except for restricted cases such as deformations with infinitesimal strains. The issue seems to be far from being resolved. It seems, therefore in general, Lee's theory is more mathematically and numerically involved, while the additive decomposition due to Green and Naghdi, and Nemat-Nasser is more flexible. As to the differences between the two decompositions and the theories thus followed, Lubarda and Lee [6.39] showed that in the case of small elastic strain with

large plastic strain Lee's theory becomes essentially that of Green-Naghdi. It is interesting to notice the comparison made in reference [6.46] which found that the differences were obvious in large strain cases. Though this observation is expected, the comparison in reference [6.34] is not convincing in the sense that, when choosing constitutive relation for the "elastic" part of strain, it employed Hooke's law in conjunction with Green-Naghdi's theory, and a quadratic equation, equation (3) of reference [6.46], with Lee's theory. This inconsistency leaves one to wonder whether the differences that Chiou and co-workers [6.46] observed are due to different constitutive relation or due to different decomposition adopted. The implementation of Lee's theory in conjunction with the total or updated Lagrangian formulation has been presented in references [6.34, 6.47]. Similar development can also be found in references [6.48-50].

A final point here is that, in all aforementioned theories, the "plastic" part of the strain, or the strain rate, or the deformation gradient, is defined on the physical ground that unloading should involve no additional plastic flow, or unloading is completely elastic. This implies that these theories are applicable to elasto-plastic materials which recover the "elastic" part of the deformation, as opposed to some other types of material, such as "elastro-plastic" materials which, upon unloading from a deformed configuration, recover only a certain portion of strains [6.37,6.51].

(4) *Large rotations*

Nonlinear analysis involving large rotations has drawn much attention in recent years [6.22, 6.31-32, 6.52-74] with early publications of the topic appearing in the late 1960's, as noted by Wempner [6.53]. At the present time, it seems that the treatment of finite rotations can be classified into the following four approaches.

The first one [6.54-55] was based on the observation that the motion of an individual element to a large extent consists of rigid body motion. Therefore, if the rigid body motion can be eliminated from the total displacements, the deformation part of the motion is always a small quantity relative to the local element axes. When this is done, shell elements developed for small displacement analysis, in conjunction with the updated Lagrangian formulation [6.54] or the co-rotational total Lagrangian formulation [6.55], may be applied to the nonlinear analysis of shells in which large displacements and rotations are involved. The precursors of this approach can be traced back to references [6.31-32, 6.75], for instance. In references [6.31-32], convected displacements were separated from the total displacements and were then used to calculate convected strains. The natural modes of reference [6.75] are in fact pre-identified deformation modes. Note that, though the principle of splitting total displacements into its rigid body motion part and deformation part holds true theoretically, it is practically not an easy task, particularly with large strain cases. Furthermore, owing to the non-commutative nature of large rotations, the sequence by which the rigid rotations are separated from the total displacements (rotations) will no doubt affect the resulting deformation part of the motion, and consequently other quantities involved in the incremental and updating process. In

reference [6.73] Argyris proposed to circumvent the non-commutativity by using the "semi-tangential" angles to represent finite rotations.

The second approach [6.52, 6.56-57, 6.74] retained the nonlinear nodal rotation terms in the displacement interpolation function, which are mainly sines and cosines of the nodal rotations. Thus, it removed the restriction of small nodal rotations between two successive load increments. Yet this approach complicates the derivation of element matrices, and numerical integration has to be employed because of the existence of sine and cosine terms.

The third approach was proposed by Bathe and Bolourchi [6.12]. With particular reference to the updated Lagrangian formulation, Bathe and Bolourchi proposed to write the transformation matrix between the current (deformed) local axes and the original (undeformed) global axes as product of two matrices, one for transformation between the current local axes and the original local axes, the other for transformation between the original local axes and the original global axes. Then, the former was sub-divided into product of transformation matrix due to the relative translational displacements of the two nodes of a beam element and transformation matrix taking into account the axial rotation of the beam. Note that in this approach the transformation matrices are written in terms of displacements and rotations of the beam element which may be large in magnitude. This approach is in fact equivalent to evaluating the transformation matrix using Euler angles, as presented by Besseling [6.76] who gave the transformation matrix expressed in terms of Euler angles. The drawback of this approach is that it may be difficult to

generalize to triangular elements, and relatively large amount of algebra is involved. In addition, for zero nutation angles the corresponding precession and spin angles become undefined.

The fourth approach [6.22, 6.58-72] starts by noting that the spatial configuration of a shell can be defined by the position vector field for points on the mid-surface of the shell as well as the director vector field that gives the orientations of thickness vectors emanating from the mid-surface points. The description of the position vector field is straightforward. It is not so for the director field due to the fact that finite rotations in space can not be treated as vectors. That is, finite rotations are not commutative. Therefore, the fourth approach focuses on defining a transformation matrix for any magnitude of the director rotation increment from time instant "t" to that at "$t+\Delta t$" in the updating procedure of the director vector field . This transformation matrix or the so-called exponential mapping is able to map an infinitesimal rotation into a large rotation, and a large rotation into another large rotation. Consequently, the change of the orientations of the directors can be correctly represented and the director field can be updated accurately. The exponential mapping also preserves the length of the director so that the inextensibility of the director will not be violated. Another concern is the representation of the director vector field which is complicated by the non-commutativity of large rotations. Consequently, several definitions of rotational parameters are introduced, the most common one being the Rodrigues parameters [6.22, 6.58-59, 6.61-73]. Here, a large rotation is represented by the so-called rotational pseudo-vector, or the axial vector [6.73]. Similar to any other vectors, the rotational pseudo-vector can be

expressed in terms of its components along a set of orthogonal axes. However, these components can not be interpreted as the component rotations about those orthogonal axes. In the limiting case of infinitesimal rotations, such an interpretation applies. This aspect has been well demonstrated by Oliver and Onate [6.57] which used, considering large rotations, as nodal degrees-of-freedom, the two in-plane components of the rotational pseudo-vector and expressed them in terms of two other angles that have physical meanings but are still not the rotations about the basis Cartesian axes. These two angles represent rotations about the basis Cartesian axes when the rotational pseudo-vector approaches the basis Z-axis as a result of the rotations approaching the infinitesimal limiting case. In reference [6.22] the incremental rotations about the time-dependent "fibre" co-ordinates, equivalent to the moving frame of references [6.58-59, 6.61] and the director orthogonal frame in references [6.62-67], at time "t" was taken as the components of the rotational pseudo-vector and subsequently used to construct the exponential mapping and to update the "fibre" co-ordinates. Similarly, Simo and Vu-Quoc [6.58-59, 6.61] specified infinitesimal displacement and infinitesimal rotation as the incremental variables of the three dimensional finite strain rod model. In their later work studying more complicated and general shell problems, Simo and co-workers [6.62-67] assumed two separate incremental fields, the incremental mid-surface displacement field and the incremental director field which was related to the field of incremental rotational pseudo-vector. It was then assumed that the incremental rotation component along the director direction was irrelevant. With such an assumption, spatially, the incremental rotational pseudo-vector is perpendicular to the current director, while the incremental

director is also perpendicular to both the incremental rotational pseudo-vector and the current director, and is equal to the cross product of the two, see equation (6.5a) of reference [6.62]. Note that, since references [6.62-67] defined the incremental rotational pseudo-vector or the incremental component rotations rather than incremental rotations about certain axes, they allowed the incremental rotation to be of any magnitude.

Obviously, the fourth approach is based on the notion that director vector field exists and is unique. In reality, this may not always be the case since intersecting shell structures can have discontinuous directors, for instance. Furthermore, when the shell structures are complex the determination of the directors becomes difficult. Formulations that can accommodate such applications are, therefore, useful and necessary. This is one of the aspects that the present study considers and will be discussed in Sub-section 6.3.6.

(5) *Dynamic analysis*

When extending a finite element formulation to cover dynamic analysis from a static one, the common approach is to add the consistent or lumped mass matrix. Originally, this approach took into account only the effect of translational inertia [6.77-78]. Then the effects of rotary inertia due to bending and associated with the drilling degrees-of-freedom (DDOF) were included in Chapter 5. Such an approach is accurate if the rotational motions involved are of relatively low angular velocity and acceleration. For those problems exhibiting considerable amount of angular velocity and acceleration,

reference [6.61] concluded that the part of mass matrix associated with the rotational degrees-of-freedom is nonsymmetric and configuration dependent. It should be emphasized that the focus of the current phase of the present investigation is on problems with symmetric stiffness and mass matrices. Cases with non-symmetric stiffness and mass matrices, and their comparison are one of the author's further research interests and results of the investigation that considers non-symmetric mass and stiffness matrices will be reported in due course.

(6) *Algorithmic development*

Concerning the development of efficient algorithms, references [6.80-81] offered detailed discussions. For example, it was suggested that implicit integration techniques would be more effective for structural dynamic problems. Note that when mass and damping matrices are not diagonal, the central difference method is an implicit one.

An ultimate objective in the present investigation is the determination of the response statistics of nonlinear structures. To this end the stochastic central difference method [6.82-87] shall be applied to determine the variances and covariances of responses of shell structures under various random excitations. During such a computing process, one also needs to, in parallel to the stochastic central difference method, employ the deterministic central difference method to conduct a transient dynamic nonlinear analysis of the shell structure. Here the deterministic central difference method is modified in such a way that its recursive expression is written with respect to displacements only. This is consistent with the stochastic central difference method. It also saves the cost of updating

angular velocity and acceleration through exponential mapping. Another consideration is that the central difference method, deterministic or stochastic, is conditionally stable. It has been found [6.82-88] that the critical time step size of the stochastic central difference method is smaller than its deterministic counterpart, given that the system without the excitations is the same. The actually used time step size for the stochastic central difference method depends mainly on accuracy and has again been found to be smaller than its deterministic counterpart [6.82-88]. This means that the time step size should be chosen in accordance with the stochastic central difference method in conjunction with the time co-ordinate transformation and adaptive time schemes that were proposed earlier in Chapter 2.

In closing this section, an outline of the nonlinear analysis of this thesis (see the remaining sections of this chapter and Chapter 7) is given in the following. It is to develop nonlinear hybrid strain based finite element models for the dynamic nonlinear analysis of shell structures of arbitrary shapes. The finite elements are of flat triangular geometry with 3 corner nodes and 18 degrees-of-freedom (DOF), including 3 translational and 3 rotational DOF for each node. The derivation of these elements starts with the assumption that each node on the shell surface has a unique director. When simplified, the linear parts of these elements reduce to those identified as $AT+k_1$ and $AT+(k_1^3)'$ in Chapter 3, or those denoted by NFORMU=14 and 16 in Chapter 5. Note that in Chapters 3 through 5 the director of a node was not uniquely defined. Rather, the three nodes of an element shared the same "director". The updated Lagrangian approach is

adopted in conjunction with an incremental Hellinger-Reissner variational principle which takes incremental displacements and incremental strains as the two independently assumed fields. Corresponding to the selected incremental formulation and variational principle, the incremental second Piola-Kirchhoff stress and the incremental Washizu strain are chosen as the incremental stress and strain measure, respectively. Explicit expressions for the linear or small displacement stiffness matrix, the initial stress or the geometric stiffness matrix and the pseudo-load vector are obtained and written in terms of variables of the reference configuration. To account for large rotations, exponential mapping is employed for configuration updating. Both geometric and material nonlinear problems are studied. In the latter case, the J_2 flow theory of plasticity is employed in conjunction with Ilyushin's yield criterion for thin shells [6.92]. In terms of solving the nonlinear final equilibrium equation, the incremental-corrective scheme is applied. Finally, the deterministic and stochastic central difference methods are executed at the same time to determine the time-dependent tangent stiffness matrix, mean as well as mean square and variance of responses of a shell structure. To this end, strategies such as time co-ordinate transformation and adaptive time schemes (see Chapter 2) will be incorporated so that the execution of the deterministic and stochastic central difference method is more effective and accurate.

6.2 Incremental Variational Principle and Its Linearization

As in any nonlinear analysis, the fundamental difficulty is that the configuration of a body at time "t+Δt" is unknown. In seeking for approximate solution of these nonlinear analysis, incremental formulations assume that the static and kinematic variables in the current configuration C^t are known. And their values in an unknown neighbouring configuration $C^{t+\Delta t}$ at a later time "t+Δt" are then determined from these known solutions. The starting point of such incremental analysis is an appropriate incremental variational principle, which is, in the present study, the Hellinger-Reissner variational principle in the incremental form. It has two independently assumed fields, the incremental displacements (and rotations) and the incremental strains. The principle takes the following form:

$$\Delta\pi_{HR}(\Delta u,\Delta e) = \int_{V^t}\left[-\frac{1}{2}(\Delta e)^T\tilde{D}(\Delta e) + \sigma^T(\Delta\bar{e}) + (\Delta e)^T\tilde{D}(\Delta\bar{e})\right]dV - W^{t+\Delta t} \tag{6.1}$$

where the integration is carried out over the reference volume V^t, and

Δu is the vector of assumed incremental displacement;

Δe is the vector of assumed incremental Green strain;

$\Delta\bar{e}$ is the vector of incremental Washizu strain calculated from the vector Δu, see equation (6.2);

$\tilde{D}$ is the time-dependent material elastic matrix so that $\Delta S = \tilde{D}\Delta e$ with ΔS being the incremental second Piola-Kirchhoff stress vector, see Section 6.5;

σ is the Cauchy stress vector at time "t"; and

$W^{t+\Delta t}$ is the work-equivalent term corresponding to prescribed body-force and surface traction in configuration $C^{t+\Delta t}$.

In equation (6.1), the incremental Washizu strain $\Delta\bar{e}$ is, in component form

$$\Delta\bar{e}_{ij} = \Delta\varepsilon_{ij} + \Delta\eta_{ij} ,$$
$$\Delta\varepsilon_{ij} = \frac{1}{2}(\Delta u_{i,j} + \Delta u_{j,i}) , \qquad (6.2)$$
$$\Delta\eta_{ij} = \frac{1}{2}\Delta u_{k,i}\Delta u_{k,j}$$

where the Einstein summation convention for indices has been adopted (for k) and the differentiation is with respect to reference co-ordinates, x_i^t (i = 1,2,3) at time "t".

Now, assuming that within every element it can be written

$$\Delta u = N\Delta q , \quad \Delta e = \tilde{P}\Delta\beta \qquad (6.3)$$

where Δq is the vector of incremental nodal displacements and $\Delta\beta$ the vector of incremental strain parameters. And N and $\tilde{P}$ are the matrices of displacement interpolation function and strain distribution function. Details of the two matrices will be

introduced in Section 6.3. Substituting equation (6.3) into (6.1) gives, with V_e being the volume of an element of the reference configuration

$$\begin{aligned}\Delta\pi_{HR}(\Delta u,\Delta e) - \Delta\pi_{HR}(\Delta q,\Delta\beta) \\ - \sum\{\int_{V_e}[-\frac{1}{2}(\Delta\beta)^T\tilde{P}^T\tilde{D}\tilde{P}(\Delta\beta) + \sigma^T B_L\Delta q \\ + \frac{1}{2}(\Delta q)^T(B_{NL})^T\bar{\sigma}^T B_{NL}(\Delta q) + (\Delta\beta)^T\tilde{P}^T\tilde{D}B_L\Delta q \\ + (\Delta e)^T\tilde{D}(\Delta\eta)\,]dV - W^{t+\Delta t}(\Delta q)\}\,.\end{aligned} \tag{6.4}$$

Note that in arriving at equation (6.4) it has been defined that

$$\begin{aligned}\Delta\varepsilon &= (B_L)(\Delta q) \\ \sigma^T\Delta\eta &= \frac{1}{2}(\Delta q)^T(B_{NL})^T(\bar{\sigma})^T(B_{NL})(\Delta q)\end{aligned} \tag{6.5}$$

where B_L and B_{NL} are the so-called linear and non-linear strain-displacement matrices and will be discussed in Section 6.3. And $\bar{\sigma}$ is a matrix that contains the Cauchy stress components at time "t". The construction of $\bar{\sigma}$ from σ is given in Sub-section 6.3.6. The last term inside the square brackets on the RHS of equation (6.4) contains "third-order" product of Δq and $\Delta\beta$, and will therefore be disregarded when linearizing equation (6.1) or (6.4). Next, defining

$$\tilde{H} = \int_{V_e} \tilde{P}^T \tilde{D} \tilde{P} dV ,$$

$$G_e = \int_{V_e} \tilde{P}^T \tilde{D} B_L dV ,$$

$$k_{NL} = \int_{V_e} (B_{NL})^T \bar{\sigma} B_{NL} dV , \tag{6.6}$$

$$F_1 = \int_{V_e} B_L^T \sigma dV ,$$

and substituting equation (6.6) into (6.4) leads to

$$\Delta\pi_{HR}(\Delta q, \Delta\beta) = \sum \{ -\frac{1}{2}(\Delta\beta)^T \tilde{H}(\Delta\beta) + F_1(\Delta q) + \frac{1}{2}(\Delta q)^T k_{NL}(\Delta q) + (\Delta\beta)^T G_e(\Delta q) - [F(t+\Delta t)]^T(\Delta q) \} \tag{6.7}$$

with F(t+Δt) being the external nodal force vector, in configuration $C^{t+\Delta t}$, associated with the $W^{t+\Delta t}(\Delta q)$ term of equation (6.4). Seeking stationarity of equation (6.7) with respect to Δβ yields

$$\Delta\beta = \tilde{H}^{-1} G_e(\Delta q) . \tag{6.8}$$

Substituting equation (6.8) into (6.7) and seeking stationarity with respect to Δq result in the following "equilibrium equation":

$$(k_L + k_{NL})(\Delta q) = F(t+\Delta t) - F_1 \tag{6.9}$$

where

$$k_L = G_e^T \bar{H}^{-1} G_e \tag{6.10}$$

is the element linear (or small displacement) stiffness matrix. The matrix k_{NL}, as defined by equation (6.6), is the element initial stress stiffness matrix. On the RHS of equation (6.9) F_1 is the pseudo-force vector. Rewriting $F(t+\Delta t) - F_1$ as $\Delta F + F(t) - F_1$, it can be seen that $F(t+\Delta t) - F_1$ consists of, ΔF, the incremental external force from "t" to "t+Δt", as well as $F(t) - F_1$, the equilibrium imbalance at time "t". If the equilibrium at time "t" is satisfied in an average sense, $F(t) - F_1$ vanishes and $F(t+\Delta t) - F_1$ reduces to the increment of external force from "t" to "t+Δt", that is, ΔF. Note that equation (6.1) differs from those presented by Boland and Pian [6.11], and Saleeb and co-workers [6.22]. The variational principle applied in references [6.11, 6.22] was based on the hybrid stress formulation and it contained one additional term, which is, in the present notation, $\int_{V^e} [\ (\Delta e)^T \tilde{D}(e - \bar{e})\ ] dV$, where Δe and $\tilde{D}$ have the same meaning as defined in equation (6.1), e is the vector of the Almansi strain accumulated from Δe and $\bar{e}$ is the Almansi strain calculated from the total displacement, respectively. Note that $\bar{e} = \frac{1}{2}(u_{i,j} + u_{j,i} - u_{k,i} u_{k,j})$. The aforementioned additional term accounts for compatibility mismatch due to inaccurate total displacements and strains. Boland and Pian

[6.11] argued that the term should not be expected to vanish. On the other hand, the numerical experiments of Saleeb and co-workers [6.22] showed that, though totally discarding the term resulted in convergence difficulties, including the term in *only* the first iteration of every load step yielded essentially the same results as those having the term under all circumstances. In the present study, the compatibility mismatch term vanishes as a consequence of the presently employed hybrid strain formulation. This is because in the present formulation $e = \bar{e}$.

The above element level formulas are applied to every element. Once all element matrices are determined they are assembled to form the global "equilibrium equation". This equation is then solved for the displacement increments.

Finally, it should be pointed out that, the incremental Washizu strain can be recovered from $\Delta\beta$ through

$$\Delta e = \tilde{P}(\Delta\beta) = \tilde{P}\tilde{H}^{-1}G_e(\Delta q) \tag{6.11}$$

and the incremental second Piola-Kirchhoff stress can be found as

$$\Delta S = \tilde{D}\Delta e \ . \tag{6.12}$$

6.3 Element Stiffness Matrices

This section is concerned with the derivation of element stiffness matrices. Sub-section 6.3.1 introduces the element geometry and co-ordinate systems. Sub-section 6.3.2 deals with the assumed incremental displacement field within an element while Sub-section 6.3.3 considers the assumed incremental strain field within an element. Derivation of the linear stiffness matrix is included in Sub-section 6.3.4 whereas derivation of the initial stress stiffness matrix is presented in Sub-section 6.3.5. Sub-section 6.3.6 is concerned with a simplified version of stiffness matrices from those derived with the nonlinear formulation investigated in Sub-sections 6.3.4 and 6.3.5.

6.3.1 Element geometry and co-ordinate systems

The finite elements under consideration are a 3-node flat shell element with triangular geometry, shown in Figure 6.1. The three nodes are allocated at the three corners of the mid-surface of the triangular element. A local rectangular co-ordinate system is attached to node 1, with its r-axis coinciding with the side 1-2, its t-axis being parallel to the normal of the element and its s-axis perpendicular to the r-t plane. With such a co-ordinate system, the r and s co-ordinates of nodes 1, 2, and 3 are: (0,0), $(r_2,0)$ and (r_3,s_3), respectively. Also defined is the director orthogonal frame, V_r, V_s and V, at any points on the mid-surface. In the undeformed configuration, the director V coincides with the normal of the shell. However, as the shell deforms, the director is, in general, not normal to the mid-surface. Consequently, the director orthogonal frame differs from point to point and from the r-s-t system. Note that the setting of the two co-ordinate

systems for each element is necessary to capture the large extent to which the shell deforms, especially for large strain deformations. Here the director orthogonal frame serves as a basis of measuring and recording the change of orientation of points situated on the mid-surface.

The six nodal degrees-of-freedom (DOF) are

u the displacement in the r-direction,

v the displacement in the s-direction,

w the displacement in the t-direction,

θ_r the rotation component along the r-axis,

θ_s the rotation component along the s-axis, and

θ_t the rotation about the t-axis, or the drilling DOF (DDOF).

and they are considered positive if along the positive directions of corresponding axes.

As will be seen later, the present development of finite element formulation differs from that of references [6.62-67] in three aspects. Firstly, the element formulations in references [6.62-67] are based on the global co-ordinates while in the present study local r-s-t co-ordinates are applied. The use of local r-s-t co-ordinates is convenient for expressing complex strain distribution within an element. Secondly, in references [6.62-67] the three mid-surface displacements and the two in-plane "rotational DOF" were chosen as the nodal DOF. References [6.62-67] seemed to suggest that the DDOF is irrelevant in the analysis of shells and can therefore be disregarded. On the other hand, previous studies of the present investigation, Chapters 3 through 5, have demonstrated the importance of incorporating the DDOF. Thirdly, unlike references [6.62-67], in the

simplified version of the present study (see Sub-section 6.3.6), the uniqueness and updating of director are not necessary. In what follows, we proceed with the derivation by first considering the case where directors are uniquely defined. Then, such directors are "removed".

6.3.2 Assumed incremental displacement field within an element

Following the isoparametric approach, the local co-ordinates (r,s,t) of an arbitrary point within the element is

$$\begin{Bmatrix} r^t \\ s^t \\ t^t \end{Bmatrix} = \sum_{i=1}^{3} \xi_i \begin{Bmatrix} \overline{r}_i^t \\ \overline{s}_i^t \\ 0 \end{Bmatrix} + \eta^t \sum_{i=1}^{3} \xi_i V_i^t \qquad (6.13)$$

where the superscript "t" denotes time "t" and the over bars indicate variables (mainly co-ordinates and translational displacements and their increments) that are defined on the mid-surface. Rotational displacements and directors and their increments are understood to be defined on the mid-surface. They will not be over-barred and confusions should not caused. V_i^t (i=1,2,3) denotes the director of node i at time "t", and ξ_i (i=1,2,3), is the natural or area co-ordinates of a triangle satisfying

$$0 \le \xi_i \le 1$$

$$\sum_{i=1}^{3} \xi_i = 1 \qquad (6.14a,b)$$

η^t is the co-ordinate along the director direction and satisfies

$$-\frac{h^t}{2} \le \eta^t \le \frac{h^t}{2} \tag{6.14c}$$

with h^t being the thickness of the shell at time "t", which is considered constant over the entire element in the present study. Note that the first summation of equation (6.13) represents the position of the mid-surface while the second summation indicates that the director orthogonal frame is interpolated in exactly the same way as the mid-surface r and s co-ordinates. In references [6.62-67], such an interpolation scheme is called continuum consistent interpolation. Compared with the other two interpolation schemes proposed in references [6.62-67], continuum consistent interpolation is simple and easy to implement.

The incremental displacements of any point within the element from time "t" to "t+Δt" can be expressed as

$$\begin{Bmatrix} \Delta u^t \\ \Delta v^t \\ \Delta w^t \end{Bmatrix} = \sum_{i=1}^{3} \xi_i \begin{Bmatrix} \overline{\Delta u_i^t} \\ \overline{\Delta v_i^t} \\ \overline{\Delta w_i^t} \end{Bmatrix} + \eta^t \sum_{i=1}^{3} \xi_i \, (\Delta V_i^t) \; . \tag{6.15}$$

In equation (6.15) the first summation represents the incremental displacements of any points located on the mid-surface. The second summation reflects the change in orientation of director of any points on the mid-surface which is interpolated from ΔV_i^t, i=1,2,3, the increment of director of node i from time "t" to "t+Δt". ΔV_i^t can be expressed as, by making use of equation (6.6.5a) of reference [6.62]

$$\Delta V_i^t = (\Delta\theta_i')^t \times V_i^t = -V_i^t \times (\Delta\theta_i')^t$$
$$= -\Omega_i^t (\Delta\theta_i')^t \qquad (6.16a)$$

where $(\Delta\theta_i')^t$ is the incremental rotational vector of node i from time "t" to time "t + Δt", relative to the director orthogonal frame attached to the same node. The expression Ω_i^t is a skew-symmetric matrix associated with V_i^t of node i and time "t". That is, if V_i^t is, in its component form, $[V_{ri}^t, V_{si}^t, V_{ti}^t]^T$, Ω_i^t is constructed according to the following equation

$$\Omega_i^t = \begin{bmatrix} 0 & -V_{ti}^t & V_{si}^t \\ V_{ti}^t & 0 & -V_{ri}^t \\ -V_{si}^t & V_{ri}^t & 0 \end{bmatrix}. \qquad (6.16b)$$

Note that $(\Delta\theta_i')^t$ is defined with respect to V_i^t which is generally not coincident with the t-axis. The transformation between $(\Delta\theta_i')^t$ and $(\Delta\theta_i)^t$, the incremental rotational vector relative to the r-s-t axes is the so-called exponential mapping and according to references [6.62-67] it can be written as

$$(\Delta\theta_i')^t = \Gamma_i^t (\Delta\theta_i)^t \qquad (6.17a)$$

where Γ_i^t is an orthogonal matrix associated with node i at time "t". The same matrix Γ_i^t satisfies

$$V_i^t = \Gamma_i^t e_3 \qquad (6.17b)$$

with e_3 being the unit vector of the t-axis. That is, $e_3=[0,0,1]^T$. V_i^t is the position vector of director at node i of the reference configuration and should be known from configuration updating (see Sub-section 6.6.1). Therefore, Γ_i^t can be determined through the relation of equation (6.17b). Another expression for the determination of Γ_i^t is, based on references [6.62-67]

$$\Gamma_i^t = aI_3 + \hat{B} + \frac{1}{1+a} B B^T \tag{6.17c}$$

where I_3 is the 3×3 identity matrix, $a = V_i^t \cdot e_3$, $B = e_3 \times V_i^t$ and $\hat{B}$ is a skew-symmetric matrix constructed from vector $B= [B_1, B_2, B_3]^T$ according to the following equation

$$\hat{B} = \begin{bmatrix} 0 & -B_3 & B_2 \\ B_3 & 0 & -B_1 \\ -B_2 & B_1 & 0 \end{bmatrix} \tag{6.17d}$$

In equation (6.16a), ΔV_i^t, the change in orientation of director V_i^t, serves to bring the director to a new position that lies in the plane containing V_i^t and ΔV_i^t. Note that equation (6.15a) indicates that these two vectors are perpendicular to one another. The change in orientation is due to $(\Delta\theta_i')^t$, the incremental rotation. Consequently, the incremental rotational vector is perpendicular to V_i^t, as well as ΔV_i^t. In other words, V_i^t, ΔV_i^t and $(\Delta\theta_i')^t$ are mutually normal. Considering the normality condition between $(\Delta\theta_i')^t$ and V_i^t, one writes

$$
\begin{aligned}
(\Delta\theta_i')^t \cdot V_i^t &= 0 \\
&= \left[(\Delta\theta_i')^t\right]^T V_i^t = \left[(\Delta\theta_i)^t\right]^T (\Gamma_i^t)^T \Gamma_i^t\, e_3 \\
&= \left[(\Delta\theta_i)^t\right]^T e_3 = (\Delta\theta_i)^t \cdot e_3 \ .
\end{aligned}
\tag{6.18a}
$$

Equation (6.18a) is satisfied only if $\Delta\theta_{ti}^t=0$, which can be shown explicitly since

$$
(\Delta\theta_i)^t \cdot e_3 = \begin{Bmatrix} \Delta\theta_{ri}^t \\ \Delta\theta_{si}^t \\ \Delta\theta_{ti}^t \end{Bmatrix} \cdot \begin{Bmatrix} 0 \\ 0 \\ 1 \end{Bmatrix} = \Delta\theta_{ti}^t = 0 \ . \tag{6.18b}
$$

Next, substituting equations (6.16a) and (6.17a) into (6.15), and disregarding the DDOF lead to

$$
\begin{Bmatrix} \Delta u^t \\ \Delta v^t \\ \Delta w^t \end{Bmatrix} = \sum_{i=1}^{3} \xi_i \begin{Bmatrix} \overline{\Delta u_i^t} \\ \overline{\Delta v_i^t} \\ \overline{\Delta w_i^t} \end{Bmatrix} + \eta^t \sum_{i=1}^{3} \xi_i \begin{bmatrix} \Lambda_{i(11)}^t & \Lambda_{i(12)}^t \\ \Lambda_{i(21)}^t & \Lambda_{i(22)}^t \\ \Lambda_{i(31)}^t & \Lambda_{i(32)}^t \end{bmatrix} \begin{Bmatrix} \Delta\theta_{ri}^t \\ \Delta\theta_{si}^t \end{Bmatrix} \tag{6.19}
$$

where the 3×2 matrix Λ_i^t is defined as

$$
\Lambda_i^t = -\Omega_i^t \bar{\Gamma}_i^t \tag{6.20}
$$

with $\bar{\Gamma}_i^t$ consisting of the first two columns of Γ_i^t. Note that both Ω_i^t and Γ_i^t are dependent of the director V_i^t. Consequently, Λ_i^t also depends on the current position of the director. As will be seen later in equations (6.23) and (6.24a,b), the interpolation of incremental

displacements requires Λ_i^t for every node at every time step. Therefore, it is necessary to update the director. This is part of the configuration updating discussed later in Subsection 6.6.1. Forming Λ_i^t through equation (6.20) excludes the DDOF to ensure the preservation of the normality condition stated in equations (6.18a,b). Note that the derivations in references [6.62-67] require the satisfaction of equations (6.18a,b) under all circumstances. This, in turn, requires to exclude any DDOF, as was the case in references [6.62-67]. However, Chapters 3 through 5 have found that the DDOF should not and can not be ignored. Therefore, as in previous chapters, Allman's formula [6.93] of incorporating DDOF with in-plane displacements u and v, and Tessler and Hughes's formula [6.94] of coupling lateral displacement w with the two bending rotations θ_r and θ_s are introduced so that equation (6.19) is extended to

$$\begin{Bmatrix} \Delta u^t \\ \Delta v^t \\ \Delta w^t \end{Bmatrix} = \sum_{i=1}^{3} \xi_i \begin{Bmatrix} \overline{\Delta u_i^t} \\ \overline{\Delta v_i^t} \\ \overline{\Delta w_i^t} \end{Bmatrix} + \eta^t \sum_{i=1}^{3} \xi_i \begin{bmatrix} \Lambda_{i(11)}^t & \Lambda_{i(12)}^t \\ \Lambda_{i(21)}^t & \Lambda_{i(22)}^t \\ \Lambda_{i(31)}^t & \Lambda_{i(32)}^t \end{bmatrix} \begin{Bmatrix} \Delta\theta_{ri}^t \\ \Delta\theta_{si}^t \end{Bmatrix} + \sum_{i=1}^{3} \begin{bmatrix} 0 & 0 & \bar{p}_i \\ 0 & 0 & \bar{q}_i \\ -\bar{p}_i & -\bar{q}_i & 0 \end{bmatrix} \begin{Bmatrix} \Delta\theta_{ri}^t \\ \Delta\theta_{si}^t \\ \Delta\theta_{ti}^t \end{Bmatrix} \tag{6.21}$$

where the terms $\bar{p}_i$ and $\bar{q}_i$ are defined as

$$\begin{aligned} \bar{p}_1 &= (a_{31}\xi_3 - a_{12}\xi_2)\xi_1 \\ \bar{p}_2 &= (a_{12}\xi_1 - a_{23}\xi_3)\xi_2 \\ \bar{p}_3 &= (a_{23}\xi_2 - a_{31}\xi_1)\xi_3 \end{aligned} \tag{6.22a}$$

$$\begin{aligned} \bar{q}_1 &= (b_{31}\xi_3 - b_{12}\xi_2)\xi_1 \\ \bar{q}_2 &= (b_{12}\xi_1 - b_{23}\xi_3)\xi_2 \\ \bar{q}_3 &= (b_{23}\xi_2 - b_{31}\xi_1)\xi_3 \end{aligned} \tag{6.22b}$$

and with reference to Figure 6.2,

$$a_{12} = \frac{1}{2}\ell_{12}\cos\gamma_{12} \quad , \quad b_{12} = \frac{1}{2}\ell_{12}\sin\gamma_{12} \, ,$$

$$a_{23} = \frac{1}{2}\ell_{23}\cos\gamma_{23} \quad , \quad b_{23} = \frac{1}{2}\ell_{23}\sin\gamma_{23} \, ,$$

$$a_{31} = \frac{1}{2}\ell_{31}\cos\gamma_{31} \quad , \quad b_{31} = \frac{1}{2}\ell_{31}\sin\gamma_{31} \, .$$

Equation (6.21) can also be recast into a more compact form

$$\begin{aligned} &\left[\Delta u^t \;\; \Delta v^t \;\; \Delta w^t \right]^T = \\ &N \left[\overline{\Delta u_1^t} \;\; \overline{\Delta v_1^t} \;\; \overline{\Delta w_1^t} \;\; \Delta\theta_{r1}^t \;\; \Delta\theta_{s1}^t \;\; \Delta\theta_{t1}^t \;\; \overline{\Delta u_2^t} \;\; \ldots \;\; \Delta\theta_{s3}^t \;\; \Delta\theta_{t3}^t \right]^T \end{aligned} \tag{6.23}$$

where

$$N = \left[[N_1]_{3\times6} \;\; [N_2]_{3\times6} \;\; [N_3]_{3\times6} \right]_{3\times18} \tag{6.24a}$$

and the 3×6 sub-matrix $[N_i]$ is

$$N_i = \begin{bmatrix} \xi_i & 0 & 0 & \eta\,\xi_i\Lambda^t_{i(11)} & \eta^t\xi_i\Lambda^t_{i(12)} & \bar{p}_i \\ 0 & \xi_i & 0 & \eta^t\xi_i\Lambda^t_{i(21)} & \eta^t\xi_i\Lambda^t_{i(22)} & \bar{q}_i \\ 0 & 0 & \xi_i & \eta^t\xi_i\Lambda^t_{i(31)} - \bar{p}_i & \eta^t\xi_i\Lambda^t_{i(32)} - \bar{q}_i & 0 \end{bmatrix}. \tag{6.24b}$$

The interpolation function for DDOF, which is needed for the derivation of the present element but not included in usual isoparametric formulations, is

$$\Delta\theta^t = \sum_{i=1}^{3} \xi_i\left(\Delta\theta^t_i\right) \tag{6.25}$$

which is defined on the mid-surface of the shell.

Finally, it should be pointed out that the introduction of the terms under the third summation sign of equation (6.21) makes the present elements sub-parametric since different interpolation schemes are used for geometry and displacements.

6.3.3 Assumed incremental strain field within an element

Similar to Chapter 3, the assumed strain field for any point within the element is

$$\begin{aligned} &\left\{ \Delta\varepsilon_r \;\; \Delta\varepsilon_s \;\; \Delta\varepsilon_{rs} \;\; \Delta\varepsilon_{st} \;\; \Delta\varepsilon_{tr} \;\; \Delta\varepsilon^s_{rs} \right\}^T = \\ &\qquad \tilde{F}\left\{ \Delta\beta_1 \;\; \Delta\beta_2 \;\; \ldots \;\; \Delta\beta_9 \;\; \Delta\beta_{10} \right\}^T \end{aligned} \tag{6.26}$$

where

$$\tilde{P} = \begin{bmatrix} [P_5]_{5\times 9} & [0]_{5\times 1} \\ [0]_{1\times 9} & [1]_{1\times 1} \end{bmatrix}_{6\times 10} \tag{6.27a}$$

and

$$P_5 = \begin{bmatrix} 1 & 0 & 0 & \eta^t & 0 & 0 & 0 & 0 & 0 \\ 0 & 1 & 0 & 0 & \eta^t & 0 & 0 & 0 & 0 \\ 0 & 0 & 1 & 0 & 0 & \eta^t & 0 & 0 & 0 \\ 0 & 0 & 0 & 0 & 0 & 0 & -s_3(1-2\xi_2) & s_3(2\xi_2+2\xi_3-1) & 0 \\ 0 & 0 & 0 & 0 & 0 & 0 & -r_3(1-2\xi_2) & r_{32}(2\xi_2+2\xi_3-1) & r_2(1-2\xi_3) \end{bmatrix}_{5\times 9} \tag{6.27b}$$

with $r_{32} = r_3 - r_2$ and superscript "s" denoting the skew-symmetric part of the strain tensor. Note that the assumed strain components $\Delta\varepsilon_{rs}$, $\Delta\varepsilon_{st}$, and $\Delta\varepsilon_{tr}$ use the so-called engineering definition. Among the strain parameters, $\Delta\beta_1$ through $\Delta\beta_3$ are associated with membrane strains, $\Delta\beta_4$ through $\Delta\beta_6$ bending strains, $\Delta\beta_7$ through $\Delta\beta_9$ transversal strains and $\Delta\beta_{10}$ the skew-symmetric strain component.

6.3.4 Element stiffness matrix k_L

Section 6.2 showed that at any time instant the total element stiffness matrix is the sum of linear and initial stress stiffness matrices, k_L and k_{NL}. The derivation of the linear stiffness matrix k_L is discussed in this Sub-section while the initial stress stiffness matrix k_{NL} will be dealt with in the next sub-section.

The derivatives of the incremental displacement, equation (6.23), with respect to local co-ordinates r^t, s^t and t^t, are

$$\begin{aligned} &\left[\Delta u_{,r}^t \;\; \Delta v_{,r}^t \;\; \Delta w_{,r}^t \;\; \Delta u_{,s}^t \;\; \Delta v_{,s}^t \;\; \Delta w_{,s}^t \;\; \Delta u_{,t}^t \;\; \Delta v_{,t}^t \;\; \Delta w_{,t}^t \right]^T \\ &\qquad = \sum H_i \left[\overline{\Delta u_i^t} \;\; \overline{\Delta v_i^t} \;\; \overline{\Delta w_i^t} \;\; \Delta\theta_{ri}^t \;\; \Delta\theta_{si}^t \;\; \Delta\theta_{ti}^t \right]^T \end{aligned} \tag{6.28}$$

with

$$H_i = \begin{bmatrix} H_{i(r)} \\ H_{i(s)} \\ H_{i(t)} \end{bmatrix}_{9\times 6}, \tag{6.29a}$$

$$H_{i(r)} = \begin{bmatrix} \xi_{i,r} & 0 & 0 & \eta^t \xi_{i,r} \Lambda^t_{i(11)} & \eta^t \xi_{i,r} \Lambda^t_{i(12)} & \bar{p}_{i,r} \\ 0 & \xi_{i,r} & 0 & \eta^t \xi_{i,r} \Lambda^t_{i(21)} & \eta^t \xi_{i,r} \Lambda^t_{i(22)} & \bar{q}_{i,r} \\ 0 & 0 & \xi_{i,r} & \eta^t \xi_{i,r} \Lambda^t_{i(31)} - \bar{p}_{i,r} & \eta^t \xi_{i,r} \Lambda^t_{i(32)} - \bar{q}_{i,r} & 0 \end{bmatrix}, \tag{6.29b}$$

and

$$H_{i(t)} = \begin{bmatrix} 0 & 0 & 0 & \xi_i \Lambda^t_{i(11)} & \xi_i \Lambda^t_{i(12)} & 0 \\ 0 & 0 & 0 & \xi_i \Lambda^t_{i(21)} & \xi_i \Lambda^t_{i(22)} & 0 \\ 0 & 0 & 0 & \xi_i \Lambda^t_{i(31)} & \xi_i \Lambda^t_{i(32)} & 0 \end{bmatrix}. \tag{6.29c}$$

The matrix $H_{i(s)}$ is similar in form to equation (6.29b) except that the derivatives with respect to r in equation (6.29b) are replaced by those with respect to s. The derivatives of ξ_i (i=1,2,3) with respect to r^t and s^t are

$$\xi_{1,r} = -\frac{1}{r_2^t}\,, \qquad \xi_{1,s} = \frac{r_3^t - r_2^t}{r_2^t s_3^t}\,,$$

$$\xi_{2,r} = \frac{1}{r_2^t}\,, \qquad \xi_{2,s} = -\frac{r_3^t}{r_2^t s_3^t}\,, \tag{6.30}$$

$$\xi_{3,r} = 0\,, \qquad \xi_{3,s} = \frac{1}{s_3^t}\,.$$

The incremental strain-displacement relations for any points within the element, using engineering definition of strains, are

$$\begin{aligned}
\Delta\varepsilon_r^t &= \Delta u_{,r}^t\,, \qquad \Delta\varepsilon_s^t = \Delta v_{,s}^t\,,\\
\Delta\varepsilon_{rs}^t &= \Delta u_{,s}^t + \Delta v_{,r}^t\,,\\
\Delta\varepsilon_{st}^t &= \Delta v_{,t}^t + \Delta w_{,s}^t\,,\\
\Delta\varepsilon_{tr}^t &= \Delta w_{,r}^t + \Delta u_{,t}^t\,,\\
(\Delta\varepsilon_{rs}^s)^t &= \Delta\theta_t^t - \frac{1}{2}\left(\Delta v_{,r}^t - \Delta u_{,s}^t\right)\,,
\end{aligned} \tag{6.31}$$

or in a more compact form

$$\begin{aligned}
&\left[\,\Delta\varepsilon_r^t \;\; \Delta\varepsilon_s^t \;\; \Delta\varepsilon_{rs}^t \;\; \Delta\varepsilon_{st}^t \;\; \Delta\varepsilon_{tr}^t \;\; (\Delta\varepsilon_{rs}^s)^t\,\right]^T\\
&= \sum_{i=1}^{3} \left(\, I_I H_i + J_J \,\right)\left[\,\overline{\Delta u_i^t} \;\; \overline{\Delta v_i^t} \;\; \overline{\Delta w_i^t} \;\; \Delta\theta_{ri}^t \;\; \Delta\theta_{si}^t \;\; \Delta\theta_{ti}^t\,\right]^T
\end{aligned} \tag{6.32}$$

with

$$I_J = \begin{bmatrix} 1 & 0 & 0 & 0 & 0 & 0 & 0 & 0 & 0 \\ 0 & 0 & 0 & 0 & 1 & 0 & 0 & 0 & 0 \\ 0 & 1 & 0 & 1 & 0 & 0 & 0 & 0 & 0 \\ 0 & 0 & 0 & 0 & 0 & 1 & 0 & 1 & 0 \\ 0 & 0 & 1 & 0 & 0 & 0 & 1 & 0 & 0 \\ 0 & -\frac{1}{2} & 0 & \frac{1}{2} & 0 & 0 & 0 & 0 & 0 \end{bmatrix}_{6\times 9} \tag{6.33}$$

and J_J is a 6×6 square matrix whose only non-zero element is located at the 6-th row and 6-th column. This non-zero element has a value of unity. Note that $(I_I H_i + J_J)$ is, in fact, the linear strain-displacement matrix B_{Li}. In Chapter 3 it was decomposed into four parts which are included here for completeness and consistency in notations,

$$B_{L_{ai}} = \begin{bmatrix} \xi_{i,r} & 0 & 0 & 0 & 0 & \bar{p}_{i,r} \\ 0 & \xi_{i,s} & 0 & 0 & 0 & \bar{q}_{i,s} \\ \xi_{i,s} & \xi_{i,r} & 0 & 0 & 0 & \bar{p}_{i,s} + \bar{q}_{i,r} \\ 0 & 0 & 0 & 0 & 0 & 0 \\ 0 & 0 & 0 & 0 & 0 & 0 \\ 0 & 0 & 0 & 0 & 0 & 0 \end{bmatrix}, \tag{6.34}$$

$$B_{L_{bi}} = \begin{bmatrix} 0 & 0 & 0 & \eta^t \xi_{i,r} \Lambda^t_{i(11)} & \eta^t \xi_{i,r} \Lambda^t_{i(12)} & 0 \\ 0 & 0 & 0 & \eta^t \xi_{i,s} \Lambda^t_{i(21)} & \eta^t \xi_{i,s} \Lambda^t_{i(22)} & 0 \\ 0 & 0 & 0 & \eta^t (\xi_{i,r} \Lambda^t_{i(21)} + \xi_{i,s} \Lambda^t_{i(11)}) & \eta^t (\xi_{i,r} \Lambda^t_{i(22)} + \xi_{i,s} \Lambda^t_{i(12)}) & 0 \\ 0 & 0 & 0 & 0 & 0 & 0 \\ 0 & 0 & 0 & 0 & 0 & 0 \\ 0 & 0 & 0 & 0 & 0 & 0 \end{bmatrix} \tag{6.35}$$

$$B_{L_{ui}} = \begin{bmatrix} 0 & 0 & 0 & 0 & 0 & 0 \\ 0 & 0 & 0 & 0 & 0 & 0 \\ 0 & 0 & 0 & 0 & 0 & 0 \\ 0 & 0 & \xi_{i,s} & \eta^t \xi_{i,s} \Lambda^t_{i(31)} & \eta^t \xi_{i,s} \Lambda^t_{i(32)} & 0 \\ & & & -\bar{p}_{i,s} + \xi_t \Lambda^t_{i(21)} & -\bar{q}_{i,s} + \xi_t \Lambda^t_{i(22)} & \\ 0 & 0 & \xi_{i,r} & \eta^t \xi_{i,r} \Lambda^t_{i(31)} & \eta^t \xi_{i,r} \Lambda^t_{i(32)} & 0 \\ & & & -\bar{p}_{i,r} + \xi_t \Lambda^t_{i(11)} & -\bar{q}_{i,r} + \xi_t \Lambda^t_{i(12)} & \\ 0 & 0 & 0 & 0 & 0 & 0 \end{bmatrix} \tag{6.36}$$

and

$$B_{L_{di}} = \frac{1}{2} \begin{bmatrix} 0 & 0 & 0 & 0 & 0 & 0 \\ 0 & 0 & 0 & 0 & 0 & 0 \\ 0 & 0 & 0 & 0 & 0 & 0 \\ 0 & 0 & 0 & 0 & 0 & 0 \\ 0 & 0 & 0 & 0 & 0 & 0 \\ \xi_{i,s} & -\xi_{i,r} & 0 & \eta^t(\xi_{i,s}\Lambda^t_{i(11)} - \xi_{i,r}\Lambda^t_{i(21)}) & \eta^t(\xi_{i,s}\Lambda^t_{i(12)} - \xi_{i,r}\Lambda^t_{i(22)}) & 2\xi_t + (\bar{p}_{i,s} - \bar{q}_{i,r}) \end{bmatrix}. \tag{6.37}$$

Note that in B_{Ldi} the director direction co-ordinate η^t should be set to zero due to the fact that the skew-symmetric part of the strain tensor is defined on the mid-surface only. This, on the other hand, implies that the skew-symmetric part is constant over the thickness.

With such an observation, equation (6.37) can be re-written as

$$B_{L_{di}} = \frac{1}{2}\begin{bmatrix} 0 & 0 & 0 & 0 & 0 & 0 \\ 0 & 0 & 0 & 0 & 0 & 0 \\ 0 & 0 & 0 & 0 & 0 & 0 \\ 0 & 0 & 0 & 0 & 0 & 0 \\ 0 & 0 & 0 & 0 & 0 & 0 \\ \xi_{i,s} & -\xi_{i,r} & 0 & 0 & 0 & 2\xi_i + (\bar{p}_{i,s} - \bar{q}_{i,r}) \end{bmatrix}. \qquad (6.38)$$

Now, the stiffness matrix k_L can be obtained by following the steps illustrated in Section 3.3 such that

$$\begin{aligned} k_{L_m} &= (G_e)_{L_m}^T \, \tilde{H}^{-1} \, (G_e)_{L_m} , \\ k_{L_b} &= (G_e)_{L_b}^T \, \tilde{H}^{-1} \, (G_e)_{L_b} , \\ k_{L_s} &= (G_e)_{L_s}^T \, \tilde{H}^{-1} \, (G_e)_{L_s} , \\ k_{L_d} &= (G_e)_{L_d}^T \, \tilde{H}^{-1} \, (G_e)_{L_d} , \\ k_L &= k_{L_m} + k_{L_b} + k_{L_s} + k_{L_d} \end{aligned} \qquad (6.39a,b,c,d,e)$$

where

$$\bar{H} = \int_V \bar{P}^T \bar{D} \bar{P}\, dV \ ,$$

$$(G_e)_{L_m} = \int_V \bar{P}^T \bar{D} B_{L_m}\, dV \ ,$$

$$(G_e)_{L_b} = \int_V \bar{P}^T \bar{D} B_{L_b}\, dV \ ,$$

$$(G_e)_{L_s} = \int_V \bar{P}^T \bar{D} B_{L_s}\, dV \ , \qquad (6.40a,b,c,d,e,f)$$

$$(G_e)_{L_d} = \int_V \bar{P}^T \bar{D} B_{L_d}\, dV \ ,$$

$$(G_e)_L = (G_e)_{L_m} + (G_e)_{L_b} + (G_e)_{L_s} + (G_e)_{L_d} \ .$$

Matrices B_{Lm} , B_{Lb} , B_{Ls} and B_{Ld} inside the integrands of equation (6.40) are defined as

$$B_{L_m} = \left[\left[B_{L_{m1}}\right] \left[B_{L_{m2}}\right] \left[B_{L_{m3}}\right] \right]_{6\times 18} \ ,$$

$$B_{L_b} = \left[\left[B_{L_{b1}}\right] \left[B_{L_{b2}}\right] \left[B_{L_{b3}}\right] \right]_{6\times 18} \ , \qquad (6.41)$$

$$B_{L_s} = \left[\left[B_{L_{s1}}\right] \left[B_{L_{s2}}\right] \left[B_{L_{s3}}\right] \right]_{6\times 18} \ ,$$

$$B_{L_d} = \left[\left[B_{L_{d1}}\right] \left[B_{L_{d2}}\right] \left[B_{L_{d3}}\right] \right]_{6\times 18} \ .$$

It should be noted that the above derivations, when simplified (see Sub-section 6.3.6), produce an element corresponding to the $AT+k_d$ of Chapter 3. To change to the $AT+(k_t^3)'$ of Chapter 3, k_{Ld} can be replaced with $(k_{Lt}^3)'$ in equation (6.39d)

$$(k_{L_t}^3)' = \frac{1}{2} Gh \int_A \bar{Y}^T \bar{Y} dA \qquad (6.42)$$

where the $\bar{y}$ vector is defined as

$$\bar{Y} = \frac{1}{2}\left[\frac{r_3-r_2}{r_2 s_3},\ \frac{1}{r_2},\ 0,\ 0,\ 0,\ 2\xi_1 - \bar{p}_{1,s} + \bar{q}_{1,r},\right.$$

$$-\frac{r_3}{r_2 s_3},\ -\frac{1}{r_2},\ 0,\ 0,\ 0,\ 2\xi_2 - \bar{q}_{2,s} + \bar{p}_{2,r}, \qquad (6.43)$$

$$\left.\frac{1}{s_3},\ 0,\ 0,\ 0,\ 0,\ 2\xi_3 - \bar{q}_{3,s} + \bar{p}_{3,r}\right]_{1\times 18} .$$

so that k_L becomes

$$k_L = k_{L_m} + k_{L_b} + k_{L_s} + (k_{L_t}^3)' \qquad (6.44)$$

6.3.5 Element stiffness matrix k_{NL}

To obtain the initial stress stiffness matrix k_{NL} one first writes the nonlinear strain-displacement matrix B_{NL}

$$B_{NL} = \left[\ [H_1]_{9\times 6}\ [H_2]_{9\times 6}\ [H_3]_{9\times 6}\ \right]_{9\times 18} \qquad (6.45)$$

where the 9×6 matrix H_i ($i=1,2,3$) has been defined in equations (6.29a,b,c).

The evaluation of k_{NL} also requires the Cauchy stress matrix $\bar{\sigma}$ which is constructed from the Cauchy stress vector $\sigma = [\sigma_r,\ \sigma_s,\ \sigma_{rs},\ \sigma_{st},\ \sigma_{tr},\ \sigma_{rs}^s]^T = [\sigma_{11},\ \sigma_{22},\ \sigma_{12},\ \sigma_{23},\ \sigma_{31},\ \sigma_{12}^s]^T$, according to the following formula

$$\bar{\sigma} = \begin{vmatrix} \sigma_{11} I_3 & (\sigma_{12}+\sigma_{12}^s) I_3 & \sigma_{31} I_3 \\ (\sigma_{12}-\sigma_{12}^s) I_3 & \sigma_{22} I_3 & \sigma_{23} I_3 \\ \sigma_{31} I_3 & \sigma_{23} I_3 & O_3 \end{vmatrix} \qquad (6.46)$$

with I_3 being the 3×3 identity matrix and O_3 a 3×3 null matrix. Note that because of σ_{12}^s, matrix $\bar{\sigma}$ is no longer symmetric. As a result, k_{NL} is non-symmetric. However, in this phase of the investigation σ_{12}^s will be disregarded so as to provide a basis for comparison to results in the next phase of the present investigation in which σ_{12}^s is included. Thus, in this phase of the investigation equation (6.46) reduces to

$$\bar{\sigma} = \begin{bmatrix} \sigma_{11}I_3 & \sigma_{12}I_3 & \sigma_{31}I_3 \\ \sigma_{12}I_3 & \sigma_{22}I_3 & \sigma_{23}I_3 \\ \sigma_{31}I_3 & \sigma_{23}I_3 & O_3 \end{bmatrix}. \tag{6.47}$$

Equations (6.11), (6.12) and (6.27a,b) indicate that, the membrane components of the incremental second Piola-Kirchhoff stress, ΔS are constant within an element. The bending components vary in the thickness direction only. However, the transverse components are mid-surface position dependent, or more precisely, are varied linearly within an element. Consequently, the second Piola-Kirchhoff and Cauchy stresses at time "t", S and σ are also a function of mid-surface position. Their updating requires storage of stresses of the three nodes. Returning to the integration of equation (6.6), if consider σ as mid-surface position dependent, it would produce very tedious expressions. Therefore, in the present study the transverse stress components of σ are considered constant over an element. That is, all the stress components of σ are calculated and updated only at the centroid of each element. This approach can be justified by recognizing that in shell structures membrane and bending stresses are usually dominant. Such an approach reduces substantially the computation efforts involved and requires much less computer storage space. Note that, in general, every σ_{ij} of equations (6.46) and

(6.47) is a combination of membrane, bending and transverse components. At any point, including the centroid of the element, membrane and transverse components are obtained by setting η^t to zero for the purpose of evaluating k_{NL}. While the total stress at the top surface can be obtained by prescribing $\eta^t = h^t/2$. The difference between the stresses at the top and the mid-surface, after divided by $h^t/2$, indicates the slope of bending stress component. Then, σ_{ij} is re-written as

$$\begin{aligned} \sigma_{ij} &= \sigma_{ij(0)} + \eta^t d\sigma_{ij} \quad , \\ d\sigma_{ij} &= \frac{2}{h^t}(\sigma_{ij(+)} - \sigma_{ij(0)}) \end{aligned} \tag{6.48}$$

where $\sigma_{ij(0)}$ and $\sigma_{ij(+)}$ denote stresses at the middle and top surfaces, respectively, while $d\sigma_{ij}$ is the slope of the bending stress. Equation (6.48) is also valid for plastic deformation. In this case, $d\sigma_{ij}$ becomes zero because of the adoption of the non-layered approach to be introduced in Section 6.5 below. Of course, for layered approach $d\sigma_{ij}$ is not zero in general.

With $\bar{\sigma}$ and B_{NL} matrices now defined, they are substituted into equation (6.6) so that explicit expressions for k_{NL} can be obtained after evaluating the required integration.

6.3.6 Simplified version of stiffness matrices

The purpose here is, (1) to demonstrate that the linear stiffness matrices derived in Chapter 3 are special cases of the linear stiffness matrices developed in the foregoing sub-sections; and (2) to obtain the simplified version of stiffness matrices, linear and

nonlinear. This is achieved by assuming that V_i^t coincides with the t-axis and it becomes $[0,0,1]^T$. In this case equation (6.13) becomes

$$\begin{Bmatrix} r^t \\ s^t \\ t^t \end{Bmatrix} = \sum_{i=1}^{3} \xi_i \begin{Bmatrix} \overline{r_i^t} \\ \overline{s_i^t} \\ 0 \end{Bmatrix} + \eta^t \begin{Bmatrix} 0 \\ 0 \\ 1 \end{Bmatrix} . \tag{6.49}$$

Note that equation (6.49) is obtained by applying equation (6.14b). Since $V_i^t=[0,0,1]^T$ $(i=1,2,3)$, equation (6.16a) and Ω_i^t become

$$\begin{aligned} \Delta V_i^t &= -\Omega_i^t \left[(\Delta\theta'_{ri})^t \;\; (\Delta\theta'_{si})^t \;\; (\Delta\theta'_{ti})^t \right]^T \\ &= \left[(\Delta\theta'_{si})^t \;\; -(\Delta\theta'_{ri})^t \;\; 0 \right]^T , \end{aligned} \tag{6.50a,b}$$

$$\Omega_i^t = \begin{bmatrix} 0 & -1 & 0 \\ 1 & 0 & 0 \\ 0 & 0 & 0 \end{bmatrix}$$

and Γ_i^t becomes an identity matrix. Applying equation (6.20) leads to

$$\Lambda_i^t = -\begin{bmatrix} 0 & -1 & 0 \\ 1 & 0 & 0 \\ 0 & 0 & 0 \end{bmatrix} \begin{bmatrix} 1 & 0 \\ 0 & 1 \end{bmatrix} = \begin{bmatrix} 0 & 1 \\ -1 & 0 \\ 0 & 0 \end{bmatrix} . \tag{6.51}$$

It may be appropriate to note that in Chapter 3 the displacement field was defined in terms of the mid-surface displacements and the rotations about the r, s and t axes. On the other hand, in the present derivation, the displacement field consists of the

displacements of an arbitrary point within the element. Therefore, one may first re-write the displacement field as

$$\begin{aligned} &\left[\ \overline{\Delta u^t}\ \ \overline{\Delta v^t}\ \ \overline{\Delta w^t}\ \ \Delta\theta_r^t\ \ \Delta\theta_s^t\ \ \Delta\theta_t^t\ \right]^T \\ &= \bar{N}\left[\ \overline{\Delta u_1^t}\ \ \overline{\Delta v_1^t}\ \ \overline{\Delta w_1^t}\ \ \Delta\theta_{r1}^t\ \ \Delta\theta_{s1}^t\ \ \Delta\theta_{t1}^t\ \ \overline{\Delta u_2^t}\ \ \ldots\ \ \Delta\theta_{s3}^t\ \ \Delta\theta_{t3}^t\ \right]^T \end{aligned} \tag{6.52}$$

with

$$\bar{N} = \left[\ [\bar{N}_1]_{6\times6}\ [\bar{N}_2]_{6\times6}\ [\bar{N}_3]_{6\times6}\ \right]_{6\times18} \tag{6.53}$$

and

$$\bar{N}_i = \begin{bmatrix} \xi_i & 0 & 0 & 0 & 0 & \bar{p}_i \\ 0 & \xi_i & 0 & 0 & 0 & \bar{q}_i \\ 0 & 0 & \xi_i & \eta^t\xi_i\Lambda^t_{i(31)} - \bar{p}_i & \eta^t\xi_i\Lambda^t_{i(32)} - \bar{q}_i & 0 \\ 0 & 0 & 0 & -\xi_i\Lambda^t_{i(21)} & -\xi_i\Lambda^t_{i(22)} & 0 \\ 0 & 0 & 0 & \xi_i\Lambda_{i(11)} & \xi_i\Lambda^t_{i(12)} & 0 \\ 0 & 0 & 0 & 0 & 0 & \xi_i \end{bmatrix}. \tag{6.54}$$

Substituting equation (6.51) into (54) results in

$$\bar{N}_i = \begin{bmatrix} \xi_i & 0 & 0 & 0 & 0 & \bar{p}_i \\ 0 & \xi_i & 0 & 0 & 0 & \bar{q}_i \\ 0 & 0 & \xi_i & -\bar{p}_i & -\bar{q}_i & 0 \\ 0 & 0 & 0 & \xi_i & 0 & 0 \\ 0 & 0 & 0 & 0 & \xi_i & 0 \\ 0 & 0 & 0 & 0 & 0 & \xi_i \end{bmatrix} \tag{6.55}$$

and the corresponding B_{Lmi}, B_{Lbi}, B_{Lsi} and B_{Ldi} matrices becomes

$$B_{L_{mi}} = \begin{bmatrix} \xi_{i,r} & 0 & 0 & 0 & 0 & \bar{p}_{i,r} \\ 0 & \xi_{i,s} & 0 & 0 & 0 & \bar{q}_{i,s} \\ \xi_{i,s} & \xi_{i,r} & 0 & 0 & 0 & \bar{p}_{i,s}+\bar{q}_{i,r} \\ 0 & 0 & 0 & 0 & 0 & 0 \\ 0 & 0 & 0 & 0 & 0 & 0 \\ 0 & 0 & 0 & 0 & 0 & 0 \end{bmatrix}, \tag{6.56}$$

$$B_{L_{bi}} = \begin{bmatrix} 0 & 0 & 0 & 0 & \eta^t\xi_{i,r} & 0 \\ 0 & 0 & 0 & -\eta^t\xi_{i,s} & 0 & 0 \\ 0 & 0 & 0 & -\eta^t\xi_{i,r} & \eta^t\xi_{i,s} & 0 \\ 0 & 0 & 0 & 0 & 0 & 0 \\ 0 & 0 & 0 & 0 & 0 & 0 \\ 0 & 0 & 0 & 0 & 0 & 0 \end{bmatrix}, \tag{6.57}$$

$$B_{L_{si}} = \begin{bmatrix} 0 & 0 & 0 & 0 & 0 & 0 \\ 0 & 0 & 0 & 0 & 0 & 0 \\ 0 & 0 & 0 & 0 & 0 & 0 \\ 0 & 0 & \xi_{i,s} & -\xi_i & 0 & 0 \\ 0 & 0 & \xi_{i,r} & 0 & \xi_i & 0 \\ 0 & 0 & 0 & 0 & 0 & 0 \end{bmatrix} \tag{6.58}$$

and

$$B_{L_{di}} = \frac{1}{2}\begin{bmatrix} 0 & 0 & 0\ 0\ 0 & 0 \\ 0 & 0 & 0\ 0\ 0 & 0 \\ 0 & 0 & 0\ 0\ 0 & 0 \\ 0 & 0 & 0\ 0\ 0 & 0 \\ 0 & 0 & 0\ 0\ 0 & 0 \\ \xi_{i,s} & -\xi_{i,r} & 0\ 0\ 0 & 2\xi_i+(\bar{p}_{i,s}-\bar{q}_{i,r}) \end{bmatrix}. \tag{6.59}$$

Comparing these matrices with those given in Chapter 3, one can find no differences. Concerning the element identified as $AT+(k_t^3)'$, the matrix $(k_{L_d}^3)'$ in equation (6.42) remains unchanged since the vector $\bar{\gamma}$ does not include terms associated with the directors.

Of course, the development in Chapter 3 did not include the initial stress stiffness matrix k_{NL}. To complete the simplified version one can obtain k_{NL} by substituting equation (6.51) into (6.29a,b,c) and proceed with the procedures outlined in Sub-section 6.3.5.

A final remark here is that, as mentioned in Section 6.1, the simplified version has its usefulness in cases where the directors are not uniquely defined, or are difficult to determine. Discussions on issues such as comparisons of accuracy will be included in Chapter 7 in which the stiffness matrices derived in Sub-sections 6.3.4 and 6.3.5 above are identified as the director version stiffness matrices or director version for simplicity and convenience of reference.

6.4 Element Consistent Mass Matrices

To limit the scope of the present study, only cases in which angular velocities and accelerations are small and therefore can be disregarded are considered. The cases in which angular velocities and accelerations are significant will be one of the arthor's future research interests and will be reported in due course. In this section it is to show that when angular velocities and accelerations are small the results in reference [6.67] reduce to those of Chapter 5.

As equation (6.13) indicated, the local co-ordinates of a point within an element can be determined by its mid-surface position vector, the director and the distance of the point to the mid-surface. Equation (6.13) can therefore be recast as

$$\Phi = \phi + \eta^t V^t \tag{6.60}$$

where Φ stands for the LHS of equation (6.13) while ϕ and V^t are the first and second summations on the RHS of equation (6.13), respectively. Then, for the point on the mid-surface, the linear and angular momentum fields are defined as, with ρ^t being the mass density per unit volume at time "t"

$$p = \int_{-\frac{h^t}{2}}^{\frac{h^t}{2}} \rho^t \dot{\Phi}\, d\eta^t = \int_{-\frac{h^t}{2}}^{\frac{h^t}{2}} \rho^t \dot{\phi}\, d\eta^t = \rho^t h^t \dot{\phi} \tag{6.61}$$

and

$$\begin{aligned}\chi &= \int_{-\frac{h^t}{2}}^{\frac{h^t}{2}} \rho^t(\Phi \cdot \varphi)\times\dot{\Phi}\, d\eta^t \\ &= \int_{-\frac{h^t}{2}}^{\frac{h^t}{2}} \rho^t\left[\eta^t V^t\times\dot{\phi} + (\eta^t)^2 V^t\times\dot{V}^t\right] d\eta^t \\ &= \int_{-\frac{h^t}{2}}^{\frac{h^t}{2}} \rho^t(\eta^t)^2 V^t\times\dot{V}^t\, d\eta^t = \rho^t\frac{(h^t)^3}{12} V^t\times\dot{V}^t\end{aligned} \tag{6.62}$$

where the integral $\int_{-\frac{h^t}{2}}^{\frac{h^t}{2}} \eta^t\, d\eta^t = 0$ has been applied.

Considering the weak form of momentum balance and defining virtual mid-surface displacement $\Delta\phi$ and virtual rotation of the director field $\Delta\alpha$ ($\Delta\phi$ and $\Delta\alpha$ are considered constant over the time period "t" to "t+Δt"), one writes

$$\begin{aligned}G_{dyn}(\Phi,\Delta\phi,\Delta\alpha) &= \int_{A^t}\left[(\Delta\phi)^T\dot{p} + (\Delta\alpha)^T\dot{\chi}\right]dA \\ &\quad + G_{sta}(\Phi,\Delta\phi,\Delta\alpha) \\ &= 0\ .\end{aligned} \tag{6.63}$$

In equation (6.63) G_{sta} is the static part of the weak form and will give the stiffness matrices, pseudo-force and consistent external load vectors. In the present study, G_{sta} is in fact the linearized incremental variational principle discussed in Section 6.2. The integral of equation (6.63) represents the effects due to the linear and angular velocities and accelerations. This integral comprises of two parts, one due to translational motion and the other rotational motion. Writing this integral as

$$
\begin{aligned}
G_{vel} &= G_{tra} + G_{rot} \\
&= \int_{A^t} (\Delta\phi)^{\cdot\cdot T} \dot{p}\, dA + \int_{A^t} (\Delta\alpha)^T \dot{\chi}\, dA
\end{aligned}
\tag{6.64}
$$

with

$$
\begin{aligned}
\dot{p} &= \rho^t h^t \ddot{\phi} \quad , \\
\dot{\chi} &= I_\rho^t (\dot{V}^t \times \dot{V}^t + V^t \times \ddot{V}^t) \\
&= I_\rho^t V^t \times \ddot{V}^t
\end{aligned}
\tag{6.65a,b}
$$

and

$$
I_\rho^t = \rho^t \frac{(h^t)^3}{12} \, . \tag{6.66}
$$

For G_{tra}, taking its variation with respect to $\dot{p}$ leads to

$$
\begin{aligned}
\Delta G_{tra} &= \int_{A^t} (\Delta\phi)^T (\Delta\dot{p})\, dA \\
&= \int_{A^t} \rho^t h^t (\Delta\phi)^T (\Delta\ddot{\phi})\, dA \\
&= (\Delta q)^T \left\{ \int_{A^t} \rho^t h^t [N_m]^T [N_m]\, dA \right\} (\Delta\ddot{q}) \\
&= (\Delta q)^T m_{tra} (\Delta\ddot{q})
\end{aligned}
\tag{6.67}
$$

where Δq is the vector of nodal DOF. That is, the vector on the RHS of equation (6.23). And $\Delta\ddot{q}$ is the vector of acceleration of the nodal DOF. In arriving at equation (6.67), the relations

$$
\Delta\phi = [N_m]\Delta q \quad , \qquad \Delta\ddot{\phi} = [N_m]\Delta\ddot{q} \tag{6.68a,b}
$$

have been applied. In equation (6.68) N_m is the interpolation function matrix for mid-surface displacements. The component matrix of N_m is N_{mi}. The latter can be obtained by setting to zero the last three rows of matrix $\bar{N}_i$ and the director direction co-ordinate η^t in equation (6.54). In other words,

$$N_{mi} = \begin{bmatrix} \xi_i & 0 & 0 & 0 & 0 & \bar{p}_i \\ 0 & \xi_i & 0 & 0 & 0 & \bar{q}_i \\ 0 & 0 & \xi_i & -\bar{p}_i & -\bar{q}_i & 0 \\ 0 & 0 & 0 & 0 & 0 & 0 \\ 0 & 0 & 0 & 0 & 0 & 0 \\ 0 & 0 & 0 & 0 & 0 & 0 \end{bmatrix} . \tag{6.69}$$

Recall that in equation (6.67) the translational part of consistent mass matrix is m_{tra} which is defined as

$$m_{tra} = \int_{A^t} \rho^t h^t [N_m]^T [N_m] dA . \tag{6.70}$$

Now, consider G_{rot} in equation (6.64). Taking the variation with respect to V^t and $\ddot{V}^t$, accordingly, one can show that

$$\begin{aligned} \Delta G_{rot} &= \int_{A^t} I_\rho^t (\Delta\alpha)^T (\Delta V^t \times \ddot{V}^t + V^t \times \Delta\ddot{V}^t)\, dA \\ &= \int_{A^t} I_\rho^t (\Delta\alpha)^T (V^t \times \Delta\ddot{V}^t)\, dA . \end{aligned} \tag{6.71}$$

Here the term $\tilde{V}^t$ represents the angular accelerations since the directors are assumed to be of unit length. Note that the term $\Delta V^t \times \tilde{V}^t$ has been disregarded because small angular velocities and accelerations have been assumed throughout this part of the thesis. By making use of equation (6.16a) and interchanging the sequence of variation and differentiation, it results in

$$\Delta \tilde{V}^t = (\Delta \tilde{\alpha} \times V^t + \Delta \alpha \times \tilde{V}^t) = \Delta \tilde{\alpha} \times V^t \tag{6.72}$$

in which the term associated with the angular accelerations has been disregarded. Substituting equation (6.72) into equation (6.71), one can write

$$\begin{aligned} \Delta G_{rot} = & \int_{A^t} I_\rho^t (\Delta \alpha)^T V^t \times (-V^t \times \Delta \tilde{\alpha})\, dA \\ & - \int_{A^t} I_\rho^t (\Delta \alpha)^T \Delta \tilde{\alpha}\, dA \\ & - (\Delta q)^T \left\{ \int_{A^t} I_\rho^t [N_r]^T [N_r]\, dA \right\} (\Delta \tilde{q}) \ . \end{aligned} \tag{6.73}$$

In deriving equation (6.73), it has been assumed that

$$\Delta \alpha = \Gamma^t [N_r]\, \Delta q \quad , \quad \Delta \tilde{\alpha} = \Gamma^t [N_r]\, \Delta \tilde{q} \tag{6.74a,b}$$

where Γ^t is the orthogonal matrix defined by equations (6.17a,b) and satisfies

$$(\Gamma^t)^T (\Gamma^t) = I_3$$

with I_3 being a 3×3 identity matrix. Note that the following identity has also been employed to obtain equation (6.73)

$$V^t \times (V^t \times \Delta\ddot{\alpha}) = -\Delta\ddot{\alpha} \ .$$

Similar to N_{mi} , N_{ri} can also be obtained by setting to zero all the elements located on the first three and the last rows of equation (6.54). That is,

$$N_{ri} = \begin{bmatrix} 0 & 0 & 0 & 0 & 0 & 0 \\ 0 & 0 & 0 & 0 & 0 & 0 \\ 0 & 0 & 0 & 0 & 0 & 0 \\ 0 & 0 & 0 & -\xi_i \Lambda^t_{i(21)} & -\xi_i \Lambda^t_{i(22)} & 0 \\ 0 & 0 & 0 & \xi_i \Lambda^t_{i(11)} & \xi_i \Lambda^t_{i(12)} & 0 \\ 0 & 0 & 0 & 0 & 0 & 0 \end{bmatrix} . \tag{6.75}$$

Equation (6.73) is the rotational part of the consistent mass matrix which is associated with the in-plane or bending rotational DOF. This rotational part of the consistent mass matrix is denoted as

$$m_{r\alpha} = \int_{A^t} I^t_\rho [N_r]^T [N_r] \, dA \ . \tag{6.76}$$

Then, it is not difficult to show that, after substituting equation (6.51) into equations (6.70) and (6.76), the consistent mass matrices derived in Chapter 5 can be recovered except for the part that corresponds to the DDOF. The reason is that reference [6.67] and the derivation up to this point do not include the DDOF. Of course, to complete the formulation for the present investigation, the part of element consistent mass

matrices associated with the DDOF derived in Chapter 5 can be added to equations (6.70) and (6.76).

To be consistent with the derivations of element stiffness matrices in Sub-section 6.3.4, the consistent element mass matrices also have their director version and simplified version. The simplified version consists of results obtained in Chapter 5 while the director version is concerned with the results derived in this section. Note that for the director version, the part of consistent mass matrices associated with the DDOF is identical to that used in the simplified version since their derivations do not depend on the directors.

In passing, it should be pointed out that the above derivation of element consistent mass matrices is with respect to the reference configuration. Therefore, the mass matrices have to be updated at every time step since the mass density, thickness of the shell and element geometry change from time to time. This approach is different from that in references [6.15, 6.23], for example. In the latter references the mass matrix was defined with respect to the undeformed configuration and was kept constant throughout the entire analysis. For the updated Lagrangian formulation, reference [6.26] obtained a consistent mass matrix that was defined with respect to the reference state. However, numerical results were not available in reference [6.26]. In the present study, the option of updating the mass matrix is introduced. Comparisons of using constant or updated mass matrices are included in the following chapter.

6.5 Constitutive Relations

This section is concerned with the constitutive relations for linear, elastic and isotropic materials with small or finite strains, and elasto-plastic materials with isotropic strain hardening. The latter case also includes deformations of small or finite strains.

6.5.1 Elastic materials

The constitutive relation for homogeneous, isotropic and linearly elastic materials undergoing deformation of small strain is

$$C_{ijkl} = \frac{E}{1+\nu}\left[\frac{\nu}{1-2\nu}\delta_{ij}\delta_{kl} + \frac{1}{2}(\delta_{ik}\delta_{jl} + \delta_{il}\delta_{jk})\right] \tag{6.77}$$

where E is the Young's moduius, ν Poisson's ratio and δ_{mn} the Kronecker delta. Equation (6.77) can be cast into a matrix form as

$$D = \begin{bmatrix} a & b & b & 0 & 0 & 0 \\ b & a & b & 0 & 0 & 0 \\ b & b & a & 0 & 0 & 0 \\ 0 & 0 & 0 & f & 0 & 0 \\ 0 & 0 & 0 & 0 & f & 0 \\ 0 & 0 & 0 & 0 & 0 & f \end{bmatrix} \tag{6.78}$$

with

$$a = \frac{E}{1+\nu}\left(\frac{1-\nu}{1-2\nu}\right), \quad b = \frac{E}{1+\nu}\left(\frac{\nu}{1-2\nu}\right), \quad f = \frac{1}{2}\left(\frac{E}{1+\nu}\right). \tag{6.79a,b,c}$$

The stress and strain vectors accompanying equation (6.78) are

$$\sigma = [\sigma_{11}, \sigma_{22}, \sigma_{33}, \sigma_{12}, \sigma_{23}, \sigma_{31}]^T ,$$
$$\varepsilon = [\varepsilon_{11}, \varepsilon_{22}, \varepsilon_{33}, \varepsilon_{12}, \varepsilon_{23}, \varepsilon_{31}]^T . \tag{6.80}$$

To take into account the skew-symmetric component of stress and strain tensors, the D matrix of equation (6.78) needs to be expanded to the following 7×7 matrix

$$\bar{D} = \begin{bmatrix} [D]_{6\times6} & [0]_{6\times1} \\ [0]_{1\times6} & f \end{bmatrix} \tag{6.81}$$

where $[0]_{6\times1}$ and $[0]_{1\times6}$ are null matrices of dimensions 6×1 and 1×6, respectively, and f has been defined in equation (6.79c). The accompanying stress and strain vectors are

$$\sigma = [\sigma_{11}, \sigma_{22}, \sigma_{33}, \sigma_{12}, \sigma_{23}, \sigma_{31}, \sigma^s_{12}]^T ,$$
$$\varepsilon = [\varepsilon_{11}, \varepsilon_{22}, \varepsilon_{33}, \varepsilon_{12}, \varepsilon_{23}, \varepsilon_{31}, \varepsilon^s_{12}]^T \tag{6.82}$$

and the superscript s denotes the skew-symmetric components.

Finally, equation (6.81) should be reduced from general three-dimensional (3D) applications to plate or shell analyses by the imposition of zero normal stress condition $\sigma_{33}=0$. Hughes and Liu [6.16] proposed to perform a transformation defined as

$$\tilde{D} = (T_c)^T \bar{D} (T_c) \tag{6.83}$$

with

$$T_c = \begin{bmatrix} 1 & 0 & 0 & 0 & 0 & 0 \\ 0 & 1 & 0 & 0 & 0 & 0 \\ t_1 & t_2 & t_4 & t_5 & t_6 & t_7 \\ 0 & 0 & 1 & 0 & 0 & 0 \\ 0 & 0 & 0 & 1 & 0 & 0 \\ 0 & 0 & 0 & 0 & 1 & 0 \\ 0 & 0 & 0 & 0 & 0 & 1 \end{bmatrix} \tag{6.84a}$$

and

$$t_i = - \frac{\bar{D}_{3i}}{\bar{D}_{33}} \tag{6.84b}$$

where $\bar{D}_{3k}$ is the element located in the third row and k-th column of $\bar{D}$ of equation (81).

For finite strain deformations, references [6.33, 6.95-96] suggested to add to equation (6.77) the following term,

$$C_{ijkl}' = - \frac{1}{2} \left(\sigma_{ik} \delta_{jl} + \sigma_{jk} \delta_{il} + \sigma_{il} \delta_{jk} + \sigma_{jl} \delta_{ik} \right) . \tag{6.85}$$

Note that this term comes as a result of transforming the Jaumann stress rate to the incremental second Piola-Kirchhoff stress. If cast into matrix form with equation (6.82) as the accompanying stress and strain vectors, the tensor equation (6.85) becomes

$$\bar{D}' = -\frac{1}{2}\begin{bmatrix} 4\sigma_{11} & 0 & 0 & 2\sigma_{12} & 0 & 2\sigma_{13} & 0 \\ 0 & 4\sigma_{22} & 0 & 2\sigma_{12} & 2\sigma_{23} & 0 & 0 \\ 0 & 0 & 4\sigma_{33} & 0 & 2\sigma_{23} & 2\sigma_{13} & 0 \\ 2\sigma_{12} & 2\sigma_{12} & 0 & \sigma_{11}+\sigma_{22} & \sigma_{13} & \sigma_{23} & 0 \\ 0 & 2\sigma_{23} & 2\sigma_{23} & \sigma_{13} & \sigma_{22}+\sigma_{33} & \sigma_{12} & 0 \\ 2\sigma_{13} & 0 & 2\sigma_{13} & \sigma_{23} & \sigma_{12} & \sigma_{11}+\sigma_{33} & 0 \\ 0 & 0 & 0 & 0 & 0 & 0 & 0 \end{bmatrix}. \quad (6.86)$$

The transformation rule of equation (6.83) also applies to $\bar{D} + \bar{D}'$, except that σ_{33} of equation (6.86) has to be set to zero.

At this stage, it may be appropriate to mention that other approaches to deal with finite strain problems include performing numerical integration on rate constitutive equations [6.16, 6.97], or on the Jaumann rate [6.23]. The approach adopted in the present study is simpler and more direct, compared with those in references [6.16, 6.23, 6.97].

6.5.2 Elasto-plastic materials with isotropic strain hardening

As mentioned in Section 6.1, notable large strain elasto-plastic deformation theories include those by, for examples, Green and Naghdi [6.45], Nemat-Nasser [6.36-38] and Lee [6.39-44]. It seems that most of the controversies arise in cases where both the elastic and plastic parts of strain are large. However, if confined to applications of small elastic, but large plastic strain (thus, large total strain) it can be shown that all different theories reduce to the so-called J_2 flow theory of plasticity [6.23, 6.33, 6.39,

6.50, 6.95-96, 6.98]. Since the material of interest in the present study is metal with small elastic, but large plastic strain, in what follows the J_2 flow theory is considered.

The small strain formulation of J_2 flow theory involves the stress deviator σ^D and the J_2 invariant of stresses which are, in Cartesian co-ordinates

$$\sigma_{ij}^{D} = \sigma_{ij} - \frac{1}{3}\sigma_{kk}\delta_{ij} , \quad J_2 = \frac{1}{2}\sigma_{ij}^{D}\sigma_{ij}^{D} . \tag{6.87a,b}$$

then, the constitutive relation in tensor form is

$$C_{ijkl}^{ep} = \frac{E}{1+\nu}\left[\frac{\nu}{1-2\nu}\delta_{ij}\delta_{kl} + \frac{1}{2}(\delta_{ik}\delta_{jl}+\delta_{il}\delta_{jk}) - \alpha\frac{\sigma_{ij}^{D}\sigma_{kl}^{D}}{\bar{\omega}}\right] \tag{6.88}$$

where

$$\bar{\omega} = \frac{2}{3}\bar{\sigma}^2\left(\frac{E-\frac{1-2\nu}{3}E_T}{E-E_T}\right). \tag{6.89}$$

In equations (6.88) and (6.89), E_T is the tangent modulus, ν Poisson's ratio, $\bar{\sigma} = \sqrt{3J_2}$ the effective stress and α is a parameter having the value of either zero or unity. When $\alpha = 0$ it is associated with elastic loading or any unloading, and when $\alpha = 1$ it is associated with plastic loading. Whether the material is undergoing plastic loading or not it can be determined through the following conditions

$$\alpha = \begin{cases} 1 & \dot{J}_2 = \sigma_{ij}^D \dot{\sigma}_{ij} \geq 0 \ \wedge \ J_2 = (J_2)_{max} \\ 0 & \dot{J}_2 < 0 \ \vee \ J_2 < (J_2)_{max} \end{cases} \tag{6.90}$$

with $\wedge$ denoting "and" and $\vee$ "or".

The above small strain formulation can be extended to finite strain cases in a similar approach to that of Sub-section 6.5.1. This is achieved by adding equation (6.85) to (6.88). Then, the matrix form of the constitutive relation becomes

$$\bar{D}^{ep} = \bar{D} + \bar{D}' + \bar{D}^{\alpha} \tag{6.91}$$

where $\bar{D}$ and $\bar{D}'$ are defined in equations (6.78) and (6.86). $\bar{D}^{\alpha}$ denotes the term associated with α in equation (6.88). It is defined as

$$\bar{D}^{\alpha} = - \beta \begin{bmatrix} \sigma_{11}^D\sigma_{11}^D & \sigma_{11}^D\sigma_{22}^D & \sigma_{11}^D\sigma_{33}^D & \sigma_{11}^D\sigma_{12} & \sigma_{11}^D\sigma_{23} & \sigma_{11}^D\sigma_{31} & \sigma_{11}^D\sigma_{12}^s \\ \sigma_{22}^D\sigma_{11}^D & \sigma_{22}^D\sigma_{22}^D & \sigma_{22}^D\sigma_{33}^D & \sigma_{22}^D\sigma_{12} & \sigma_{22}^D\sigma_{23} & \sigma_{22}^D\sigma_{31} & \sigma_{22}^D\sigma_{12}^s \\ \sigma_{33}^D\sigma_{11}^D & \sigma_{33}^D\sigma_{22}^D & \sigma_{33}^D\sigma_{33}^D & \sigma_{33}^D\sigma_{12} & \sigma_{33}^D\sigma_{23} & \sigma_{33}^D\sigma_{31} & \sigma_{33}^D\sigma_{12}^s \\ \sigma_{12}\sigma_{11}^D & \sigma_{12}\sigma_{22}^D & \sigma_{12}\sigma_{33}^D & \sigma_{12}\sigma_{12} & \sigma_{12}\sigma_{23} & \sigma_{12}\sigma_{31} & \sigma_{12}\sigma_{12}^s \\ \sigma_{23}\sigma_{11}^D & \sigma_{23}\sigma_{22}^D & \sigma_{23}\sigma_{33}^D & \sigma_{23}\sigma_{12} & \sigma_{23}\sigma_{23} & \sigma_{23}\sigma_{31} & \sigma_{23}\sigma_{12}^s \\ \sigma_{31}\sigma_{11}^D & \sigma_{31}\sigma_{22}^D & \sigma_{31}\sigma_{33}^D & \sigma_{31}\sigma_{12} & \sigma_{31}\sigma_{23} & \sigma_{31}\sigma_{31} & \sigma_{31}\sigma_{12}^s \\ \sigma_{12}^s\sigma_{11}^D & \sigma_{12}^s\sigma_{22}^D & \sigma_{12}^s\sigma_{33}^D & \sigma_{12}^s\sigma_{12} & \sigma_{12}^s\sigma_{23} & \sigma_{12}^s\sigma_{31} & \sigma_{12}^s\sigma_{12}^s \end{bmatrix} \tag{6.92}$$

where

$$\beta = \frac{\alpha}{\omega} . \tag{6.93}$$

Equation (6.91) is the constitutive relation for general 3D problems. When reducing the general 3D theory to thin or moderately thick plates or shells two aspects are to be noted. Firstly, it is usually assumed that the effects of transversal shear stresses on plastic behaviours can be disregarded [6.99]. Such an assumption leads to a simplified matrix $\bar{D}^{e}$ which becomes now

$$\bar{D}^{e} = -\beta \begin{bmatrix} \sigma_{11}^{D}\sigma_{11}^{D} & \sigma_{11}^{D}\sigma_{22}^{D} & \sigma_{11}^{D}\sigma_{33}^{D} & \sigma_{11}^{D}\sigma_{12} & 0 & 0 & \sigma_{11}^{D}\sigma_{12}^{s} \\ \sigma_{22}^{D}\sigma_{11}^{D} & \sigma_{22}^{D}\sigma_{22}^{D} & \sigma_{22}^{D}\sigma_{33}^{D} & \sigma_{22}^{D}\sigma_{12} & 0 & 0 & \sigma_{22}^{D}\sigma_{12}^{s} \\ \sigma_{33}^{D}\sigma_{11}^{D} & \sigma_{33}^{D}\sigma_{22}^{D} & \sigma_{33}^{D}\sigma_{33}^{D} & \sigma_{33}^{D}\sigma_{12} & 0 & 0 & \sigma_{33}^{D}\sigma_{12}^{s} \\ \sigma_{12}\sigma_{11}^{D} & \sigma_{12}\sigma_{22}^{D} & \sigma_{12}\sigma_{33}^{D} & \sigma_{12}\sigma_{12} & 0 & 0 & \sigma_{12}\sigma_{12}^{s} \\ 0 & 0 & 0 & 0 & 0 & 0 & 0 \\ 0 & 0 & 0 & 0 & 0 & 0 & 0 \\ \sigma_{12}^{s}\sigma_{11}^{D} & \sigma_{12}^{s}\sigma_{22}^{D} & \sigma_{12}^{s}\sigma_{33}^{D} & \sigma_{12}^{s}\sigma_{12} & 0 & 0 & \sigma_{12}^{s}\sigma_{12}^{s} \end{bmatrix}. \tag{6.94}$$

Secondly, the transformation rule of equation (6.83) is applied to $\bar{D}^{ep}$. In doing so, one can only set σ_{33} to zero. On the other hand, $\sigma_{33}{}^{D}$ is not zero.

It may be appropriate to point out that in arriving at equations (6.91) and (6.94), the von Mises criterion of yield has been employed. The von Mises criterion is considered here because the materials of interest in the present investigation are metals. The von Mises yield criterion can be expressed in terms of stresses or stress resultants. The first approach allows for the spread of plasticity over the thickness of plates and shells, and is termed "the layered approach". This approach has been adopted in reference [6.99]. The second approach, "the non-layered approach", on the other hand, employs

yield functions that are in terms of stress resultants. This approach assumes that at a point the entire cross-section becomes plastic simultaneously. Therefore, compared with the non-layered approach, the layered approach seems to be more realistic but requires larger amount of algebraic manipulations in forming element stiffness matrix. However, reference [6.99] showed that the discrepancy between the two approaches was insignificant, while reference [6.66] seemed to suggest the application of a large number of elements with the non-layered approach. In the present investigation, the non-layered approach is employed for two considerations. Firstly, it requires less computation to evaluate element stiffness matrices. Secondly, the $\bar{D}^{ep}$ matrix can be written in a simple and concise way, which enables one to obtain explicit expressions for the stiffness matrix that are of manageable size.

In the non-layered approach, the yield criterion should be expressed in terms of stress resultants. Such attempts include those proposed in references [6.66, 6.92, 6.100-101]. In 1948, Ilyushin applied the von Mises yield criterion to thin shells [6.100]. The idea was further developed by Shapiro [6.101]. Simo and Kennedy [6.66] then extended the Ilyushin-Shapiro two-surface yield condition to nonlinear shell analysis. The yield conditions of Simo and Kennedy [6.66] were written in terms of membrane forces and bending moments, and are capable of reflecting the coupling effect of membrane forces and bending moments on plastic behaviours. Because the yield conditions included two additional parameters that were deformation-path dependent, Simo and Kennedy [6.66] have constructed a complex return mapping algorithm (to bring stress points outside of the yield surface onto the surface). This technique, however, requires a very significant

amount of computational effort. On the other hand, Robinson [6.92] had shown that the Ilyushin-Shapiro yield condition reduced to a non-parametric form without loss of accuracy and generality. Consequently, the corresponding return mapping algorithm is simpler to construct and is less computationally expensive. In what follows, the yield condition [6.92] investigated by Robinson and its corresponding return mapping are introduced . The yield condition in reference [6.90] shall be called Ilyushin's yield condition henceforth.

If σ_y is the yield stress of the material in simple tension and h the thickness of the shell, one defines dimensionless membrane forces n_{11}, n_{22} and n_{12} where

$$n_{ij} = \frac{N_{ij}}{\sigma_y h} \tag{6.95}$$

and dimensionless bending moments m_{11}, m_{22} and m_{12} (note that they should not be confused with the elements of mass matrix) where

$$m_{ij} = \frac{4M_{ij}}{\sigma_y h^2} . \tag{6.96}$$

The Ilyushin yield condition proposed by Robinson [6.92] are stated as

$$Q_t + Q_m + \frac{|Q_{tm}|}{\sqrt{3}} \leq 1 \tag{6.97}$$

with

$$
\begin{aligned}
Q_t &= n_{11}^2 + n_{22}^2 - n_{11}n_{22} + 3n_{12}^2 \\
Q_m &= m_{11}^2 + m_{22}^2 - m_{11}m_{22} + 3m_{12}^2 \\
Q_{tm} &= n_{11}m_{11} + n_{22}m_{22} - \frac{1}{2}n_{11}m_{22} - \frac{1}{2}n_{22}m_{11} + 3n_{12}m_{12} \ .
\end{aligned}
\tag{6.98}
$$

It should be noted that in the above yield condition transverse shear stresses have been disregarded. Robinson [6.92] has shown that equation (6.97) is a very good approximation to the exact criterion and superior to the other linear approximations.

Note that in equations (6.95) and (6.96), the membrane forces N_{ij} and bending moments M_{ij} are related to stress components across the cross-section as

$$
\begin{aligned}
N_{ij} &= \int_{-\frac{h}{2}}^{\frac{h}{2}} \sigma_{ij}\, d\eta \ , \\
M_{ij} &= \int_{-\frac{h}{2}}^{\frac{h}{2}} \sigma_{ij}\eta\, d\eta \ .
\end{aligned}
\tag{6.99}
$$

Therefore, they are defined over a cross-section with thickness h and *unity* width.

The return mapping follows that described in reference [6.23] for general 3D problems. Noting that in the present study membrane and bending stresses are uncoupled, it is proposed to split the return mapping into two portions, one for the membrane stress and the other for bending stress. The portion for membrane stress is, in fact, a return mapping for plane stress problems. Similarly, the portion for bending stress is identical

to a return mapping for plate bending problems. Assuming that $\Delta\varepsilon^{ep}$ is the elasto-plastic strain increment which is divided into sub-increments $\Delta(\Delta\varepsilon^{ep})$ according to reference [6.15]

$$\Delta(\Delta\varepsilon^{ep}) = \frac{\gamma}{Z} \tag{6.100}$$

with

$$\gamma = \frac{\Delta\varepsilon^{ep}}{\Delta\varepsilon}\,, \qquad Z = 1 + \frac{\gamma}{30}\,. \tag{6.101a,b}$$

Therefore, the parameter γ indicates the elasto-plastic portion of total strain increment $\Delta\varepsilon$. Equations (6.100) and (6.101a,b) in fact divide $\Delta\varepsilon$ into 30 equal sub-increments, Z of which corresponds to $\Delta\varepsilon^{ep}$, the elasto-plastic portion of strain increment. For each of the Z sub-increments of the elasto-plastic strain, $\Delta(\Delta\varepsilon^{ep})$, the updating formula is

$$\tau \leftarrow \tau + \tilde{D}_3^{ep}\,\Delta(\Delta\varepsilon^{ep}) \tag{6.102}$$

where $\leftarrow$ stands for "assign to". For the membrane stress portion τ and $\Delta(\Delta\varepsilon^{ep})$ are understood to be the membrane stresses and membrane strain sub-increment, respectively. For the bending moment portion, τ and $\Delta(\Delta\varepsilon^{ep})$ are understood to be the bending

moments and bending curvature sub-increment, respectively. The 3×3 matrix $\tilde{D}_3^{ep}$ is obtained through

$$\tilde{D}_3^{ep} = (T_{c4})^T D_4^{ep} (T_{c4}) \tag{6.103}$$

where the 4×4 matrix D_4^{ep} is defined as

$$D_4^{ep} = D_4 + D_4' + D_4^a \ . \tag{6.104}$$

In equation (6.104), D_4' and D_4^a are of dimension 4×4 and can, in fact, be formed by, (i) selecting the first 4 rows and columns of $\bar{D}'$ of equation (6.86) and $\bar{D}^a$ of equation (6.92), respectively; and (ii) replacing σ by appropriate τ. Then,

$$D_4 = \lambda_1 \begin{bmatrix} 1-\nu & \nu & \nu & 0 \\ \nu & 1-\nu & \nu & 0 \\ \nu & \nu & 1-\nu & 0 \\ 0 & 0 & 0 & \dfrac{1-2\nu}{2} \end{bmatrix} \tag{6.105}$$

where

$$\lambda_1 = \frac{E}{(1+\nu)(1-2\nu)} \quad \text{for membrane stresses and}$$

$$\lambda_1 = \frac{Eh^3}{12(1+\nu)(1-2\nu)} \quad \text{for bending moments.}$$

Finally, the transformation matrix T_{c4} in equation (6.103) is given as

$$T_{c4} = \begin{bmatrix} 1 & 0 & 0 \\ 0 & 1 & 0 \\ t_1 & t_2 & t_4 \\ 0 & 0 & 1 \end{bmatrix} \tag{6.106}$$

with

$$t_k = -\frac{(D_4^{ep})_{3k}}{(D_4^{ep})_{33}} \, . \tag{6.107}$$

6.6 Configuration and Stress Updating

This section is concerned with the updating of configuration and stress at every time step. The updating of configuration is introduced in Sub-section 6.6.1 while the updating of stress is presented in Sub-section 6.6.2.

6.6.1 Updating of configuration

The updating of configuration of a shell consists of the updating of its mid-surface co-ordinates and directors. Mid-surface co-ordinates are updated by adding mid-surface displacements to mid-surface co-ordinates of the reference configuration. By setting η^t to zero in equations (6.13) and (6.15), one can write, for mid-surface co-ordinates of the reference configuration

$$\begin{Bmatrix} \overline{r^t} \\ \overline{s^t} \\ \overline{t^t} \end{Bmatrix} = \sum_{i=1}^{3} \xi_i \begin{Bmatrix} \overline{r_i^t} \\ \overline{s_i^t} \\ 0 \end{Bmatrix} \tag{6.108}$$

and for incremental displacements

$$\begin{Bmatrix} \overline{\Delta u^t} \\ \overline{\Delta v^t} \\ \overline{\Delta w^t} \end{Bmatrix} = \sum_{i=1}^{3} \xi_i \begin{Bmatrix} \overline{\Delta u_i^t} \\ \overline{\Delta v_i^t} \\ \overline{\Delta w_i^t} \end{Bmatrix} . \tag{6.109}$$

Adding displacement increments to mid-surface co-ordinates of the reference configuration results in the following updating scheme for mid-surface co-ordinates

$$\begin{Bmatrix} \overline{r^{t+\Delta t}} \\ \overline{s^{t+\Delta t}} \\ \overline{t^{t+\Delta t}} \end{Bmatrix} = \begin{Bmatrix} \overline{r^{t}} \\ \overline{s^{t}} \\ \overline{t^{t}} \end{Bmatrix} + \begin{Bmatrix} \overline{\Delta u^{t}} \\ \overline{\Delta v^{t}} \\ \overline{\Delta w^{t}} \end{Bmatrix} . \tag{6.110}$$

Note that equations (6.108) through (6.110) are written in terms of local co-ordinates. Similar construction for the global co-ordinates can be made. But for brevity, those in terms of global co-ordinates will be not presented here.

The updating procedures for the directors follow those proposed in references [6.22, 6.62-67]. Assuming that incremental rotations $(\Delta\theta_i)^t$ $(i=1,2,3)$ have been solved, $V_i^{t+\Delta t}$, the new position of director V_i^t, is updated through the following equation

$$V_i^{t+\Delta t} = T_v V_i^t \tag{6.111}$$

with

$$T_v = \cos(|\Delta\theta|) I_3 + \frac{\sin(|\Delta\theta|)}{|\Delta\theta|}(\Delta\hat{\theta}) \tag{6.112}$$

where $\Delta\theta = (\Delta\theta_i)^t$, $|\cdot|$ denotes the magnitude of the enclosed vector and $(\Delta\hat{\theta})$ is a skew-symmetric matrix constructed from $\Delta\theta$. That is,

$$\Delta\hat{\theta} = \begin{bmatrix} 0 & -\Delta\theta_t & \Delta\theta_s \\ \Delta\theta_t & 0 & -\Delta\theta_r \\ -\Delta\theta_s & \Delta\theta_r & 0 \end{bmatrix} . \tag{6.113}$$

In addtion, the following scheme [6.67] is included to update the director angular velocity field $\omega^t = V^t \times \dot{V}^t$ and director angular acceleration field $\dot{\omega}^t$

$$\omega^{t+\Delta t} = \frac{\gamma}{\beta\delta}\Delta\theta - T_v\left\{\omega^t + \left(\frac{\gamma}{\beta} - 2\right)\left[\omega^t + \frac{\delta}{2}\dot{\omega}^t\right]\right\}$$
$$\dot{\omega}^{t+\Delta t} = \frac{1}{\gamma\delta}\omega^{t+\Delta t} - T_v\left[\frac{1}{\gamma\delta}\omega^t + \left(\frac{1}{\gamma} - 1\right)\dot{\omega}^t\right] \qquad (6.114a,b)$$

in which T_v is defined by equation (6.112) and $\Delta\theta = (\Delta\theta_i)^t$. The parameters γ and β, are those of the Newmark family of direct integration algorithms. And $\delta = \Delta t$ is the time step size. Note that equations (6.114a,b) are extensions of the following updating scheme for (translational) velocity and acceleration

$$\dot{u}^{t+\Delta t} = \frac{\gamma}{\beta\delta}\Delta u - \left\{\dot{u}^t + \left(\frac{\gamma}{\beta} - 2\right)\left[\dot{u}^t + \frac{\delta}{2}\ddot{u}^t\right]\right\}$$
$$\ddot{u}^{t+\Delta t} = \frac{1}{\gamma\delta}\dot{u}^{t+\Delta t} - \left[\frac{1}{\gamma\delta}\dot{u}^t + \left(\frac{1}{\gamma} - 1\right)\ddot{u}^t\right]. \qquad (6.115a,b)$$

Equations (6.111) through (6.115a,b) are not applicable to the central difference method since in the latter $\beta = 0$. However, the deterministic central difference method will be employed in conjunction with the stochastic central difference method for the evaluation of response statistics of nonlinear shell structures. Thus, updating scheme similar to equations (6.111) through (6.115) for the central difference method has to be developed. This updating scheme together with computed results will be reported in Chapter 8.

Returning to the present updating scheme, it should be mentioned that in the limiting cases of small rotations, $\Delta\theta \to 0$. Consequently, $\cos(|\Delta\theta|) \to 1$, $\frac{\sin(|\Delta\theta|)}{|\Delta\theta|} \to 1$ and $T_v \to I_3$. In this case, the director needs not be updated, and the updating scheme for director angular velocity, equation (6.114a) and director angular acceleration, equation (6.114b), reduce to those for translational velocity and acceleration, see equations (6.115a,b).

It should also be mentioned that the above updating scheme, equations (6.111) through (6.115a,b), has embodied one implicit condition [6.22, 6.62-67]. That is, the incremental rotation vector $\Delta\theta$ is perpendicular to the director's reference position V_i^t. As discussed in Sub-section 6.3.2, this implicit condition implies that $\Delta\theta_{ti}^t = 0$. The physical interpretation is that the incremental rotational component along the director does not have any effects on the re-orientation of the director. Only those incremental rotational components lying on the plane perpendicular to the director can have effect on bringing the director to a new position. Recently, Fox and Simo [6.102] proposed to replace the exponential mapping Γ_i^t of equations (6.17a,b,c,d) with another mapping that in fact contained the product of two exponential mappings. One of these mappings was constructed from the DDOF and the director. However, Fox and Simo [6.102] showed that such a new mapping was not uniquely defined. To preserve uniqueness "drill rotation constraint" had to be applied. This no doubt complicates the computation (see reference [6.102]). As reference [6.103], the precursor of reference [6.102], pointed out, the aim was to identify the independent rotation field, which is the DDOF in the present study,

with the rotation of the continuum. This aim is realized in the foregoing formulation and derivation. The present study adopts equations (6.111) and (6.112a,b) as the director updating scheme because of two reasons. Firstly, it has good physical basis. Secondly, it involves less computational efforts. It may be appropriate to note that no numerical results were included in reference [6.102].

Finally, as a part of configuration updating, we consider the updating of mass density and thickness. Such an updating requires the calculation of "relative" deformation gradient [6.33] which is defined as

$$F_t^{t+\Delta t} = \begin{bmatrix} \frac{\partial(\Delta u^t)}{\partial u^t} & \frac{\partial(\Delta u^t)}{\partial v^t} & \frac{\partial(\Delta u^t)}{\partial t^t} \\ \frac{\partial(\Delta v^t)}{\partial u^t} & \frac{\partial(\Delta v^t)}{\partial v^t} & \frac{\partial(\Delta v^t)}{\partial t^t} \\ \frac{\partial(\Delta w^t)}{\partial u^t} & \frac{\partial(\Delta w^t)}{\partial v^t} & \frac{\partial(\Delta w^t)}{\partial t^t} \end{bmatrix} \tag{6.116}$$

where displacement increments Δu^t, Δv^t, Δw^t are as given in equation (6.15). Equation (6.116) expresses the deformations of the body occupying configuration $C^{t+\Delta t}$ with respect to the reference configuration C^t. Then,

$$\rho^{t+\Delta t} = \frac{\rho^t}{\det(F_t^{t+\Delta t})}$$

$$h^{t+\Delta t} = h^t \det(F_t^{t+\Delta t}) \frac{A^t}{A^{t+\Delta t}} \tag{6.117a,b}$$

with det(·) denoting the "determinant of" and the area of an element at time "t", A^t, is

$$A^t = \frac{r_2^t s_3^t}{2} .$$

6.6.2 Updating of stresses

As equations (6.11) and (6.12) indicated, after solving the nodal displacement increments, strain and stress increments can be recovered. This stress increment is defined with respect to the reference configuration C^t, and can therefore be added to σ^t, the Cauchy stress at time "t" since they are referred to the same reference state. The sum of σ^t and ΔS becomes $S^{t+\Delta t}$. That is, $S^{t+\Delta t} = \sigma^t + \Delta S$, which is the second Piola-Kirchhoff stress of deformation state $C^{t+\Delta t}$ measured with respect to the reference configuration C^t. The transformation of the second Piola-Kirchhoff stress $S^{t+\Delta t}$ to the Cauchy stress $\sigma^{t+\Delta t}$ is [6.23, 6.33]

$$\sigma^{t+\Delta t} = \frac{1}{\det(F_t^{t+\Delta t})} F_t^{t+\Delta t} S^{t+\Delta t} (F^{t+\Delta t})^T \qquad (6.118)$$

where $F_t^{t+\Delta t}$ is defined by equation (6.116).

6.7 Concluding Remarks

In this chapter aspects and theories of nonlinear analysis of structures, with special emphasis on structures that are discretized by the finite element method, have been discussed. The updated Lagrangian formulation and the incremental Hellinger-Reissner variational principle were employed. The independently assumed fields employed were the incremental displacements and incremental strains. Accordingly, the incremental second Piola-Kirchhoff stress and the incremental Washizu strain were selected as the incremental stress and strain measures. In turn, the incremental second Piola-Kirchhoff stress at time "t" was added to the Cauchy stress at time "t" to form the second Piola-Kirchhoff stress of deformation state $C^{t+\Delta t}$ measured with respect to the reference configuration C^{t}. Subsequently, $S^{t+\Delta t}$ was transformed to the Cauchy stress $\sigma^{t+\Delta t}$.

Two versions of linear and nonlinear element stiffness matrices were derived. These are the director version and the simplified version. In the director version, it was assumed that for each node on the shell mid-surface the director can be uniquely defined. The stiffness matrices were found to be dependent of the current position of the director, thus it required the updating of the director at every time step. The simplified version, on the other hand, was useful for cases where the director was not unique, or was difficult to determine. The linear part of the simplified version was proved identical to the elements developed in Chapter 3. In the derivation of element stiffness matrices, variable thickness of the shell was considered to take into account the "thinning effect" due to large strain.

Consistent element mass matrices were derived in Section 6.4. To be consistent with element stiffness matrices, the consistent element mass matrices had their director version and simplified version, depending on whether the director was uniquely defined and included. The mass matrices were defined with respect to the reference configuration. They were different from those referenced to the undeformed configuration [6.15, 6.23], for instance. Therefore, mass matrix was to be calculated at every time step, since mass density, thickness of the shell, positions of mid-surface nodes, and directors for the director version of formulation, changed as the shell deformed.

Material nonlinearity studied in this chapter was of elasto-plastic type with isotropic strain hardening. Here only cases in which small elastic, but large plastic strain condition applies were considered and the J_2 flow theory of plasticity, in conjunction with Ilyushin's yield criterion, was employed. To simplify the derivation of (small displacement) stiffness matrix and to facilitate the acquisition of explicit expression for the stiffness matrix, the non-layered approach was then adopted. For homogeneous, isotropic and linearly elastic material, formulations for small and large strain applications were also included.

Emphasis was also placed on the updating of director field, director velocity field and director acceleration field. Schemes to update stress and to transform the second Piola-kirchhoff stress to the Cauchy stress were introduced.

It should be mentioned that explicit expressions for the element matrices (linear and nonlinear), element consistent mass matrices and element pseudo-force vector were obtained. These expressions were written in terms of geometry and stress state of the

time step. These explicit expressions are given in reference [6.104] and will not be included here for brevity.

It should also be mentioned that this chapter only presented the derivation of two shell elements whose simplified linear parts correspond to the shell elements identified as NFORMU=14 and 16 in Chapter 5. The remaining 14 variations of the formulations of the shell elements can be obtained following the derivations shown in this chapter.

Results concerning the applications of the formulations developed so far in this chapter will be presented in the next chapter.

CHAPTER 7

STUDIES OF NONLINEAR SHELL STRUCTURES

In this chapter, the theory developed in Chapter 6 is applied to a number of examples so as to examine the correctness, accuracy and applicability of the theory. These examples are concerned with static and dynamic analysis of problems with geometrical, material, and geometrical and material nonlinearities. The chapter consists of four sections. Briefly, Section 7.1 includes static analysis of geometrically nonlinear problems while Section 7.2 deals with static analysis of materially and geometrically nonlinear problems. Dynamic analysis of generally nonlinear problems is presented in Section 7.3. Concluding remarks are given in Section 7.4.

In the computations performed in this and next chapters the shell element whose simplified linear part is labled as NFORMU=16 in Chapter 5 has been employed. Though other choices of the shell elements are available, NFORMU=16 is chosen because it does not possess spurious modes and is the most accurate among the four choices of the shell elements having no spurious modes (see Section 5.3).

7.1 Static Analysis of Geometrically Nonlinear Problems

The literature on static analysis of geometrically nonlinear problems is vast. Eight representative examples are selected and investigated in this section. They cover typical shell structures such as beams, plates, arches, cylindrical and spherical shells. The

selected examples include shell structures exhibiting stiffness hardening (cantilever beam subjected to a conservative end shear, clamped square plate subjected to uniform load, and square plate simply supported at two sides and subjected to a line force) or softening (cantilever beam subjected to an end moment, hinged cylindrical panel subjected to a central load, clamped circular arch subjected to a concentrated load and hinged and clamped spherical caps subjected to an apex load) when undergoing large deformations. The three options that are designed to provide flexibility for nonlinear static analysis of shells, namely, the "finite strain" and "small strain" formulation option, the "incorporation" and "exclusion" of director option and the "constant" and "updated" thickness option are studied. The effect of these options are discussed. Other issues addressed in this chapter include mesh topology, size of load increment and computational time.

7.1.1 Cantilever beam subjected to a conservative end shear

The cantilever beam, shown in Figure 7.1, has a length L=10.0 m, width b=1.0 m and thickness h=0.1 m. The material properties are Young's modulus $E=1.2\times10^6$ kN/m^2 and Poisson's ratio $\nu=0.0$. It is a thin beam since the aspect ratio of length to thickness is L/h=100. In the finite element discretization, two models were considered. In the first one the beam was divided into 20 equal spacing along its length. The mesh, therefore, had 22 nodes and 20 elements in total. After constraining all six degrees-of-freedom (DOF) at the fixed end, and constraining V, Θ_x and Θ_z for the remaining nodes, there were 60 unknown displacements left to be included in the final equilibrium

equation. The second model was similar to the first one except that the element connected to the fixed end in the first model was sub-divided into two. This mesh contained 24 nodes, 22 elements and 66 total unknown displacements.

As in the remaining static analyses presented in this chapter, the incremental-corrective procedure of solving nonlinear equations was adopted. In doing so, the maximum value of the conservative end shear P, 4 kN, is divided into 80 increments. That is, $\Delta P=0.05$ kN. Tip displacements U and W obtained from the two meshes are compared with those of reference [7.1] in Figure 7.2 where excellent agreement is observed. Note that, the 20 and 22 element meshes yielded almost identical results. Results plotted in Figure 7.2 were acquired by setting the following options: finite strain, inclusion of director and updated thickness. However, numerical investigations for this problem indicated that selecting small strain formulation, or not including director option, or adopting constant thickness gave insignificant difference, see Table 7.1. This seems to imply that the cantilever beam experiences small strain deformation within the range of applied load.

Table 7.1 Tip displacements U and W
(cantilever beam subjected to conservative end shear)

formulation options			tip displacements (m)	
strain	director	thickness	U	W
finite	included	updated	3.240	6.741
small	included	updated	3.240	6.741
finite	excluded	updated	3.223	6.728
finite	included	constant	3.265	6.747

7.1.2 Cantilever beam subjected to an end moment

This classical elastica problem has been widely used by many investigators as a benchmark test for large deformation analysis, see references [7.1-2], for example. As shown in Figure 7.3, the geometrical properties of the beam are, length L=12.0 m, width b=1.0 m and thickness h=1.0 m. The young's modulus of the beam is $E=3\times10^7$ N/m^2 with Poisson's ratio $\nu=0.0$. Analytical solutions show that under end moment M, the beam "rolls up" into a circular arc of radius ρ given by the following formula

$$\frac{1}{\rho} = \frac{M}{EI} . \tag{7.1}$$

when M reaches

$$M_0 = \frac{2\pi EI}{L} \tag{7.2}$$

the beam rolls up into a complete circle whose radius is

$$\rho = \frac{L}{2\pi} . \tag{7.3}$$

Applying the present geometrical and material properties, we have: $EI = 2.5 \times 10^6$ N m^2, $M_0 = 1.3 \times 10^6$ N-m and $\rho = 1.9099$ m.

In the finite element discretization, a 22 node, 20 element mesh was used. The longitudinal spacing was 1 m for the element connected to the fixed end and 1.2222 m for the remaining elements. At the fixed end, all six DOF were set to zero (constrained). While for the remaining nodes, three DOF, V, Θ_x and Θ_z, were constrained. Therefore there were 60 total unknown displacements.

Figures 7.4 through 7.9 present results obtained from the present investigation. In Figures 7.4 and 7.5, results using large and small strain formulations are compared with each other. Note that the incorporation of director and constant thickness were selected in this example. The latter choice was based on the consideration that analytical solution does not take into account the change of thickness. Figure 7.4 shows that for both the large and small strain formulations, when M/M_0 equals 1.0, tip rotation reaches 2π, tip displacement in the axial direction, U, arrives at L and tip displacement in the lateral direction, W, becomes zero. These indicate that the beam rolls up to a complete

circle, as demonstrated in Figure 7.5 which is the deformation configuration when $M/M_0=1.0$. In this configuration maximum lateral displacement 4.0557 m is observed at nodes 6 and 18 (with a distance of 7.1110 m from the fixed end). This gives approximately a radius of 2.02785 m, which is 6.176% over-estimated the analytical solution. Moreover, the identical results between large and small strain formulations demonstrate that the problem is of the category of small strain but large deformation.

However, unlike the cantilever beam discussed in Sub-section 7.1.1, in the present problem the incorporation of the director and updated thickness makes significant differences from those without the director and constant thickness. The results are presented in Figures 7.6 through 7.9. In comparison to the case with director, the case without director indicates that the beam rolls up to a complete circle at a smaller load level, which is approximately $M/M_0=0.95$. Note that when the director is not included, an element is connected to others through its three mid-surface nodes. On the other hand, with the inclusion of the director, elements are connected through not only their mid-surface nodes, but also their "cross sections". As a result, the finite element model of a shell structure when including the director tends to be stiffer than that not considering the director. This explains why the cantilever beam is able to deform to the complete circle at a lower load level when the director is not included. Note that in Figures 7.6 and 7.7, finite strain formulation was used together with the constant thickness option.

More difference is observed between results obtained using constant or updated thickness. Figures 7.8 and 7.9 present results obtained by selecting the finite strain formulation, director, and thickness updating according to the scheme discussed in Section

6.6. These two figures seem to suggest that, instead of rolling up to a complete circle, the beam shows a spiralled out trend (Figure 7.9). Note that significant differences are observed after the lateral displacement W reaches its maximum value (approximately at $M/M_0=0.4$, see Figure 7.8). One possible explanation may be that, in the case of using updated thickness, applied end moment acts not only to bend the beam, but also to stretch the beam. The stretching of the beam, or the thinning in the thickness direction is relatively small at low load level. Therefore no substantial differences are present between results based on constant and updated thickness. At high load level, however, the beam becomes thinner and its stiffness reduces, allowing itself to bend and at the same time the tip to move "outward" to make room for stretching longitudinally. On the other hand, constant thickness option may be interpreted as a constraint to enforce all the work done by the applied end moment to be transferred to the process of bending the beam and finally forming a complete circle.

In passing, the load increment for the aforementioned results was $0.08\ M_0$. That is, the steps used in the incremental-corrective solution scheme were 125.

7.1.3 Clamped square plate subjected to uniform loading

This problem is defined in Figure 7.10. Each side of the plate is of length $L=1000.0$ mm. Its thickness is 2.0 mm. Material properties are $E=2\times10^4$ kN/mm^2 and $\nu=0.3$. Due to symmetry of geometry, boundary condition and loading only one quarter of the plate was considered. Two finite element meshes were employed. These are the 25 node, 32 element mesh (Figure 7.11) and the 32 node, 46 element mesh (Figure 7.12).

The latter mesh has finer discretization around the clamped sides and therefore is able to better represent the stress distribution near the clamped boundaries. In Figures 7.11 and 7.12, the two clamped sides are designated as "B.C." implying appropriate boundary conditions are to be applied. These figures will be used later for other problems (see Sub-sections 7.1.4 and 7.1.5). The boundary conditions for the two clamped sides were $U=V=W=\Theta_x=\Theta_y=\Theta_z=0.0$. Boundary conditions for the symmetrical sides were, for the one parallel to Y-axis, $U=\Theta_y=\Theta_z=0.0$, and for the one parallel to X-axis, $V=\Theta_x=\Theta_z=0.0$, respectively. The total unknown displacements were, therefore, 73 for the 32 element mesh and 115 for the 46 element mesh.

Results of the nonlinear static analysis using the two meshes are then presented and compared with those from reference [7.3] in Figure 7.13. The units for E and uniform load q were kg/mm^2 in reference [7.3]. They have been converted to kN/mm^2 in Figure 7.13. The load increment was 0.01 kN/mm^2. Finite strain formulation was selected in conjunction with inclusion of the director and updated thickness. In Figure 7.13, good agreement is observed for the 46 element mesh. The 32 element mesh yielded smaller displacement under the same load because the mesh was inadequate to account for the "stiffening" behaviour occurring near the clamped boundaries. This indicates that, as in linear analysis, mesh topology is also very important in nonlinear analysis using finite elements.

7.1.4 Cylindrical bending of a square plate subjected to a line force

This problem deals with cylindrical bending of a very thin square plate whose aspect ratio of length to thickness is 1600. The plate is simply supported (S.S.) on two opposite edges and free on the other two sides, as shown in Figure 7.14. The geometrical and material properties are: L=680.0 mm, thickness h=0.8 mm, Young's modulus $E=2.07\times10^5$ N/mm^2, and Poisson's ratio $\nu=0.3$.

Due to symmetry of geometry, boundary condition and loading one quarter of the square plate was discretized. The 25 node, 32 element mesh of Figure 7.11 was employed. In order to ensure cylindrical bending, constraint $\Theta_x=\Theta_z=0.0$ was applied to all the nodes. In addition, for nodes on the simply supported side W=0.0 was imposed. V=0.0 and $U=\Theta_y=0.0$ were applied on the symmetrical sides parallel to the X- and Y-axis, respectively. In this case the total unknown displacements were 80.

Figure 7.15 shows results with constant and updated thicknesses. They are compared with those from references [7.1,7.4]. Results employing the constant thickness option are very close to those of references [7.1,7.4]. This suggests that the results from the latter references were based on constant thickness assumption. It is interesting to note that reference [7.1] did not restrict the thickness of the shell to be constant in its formulation. However, it did not include an updating scheme for thickness. The present results demonstrated larger displacements for updating the thickness. Considering that the shell becomes thinner as it deforms which makes the shell structure less stiff, it seems reasonable and correct to obtain larger displacements compared with the case of constant thickness. Finally, it is noticed that maximum displacements are of the order of 500 times

the original thickness of the plate. However, this is still a small strain problem since small and finite strain formulations yielded almost identical results.

7.1.5 Hinged cylindrical panel subjected to a central load

As depicted in Figure 7.16, the radius of the cylindrical panel is R=2540.0 mm, thickness h=12.7 mm, length L=2×254.0 mm. The material properties are E=3.10275 kN/mm^2 and ν=0.3. Taking into account the symmetry of geometry, boundary condition and loading, one quarter of the panel was modeled by finite elements. The mesh used was the 25 node, 32 element mesh shown in Figure 7.11. On the hinged side, boundary conditions were such that $U=V=W=\Theta_x=\Theta_z=0.0$. On the symmetrical sides, boundary conditions were, $V=\Theta_x=\Theta_z=0.0$ for the one parallel to the X-axis, and $U=\Theta_y=\Theta_z=0.0$ for the one parallel to the Y-axis. Therefore, in this example total unknown displacements were 107.

The cylindrical panel exhibits "snap-through" phenomenon when the applied load reaches certain level. For example, this load level was found to be 2.20 kN in reference [7.1]. The same value was reported in reference [7.3]. Bathe and Bolourchi observed a slightly higher value: 2.24 kN [7.5]. In the present study, the maximum load before snap-through was 2.30 kN if using a load increment of 0.1 kN and 2.25 kN with an increment 0.05 kN. The load-displacement curve for loads under the maximum value is presented in Figure 7.17. Again, excellent agreement with references [7.3,7.5] is obtained. The results of the figure also demonstrate that the effect of choosing different sizes of load increment is insignificant. This holds true for the other examples studied so far. Note that

the results in Figure 7.17 were obtained by considering finite strain, incorporating director and updating thickness.

7.1.6 Clamped circular arch subjected to a concentrated load

This problem is described by Figure 7.18 in which the radius of the arch is R=3381.10 mm, the thickness h=4.7625 mm, the width b=25.4 mm and the height of the arch over the clamped base H=27.686 mm. The material properties are $E=6.985\times10^{11}$ N/m^2 (10^7 psi) and $\nu=0.2$. Owing to symmetry one half of the arch was discretized by a 22 node, 20 element mesh. In this mesh, elements connected to the fixed end and the point of loading were of smaller length so that it could better represent the stiffening and stress concentration effects in those locations. To all nodes the constraints $V=\Theta_x=\Theta_z=0.0$ were applied. In addition, at the fixed end boundary condition $U=W=\Theta_y=0.0$ was set. For nodes situated on the symmetrical axis of the arch, $U=\Theta_y=0.0$ was applied. As a result, 56 unknown displacements were left in the final equilibrium equation.

Using a load increment of $\Delta P=6.68$ N (1.5 lb), the load-displacement curve was obtained and presented in Figure 7.19. It was found that at load level P=160.34 N (36 lb) snap-through occurred. This maximum load is very close to 159.45 N (35.8 lb) which was obtained by Hughes and Liu [7.3]. In constructing Figure 7.19, the finite strain formulation together with director and updating thickness options was selected. Numerical studies showed that the variations of the three options had insignificant influence on the results.

7.1.7 Hinged and clamped spherical caps subjected to an apex load

This sub-section first considers a spherical cap loaded at the apex and supported on a fixed hinge at the circumference, as shown in Figure 7.20. The pertinent data are, radius R=120.90 mm (4.76 in), thickness h=0.4 mm (0.1576 in), height H=2.18 mm (0.08589 in), Young's modulus $E=6.985\times10^{11}$ N/m^2 (10^7 psi) and Poisson's ratio $\nu=0.3$.

In the finite element discretization, only one quadrant of the cap was considered by exploiting the symmetry of the problem. Three meshes were employed. These are the 28 node, 36 element mesh as shown in Figure 7.21, the 46 node, 72 element mesh as presented in Figure 7.22 and the 51 node, 80 element mesh shown in Figure 7.23. Note that all three meshes had relatively fine discretization around the apex. The radial spacing was increased gradually from the apex to the hinged circumference. In the latter two meshes, the area near the hinged circumference was refined compared with the 28 node, 36 element mesh.

Boundary conditions were, on the hinged circumference, $U=V=W=\Theta_z=0.0$; on the symmetrical side parallel to the X-axis, $V=\Theta_x=\Theta_z=0.0$; on the symmetrical side parallel to the Y-axis, $U=\Theta_y=\Theta_z=0.0$; and at the apex, $U=V=\Theta_x=\Theta_y=\Theta_z=0.0$. The resulting total unknown displacements were 101, 211 and 235 for the three meshes, respectively. Results obtained by selecting finite strain formulation and updated thickness, and the exclusion of the director are presented in Figure 7.24 in which comparisons to results from reference [7.6] are also made. It can be seen that meshes having 46 and 51 nodes yielded very close results and behaved more satisfactorily than the 28 node mesh.

As in reference [7.6], the present results detected snap-through phenomenon. The maximum load before snap-through was 213.79 N (48 lb) from the 28 node, 36 element mesh and 227.15 N (51 lb) from the other two meshes. These values compare very well with that predicted by reference [7.6], which was 216.02 N (48.5 lb) according to Figure 4.13 of reference [7.6].

Comparison was also made between results obtained by incorporating and excluding the director option. These results are presented in Figure 7.25. It is interesting to notice that under a load level of approximately 100 N, the two options yielded little difference. However, it is no longer the case for higher applied loads. With director option included, the spherical cap seemed to be very stiff for applied loads ranging approximately from 160 N to 210 N. If increasing the load P further, the cap became very soft. Snap-through was also predicted but at a higher load level: 236.06 N (53 lb). Figure 7.25 suggests that, in general, incorporating the director makes the finite element model stiffer than that without the director. This agrees with the discussion of Sub-section 7.1.2 (see, Figures 7.6 and 7.7). It was also found that there was little difference between results of finite or small strain formulations, and between results of updated thickness and constant thickness.

A spherical cap loaded at the apex and clamped at the circumference, as shown in Figure 7.26, is also studied. The cap has the same geometry and material properties as the hinged one in the same sub-section. Therefore the three meshes shown in Figures 7.21 through 7.23 were also used for the clamped cap. When applying boundary conditions, the clamped circumference was constrained by $U=V=W=\Theta_x=\Theta_y=\Theta_z=0.0$.

The boundary conditions for the symmetrical sides parallel to the X- and Y-axes and the apex remained the same as those of the hinged cap. Consequently, the total unknown displacements of the three different meshes were 85, 199 and 223, respectively.

Figure 7.27 shows results for the three different meshes. The three sets of results were obtained by selecting finite strain formulation with updated thickness and disregarding the director. Similar to the hinged cap (see, Figure 7.24), the 46 and 51 node meshes gave almost identical results and were more accurate than the 28 node mesh. However, the three meshes were common in that their stiffness matrices exhibited singularity at certain load levels. These loads were, 187.07 N (42 lb) for the 28 node, 36 element mesh and 213.79 N (48 lb) for the other two meshes. Note that these loads were not snap-through loads. One of the reasons of the stiffness matrices being singular at these loads may be explained by the fact that explicit integration was used for both the linear and the initial stress stiffness matrices and therefore the present formulation is more sensitive to ill-conditioned stiffness matrices. The singularity of the stiffness matrices may also be due to the employment of the present flat triangular shell elements. On the other hand, eight node isoparametric elements in reference [7.7] and eight node axisymmetric elements in reference [7.8] were used. These two references did not report singularity in stiffness matrices. This finding also suggests that methods for dealing with singularity of this type are required. The development of such methods is one of the further research interests that the author would like to pursue.

Calculations were also performed to study the effects of small and finite strain formulations, the inclusion and exclusion of the director, and constant and updated

thickness. Results showed that insignificant differences existed except those with and without the director (see, Figure 7.28). Note that there is a common feature between Figures 7.28 and 7.25. That is, above certain load level (approximately 100 N for the hinged cap and 130 N for the clamped cap), the load-displacement curves obtained by including the director drifted away from those without the director. Beyond such a load level, the caps became very stiff and then very soft. Although, in general, incorporating the director makes the finite element model stiffer than that excluding the director, numerical causes of such drifting can not be firmly ruled out at this stage. Assuming the correctness of results from references [7.6-7], Figures 7.25 and 7.28 suggest that the exclusion of the director option would be more appropriate for the caps considered here. Moreover, for the clamped cap, if the apex load could be confined to less than, say, 180 N for the 46 and 51 node meshes, the singularity problem of the stiffness matrices would be circumvented.

7.1.8 Remarks

Before leaving this section, it may be appropriate to summarize the computing time needed for the examples investigated. This is accomplished in Table 7.2. For the eight problems studied so far, the theory and formulation developed in Chapter 6 seem to be excellent in terms of both accuracy and effectiveness. The formulation will be applied to elasto-plastic problems in the next section.

Table 7.2 Summary of computing time*

problem	total unknowns	load steps	computing time
cantilever beam (end shear)	60	80	3
cantilever beam (end moment)	60	125	5
square plate (uniform load)	73	80	4.5
	115	80	6
square plate (line force)	80	115	5.5
cylindrical panel (hinged)	107	46	2
circular arch (clamped)	56	23	1.5
spherical cap (hinged)	101	48	3
	211	51	5
	235	51	6
spherical cap (clamped)	85	42	2.5
	199	48	4
	223	48	5

* in minutes. All computing was performed on SGI 4.1 workstation.

7.2 Static Analysis of Elasto-plastic Problems

This section is concerned with elasto-plastic material behaviour. In addition to material non-linearity, the deformation of the shell structure can be small or large. The former case constitutes the so-called materially nonlinear only analysis (M.N.O.). In such

analyses no configuration updating is necessary since it is assumed that the deformation is small and the undeformed configuration is always the reference one [7.9]. Moreover, the initial stress (or the geometric, or the tangent) stiffness matrix k_{NL} (see Sub-section 6.3.5) is no longer present in equation (6.9). On the other hand, the more generally non-linear analysis in which both elasto-plastic material behaviour and large deformation are considered requires the application of the updated Lagrangian formulation in conjunction with the elasto-plastic constitutive relation discussed in Section 6.5.

In this section four examples are studied. They are: a cantilever beam subjected to an end shear, a beam built in at both ends and subjected to concentrated load, a simply supported square plate subjected to uniform loading and a clamped spherical cap subjected to apex load. For all these cases the material is of elastic-perfectly plastic type. The latter seems to be the only type that is available in the literature for comparision. Numerical examples of shell analysis of elatic-plastic materials with strain hardening behaviour would be of interest for future research.

7.2.1 Cantilever beam subjected to an end shear

This example is chosen because analytical solutions are available for both material, and geometrical and material nonlinearities [7.6]. Note that the analytical solutions are an analog to the layered approach of plasticity analysis using finite element method (see, Section 6.5). Parisch [7.6] also provided numerical results based the layered approach. The description of the problem is given in Figure 7.1 where the geometrical properties

are: length L=100.0 mm, width b=20.0 mm and thickness h=0.5 mm. In finite element discretization, a 24 node, 22 element mesh was considered. The longitudinal spacing of the beam was, starting from the fixed end, 5 mm (×2) and 10 mm (×9). That is, a finer discretization was used around the fixed end. Boundary conditions were then, $U=V=W=\Theta_x=\Theta_y=\Theta_z=0.0$ for the nodes on the fixed end and $V=\Theta_x=\Theta_z=0.0$ for the remaining nodes. Therefore the total unknown displacements came to 66.

The material of the beam is elastic-perfectly plastic with the following data: Young's modulus $E=1.8\times10^4$ kN/mm^2, Poisson's ratio $\nu=0.0$ and yield stress $\sigma_y=40.0$ kN/mm^2. Results obtained by using the 24 node, 22 element mesh and a load increment of 0.025 kN are presented in Figures 7.29 through 7.32. In Figure 7.29, the present results are compared with the analytical solutions of Parisch [7.6] for the case of M.N.O. analysis. In reference [7.6] the M.N.O. solutions were labelled "linear solution". It was found that outer layers of the beam underwent plastic deformation when the end shear reached 1/3 kN. The limit load was predicted as 0.5 kN. On the other hand, the present study found plastic deformation to occur at and the limit load to be 0.55 kN. Therefore, the predictions of the limit load were close. Closer predictions can be expected by using smaller load increments. The discrepancy in predicting the occurrence of plasticity is due to the different approaches used. The layered approach accounts for the spread of plastic zone along the thickness direction. Plastic deformation is considered to occur as soon as the outer layer(s) of the shell is plastic. The non-layered approach which is adopted in the present study (see, Section 6.5) determines the occurrence of plastic deformation based on stress resultants. When a yield condition is satisfied it means that the entire cross

section of the shell is plastic. Therefore one would expect that the layered approach predicts the occurrence of plasticity at a lower load level than the non-layered one.

Discrepancy between the two approaches also appeared in Figure 7.29 when load level is higher than 0.35 kN, approximately. Reference [7.6] predicted the occurrence of plastic deformation at a load level of 1/3 kN, using the layered approach. Therefore, for applied loads higher than this value, the beam became less stiff due to the existence of plastic layers. In the non-layer approach the beam had the same stiffness until the entire cross-section of the fixed end was plastic. This explains why the layered approach yielded larger displacement.

This explanation also holds true for analysis in which the combined effect of both material and geometrical nonlinearities is studied (Figure 7.30). Compared Figure 7.30 with 7.29 it can be seen that, in the U.L. analysis discrepancy between the layered and non-layered approaches also existed, but appeared at a higher load level (approximately 0.45 kN, compared with the 0.35 kN in M.N.O. analysis). Moreover, in terms of limit load, reference [7.6] predicted 1.825/3 = 0.608 kN. On the other hand, the present study observed a 0.625 kN. With respect to the limit loads found in reference [7.6], the percentage discrepancy of the present results is 10.0 and 2.80 for M.N.O. and U.L. analyses, respectively. In other words, the difference between the layered and non-layered approaches depends on the type of analysis performed. In particular, when predicting limit load, the non-layered approach gives better estimates in analysis where both geometrical and material non-linearities are concerned than in M.N.O. analysis. In terms of evaluating displacements, the non-layered approach seems to be stiffer than the layered

counterpart in the applied load range that causes only portion of the cross-section to be plastic.

Since the U.L. analysis observed a higher limit load than the M.N.O. analysis, one may recognize that plastic designs based on the M.N.O. analysis would be conservative ones.

In Figure 7.30, the three formulation options were set: finite strain, inclusion of the director and updated thickness. It was found that switching to small strain, or excluding the director, or constant thickness yielded insignificant difference. The most observable difference was between constant and updated thicknesses (see Figure 7.31). It should, however, be mentioned that in the examples to follow differences exist among various options. This is, therefore, a problem dependent issue, as in the geometrically non-linear static analysis of Section 7.1.

Finally it may be appropriate to discuss the following issue. According to the elementary solution, in M.N.O. analysis using the non-layered approach, as soon as the plastic hinge at the fixed end is formed, the beam loses end shear bearing capability and its stiffness matrix becomes singular due to the presence of rigid body rotation about the hinge. However, in the numerical analysis, such as that employing the finite element method, it may be different. In the present investigation, the stiffness matrix of the cantilever beam remained positive-definite several load increments beyond the limit load (see, Figure 7.32). During these several load increments the lateral displacement W grew at a faster rate than that before the formation of the plastic hinge. With subsequent load increments, the stiffness matrix eventually became singular. One possible explanation is

that the lateral displacement can only jump to any value theoretically but not computationally. Physically, a hinge cannot be formed until upper and lower fibres of the fixed end undergo very large deformation, which implies that prior to the final collapse, the actual beam can still sustain some loads even though the plastic hinge has already formed. If only one hinge is possible and only one limit load is concerned, the above-mentioned discrepancy between theory and computation does not affect the accuracy of the prediction of the limit load. When the structure has more than one hinge, such as the beam to be studied in Sub-section 7.2.2, one may observe, with respect to the elementary solutions, over-estimates (with respect to the elementary solutions) of limit loads corresponding to the second hinge and those that follow.

7.2.2 A beam built in at both ends and subjected to a concentrated load

A elastic-perfectly plastic beam built in at both ends and subjected to a concentrated load at the 3/4 point along its span is considered here. The beam is given in Figure 7.33. The length of the beam is L=10.0 m, width and thickness b=h=1.0 m. The finite element meshes used for this beam included a 46 node, 44 element mesh and a 50 node, 48 element mesh. The first mesh had refinements at the two built in ends. Such refinement was added to the neighbourhood of the point of loading in the second mesh. Note that the two built in ends and the load point are the locations of the onset of plastic hinges, as will be seen in later discussions in this sub-section. Boundary conditions applied to the beam were similar to those of the cantilever beam studied in Sub-section 7.2.1. That is, $U=V=W=\Theta_x=\Theta_y=\Theta_z=0.0$ for nodes on the two built in ends and

$V=\Theta_x=\Theta_z=0.0$ for the remaining nodes. The resulting total unknown displacements were, 120 for the 46 node, 44 element mesh and 138 for the 50 node, 48 element mesh, respectively.

Simo and Kennedy [7.2] studied this example with the objective to compare with the Bernoulli-Euler (bending dominated) elementary solution in predicting the onset of plastic hinges. This remains as the objective of the present investigation of the beam. Though both reference [7.2] and the present study employed the layered approach and yield conditions that are written in terms of stress resultants, there were differences. One of such differences is that reference [7.2] treated the rigidities associated with membrane (Eh), bending ($Eh^3/12$) and transverse shear ($\kappa_s Gh$) as independent parameters in order to simulate the elementary bending dominated solution. Similarly, the yield parameters $n_0=\sigma_y h$, $m_0=\sigma_y h^2/4$ and $q_0=\sigma_y h$ were chosen independently. As a result Young's modulus E and yield stress σ_y were not given uniquely and explicitly in reference [7.2]. The intent of the present study was to use shell model to predict the onset of plastic hinges and then compare it with the elementary solution. Therefore, unlike reference [7.2], Young's modulus and yield stress were $E=2.5\times10^7$ kN/m^2 and $\sigma_y=90$ kN/m^2. Rigidities and yield parameters were then determined accordingly.

Subsequently, the following calculations were performed: M.N.O. and U.L. analyses on the two meshes. In the U.L. analysis, finite strain formulation was selected together with the director and updated thickness. It was found that the M.N.O. and U.L. analyses yielded little difference for the interested range of applied load (see, Figure 7.34). Table 7.3 summarizes the load levels and corresponding lateral displacements of

the load point when plastic hinges occur at points B, C and A, respectively. This sequence of forming plastic hinges is in agreement with the Bernoulli-Euler elementary solution: first at the built in end closest to the load point, next at the point of loading, and thirdly at the boundary furthest from the load point. Such load levels were not reported in reference [7.2]. Figure 7.34 presents a comparison between the present study and that of reference [7.2]. It can be seen that there is discrepancy after the first plastic hinge is formed. The loads at which the second and third plastic hinges occurred were higher than those of reference [7.2] (based on readings from its figure). This phenomenon is also observed for the simply supported square plate discussed later in Sub-section 7.2.3. The cause has been explained in Sub-section 7.2.1.

Subsequently, the beam is still able to sustain further increase of applied load after the formation of the third plastic hinge. This is contrary to the bending dominated elementary solution. For the M.N.O. analysis, this has been discussed in the last paragraph of Sub-section 7.2.1. In the U.L. analysis, configuration changes allow the beam to become a truss structure after the formation of all possible plastic hinges. Our shell elements are capable of representing such a truss structure. As a result, unlike in the M.N.O. analysis, the load-displacement curve in the U.L. analysis reflects the load bearing capability of the beam as a truss after the onset of all plastic hinges.

Though little difference was observed between the M.N.O. and U.L. analyses for the load range shown in Figure 7.34, it was found that, in the M.N.O. analysis, singularity of the stiffness matrix could be observed when further increasing the applied load. For example, using the 46 node, 44 element mesh the stiffness matrix became

singular at an applied load of 47.0 kN. However, the U.L. analysis did not encounter such singularity. In the last paragraph of Sub-section 7.2.1 the singularity phenomenon has been discussed and the same interpretation applies here. Results obtained from the two meshes are also compared in Figure 7.34.

Table 7.3 The onset of plastic hinges

46 node, 44 element mesh				
plastic hinge	M.N.O. analysis		U.L. analysis	
	load level (kN)	displacement ($\times 10^{-5}$)	load level (kN)	displacement ($\times 10^{-5}$)
B	19.0	2.974	19.0	2.974
C	29.0	5.491	29.0	5.491
A	36.0	8.796	37.0	9.501
50 node, 48 element mesh				
plastic hinge	M.N.O. analysis		U.L. analysis	
	load level (kN)	displacement ($\times 10^{-5}$)	load level (kN)	displacement ($\times 10^{-5}$)
B	19.0	2.989	19.0	2.989
C	29.0	5.507	29.0	5.507
A	36.0	8.913	37.0	9.631

7.2.3 Simply supported square plate subjected to uniform load

This problem is depicted in Figure 7.35. Every side of the plate has a length L=1.0 m. The material is elastic-perfectly plastic with Young's modulus $E=10.92\times10^6$ N/m^2, Poisson's ratio $\nu=0.3$ and yield stress $\sigma_y=1600.0$ N/m^2. Considering bending dominated analytical solution, reference [7.10] suggests the following formula to calculate the limit load q_{max}

$$M_p = \frac{\sigma_y h^2 L}{4}, \qquad q_{max} = \frac{24}{L^2} M_p . \tag{7.4a,b}$$

It should be noted that the formula is suitable for thick plates [7.10]. The solution also suggests plastic hinges to occur along the diagonals of the plate. If the thickness of the plate is 0.1 m, it is found that $M_p=4$ N-m and $q_{max}=96.0$ N/m^2.

In the present finite element discretization, only one quarter of the plate was considered due to symmetry of geometry, boundary condition and loading. The mesh used is the one with 25 node, 32 element mesh shown in Figure 7.11. Boundary conditions applied at the simply supported edge that is parallel to the X-axis were $U=V=W=\Theta_y=\Theta_z=0.0$. At the simply supported boundary parallel to the Y-axis one had $U=V=W=\Theta_x=\Theta_z=0.0$. On the symmetrical side parallel to the X-axis they were $V=\Theta_x=\Theta_z=0.0$. Finally, boundary conditions for the symmetrical side parallel to the Y-axis were $U=\Theta_y=\Theta_z=0.0$. After eliminating the constrained DOF, there were 48 total unknowns.

Both the M.N.O. and U.L. analyses were performed using the 25 node, 32 element mesh. Both analyses predicted the first occurrence of plastic deformation at a

load level of $q=82.7$ N/m^2 and at the corner formed by the two simply supported edges (see, Figure 7.36). The progression of plastic zone is portrayed in Figures 7.36 through 7.43. The load-displacement curve is presented in Figure 7.44 which shows that for thickness $h=0.1$ m the M.N.O. and U.L. analyses had no significant differences. Although plastic deformation first occurred at the load level of 82.7 N/m^2, significant change of the gradient of the load-displacement curve did not happen until the load q was further increased to approximately 110 N/m^2. Referring to Figures 7.38 and 7.39, at such a load level the entire diagonal of the square plate has undergone plastic deformation. Note that even after the entire plate became plastic (at a load level of $q=163.5$ N/m^2, see Figure 7.43), the plate was still able to sustain further increase of applied load. Explanations for the causes of this phenomenon have been offered in previous sub-sections.

Investigations were also carried out on the same plate but with a smaller thickness $h=0.01$ m. In this case q_{max} becomes 0.96 N/m^2. The obtained load-displacement curves for both the M.N.O. and U.L. analyses are shown in Figures 7.45 and 7.46. Unlike the case with $h=0.1$ m, now M.N.O. and U.L. analyses yielded substantial difference. The reason is that the plate is thin and that the applied load is intense enough to allow the plate to undergo large deformation. In this case, the displacement is reduced compared with the M.N.O. solution because of stiffness hardening (also see Sub-section 7.3.2). Computational results indicate that plasticity occurs firstly at the corner formed by the two simply supported edges and at load levels $q=0.87$ and 0.98 N/m^2 for the M.N.O. and U.L. analyses, respectively. The load levels at which the entire diagonal of the plate

becomes plastic are, based on Figures 7.45 and 7.46, approximately 1.1 and 1.4 N/m^2 for the M.N.O. and U.L. analyses, respectively. The increase from 1.1 to 1.4 N/m^2 is due to the stiffness hardening mechanism which reduces the displacement as well as stress levels so that plasticity may occur at higher level of applied load. This suggests that for the thin plate, the M.N.O. analysis would give a conservative estimate in its elasto-plastic design.

7.2.4 Clamped spherical cap subjected to an apex load

The geometry of the cap has been portrayed by Figure 7.26 and included in Sub-section 7.1.7. For easy reference they are repeated here: radius R = 120.90 mm (4.76 in), thickness h = 0.4 mm (0.01576 in) and height H = 2.18 mm (0.08589 in). The material of the cap is considered to be elastic-perfectly plastic with Young's modulus $E = 6.985 \times 10^{10}$ N/m^2 (10^7 psi), Poisson's ratio $\nu = 0.3$ and yield stress $\sigma_y = 1.397 \times 10^8$ N/m^2 (2×10^4 psi). Similar to Sub-section 7.1.7, only one quadrant of the cap was discretized by shell finite elements. The finite element meshes used were the same as those in the geometrically nonlinear analysis. That is, the 28 node, 36 element mesh (Figure 7.21), the 46 node, 72 element mesh (Figure 7.22) and the 51 node, 80 element mesh (Figure 7.23). Finally, same boundary conditions as those used in Sub-section 7.1.7 were applied to the meshes resulting in 85, 199 and 223 total unknown displacements for the three meshes, respectively.

In Figure 7.47 load-displacement curves using the meshes are demonstrated and compared with results from reference [7.7]. Finite strain, updated thickness and excluding

director were considered. Comparison among the three meshes shows that the 51 node, 80 element mesh gave the most satisfactory result. Results using this mesh also compare very well with the layered approach of reference [7.7] up to the load level of approximately 190 N at which the stiffness matrix became singular. In fact, the other two meshes encountered singular stiffness matrices at about the same load level (170-185 N). This observation agrees with that of Sub-section 7.1.7 where the same range of applied load was found to be associated with singularity of stiffness matrices. As to the distribution of plastic zone, reference [7.7] indicated that it was found mainly over the outer and inner surfaces of the cap. In the present study, since the non-layered approach is employed, plastic zone was found to form around the apex. For example, a plastic zone with a radius of approximately 5.94 mm (0.225 in) from the axis of symmetry was formed at load P= 155.89 N (35 lb).

Recalling that in the geometrically non-linear analysis of the same cap (see Sub-section 7.1.7) incorporation of the director had significant effects, the director effect on elasto-plastic deformation of the cap was considered. Figure 7.48 presents a comparison between results without the director and with the director. The "drifting away" phenomenon also started at a load of approximately 130 N but the load-displacement curve did not possess the very stiff and very soft segments. The stiffness matrix subsequently became singular at a load level of 230 N which was not observed in Sub-section 7.1.7. Judging from the closeness to the result of reference [7.7], the case without the director appears again to be more appropriate for the elasto-plastic deformation analysis of the clamped cap. Similar to the analysis of Sub-section 7.1.7, if the applied

load could be confined to be less than approximately 180 N, the singularity of the stiffness matrices would be circumvented.

Comparisons about the other two formulation options were also made and are presented in Figures 7.49 and 7.50. For the cap, it seems that its thickness changed little for the range of applied load interested since the selection of the updated and constant thickness yielded essentially the same results (Figure 7.50). As to the small and finite strain formulations, the mathematical difference is the matrix $\bar{D}'$ defined by equation (6.86). Whether the inclusion of equation (6.86) will increase or reduce the stiffness of the structure depends on the signs of the stress components. Therefore, it is possible to observe stiffer or softer shell behaviours from the finite strain formulation than from the small strain one. In the present case, stiffer shell behaviours were observed and the results using the finite strain option agreed with those of reference [7.7] better than the small strain formulation.

7.3 Dynamic Analysis of Generally Nonlinear Problems

Static analysis including geometric, material, and geometric and material nonlinearities has been presented in Sections 7.1 and 7.2. They have demonstrated the correctness, accuracy and applicability of the formulations developed in Chapter 6. This section is to further examine the issues within the framework of dynamic responses. The three formulation options associated with static analysis (or the stiffness matrix), that is, the option of finite or small strain formulation, the option of including or excluding the

director, and the option of updated or constant thickness are retained here. In addition, one more option is available in the present study for selecting updated or constant consistent mass matrix (also, see Section 6.4). This option enables one to investigate the difference, if any, between results with constant and updated consistent mass matrices. this is an important issue to be addressed as the existing literature commonly adopts a constant consistent mass matrix, see reference [7.8] for example.

This section contains two examples, a clamped spherical cap subjected to an apex load and a simply supported rectangular plate subjected to a center load.

7.3.1 Clamped spherical cap subjected to an apex load

This clamped spherical cap has been studied in Sub-sections 7.1.7 and 7.2.4 for geometrically, and geometrically and materially non-linear analyses. The material of the cap is either elastic with Young's modulus $E=6.985\times10^{10}$ N/m^2 (10^7 psi), Poisson's ratio $\nu=0.3$ and mass density per unit volume $\rho=2621.54$ kg/m^3 (0.000245 lb-sec^2/in^4), or elastic-perfectly plastic with yield stress $\sigma_y=1.397\times10^8$ N/m^2 (2×10^4 psi). Other pertinent data have been included in Sub-section 7.2.7

In the finite element discretization only one quadrant of the cap was modeled because of symmetry of geometry, boundary condition and loading. The 46 node, 72 element mesh (Figure 7.22) was employed in the dynamic analysis for two reasons: (i) the mesh performed satisfactorily in the static analysis; and (ii) computationally the size of the problem is moderate so that it can be dealt with by a workstation, such as the SGI 4.1 machine. The boundary conditions applied to the mesh were the same as those used

in Sub-section 7.1.7. The resulting total unknown displacements were 199. The applied load in the apex has one of the following two definitions: a step function or impulse-type function.

Firstly, consider the case of a step apex load whose time history is shown in Figure 7.51 with $P_0=155.89$ N (35 lb). The calculated dynamic responses for linear and geometrically nonlinear cases are plotted and compared with those of reference [7.8] in Figure 7.52. The results from reference [7.8] were obtained by employing ten eight-node axisymmetric elements and the updated Lagrangian formulation. The small strain formulation was applied. Constant consistent mass matrix was also chosen. On the other hand, the present results shown in Figure 7.52 were obtained by selecting finite strain formulation, excluding the director, updated thickness and constant consistent mass matrix. When performing direct integration, both the present study and reference [7.8] adopted the trapezoidal rule with a time step size $\Delta t=0.22\times10^{-5}$ second. This time step size is one-fiftieth of the fundamental period of the cap which is 0.116×10^{-3} second [7.8]. Figure 7.52 shows that the nonlinear response has a large amplitude and a longer period compared with the linear one. Roughly speaking, both the nonlinear amplitude and period are 4.5 times of their linear counterparts. These are indication of stiffness softening effect. Such stiffness softening effect agrees with the observation in Sub-section 7.1.7 (see, Figure 7.27).

Calculations were then repeated for the geometrically non-linear response. Instead of choosing a constant consistent mass matrix, this time the mass matrix was updated at every time step. A comparison is shown in Figure 7.53. It can be seen that noticeable

difference is observed when and after the displacement reaches its maximum value. The result from updated mass matrix seems to predict a longer period of vibration. One should, therefore, recognize that there are differences between using updated and constant mass matrices when large displacement is involved, such as in the cases of stiffness softening. Employing updated consistent mass matrix in conjunction with the updated Lagrangian formulation is more rigorous from the theoretical point of view, but at the same time more computations are required. If the change of configuration is not significant, using constant consistent mass matrix is an economical and accurate approach.

We next considered the case of impulse-type applied load whose time history is given in Figure 7.54 in which $P_0=133.62$ N (30 lb) and $t_0=0.0005$ second. The material of the cap was taken to be elastic-perfectly plastic. More generally nonlinear analysis was performed, which included both material and geometrical nonlinearities. Results from finite and small strain formulations were obtained and are presented in Figure 7.55. In the latter the linear solution and the result of general nonlinear analysis from reference [7.8] are also included for comparison. The formulation of reference [7.8] is concerned with small strain deformation and layered approach for the elasto-plastic analysis. On the other hand, the present formulation uses the non-layered approach. The other formulation options for the results of Figure 7.55 were, excluding the director, updated thickness and constant consistent mass matrix. For direct integration, the time step size was again 0.22×10^{-5} second. Figure 7.55 shows that the present study, using finite and small strain formulations, and reference [7.8] predicted very close dynamics patterns. In terms of the displacement, the present study seemed to yield higher values. Between the finite and

small strain formulations, the latter was closer to the formulation of reference [7.8]. Overall, the qualitative and quantitative agreements between the present study and reference [7.8] are very good.

7.3.2 Simply supported rectangular plate subjected to a center load

This simply supported plate has been studied in reference [7.8] for linear dynamic response analysis. Here the investigation is to be extended to more complicated cases using the present formulation. The plate is shown in Figure 7.56. Its geometrical dimension is, a=1016 mm (40 in), b=1524 mm (60 in) and thickness h=25.4 mm (1 in). The material properties are, Young's modulus $E=2.0955\times10^8$ N/m^2 (3×10^4 psi), Poisson's ratio $\nu=0.25$, yield stress $\sigma_y=2.0955\times10^5$ N/m^2 (30 psi) and mass density per unit volume $\rho=3210.05$ kg/m^3 (0.0003 lb-sec^2/in^4).

Owing to symmetry of geometry, boundary condition and loading, one quarter of the plate was discretized by the finite elements developed earlier in Chapters 3 through 6. The mesh consisted of 25 nodes and 32 elements. Its layout is portrayed by Figure 7.11. Boundary conditions have been described in Sub-section 7.2.3 and will not be repeated here for brevity. The total unknown displacements were 48.

For direct integration the trapezoidal scheme was employed and the time step size was 0.002 second as suggested by reference [7.8].

Similar to Sub-section 7.3.1, two types of dynamic loads were considered: a step function and an impulse-type function. Figure 7.57 shows the step function. The difference between Figures 7.51 and 7.57 is that the latter allows a period t_0 so that the

load is increased to its full value instead of a jump at t=0. The period t_0 is set to 0.006 second throughout this example. P_0 was first chosen to be 44.54 N (10 lb). Note that P_0 is the force acting on a quarter of the plate. A linear dynamic analysis was performed. The result is plotted and compared with that of reference [7.8] in Figure 7.58. Very good agreement is observed. Geometrically nonlinear analysis was calculated under the same applied load (see Figure 7.59). The nonlinear result had smaller amplitude and shorter period compared with the linear solution, which indicates stiffness hardening. The existence of stiffness hardening was further confirmed by increasin, P_0 to 89.08 N (20 lb), see Figure 7.60. It can be seen that, when P_0=89.08 N, the reduction of amplitude and period with respect to the corresponding linear solution is increased compared with the case of P_0=44.54 N (Figure 7.59).

The more general analysis where both material and geometric nonlinearities are included was considered here. Figure 7.60 illustrates the dynamic responses using linear, geometrically nonlinear, and materially and geometrically nonlinear analyses and subjected to a load P_0=89.08 N (20 lb). When both material and geometric non-linearities were present, the plate had a very small vibrating amplitude compared with the linear and geometrically nonlinear responses. The vibration period was the shortest when both nonlinearities were included. These are indications that plastic deformation further hardens the plate.

Finally, the impulse-type loading as depicted by Figure 7.61 was applied to the center of the plate. P_0 was again set to 44.54 N (10 lb). Four analyses were carried out: linear, geometrically nonlinear, material nonlinear only and materially and geometrically

nonlinear analyses. The obtained dynamic responses are presented in Figure 7.62. Geometrically nonlinear and material nonlinear only analyses revealed stiffness hardening and softening effects, respectively. The combined effect of material and geometric nonlinearities seemed to preserve the linear vibration period but at the same time reduce the vibration amplitude.

The effect of using updated or constant consistent mass matrix was also investigated. Results for the rectangular plate presented in Figures 7.59 and 7.60 suggested that constant mass matrix had satisfactory accuracy. This is because of the stiffness hardening effect that exists when the plate is under large applied load.

7.4 Concluding Remarks

This chapter emphasized the application of the theoretical development of Chapter 6. Static and dynamic analyses of problems with geometrical, material, and geometrical and material nonlinearities were performed. The purposes of these numerical studies were to: (i) examine the correctness, accuracy and applicability of the present formulation; and (ii) study the effects of the four formulation options. The numerical studies included nine different examples. Overall, the present formulations are accurate, flexible and applicable to different types of shell structures with geometric or material, or both geometric and material nonlinearities. The four formulation options provide flexibility in generally nonlinear analysis.

The issues of snap-through buckling and bifurcation, and their associated computational strategies were not addressed in detail in this chapter. As they are very

important in the analysis of nonlinear shell structures their studies require a separate and concentrated effort. Therefore, such an effort is recommended for further investigation. However, it should be mentioned that in the foregoing nonlinear problems the incremental-corrective scheme [7.11-12] have been employed for the computation.

CHAPTER 8

RESPONSE STATISTICS OF SHELL STRUCTURES WITH GEOMETRICAL AND MATERIAL NONLINEARITIES

The previous five chapters have focused on several hybrid strain based 3-node flat triangular shell elements. It has been found that results obtained by using these elements are accurate. These elements are free from shear locking, computationally effective and applicable to thin to moderately thick shell structures. Therefore, they are employed in the determination of random responses of a relatively wide class of shell structures with material and geometrical nonlinearities. The excitations considered are nonstationary random. They represent a variety of intensive transient excitations, such as earthquake excitations, blast loads of rockets and atmospheric turbulences, to name but a few. The methodologies of calculating random responses of linear and nonlinear systems have been studied in Chapter 2. Owing to their advantageous features over various other existing methods, the techniques proposed in Chapter 2 are employed and further developed for the computation of nonlinear response statistics of shell structures under nonstationary random excitations. The techniques are the stochastic central difference (SCD) method in conjunction with time co-ordinate transformation (TCT) and adaptive time schemes (ATS). A brief summary of these techniques with their further extension to include excitations treated as a combination of a deterministic component and a stochastic part, is given in Section 8.1. Three numerical examples are studied and presented in Section 8.2 followed by concluding remarks in Section 8.3.

8.1 Computational Techniques and Strategies

This section is concerned with the computational techniques and strategies employed in the present investigation for the determination of response statistics of shell structures. These response statistics include ensemble averages, time-dependent mean squares and cross-correlations, variances and covariances of displacements. A general dynamic system having time-dependent mass, damping and stiffness characteristics is considered. The recursive expressions for the random responses of the structure are given in Sub-section 8.1.1. As discussed in Chapter 2, when the dynamic system under consideration is stiff the time co-ordinate transformation (TCT) technique becomes necessary. Moreover, the adaptive time schemes (ATS) developed is adopted here so that general nonlinear systems may be investigated. Therefore, the TCT and ATS techniques are briefly outlined in the following sub-sections. The final sub-section deals with the implementation of the above strategies with particular reference to nonlinear dynamic systems idealized by the finite elements.

8.1.1 The stochastic central difference (SCD) method

Consider a general dynamic system governed by the following matrix equation of motion

$$M(t)\ddot{X} + C(t)\dot{X} + K(t)X = p(t) + r(t) \tag{8.1}$$

where M(t), C(t) and K(t) are assembled matrices of time-dependent consistent mass, damping and stiffness, respectively. In the most general case these assembled matrices are stochastic functions of time t. However, for simplicity the assembled matrices are assumed to be deterministic function of time t and therefore at every time step they can be treated as constant. $\ddot{X}$, $\dot{X}$ and X are vectors of acceleration, velocity and displacement, respectively. On the right hand side (RHS) of equation (8.1), the excitation vector is a combination of a deterministic component p(t) and a stochastic one r(t). Throughout the present study, it is assumed that the random excitation vector r(t) is defined by

$$r(t) = \bar{e}(t)w(t) \tag{8.2}$$

where $\bar{e}(t)$ is a vector of deterministic amplitude modulating functions and w(t) a stationary Gaussian white noise with zero mean and spectral intensity S_0. That is, $<w(t)> = 0.0$ and $<w(t)^2> = 2\pi S_0\delta(0)$, with $\delta(z)$ being the Kronecker delta such that $\delta(0) = 1.0$ or otherwise zero. The element e(t) of the vector of deterministic amplitude modulating functions is given as

$$e(t) = E_r\left(e^{-\alpha_{r1}t} - e^{-\alpha_{r2}t}\right) \tag{8.3}$$

in which α_{r1} and α_{r2} are positive constants satisfying $\alpha_{r1} < \alpha_{r2}$. E_r is a constant used to normalize e(t) such that its maximum value is unity. That is, *max* {e(t)} = 1.0. Note that equation (8.2) is general and can be applied to model a wide class of nonstationary random excitations by adjusting the constants α_{r1} and α_{r2}.

Since equation (8.1) is valid for any given time instant t_s, one can therefore, after applying the central difference approximation, write the acceleration and velocity vectors at time t_s in terms of displacement vectors as

$$\dot{X}_s = \frac{1}{2\Delta t}\left(X_{s+1} - X_{s-1}\right),$$
$$\ddot{X}_s = \frac{1}{(\Delta t)^2}\left(X_{s+1} - 2X_s + X_{s-1}\right) \tag{8.4a,b}$$

where the subscripts indicate the time instants and Δt is the time step size such that $\Delta t = t_{s+1} - t_s$. Then direct substitution of equation (8.4) into (8.1) and re-arrangement of terms result in

$$X_{s+1} = (\Delta t)^2 N_1 f_s + N_2 X_s + N_3 X_{s-1} \tag{8.5}$$

with

$$f_s = p_s + r_s \tag{8.6}$$

and

$$\begin{aligned} N_1 &= \left[M_s + \frac{1}{2}(\Delta t)C_s\right]^{-1}, \\ N_2 &= N_1\left[2M_s - (\Delta t)^2 K_s\right], \\ N_3 &= N_1\left[\frac{1}{2}(\Delta t)C_s - M_s\right] \end{aligned} \tag{8.7}$$

in which the superscript " - 1" indicates the inverse of a matrix.

Taking the ensemble average of equation (8.5) leads to

$$\langle X_{s+1}\rangle = (\Delta t)^2 N_1 \langle f_s\rangle + N_2\langle X_s\rangle + N_3\langle X_{s-1}\rangle \tag{8.8}$$

where the angular brackets denote "ensemble average" of the enclosed quantity. Since

$$\langle f_s\rangle = \langle \eta_s\rangle + \langle r_s\rangle = p_s + e_s\langle w_s\rangle = p_s \tag{8.9}$$

one has

$$\langle X_{s+1}\rangle = (\Delta t)^2 N_1 p_s + N_2\langle X_s\rangle + N_3\langle X_{s-1}\rangle . \tag{8.10}$$

Equation (8.10) is, in fact, the recursive expression for the ensemble average of displacements of the discretized structure. This particular relation is the deterministic central difference (DCD) scheme that is to be used in parallel to the SCD method to be derived later in the same sub-section. For the present nonlinear analysis equation (8.10) is applied to updating the co-ordinates and element matrices at every time step. Strictly speaking, for co-ordinate updating, and evaluating element stiffness and mass matrices, equation (8.5) should be employed instead of equation (8.10). The latter is applied presently for two main reasons. Firstly, it is relatively easy and economical to employ. Secondly, it can be used as a basis for comparison to results obtained by applying equation (8.5). These results and their comparison to those obtained in the present phase of the investigation is recommended for future investigation.

Returning to the SCD scheme, one takes the transpose of X_{s+1}, multiplies X_{s+1} by X_{s+1}^T, takes the ensemble average of the product and re-arranges terms. Finally, one can show that the expression for the time-dependent mean squares of displacements is

$$
\begin{aligned}
R(s+1) = {} & (\Delta t)^4 N_1 [B(s) + P(s)] N_1^T \\
& + N_2 R(s) N_2^T + N_3 R(s-1) N_3^T \\
& + N_2 D(s) N_3^T + N_3 D(s) N_2^T \\
& + (\Delta t)^2 N_1 p_s \langle X_s \rangle^T N_2^T + (\Delta t)^2 N_2 \langle X_s \rangle p_s^T N_1^T \\
& + (\Delta t)^2 N_1 p_s \langle X_{s-1} \rangle^T N_3^T + (\Delta t)^2 N_3^T \langle X_{s-1} \rangle p_s^T N_1^T
\end{aligned}
\tag{8.11a}
$$

and

$$
\begin{aligned}
D(s) = {} & (\Delta t)^2 N_1 p_{s-1} \langle X_{s-1} \rangle^T \\
& + N_2 R(s-1) + N_3 D(s-1)^T
\end{aligned}
\tag{8.11b}
$$

in which

$$
\begin{aligned}
R(s) &= \langle X_s X_s^T \rangle , \\
D(s) &= \langle X_s X_{s-1}^T \rangle , \\
B(s) &= 2\pi S_0 \bar{e}_s \bar{e}_s^T , \\
P(s) &= p_s p_s^T .
\end{aligned}
\tag{8.12a,b,c,d}
$$

Note that for every given spectral intensity of the discrete white noise process, the matrix B(s) in equation (8.12c) is a deterministic relation since $\bar{e}_s$ is deterministic.

Equation (8.11) is the recursive expression for the time-dependent cross-correlations of displacements. By making use of equation (8.11) one can obtain the recursive expression for the time-dependent covariance matrix of displacements as

$$\begin{aligned} V(s+1) &= (\Delta t)^4 N_1 B(s) N_1^T \\ &\quad + N_2 V(s) N_2^T + N_3 V(s-1) N_3^T \\ &\quad + N_2 A(s) N_3^T + N_3 A(s)^T N_2^T , \end{aligned} \tag{8.13a,b}$$

$$A(s) = N_2 V(s-1) + N_3 A(s-1)^T$$

where

$$\begin{aligned} V(s) &= R(s) - \langle X_s \rangle \langle X_s \rangle^T , \\ A(s) &= D(s) - \langle X_s \rangle \langle X_{s-1} \rangle^T . \end{aligned} \tag{8.14a,b}$$

Equations (8.11a,b) and (8.13a,b) constitute the SCD scheme. One route is to use equations (8.11a,b) to obtain the time-dependent cross-correlations of displacements and then determine the covariances of displacements by equation (8.14a,b). The other route is to employ equation (8.13a,b) to obtain the covariances of displacements directly. If desired, one then uses equation (8.14a,b) to calculate the time-dependent cross-correlations of displacements. Computationally, the latter route is more efficient because equation (8.13a,b) requires less amount of algebraic manipulations. This route is adopted in the present study.

8.1.2 Time co-ordinate transformation (TCT)

Time co-ordinate transformation is a strategy for dealing with the computational instability associated with the DCD and SCD, and increasing the efficiency of the DCD and SCD algorithms. Details of this strategy have been introduced in Chapter 2 and are repeated here for completeness. In this strategy it is assumed that the stiff system governed by equation (8.1) has its highest natural frequency Ω. Dividing both sides of equation (8.1) by the square of Ω and transforming the resulting equation of motion from time co-ordinate t to dimensionless time co-ordinate τ such that

$$M(\tau)x'' + \frac{1}{\Omega} C(\tau) x' + \frac{1}{\Omega^2} K(\tau) x = \frac{1}{\Omega^2} f(\tau) \tag{8.15}$$

where the prime and double prime designate the first and second order derivatives with respect to the dimensionless time τ. The matrices $M(\tau)$, $C(\tau)$ and $K(\tau)$, the response vector $x(\tau)$ and the forcing vector $f(\tau)$ are all functions of τ which is being chosen as

$$\tau = \Omega t . \tag{8.16}$$

The variance and covariance of displacements for the system described by equation (8.15) can then be evaluated by equation (8.13a,b) in which the assembled mass matrix M is identical to that in equation (8.1), the damping matrix C is equal to the original damping matrix C in equation (8.1) divided by Ω, the stiffness matrix K is equal to the original stiffness matrix K in equation (8.1) divided by Ω^2, and the excitation vector f is

equal to the original forcing vector in equation (8.1) divided by Ω^2. In other words, if we write the equation in the τ co-ordinate

$$M_\tau \frac{d^2x}{d\tau^2} + C_\tau \frac{dx}{d\tau} + K_\tau x = f_\tau \,, \tag{8.17}$$

then

$$M_\tau = M \,,\quad C_\tau = \frac{1}{\Omega} C \,,\quad K_\tau = \frac{1}{\Omega^2} K \,,\quad f_\tau = \frac{1}{\Omega^2} f \,, \tag{8.18}$$

where M, C, K and f are defined in the original time co-ordinate t. Equation (8.13a,b) can then be applied to evaluate the variance and covariance of displacements of the discretized structure in dimensionless time τ. When applying equation (8.13a,b) to obtain the variance and covariance of displacements in the dimensionless time co-ordinate τ, matrices M, C, K, and vector f_s in equation (8.13a,b) have to be replaced respectively with M_τ, C_τ, K_τ, and $f_{\tau s}$. Note that $f_{\tau s}$ is f_τ at the dimensionless time step τ_s. Moreover, Δt in equation (8.13a,b) is replaced by $\Delta\tau$.

Once the variances and covariances in the τ co-ordinate are determined by using equation (8.13a,b) they are converted back to the t co-ordinate. The variances and covariances in the two time co-ordinates are related by the following expressions

$$V_t(s) = \Omega\, V(s)\,, \qquad t = \frac{\tau}{\Omega} \tag{8.19}$$

where the subscript t denotes the t co-ordinate solution while V(s) is understood to be in the dimensionless time τ. Equation (8.19) can be easily verified if one considers the stationary variance of displacement for a single degree-of-freedom (SDOF) linear system excited by a zero mean Gaussian white noise.

For the evaluation of ensemble average of displacements using equation (8.10), matrices M, C and K and vector f follow the transformation rule defined by equation (8.18). Similarly, Δt is replaced with $\Delta\tau$. However, the ensemble average calculated in the τ co-ordinate is equal to that in the original time co-ordinate t and therefore no conversion is necessary. In other words, the following relation holds

$$\langle X_s \rangle_t = \langle x_s \rangle \tag{8.20}$$

here the subscript t also denotes the t co-ordinate solution. The proof of equation (8.20) is similar to that for equation (8.19).

8.1.3 Adaptive time schemes (ATS)

The time step size used in the actual computation of the SCD algorithm is reduced with increasing natural frequency [8.1-2]. This suggests that for nonlinear systems the time step size at every time step has to be changed in accordance with the time-dependent natural frequency. Consequently, some time step size updating strategies have to be

incorporated into the SCD algorithm. In Chapter 2 three representative strategies have been proposed. These are:

SCD-ATS which is the stochastic central difference with adaptive time scheme,

SCD-ATST which is the stochastic central difference and adaptive time scheme with time co-ordinate transformation, and

SCD-TATS which is the stochastic central difference with time co-ordinate transformation and adaptive time scheme.

Therefore, every of the above three strategies has an ATS which shall be described later in this sub-section. However, the TCT is executed at different stage of individual strategy. In the SCD-ATS, the TCT is not incorporated. Consequently, it is not suitable for stiff systems. The second strategy, the SCD-ATST, requires the TCT at every time step. On the other hand, for the third strategy, the SCD-TATS, the TCT is performed only once at the first time step on the corresponding linearized system. From the viewpoint of computational effectiveness, the SCD-TATS is less expensive than the SCD-ATST, especially for nonlinear systems with many DOF. This is because the latter approach requires the evaluation of the highest natural frequency at every time step. In terms of accuracy, results in Chapter 2 have demonstrated that the three strategies can give equally good agreement. Therefore, in terms of computational effectiveness and accuracy, the SCD-TATS is a better approach.

Returning to the ATS, it is essentially a process in which the time step size is related to the representative natural frequency of the system at every time step. Chapter

2 suggested to select the fundamental natural frequency as the representative natural frequency of the system. The rationale behind is that such selection can better represent response generated by the fundamental mode. Such a response is, in general, dominant in a system with MDOF. Bathe and Wilson gave the same reasoning in reference [8.3] for deterministic responses. A summary of the time step size and fundamental natural frequency relation observed in Chapter 2 is given as Table 8.1 where the fundamental natural frequency ω and the time step size $\Delta\tau$ are associated with time co-ordinate τ. In particular, if ω is less than 0.1, $\Delta\tau$ can be simply chosen as 1.0.

Another advantage of the SCD-ATST and SCD-TATS is their numerical stability. This is because the time step size, in the dimensionless time co-ordinate τ, can not exceed unity, which is well below the critical time step size $(\Delta\tau)_{cr} = 2^{1/2} = 1.414$. The discussion of critical time step size of the SCD algorithm can be found in reference [8.4].

8.1.4 Implementation of the strategies

As mentioned in Sub-section 8.1.3, in terms of accuracy the SCD-ATST and SCD-TATS can give equally good results. However, in term of computational effectiveness, the SCD-TATS is a better approach because the highest natural frequency of the system needs to be calculated only once at the beginning instead of being calculated at every time step. In the present study the SCD-TATS is mainly employed due to its

Table 8.1 Relation of time step size and fundamental frequency

range of frequency ω	time step size $\Delta\tau$
$1.0 \le \omega \le 5.0$	$\Delta\tau = 0.83 - 0.72 \log_{10}\omega$
$\omega \le 1.0$	$\Delta\tau = 1.0 - 0.053\omega - 0.12\omega^2$

computational effectiveness and accuracy, and the following observation. It has been found, by monitoring the change of the natural frequencies, that the highest natural frequency changes at a slower pace than the fundamental one and remains essentially unchanged for the time period of interest (see next section for details). Therefore, the calculation of the highest natural frequency and the TCT at every time step seem unnecessary.

It has also been observed that the fundamental natural frequency of the system in the dimensionless time co-ordinate τ for a large class of nonlinear systems is well below 0.1. As a result, $\Delta\tau$ can be simply set to 1.0. This time step size ($\Delta\tau = 1.0$) has been coded as the default time step size in conjunction with the SCD-TATS strategy. Of course, for some nonlinear systems in the dimensionless time co-ordinate τ their fundamental natural frequencies may be greater than 0.1 such that steps are necessary for selecting the corresponding $\Delta\tau$.

8.2 Nnonlinear Random Responses of Shell Structures

The computational techniques and strategies included in Section 8.1 are now applied to shell structures disturbed by nonstationary random excitations. Every one of the latter is treated as a combination of a deterministic component and a stochastic component which is a product of a deterministic modulating function and a zero mean Gaussian white noise process. Three examples are included here. These are: a square plate clamped at one side, a simply supported rectangular plate and a clamped spherical cap. The first two examples are associated with stiffness hardening while the last one with stiffness softening.

The assembled mass matrix is considered constant. This is justified because the time duration during which the random excitation is effectively acting on the shell structure is relatively short. Moreover, for the numerical studies in this paper Rayleigh damping is assumed so that damping matrix can easily be constructed based on the first two modes of the corresponding linear system. It should be emphasized that the damping matrix in Section 8.1 is general. The Rayleigh damping assumption adopted here is mainly for convenience rather than mathematical rigor and generality. This definition of Rayleigh damping naturally leads to a constant damping matrix. That is, it is formed at the first time step and then remains unchanged throughout the entire computation.

For computational effectiveness in the finite element analysis of structures under static loads or deterministic excitations, it has been a common practice to exploit geometric symmetry of the structure. Whether such a practice is applicable or not to stochastic dynamic analysis in which variances and covariances are required remains an

open question. This issue has not yet been addressed in the literature, and therefore it would be an interesting and important subject of investigation. The present study does not deal with the issue of symmetry as the main objective of the study is the application of computational techniques and strategies presented in Section 8.1.

8.2.1 Square plate clamped at one side and subjected to a concentrated load

This cantilever plate is chosen because it has been studied in Chapter 2 where the high precision triangular plate bending element reported in reference [8.5] was used to represent the entire plate and to test the TCT strategy. In the present study the high precision triangular plate bending element is employed so as to compare with the shell elements presented in Chapters 3 through 7.

The geometrical and material properties of the plate are: dimensions $1.0 \times 1.0 \times 0.005$ m^3, Young's modulus $E=2\times10^{11}$ N/m^2, Poisson's ratio $\nu=0.3$ and mass density per unit volume $\rho=7830.0$ kg/m^3. In the finite element discretization the entire plate was idealized by either 8 high precision triangular plate bending elements or 8 shell elements as shown in Figure 8.1. This resulted in 27 total unknown displacements for the plate element model and 24 for the shell element discretization. The boundary conditions applied were: $U=V=W=\Theta_x=\Theta_y=\Theta_z=0.0$ on the clamped side. In addition, $U=\Theta_z=0.0$ was imposed on all the nodes so that no twisting would be allowed to occur. For the 8 shell element model, the first two and the highest natural frequencies as well as Rayleigh damping coefficients corresponding to 5% damping for the first and second modes are obtained and listed in Table 8.2.

Table 8.2 Natural frequencies and damping coefficients

model	8 shell elements	4 shell elements
unknown displacements	24	14
ω_1 (rad/sec)	28.10	28.21
ω_2 (rad/sec)	136.5	276.9
Ω (rad/sec)	2.492×105^5	1.211×10^5
λ_m	2.330	2.560
λ_k	6.075×10^{-4}	3.278×10^{-4}

For such a finite element representation linear analysis was performed so as to make comparison with the result using the plate element of reference [8.5]. The stochastic excitation was assumed to be a concentrated load and was applied to the middle of the free side opposite to the clamped one. That is, node 8 of Figure 8.1. The amplitude modulating function was

$$e_r(t) = 9.4815(e^{-45t}-e^{-60t}) \tag{8.21}$$

where the subscript r is the integer corresponding to the nodal DOF of the point of load, and the spectral intensity was $S_0=1.0$.

The computed variance of displacement at node 8 is presented in Figure 8.2 which also includes the result from Chapter 2. Excellent agreement can be seen in Figure 8.2. Recalling that in Chapter 2, the first 6 modes were set to have equal damping ratio 0.05.

Consequently, all the modes that have a natural frequency less than or in the neighbourhood of 136.5 rad/sec were 5% critically damped. This is why the results from Chapter 2 can be directly used to compare with the those using the shell elements and Rayleigh damping.

To partially investigate the effect of symmetry and the reduction in computational time a half of the plate represented by 4 shell elements, as shown in Figure 8.3, was studied. In addition to the boundary conditions applied on the clamped side and at every node to circumvent twisting of the plate, $U=\Theta_y=\Theta_z=0.0$ were imposed on the symmetric side. The resulting finite element model had 14 total unknown displacements. Its natural frequencies and Rayleigh damping coefficients are given in Table 8.2. The computed maximum variance and covariance, with $S_0=1.0$, of displacements at nodes 4 and 6 of Figure 8.3 are presented in Table 8.3. Those from the 8 element model with $S_0=1.0$ are also included in Table 8.3. It is interesting to note that the variance and covariance of displacements from the 4 element model were close to those from the 8 element model. However, as a caveat this finding is not general. In fact, in the course of computational experiments it was observed that the rule for geometrical symmetry of structures under deterministic excitations did not apply to systems with stochastic excitations. Another noteworthy feature is the large difference in computing time: 10 minutes for the 4 element model versus 100 minutes for the 8 element model. The advantage of discretizing a half of the plate rather than the entire one is that, in addition to having system matrices of smaller size (14 versus 24), Ω can be reduced (1.211×10^5 versus 2.492×10^5 rad/s, see Table II). In turn, a smaller number of time steps is required to cover the same interval

in the time co-ordinate t (15500 versus 32000 steps in this particular problem). The reductions in both the system matrix size and the highest natural frequency Ω make the computation much more economical if one can have rule of symmetry mentioned above.

Table 8.3 Maximum variance and covariance of displacements

model	8 shell elements	4 shell elements
total unknowns	24	14
S_0	1.0	1.0
variance of displacement at node 6	47.82×10^{-7}	48.36×10^{-7}
variance of displacement at node 4	4.696×10^{-7}	4.828×10^{-7}
covariance of displacements at nodes 4 and 6	14.51×10^{-7}	15.15×10^{-7}
computing time in minutes	100	10

Using the 4 element model in Figure 8.3 calculations were further performed to obtain the variances and covariances of displacements of the plate with geometrical nonlinearity. The nonstationary random excitation as defined on the RHS of equation (8.1) was applied laterally at node 6. The deterministic component of the nonstationary random excitation had a time function p(t) described in Figure 8.4 where t_0 was 0.006 seconds and P either 500 N or 1250 N. The latter two values for P were selected so as to achieve different degree of geometrical nonlinearity. Moreover, the spectral intensity S_0 was also varied with nonlinearity: $S_0=10^5$ for linear analysis; 2.5×10^5 for nonlinear analysis with P=500 N and 5×10^5 with P=1250 N. Note that P and S_0 are referred to the half plate only. Some representative results, such as variances and covariances of transversal displacements and rotations at nodes 4 and 6 are shown in Figures 8.5 through 8.10. It can be seen that variances and covariances were reduced with increased degree of nonlinearity. This has much to do with the stiffness hardening of the structure. It is interesting to note that the covariance of rotations at nodes 4 and 6 became negative when nonlinearity was present in the structure, as shown in Figure 8.10. The time-dependent mean square and variance of transversal displacement at node 6 are given and compared in Figures 8.11 through 8.13. In the linear case, the time-dependent mean square and variance were close to one another because the ensemble average of displacement was relatively small as shown in Figure 8.11. With the presence of nonlinearity in the structure the difference between the time-dependent mean square and variance remained small prior to the occurrence of peak value of the variance. After that, the time-dependent

mean square became more significant than the variance due to the relatively large value of the ensemble average of displacement.

Note that in all the above calculations, the SCD-TATS scheme was used exclusively. This is because the change of the highest natural frequency is negligible. For example, with a load level of P=500 N, it was observed that the fundamental and the highest natural frequencies were both increased: ω_1 from 28.21 to 32.46 rad/s and Ω from 1.211×10^5 to 1.217×10^5 rad/s. The percentage increase for ω_1 and Ω was 15.1 and 0.5, respectively. Therefore, the exclusive use of SCD-TATS is justified from the viewpoint of both accuracy and computational effectiveness. It was also observed that the time used to perform a nonlinear SCD-TATS computation was 95 minutes and the time to compute the natural frequencies approximately 5 minutes (accumulated over the required 15500 time steps). It was observed during the computational experiments that for the present example the computing time of SCD-ATST was not substantially more than that of SCD-TATS. The reason is that the total unknown displacements were only 14. However, the portion of computing time used to calculate natural frequencies at every time step will be drastically increased for systems having many DOF (see discussion in Sub-section 8.2.3).

8.2.2 Simply supported rectangular plate subjected to a center load

This plate has been studied in Sub-section 7.3.2. Owing to symmetry of geometry, boundary conditions and loading, only one quarter of the plate is considered here. For the quarter plate, its geometrical dimensions are 508 × 762 × 25.4 mm^3 (20 × 30 × 1 in^3). The material properties are: Young's modulus $E=2.0955\times10^8$ N/m^2 (3×10^4 psi),

Poisson's ratio $\nu=0.25$, yield stress $\sigma_y=2.0955\times10^5$ N/m^2 (30 psi) and density $\rho=3210.05$ kg/m^3 (0.0003 lb-sec^2/in^4).

The finite element mesh for the quarter plate consisted of 25 nodes and 32 elements. The mesh layout shown in Figure 8.14 was employed. Boundary conditions applied on the simply supported boundary that is parallel to the X-axis were $U=V=W=\Theta_y=\Theta_z=0.0$. On the simply supported boundary parallel to the Y-axis one had $U=V=W=\Theta_x=\Theta_z=0.0$. Then on the symmetrical side parallel to the X-axis it was set that $V=\Theta_x=\Theta_z=0.0$. Finally, boundary conditions for the symmetrical side parallel to the Y-axis were $U=\Theta_y=\Theta_z=0.0$. After discarding constrained DOF, there were 48 total unknowns. The first two and the highest natural frequencies were 27.21, 102.8 and 1.399×10^4 rad/s, respectively. The Rayleigh damping coefficients were $\lambda_m=2.152$ and $\lambda_k=0.7692\times10^{-4}$ which correspond to 5% critically damped for the first two modes.

The applied load consisted of a deterministic and a stochastic component acting on the transversal direction of the center of the plate. That is, node 21 in Figure 8.14. For the quarter plate, the deterministic load had the same time function as depicted in Figure 8.4. The time t_0 was 0.006 seconds while the load level P was either 44.54 N (10 lb) or 89.08 N (20 lb). The amplitude modulating function defined by equation (8.21) was employed. Spectral intensity S_0 was kept constant at a level of $S_0=1.0$ except for materially and geometrically nonlinear analysis where $S_0 = 5.0$ was applied.

Using the finite element discretization of Figure 8.14 under the loading condition described in the previous paragraph, computations were carried out to obtain ensemble average, time-dependent mean square and cross-correlation, variance and covariance of

displacements of the plate. To begin with, results for linear and geometrically nonlinear analyses are presented. Note that, though results were available for every active DOF, only the representative ones are given here. They are: ensemble average, time-dependent mean square and variance of transversal displacements at node 21 (Figures 8.15 through 8.17), 17 (Figures 8.18 through 8.20), rotation Θ_x at node 16 (Figures 8.21 through 8.23) and rotation Θ_y at node 22 (Figures 8.24 through 8.26). Similar to the cantilever plate discussed in Sub-section 8.2.1, one can observe that the variances of transversal displacements were reduced with increasing geometrical nonlinearity, or more specifically, with increasing degree of stiffness hardening (comparing with Figures 8.5 and 8.7, for example). In addition to time-dependent mean squares and variances, time-dependent cross-correlations and covariances are also presented. For example, cross-correlation and covariance between transversal displacements at nodes 21 and 17 (Figures 8.27 and 8.28), transversal displacement at node 21 and rotation Θ_x at node 16 (Figures 8.29 and 8.30) and transversal displacement at node 21 and rotation Θ_y at node 22 (Figures 8.31 and 8.32). For the transversal displacement at the center point, time-dependent mean square and variance are also compared (Figures 8.33 through 8.35). It is found that the peak variance to peak mean square ratios are 0.293, 0.310 and 0.128 for the linear analysis with P=44.54 N, nonlinear analysis with P=44.54 N and nonlinear analysis with P=89.08 N, respectively. Or in terms of standard deviation to root mean square ratio, they are 0.541, 0.556 and 0.358, respectively. These indicate that the stochastic loading has significant effect compared with the deterministic one.

Results from nonlinear analysis including both material and geometrical nonlinearities are presented in Figures 8.36 through 8.40 which include ensemble average, mean square and variance of transversal displacements at node 21 (Figures 8.36 and 8.37) and at node 17 (Figures 8.38 and 8.39), and cross-correlation and covariance of transversal displacements at nodes 21 and 17 (Figure 8.40). In such an analysis, the deterministic loading was kept at the level of P=89.08 N while the spectral intensity was either S_0=1.0 or S_0=5.0. Owing to the presence of plastic deformation, the ensemble average of displacement was increased compared with the case of geometrical nonlinearity. For example, node 21 experienced a maximum displacement of 0.84 × 25.4 mm when only geometrical nonlinearity was considered (see Figure 8.15). The displacement was increased to 0.93 × 25.4 mm when both material and geometrical nonlinearities existed (Figure 8.36). It is interesting to note that the variance of displacement was also increased after introducing plastic deformation. The variance of displacement at node 21 were, with S_0=1.0, 0.103 × 645.16 mm^2 (Figure 8.17) and 0.117 × 645.16 mm^2 (Figure 8.37) for geometrically, and materially and geometrically nonlinear analysis, respectively. This increase in the variance is the result of stiffness softening (also see Sub-section 8.2.3). However, since the ensemble average of the transversal displacement at node 21 was increased faster than the variance, the variance to mean square ratio was reduced to 0.094 compared with 0.128 for the case of geometrical nonlinearity only. When increasing S_0 to 5.0, the same ratio became 0.354. The corresponding standard deviation to root mean square ratio was 0.595. Therefore, the effect of stochastic loading is significant.

Finally, it should be mentioned that the above results were obtained using the SCD-TATS scheme. The rationale behind is similar to that of Sub-section 8.2.1 for the cantilever plate: the change of the highest natural frequency is negligible. The monitoring of natural frequencies showed that, for the geometrically nonlinear analysis with P=44.54 N, the highest natural frequency Ω remained 1.399×10^4 rad/sec over the time duration of interest. During the same duration, the fundamental frequency ω_1 had its minimum 27.21 rad/sec and maximum 41.04 rad/sec, the percentage increase of ω_1 being 50.7. The time used for computation of natural frequencies over 2500 time steps was approximately 8 minutes, compared with 155 minutes of the total time for performing a geometrically nonlinear SCD-TATS calculation. On the other hand, the time required for linear, and materially and geometrically nonlinear analysis using the SCD-TATS scheme was 60 and 180 minutes, respectively. In the foregoing computations 2500 time steps were considered in every run of the digital computer program.

8.2.3 Clamped spherical cap subjected to an apex load

This clamped spherical cap has been studied in Sub-sections 7.1.7, 7.2.4 and 7.3.1 for deterministic static and dynamic analysis with geometrical, and material and geometric nonlinearities. The geometry of the cap is shown in Figure 8.41, where the radius of the cap is R=120.90 mm (4.76 in), thickness h=0.4 mm (0.01579 in) and height H=2.18 mm (0.08589 in). The material of the cap is either elastic with Young's modulus $E=6.985\times10^{10}$ N/m^2 (10^7 psi), Poisson's ratio $\nu=0.3$ and density $\rho=2621.54$ kg/m^3

(0.000245 lb-sec^2/in^4), or elastic-perfectly plastic with yield stress $\sigma_y = 1.397 \times 10^8$ N/m^2 (2×10^4 psi).

In the finite element discretization only one quadrant of the cap was modeled because of symmetry of geometry, boundary conditions and loading. The 28 node, 36 element mesh (Figure 8.42) was employed. Boundary conditions were, on the clamped circumference, $U = V = W = \Theta_x = \Theta_y = \Theta_z = 0.0$; on the symmetrical side parallel to the X-axis, $V = \Theta_x = \Theta_z = 0.0$; on the symmetrical side parallel to the Y-axis, $U = \Theta_y = \Theta_z = 0.0$; and at the apex, $U = V = \Theta_x = \Theta_y = \Theta_z = 0.0$. The resulting total unknown displacements were therefore 85.

The first two and the highest natural frequencies are 5.858×10^4, 7.348×10^4 and 1.225×10^7 rad/sec, respectively. Setting the damping ratio of the first two modes to 0.05 the corresponding Rayleigh damping coefficients were $\lambda_m = 3.259 \times 10^3$ and $\lambda_k = 7.572 \times 10^{-7}$.

With regard to the external loading on the quadrant of the cap, the deterministic component had the same time function as depicted in Figure 8.4. The time t_0 was chosen as 0.00003 seconds while the load level P was 38.9725 N (8.75 lb). The amplitude modulating function $e_r(t)$ was defined as

$$e_r(t) = 9.4815(e^{-18000t} - e^{-24000t}) \tag{8.22}$$

and the spectral intensity S_0 was kept constant at a level of $S_0 = 1.0$.

Computations were carried out to obtain random responses of the cap. Three cases were considered: linear, geometrically nonlinear and materially and geometrically

nonlinear. Results of these computations are presented in Figures 8.43 through 8.49. These are the variance of transversal displacements at nodes 1, 3, 6, and 10 (Figures 8.43 through 8.46), and covariance of transversal displacements at nodes 1 and 3, 3 and 6, and 6 and 10 (Figures 8.47 through 8.49). It can be seen that compared with the linear solution the variances from the two nonlinear analyses were increased; at the same time, the time instant at which the peak value of variance occurred was delayed for the geometrically nonlinear case, and advanced for the materially and geometrically nonlinear case. The increase in peak value of variance and the delay in time instant corresponding to the peak value are associated with the stiffness softening behaviour that the cap exhibits in the nonlinear regime. It is also noticed that with both material and geometrical nonlinearities present in the cap, the variance of transversal displacement at node 1 was reduced to 1.811×645.16 mm^2 from 2.243×645.16 mm^2 of the geometrical nonlinearity only solution (Figure 8.43). But the opposite trend holds for the rectangular plate of Sub-section 8.2.2. The maximum variance of transversal displacement at node 21 of the plate was 0.103×645.16 mm^2 for geometrically nonlinear analysis (Figure 8.17) and 0.117×645.16 mm^2 for the case with both material and geometrical nonlinearities (Figure 8.37). That is, the variance of the displacement was increased rather than reduced.

In the above computation 1900 time steps were considered. The times used for the computations were: 6 hours for linear analysis, 9.5 hours for geometrically nonlinear analysis and 10 hours for both materially and geometrically nonlinear analysis.

Similar to the two previous examples, the SCD-TATS scheme was mainly employed. In the monitoring of natural frequencies it was found that for the cap the fundamental frequency was reduced from 5.858×10^{4} rad/sec to its minimum 8.194×10^{3} rad/sec, a 86.0% reduction. Meanwhile, the highest natural frequency Ω was increased from 1.225×10^{7} rad/sec to 1.238×10^{7} rad/sec. the increase being 1.1%. Since the change of Ω is very small, the use of the SCD-TATS scheme is well justified. However, to demonstrate the computational effectiveness of the SCD-TATS strategy, and to substantiate the comment made previously that the SCD-TATS is a better choice than the SCD-ATST. The latter approach was employed to re-calculate the random response of the geometrically nonlinear case. Results of the SCD-ATST scheme were found to be almost identical to those from the SCD-TATS (see Figures 8.50 through 8.52 for comparison of variance of displacement at node 1 and 3, and covariance of displacements at nodes 1 and 3). But it took 12 hours to complete the SCD-ATST computation instead of the 9.5 hours for the SCD-TATS scheme. The 2.5 hours reduction in computing time by using the SCD-TATS is mainly due to the elimination of computations for natural frequencies at every time step. Recalling that the portion of time used for natural frequency calculation was much smaller for the cantilever plate and the rectangular plate which have 14 and 48 total unknown displacements, respectively. One should therefore anticipate a drastic increase of computing time when adopting the SCD-ATST scheme over the SCD-TATS algorithm for a system with many effective DOF.

8.3 Concluding Remarks

In this chapter the methodologies for determination of random responses of structures discretized by finite elements were summarized and the formulations of the stochastic central difference method was extended to include a relatively general nonstationary random excitation that consists of a deterministic and stochastic components. These methodologies were applied to three examples. These examples covered different shell geometry (plate and spherical cap) and exhibited stiffness hardening (the cantilever plate and the simply supported rectangular plate) or softening (the clamped spherical cap) in the nonlinear range. In the nonlinear problems the DCD and the SCD-TATS as well as the SCD-ATST are executed in parallel. Results of these problems have been presented. It may be appropriate to note that many of these results have not been found in the literature.

The results revealed some interesting features. For example, in the geometrically nonlinear analysis, if stiffness hardening exists, the variances of displacements are reduced and at the same time their peaks advanced temporally, with respect to their linear counterparts. The opposite trend, that is, increased variances and delayed peaks of the variances, hold for stiffness softening cases. Moreover, plastic deformation seems to, compared with the geometrically nonlinear solution, reduce the variances of displacements if the structure experiences stiffness softening and increase the variances of displacements if the structure exhibits stiffness hardening.

In addition, the SCD-TATS and SCD-ATST were compared. It is now appropriate to state that the SCD-TATS is indeed a more computationally effective algorithm than the

SCD-ATST. To further achieve computational effectiveness, symmetry conditions have been employed in the finite element discretizations. However, a thorough study on making use of symmetry conditions in stochastic dynamic analysis has not been attempted at the present time. It is recommended for future study. Furthermore, for future study and comparison to the present method an approach which incorporates randomness into configuration updating and therefore into the evaluation of stiffness matrices is also recommended.

CHAPTER 9

CONCLUSIONS AND RECOMMENDATIONS

In this concluding chapter, it first summarizes the investigation that has been accomplished (Section 9.1). Conclusions are accordingly derived from the investigation. Recommendations for further study are given in Section 9.2.

9.1 Summary and Conclusions

The investigation reported in the thesis consisted of three integral parts. These are: (1) a series of hybrid strain based three node flat triangular shell elements that are applicable to thin to moderately thick shell structures, and to general nonlinear analysis, (2) the strategies, such as the stochastic central difference (SCD) method, the time co-ordinate transformation (TCT) and the adaptive time schemes (ATS), that are used to determine the random responses of structures with explicit or implicit nonlinearities subjected to stationary and nonstationary Gaussian random excitations, and (3) response statistics of shell structures with geometrical and material nonlinearities under stationary and nonstationary Gaussian random excitations.

In accomplishing the three integral parts, the investigation was conducted in three related phases. The first phase was to develop the hybrid strain based three node flat triangular shell elements and to apply them to linear static and dynamic analysis. This phase was also involved with, at the same time, the study of computational aspects of the SCD method in conjunction with the TCT and ATS techniques. The second phase consisted of the extension of the shell elements derived in the first phase to general

nonlinear shell structural analysis with an emphasis of elasto-plastic deformations of finite strains. In the final phase, the developed shell elements and the SCD method with the TCT and ATS techniques were applied to evaluate response statistics of several representative shell structures under random loadings. The finite element method (FEM) and the SCD method were the two main investigation tools. The results of the investigation were reported in Chapters 1 through 8, and Appendices A through C.

The conclusions with highlights of the investigation are grouped into the following parts: (1) the hybrid strain based three node flat triangular shell elements, (2) linear static and dynamic analysis using the shell elements, (3) nonlinear analysis of shell structures, (4) application of the stochastic central difference method with associated computational strategies, and (5) response statistics of general nonlinear shell structures.

9.1.1 Hybrid strain based three node flat triangular shell elements

Combining the results in Sections 3.2 and 3.3 in which the Hellinger-Reissner variational principle was employed, a series of flat triangular shell elements with three corner nodes and six degree-of-freedom (DOF) per node was obtained. The elements have a simple geometry and contain only basic nodal DOF that are either displacements or rotations. Each of these elements was obtained by combining a triangular bending element and a plane stress element. The bending component element is degenerate and isoparametric in nature and adopts the specially designed strain distribution, equation (3.22), to suppress shear-locking in the "thin" limit. It is thus generally applicable to thin and thick problems. The plane stress component element is built on the basis of constant

strain triangle (CST) or Allman's triangle (AT), with much effort being directed to include the drilling degree-of-freedom (DDOF) and couple them with the in-plane displacements. Such attempts have led to six variations of the element stiffness matrix k, depending on how the DDOF are treated and whether CST or AT is employed. These variations are identified as CST+k_t^1, CST+k_t^3, CST+k_d AT+$(k_t^1)'$, AT+$(k_t^3)'$ and AT+k_d, and their characteristics summarized as follows.

CST+k_t^1 is $k = k_m+k_b+k_s+k_t^1$. Stiffness associated with DDOF enters k via the displacement-based k_t^1. The interpolation function for θ_t is constant over the shell element.

CST+k_t^3 is $k = k_m+k_b+k_s+k_t^3$. The inclusion of DDOF is through matrix k_t^3 which is derived by displacement-based method and makes use of linearly varied interpolation function for θ_t.

CST+k_d is $k = k_m+k_b+k_s+k_d$. Strain associated with shear caused by DDOF and the "true" normal rotations is accounted for by forming k_d based the hybrid formulation. θ_t can be constant or linear over the element.

AT+$(k_t^1)'$ is $k = (k_m)'+k_b+k_s+(k_t^1)'$. Similar to CST+$k_t^1$ except that Allman's formulation is incorporated such that $(k_m)'$ replaces k_m and k_t^1 is substituted by $(k_t^1)'$.

AT+$(k_t^3)'$ is $k = (k_m)'+k_b+k_s+(k_t^3)'$. Similar to AT+$(k_t^1)'$ except that θ_t is varied linearly over an element.

AT+k_d is $k = (k_m)'+k_b+k_s+k_d$. Similar to CST+k_d except that the AT is employed instead of CST.

Explicit expressions of the stiffness matrices were obtained by making use of a combination of manual and computer assisted derivations. These explicit expressions eliminate the need for numerical integration and thereby improve significantly the computational time.

Explicit expressions for the corresponding consistent mass matrices employing the same displacement interpolation functions were also presented. Note that these consistent mass matrices incorporate the effects of rotary inertia due to bending rotations and the DDOF.

It has been shown in Chapter 3 that the DDOF can be included in a mathematically rigorous manner. No similar detailed study of the DDOF incorporating the hybrid formulation has been reported in the literature.

Consequently the proposed shell elements are accurate, computationally effective and versatile to be applied to a large class of thin to moderately thick shell structures.

9.1.2 Linear static and dynamic analysis of shell structures

In Chapters 4 and 5 results of numerical studies for various plate and shell problems, static and dynamic, including those in the obstacle course [4.1], were presented. These results were obtained with the six (for static analysis) and the sixteen (for dynamic analysis) hybrid strain based flat triangular shell finite elements.

(1) The present investigation considered more than ten static examples, covering plane stress, plate and shell problems. The proposed elements gave excellent results for plane stress, plate and shallow shell applications. When the shells are deep, the

present elements seem to either converge relatively slowly, or lead to results that are slightly larger than the desired ones. For all the examples, the six proposed elements exhibit a consistently convergence pattern: approaching the exact solutions from below. The finite element results also serve as lower bounds to the exact solutions when used in shallow shell analysis.

(2) The six proposed elements have been tested in both thin and thick problems. In the thin limit, the assumed strain field offers discrete Kirchhoff type shear constraints. Thus, it effectively circumvents shear-locking. Mesh topology, too, has much to do with reducing shear-locking, and over-stiff phenomenon associated with clamped boundary conditions. In this regard, cross-diagonal mesh and refined mesh along the clamped boundaries appear to be better choices.

(3) Mesh topology is a critical consideration of finite element modelling by triangular elements. Four representative types of meshes have been examined. Type D mesh seems to be superior to the others in plane stress and plate problems. However, in shell applications, shallow or deep, this may not be true. Overall, for plane stress, plate and shell problems type A mesh appears to be favourable in terms of accuracy, convergence and cost effectiveness.

(4) It has been found that the incorporation of matrix k_d, k_t^1 or k_t^3 with the other component element stiffness matrices has no contribution to accuracy and convergence of the final (displacement) results. However, the incorporation secures rank sufficiency of the element and global stiffness matrices, even when several elements connected to a node are coplanar.

(5) It was also found that when $(k_m)'$, and/or $(k_t^1)'$ or $(k_t^3)'$ were employed instead of k_m, k_t^1 or k_t^3, the accuracy and convergence of the corresponding elements were improved to a very large extent. Since matrices $(k_m)'$, $(k_t^1)'$ and $(k_t^3)'$ are capable of representing the coupling effects between the two in-plane displacements and the DDOF. The conclusion is that the DDOF should not and can not be disregarded. In fact, they play a crucial role in achieving satisfactory accuracy and convergence of shell elements.

(6) Comparing the performance of the six elements, $AT+(k_t^1)'$ generally out-performs the others. In terms of mathematical and formulation consistency, accuracy and computational effectiveness, $AT+k_d$ is, however, the best.

(7) The convergent pattern of natural frequency solution using the present shell finite elements was observed to be approaching the exact solutions from above. It was also observed that mesh types C and D were more capable of representing repetitive natural frequencies than types A and B. Meanwhile, mesh types A and B showed little difference in evaluating natural frequencies.

(8) The proposed finite element formulations seem to be capable of representing vibration behaviours of general plate and shell structures. Numerical results reported in Chapter 5 indicate that the shell elements have good convergence rates. Consequently, the presented elements are attractive to be employed for vibration analysis of general plate and shell structures. In particular, the four elements identified by NFORMU = 4, 8, 12 and 16 correctly give six rigid body modes.

9.1.3 Nonlinear analysis of shell structures

In Chapter 6, aspects and theories of nonlinear analysis of structures have been discussed. The updated Lagrangian formulation and the incremental Hellinger-Reissner variational principle were applied. The independently assumed fields employed were the incremental displacements and incremental strains. Accordingly, the incremental second Piola-Kirchhoff stress and the incremental Washizu strain were selected as the incremental stress and strain measures. Two versions of linear and nonlinear element stiffness matrices were derived. These are the director version and the simplified version. In the director version, it was assumed that for each node on the shell mid-surface the director can be uniquely defined. The stiffness matrices were found to be dependent of the current position of the director, thus it required the updating of the director at every time step. The simplified version, on the other hand, was useful for cases where the director was not unique, or was difficult to determine. The linear part of the simplified version was proved identical to the elements developed in Chapter 3. In the derivation of element stiffness matrices, variable thickness of the shell was considered to take into account the "thinning effect" due to large strain. Explicit expressions for the linear and nonlinear parts of the stiffness matrices were obtained.

To be consistent with the element stiffness matrices, the consistent element mass matrices had their director version and simplified version, depending on whether the director was uniquely defined and included. The mass matrices were defined with respect to the reference configuration. They were different from those referenced to the undeformed configuration. Therefore, mass matrix was to be calculated at every time

step, since mass density, thickness of the shell, positions of mid-surface nodes, and directors for the director version of formulation, changed as the shell deformed. It may be appropriate to stress that explicit expressions for the two versions of element consistent mass matrices were also obtained.

Material nonlinearity studied in Chapter 6 was of elasto-plastic type with isotropic strain hardening. Here only cases in which small elastic, but large plastic strain condition applies were considered and the J_2 flow theory of plasticity, in conjunction with Ilyushin's yield criterion, was employed. To simplify the derivation of (small displacement) stiffness matrix and to facilitate the acquisition of explicit expression for the stiffness matrix, the non-layered approach was then adopted. Explicit expressions for the nonlinear part of the stiffness matrices in this phase of the investigations were also obtained. For homogeneous, isotropic and linearly elastic material, formulations for small and large strain applications were also included.

Emphasis was also placed on the updating of director field, director velocity field and director acceleration field. Schemes to update stress and to transform the second Piola-kirchhoff stress to the Cauchy stress were introduced.

Four formulation options were included. These are: the option of "finite" or "small" strain formulations, the option of "including" and "excluding" directors, the option of "updated" or "constant" thickness, and the option of "updated" or "constant" consistent mass matrix. The latter two options have very frequently been kept to "constant" thickness and consistent mass matrix in the literature. Thus, the four options

in the currently developed computer program provided an added flexibility in general nonlinear analysis of shell structures.

Chapter 7 emphasized the application of the theoretical development of Chapter 6. Static and dynamic analyses of problems with geometrical, material, and geometrical and material nonlinearities were performed. The numerical studies included nine different examples. They covered typical shell structures exhibiting stiffness hardening and softening behaviour in the nonlinear range. Overall, the present formulations are accurate, flexible and applicable to different types of shell structures with geometrical or material, or both geometrical and material nonlinearities. For material nonlinearity only elastic-perfectly plastic behaviour was investigated in the numerical studies due to ready availability of the literature.

9.1.4 Application of the SCD method and associated computational strategies

The SCD method, when applied to structures discretized by finite elements, has many advantages, including low computational cost, no normal mode analysis and being capable of handling geometrical and material nonlinearities. The problems encountered when applying the SCD method to finite element discretizations, such as large size of system matrices and wide range of natural frequency, as well as computational instability, were resolved by the TCT technique. Linear beams and plates were chosen to apply the SCD method with the TCT. The numerical results showed that the SCD-TCT method has excellent accuracy and effectiveness, and does not cause computational instability.

For nonlinear structures, it was suggested to employ the SCD method in conjunction with the TCT and ATS strategies. Three schemes, that is, the SCD-ATS, SCD-TATS and SCD-ATST were therefore proposed. A single degree-of-freedom (SDOF) Duffing's oscillator disturbed by a nonstationary random excitation, and a 2 DOF nonlinear system under a nonstationary random process were studied. It showed that the three schemes are very efficient to apply compared with digital simulation. Moreover, they are free from computational instability and give very accurate results for highly nonlinear systems.

The 2 DOF nonlinear system used for the study of the three schemes is with explicitly defined non-symmetric nonlinear stiffness. By applying the stochastic central difference in conjunction with the statistical linearization (SCD-SL) technique, recursive expressions of random responses of the 2 DOF system were obtained. Four sets of such recursive expressions were presented. Numerical results from the SCD-SL approaches compare well with those from digital simulations and from the SCD-ATS, SCD-TATS and SCD-ATST schemes.

Relations between the time step size and the natural frequency of any MDOF system were also presented. These relations are required in the implementation of the three proposed ATS.

9.1.5 Response statistics of general nonlinear shell structures

In Chapter 8, the methodologies for determination of random responses of structures discretized by finite elements were summarized and the formulations of the

stochastic central difference method was extended to include a relatively general nonstationary random excitation that consists of a deterministic and stochastic components. These methodologies were applied to three examples. These examples covered different shell geometry (plate and spherical cap) and exhibited stiffness hardening (the cantilever plate and the simply supported rectangular plate) or softening (the clamped spherical cap) in the nonlinear range. In the nonlinear analysis the DCD and the SCD-TATS as well as the SCD-ATST were executed in parallel. Results of these problems have been presented. It may be appropriate to note that many of these results have not been found in the literature.

The numerical results revealed some interesting features. For example, in the geometrically nonlinear analysis, if stiffness hardening exists, the variances of displacements are reduced and at the same time their peaks advanced temporally, with respect to their linear counterparts. The opposite trend, that is, increased variances and delayed peaks of the variances, holds for stiffness softening cases. Moreover, plastic deformation seems to, compared with the geometrically nonlinear solution, reduce the variances of displacements if the structure experiences stiffness softening and increase the variances of displacements if the structure exhibits stiffness hardening.

In addition, the SCD-TATS and SCD-ATST were compared. It may be appropriate to state that the SCD-TATS is indeed a more computationally effective algorithm than the SCD-ATST.

9.2 Recommendations

In the investigation reported in this thesis, various areas of further research were identified. However, the main areas of immediate interests and importance for future investigation are recommended in the following.

(1) An analysis of shell structures with non-symmetric consistent mass and stiffness matrices should be performed. Such an analysis will find many applications in areas such as multi-body dynamics and robotic manipulators.

(2) The issues of snap-through buckling and bifurcation and their associated computational strategies should be addressed. This is because many shell structures under intensive excitations frequently experience the snap-through buckling and bifurcation, and their computational strategies available in the literature to-date are far from satisfactory.

(3) A thorough study on making use of symmetry conditions in stochastic dynamic analysis should be performed. The importance of such an investigation is that it can drastically reduce the computational time for systems with many DOF. This is particularly true for the SCD method.

(4) An approach which incorporates randomness into configuration updating and therefore into the evaluation of mass and stiffness matrices should be formulated and studied. Such a formulation will find many application in the fields of geotechnical engineering and off-shore engineering structures which have material and geometrical imperfections, and are under random loadings.

(5) Numerical examples of shell analysis of elastic-plastic materials with strain hardening behaviour should also be included for future research.

RESPONSE STATISTICS OF SHELL STRUCTURES WITH GEOMETRICAL AND MATERIAL NONLINEARITIES

Volume II

by

Meilan Liu

Department of Mechanical Engineering
Faculty of Engineering Science

Submitted in partial fulfilment of
the requirement for the degree of
Doctor of Philosophy

Faculty of Graduate Studies
The University of Western Ontario
London, Ontario, Canada
July, 1993

TABLE OF CONTENTS

Volume II

LIST OF FIGURES

LIST OF FIGURES
(cont'd)

LIST OF FIGURES
(cont'd)

LIST OF FIGURES
(cont'd)

LIST OF FIGURES
(cont'd)

LIST OF FIGURES
(cont'd)

LIST OF FIGURES
(cont'd)

LIST OF FIGURES
(cont'd)

LIST OF FIGURES
(cont'd)

LIST OF FIGURES
(cont'd)

LIST OF FIGURES
(cont'd)

LIST OF APPENDICES

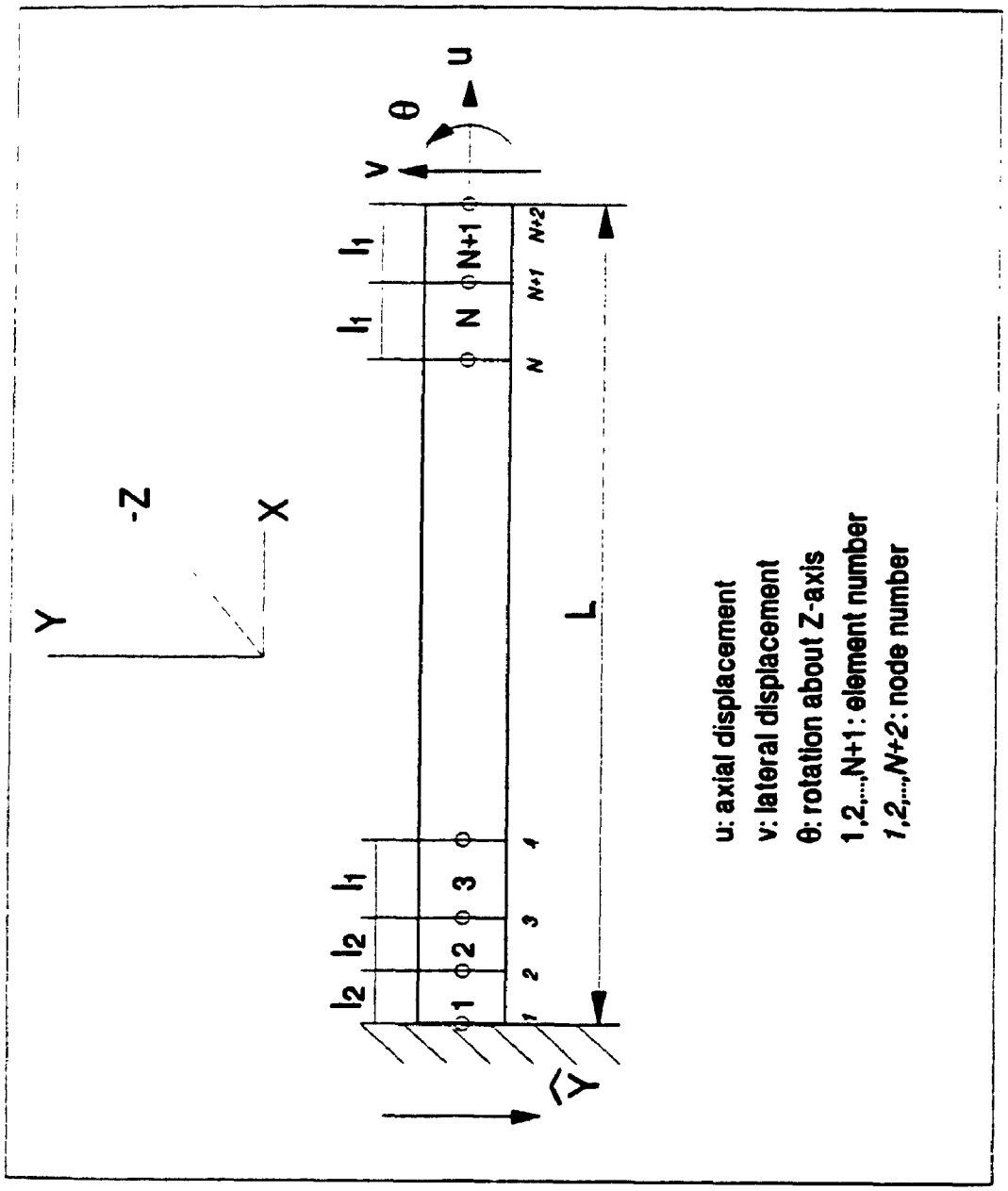

Figure 2.1 The discretized beam structure

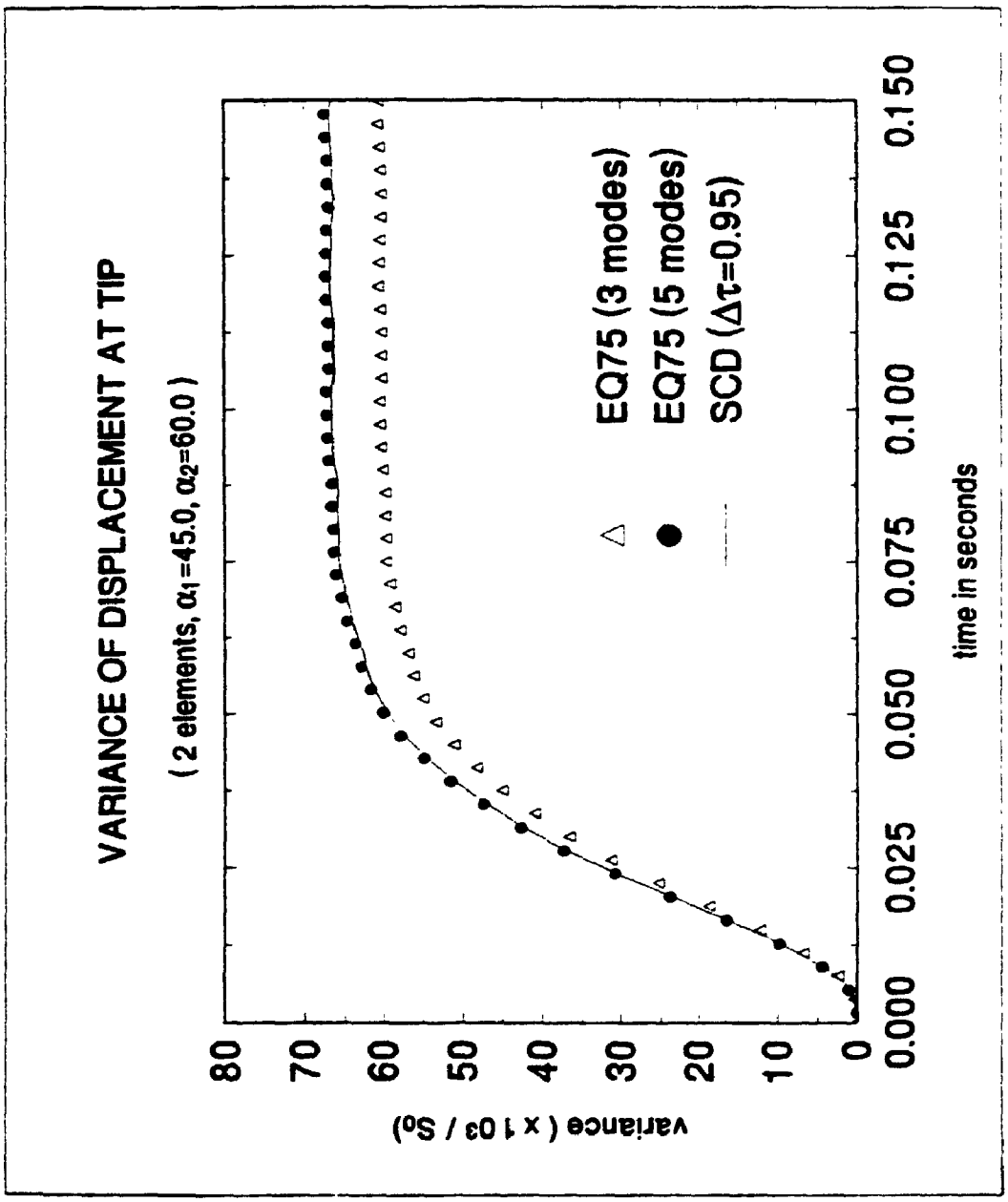

Figure 2.2 Variance of displacement at tip (2 elements, zero damping)

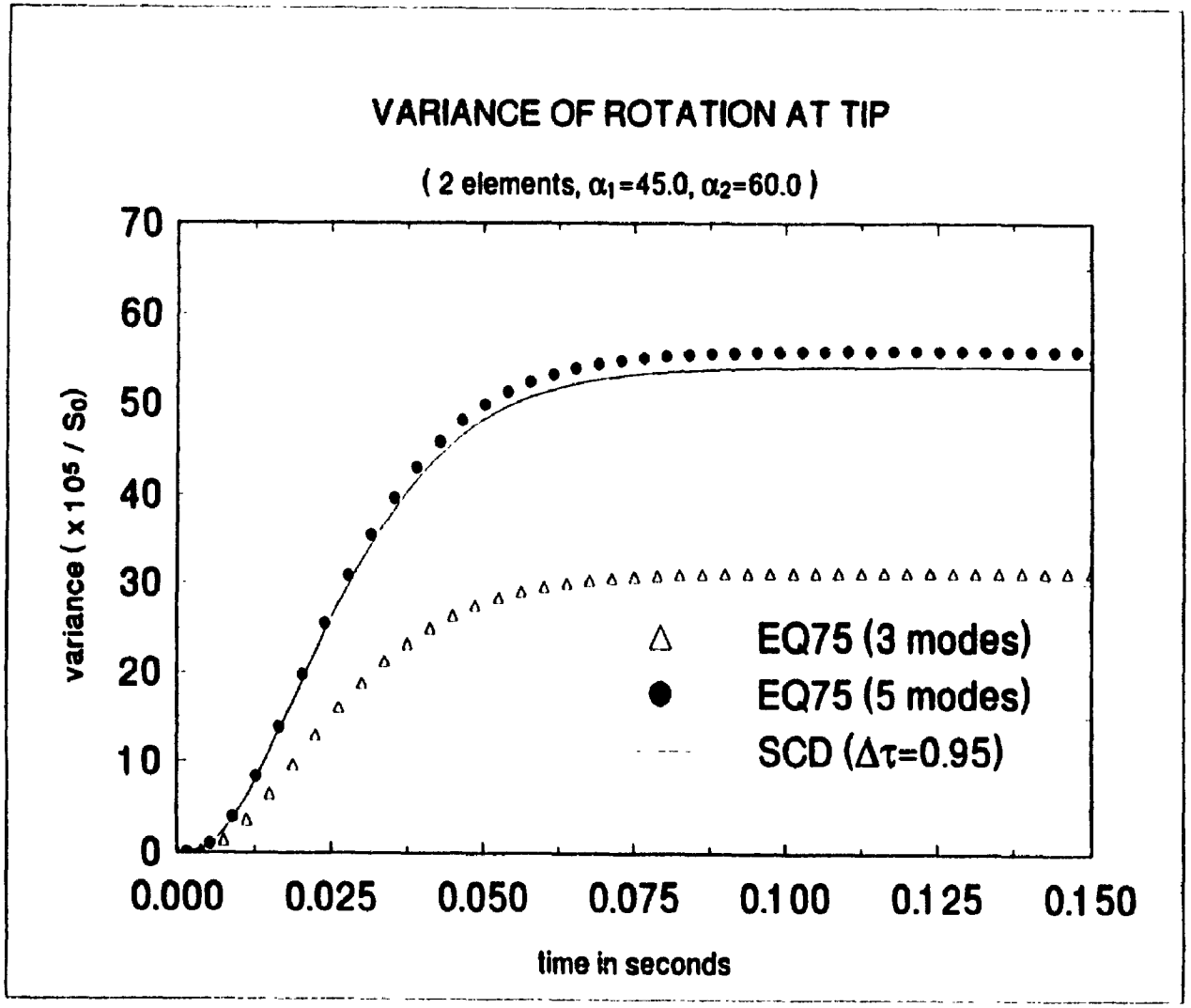

Figure 2.3 Variance of rotation at tip (2 elements, zero damping)

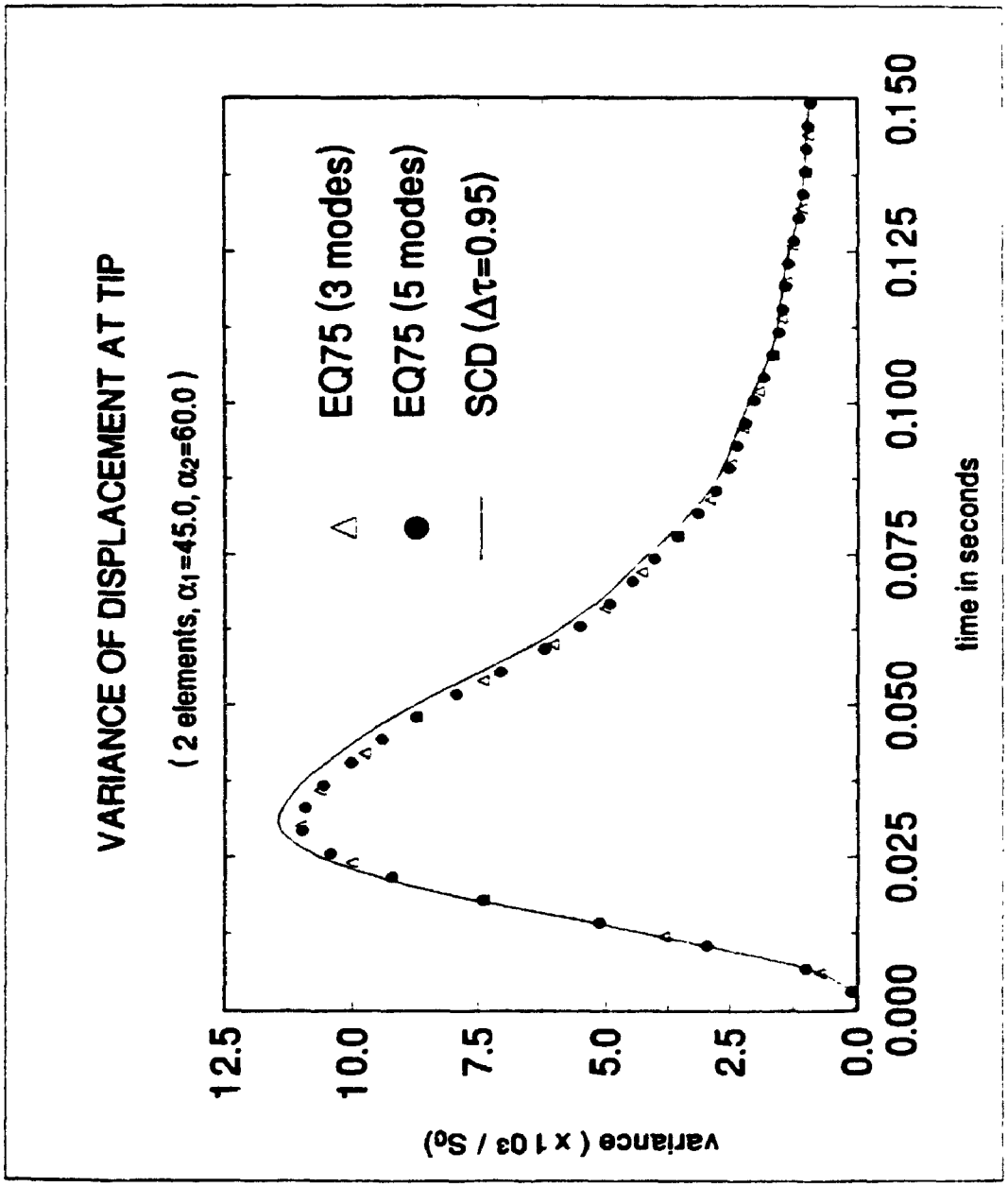

Figure 2.4 Variance of displacement at tip (2 elements)

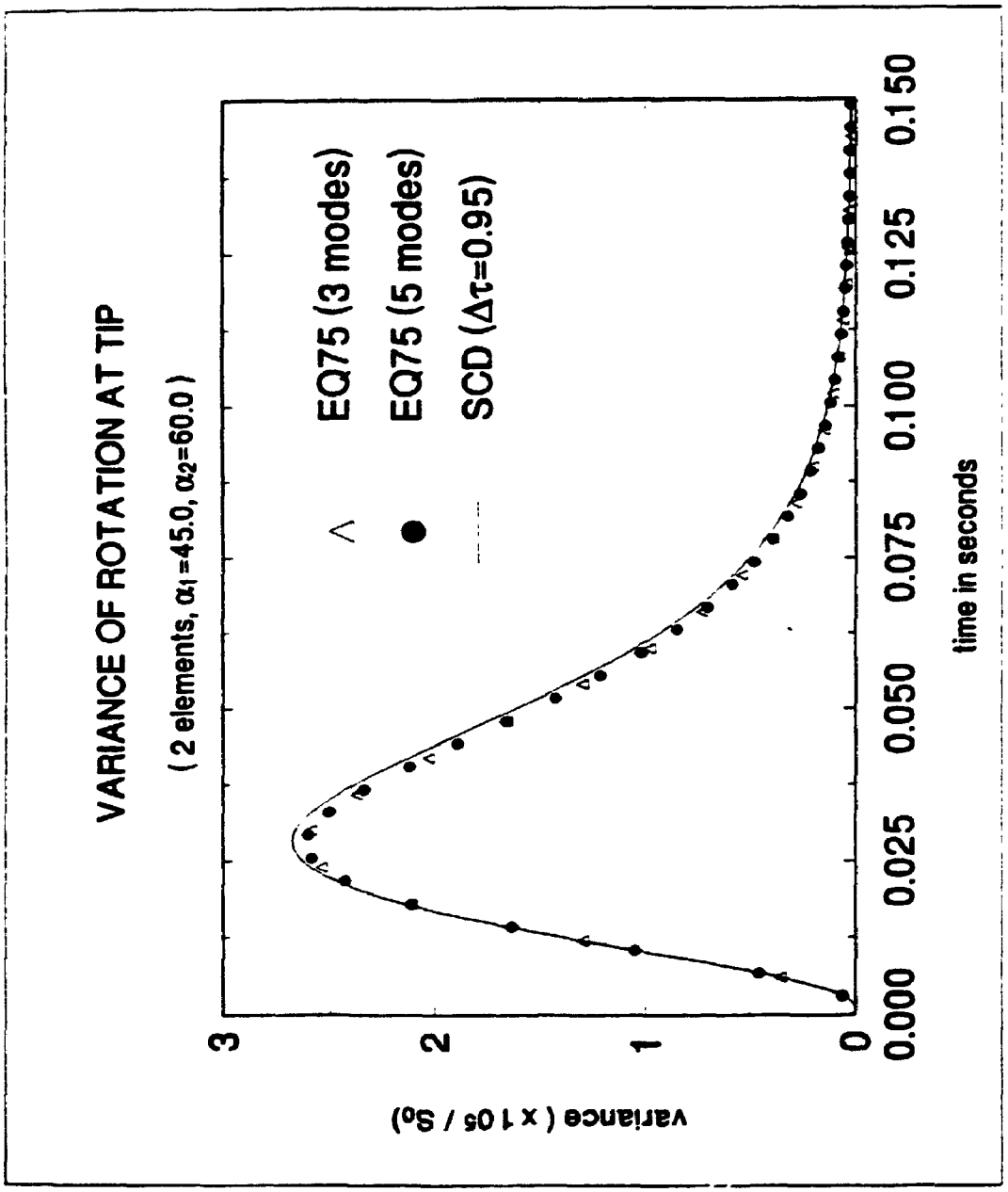

Figure 2.5 Variance of rotation at tip (2 elements)

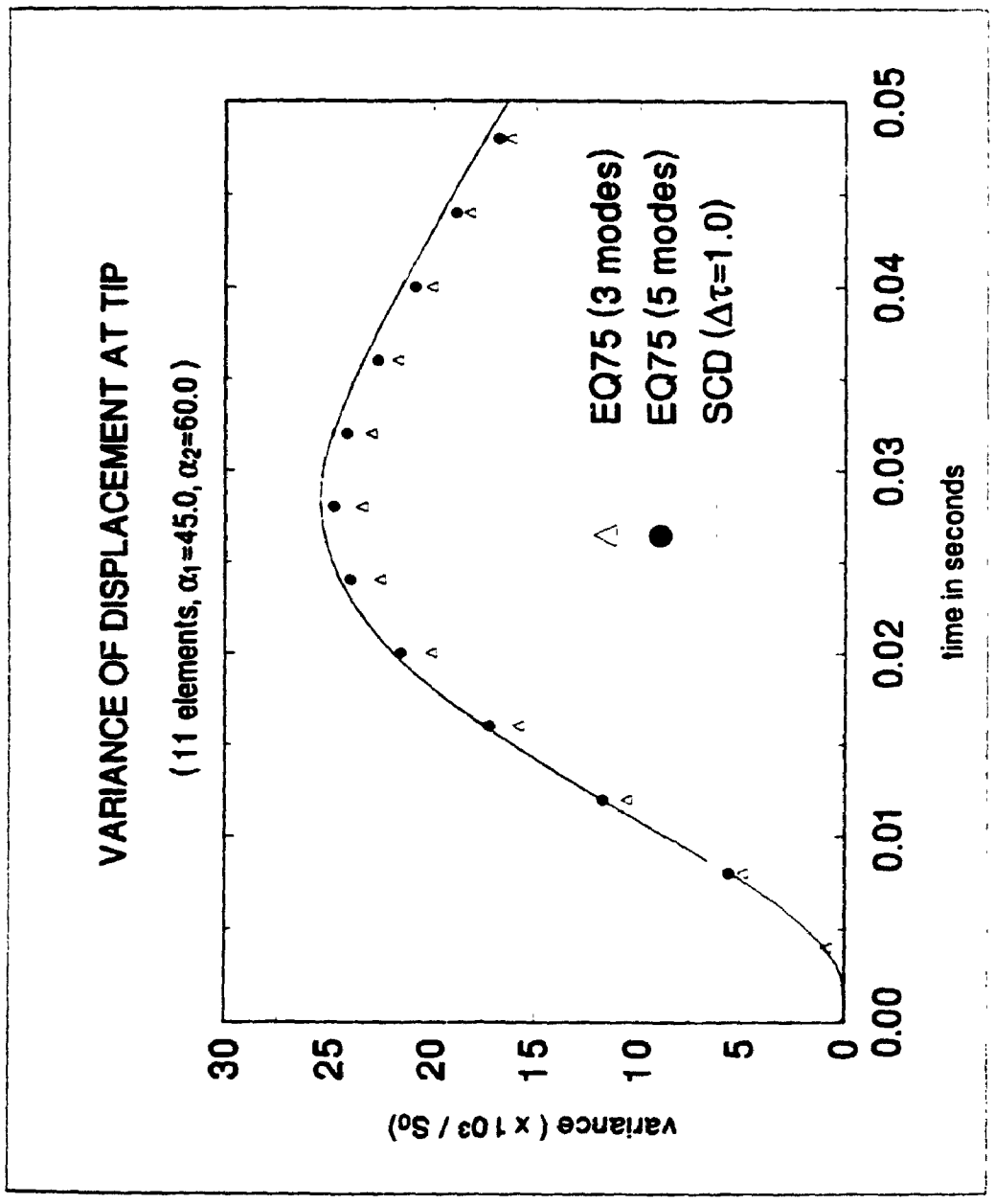

Figure 2.6 Variance of displacement at tip (11 elements)

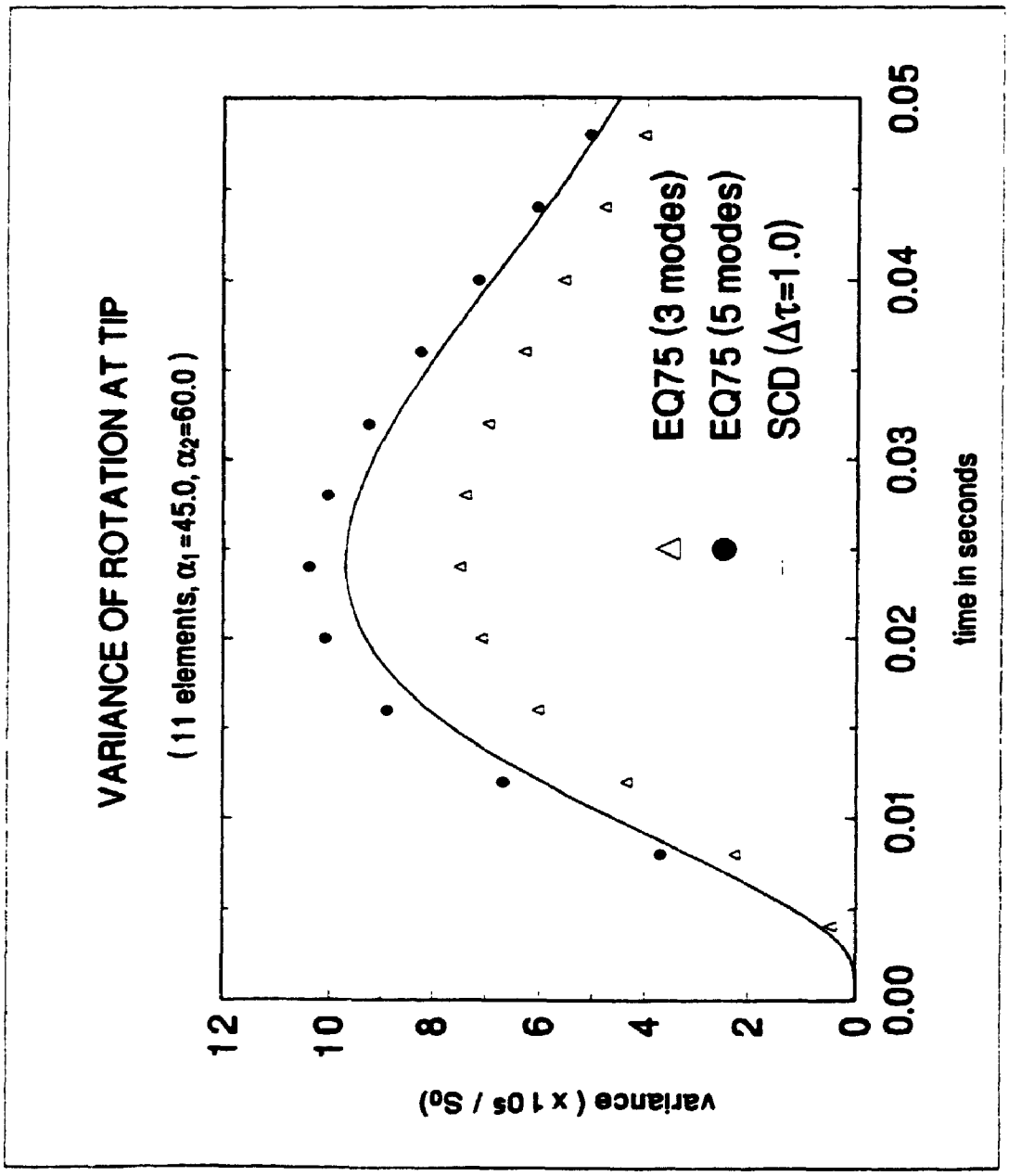

Figure 2.7 Variance of rotation at tip (11 elements)

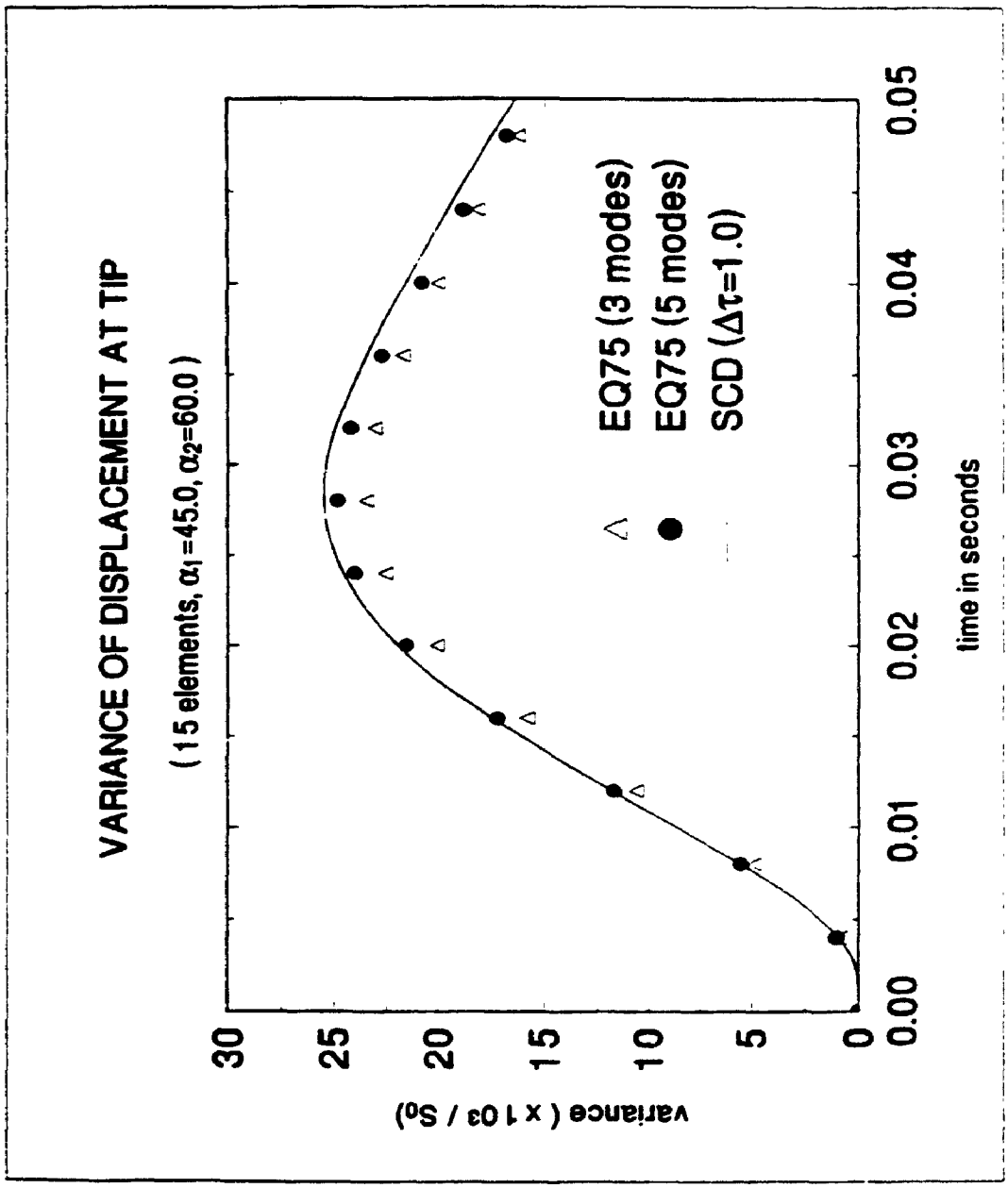

Figure 2.8 Variance of displacement at tip (15 elements)

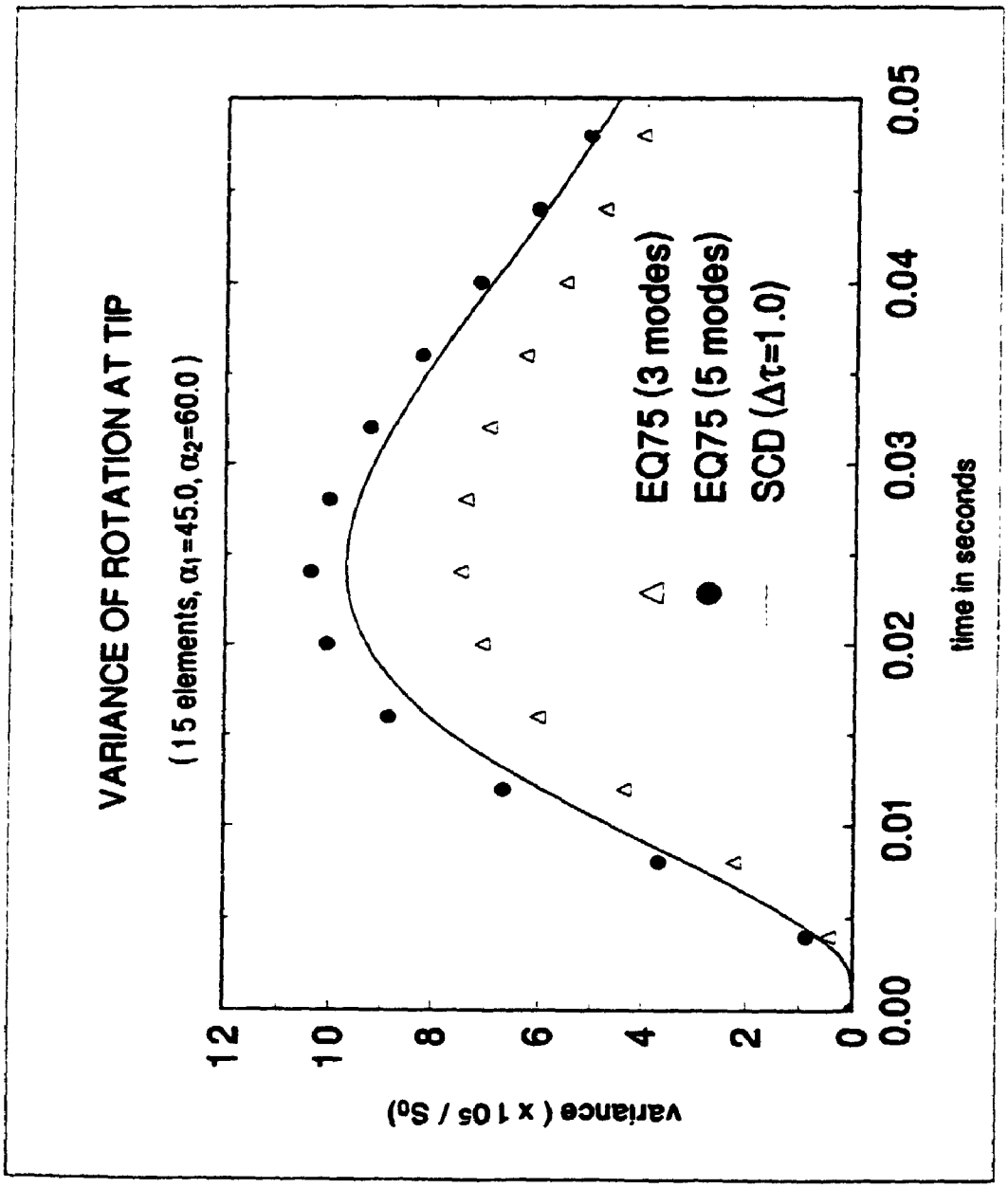

Figure 2.9 Variance of rotation at tip (15 elements)

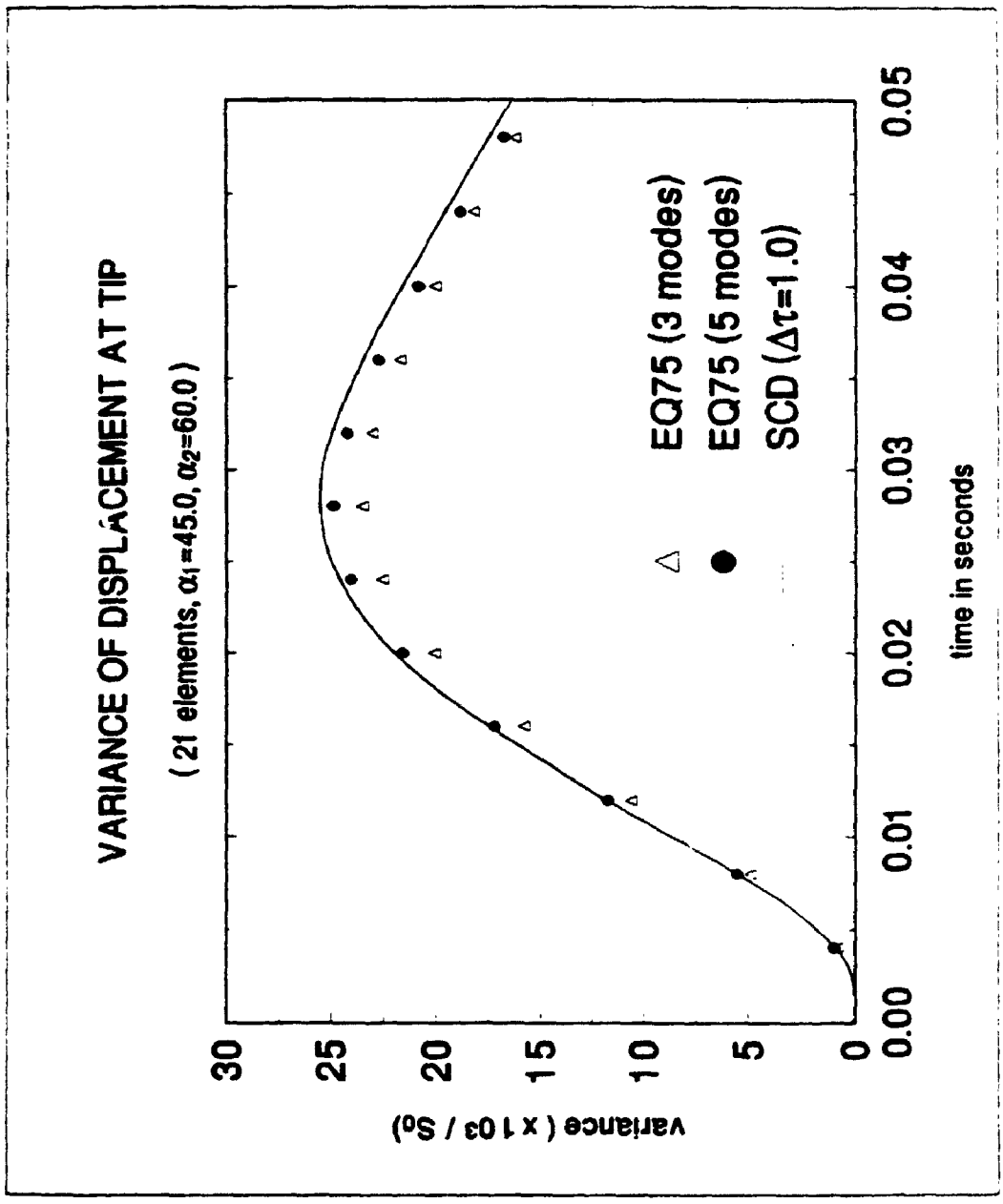

Figure 2.10 Variance of displacement at tip (21 elements)

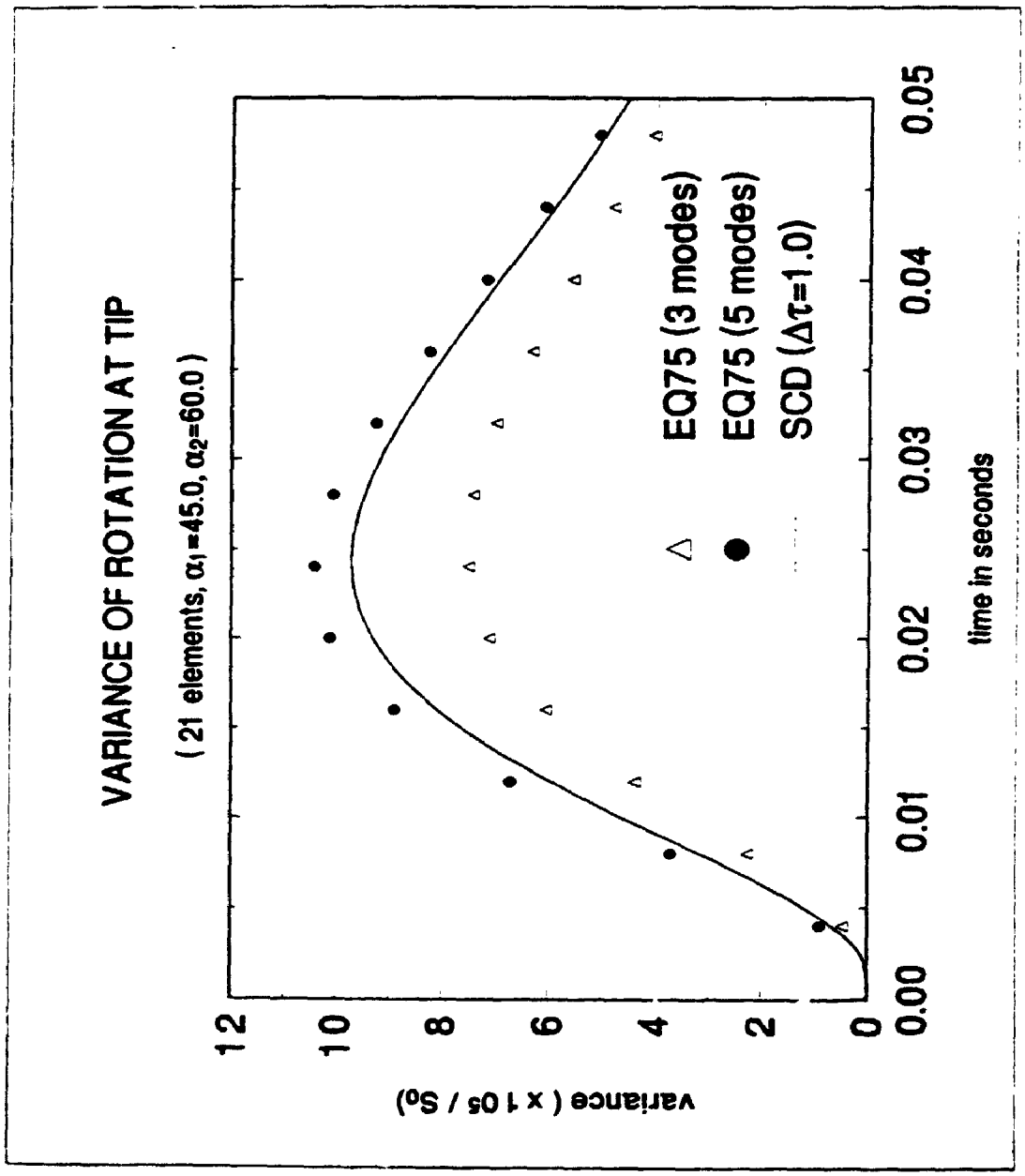

Figure 2.11 Variance of rotation at tip (21 elements)

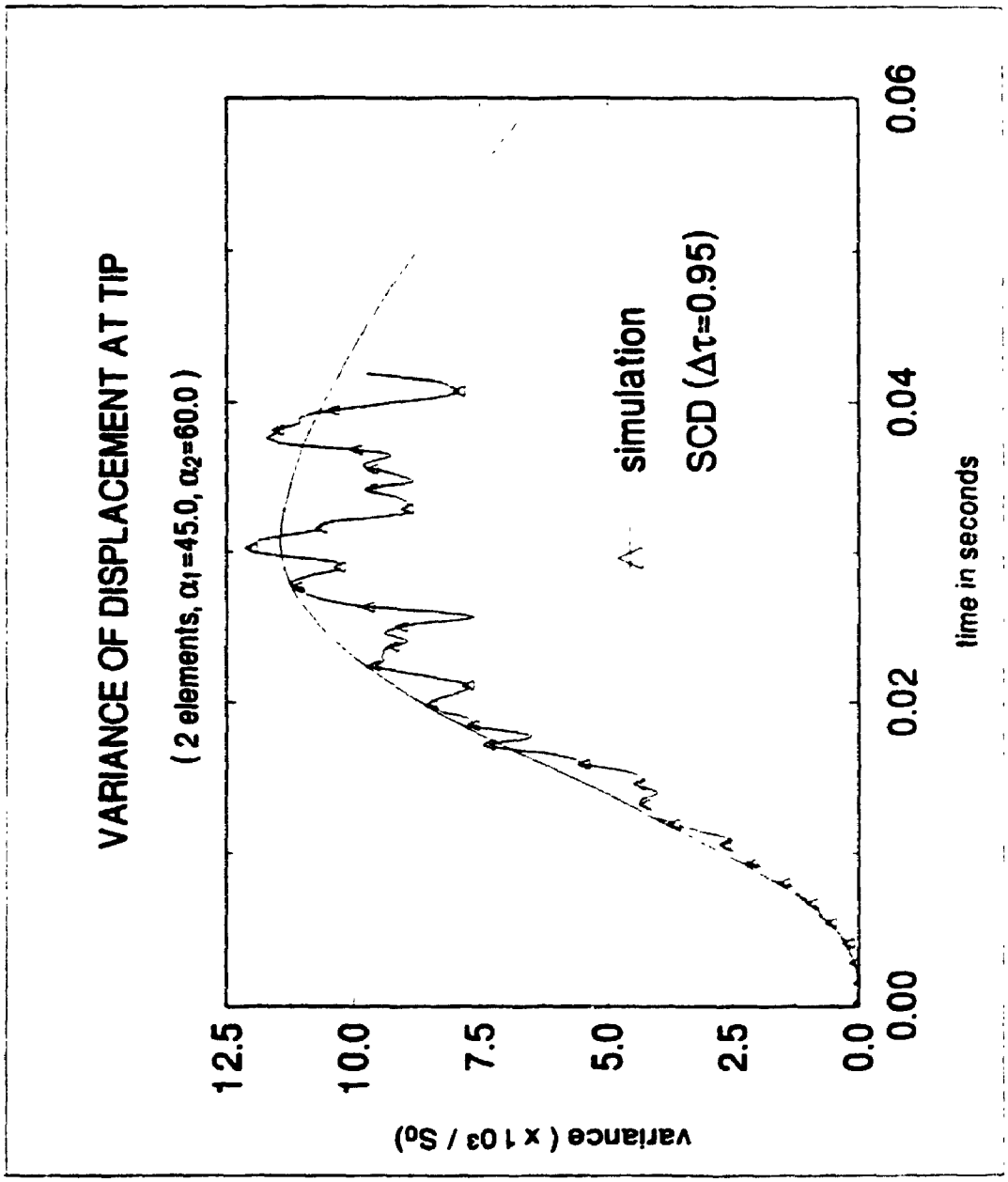

Figure 2.12 Variance of displacement at tip
(2 elements, comparison to MCS)

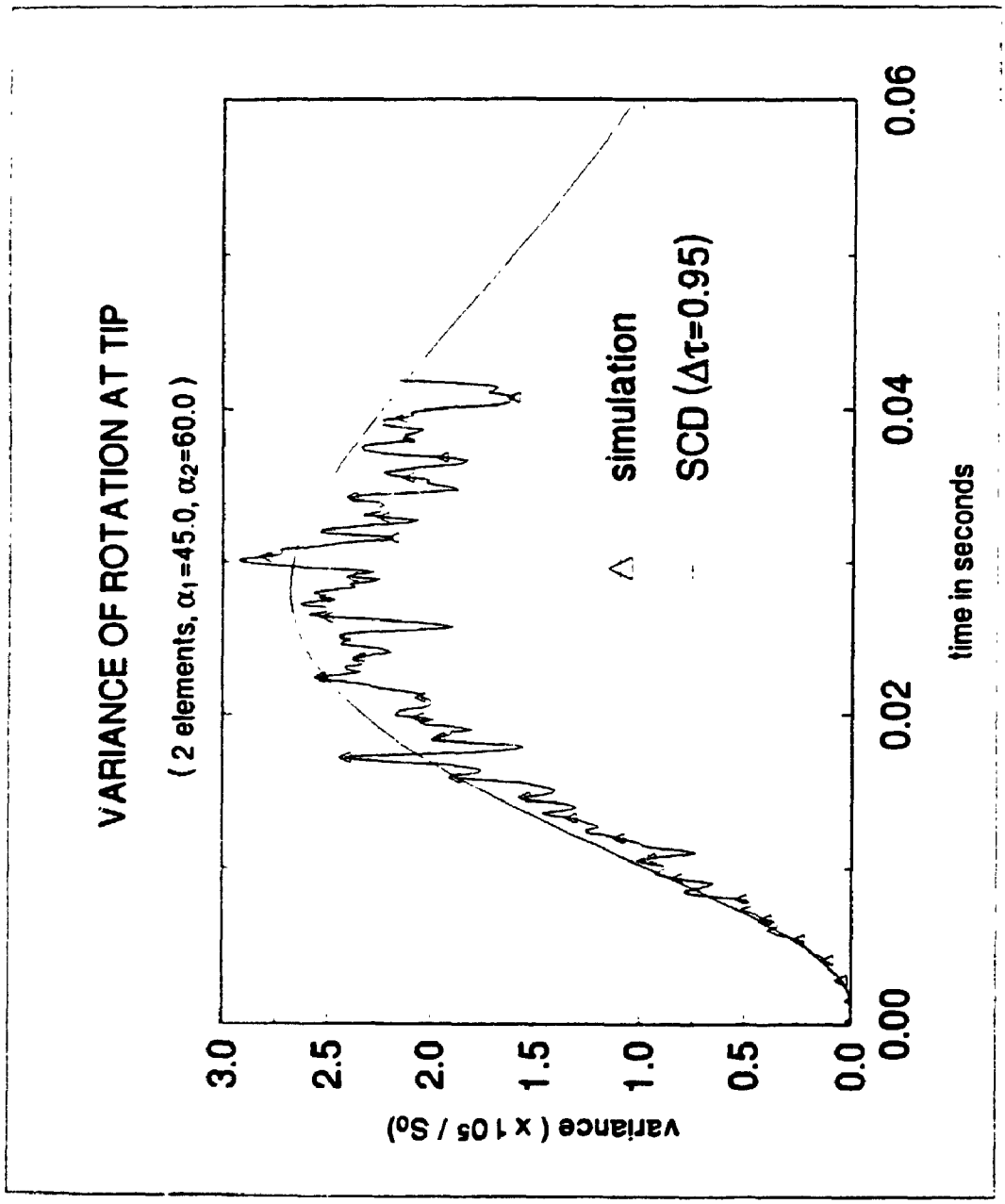

Figure 2.13 Variance of rotation at tip
(2 elements, comparison to MCS)

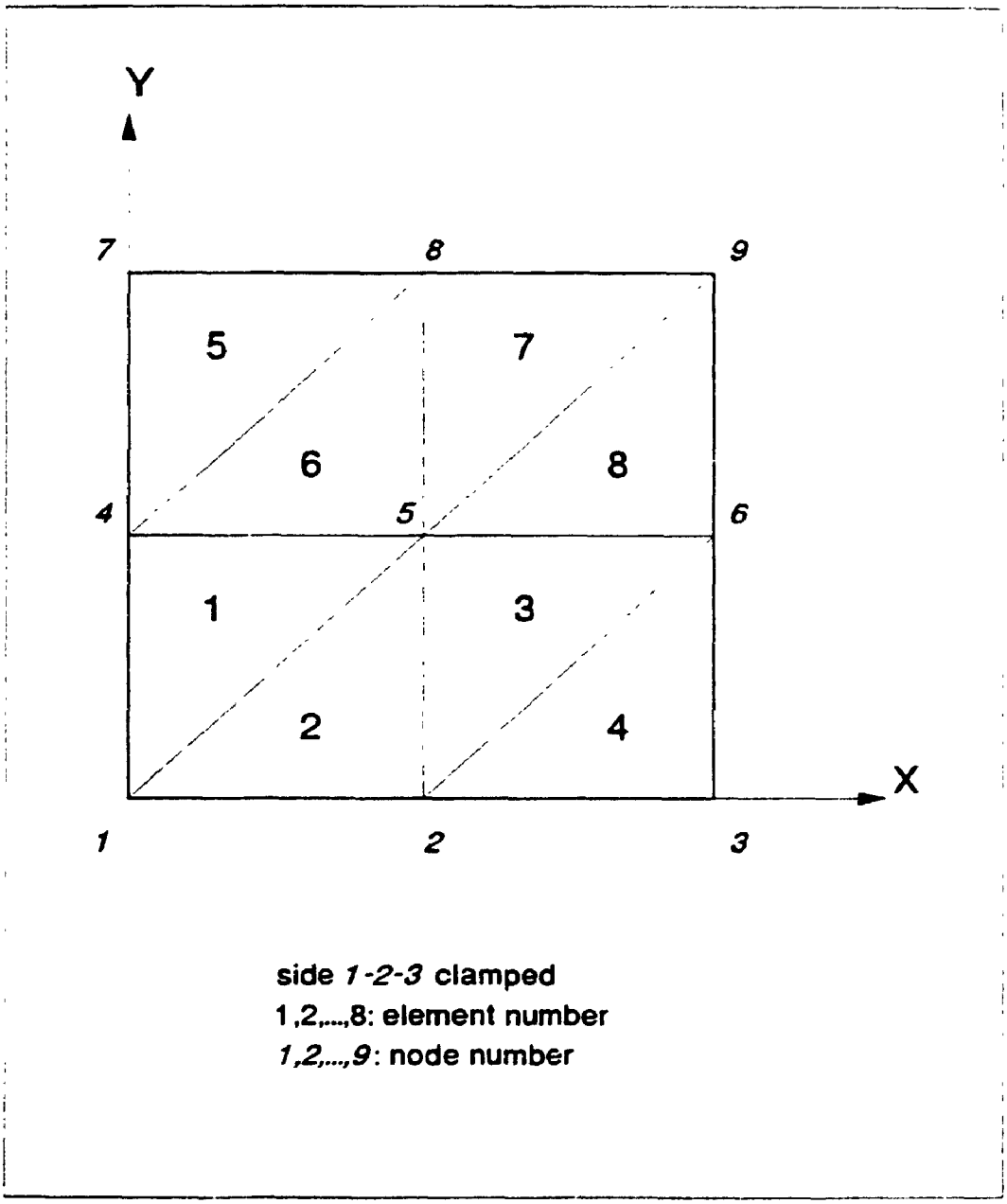

Figure 2.14 The discretized plate structure (CF3 plate)

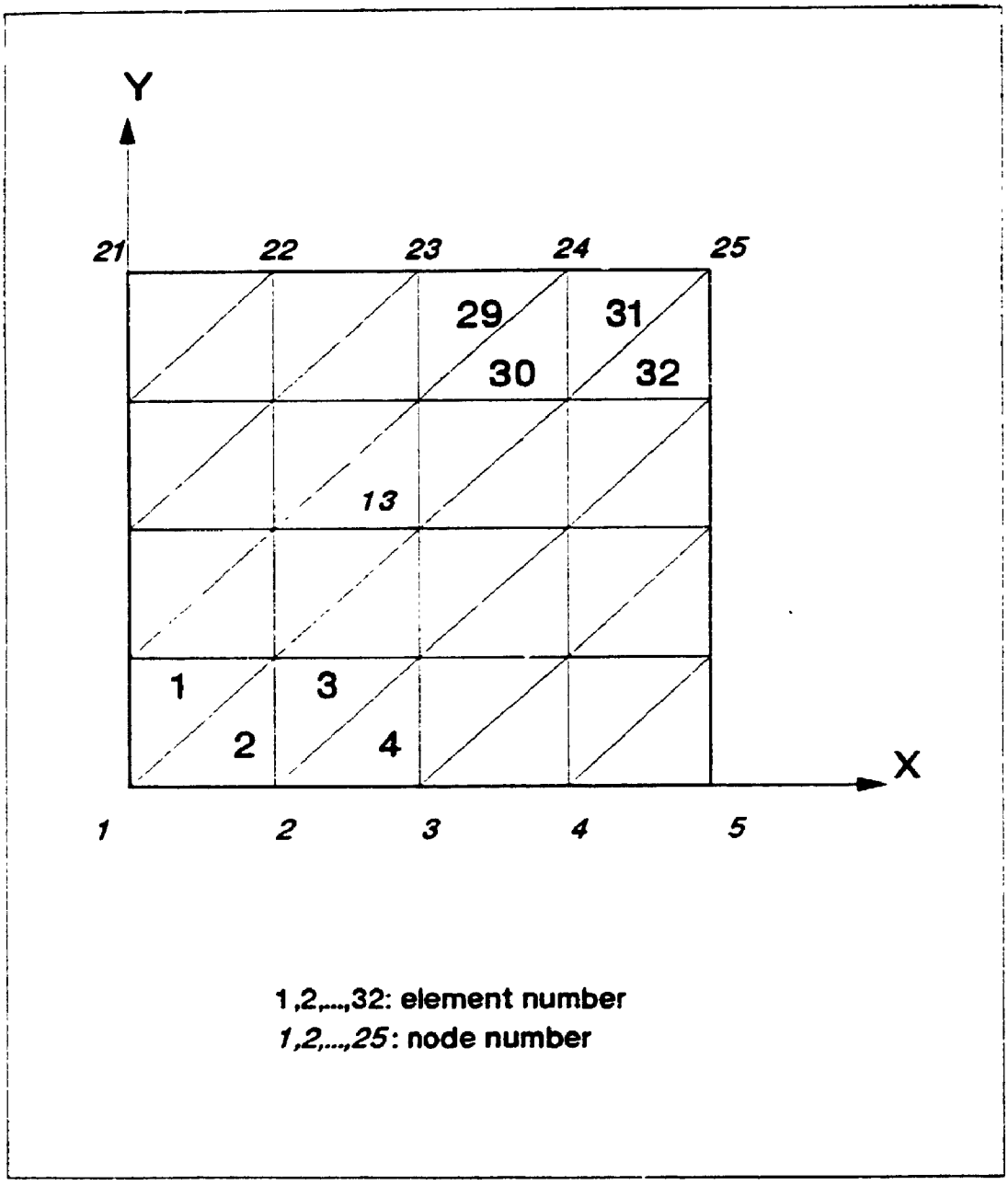

Figure 2.15 The discretized plate structure (C4 plate)

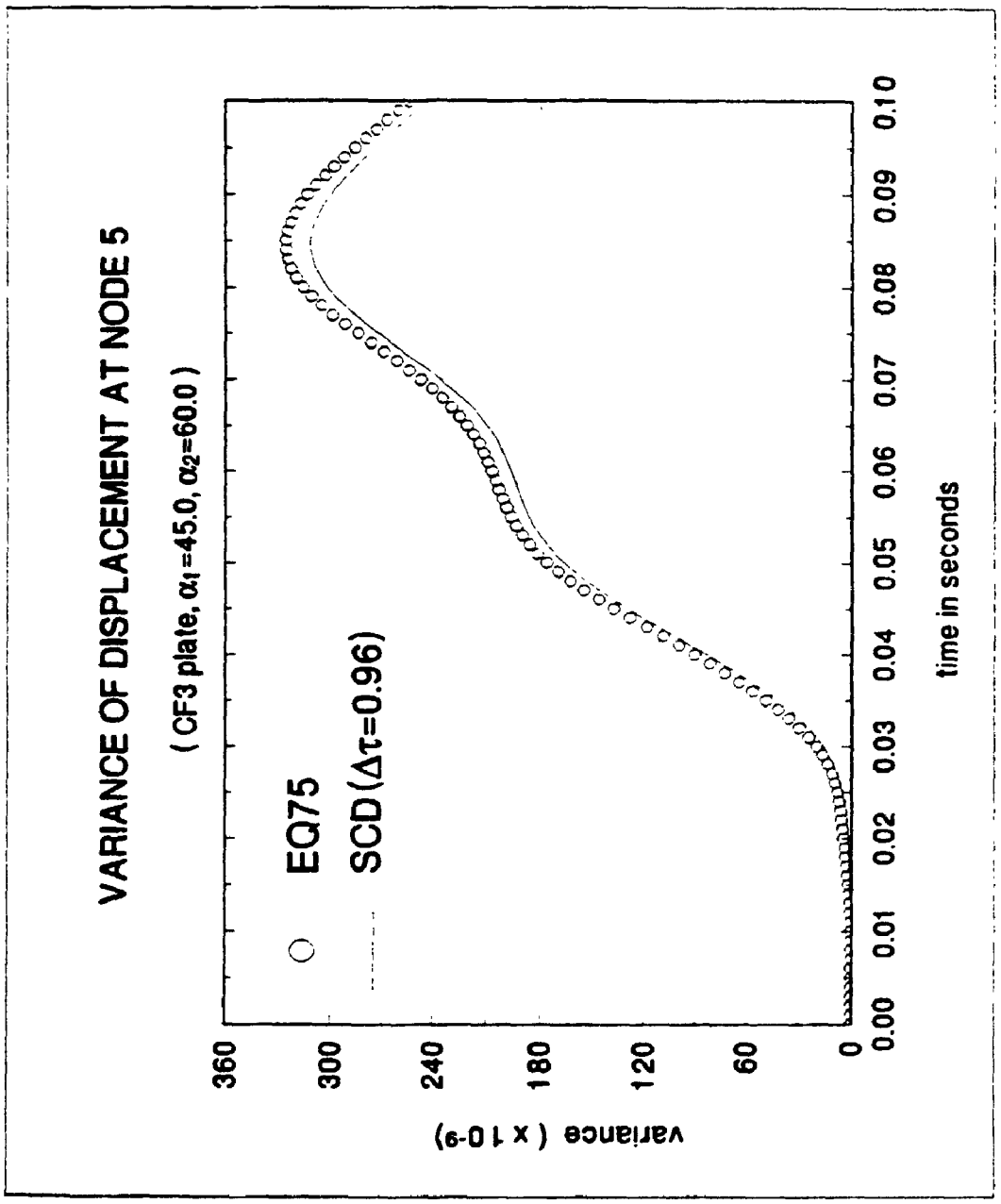

Figure 2.16 Variance of displacement at node 5 (CF3 plate)

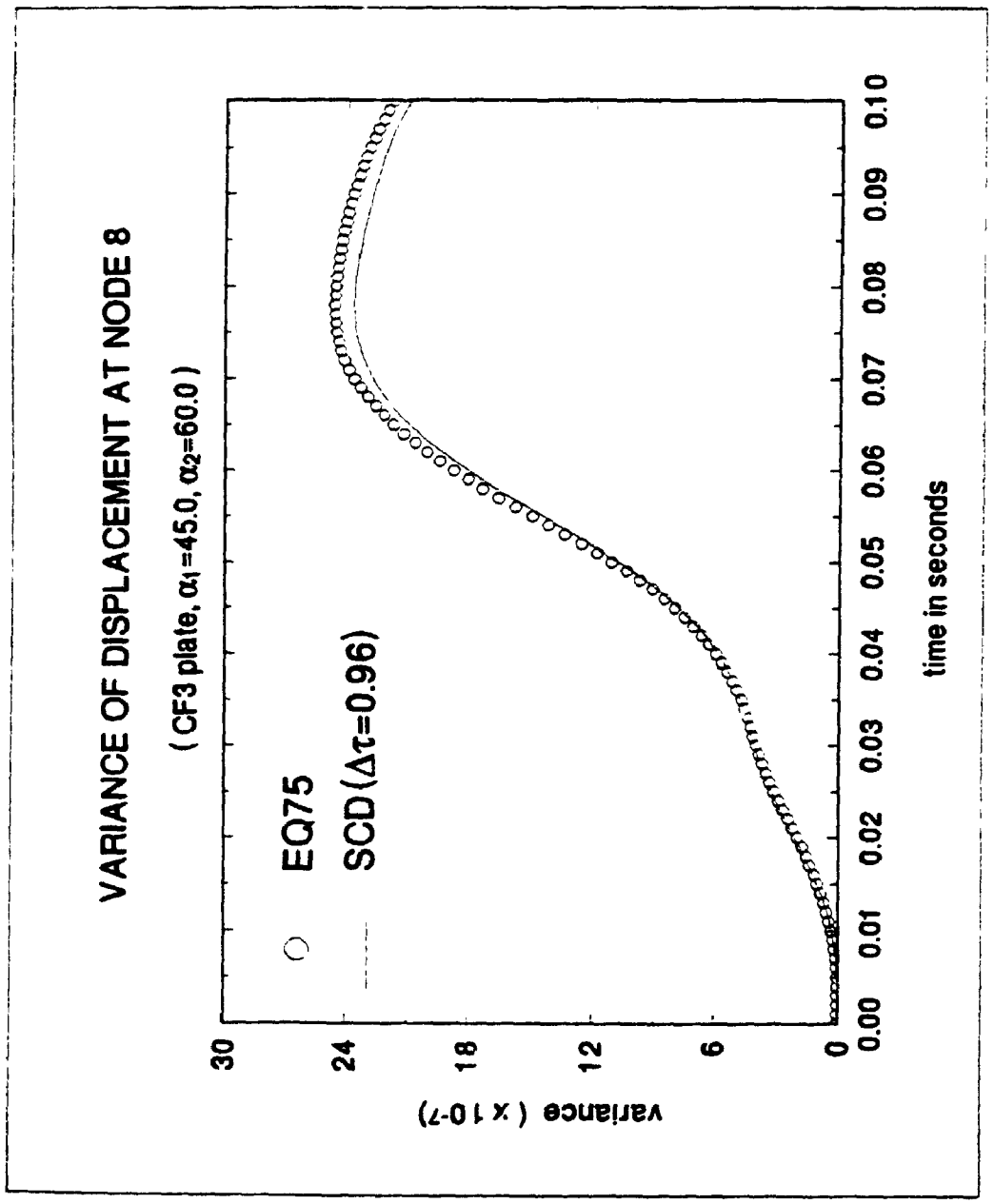

Figure 2.17 Variance of displacement at node 8 (CF3 plate)

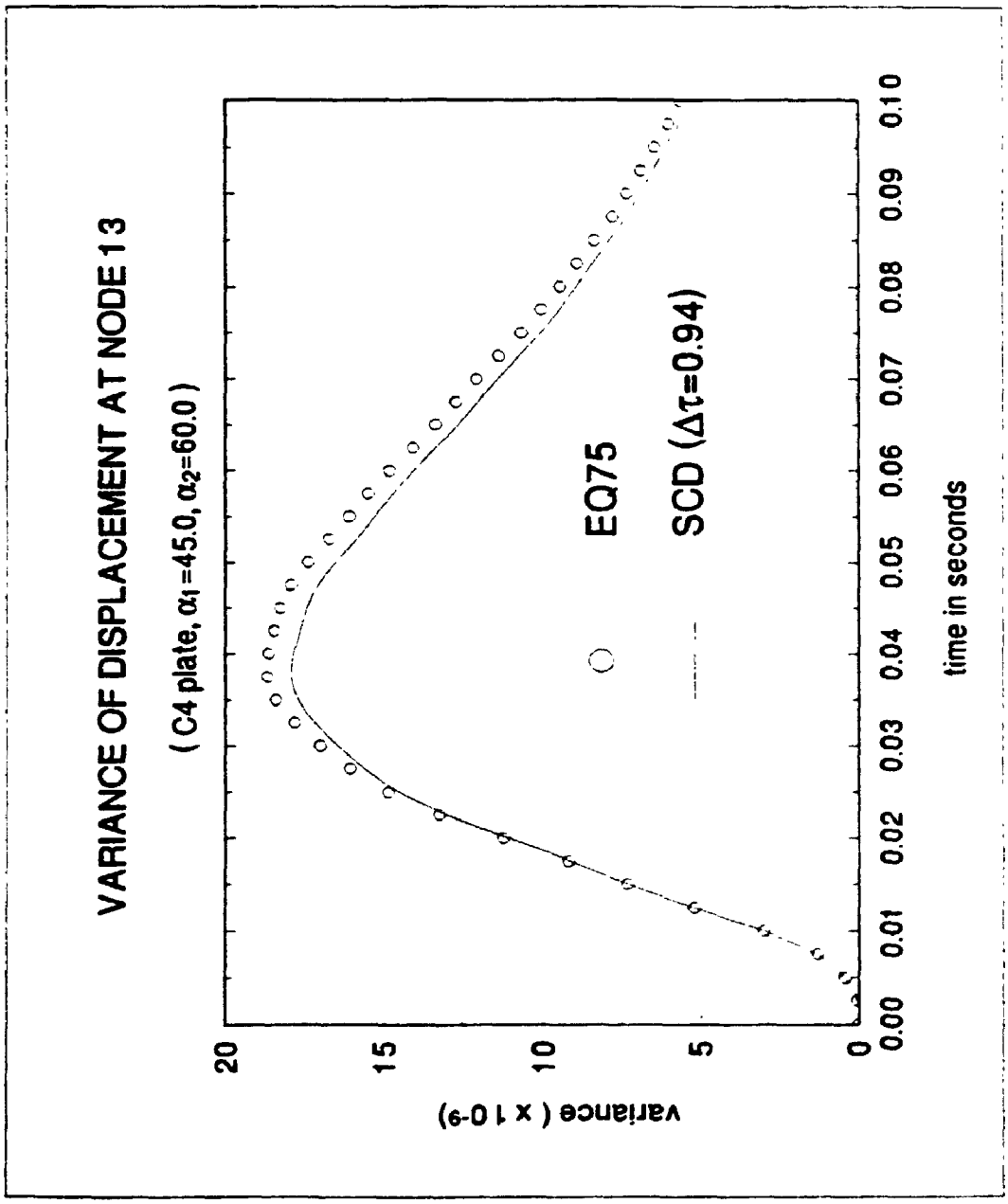

Figure 2.18 Variance of displacement at node 13 (C4 plate)

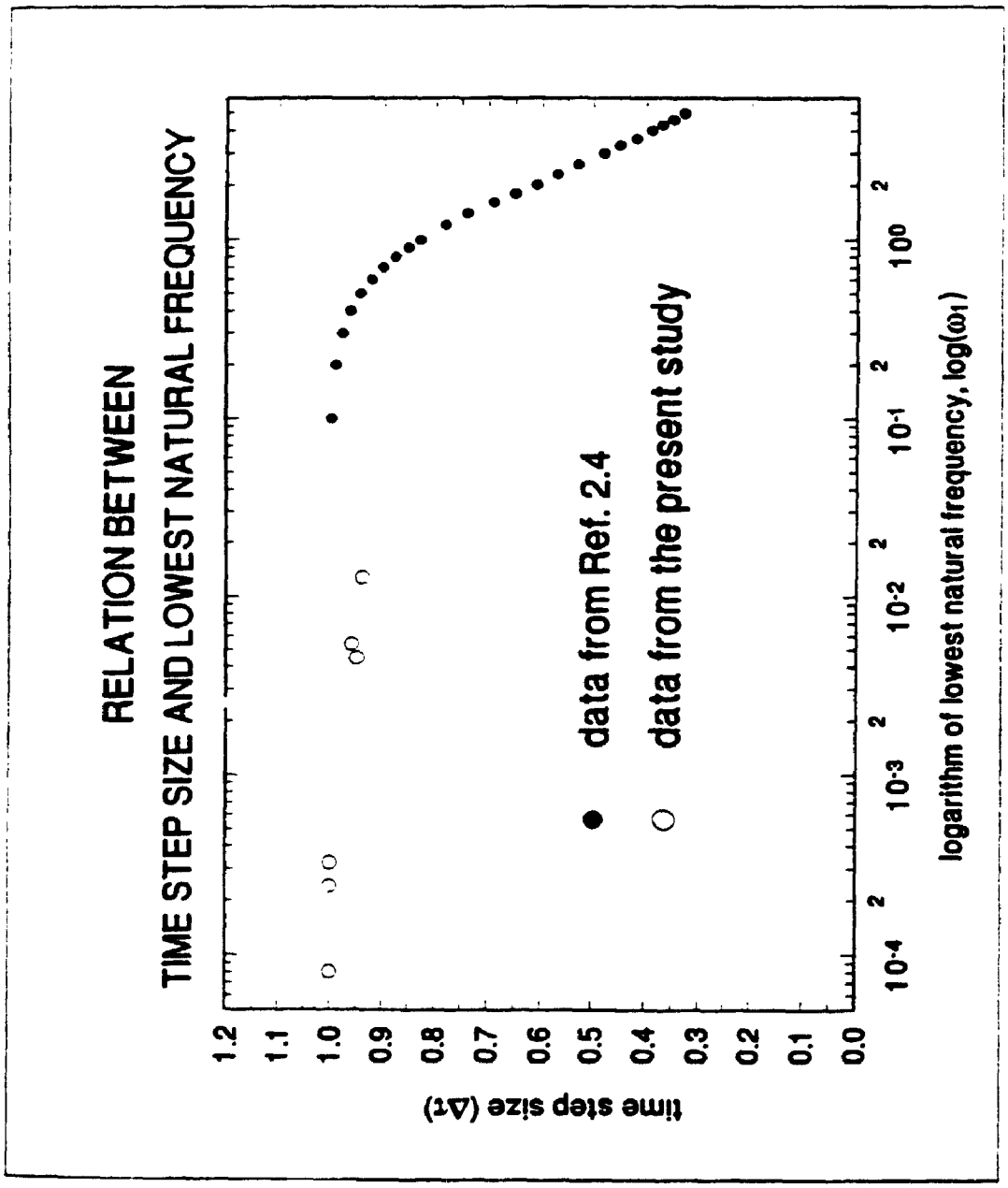

Figure 2.19 Relation between time step size and lowest natural frequency

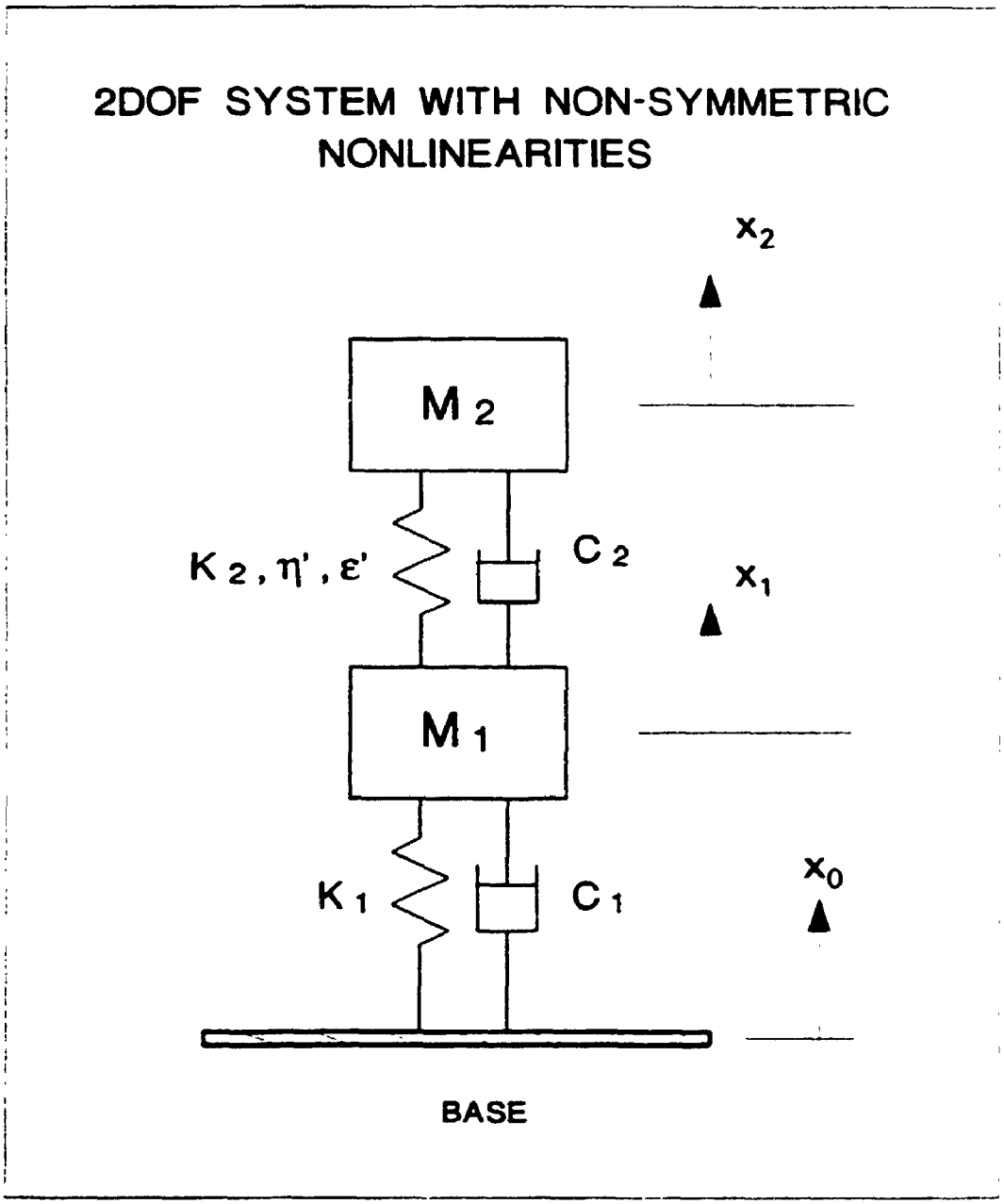

Figure 2.20 The 2 DOF non-symmetric nonlinear system

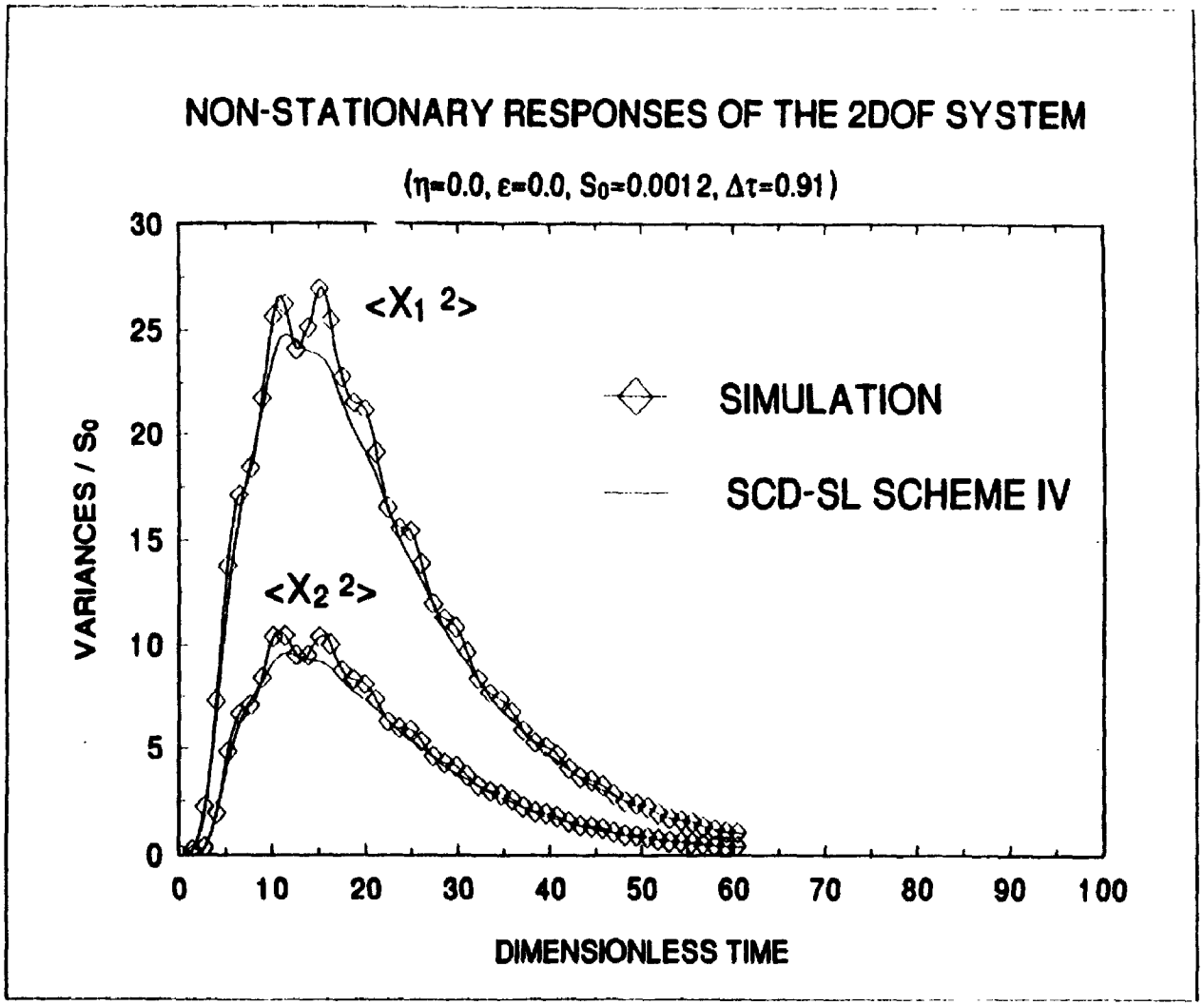

Figure 2.21 Non-stationary responses of the 2 DOF system ($\eta = 0.0, \varepsilon = 0.0$)

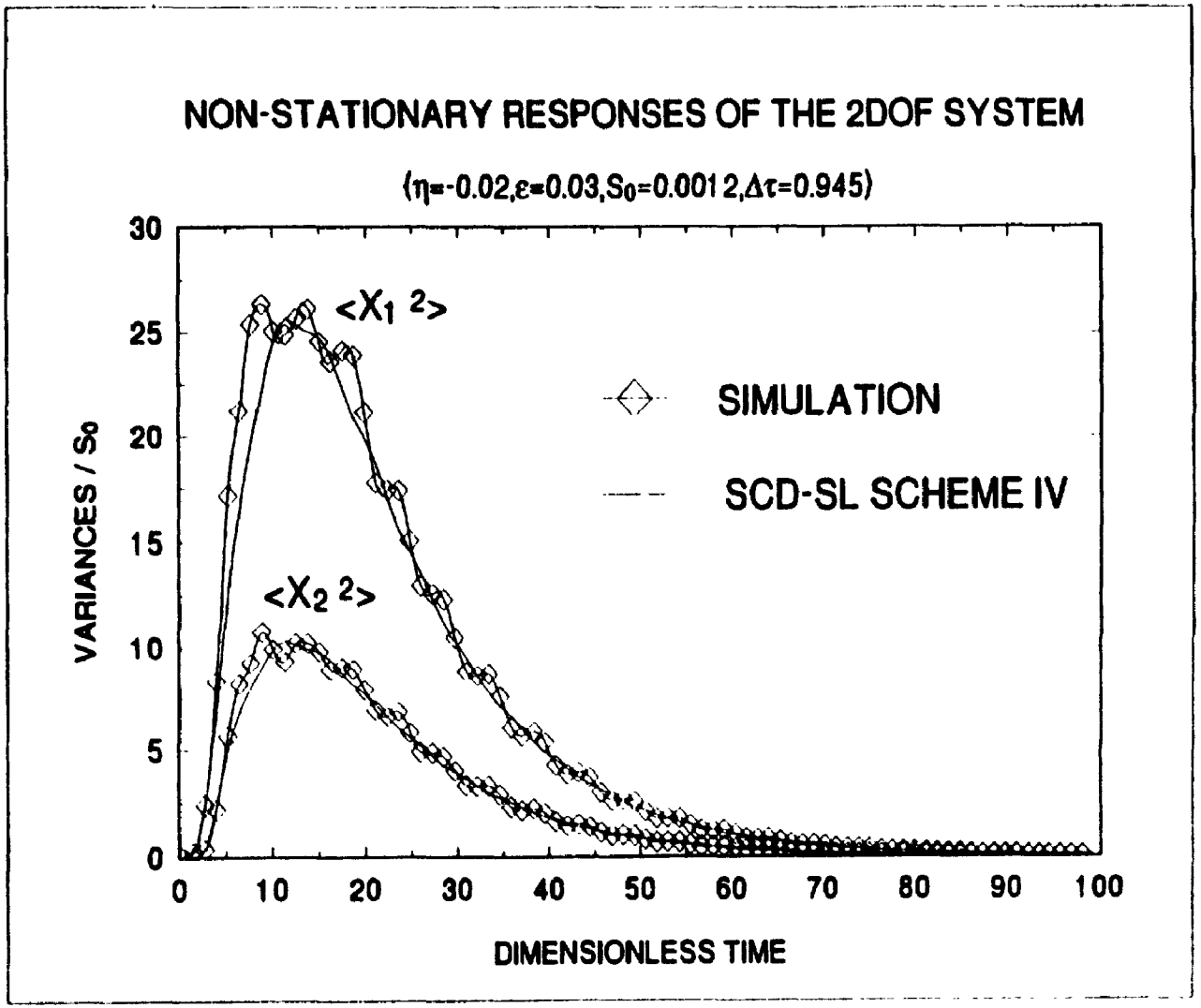

Figure 2.22 Non-stationary responses of the 2 DOF system ($\eta = -0.02, \varepsilon = 0.03$)

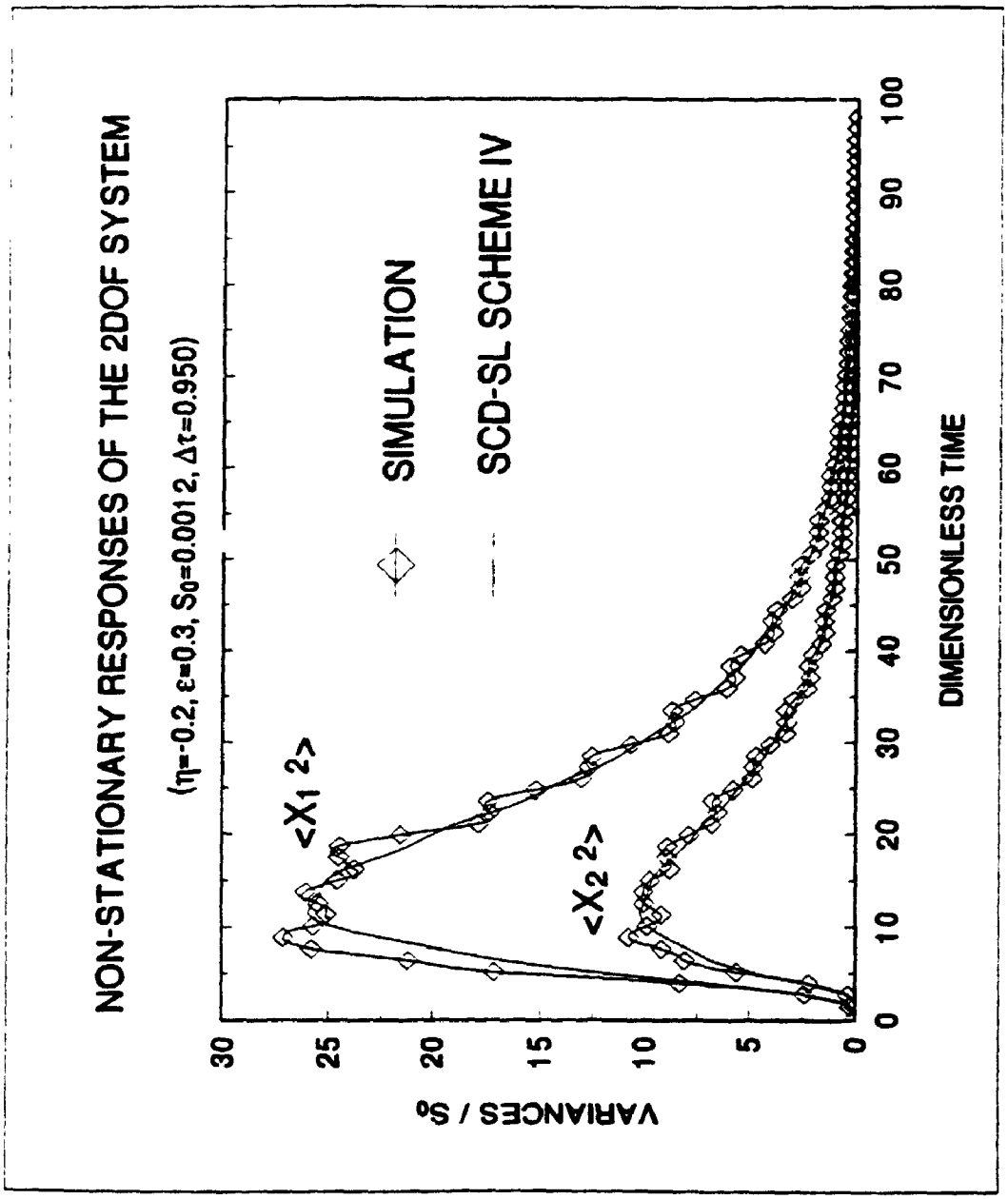

Figure 2.23 Non-stationary responses of the 2 DOF system ($\eta = -0.2, \varepsilon = 0.3$)

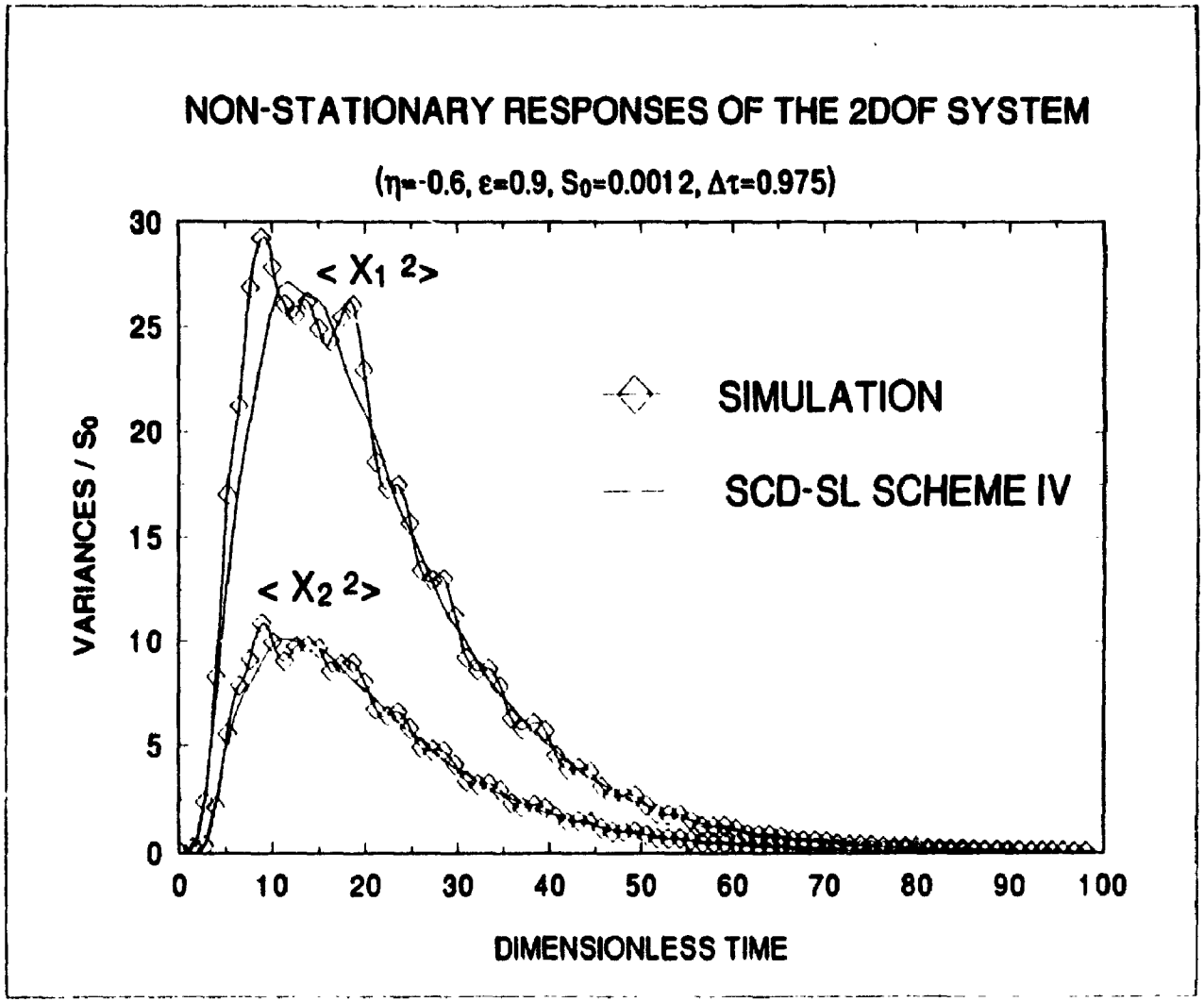

Figure 2.24 Non-stationary responses of the 2 DOF system ($\eta = -0.6, \varepsilon = 0.9$)

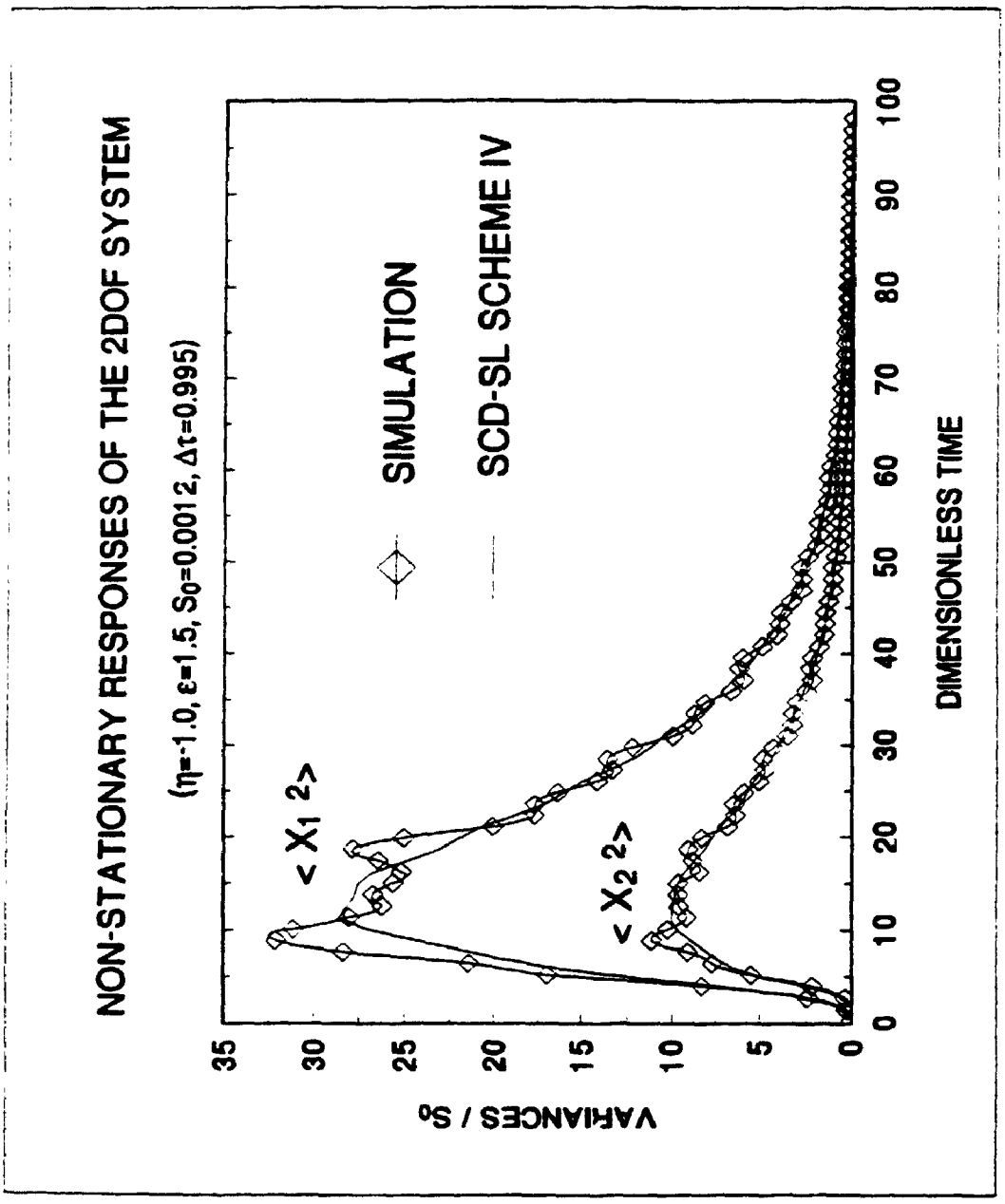

Figure 2.25 Non-stationary responses of the 2 DOF system ($\eta = -1.0, \varepsilon = 1.5$)

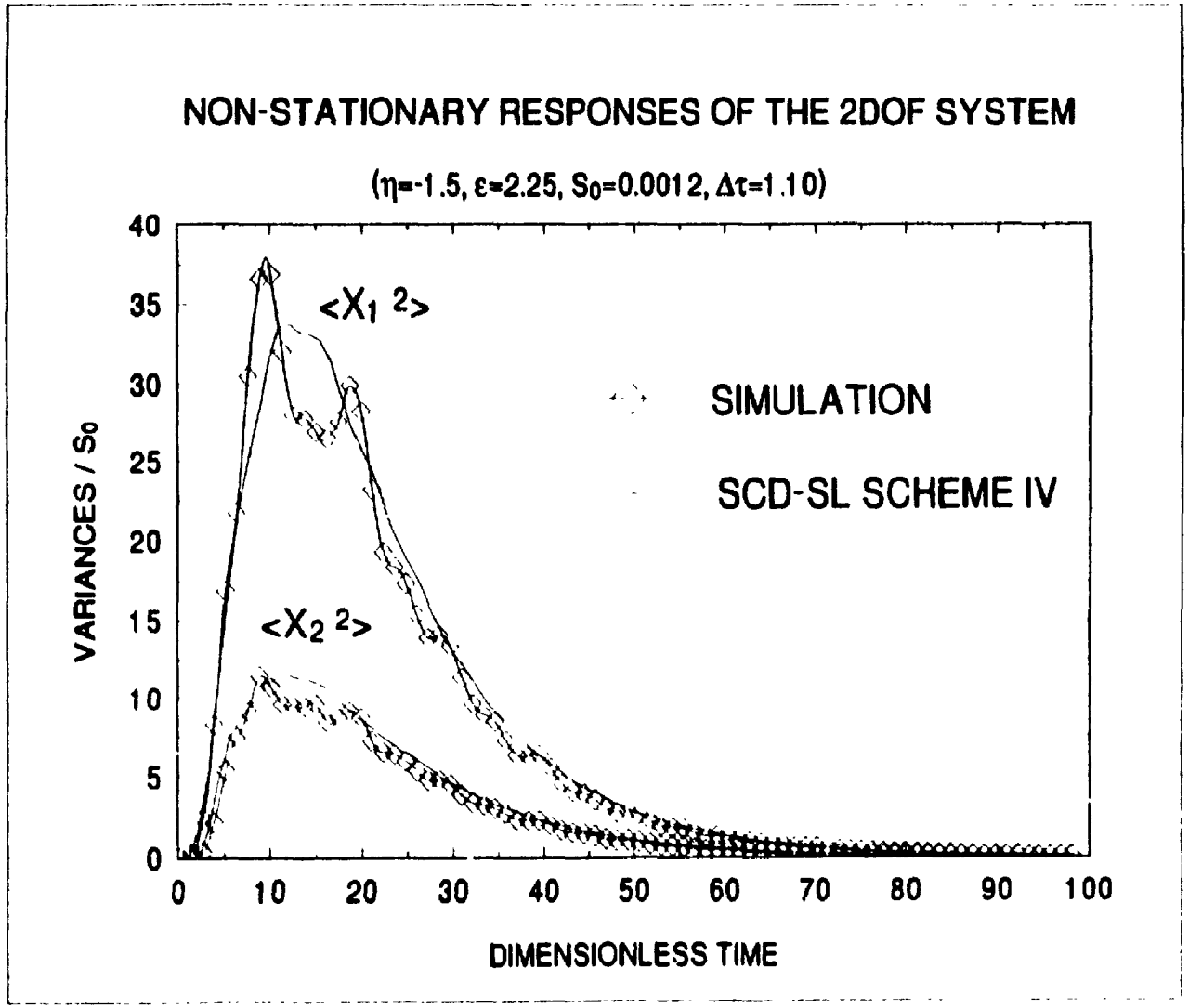

Figure 2.26 Non-stationary responses of the 2 DOF system ($\eta = -1.5, \varepsilon = 2.25$)

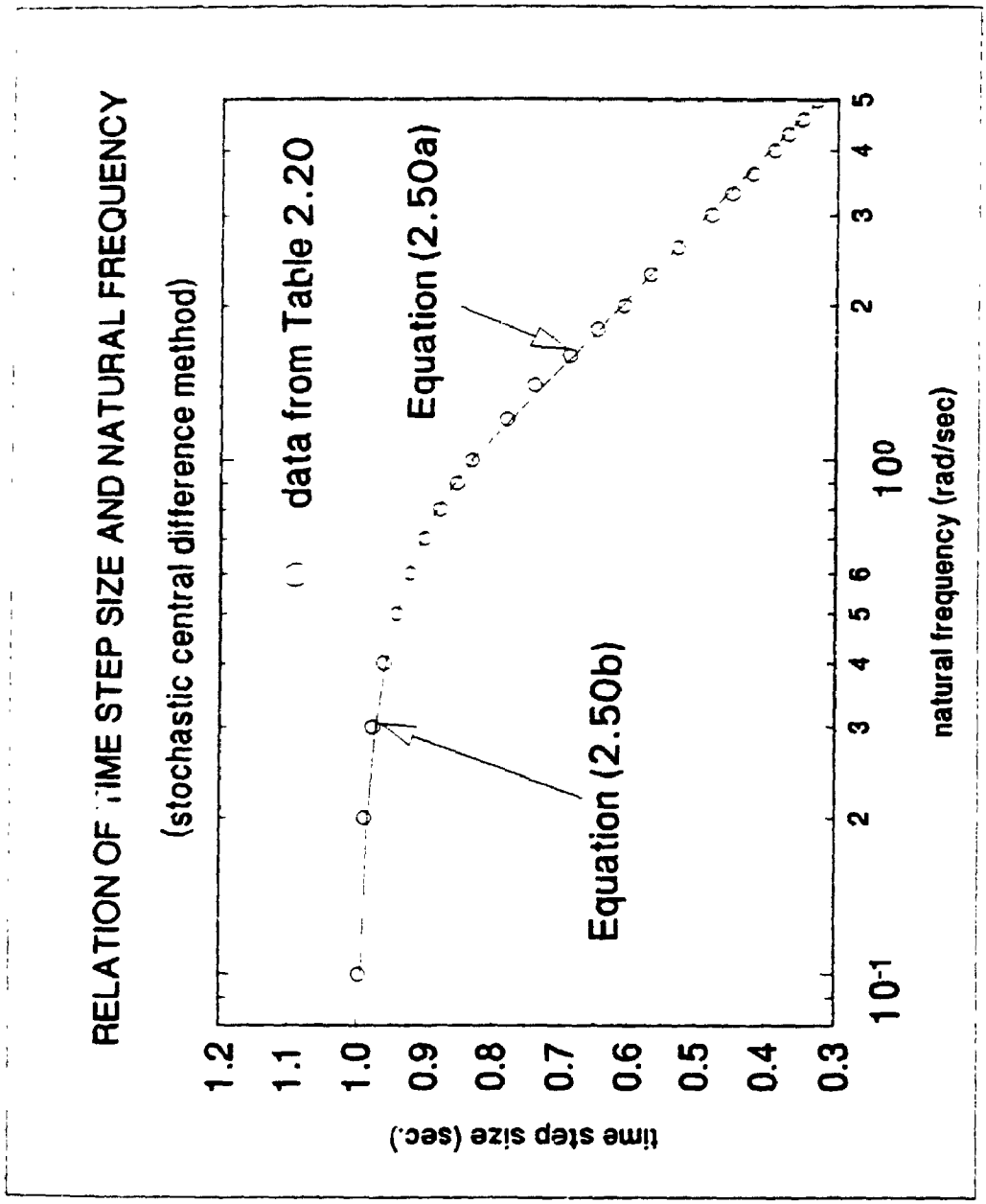

Figure 2.27 Relation of time step size and natural frequency

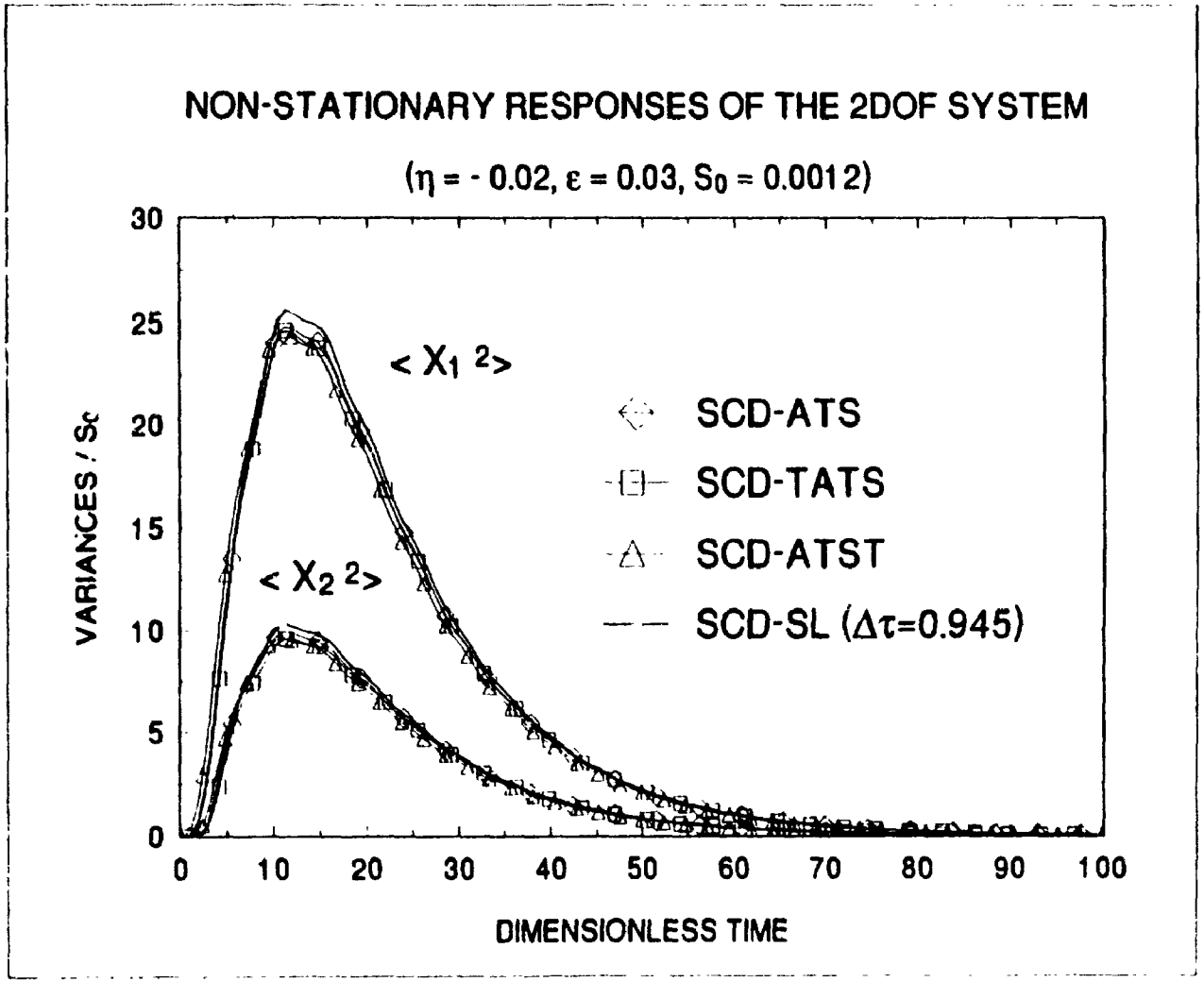

Figure 2.28 Non-stationary responses of the 2 DOF system ($\eta = -0.02, \varepsilon = 0.03$)

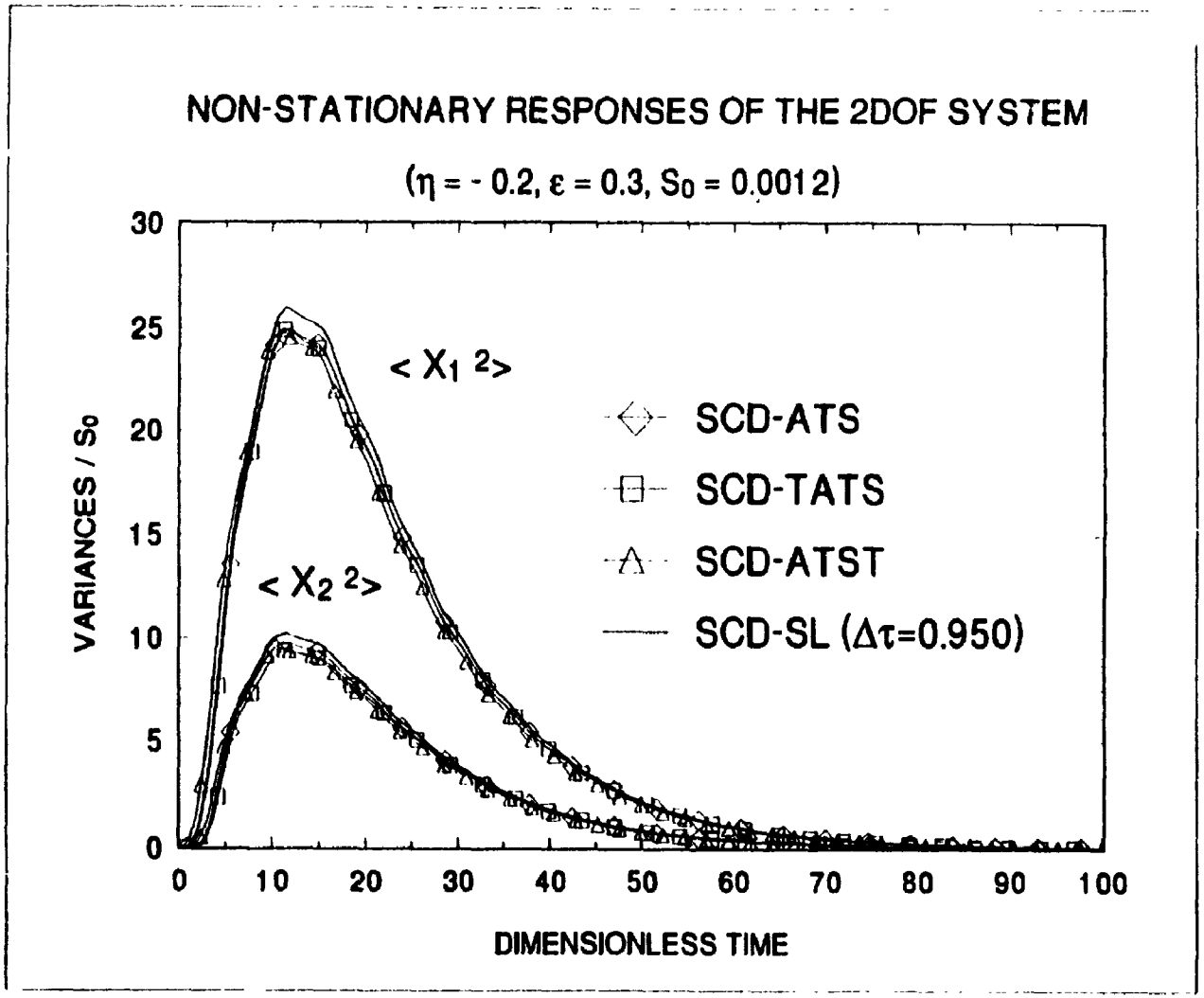

Figure 2.29 Non-stationary responses of the 2 DOF system ($\eta = -0.2, \varepsilon = 0.3$)

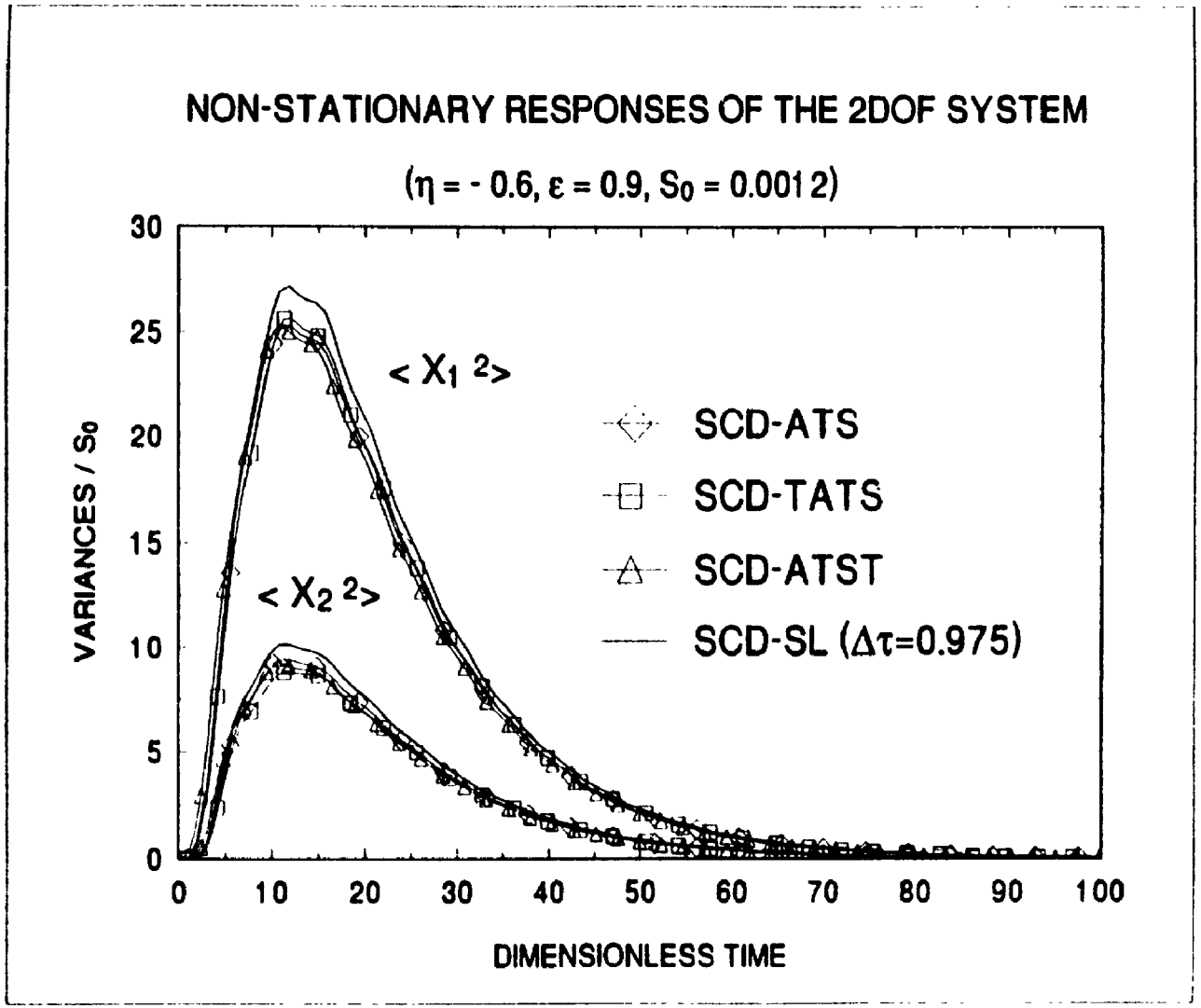

Figure 2.30 Non-stationary responses of the 2 DOF system ($\eta = -0.6, \varepsilon = 0.9$)

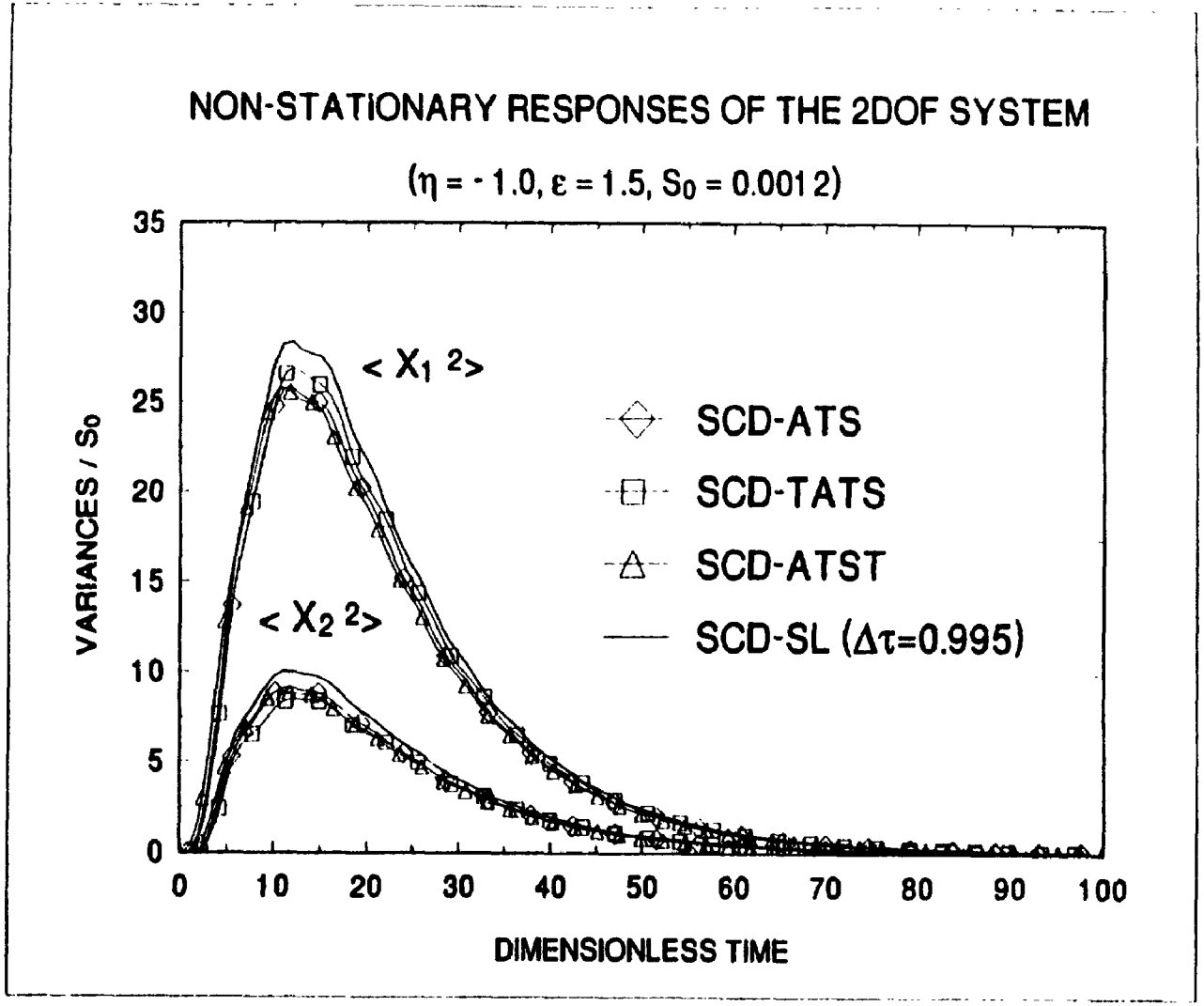

Figure 2.31 Non-stationary responses of the 2 DOF system ($\eta = -1.0, \varepsilon = 1.5$)

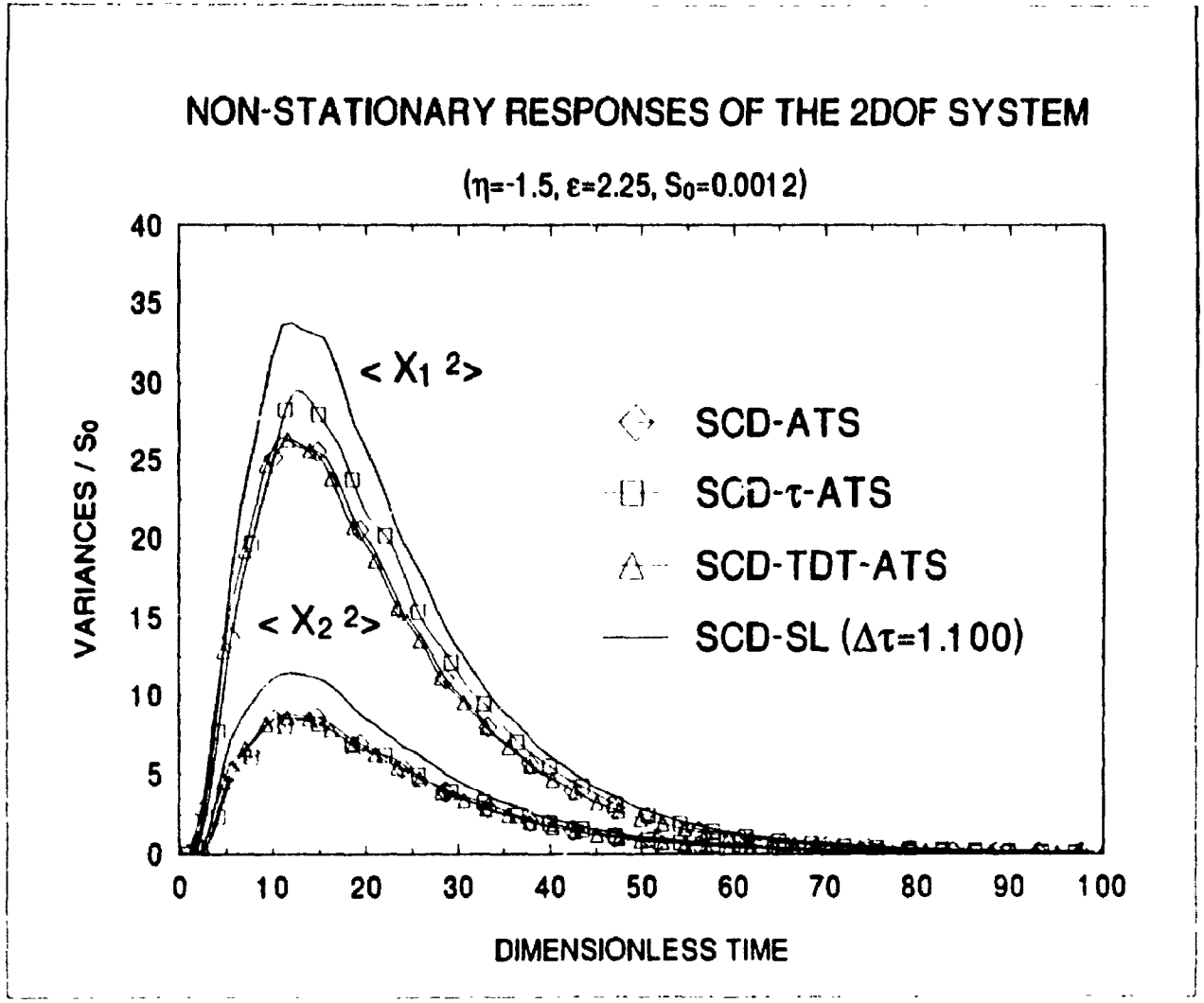

Figure 2.32 Non-stationary responses of the 2 DOF system ($\eta = -1.5, \varepsilon = 2.25$)

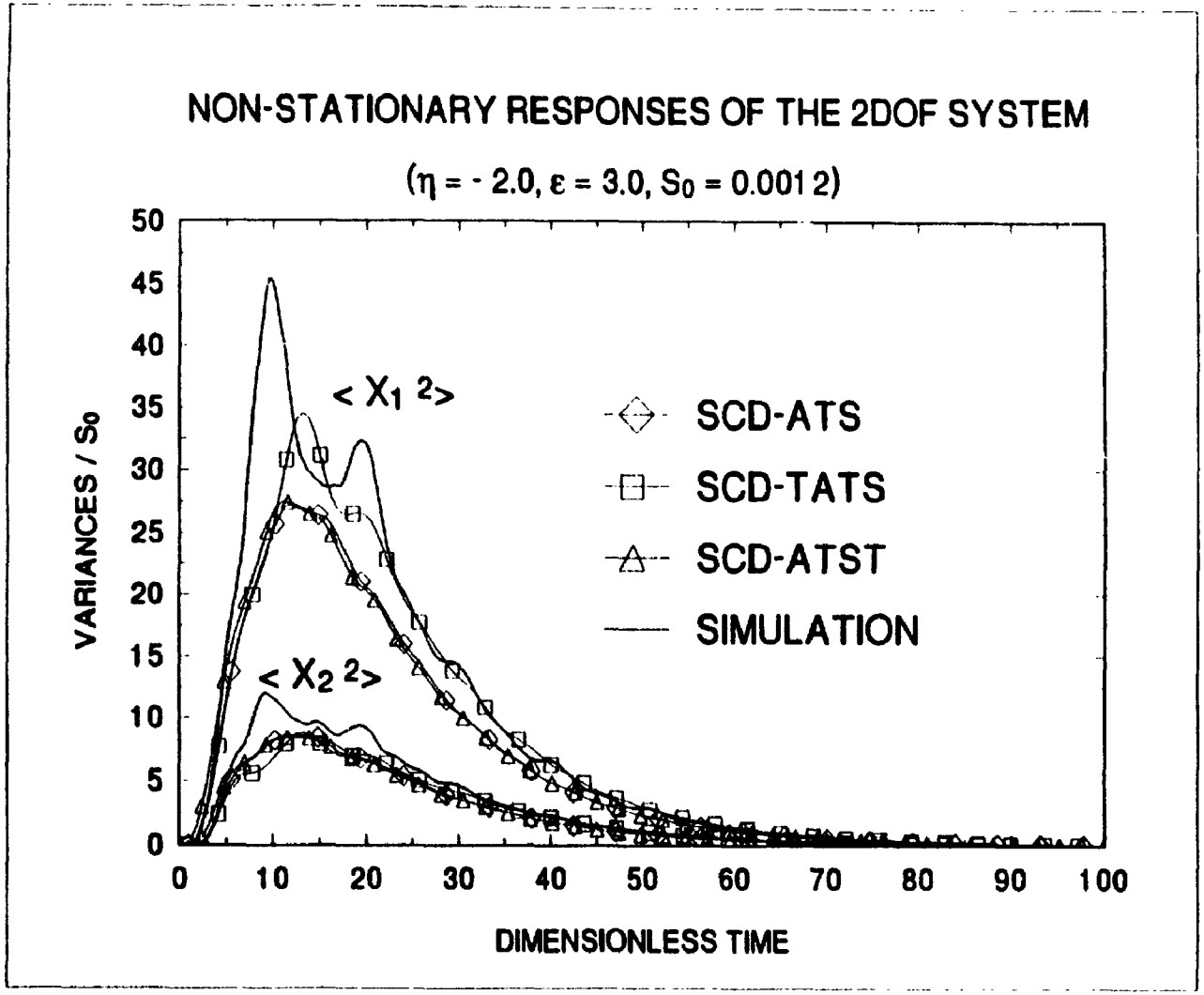

Figure 2.33 Non-stationary responses of the 2 DOF system ($\eta = -2.0, \varepsilon = 3.0$)

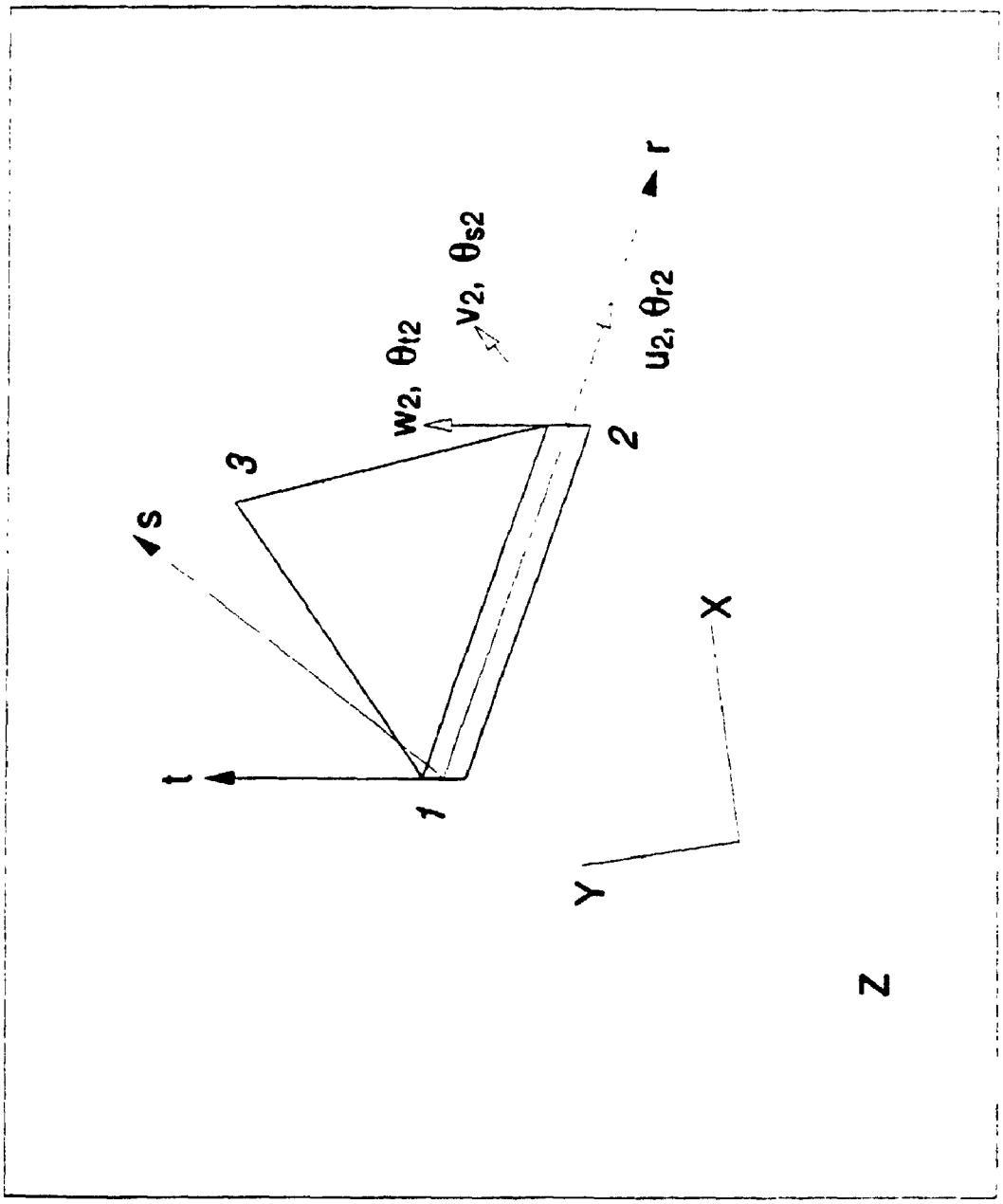

Figure 3.1 A representative 3 node flat triangular shell element

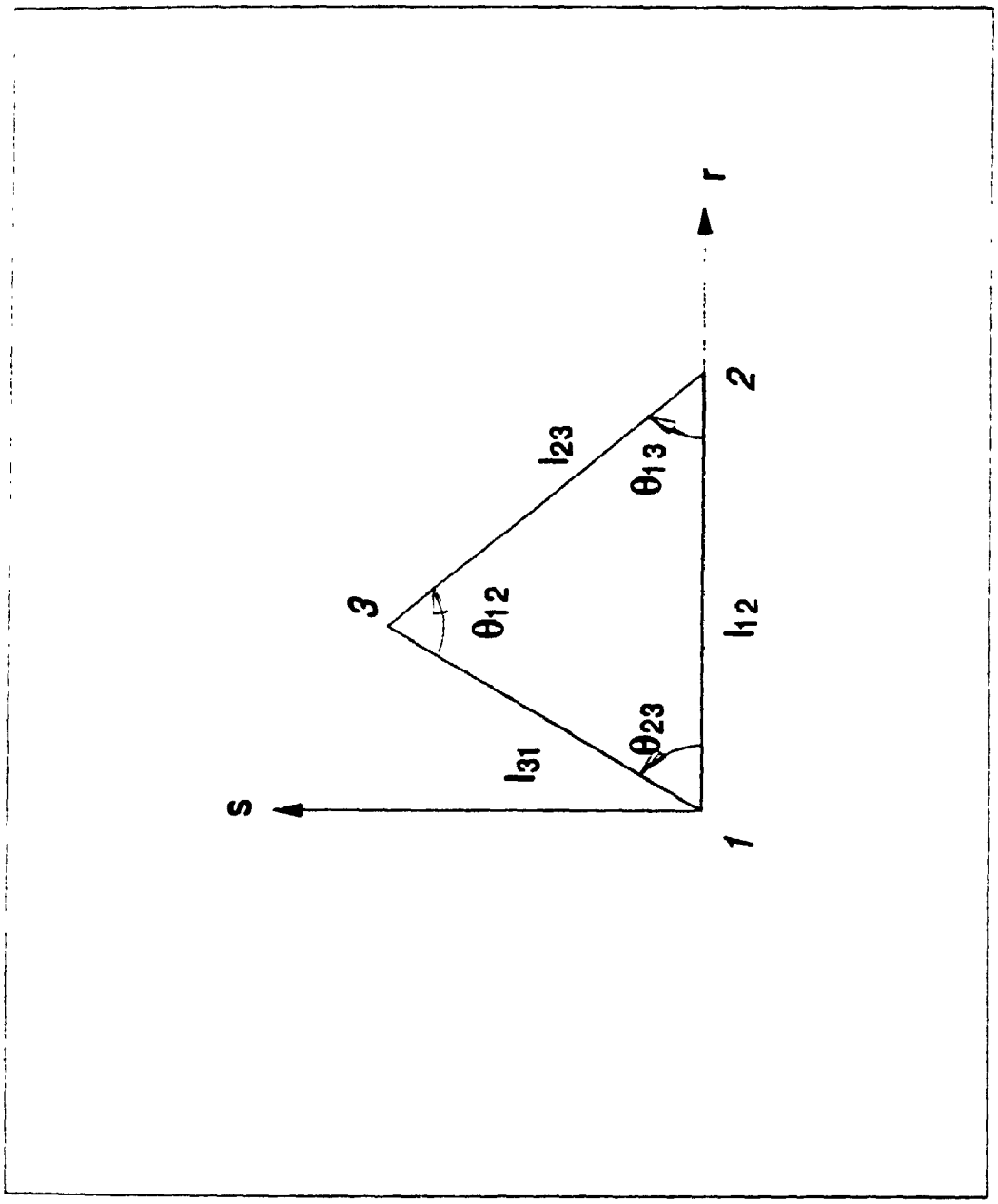

Figure 3.2 The geometry of the shell element

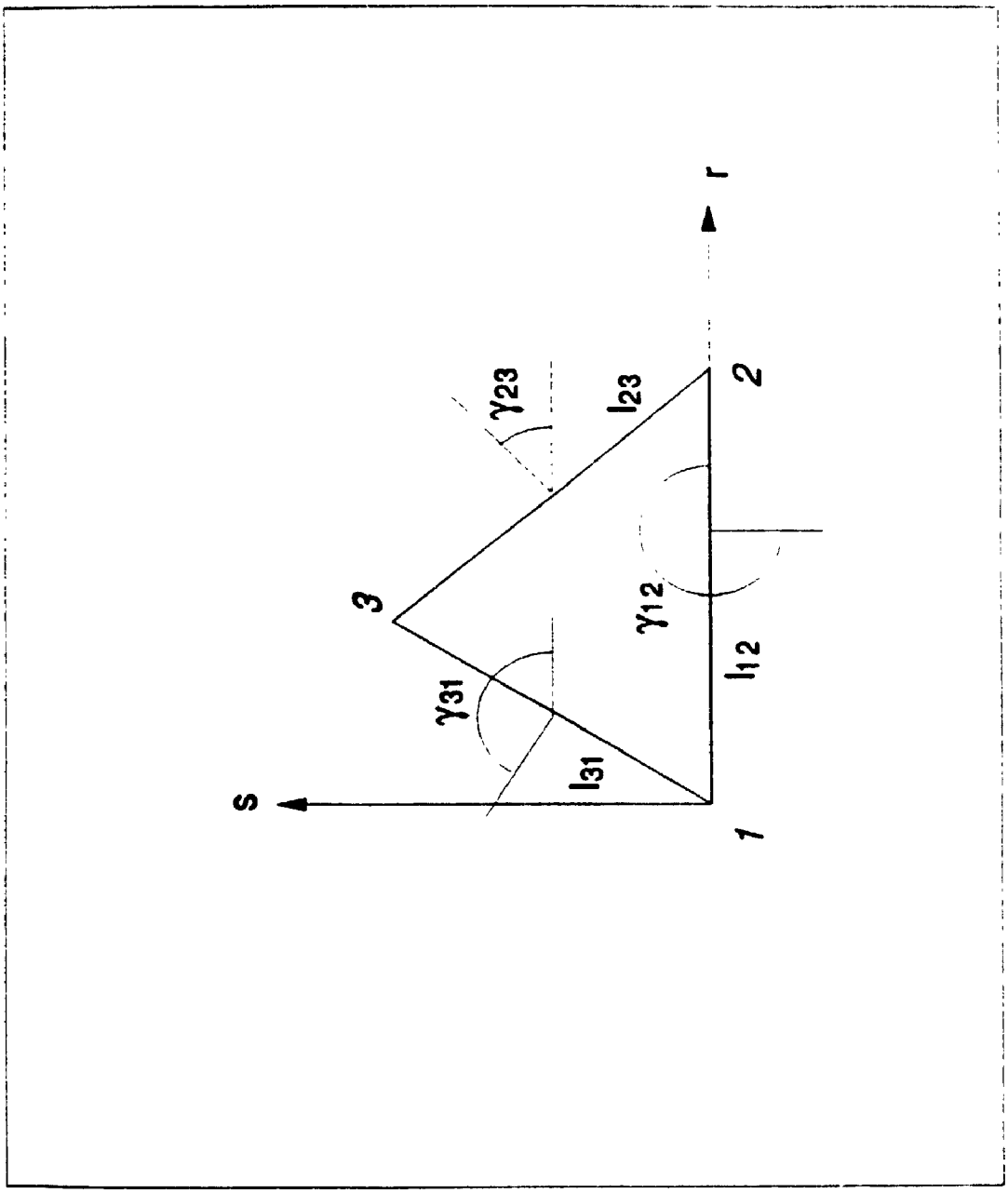

Figure 3.3 The geometry of the shell element

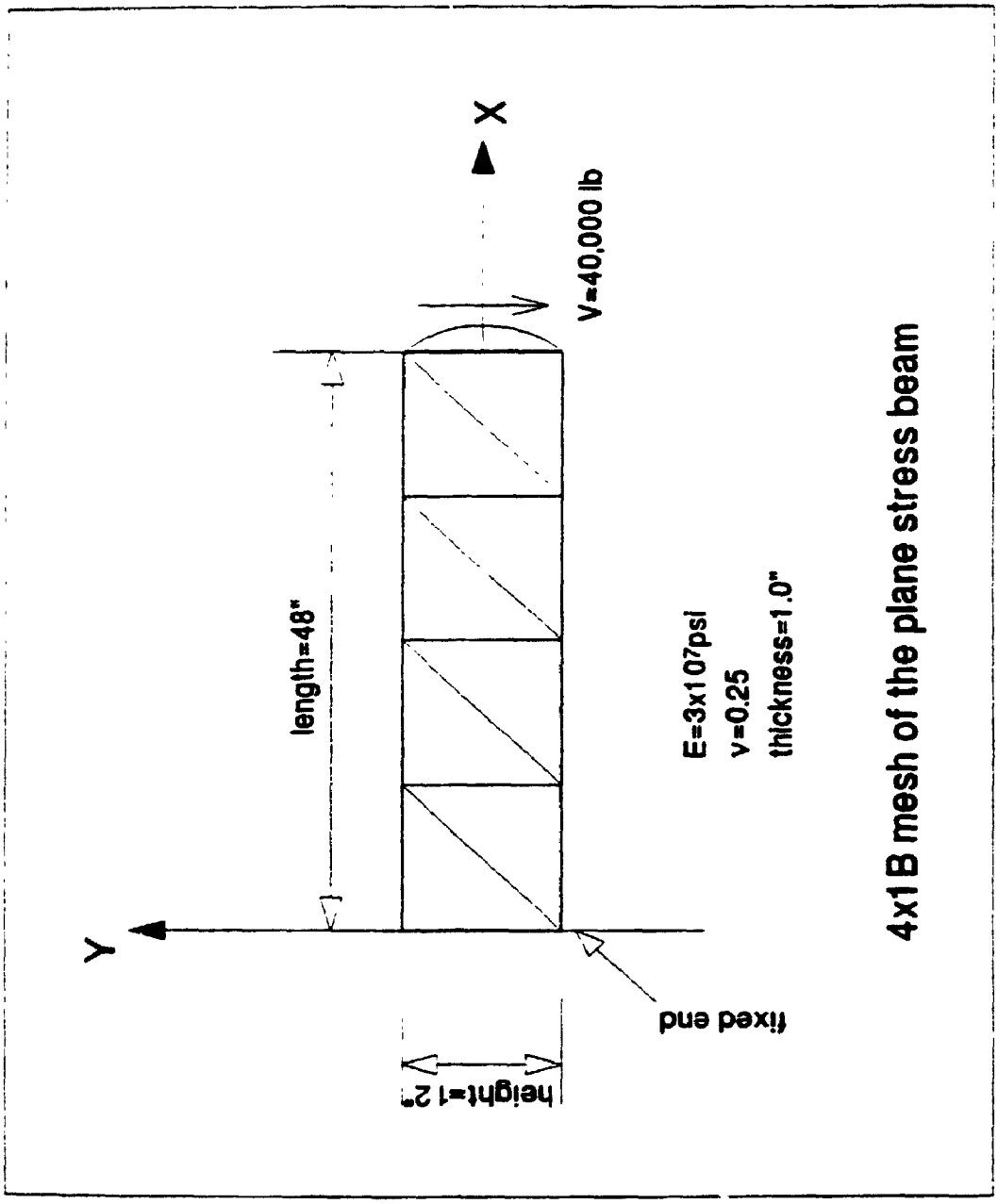

Figure 4.1 4 × 1 B mesh of the plane stress beam

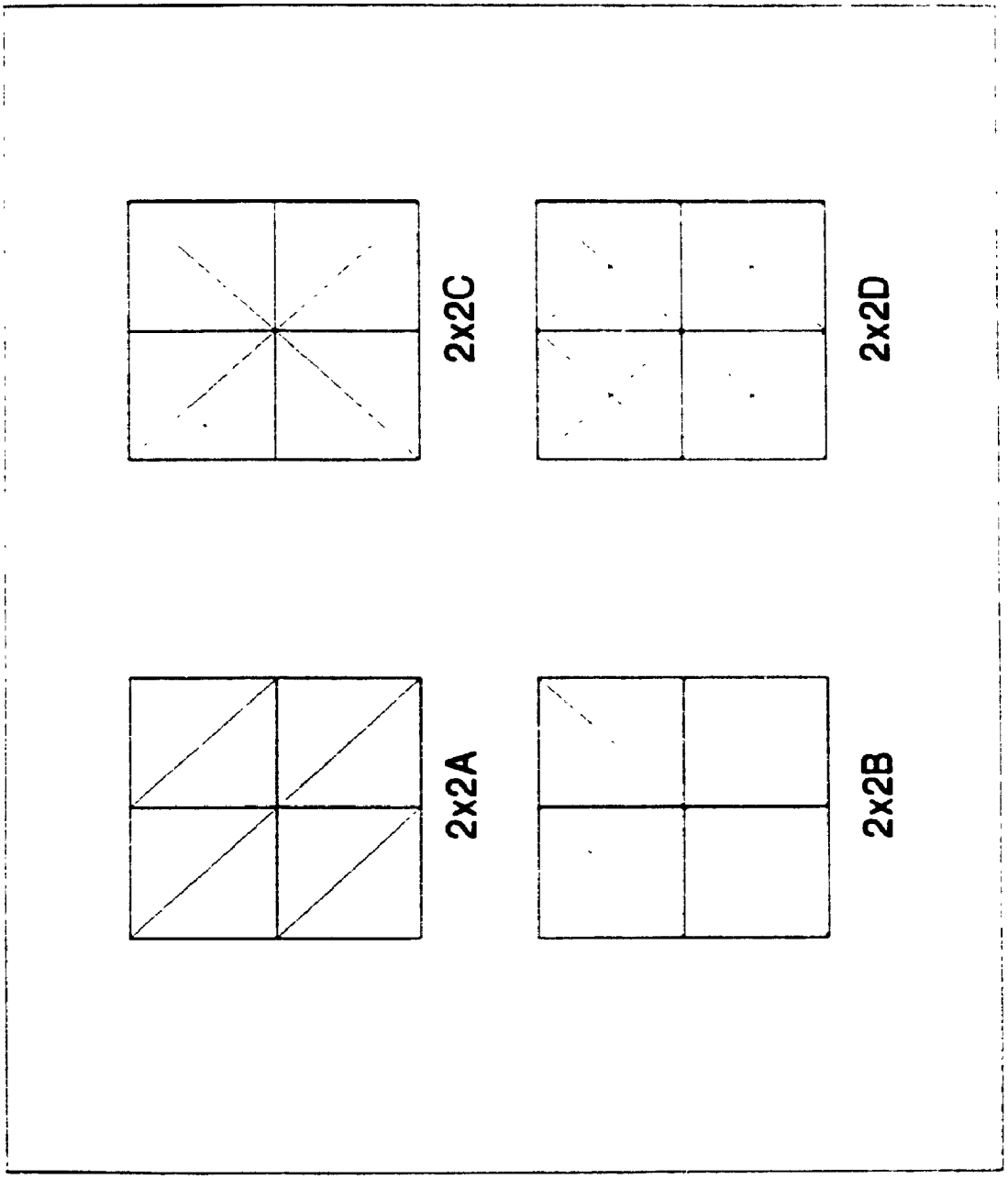

Figure 4.2 The four types of mesh layout

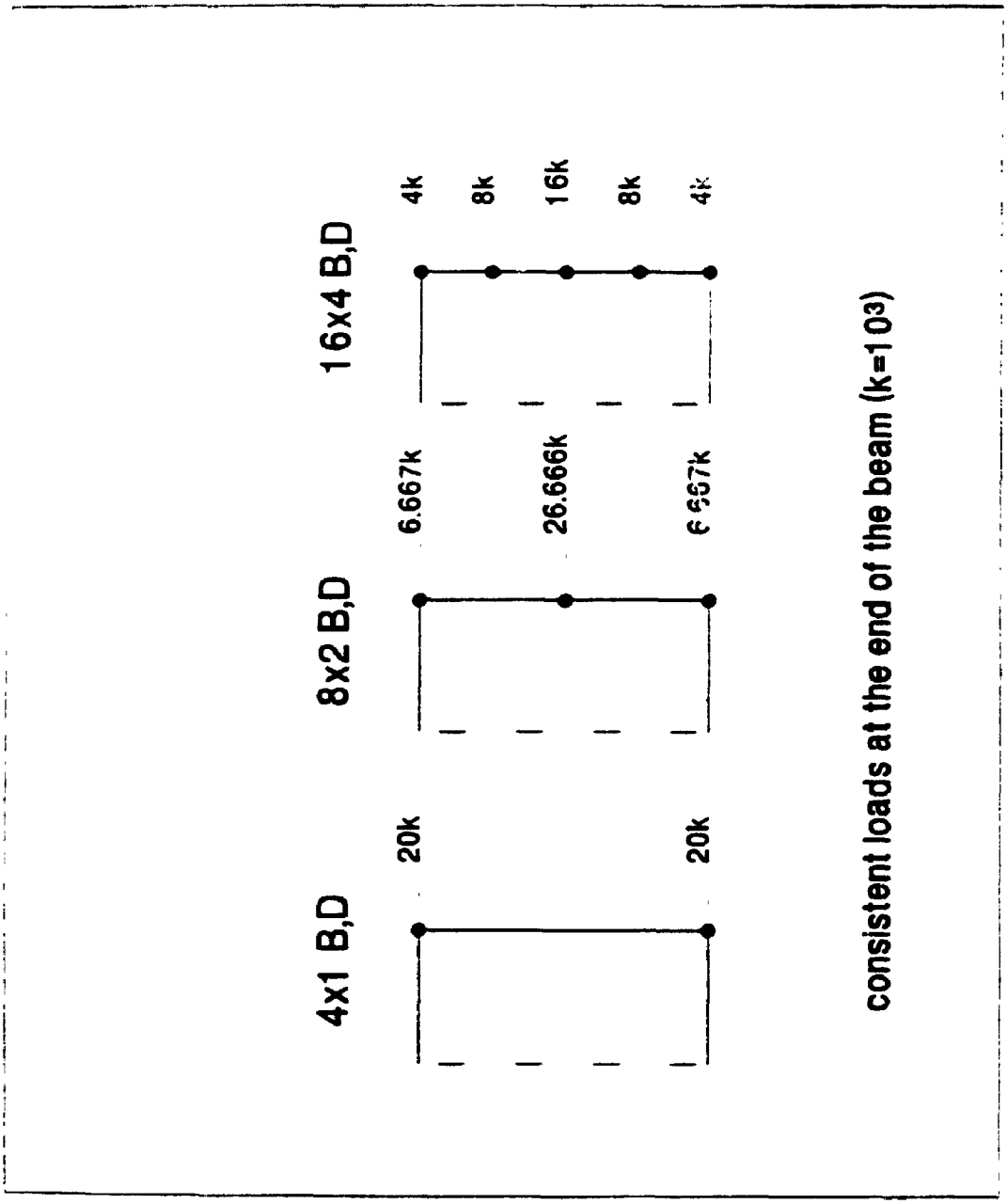

Figure 4.3 Consistent loads at the end of the plane stress beam

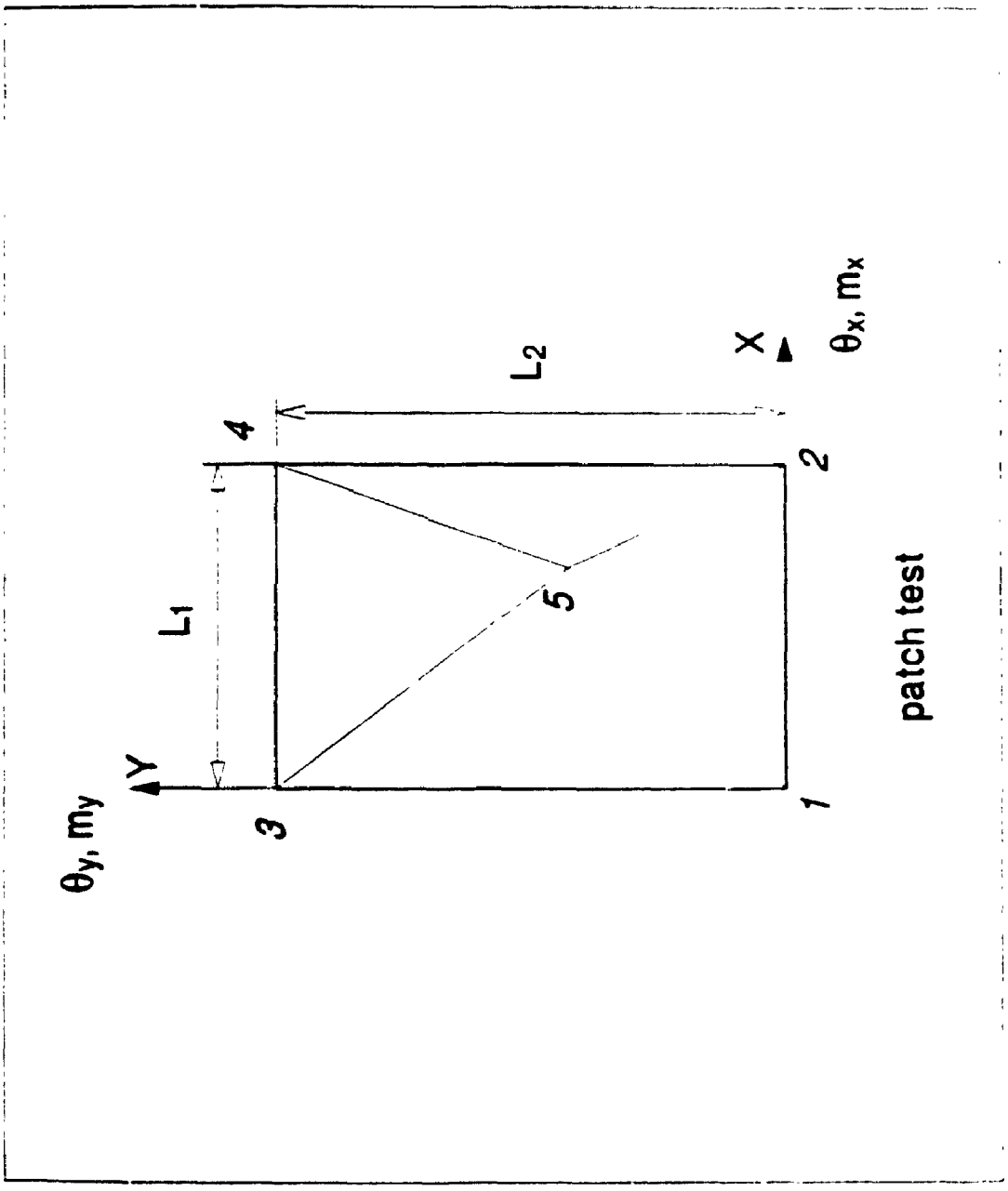

Figure 4.4 Patch test for bending

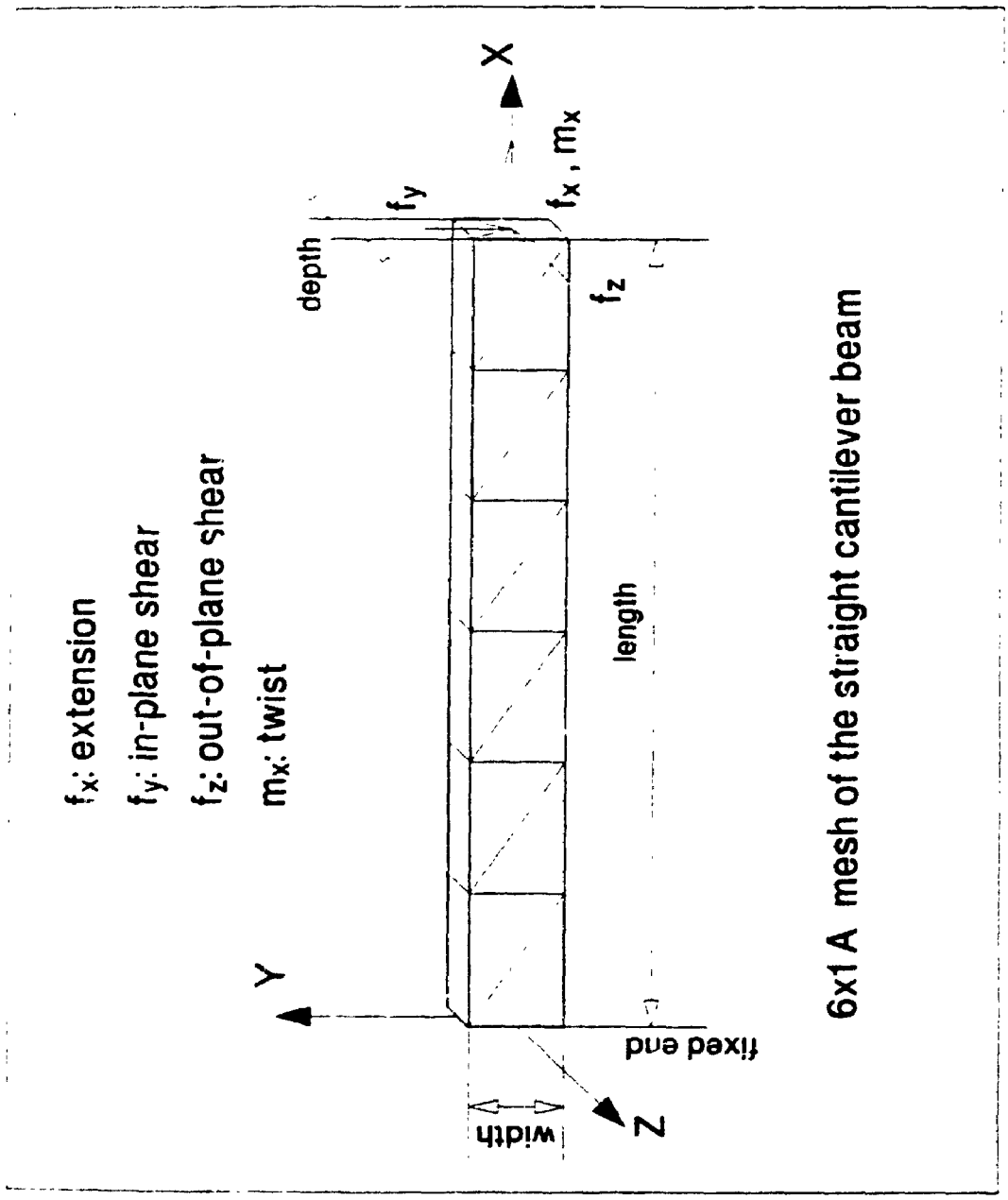

Figure 4.5 6×1 A mesh of the straight cantilever beam

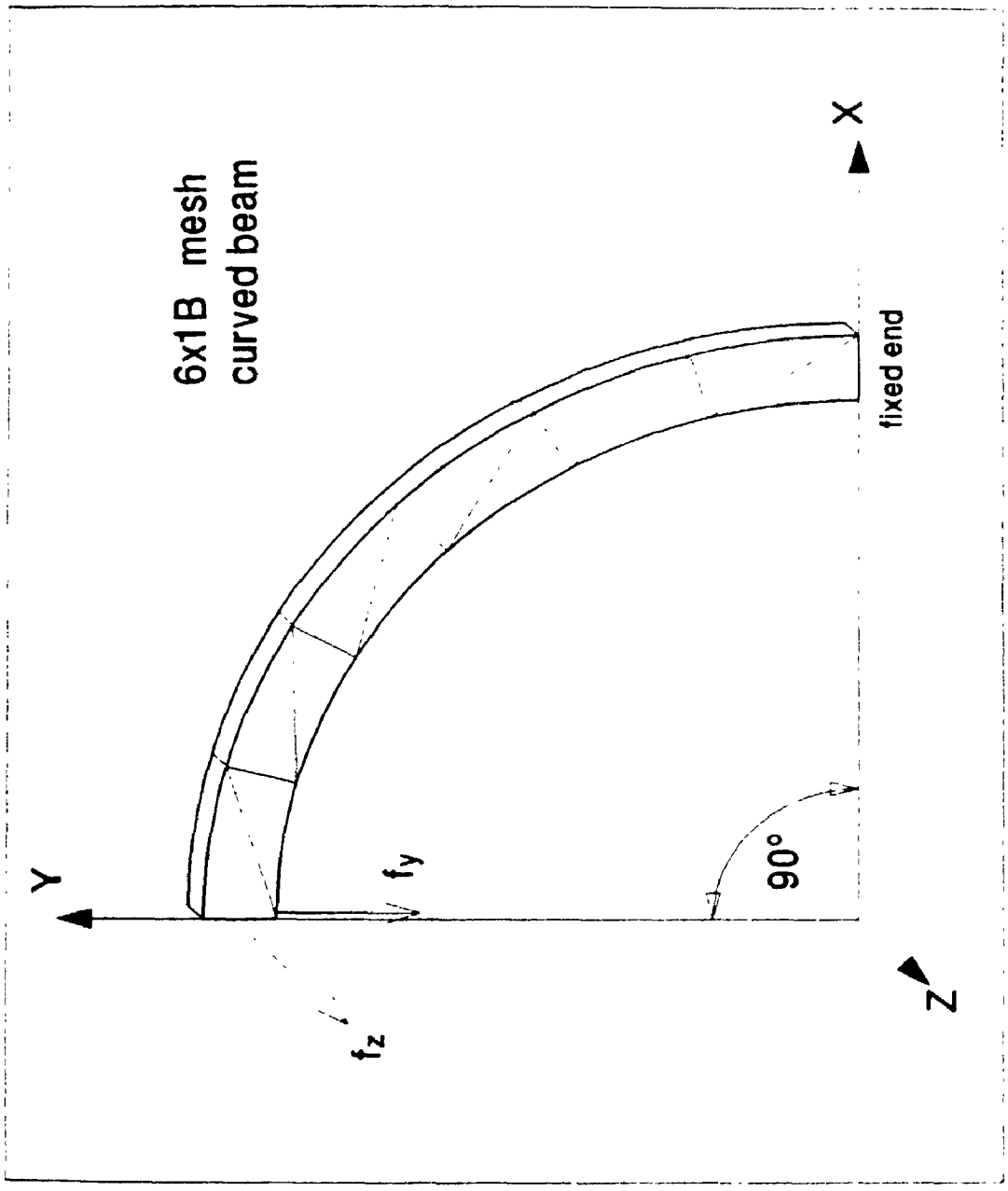

Figure 4.6 6×1 B mesh of the curved beam

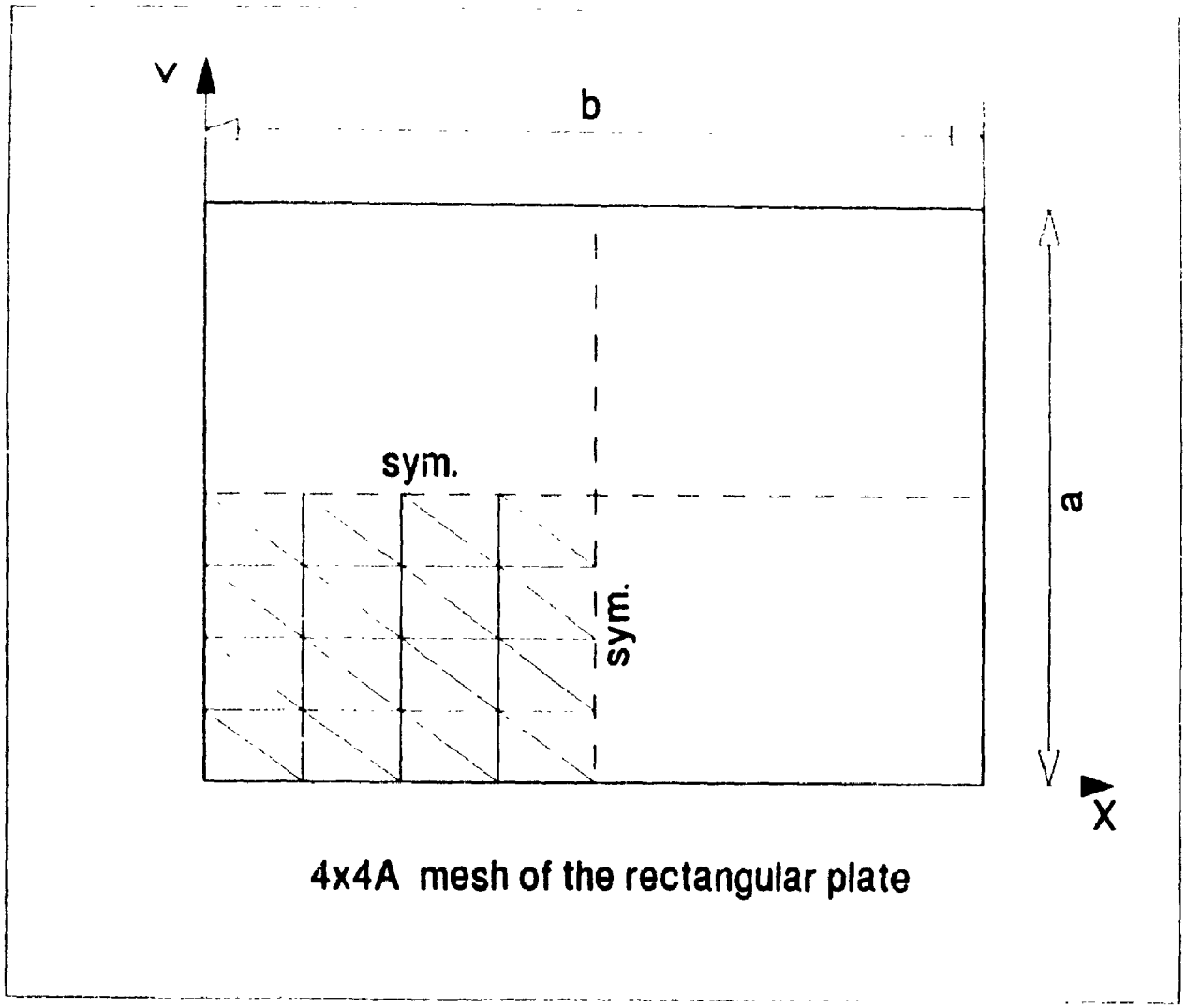

Figure 4.7 4×4 A mesh of the rectangular plate

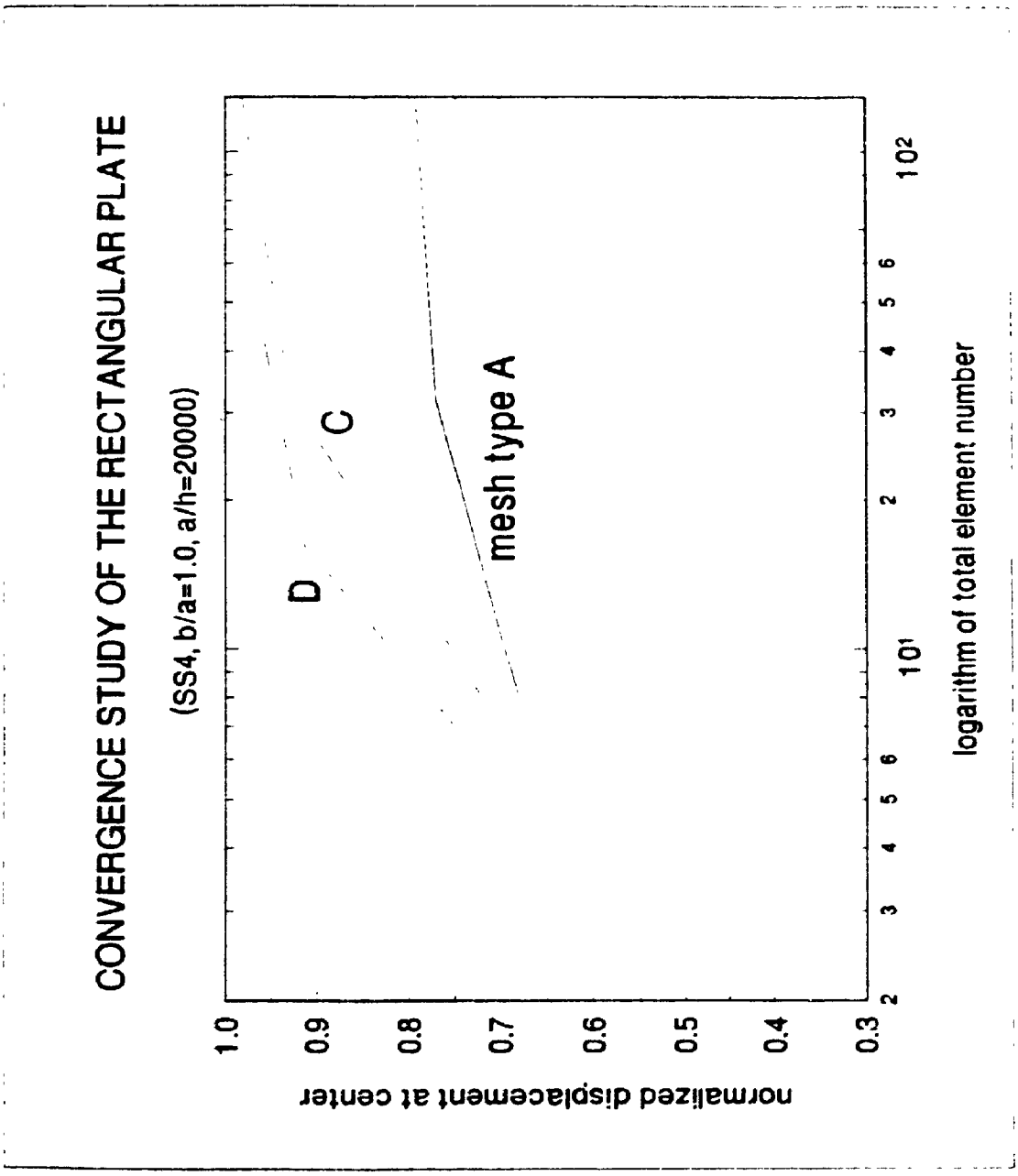

Figure 4.8 Convergence study of the rectangular plate (SS4, b/a = 1.0, a/h = 20000.0)

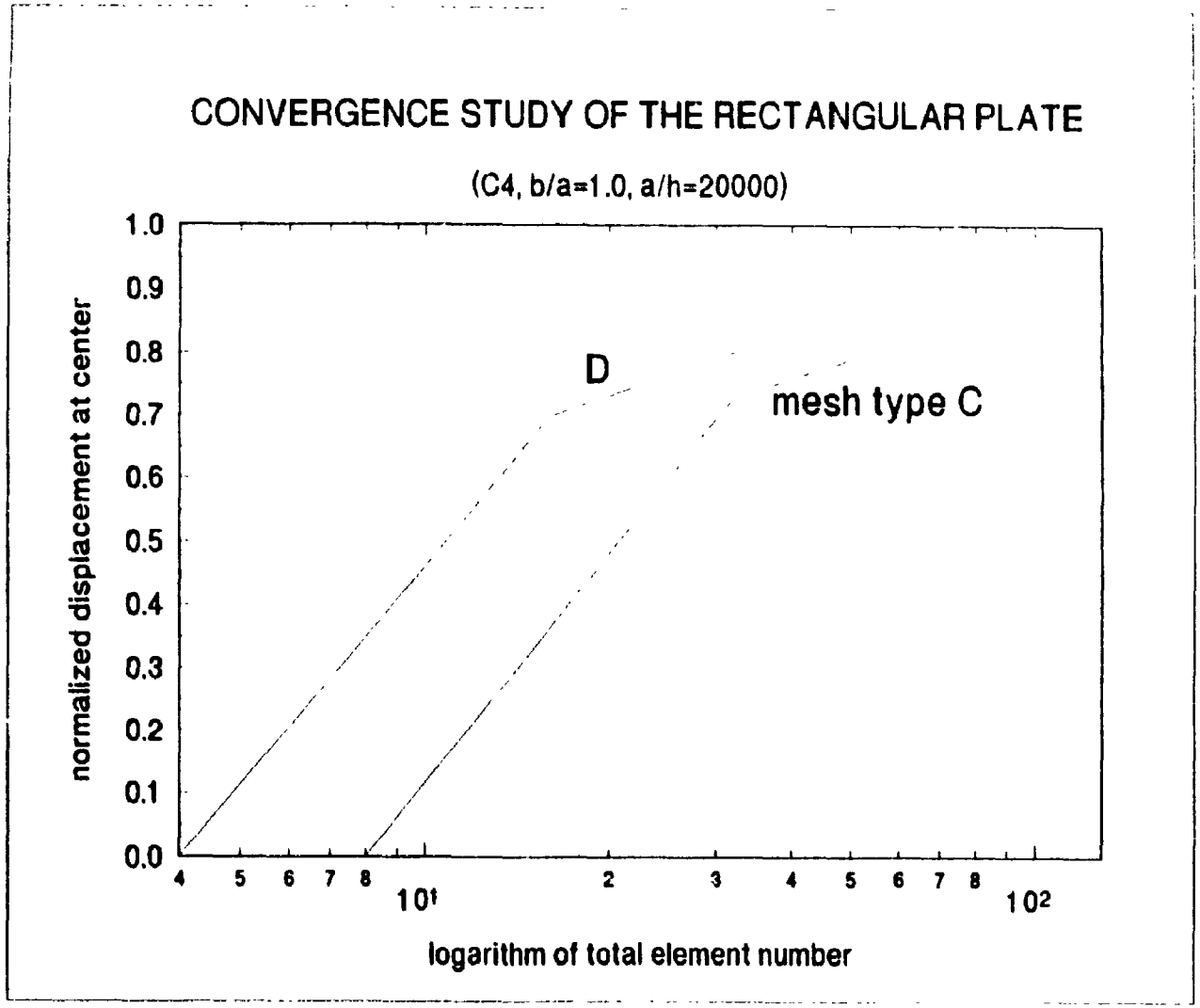

Figure 4.9 Convergence study of the rectangular plate (C4, b/a=1.0, a/h=20000.0)

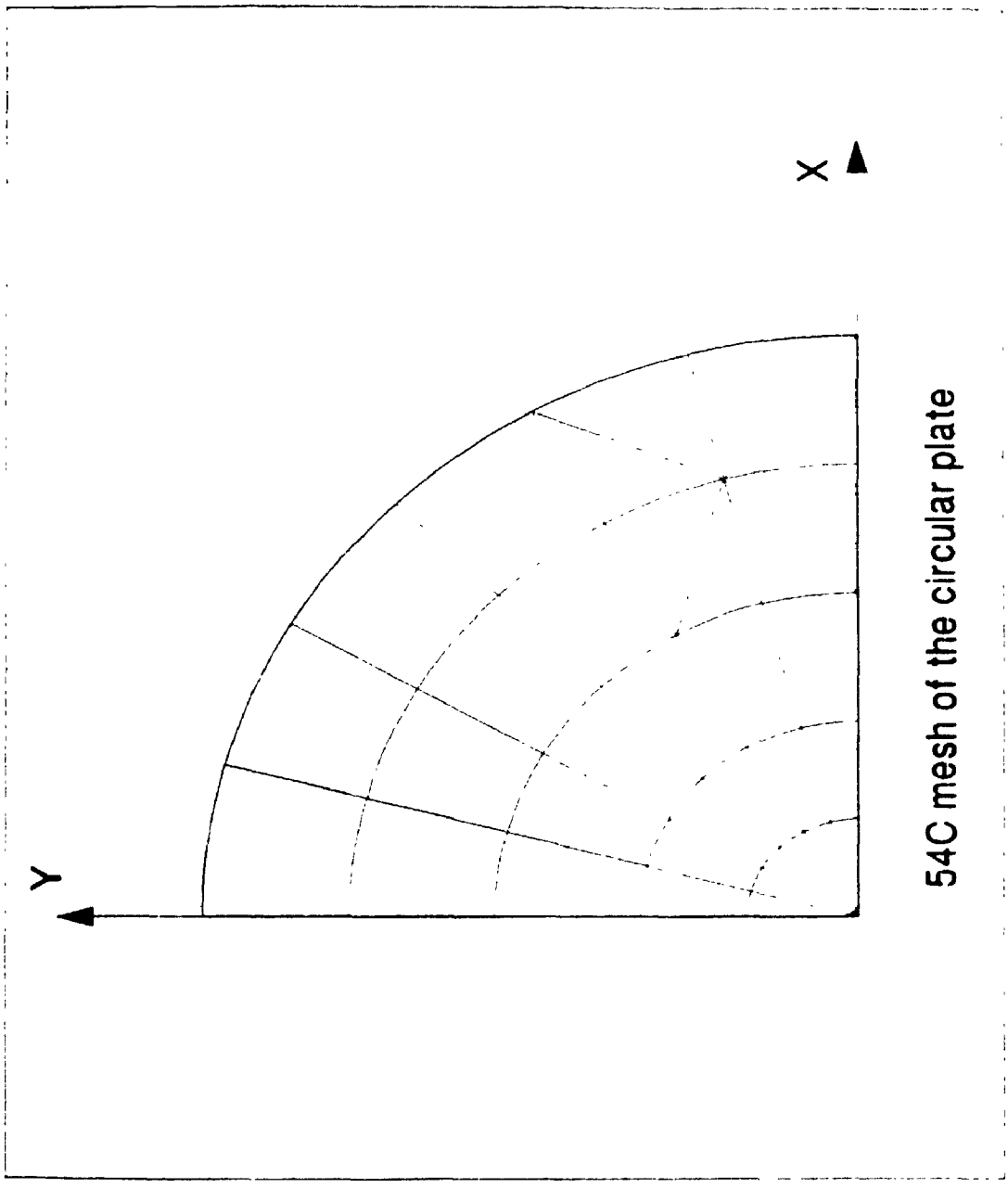

Figure 4.10 54 C mesh of the circular plate

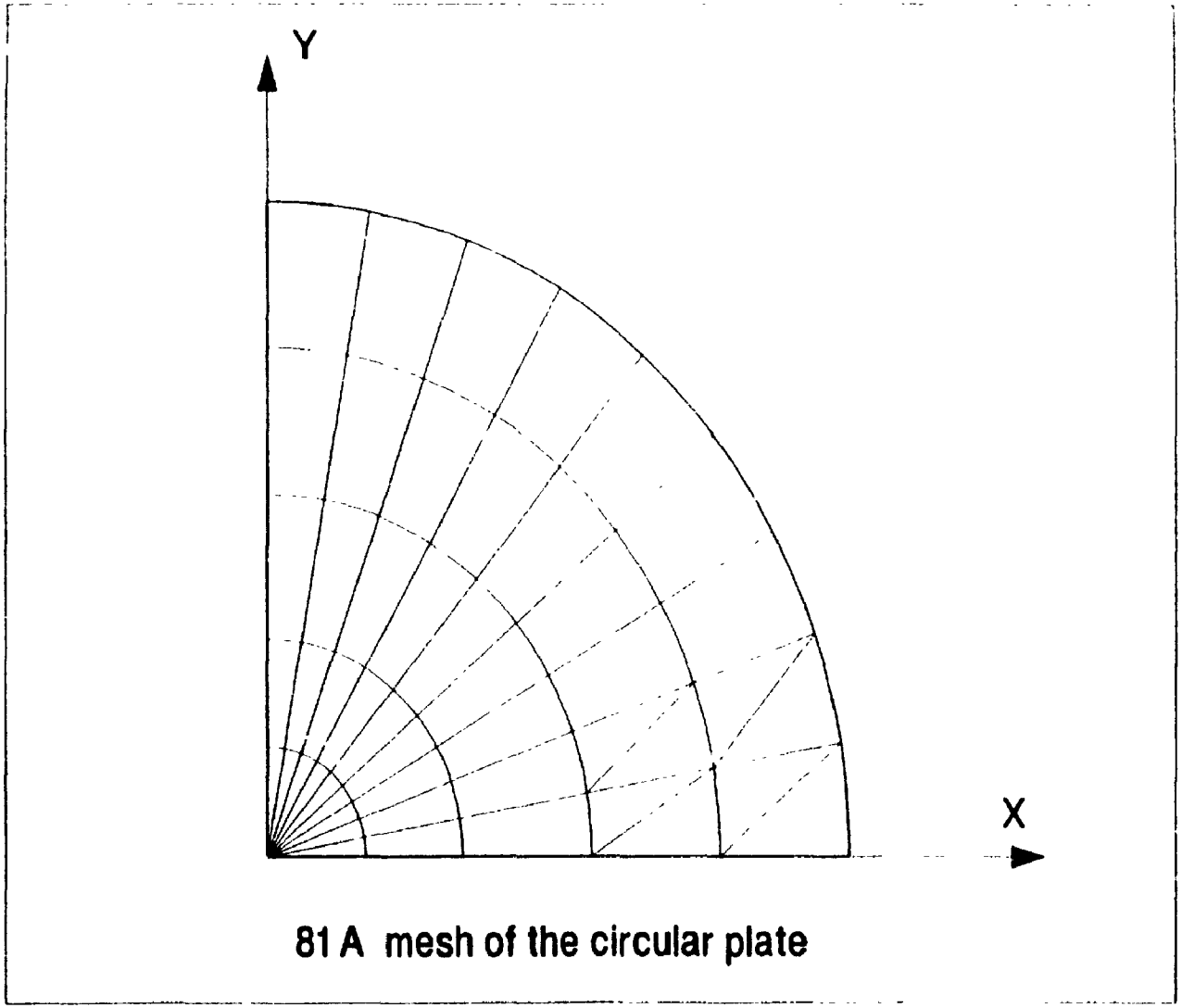

Figure 4.11 81 A mesh of the circular plate

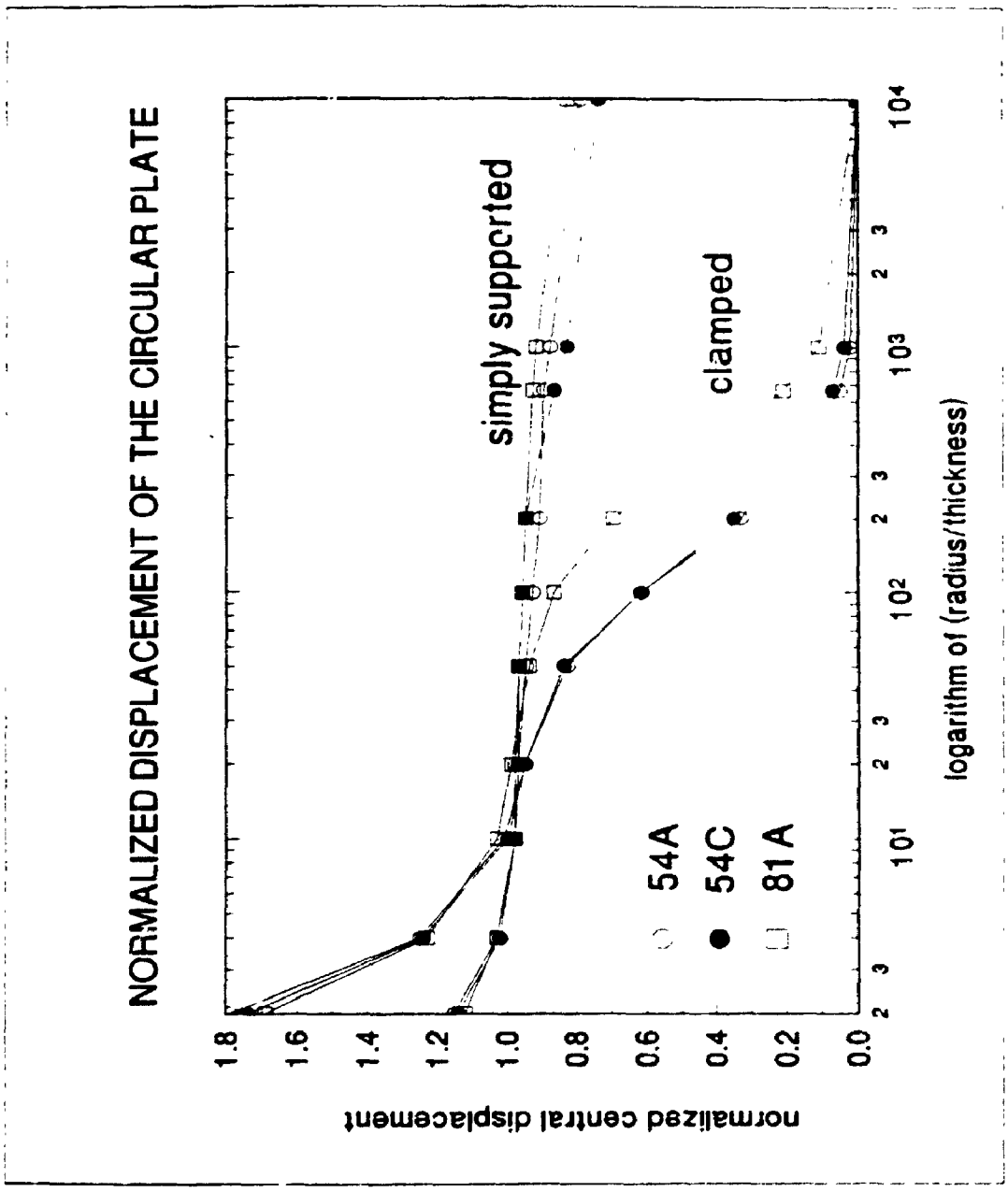

Figure 4.12 Normalized displacement of the circular plate

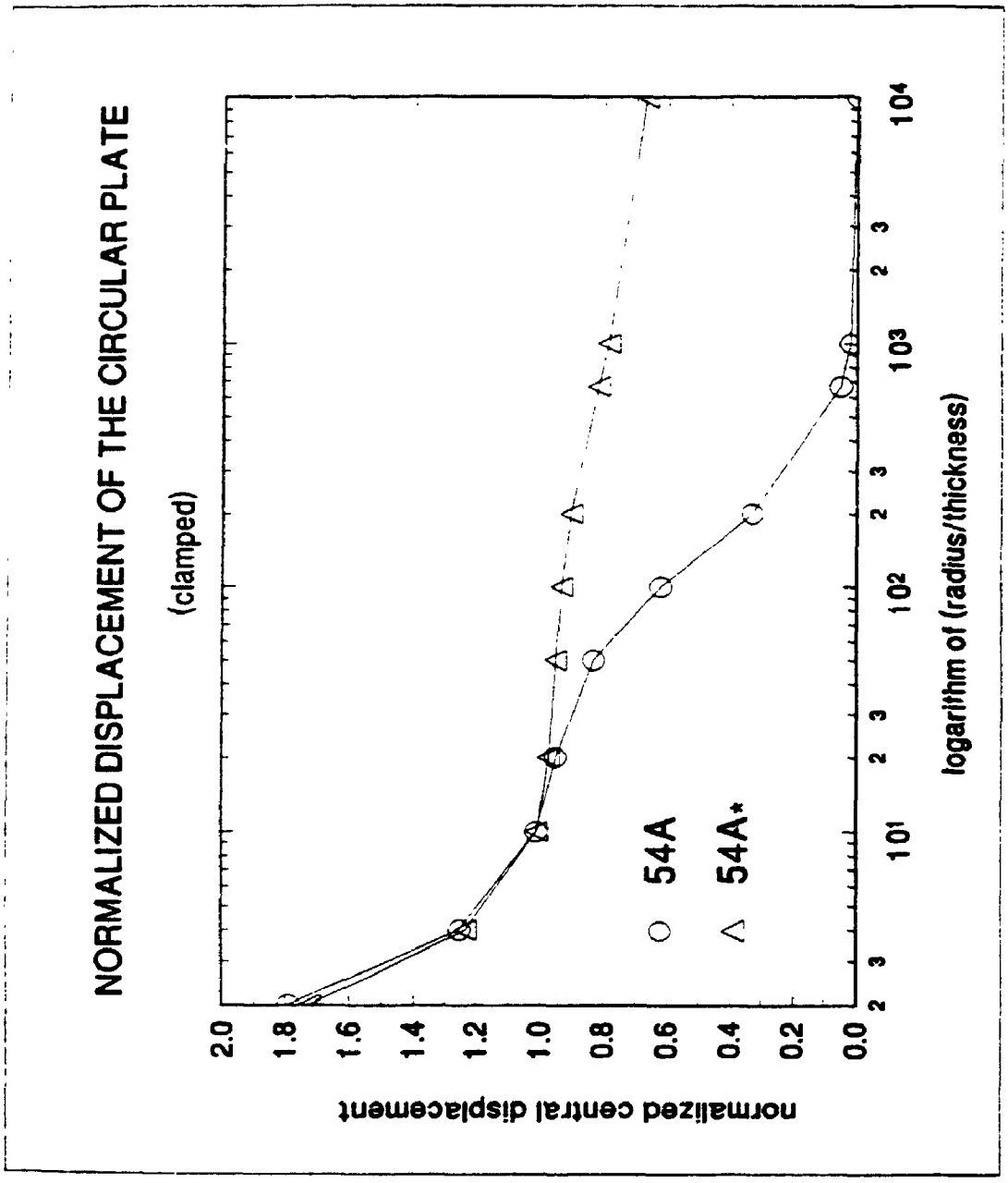

Figure 4.13 Normalized displacement of the clamped circular plate

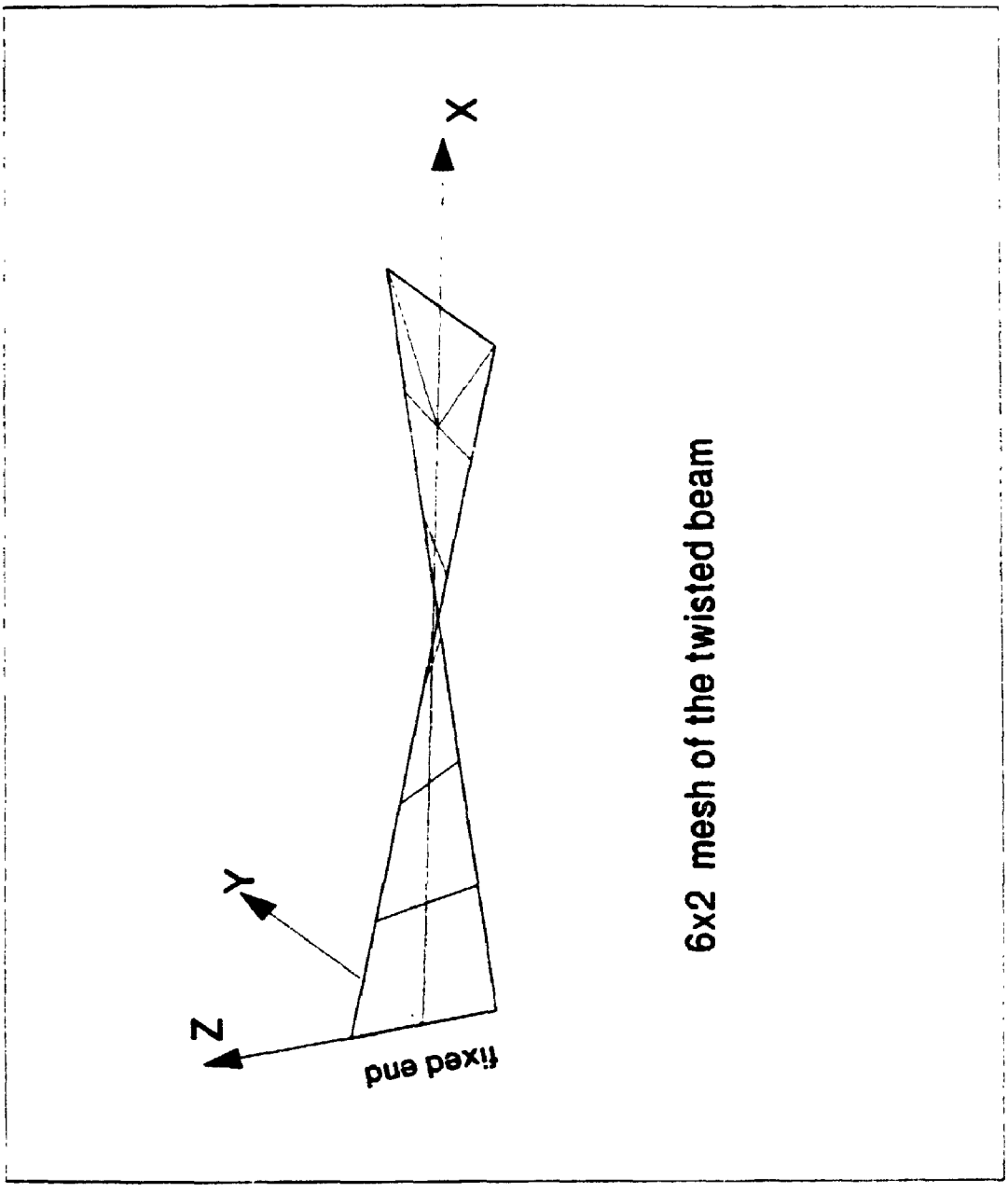

Figure 4.14 6×2 mesh of the twisted beam

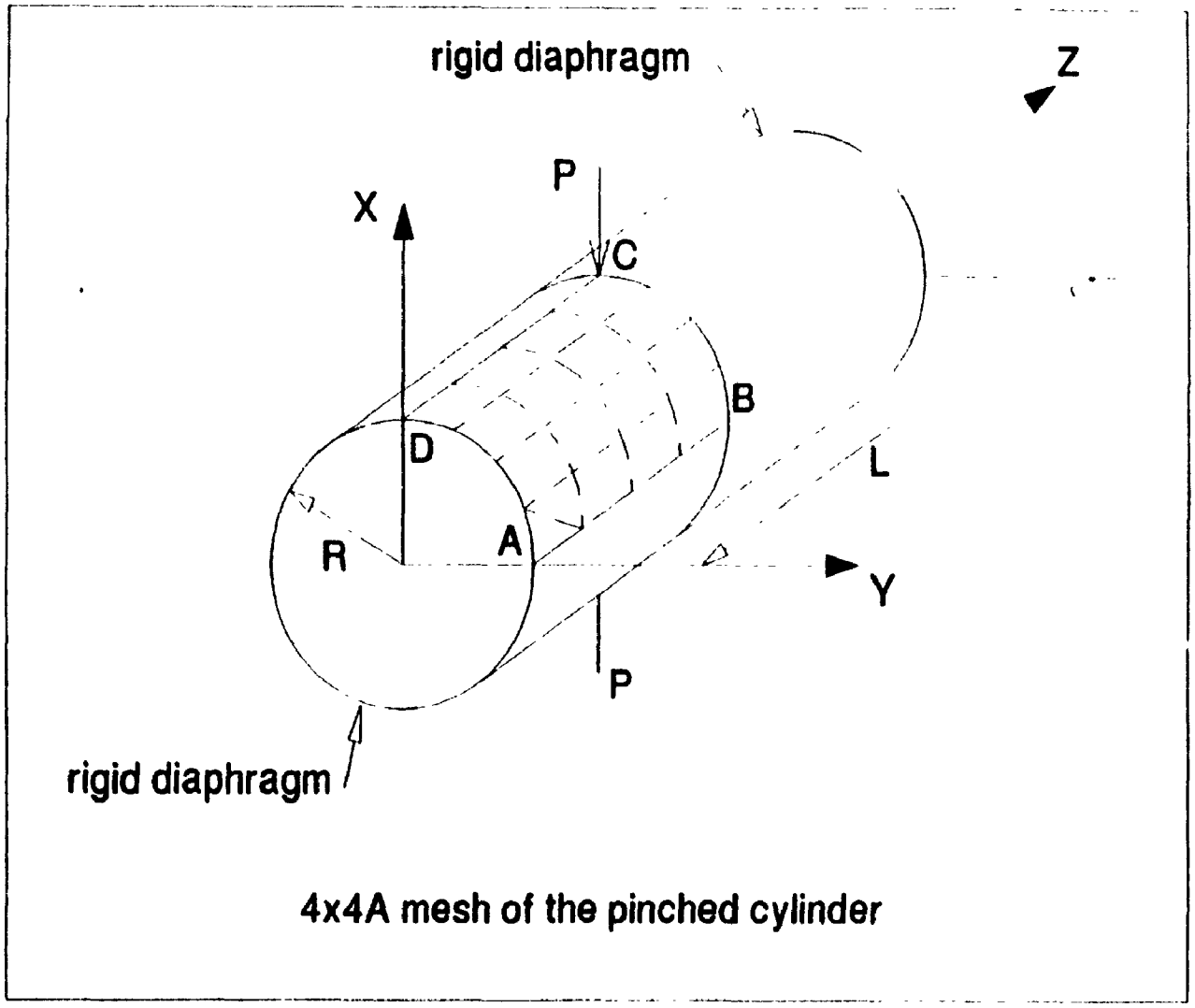

Figure 4.15 4×4 A mesh of the pinched cylinder

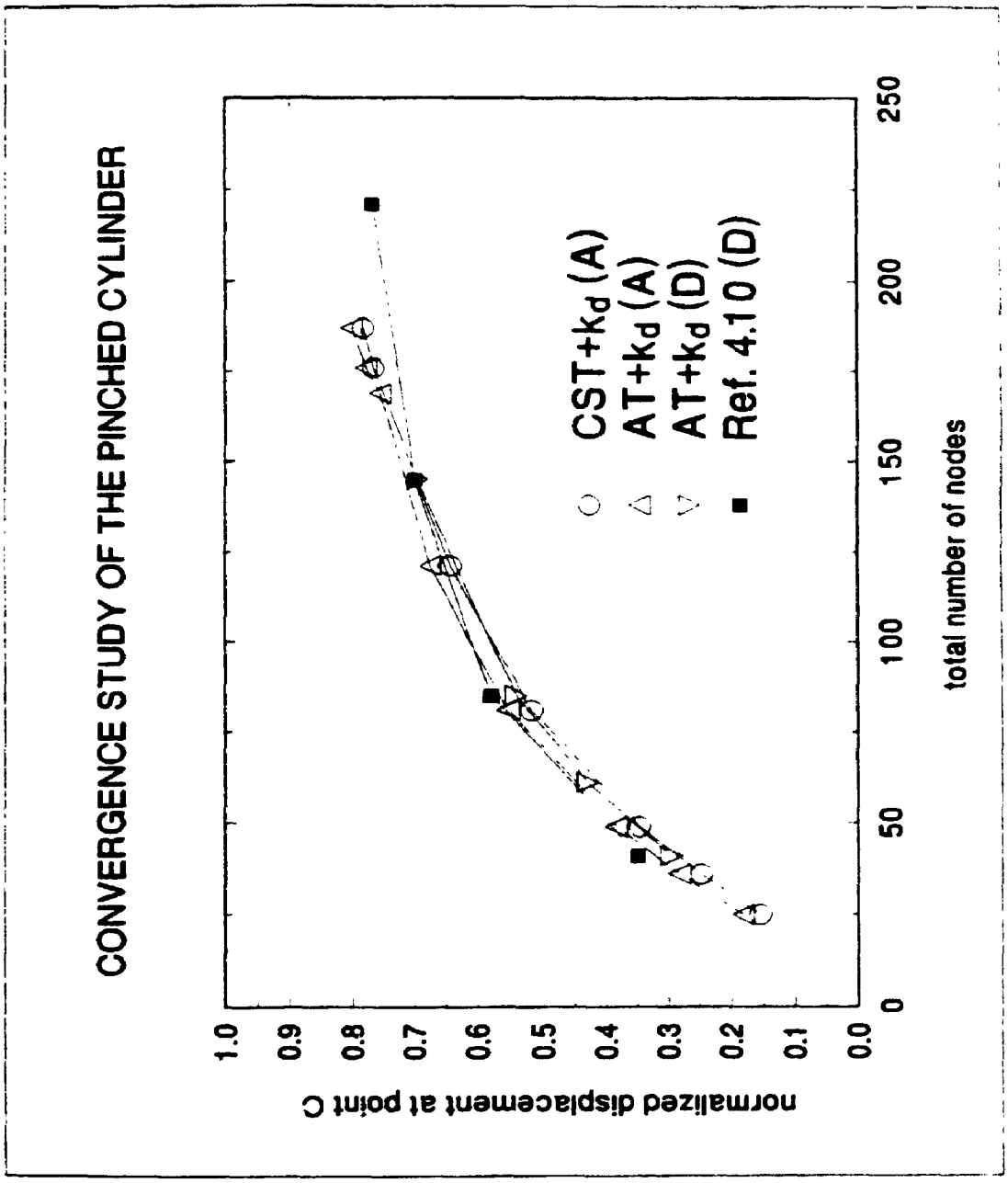

Figure 4.16 Convergence study of the pinched cylinder

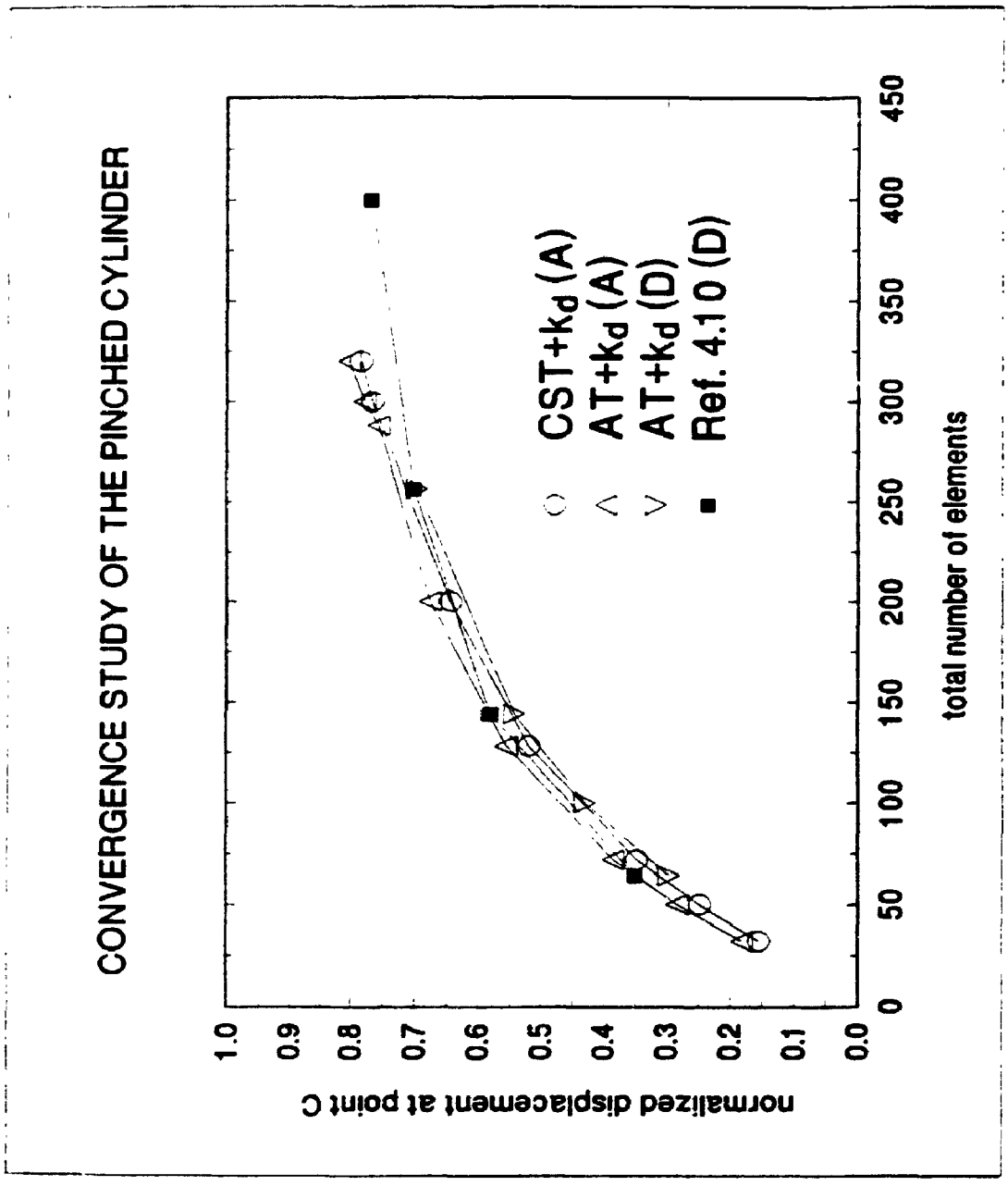

Figure 4.17 Convergence study of the pinched cylinder

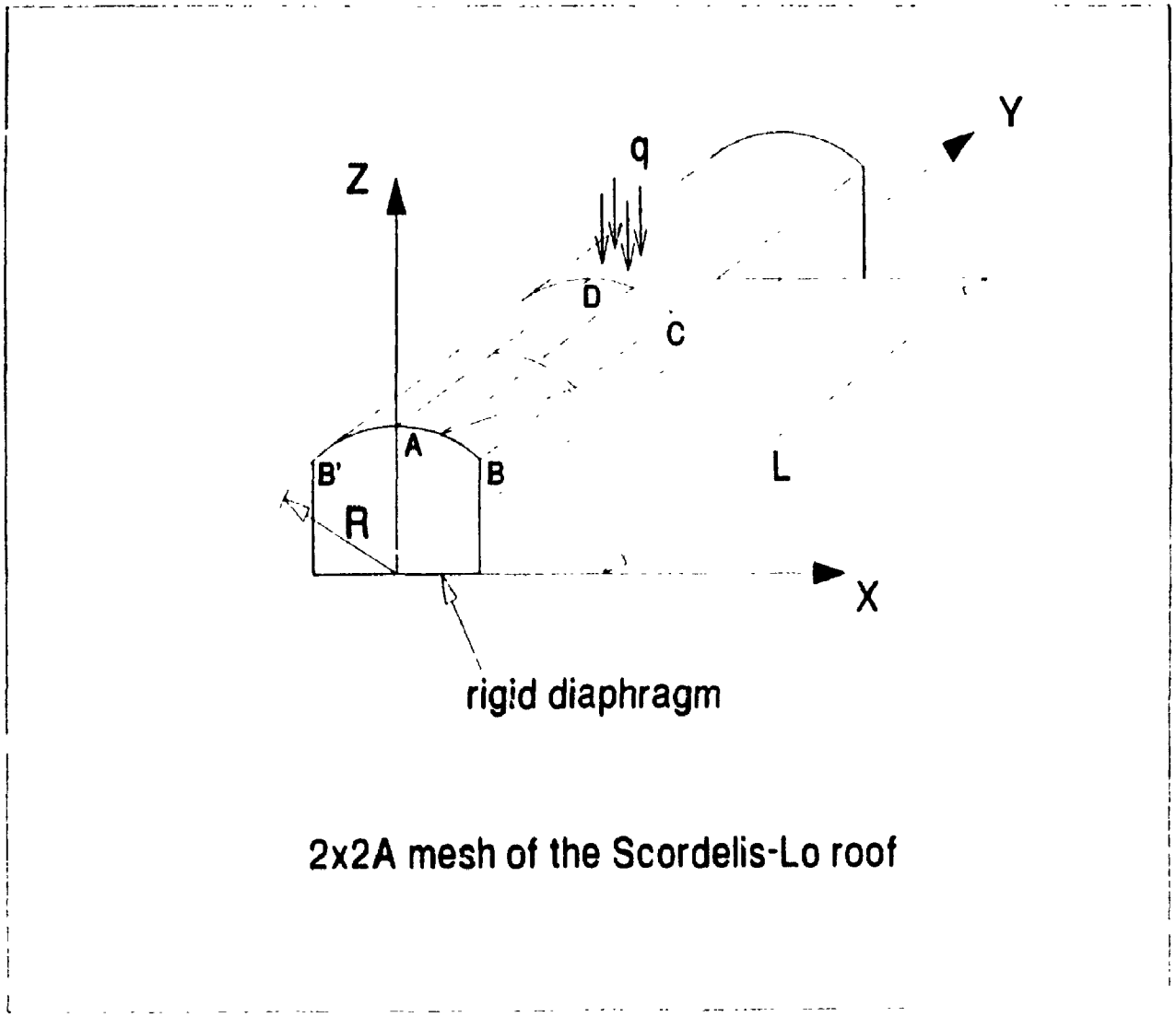

Figure 4.18 2×2 A mesh of the Scordelis-Lo roof

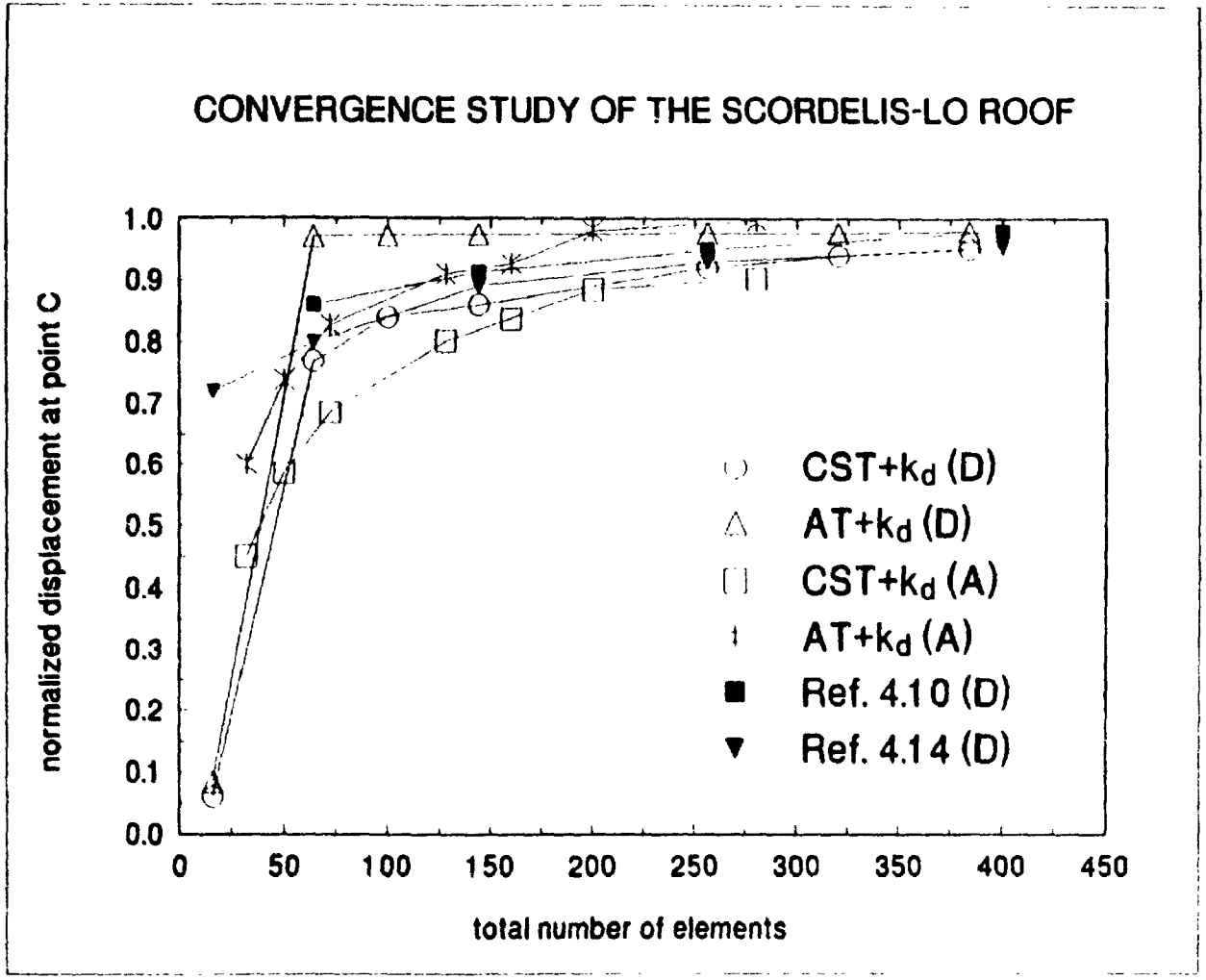

Figure 4.19 Convergence study of the Scordelis-Lo roof

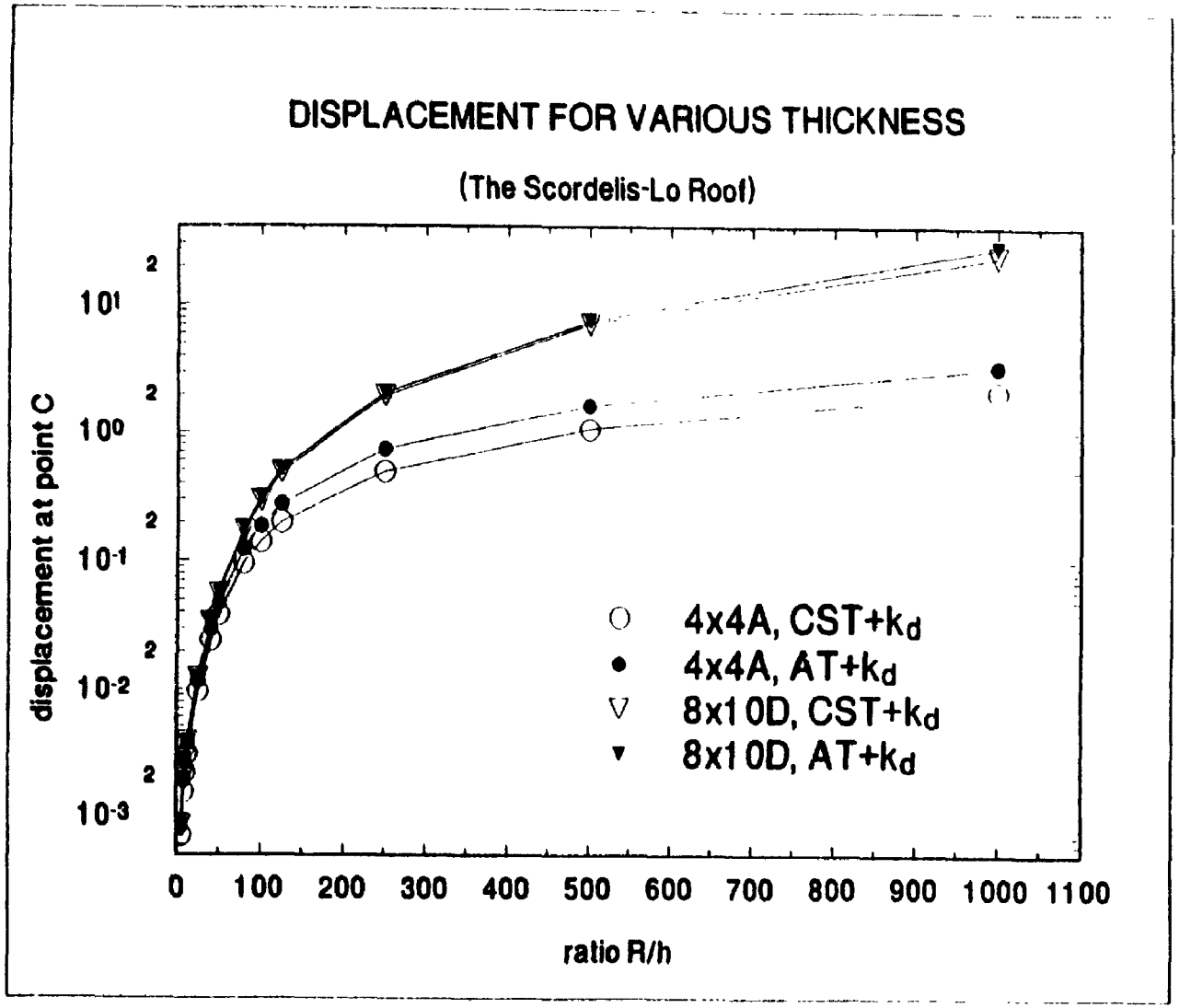

Figure 4.20 Displacement for various thickness of the Scordelis-Lo roof

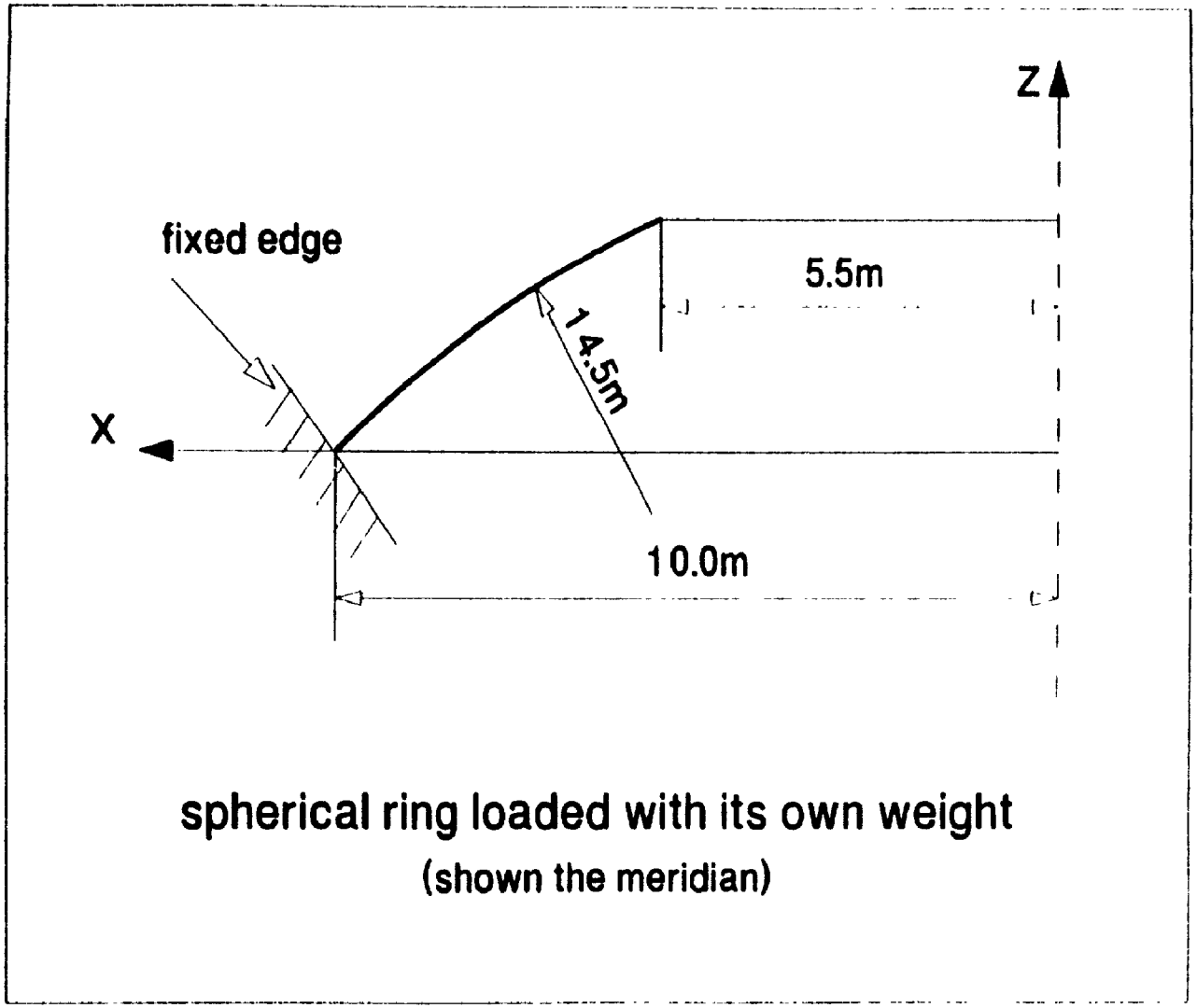

Figure 4.21 The spherical ring loaded with its own weight

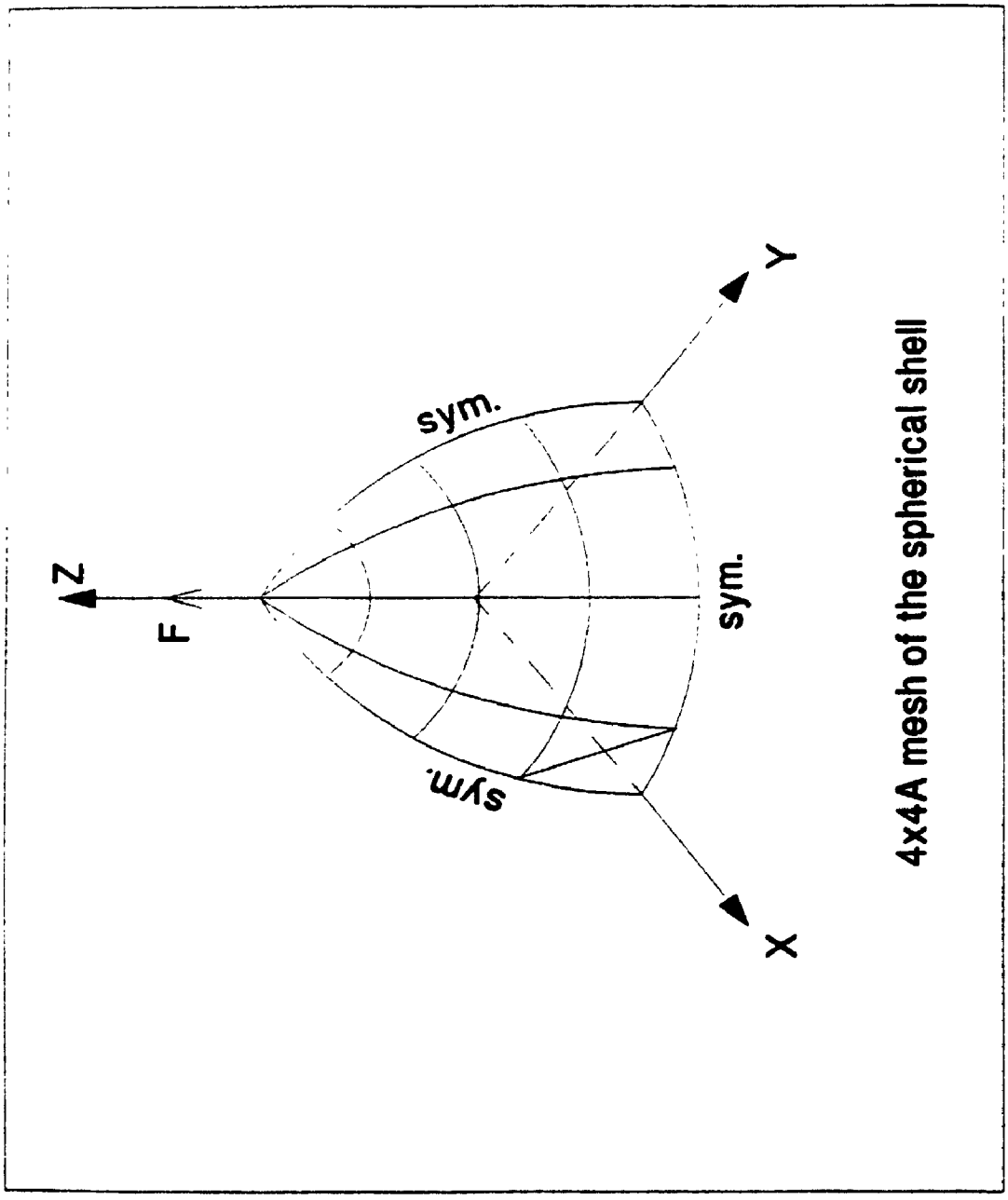

Figure 4.22 4×4 A mesh of the spherical shell

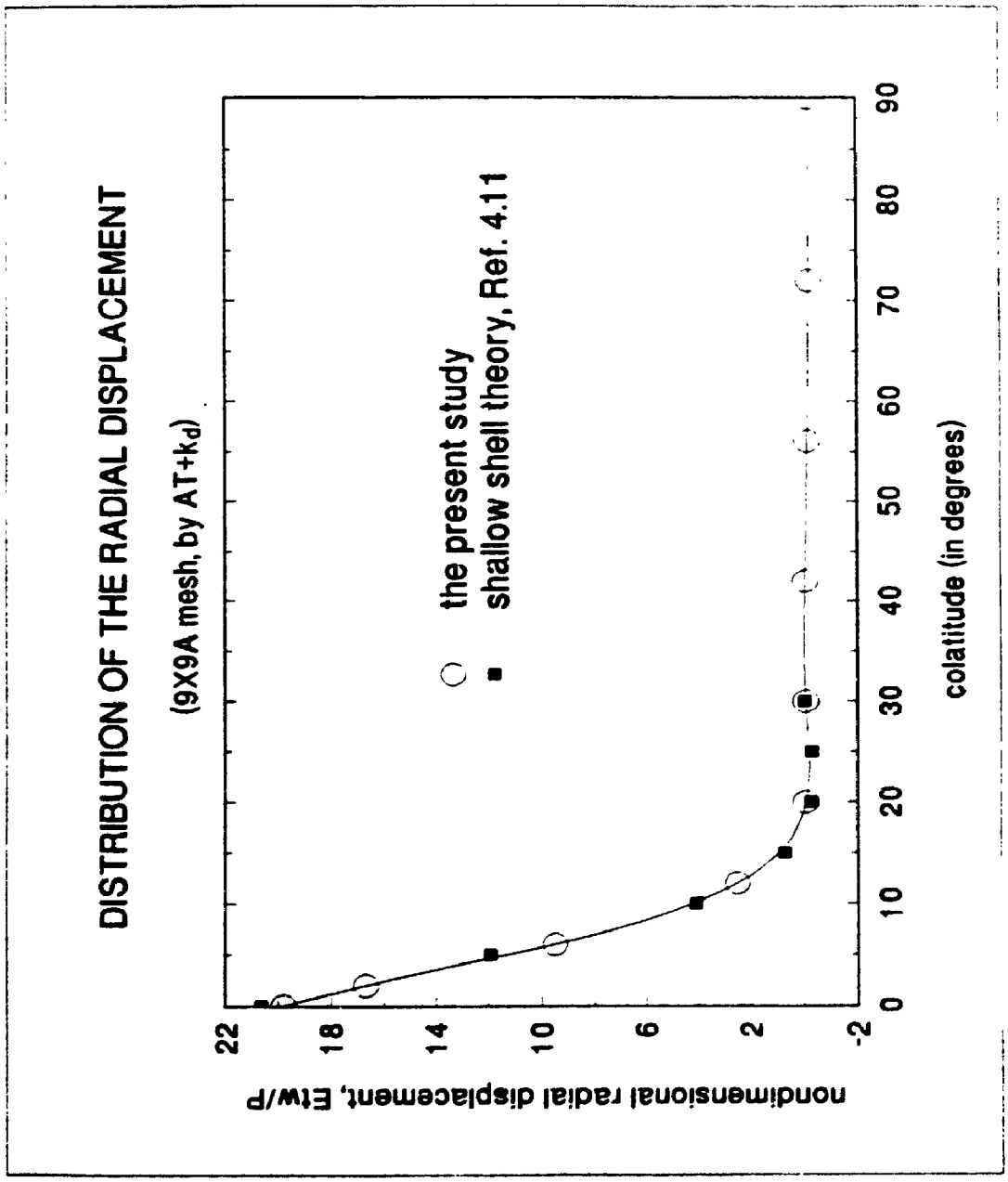

Figure 4.23 Distribution of the radial displacement

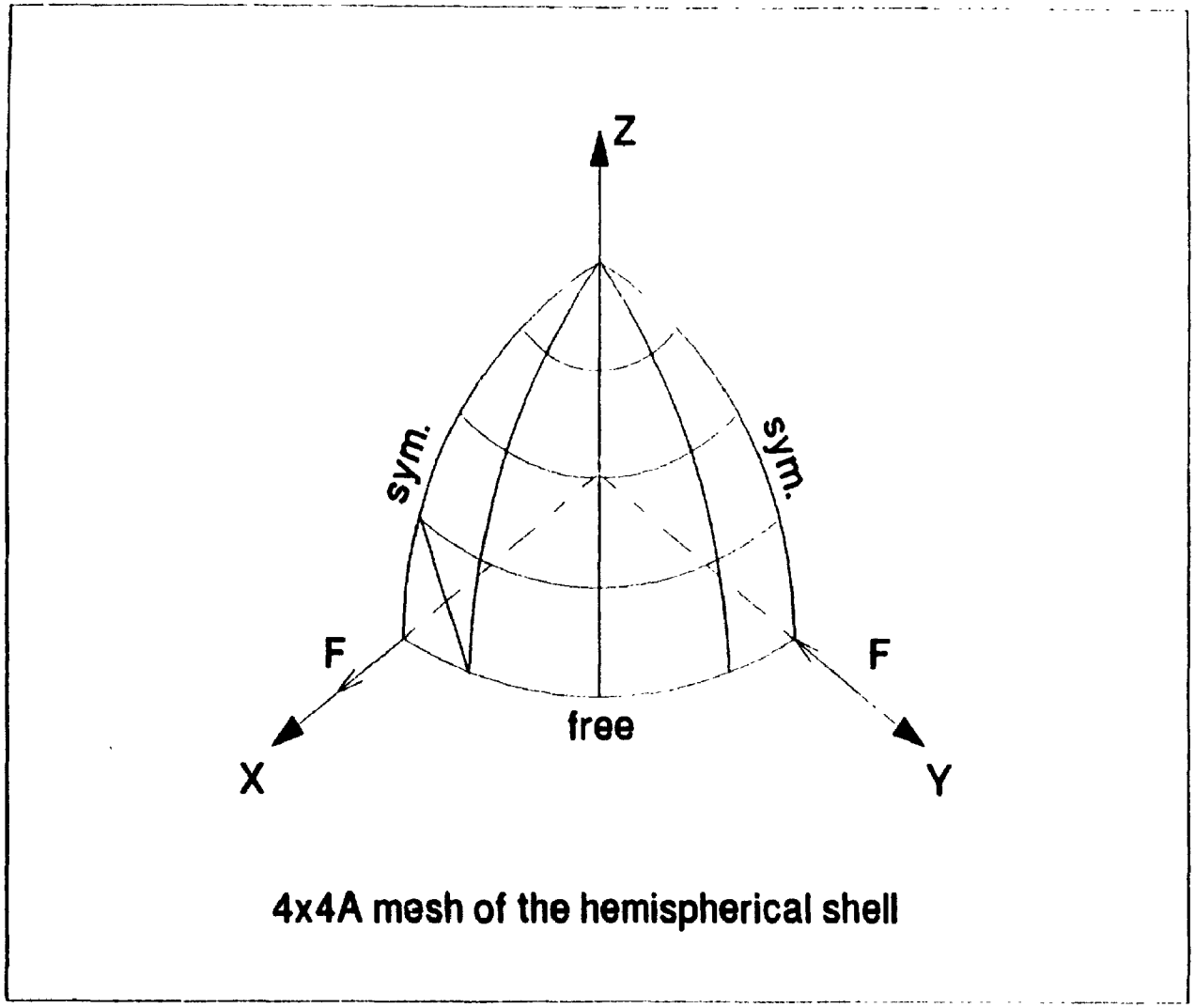

Figure 4.24 4×4 A mesh of the hemispherical shell

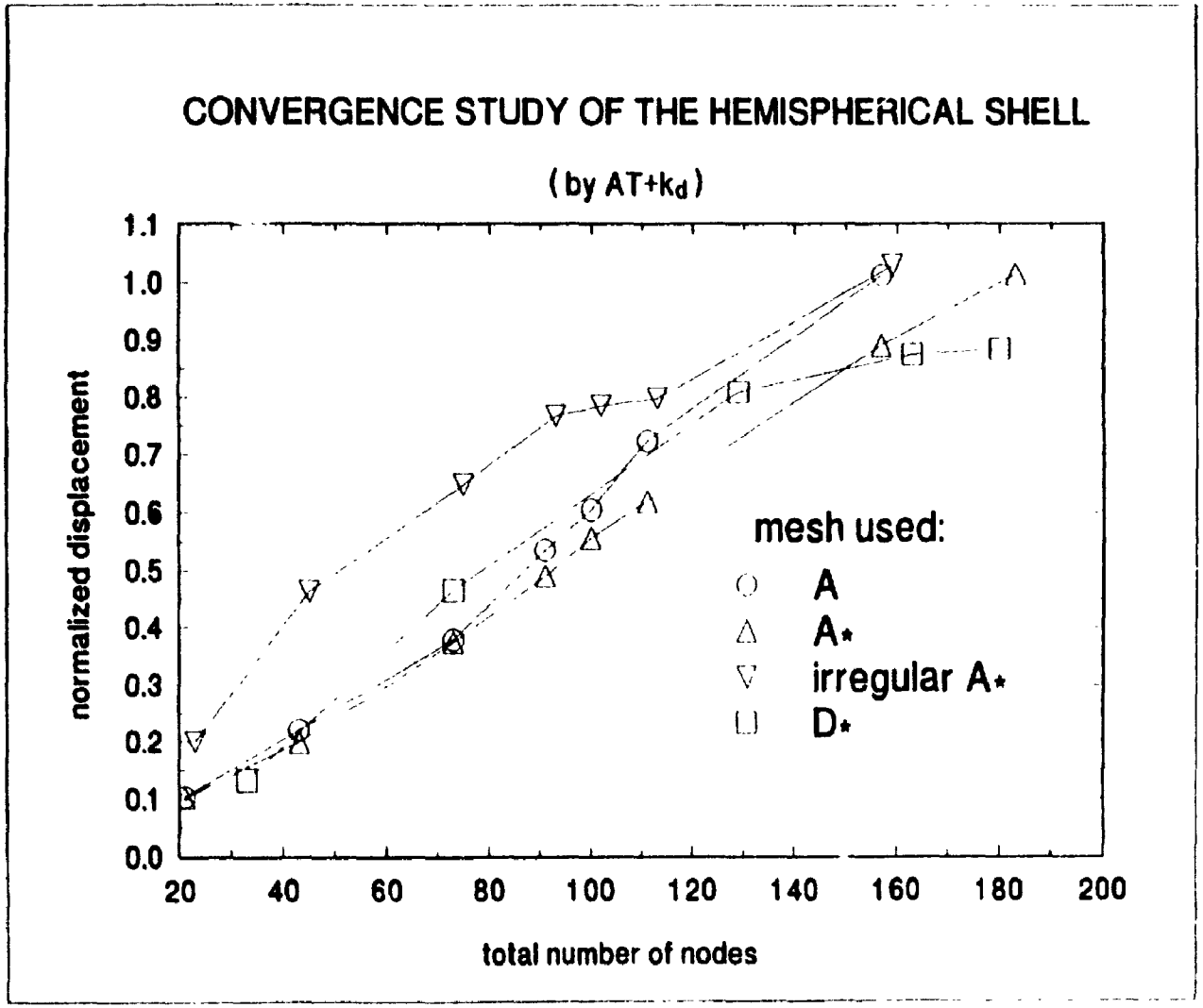

Figure 4.25 Convergence study of the hemispherical shell

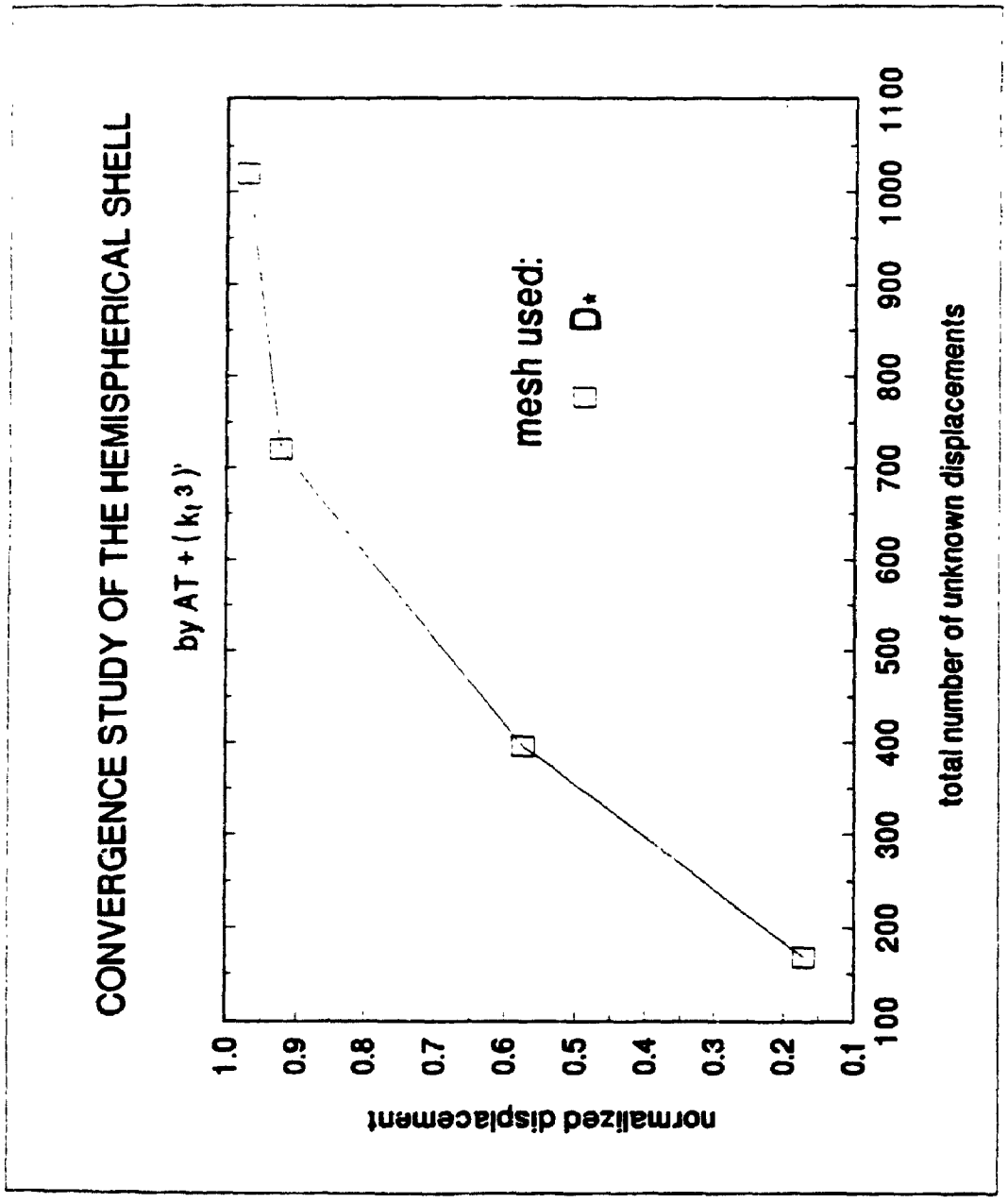

Figure 4.26 Convergence study of the hemispherical shell

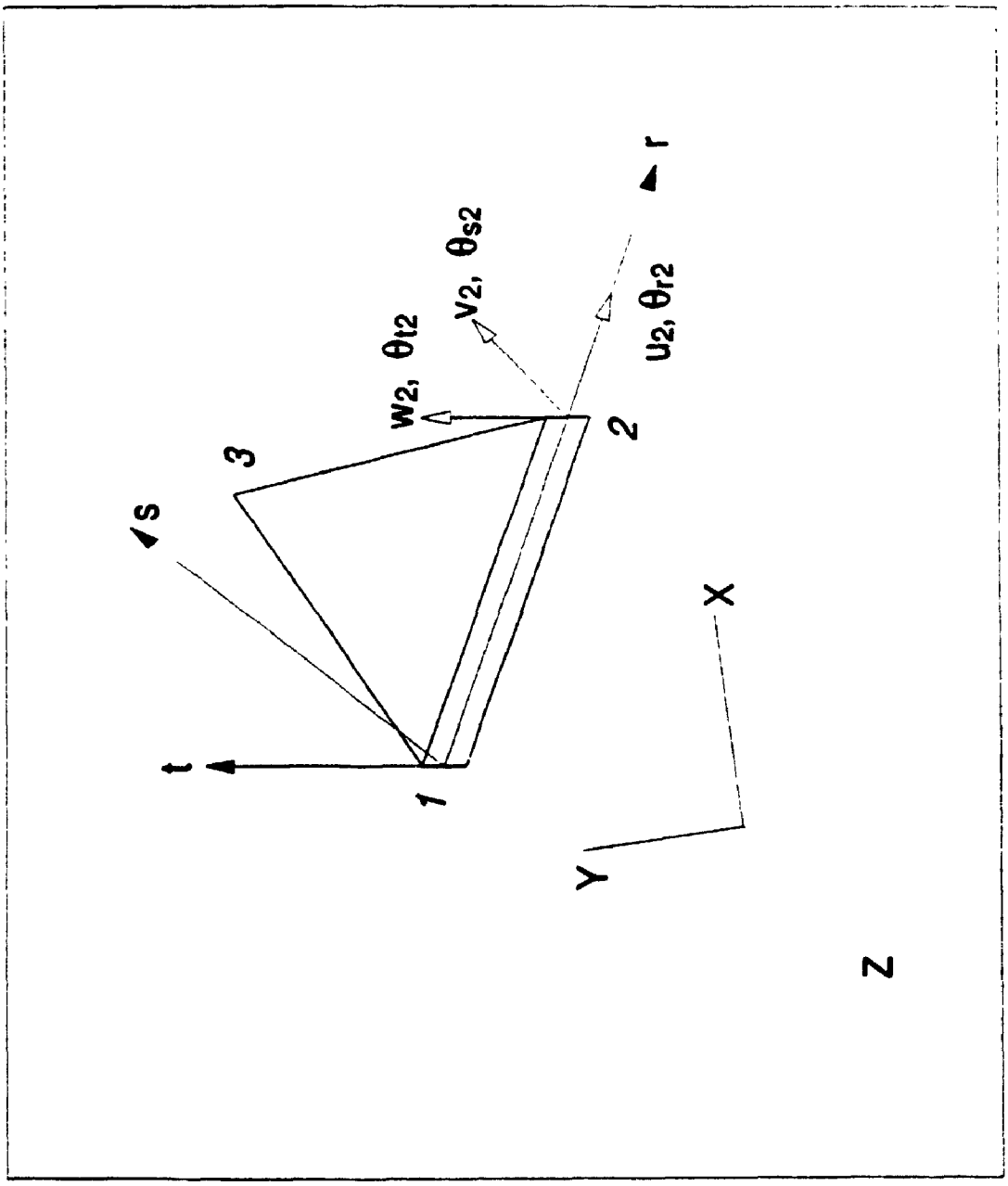

Figure 5.1 A representative 3 node flat triangular shell element

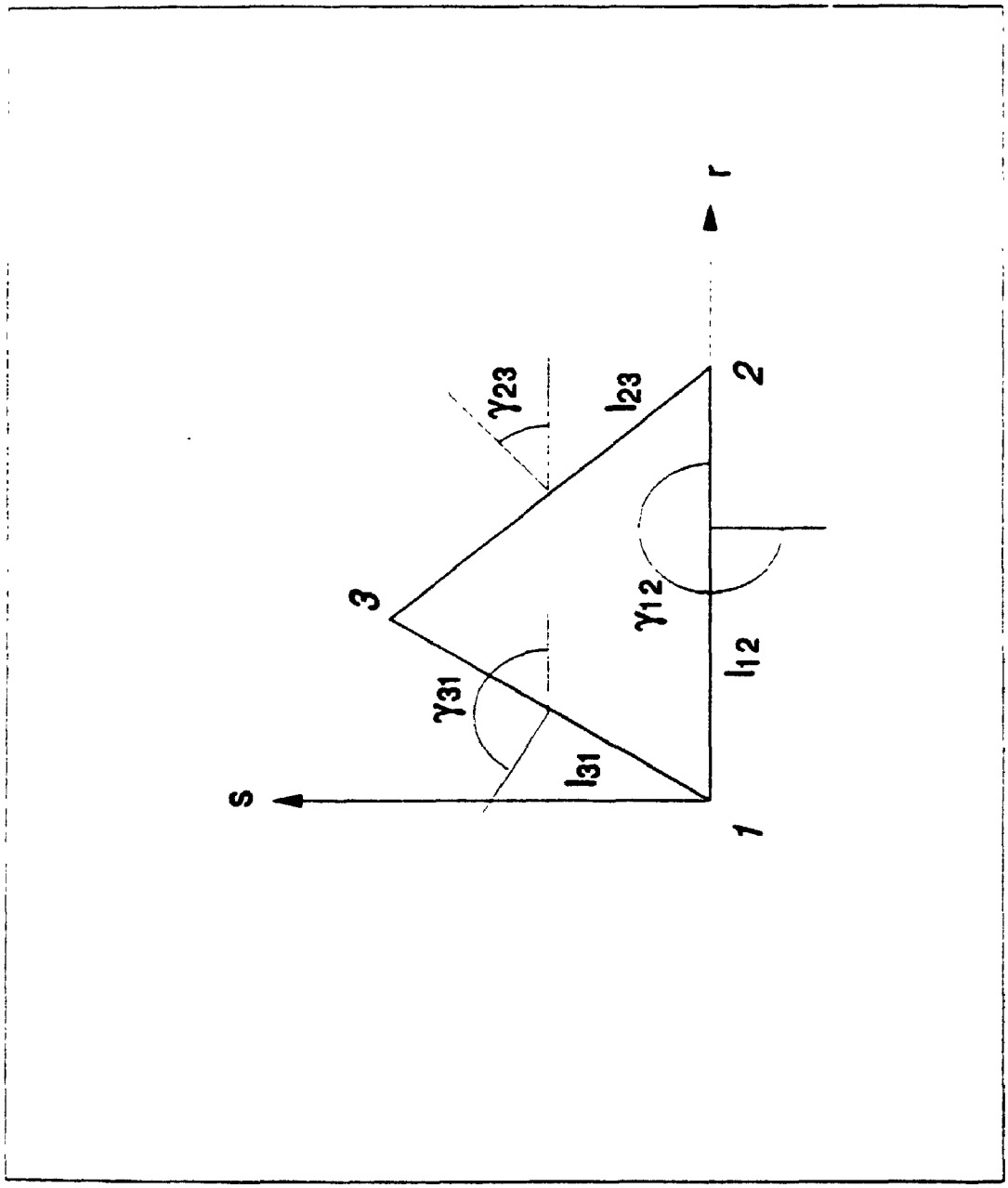

Figure 5.2 The geometry of the shell element

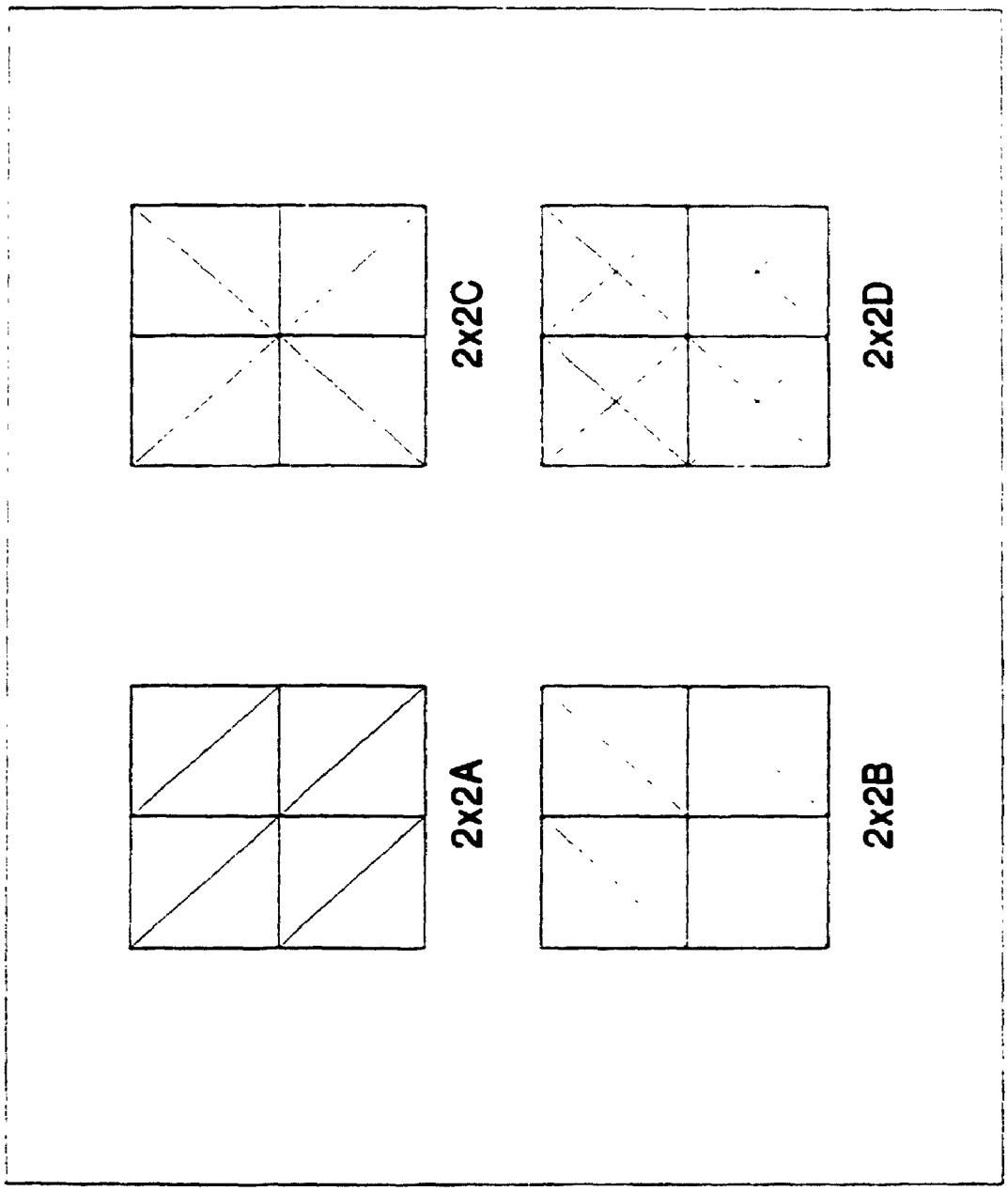

Figure 5.3 The four types of mesh layout

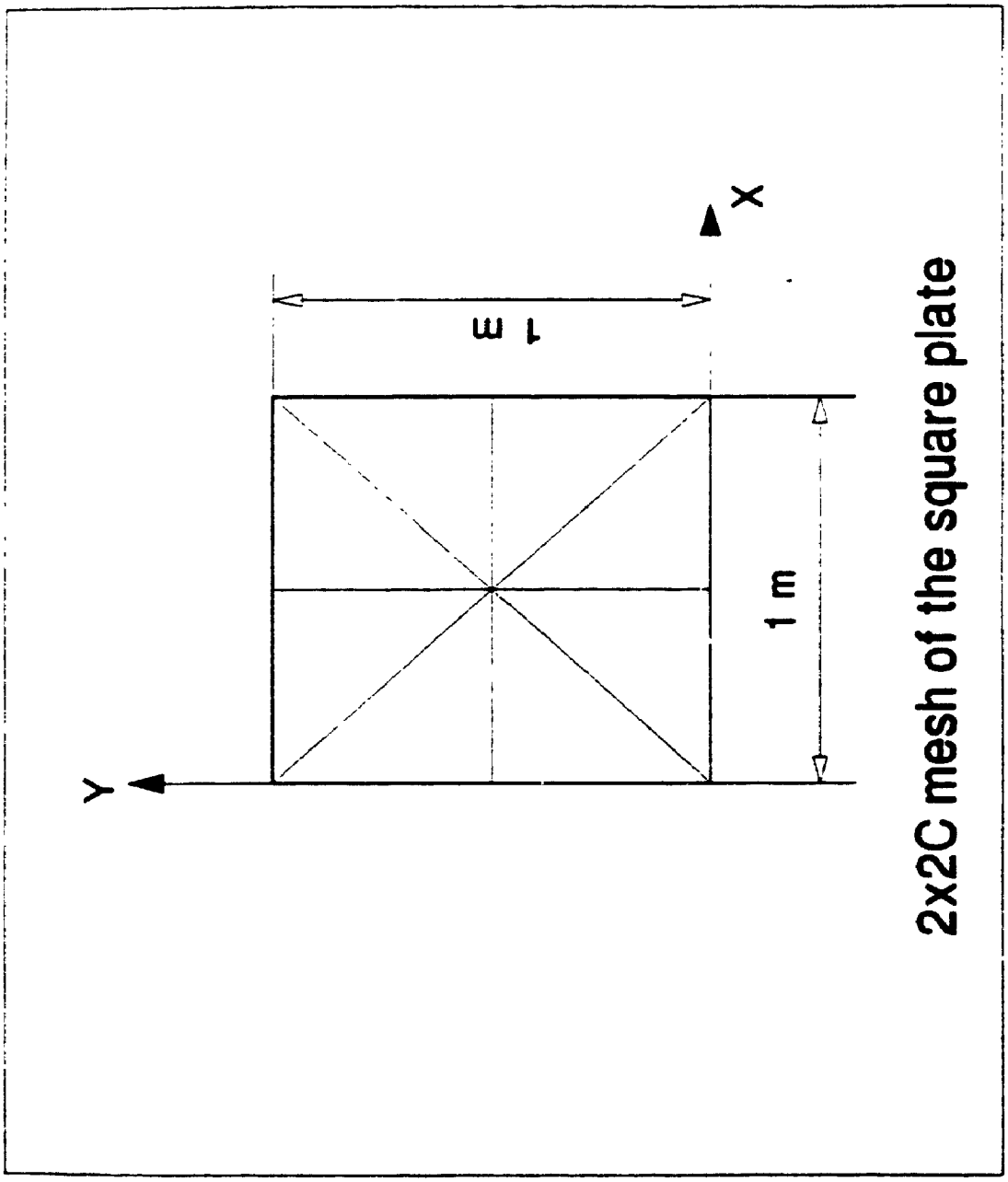

Figure 5.4 2×2 C mesh of the square plate

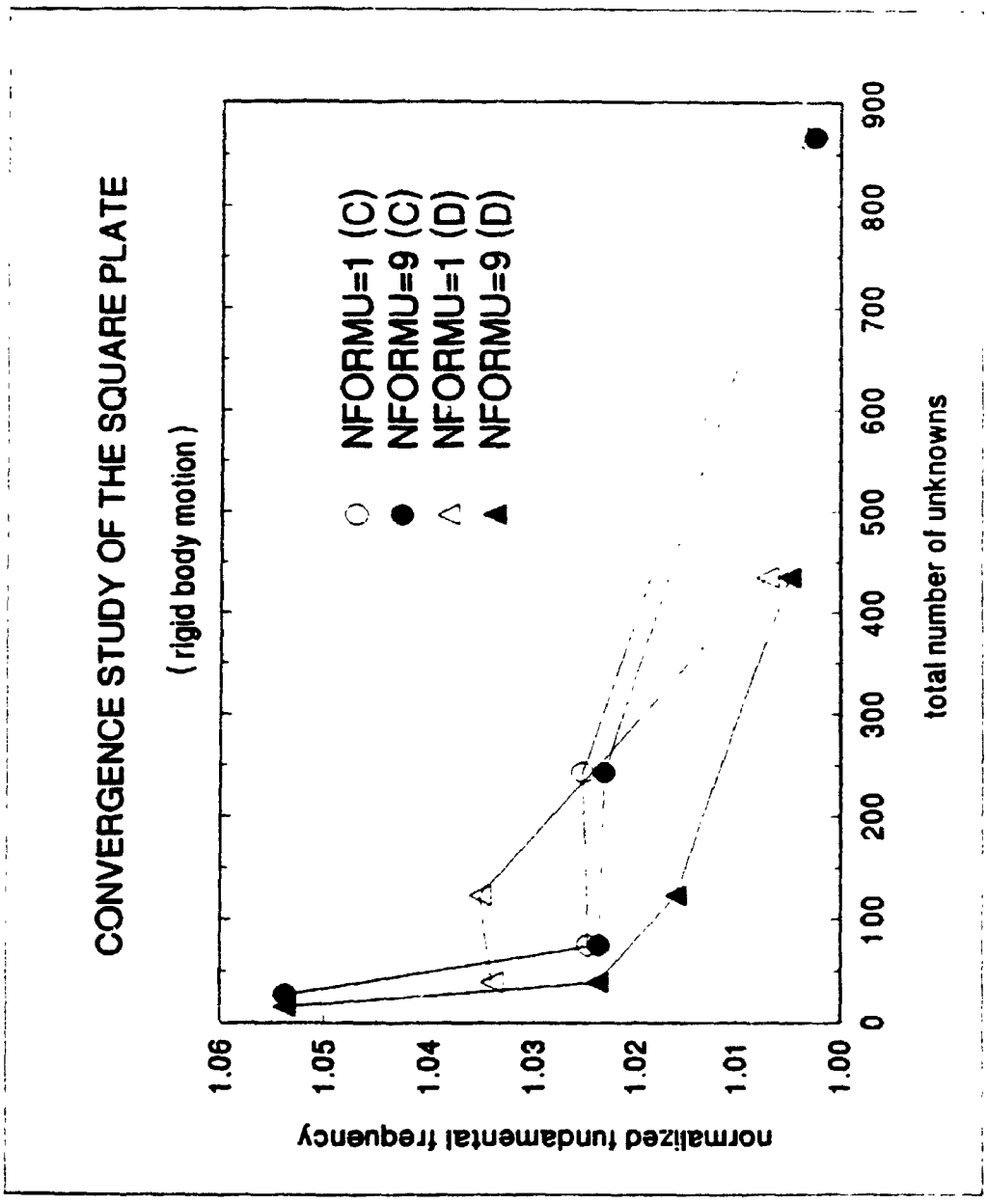

Figure 5.5 Convergence study of the square plate
(first non-zero frequency of rigid body motion)

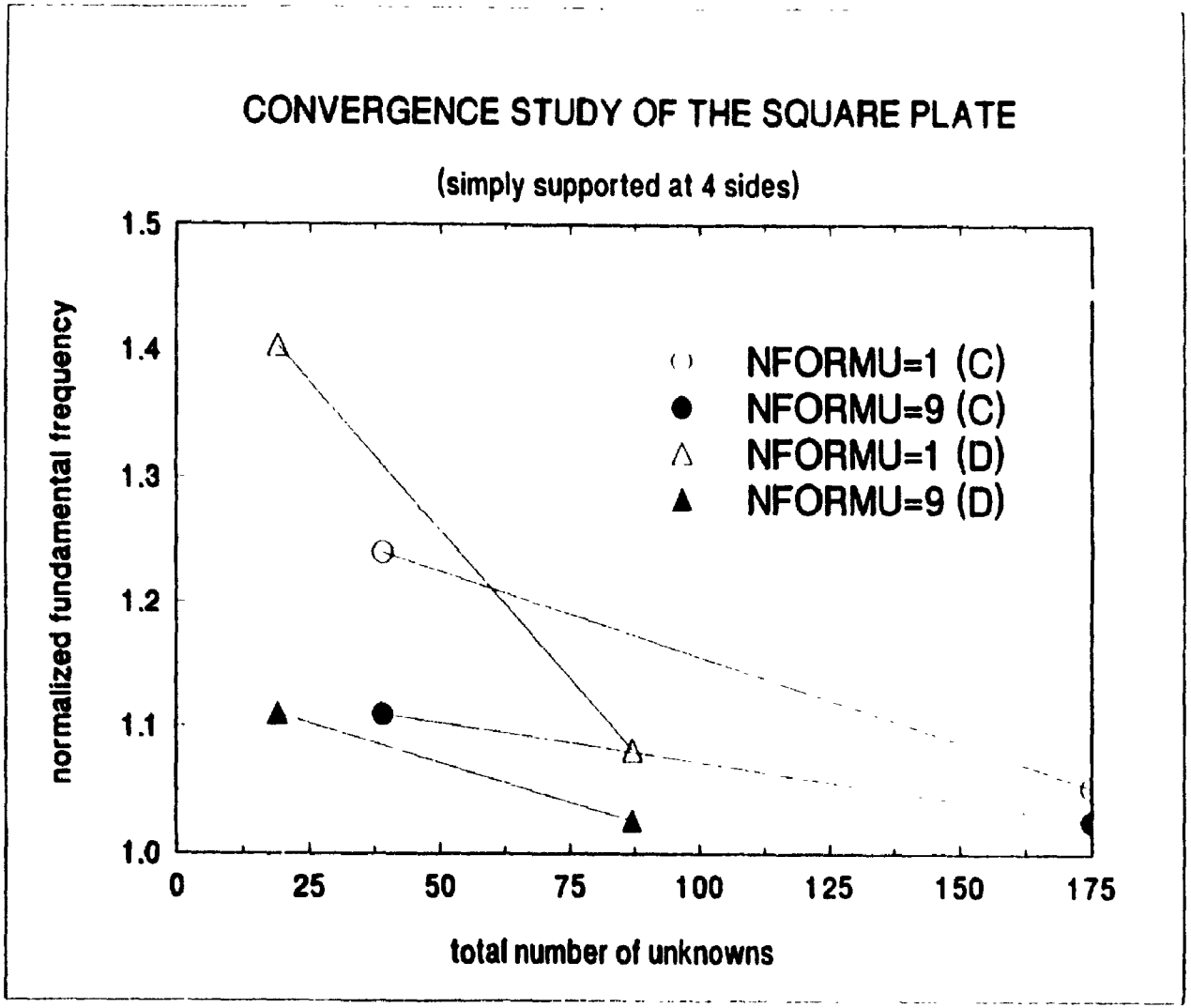

Figure 5.6 Convergence study of the square plate
(fundamental frequency, simply supported at 4 sides)

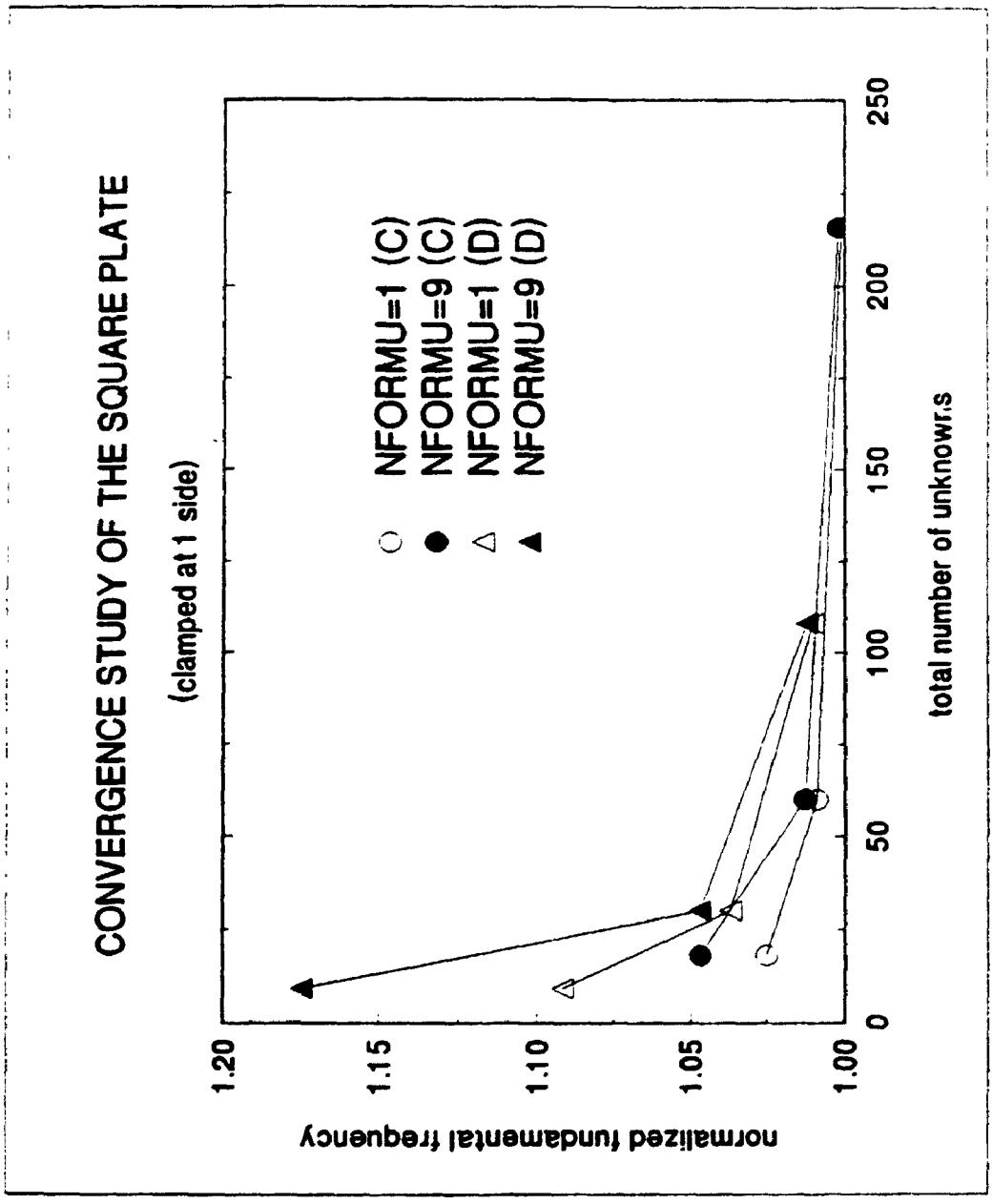

Figure 5.7 Convergence study of the square plate (fundamental frequency, clamped at 1 side)

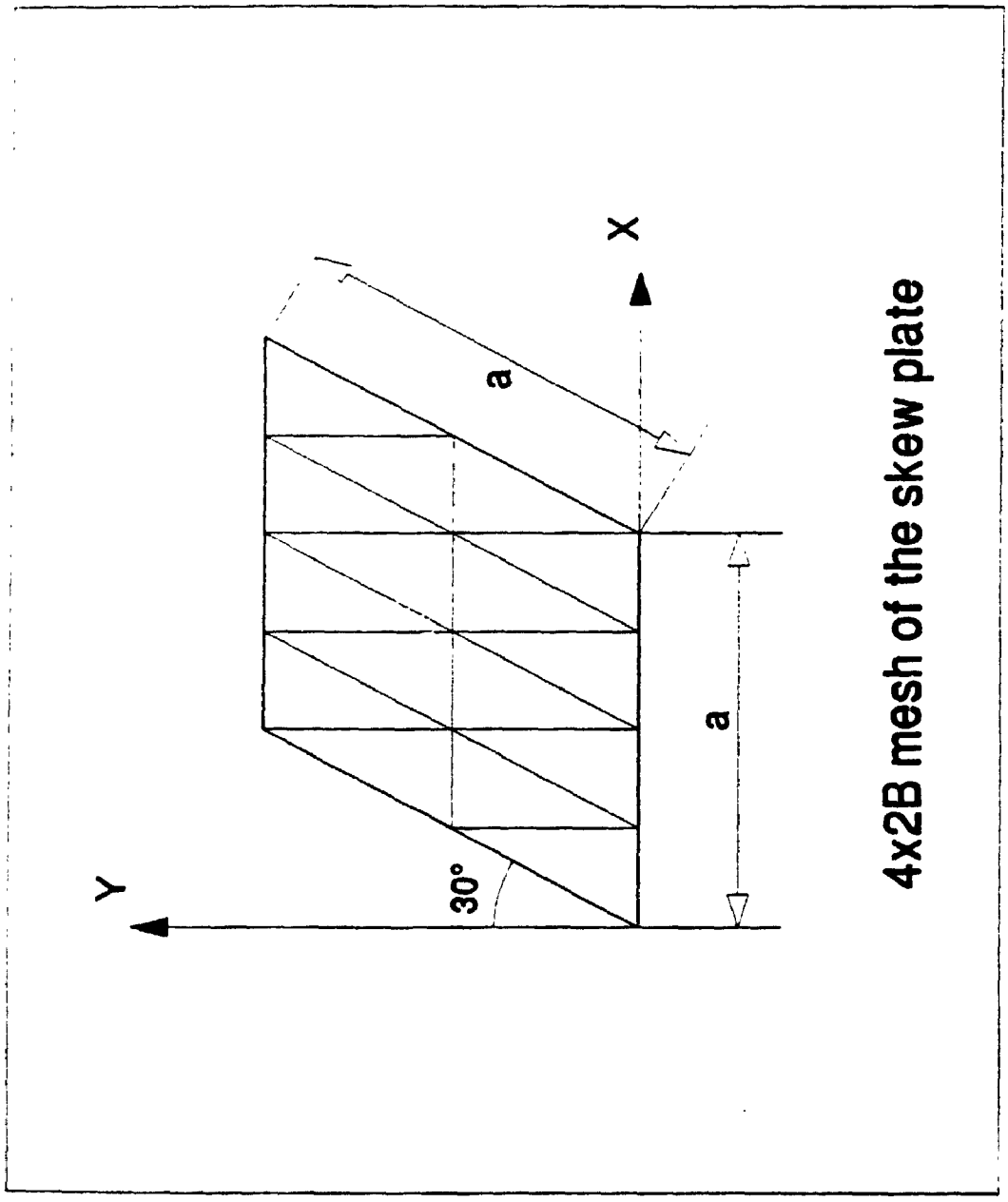

Figure 5.8 4×2 B mesh of the skew plate

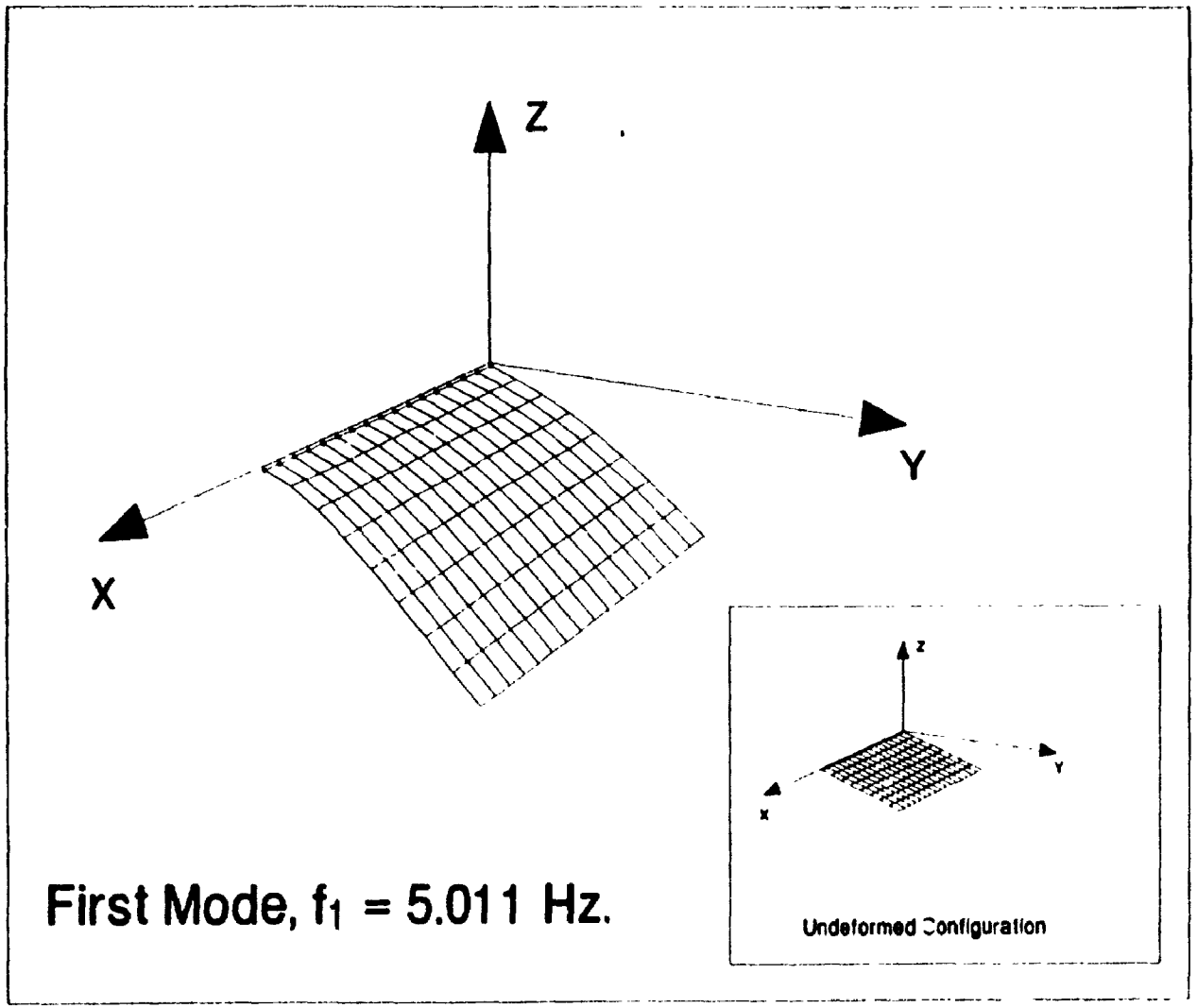

Figure 5.9 First mode shape of the skew plate (f_1 = 5.011 Hz)

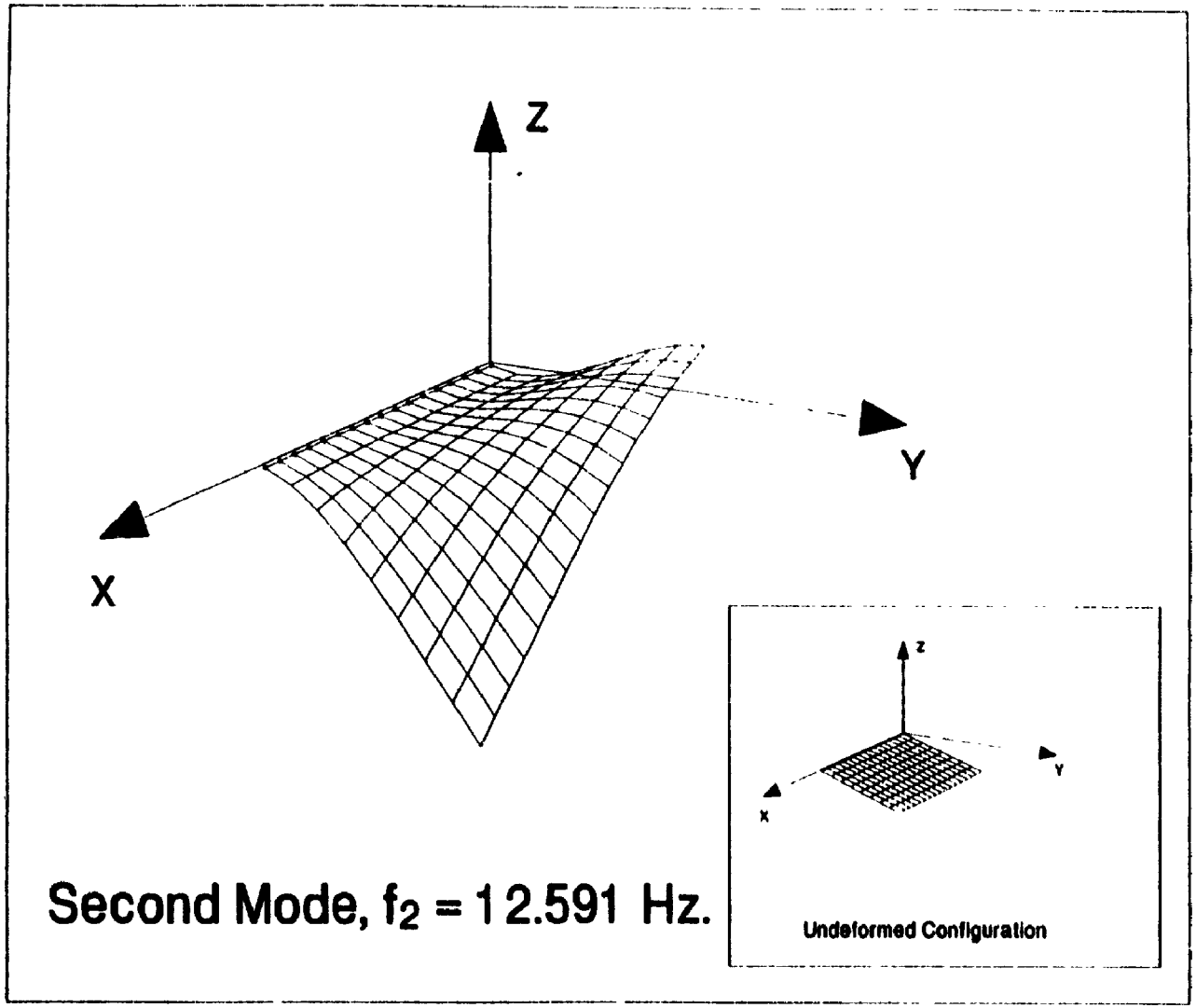

Figure 5.10 Second mode shape of the skew plate (f_2 = 12.591 Hz)

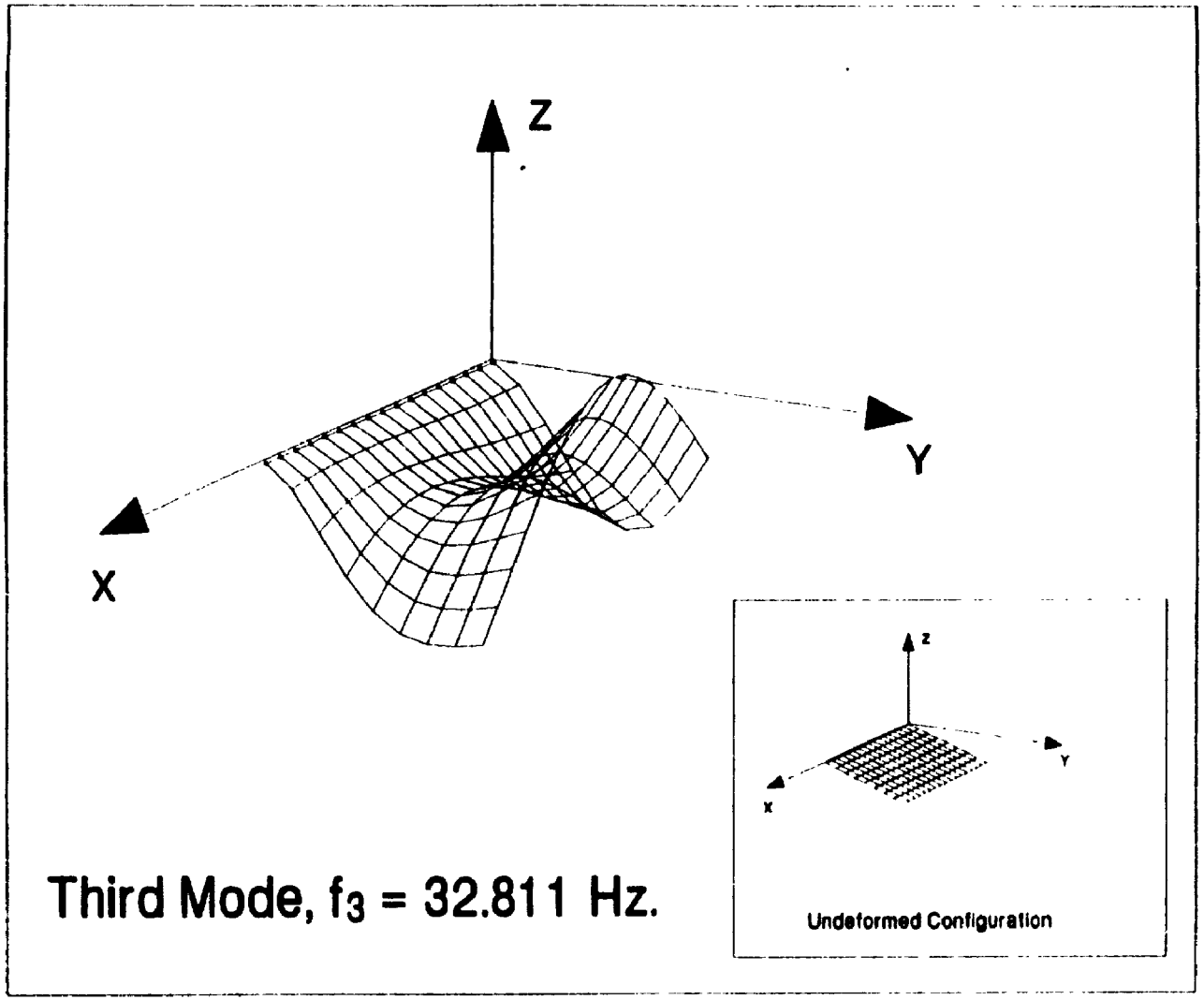

Figure 5.11 Third mode shape of the skew plate (f_3=32.811 Hz)

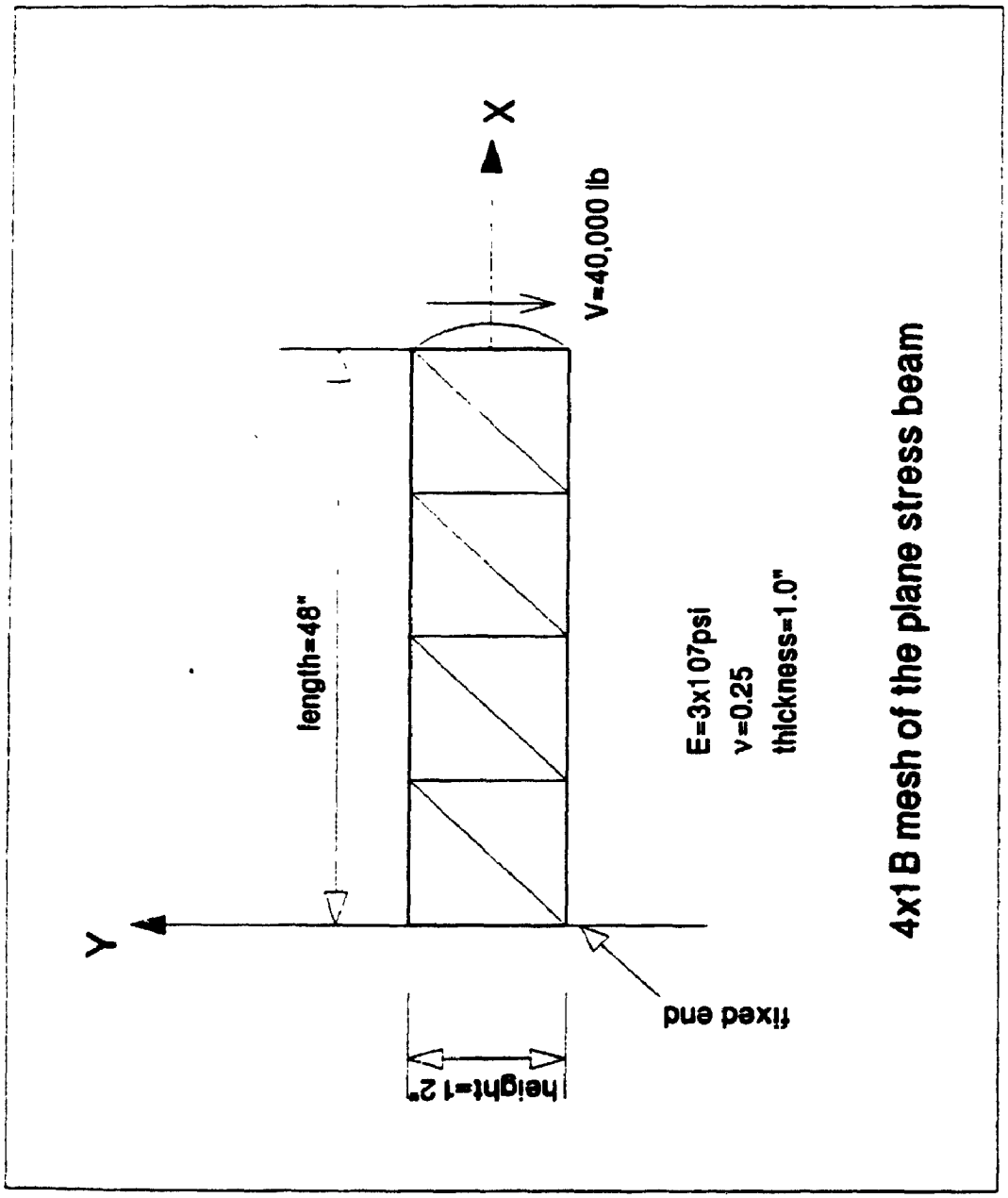

Figure 5.12 4×1 B mesh of the plane stress beam

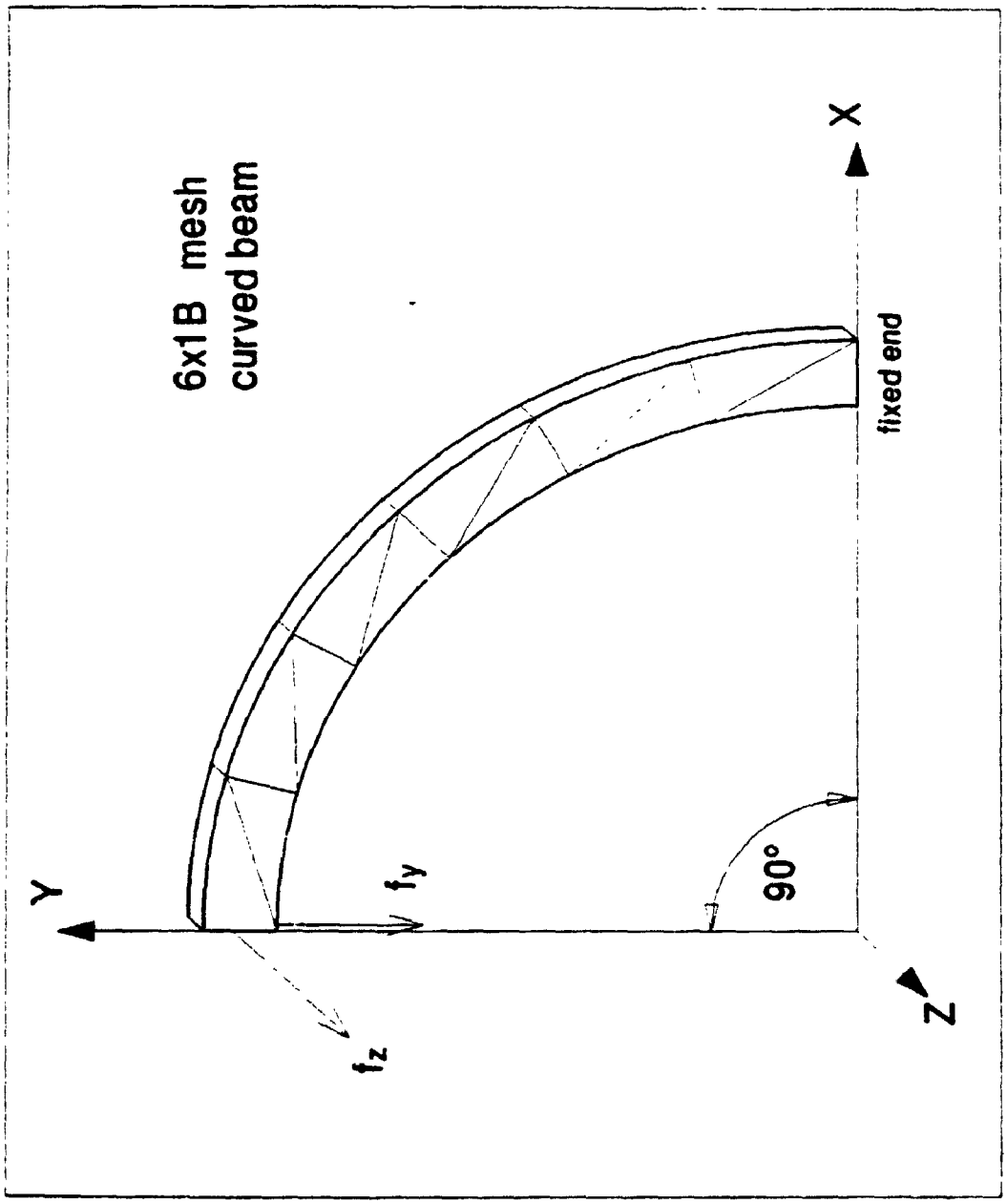

Figure 5.13 6×1 B mesh of the curved beam

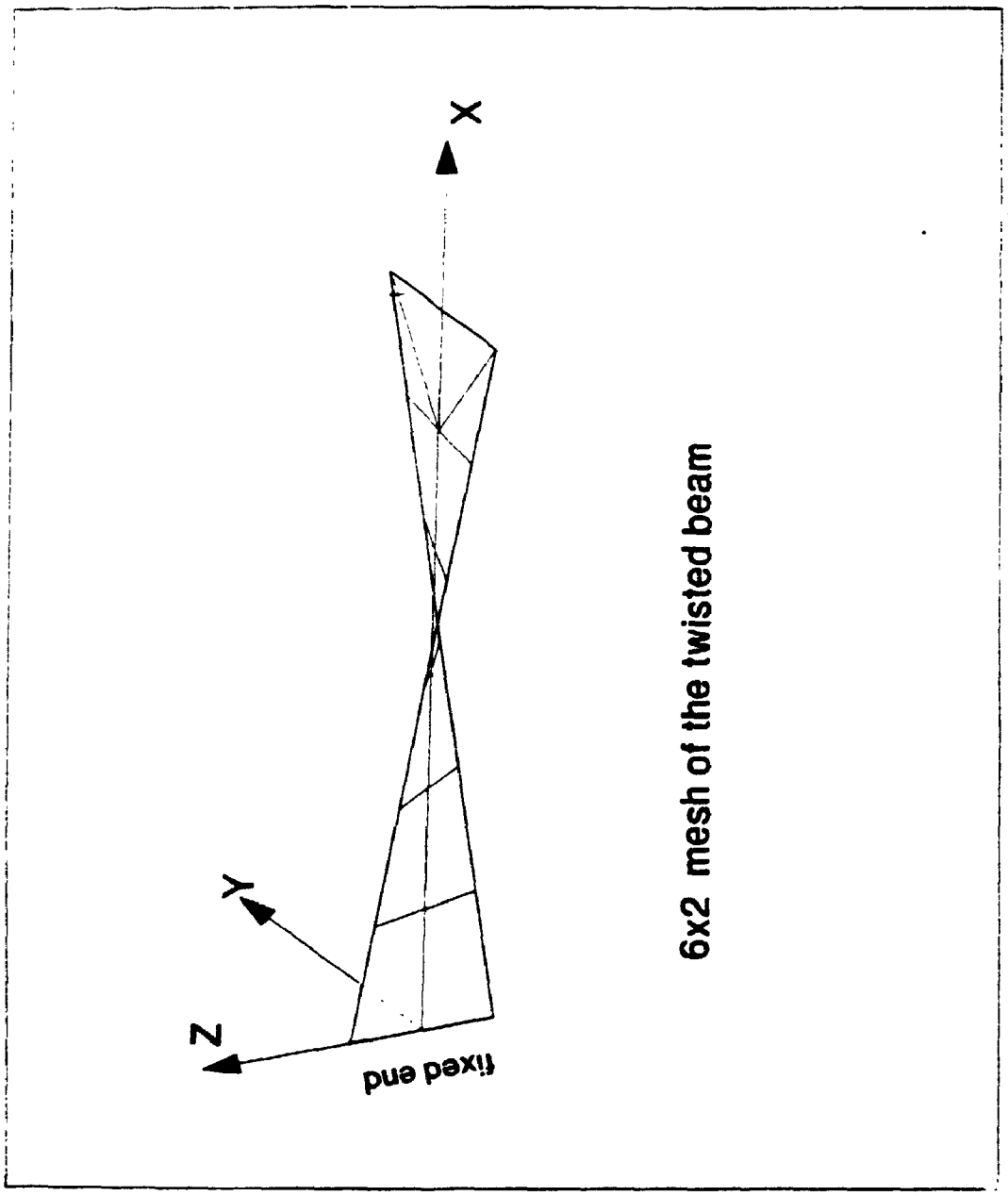

Figure 5.14 6×2 mesh of the twisted beam

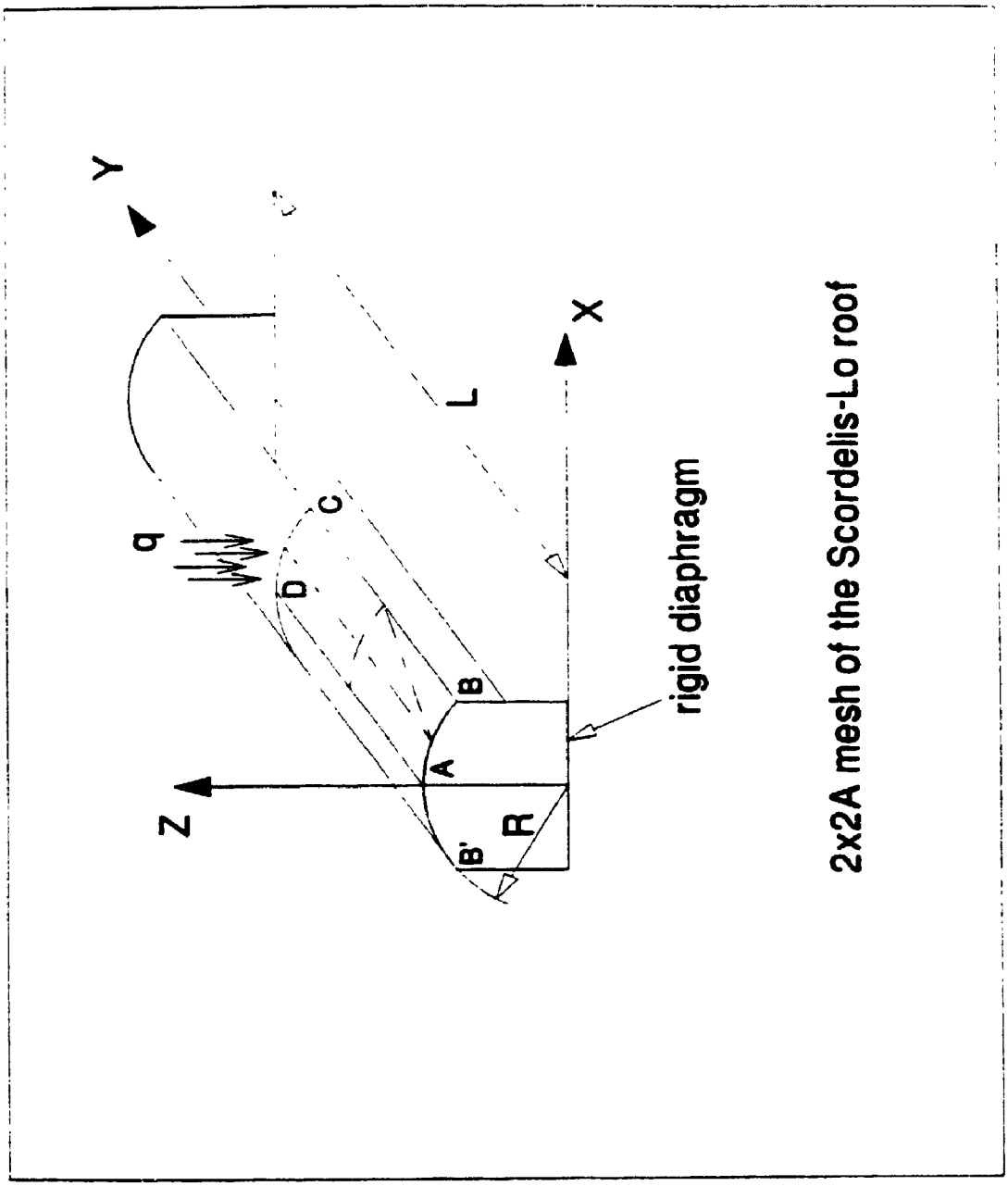

Figure 5.15 2×2 A mesh of the Scordelis-Lo roof

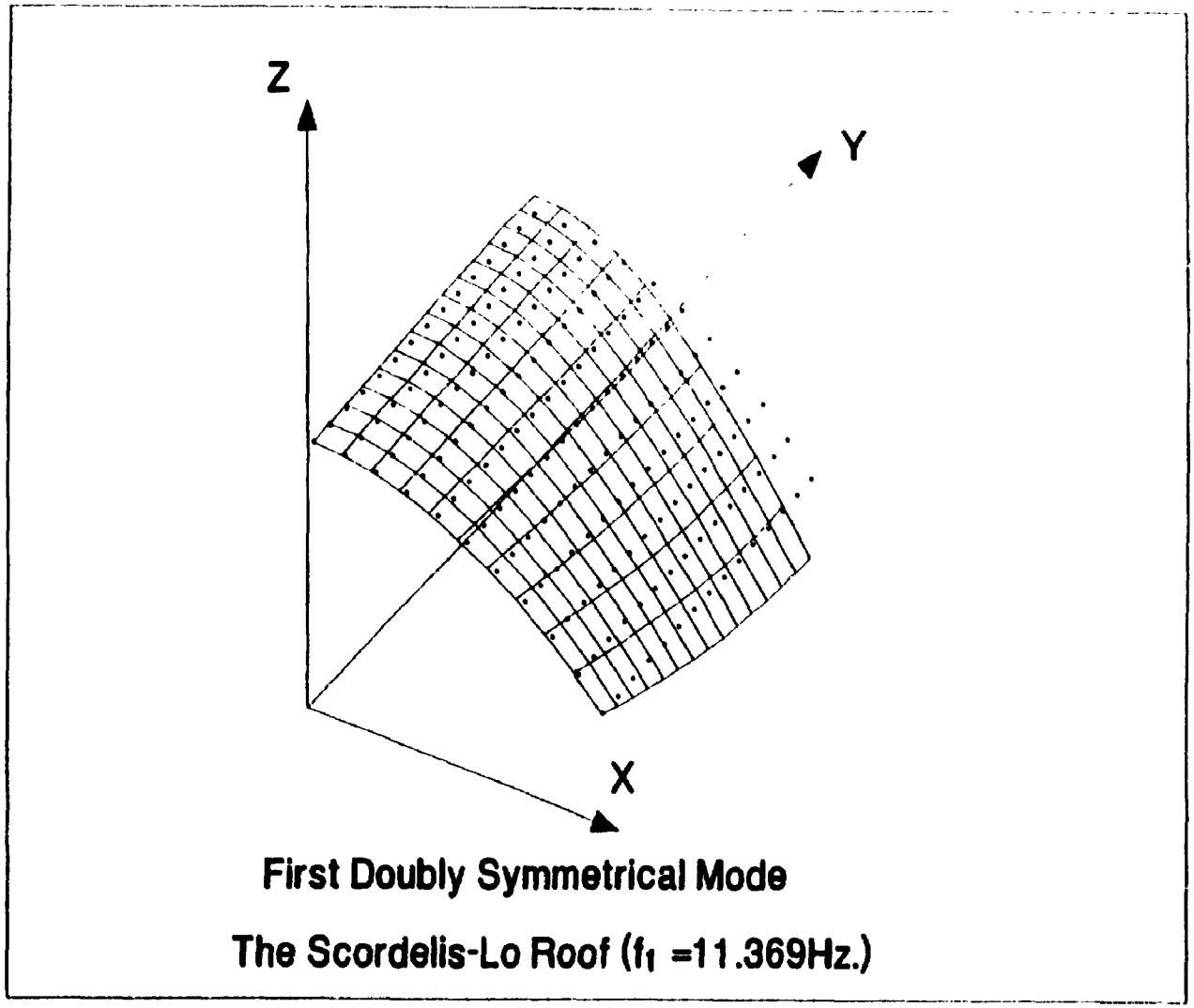

Figure 5.16 First mode shape of the Scordelis-Lo roof (f_1 = 11.369 Hz)

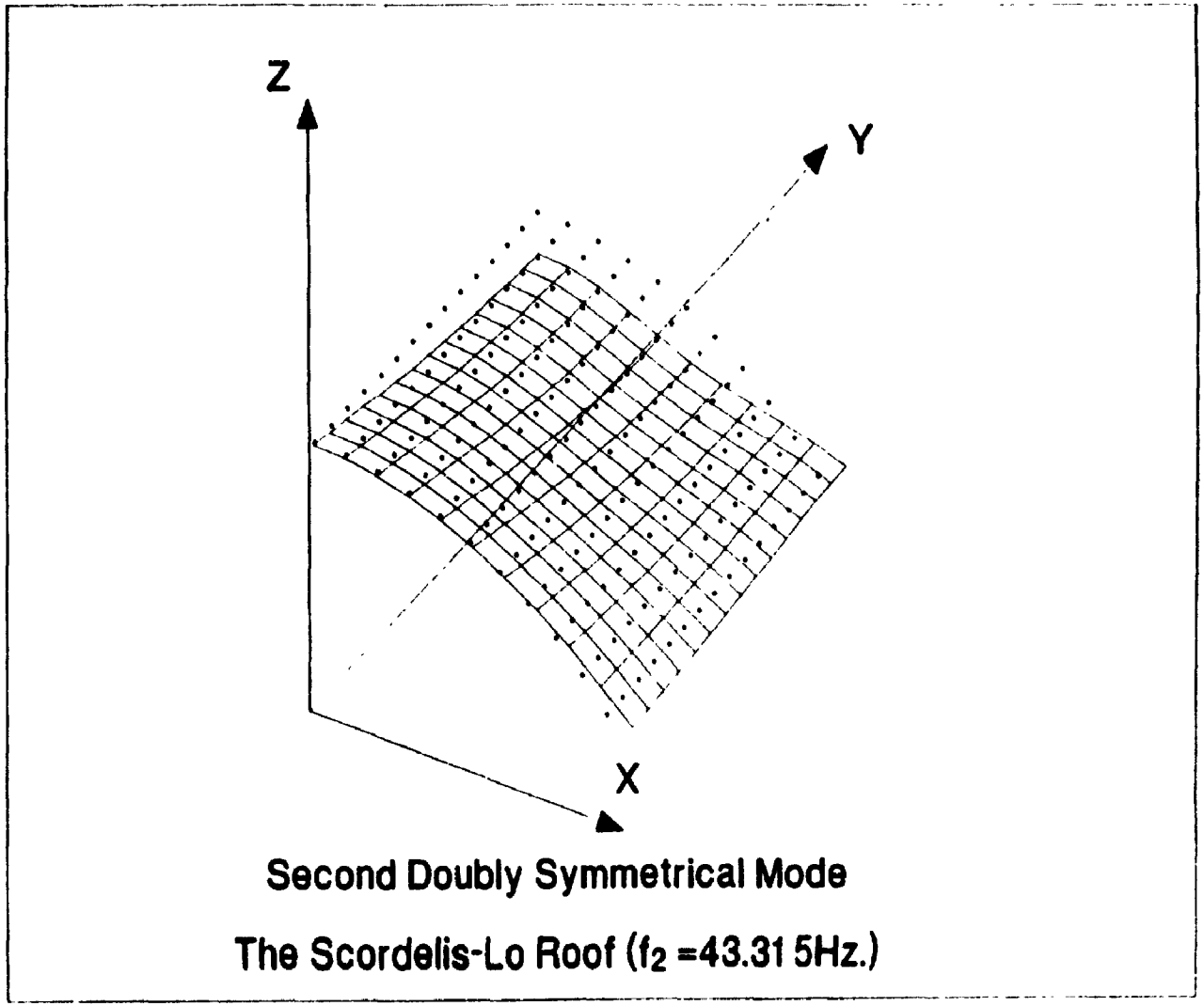

Figure 5.17 Second mode shape of the Scordelis-Lo roof (f_2=43.315 Hz)

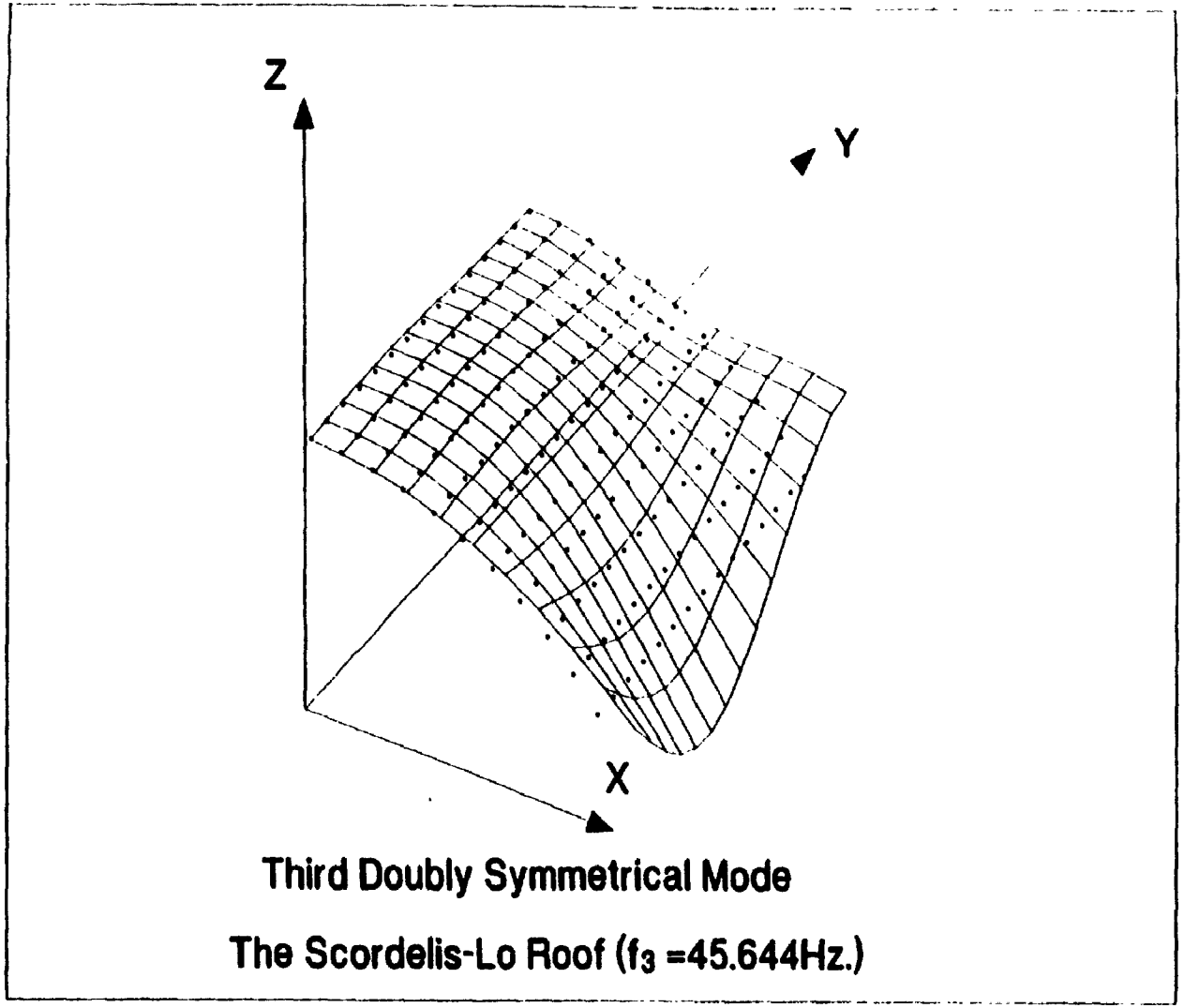

Figure 5.18 Third mode shape of the Scordelis-Lo roof (f_3=45.644 Hz)

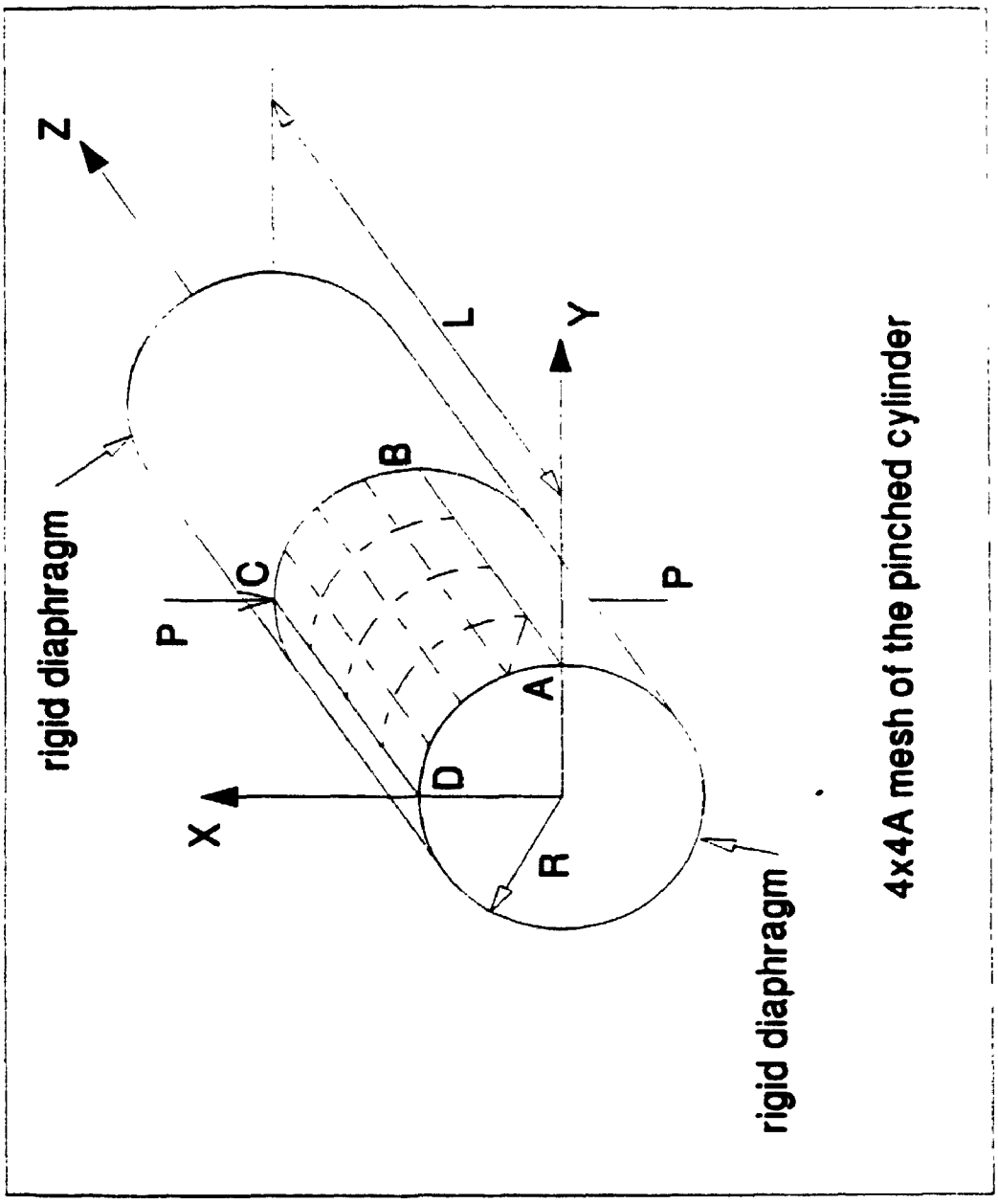

Figure 5.19 4×4 A mesh of the pinched cylinder

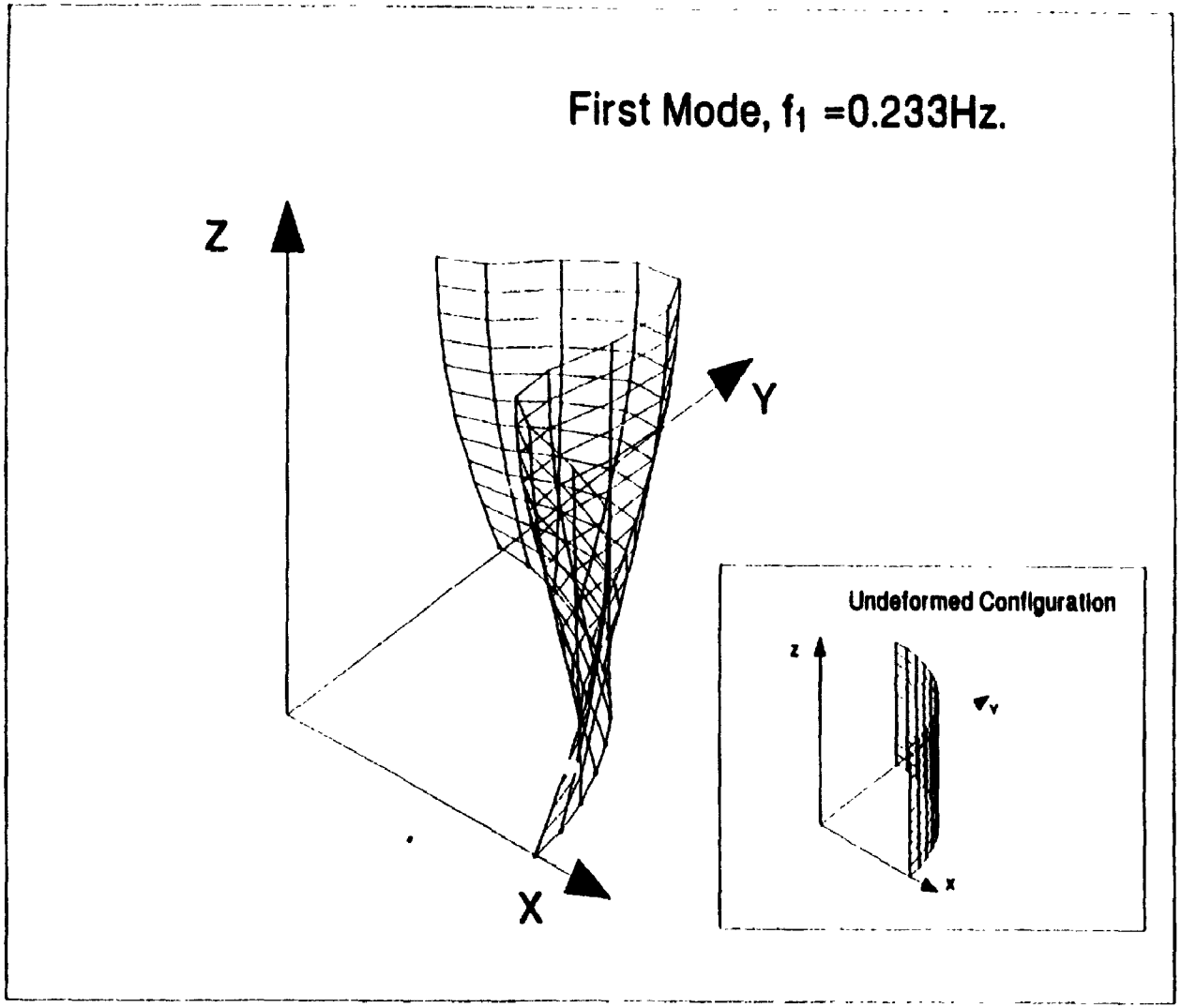

Figure 5.20 First mode shape of the pinched cylinder (f_1=0.233 Hz)

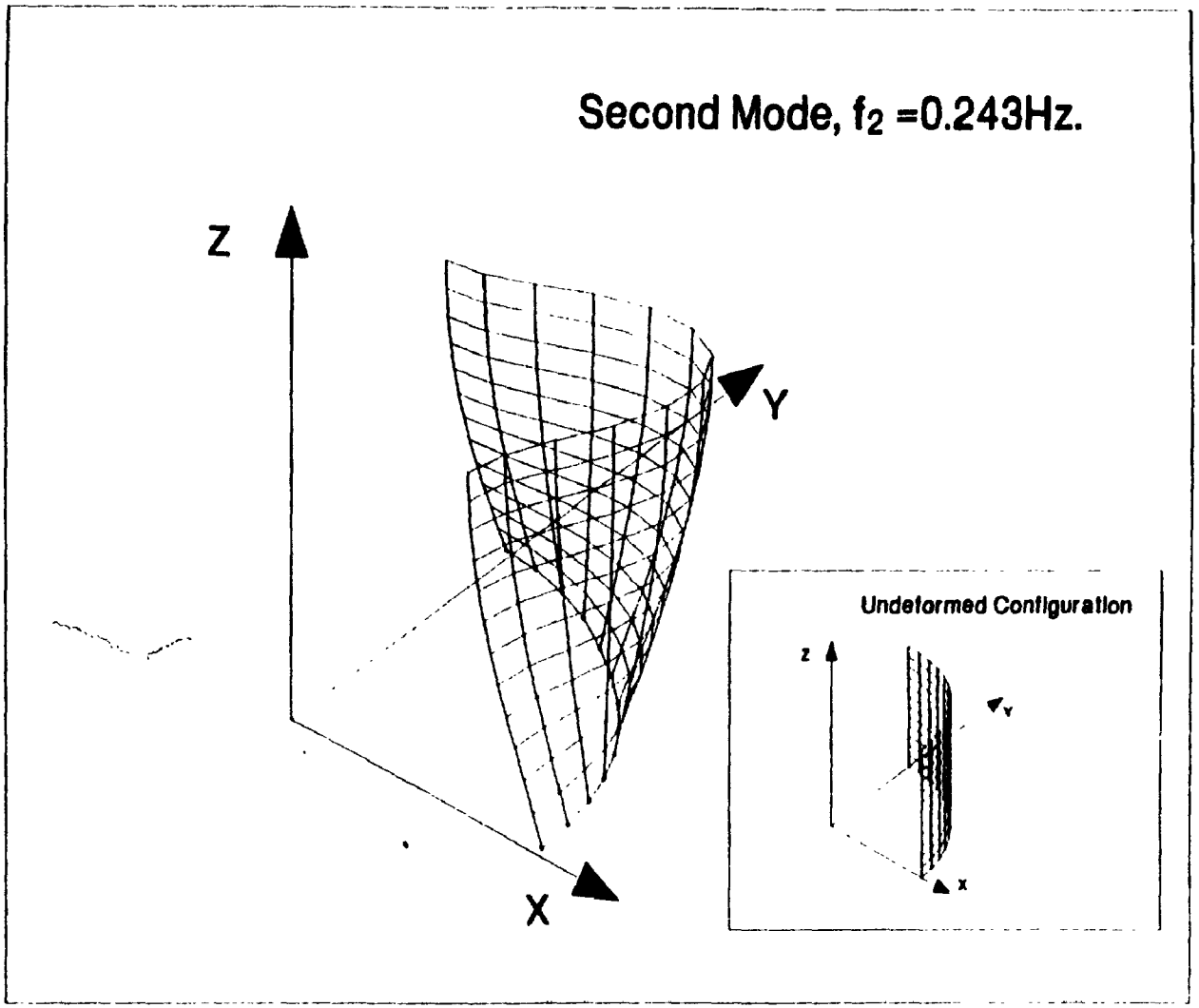

Figure 5.21 Second mode shape of the pinched cylinder (f_2=0.243 Hz)

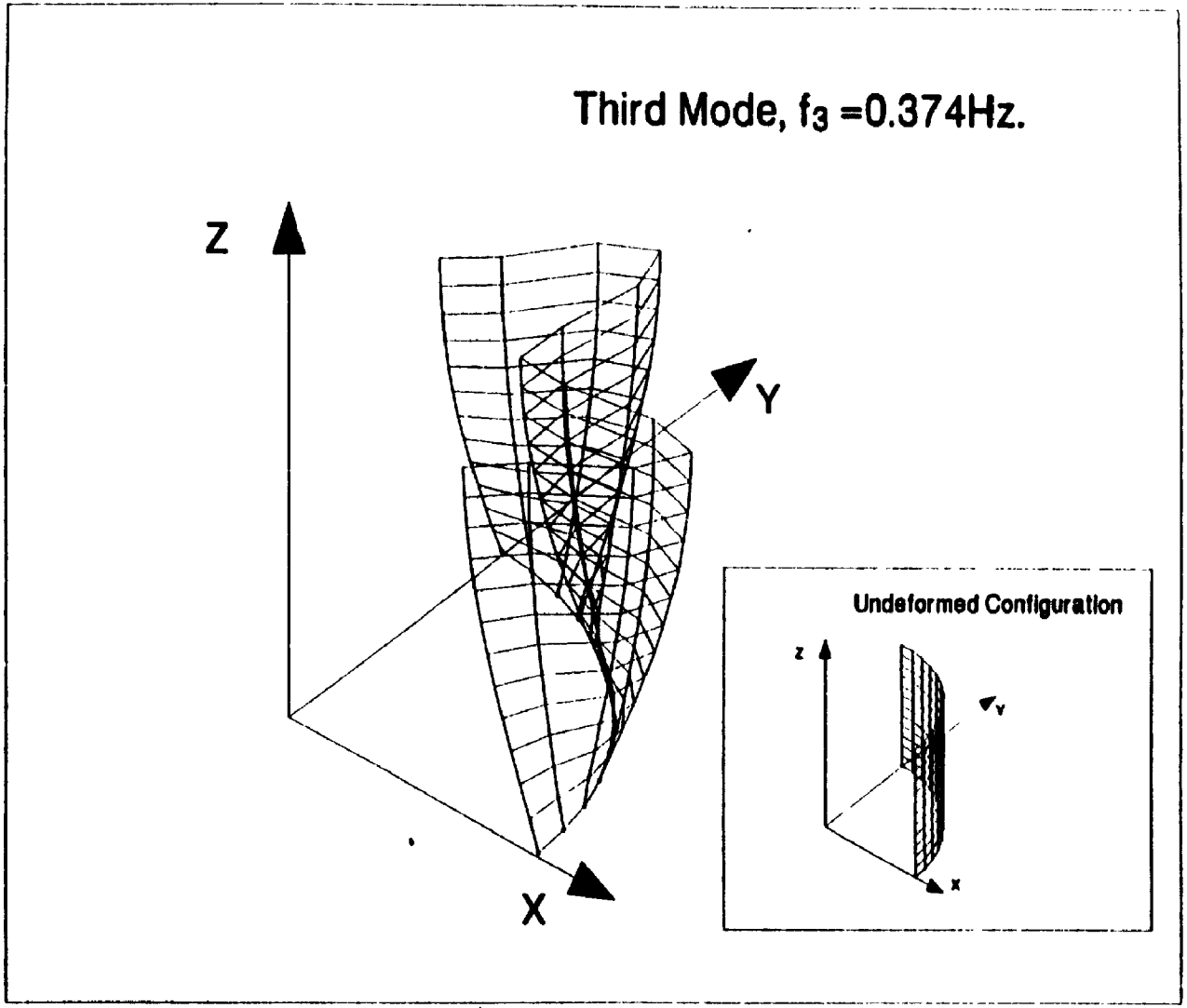

Figure 5.22 Third mode shape of the pinched cylinder ($f_3 = 0.374$ Hz)

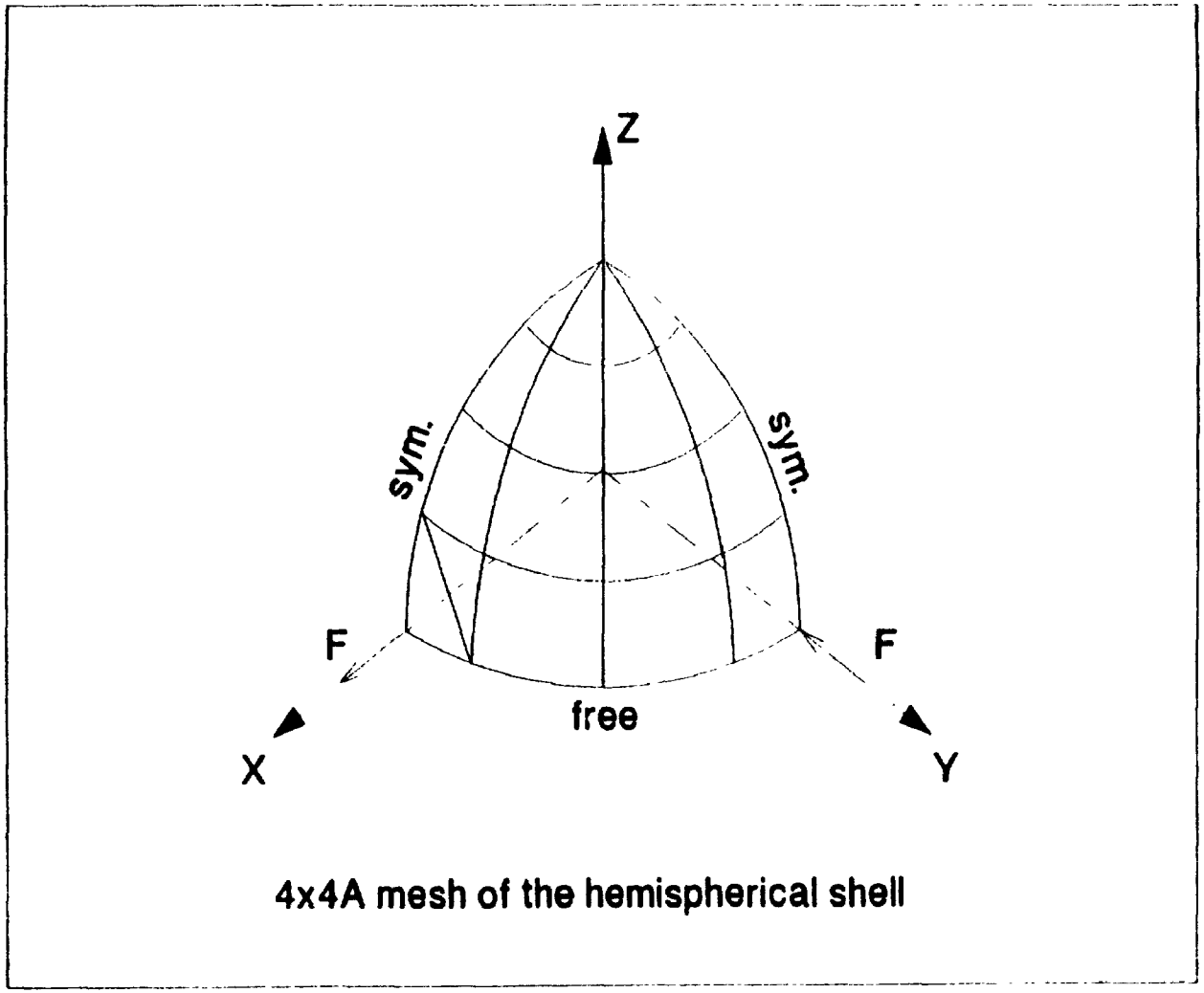

Figure 5.23 4×4 A mesh of the hemispherical shell

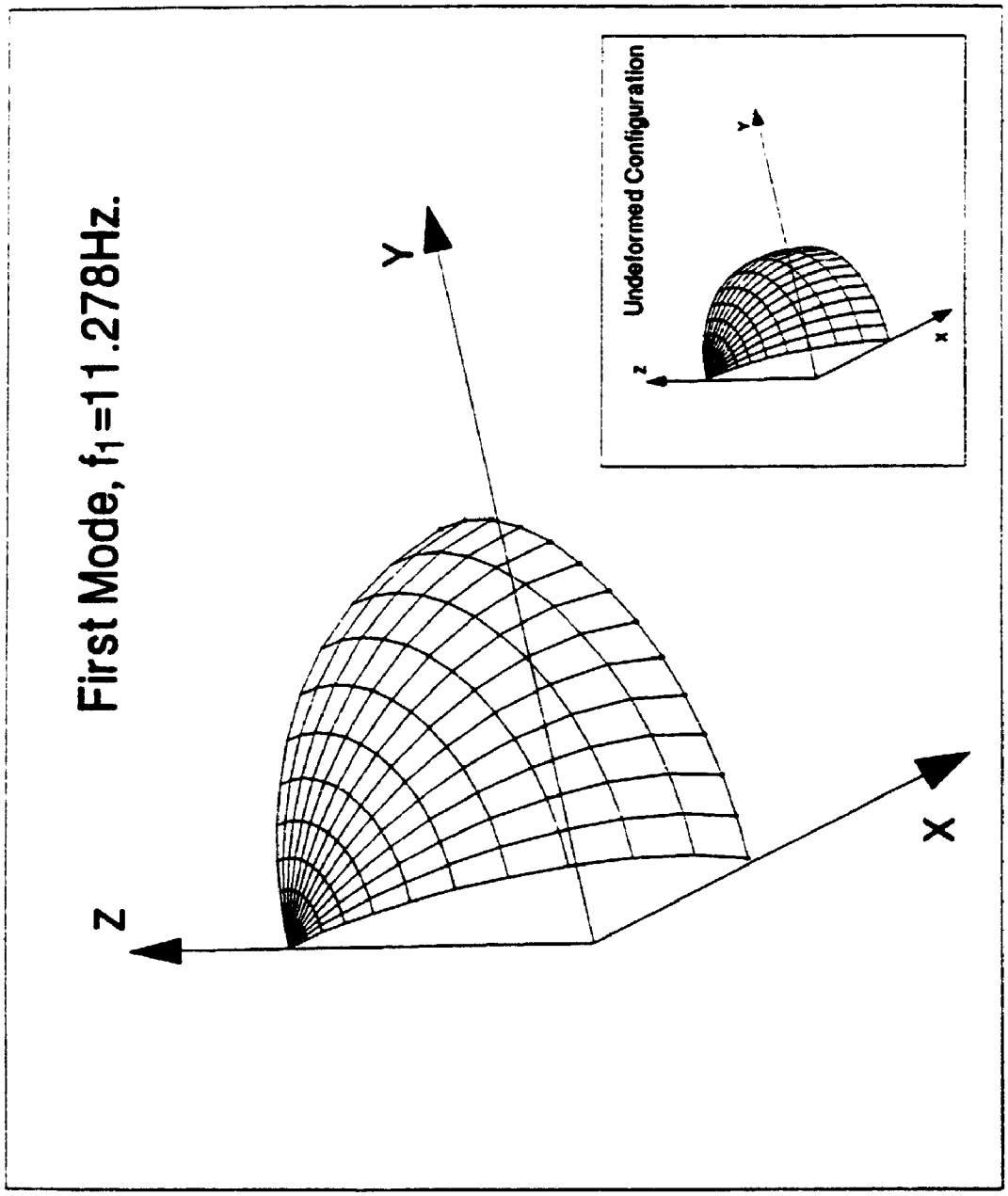

Figure 5.24 First mode shape of the hemispherical shell ($f_1 = 11.278$ Hz)

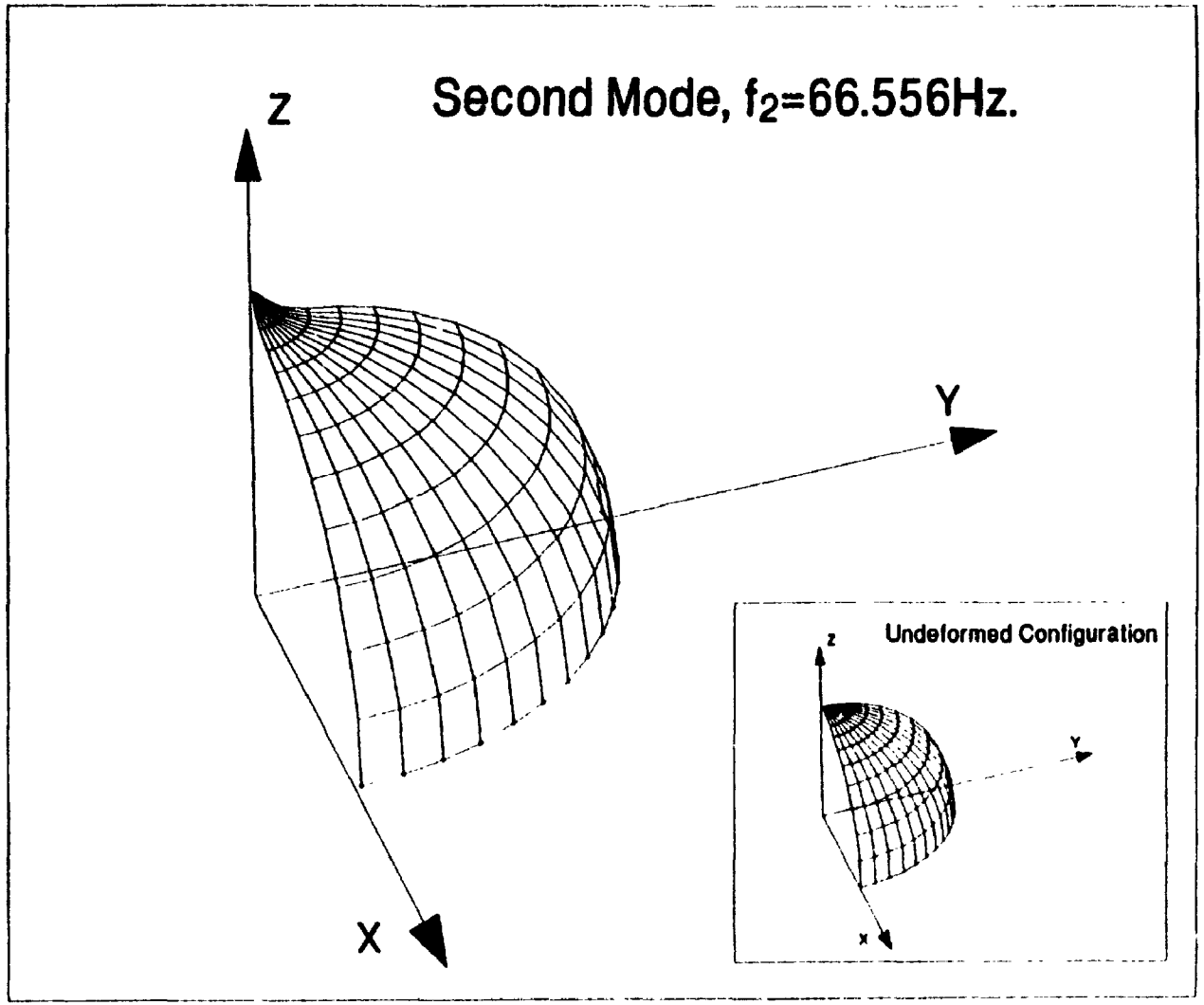

Figure 5.25 Second mode shape of the hemispherical shell ($f_2 = 66.556$ Hz)

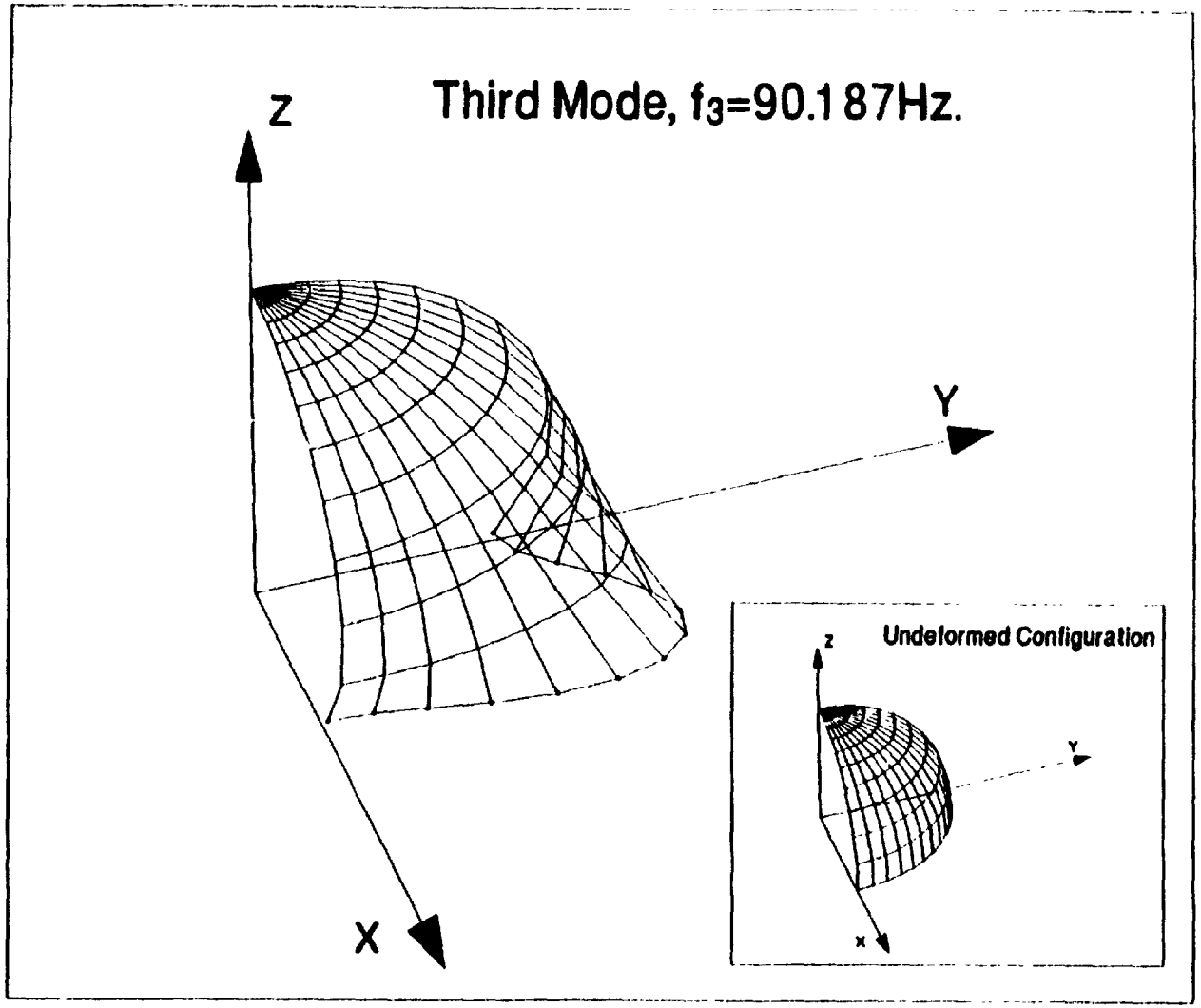

Figure 5.26 Third mode shape of the hemispherical shell (f_3 =90.187 Hz)

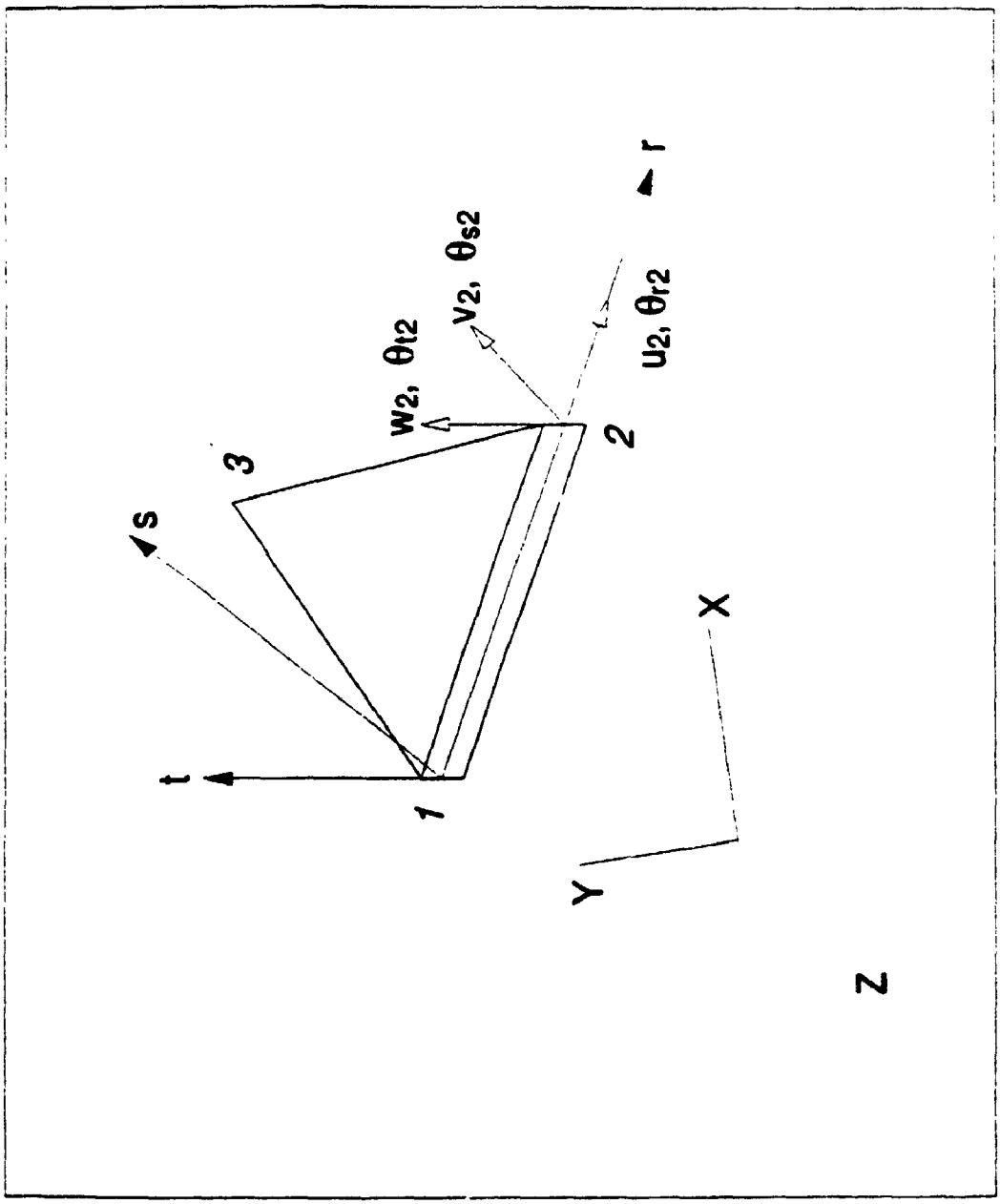

Figure 6.1 A representative 3 node flat triangular shell element

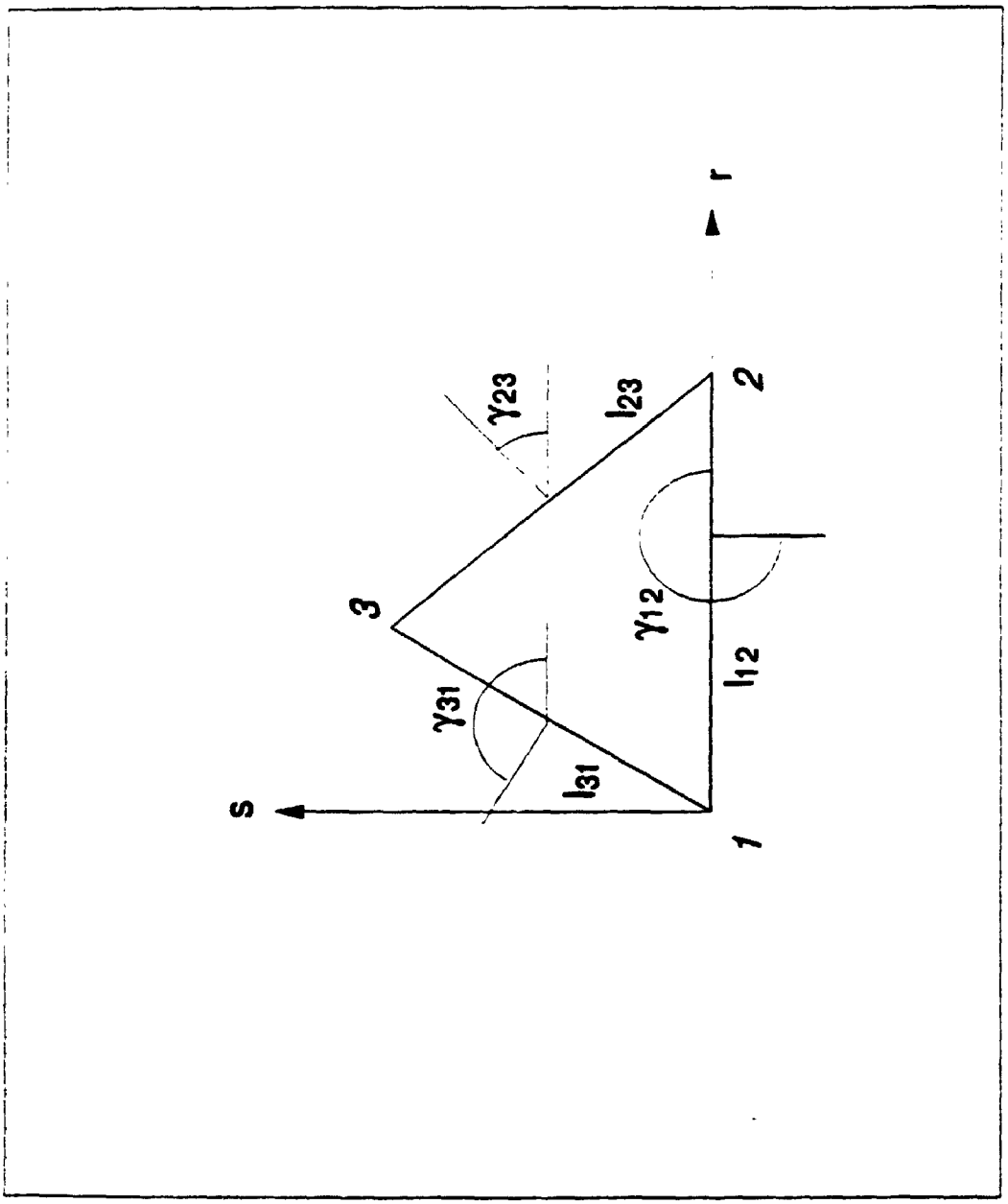

Figure 6.2 The geometry of the shell element

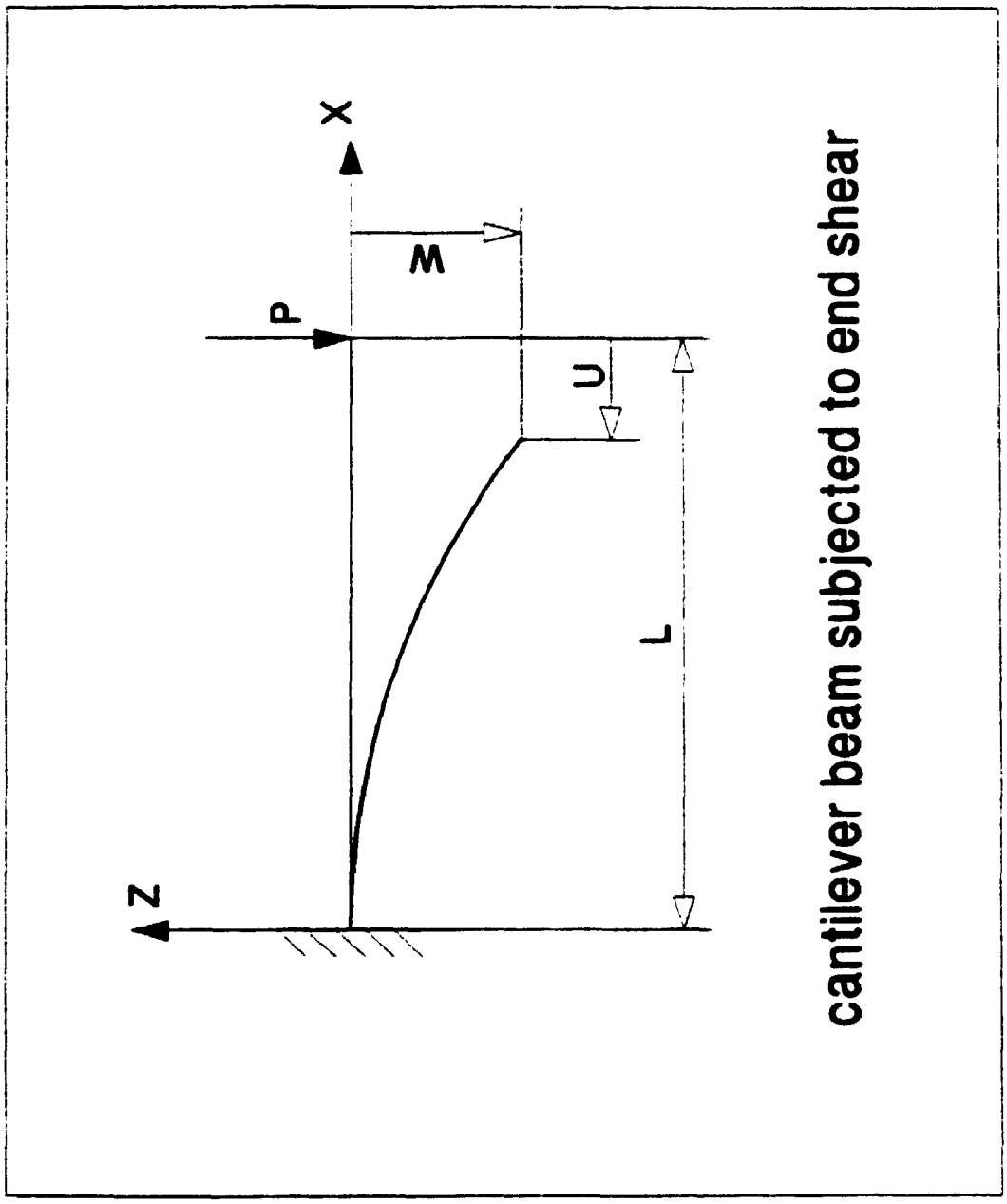

Figure 7.1 A cantilever beam subjected to a conservative end shear

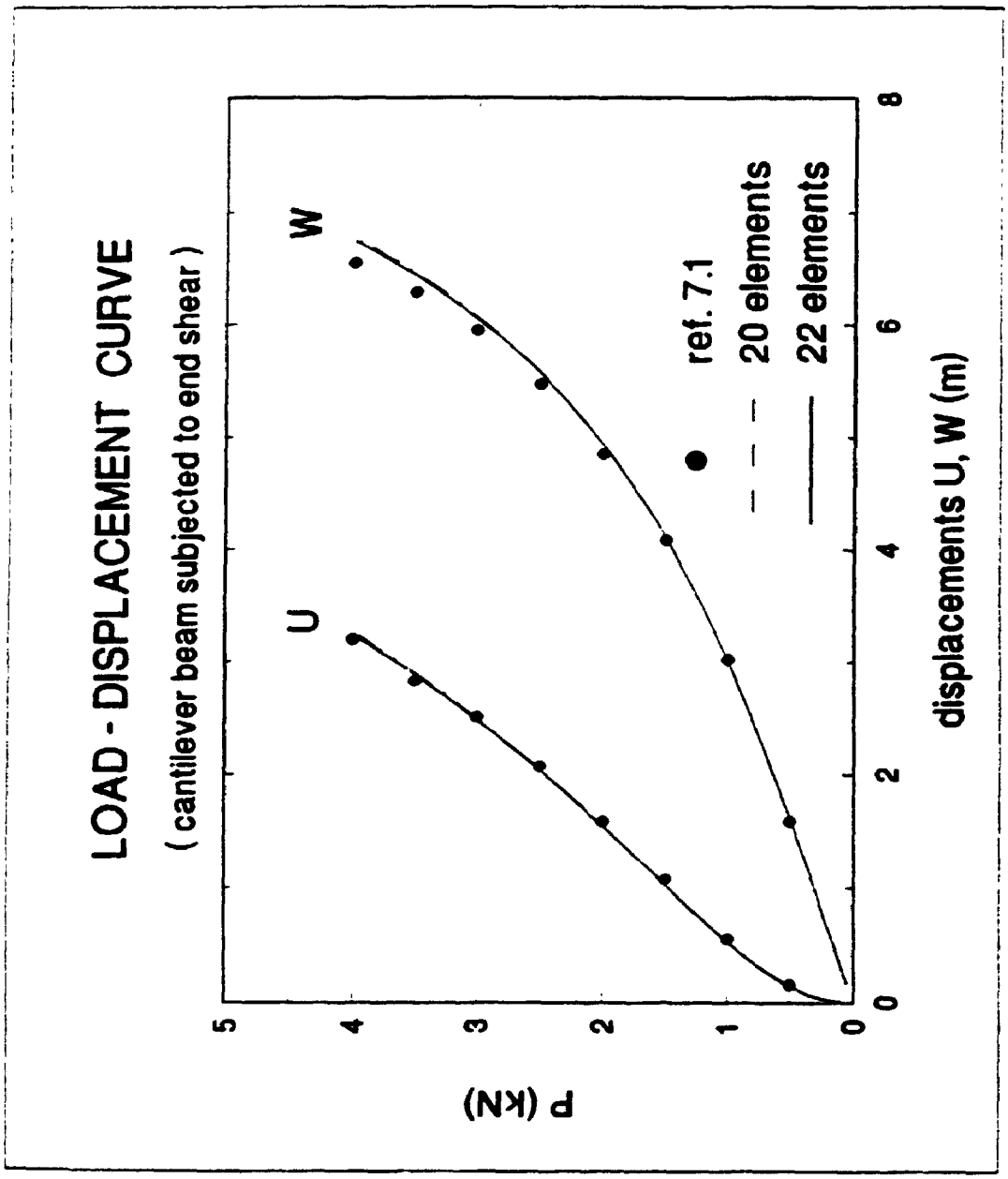

Figure 7.2 Load-displacement curve for the cantilever beam

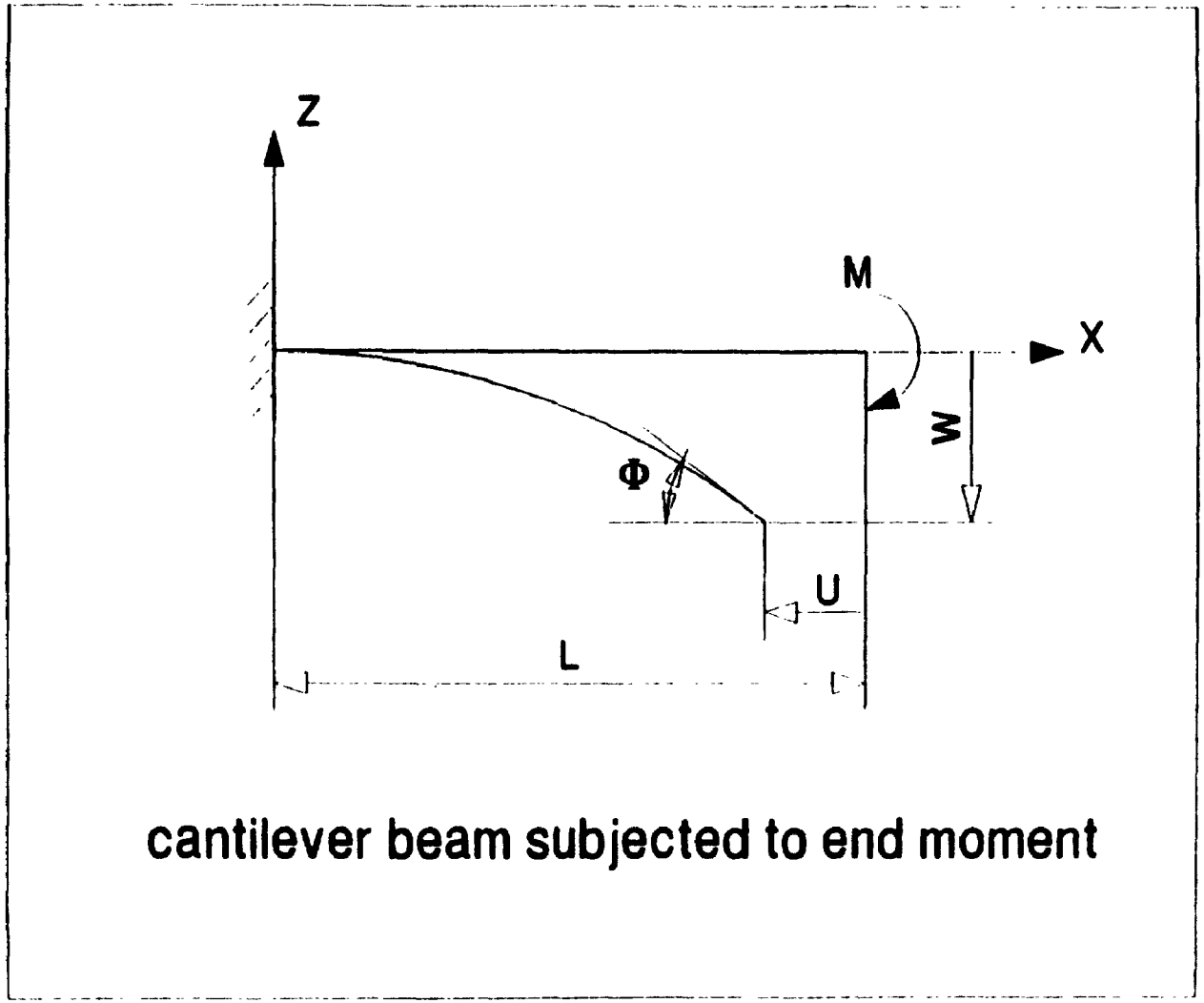

Figure 7.3 A cantilever beam subjected to an end moment

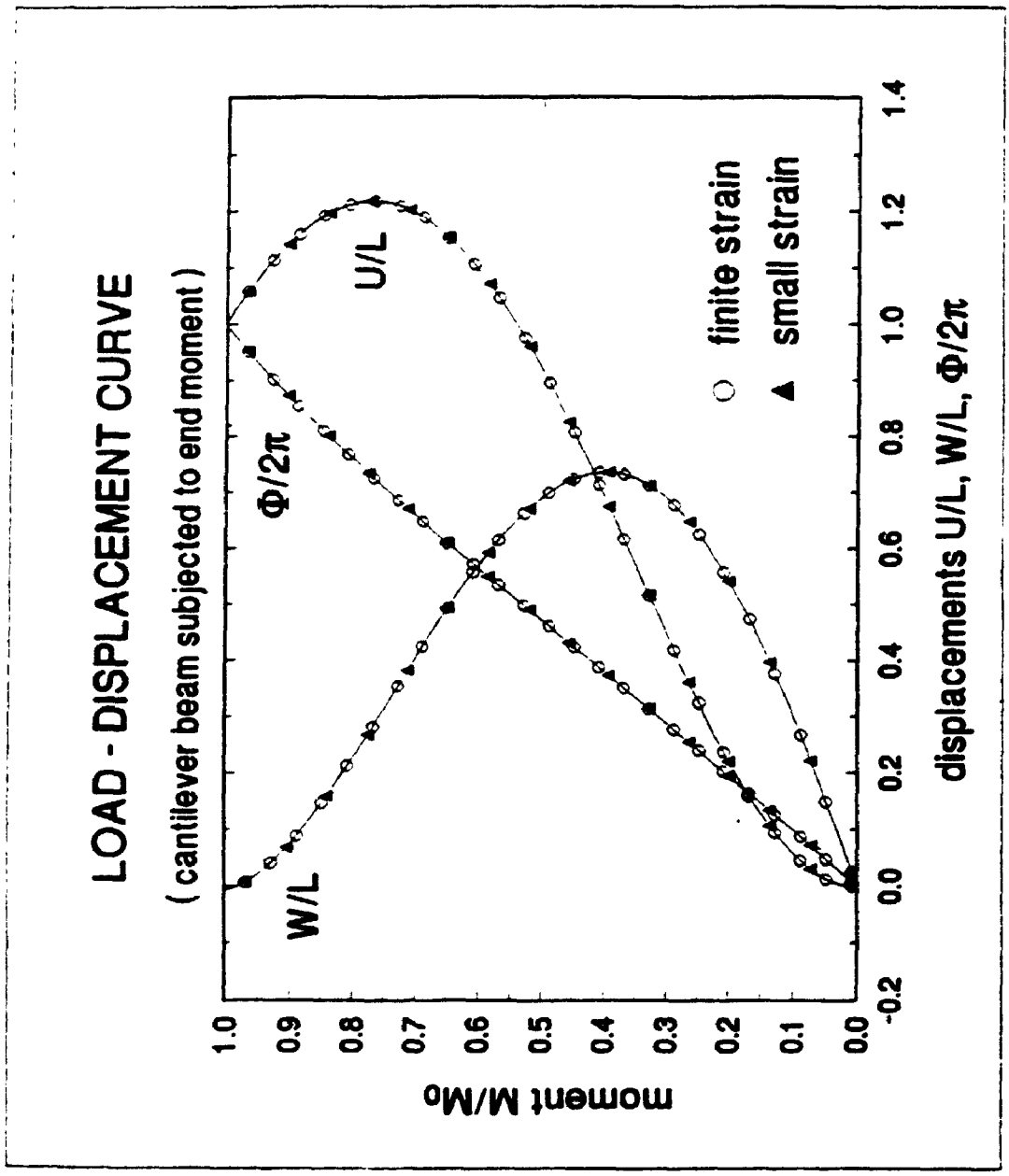

Figure 7.4 Load-displacement curve for the cantilever beam

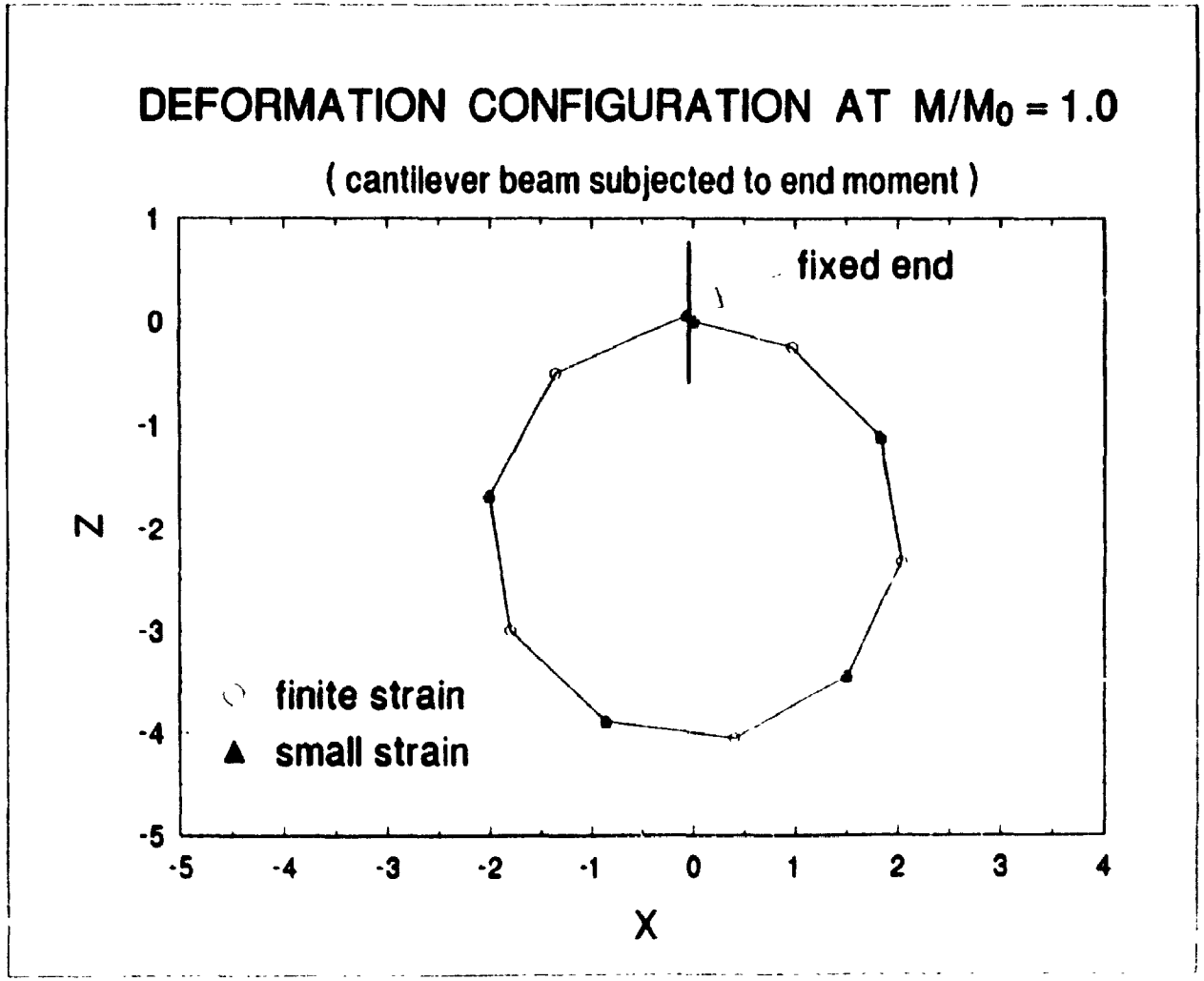

Figure 7.5 Deformation configuration of the cantilever beam at $M/M_0 = 1.0$

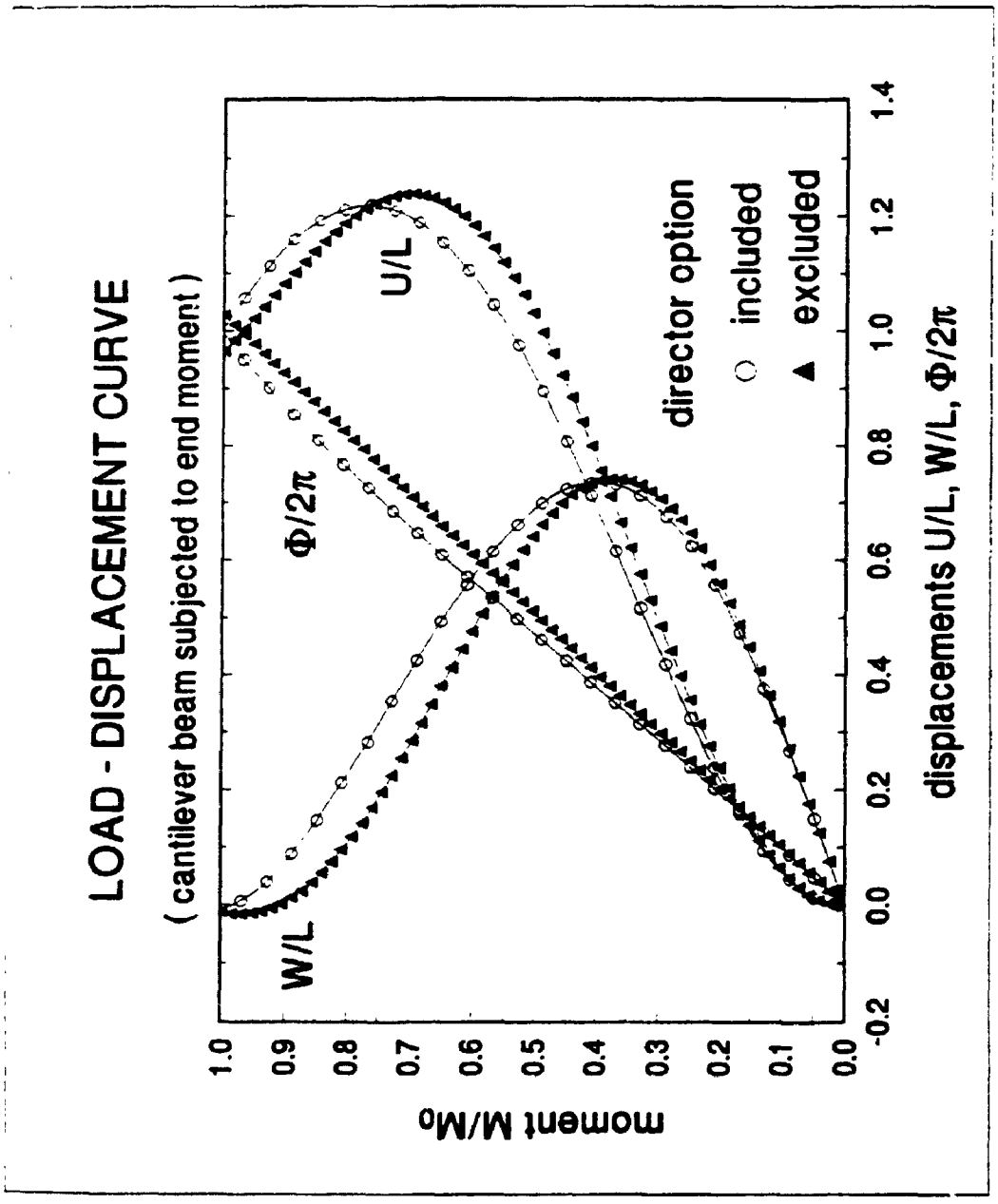

Figure 7.6 Load-displacement curve for the cantilever beam

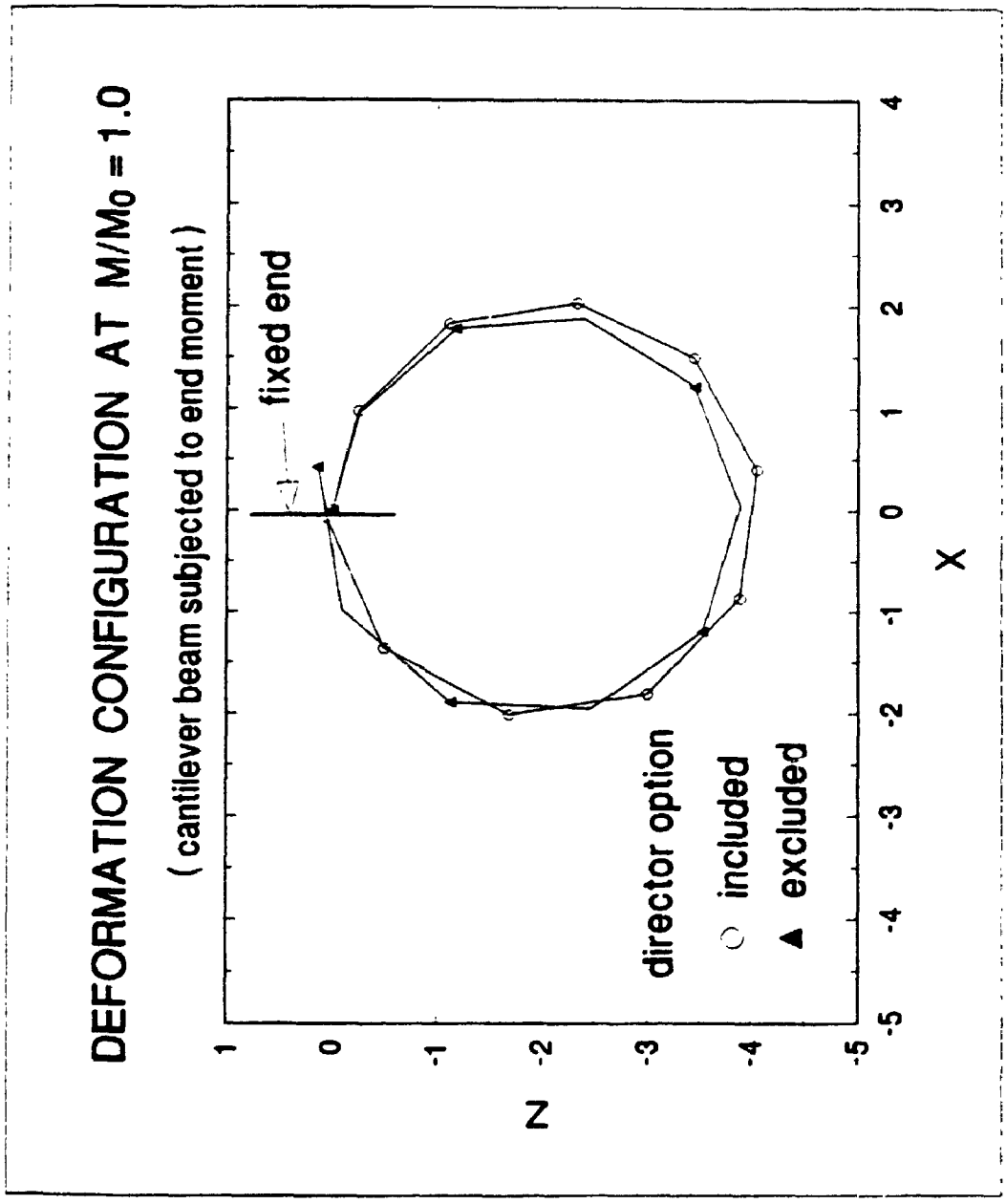

Figure 7.7 Deformation configuration of the cantilever beam at $M/M_0 = 1.0$

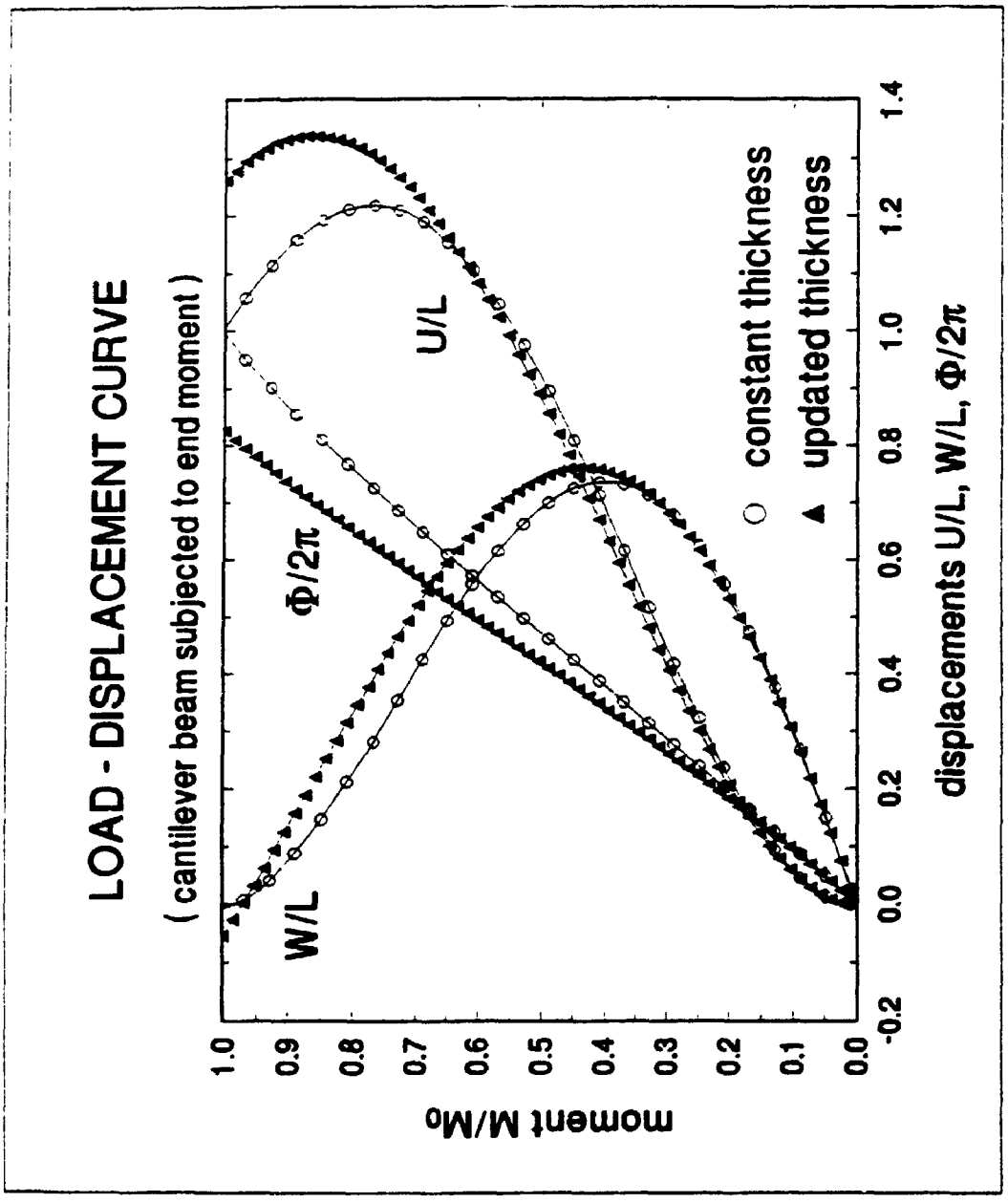

Figure 7.8 Load-displacement curve for the cantilever beam

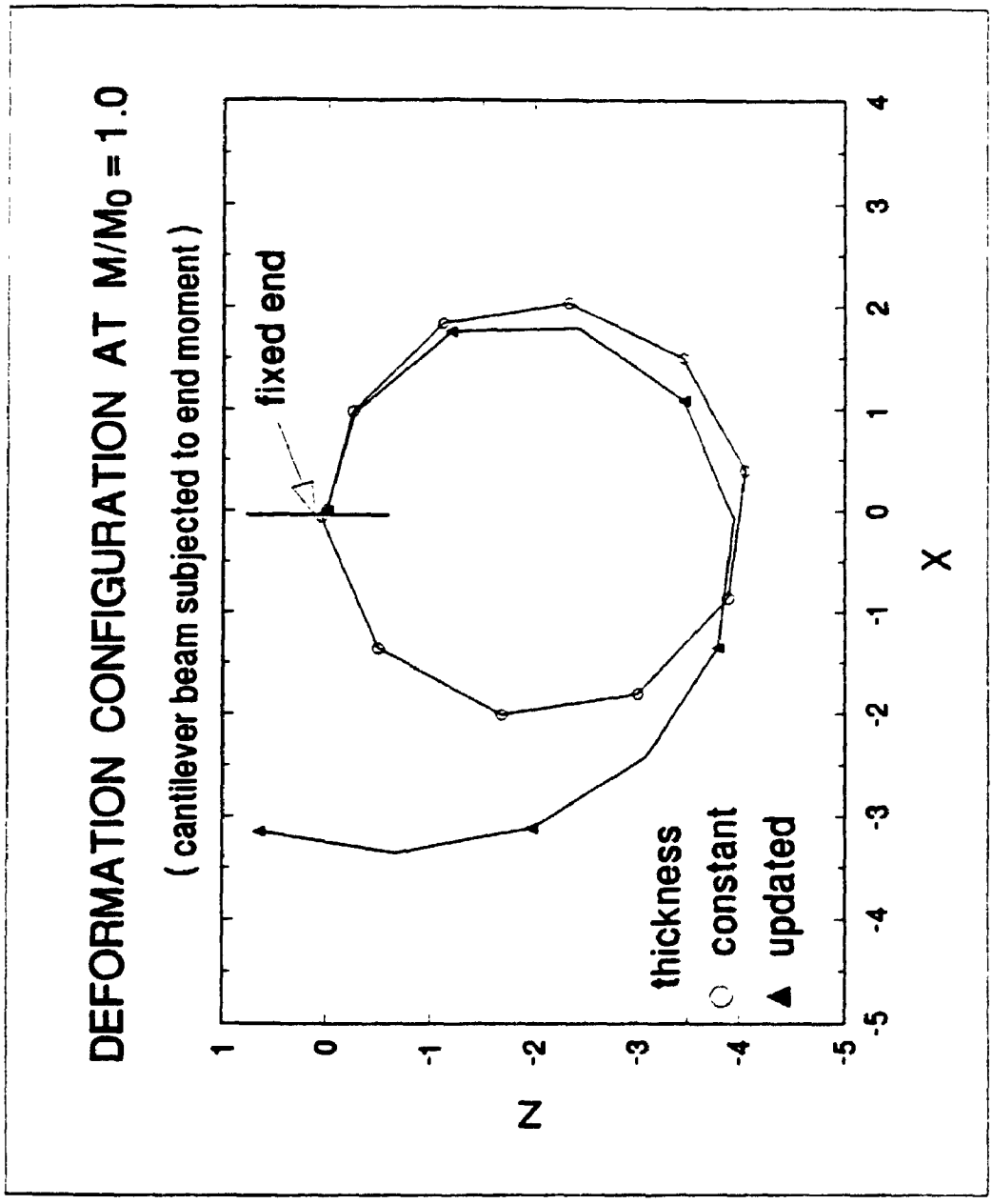

Figure 7.9 Deformation configuration of the cantilever beam at $M/M_0 = 1.0$

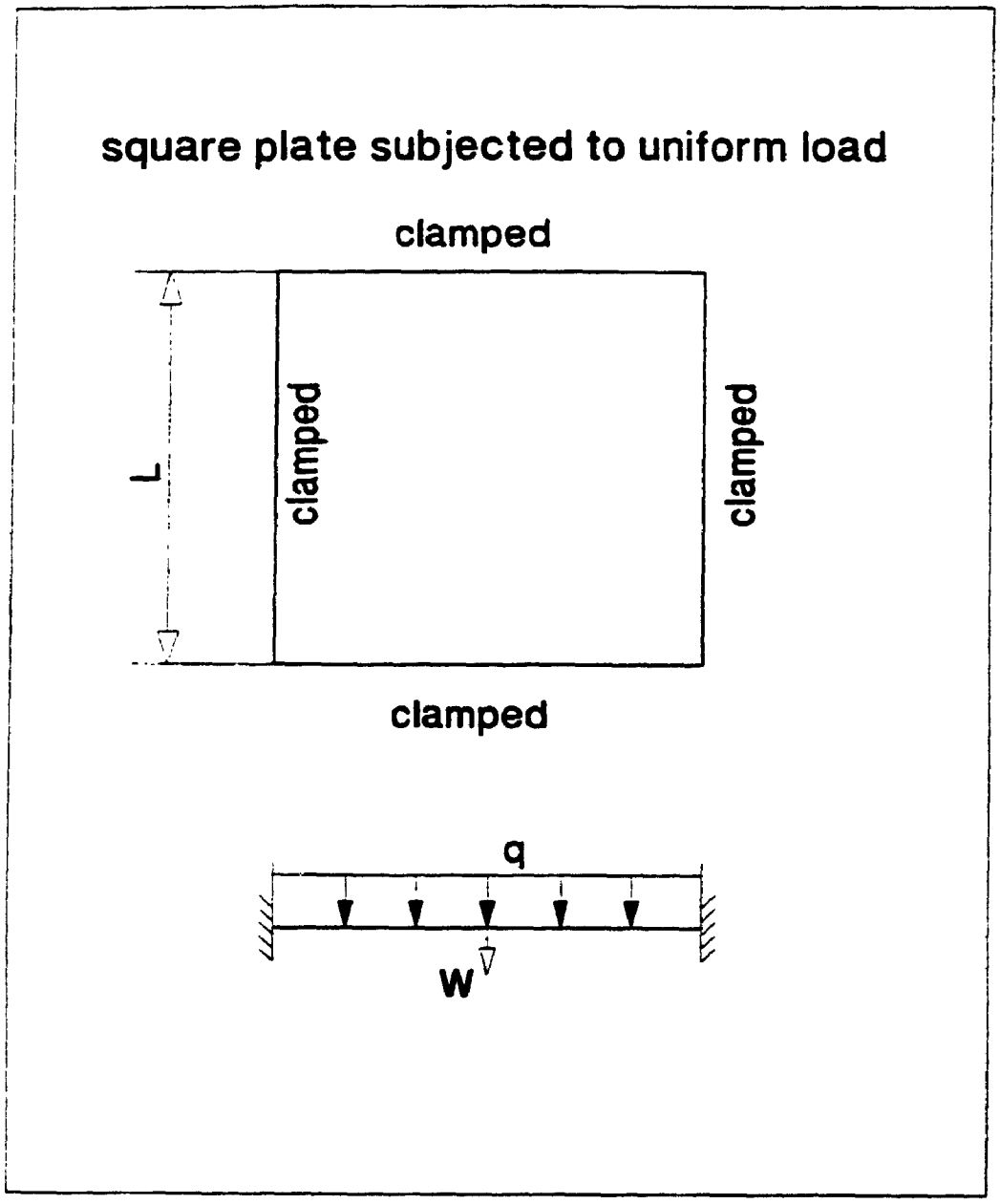

Figure 7.10 A clamped square plate subjected to uniform load

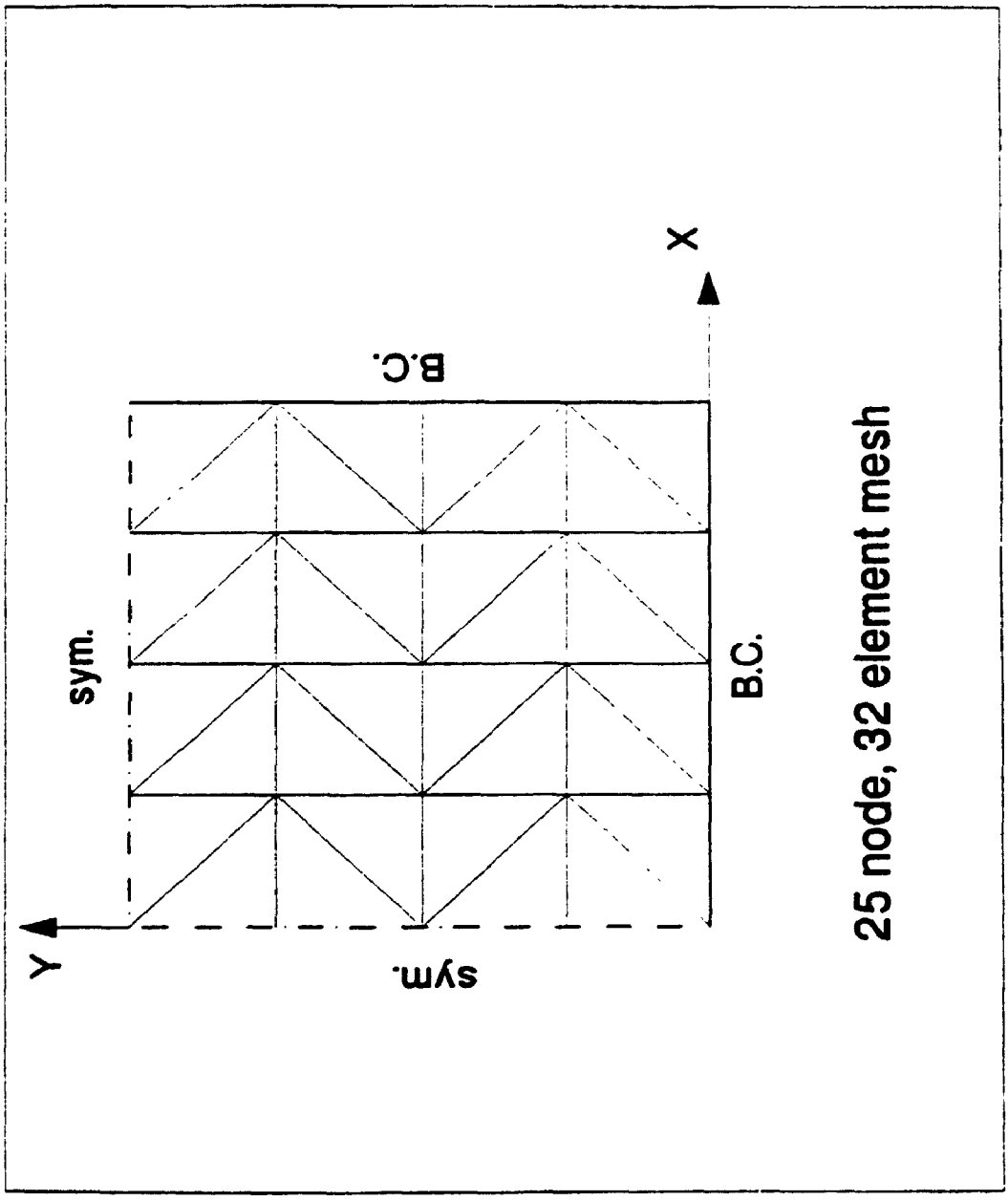

Figure 7.11 The 25 node, 32 element mesh

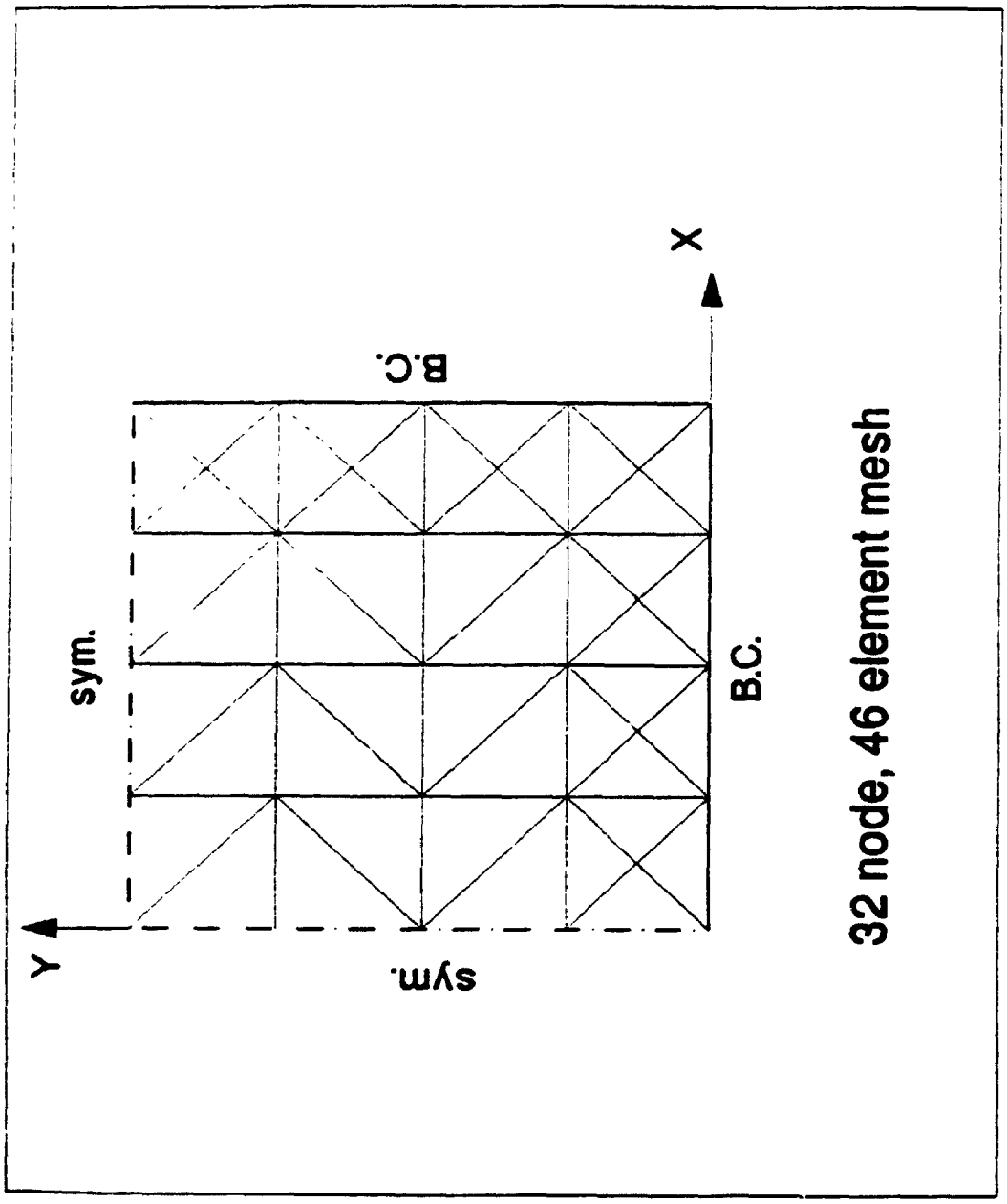

Figure 7.12 The 32 node, 46 element mesh

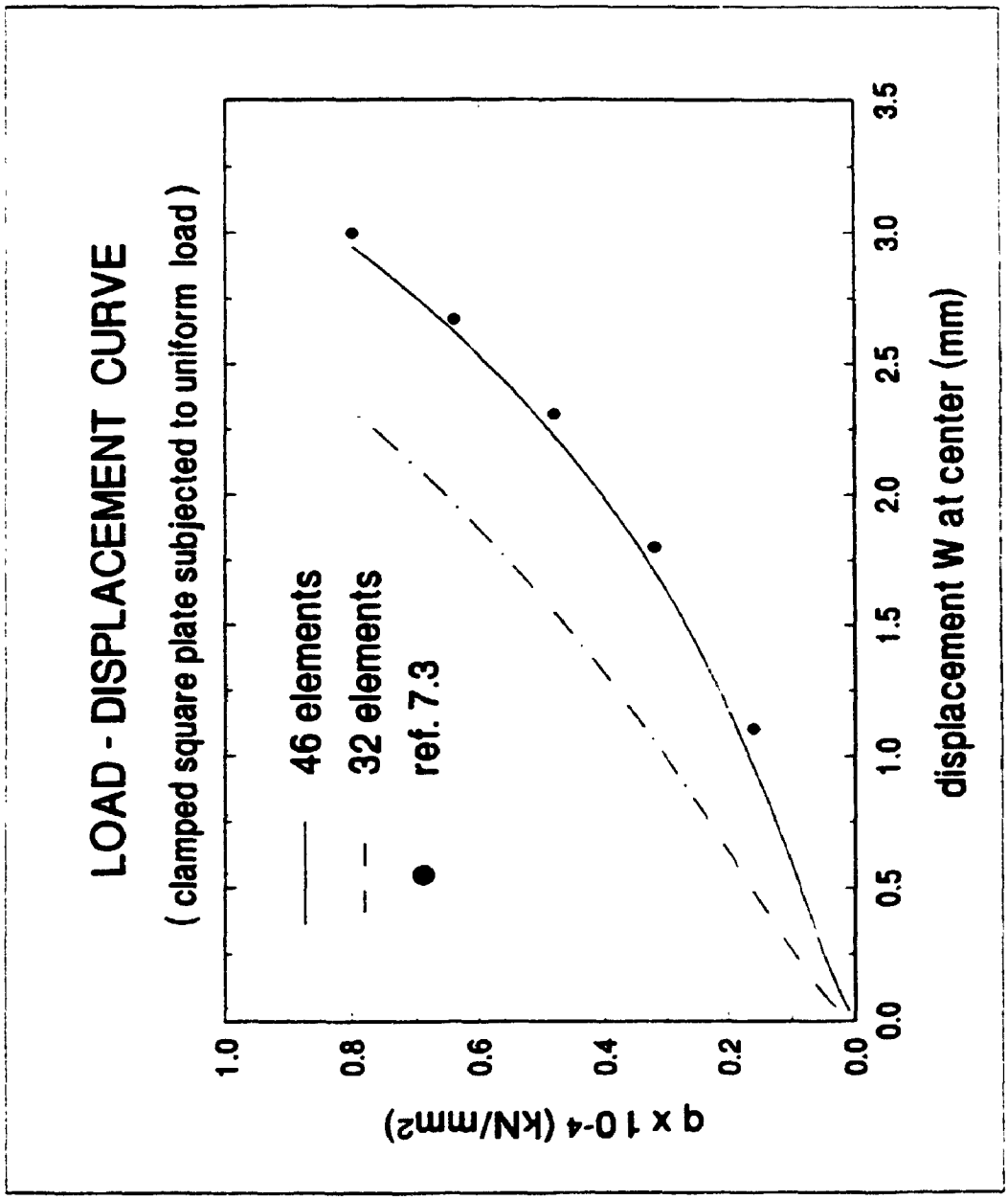

Figure 7.13 Load-displacement curve for the clamped square plate

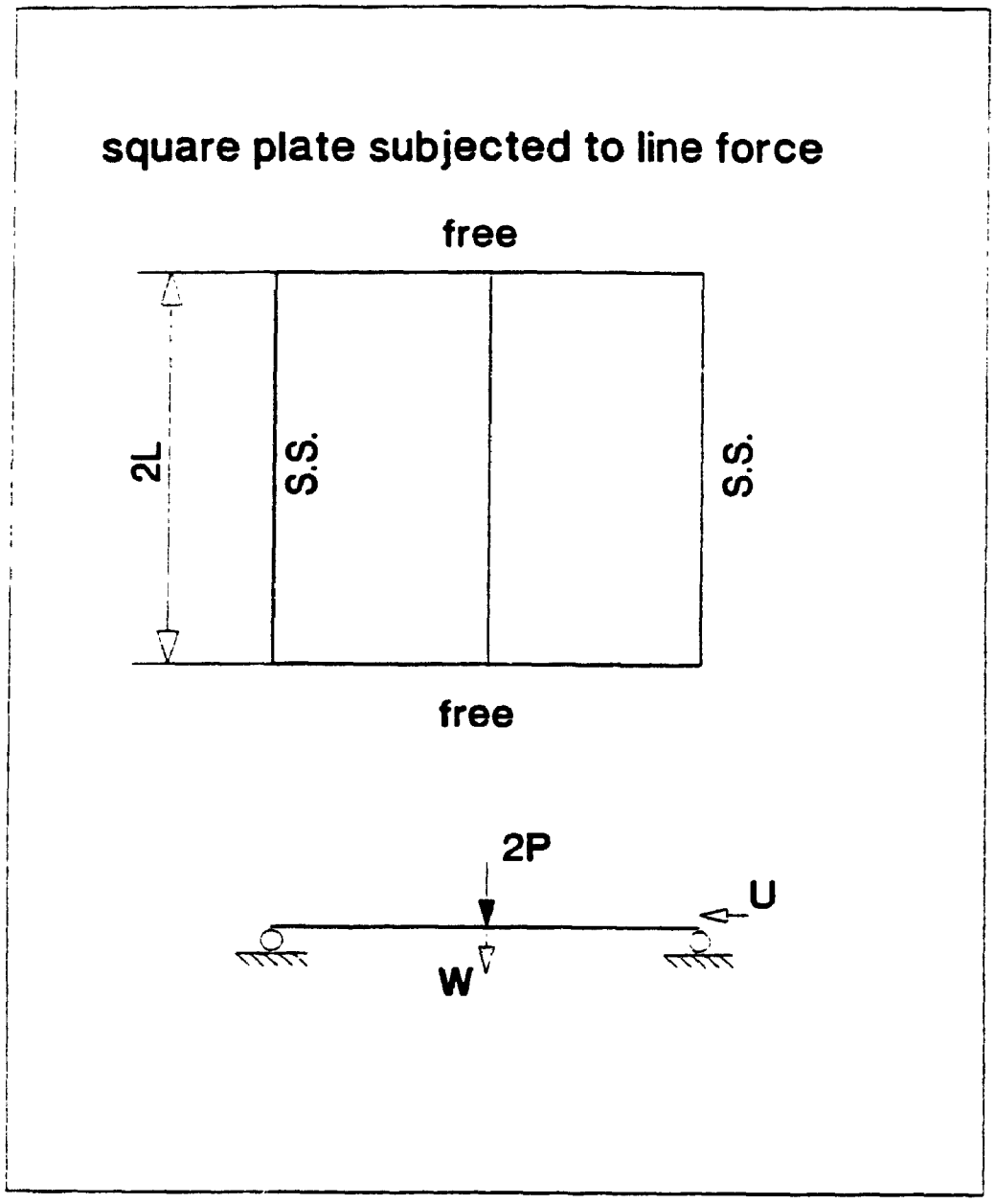

Figure 7.14 A square plate subjected to a line force

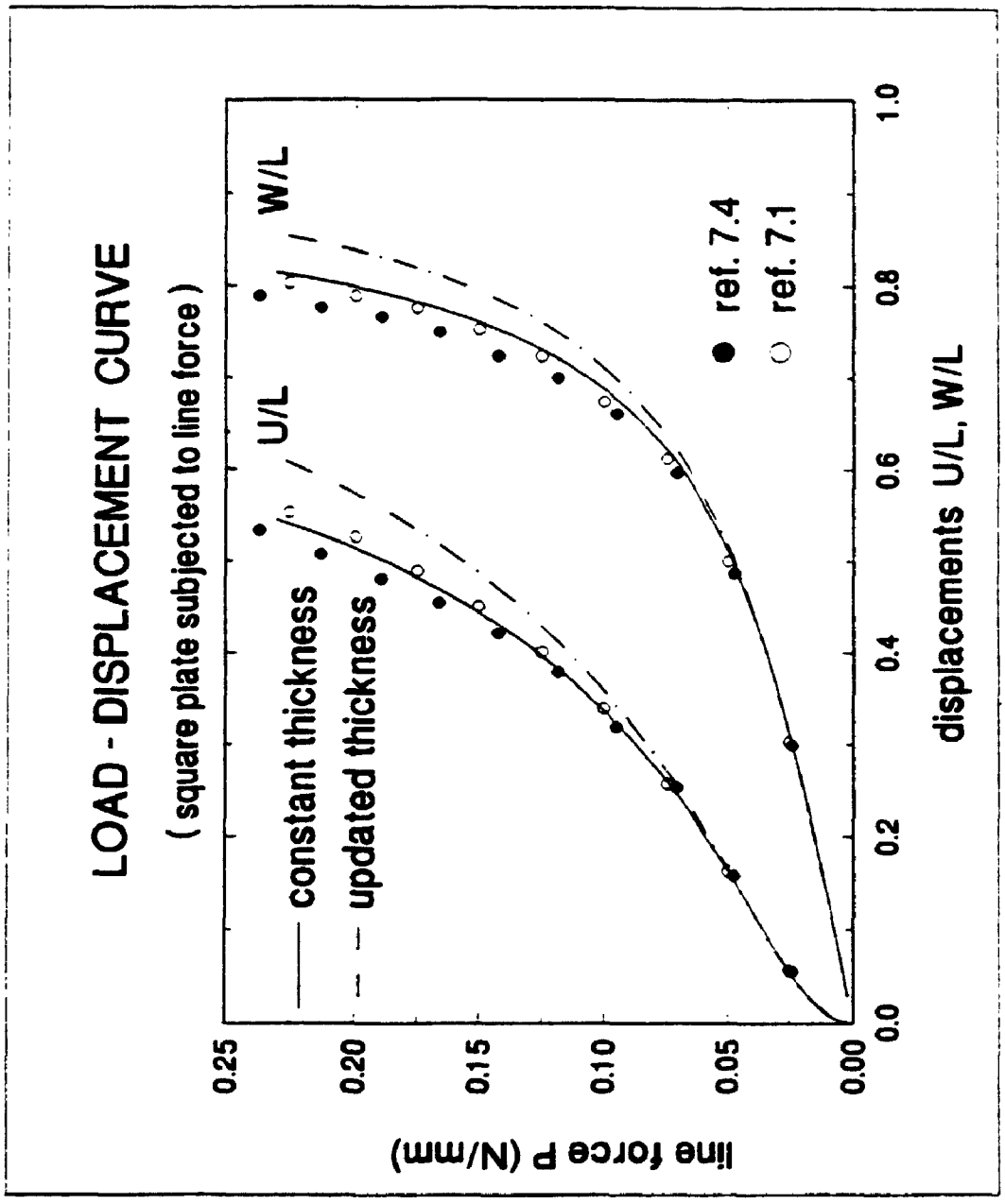

Figure 7.15 Load-displacement curve for the square plate

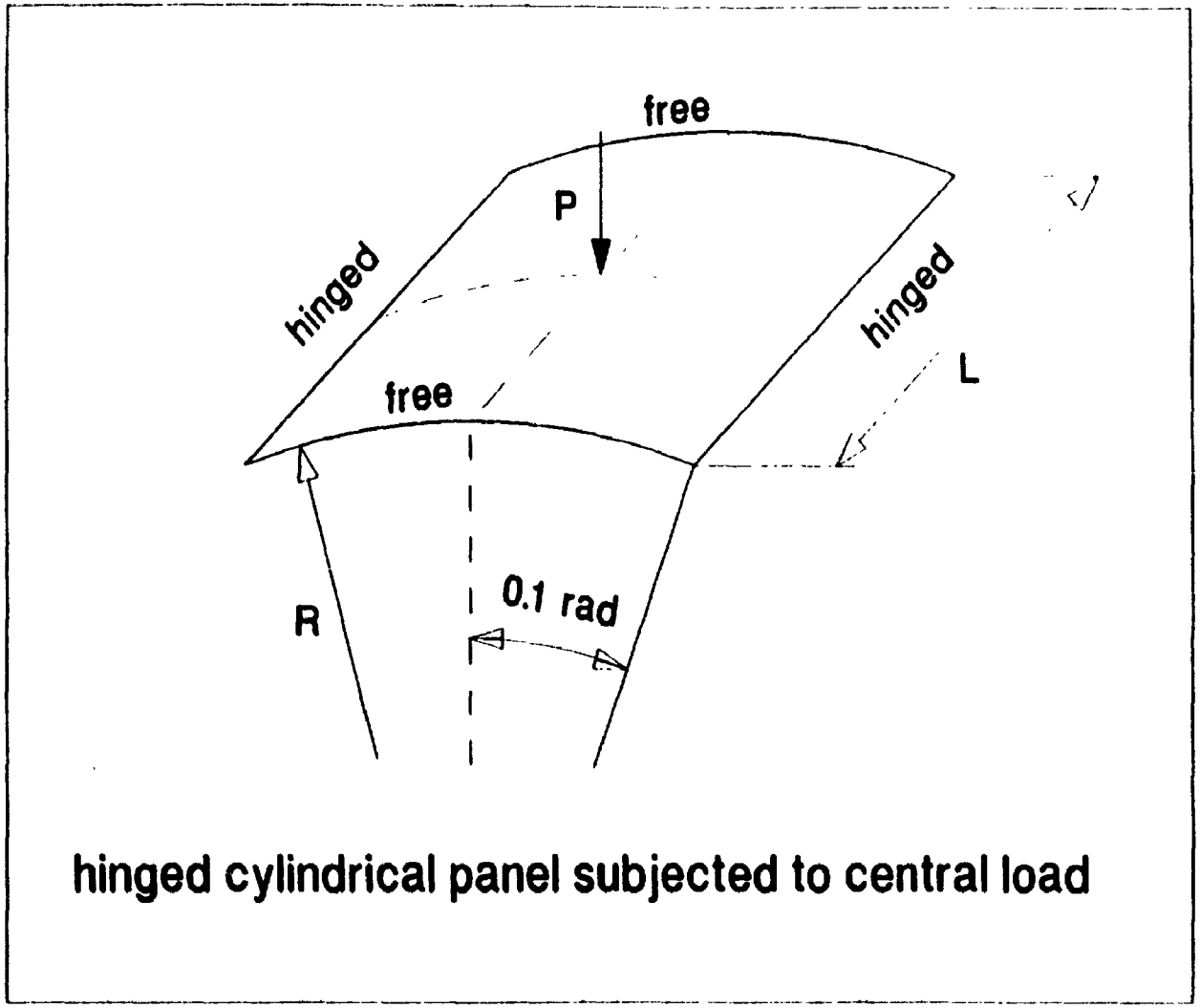

Figure 7.16 The hinged cylindrical panel subjected to a central load

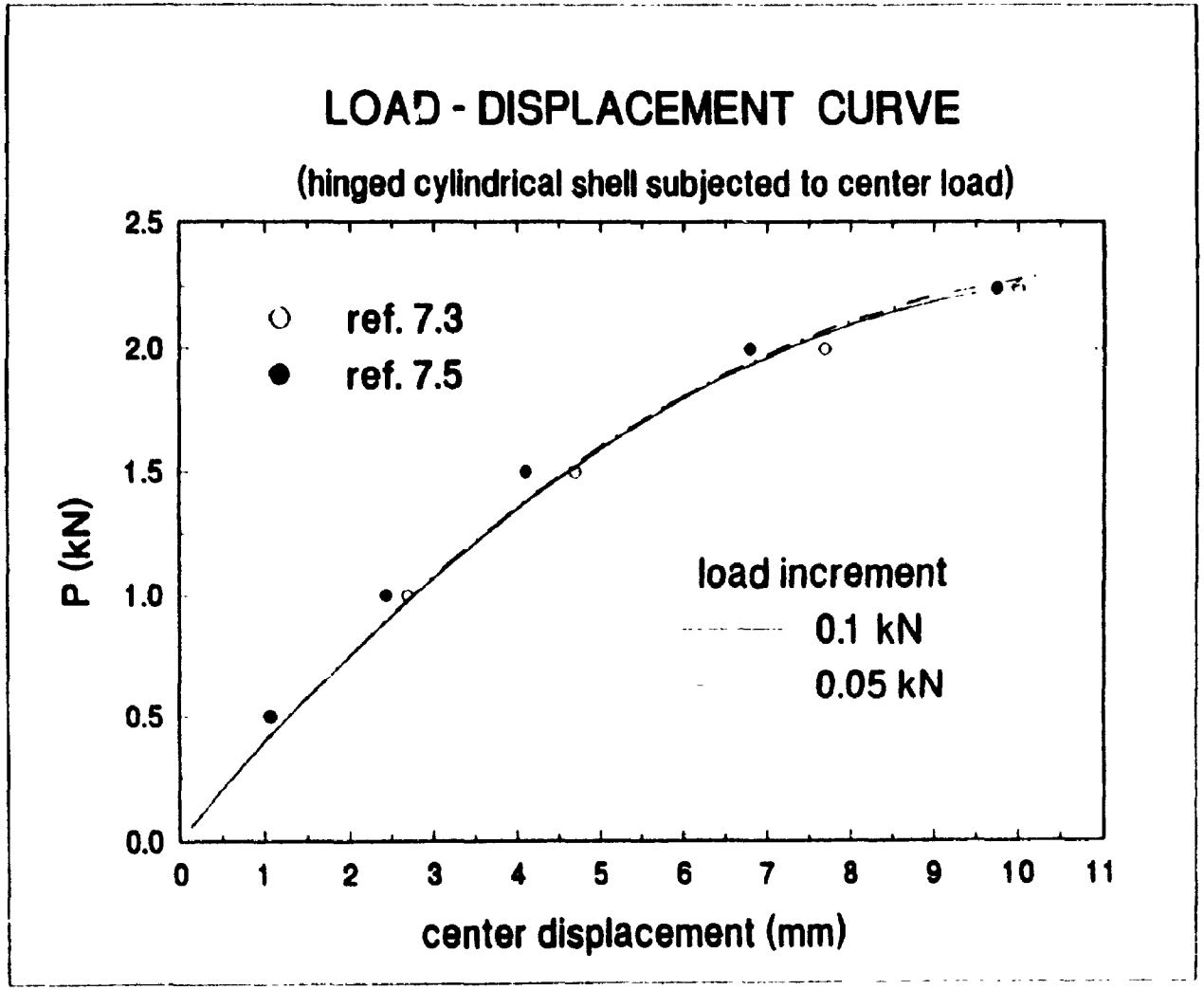

Figure 7.17 Load-displacement curve for the hinged cylindrical shell

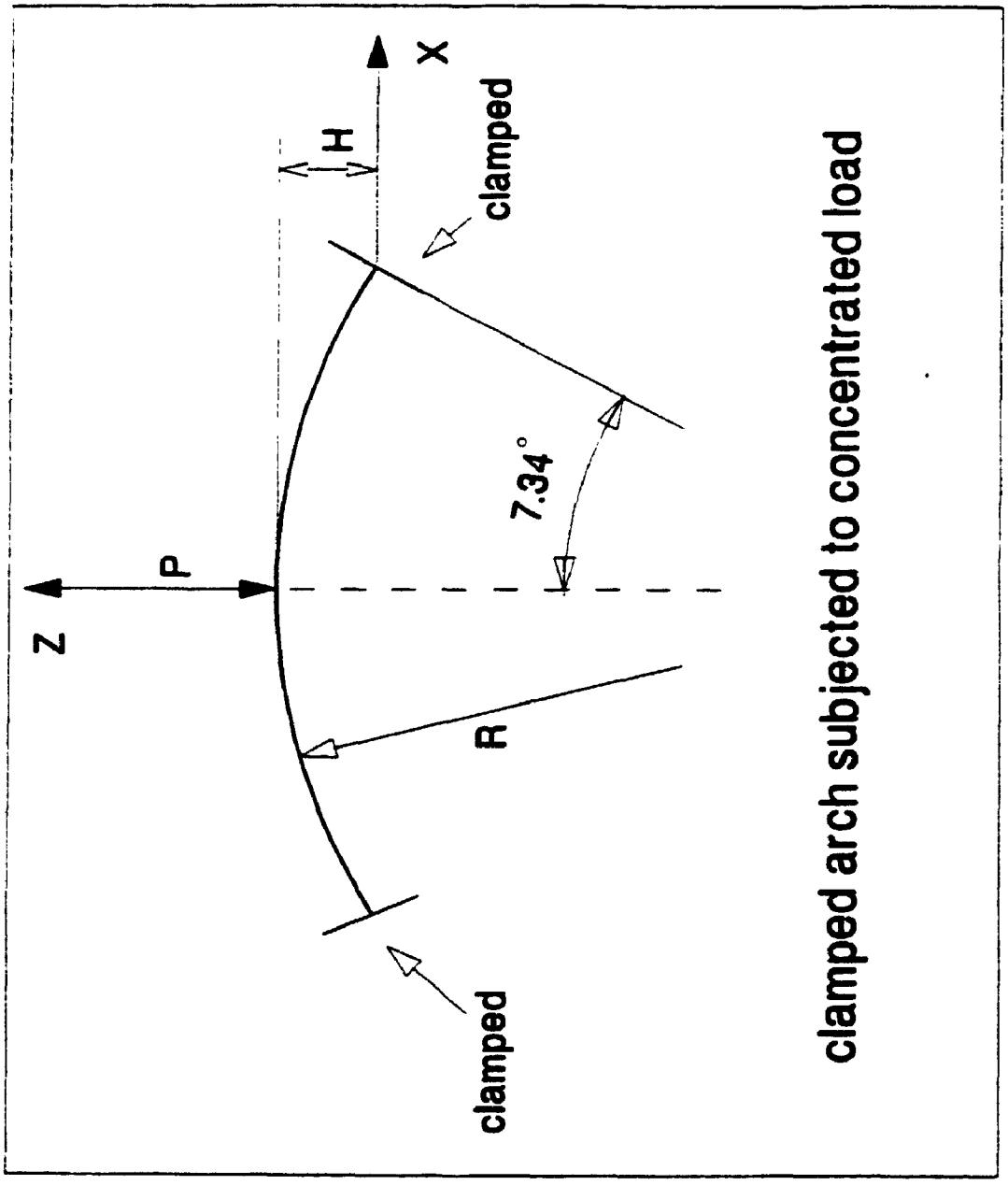

Figure 7.18 The clamped arch subjected to a concentrated load

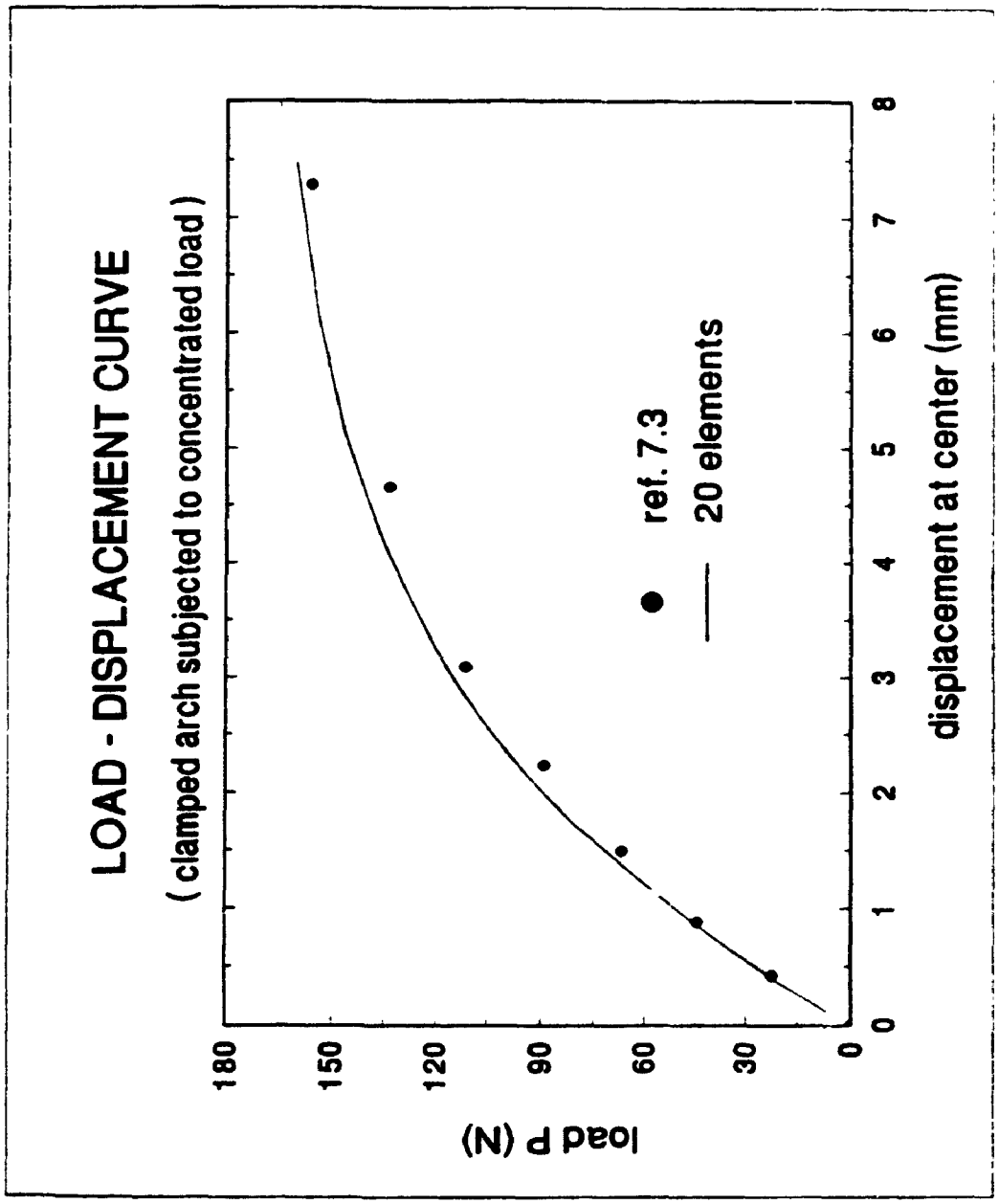

Figure 7.19 Load-displacement curve for the clamped arch

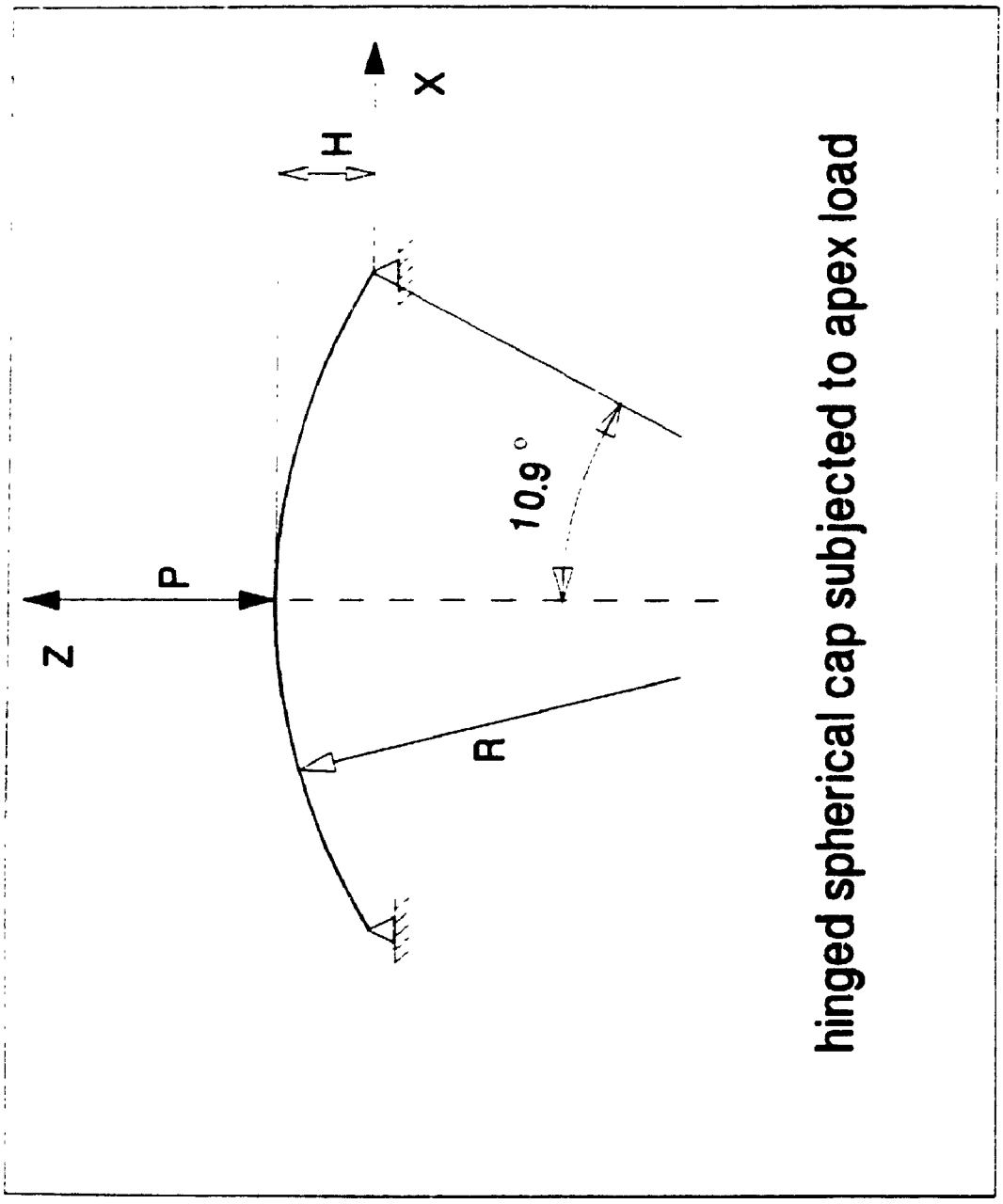

Figure 7.20 The hinged spherical cap subjected to an apex load

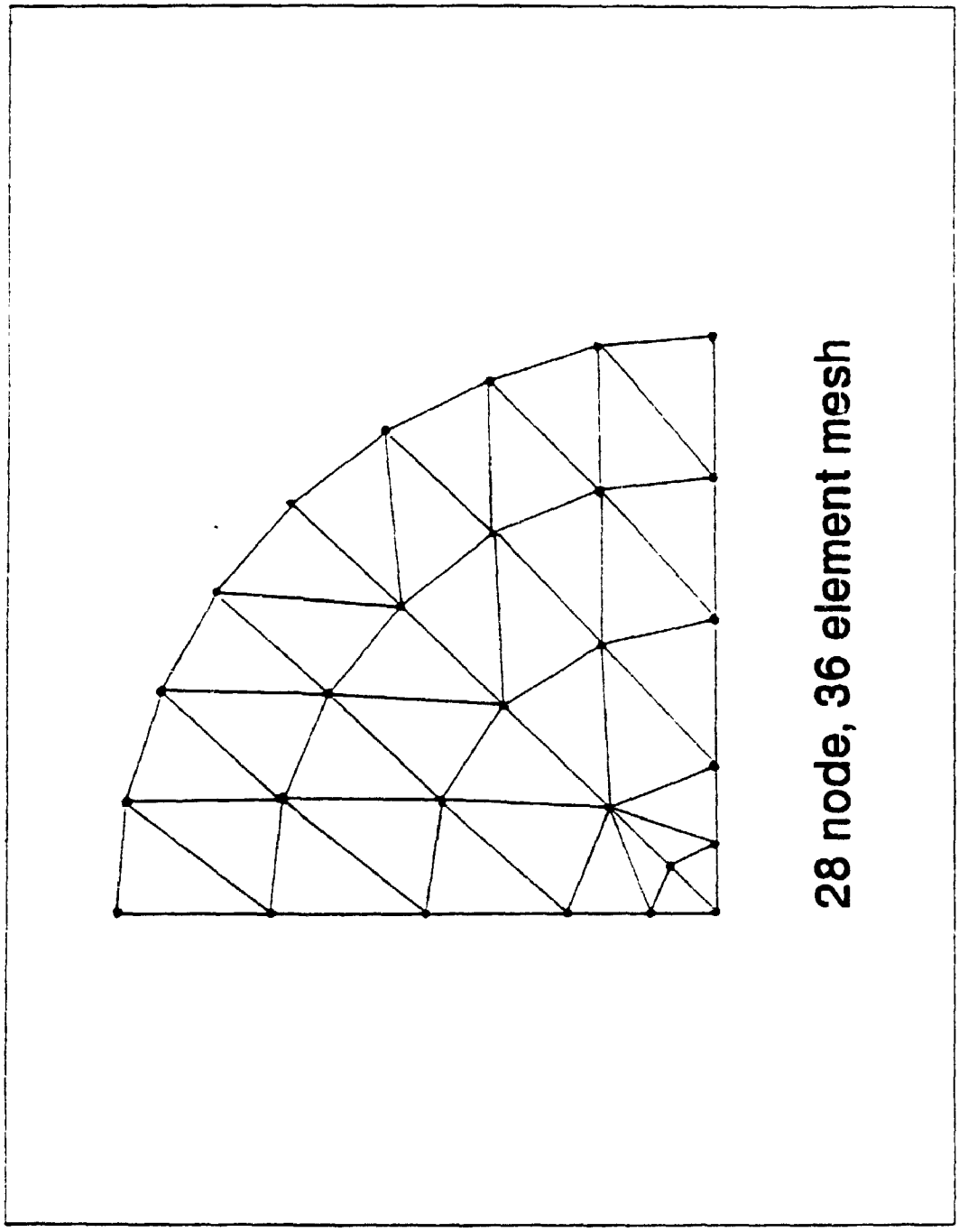

Figure 7.21 The 28 node, 36 element mesh

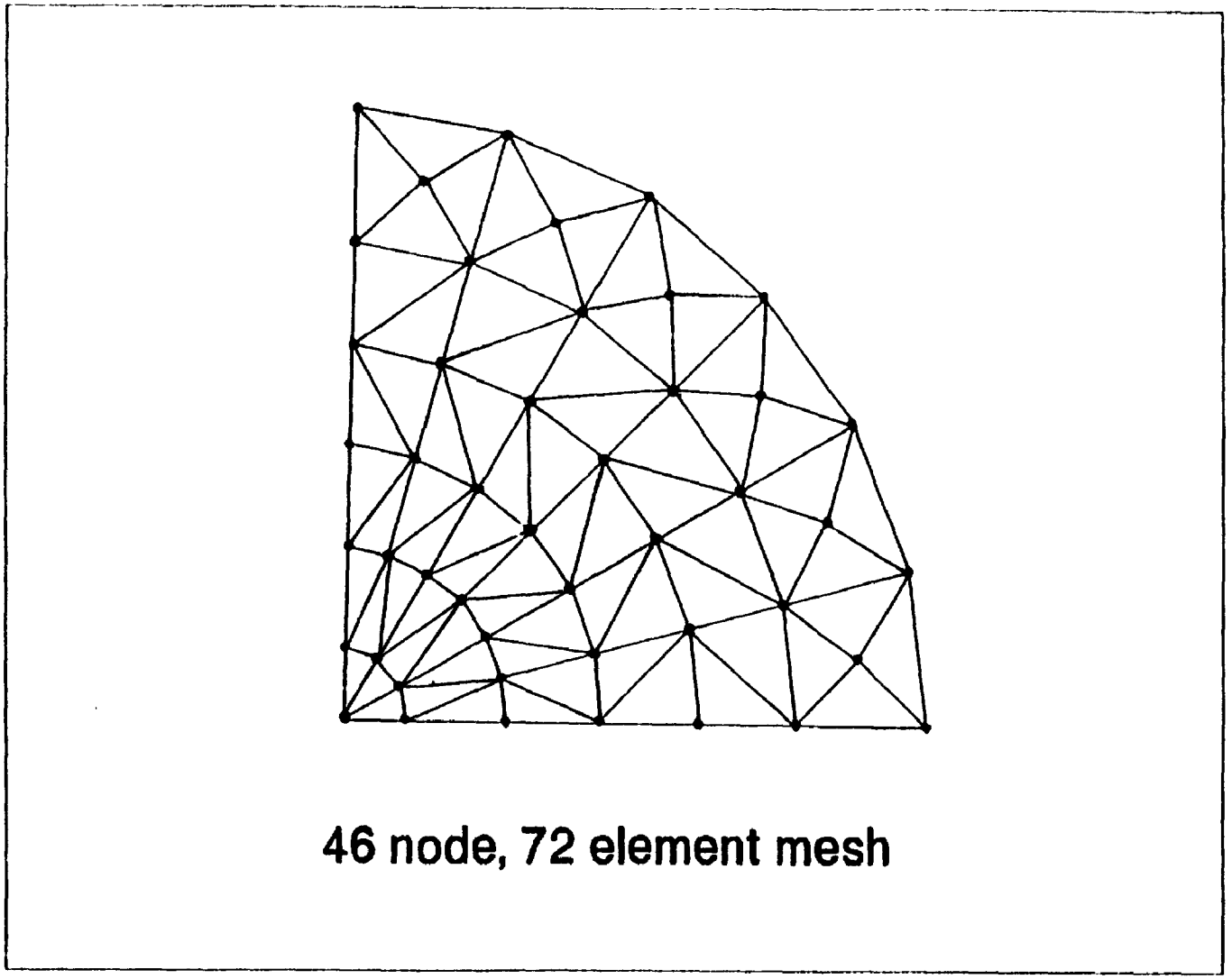

Figure 7.22 The 46 node, 72 element mesh

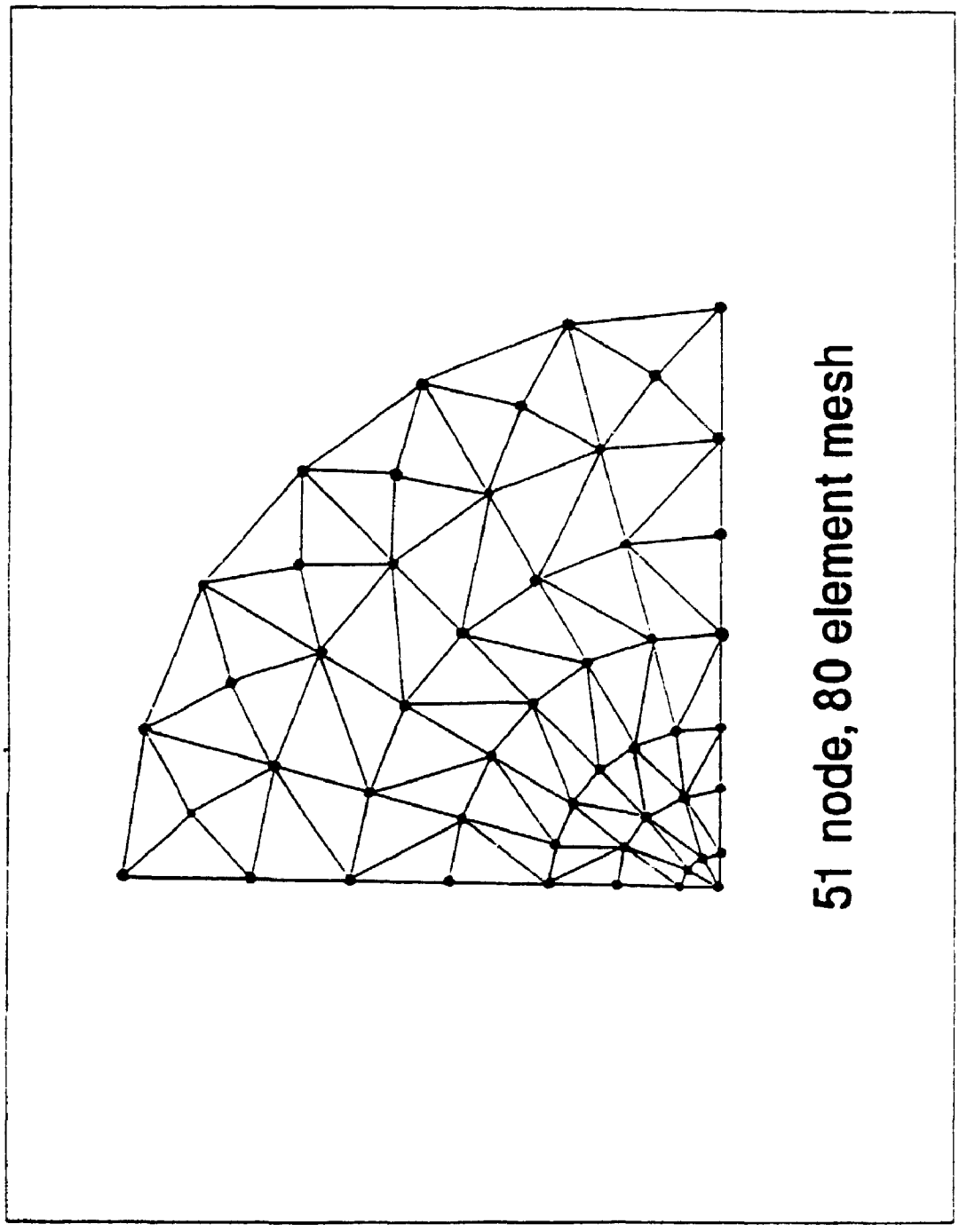

Figure 7.23 The 51 node, 80 element mesh

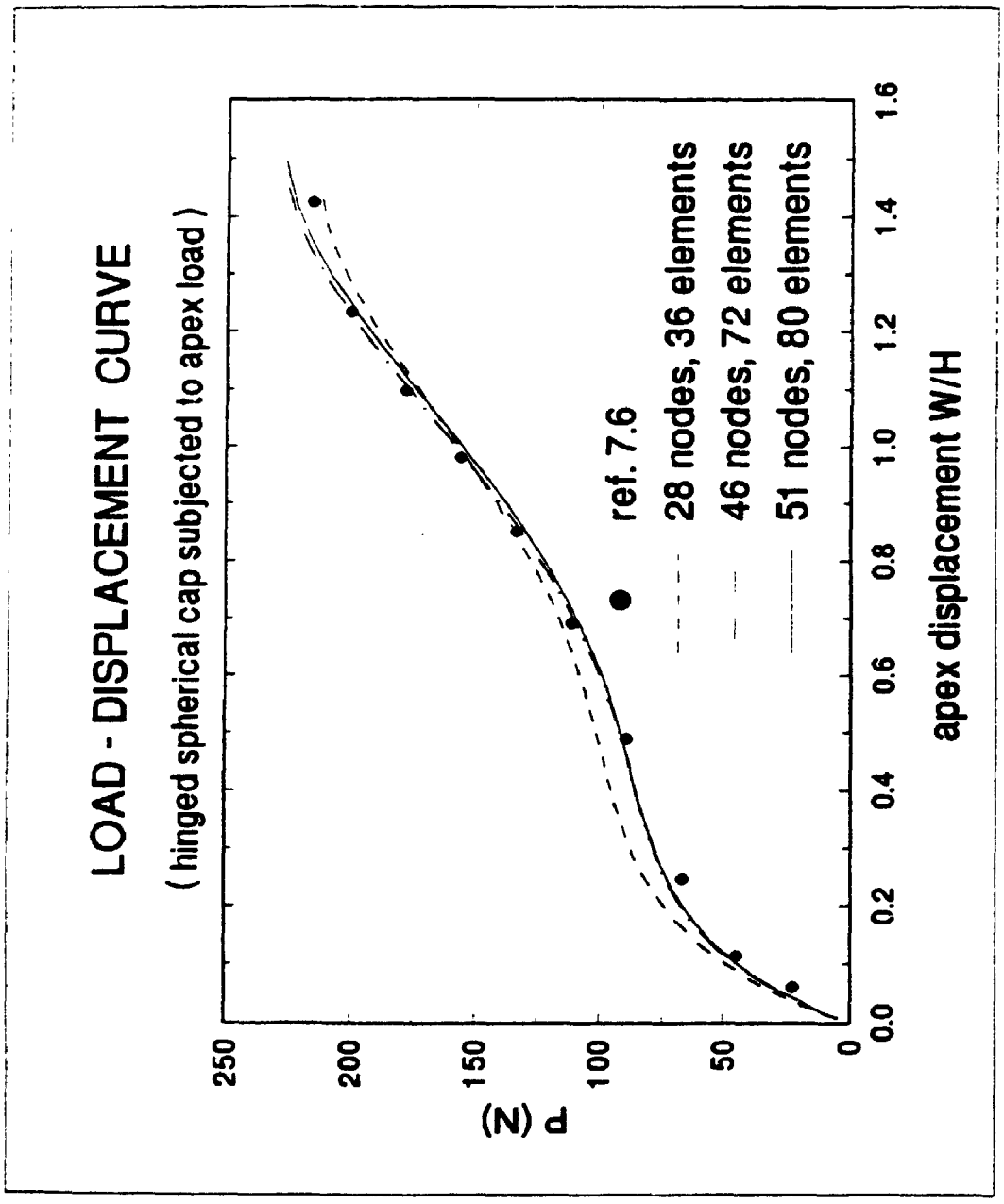

Figure 7.24 Load-displacement curve for the hinged spherical cap

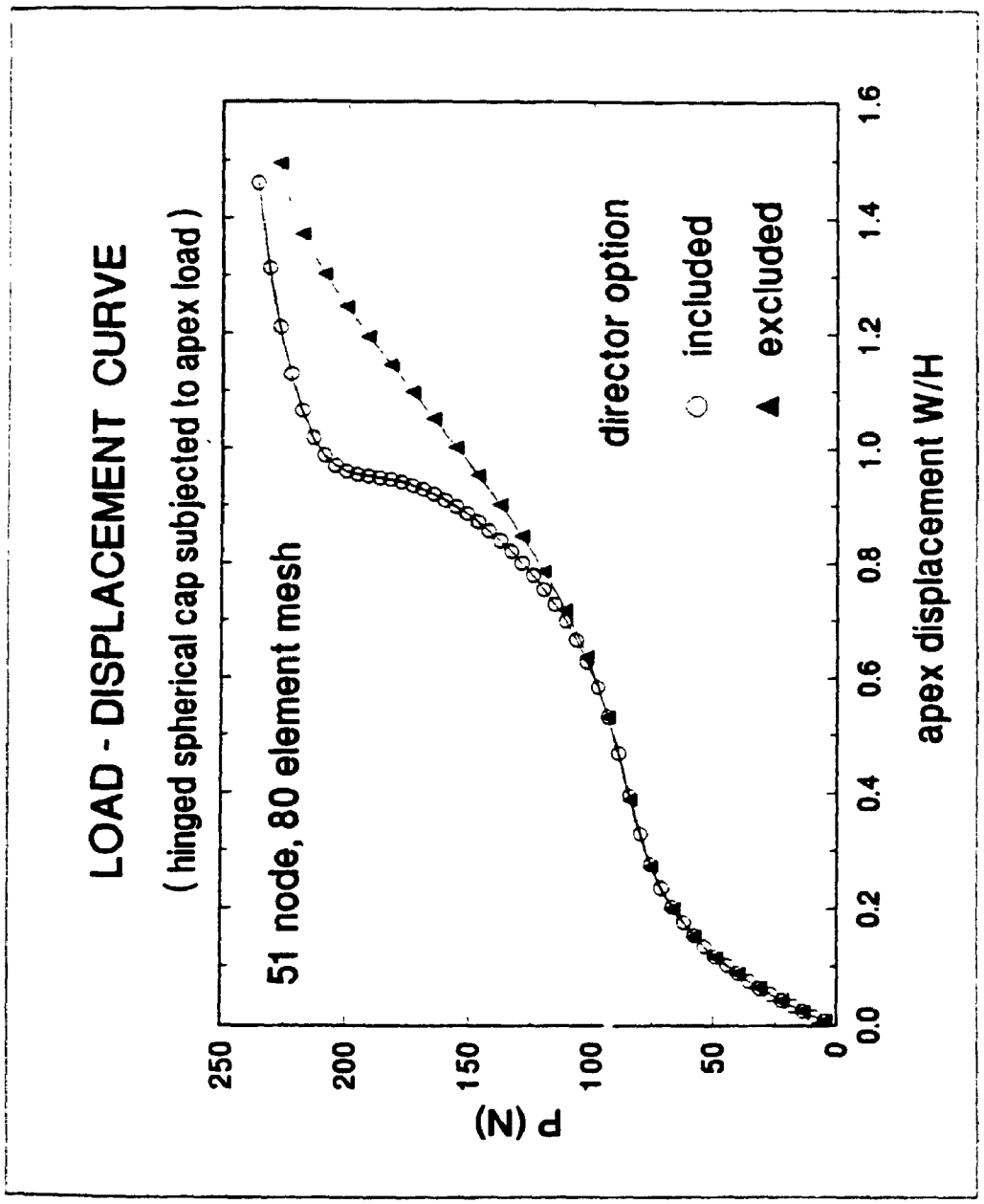

Figure 7.25 Load-displacement curve for the hinged spherical cap

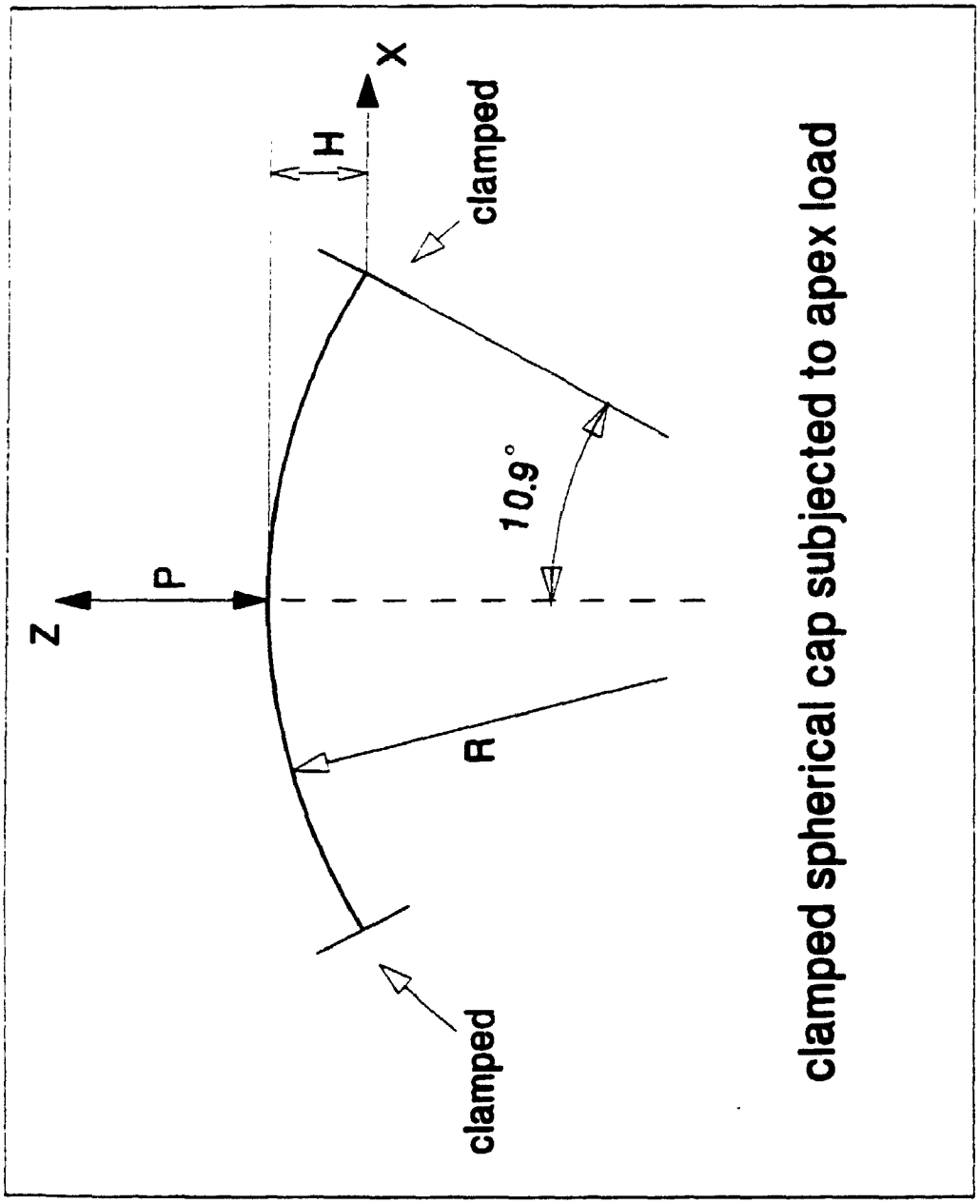

Figure 7.26 The clamped spherical cap subjected to an apex load

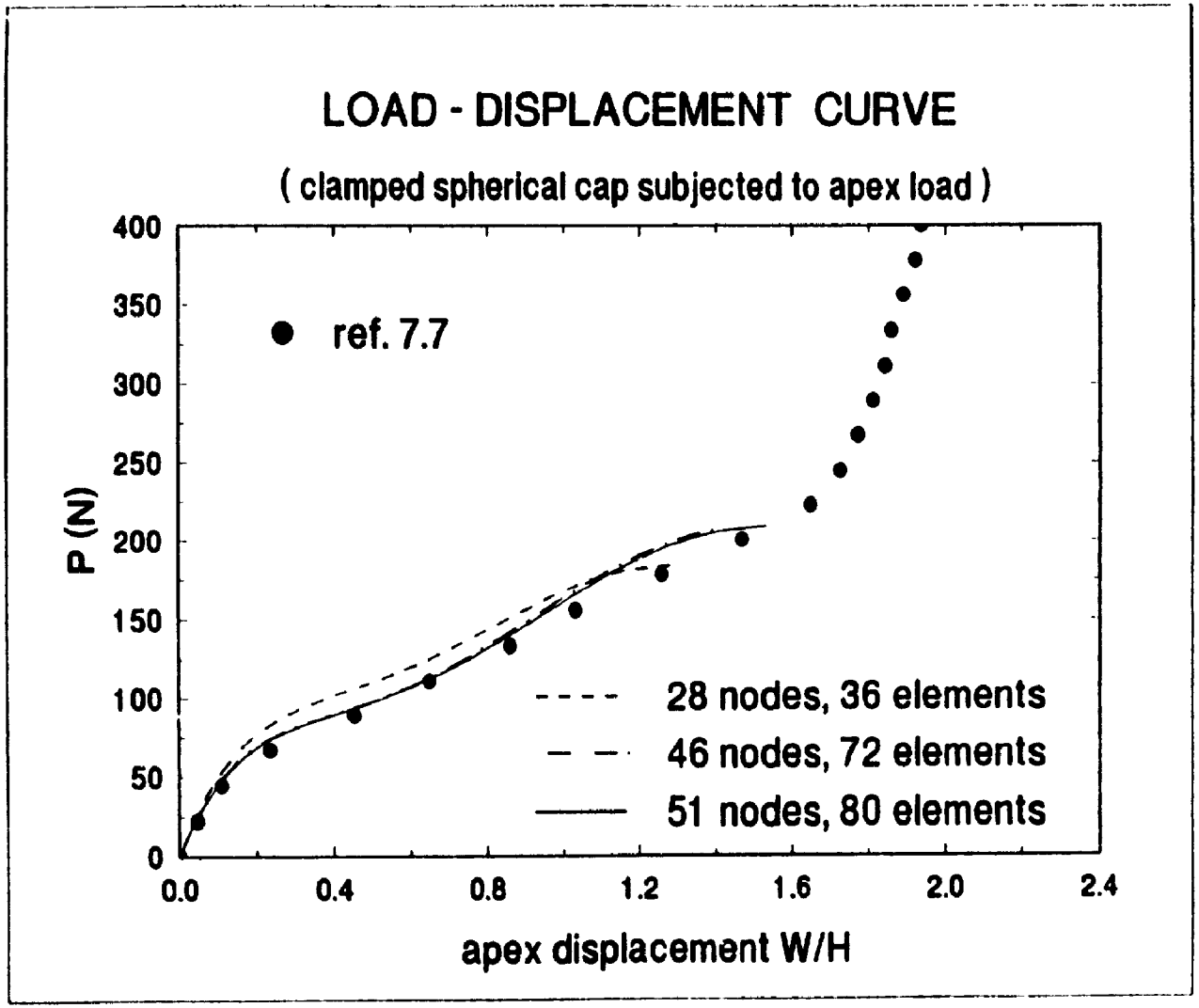

Figure 7.27 Load-displacement curve for the clamped spherical cap

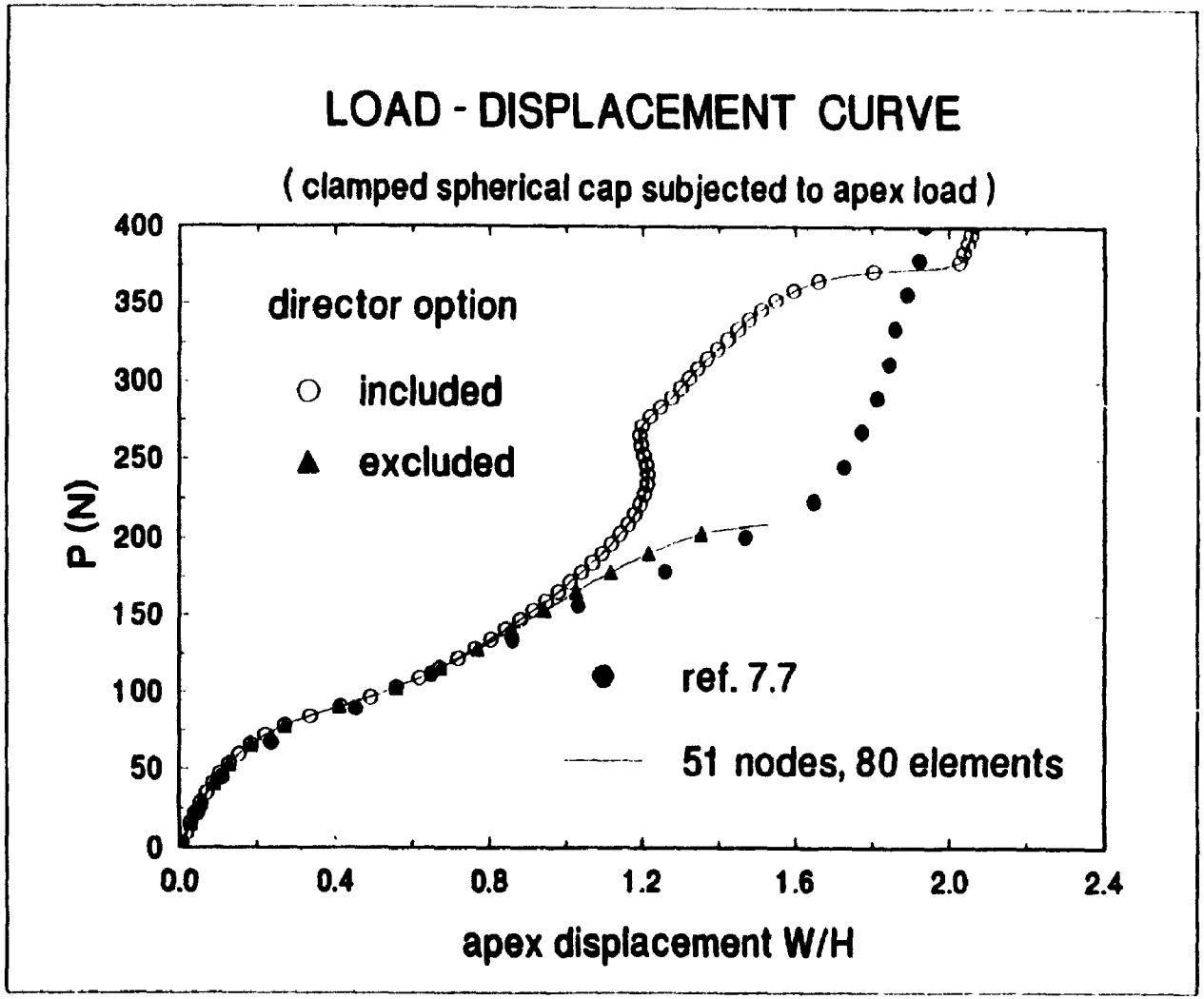

Figure 7.28 Load-displacement curve for the clamped spherical cap

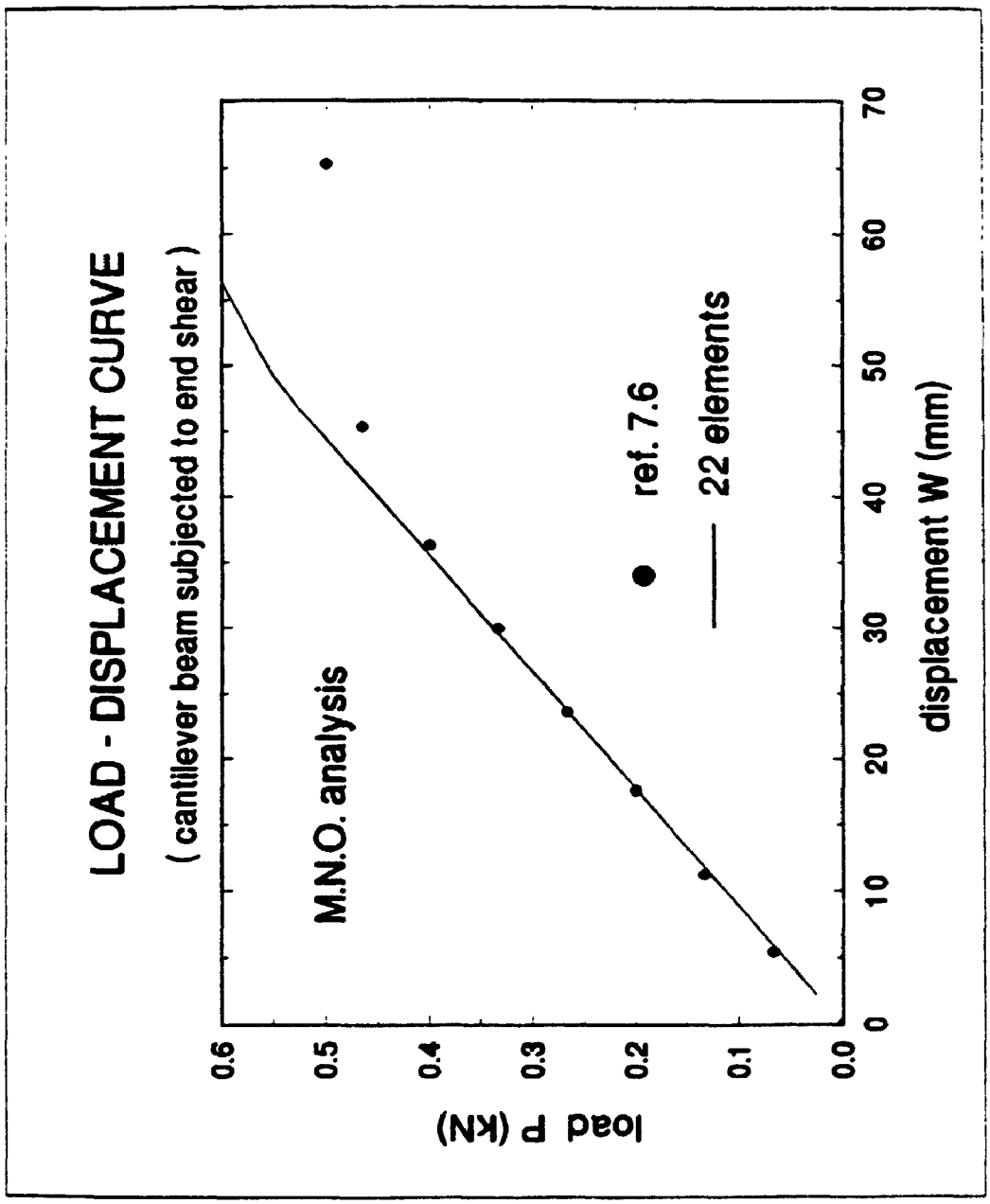

Figure 7.29 Load-displacement curve for the cantilever beam

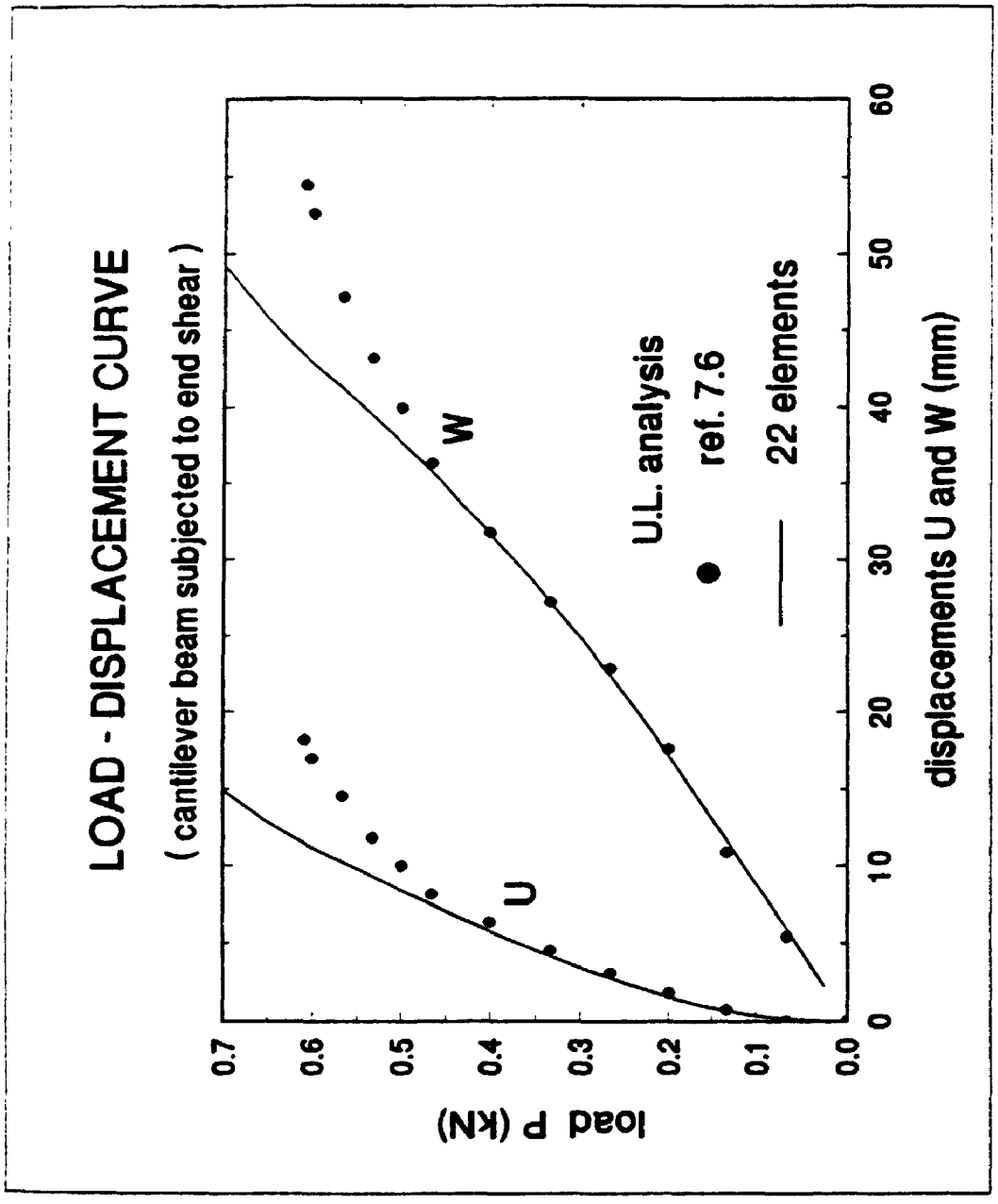

Figure 7.30 Load-displacement curve for the cantilever beam

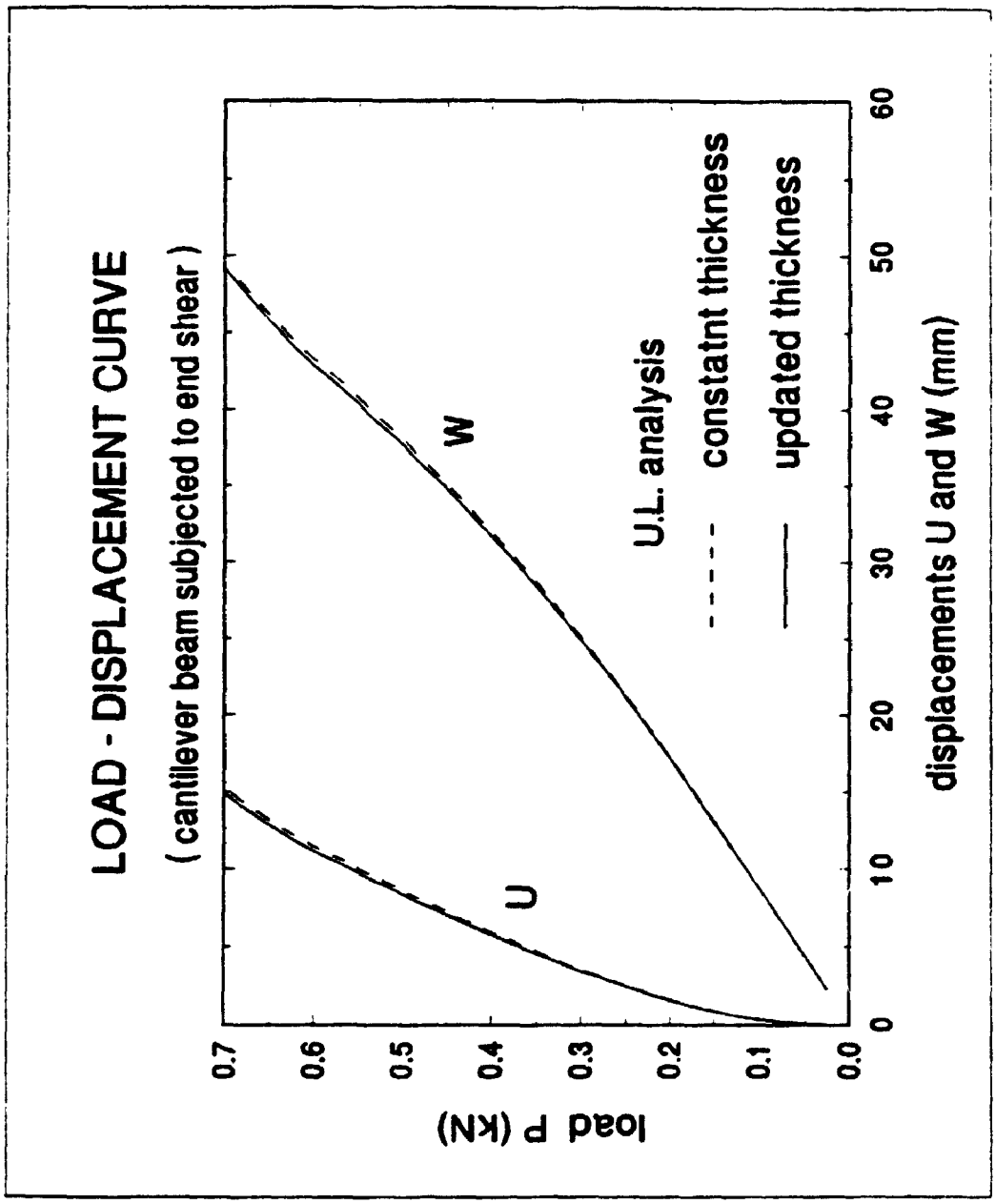

Figure 7.31 Load-displacement curve for the cantilever beam

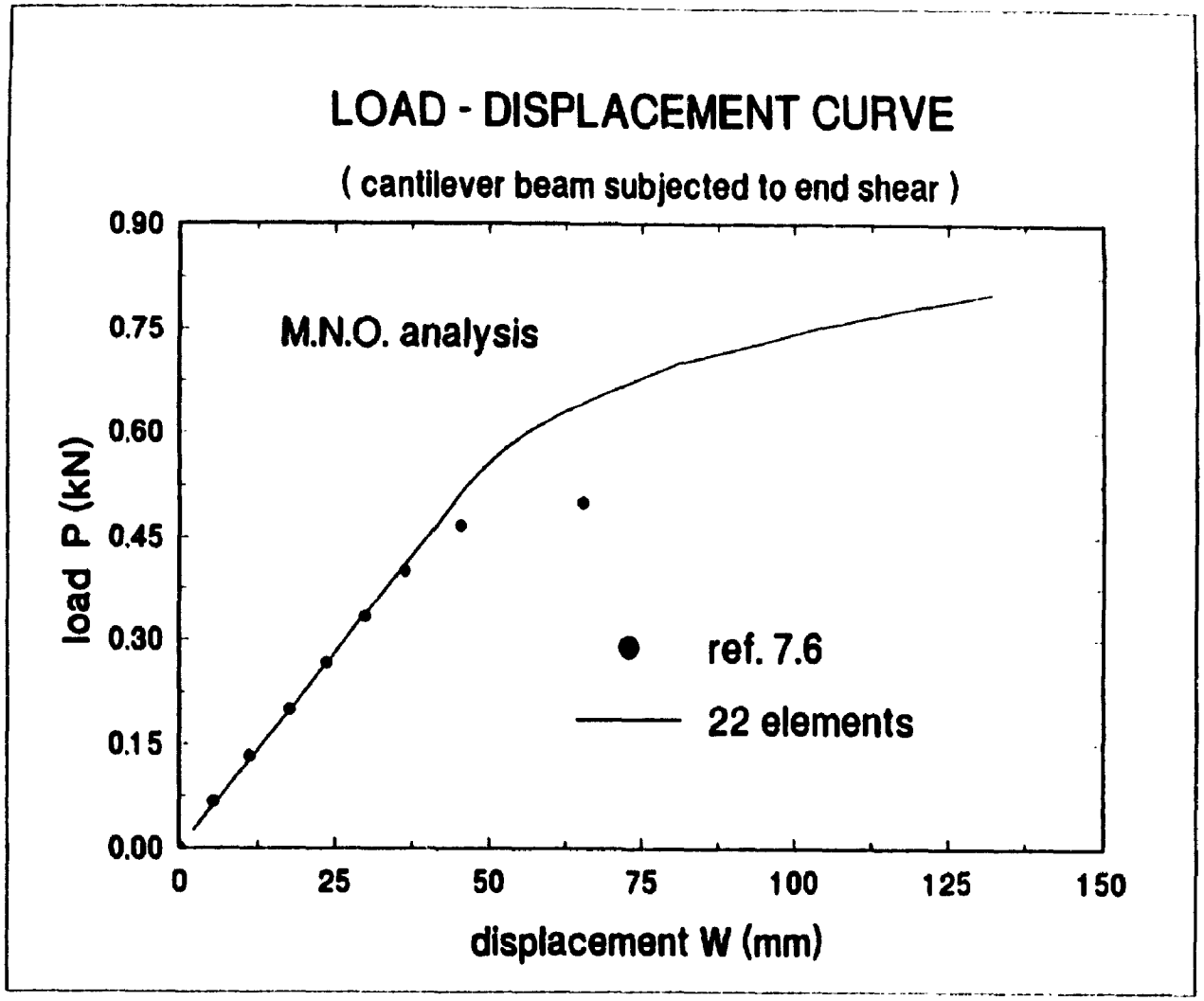

Figure 7.32 Load-displacement curve for the cantilever beam

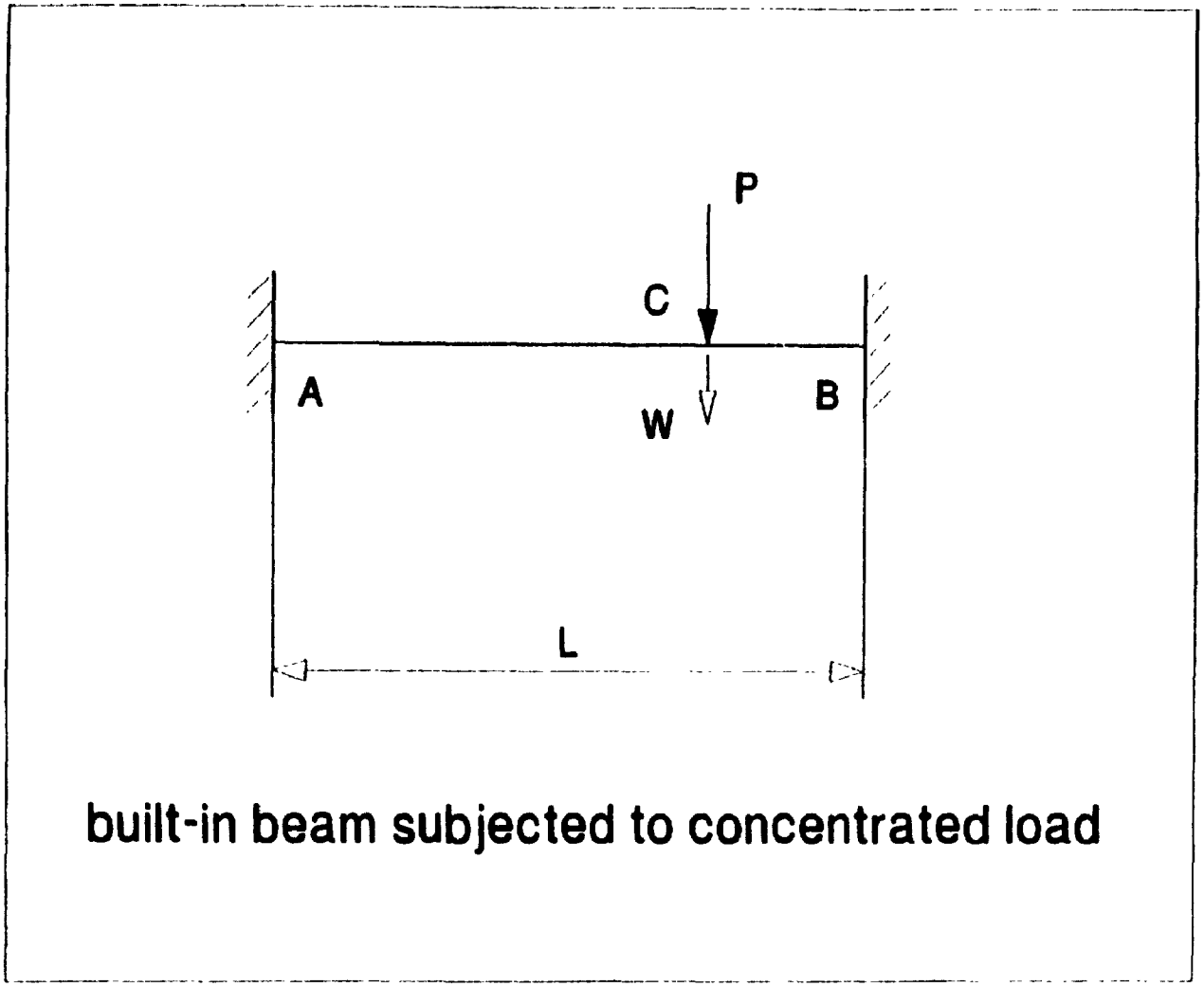

Figure 7.33 A beam built in at both ends subjected to a concentrated load

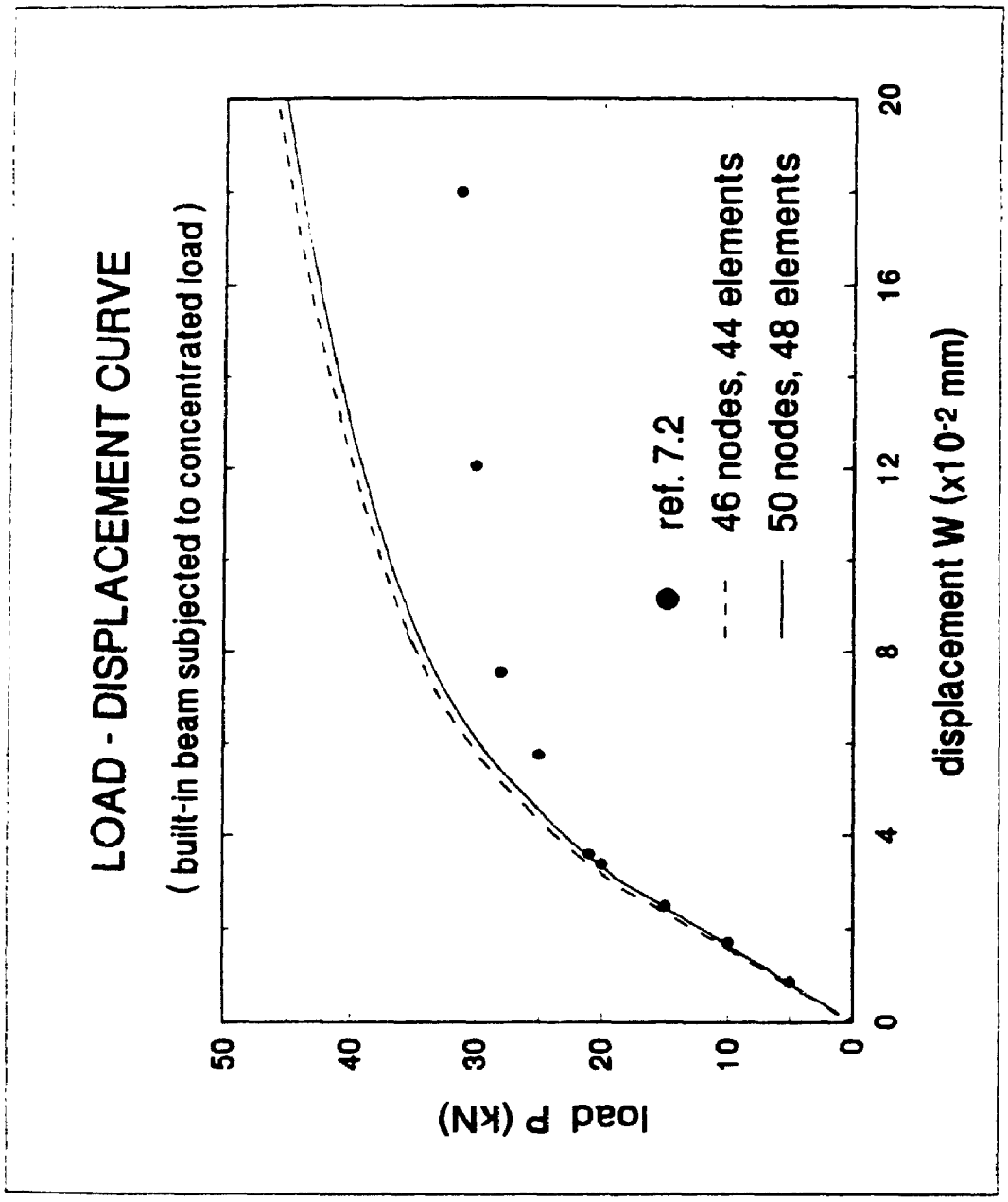

Figure 7.34 Load-displacement curve for the built-in beam

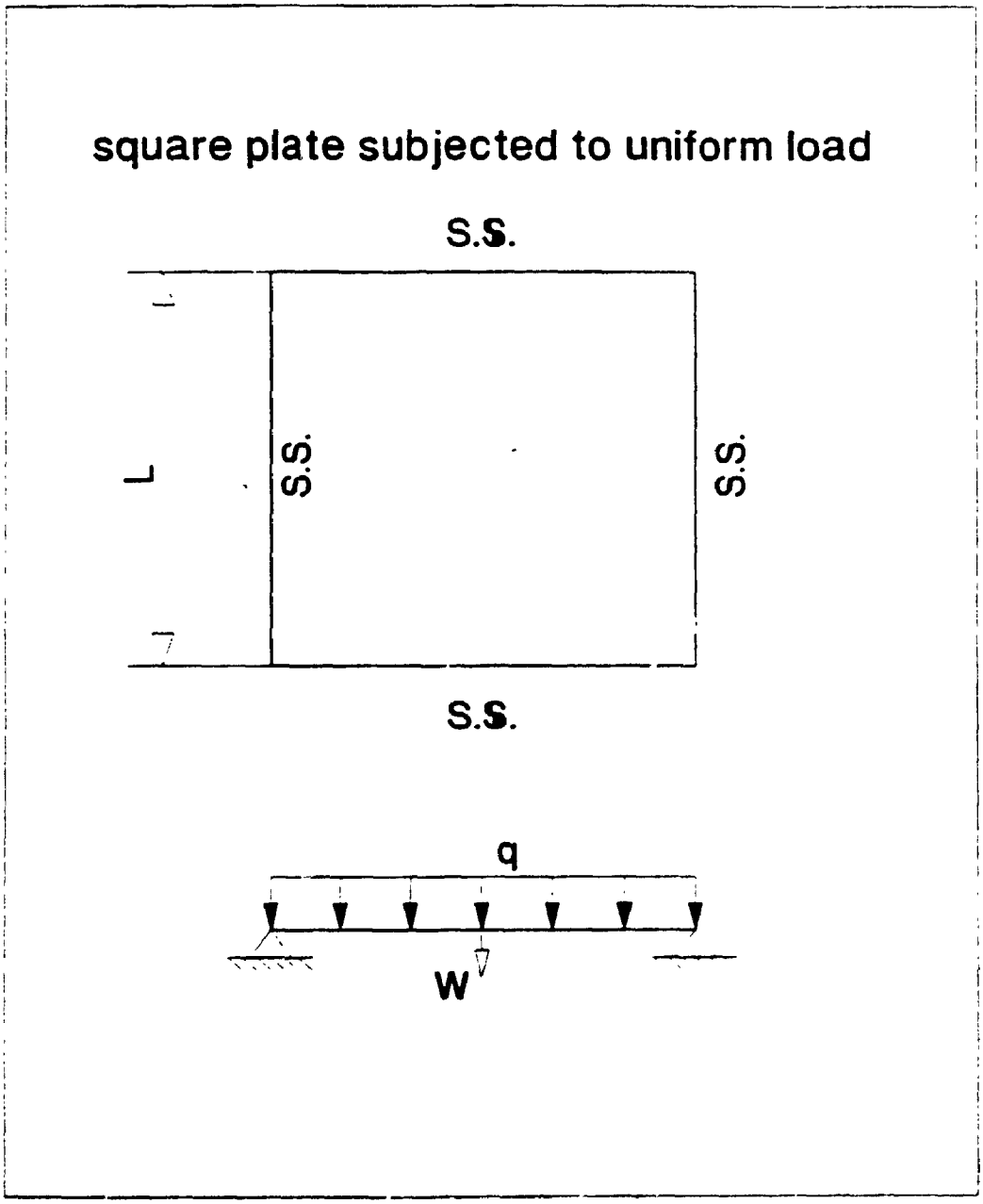

Figure 7.35 A simply supported square plate subjected to uniform load

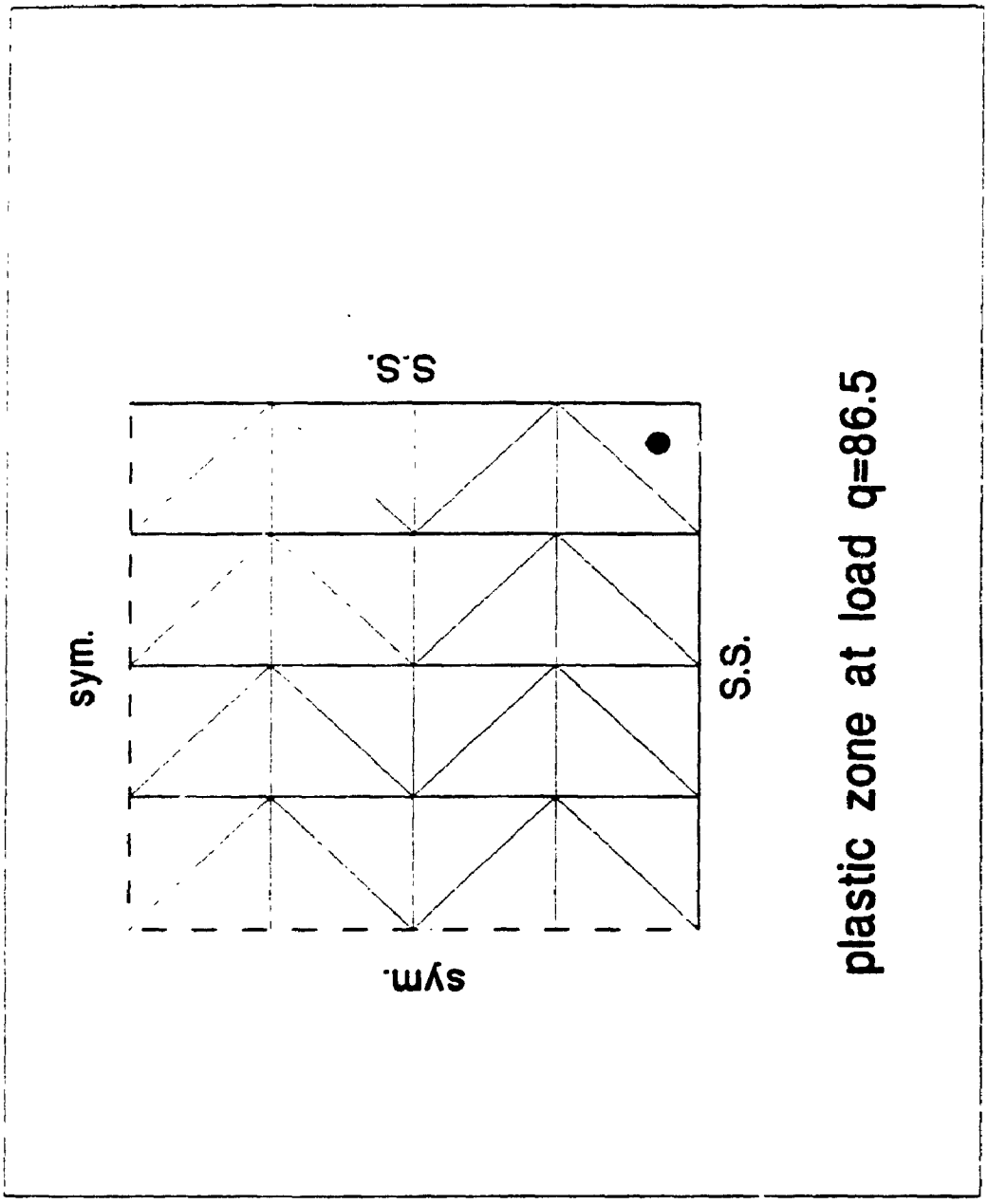

Figure 7.36 Plastic zone at load q=86.5

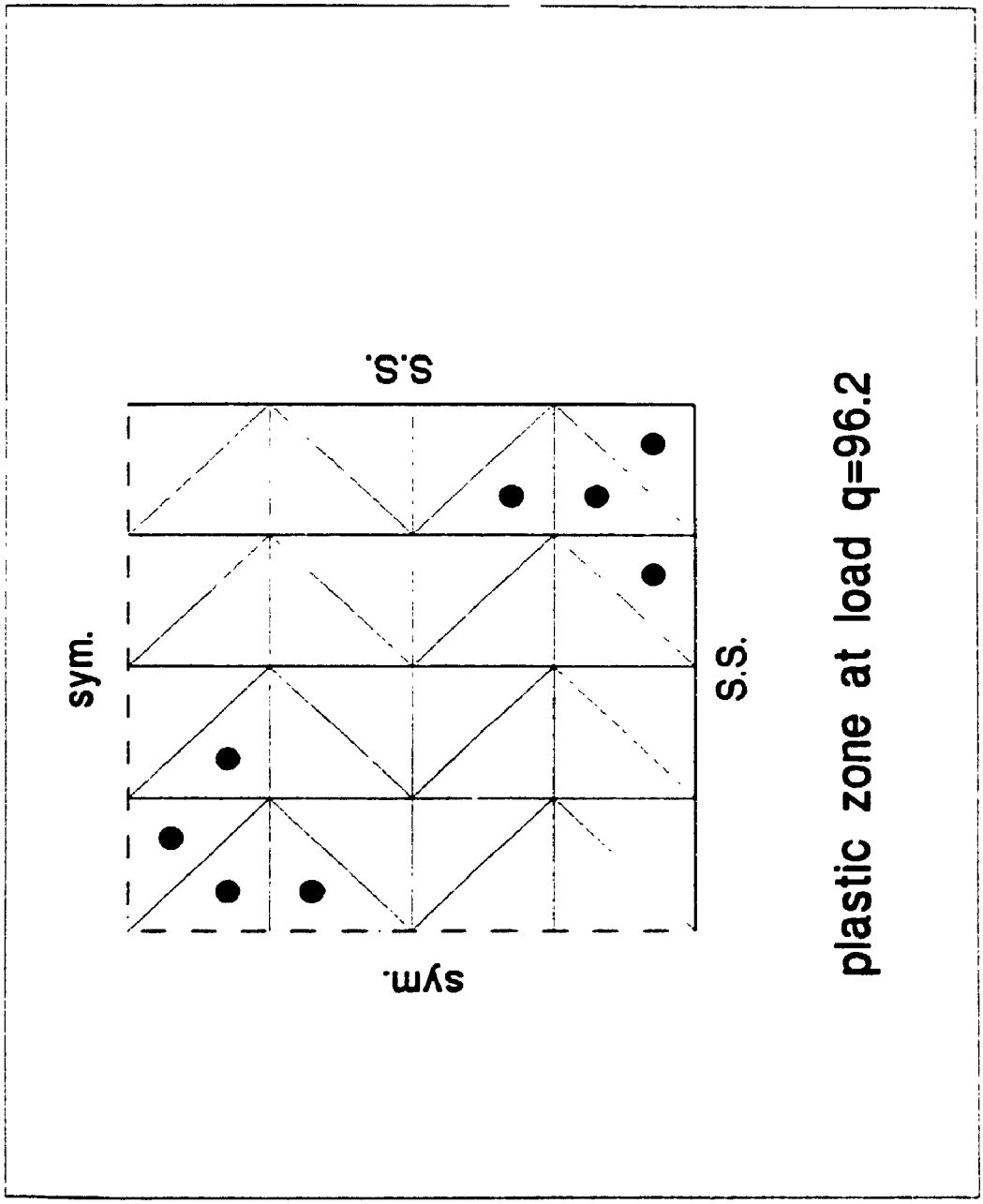

Figure 7.37 Plastic zone at load q=96.2

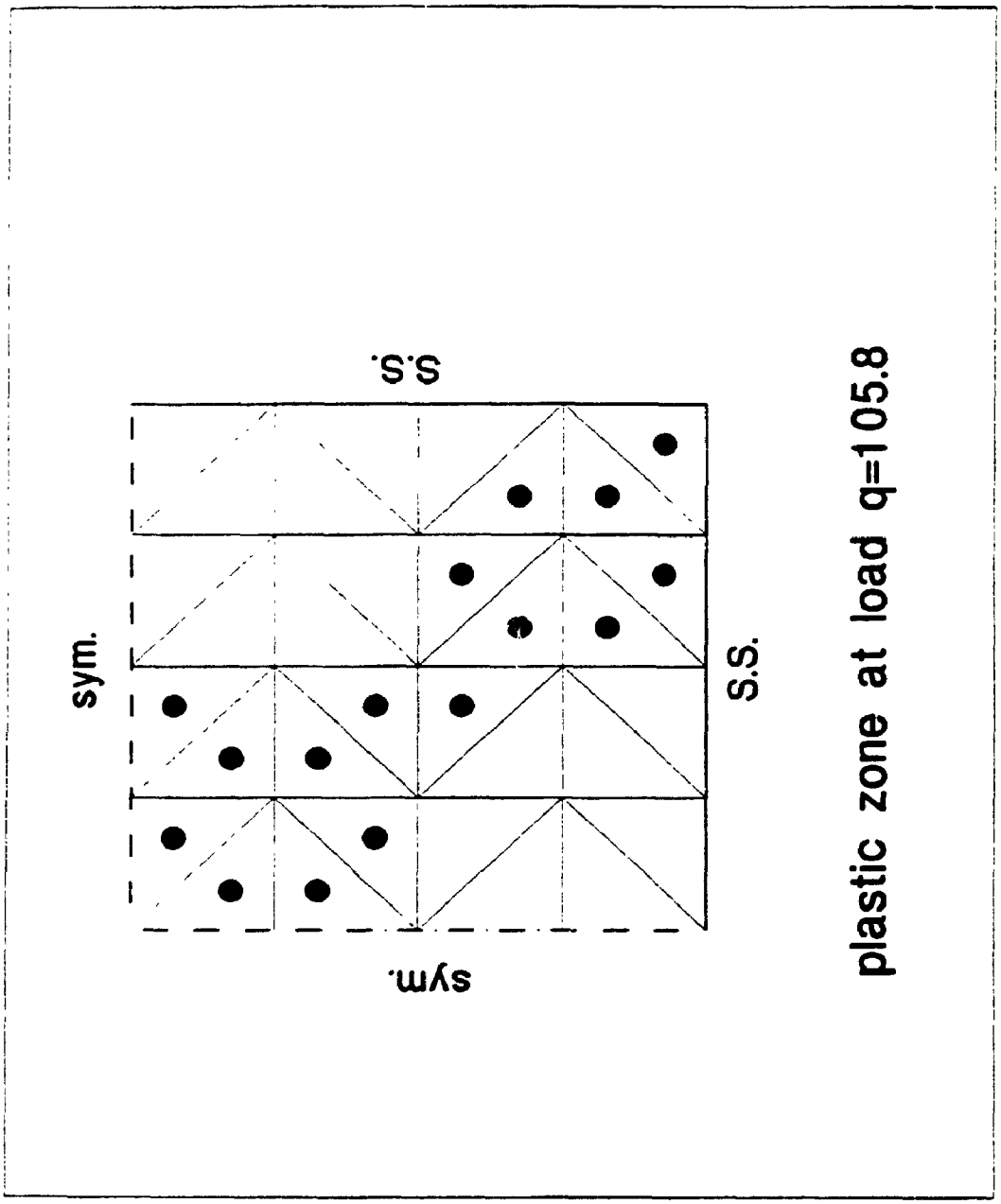

Figure 7.38 Plastic zone at load q=105.8

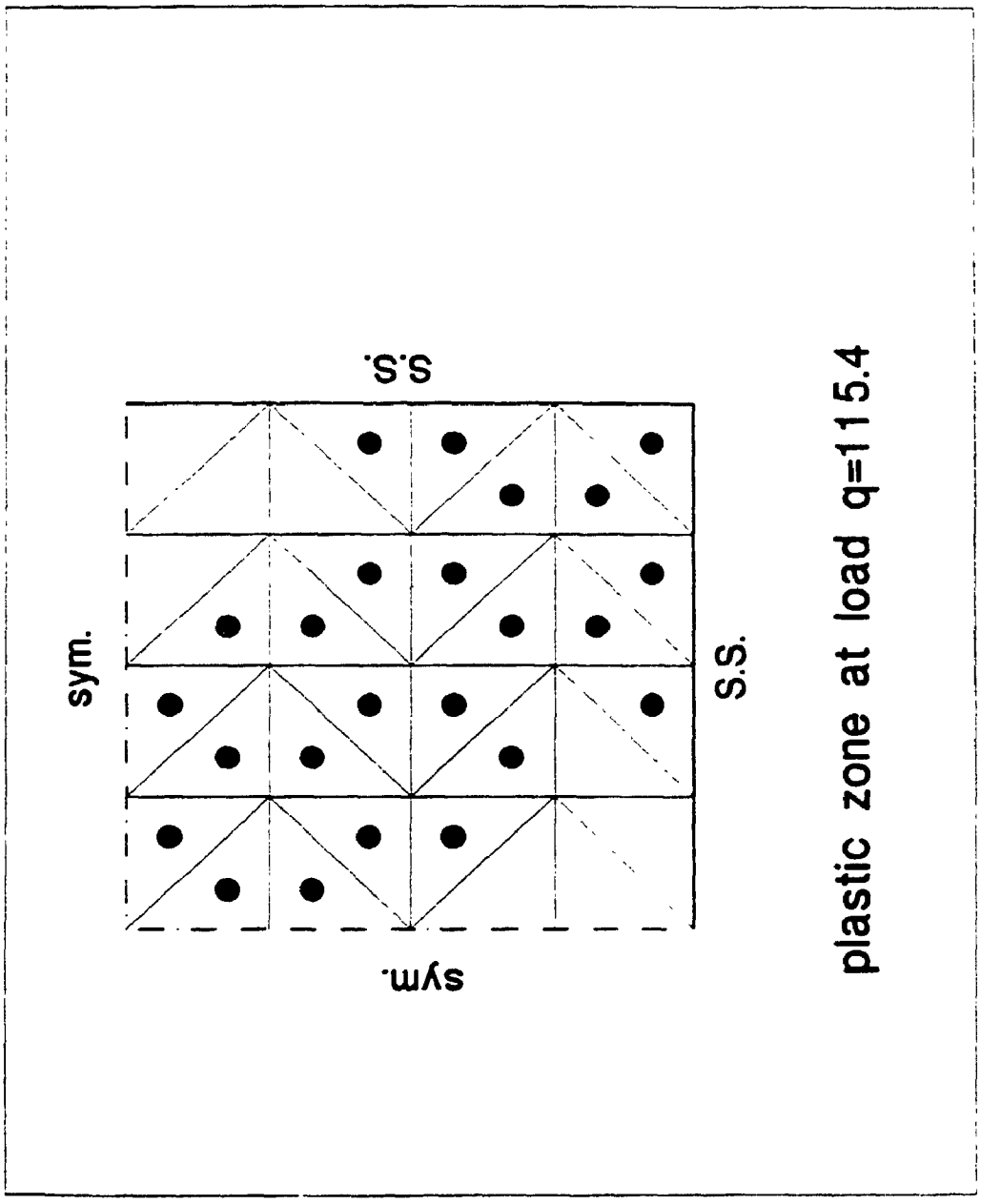

Figure 7.39 Plastic zone at load q=115.4

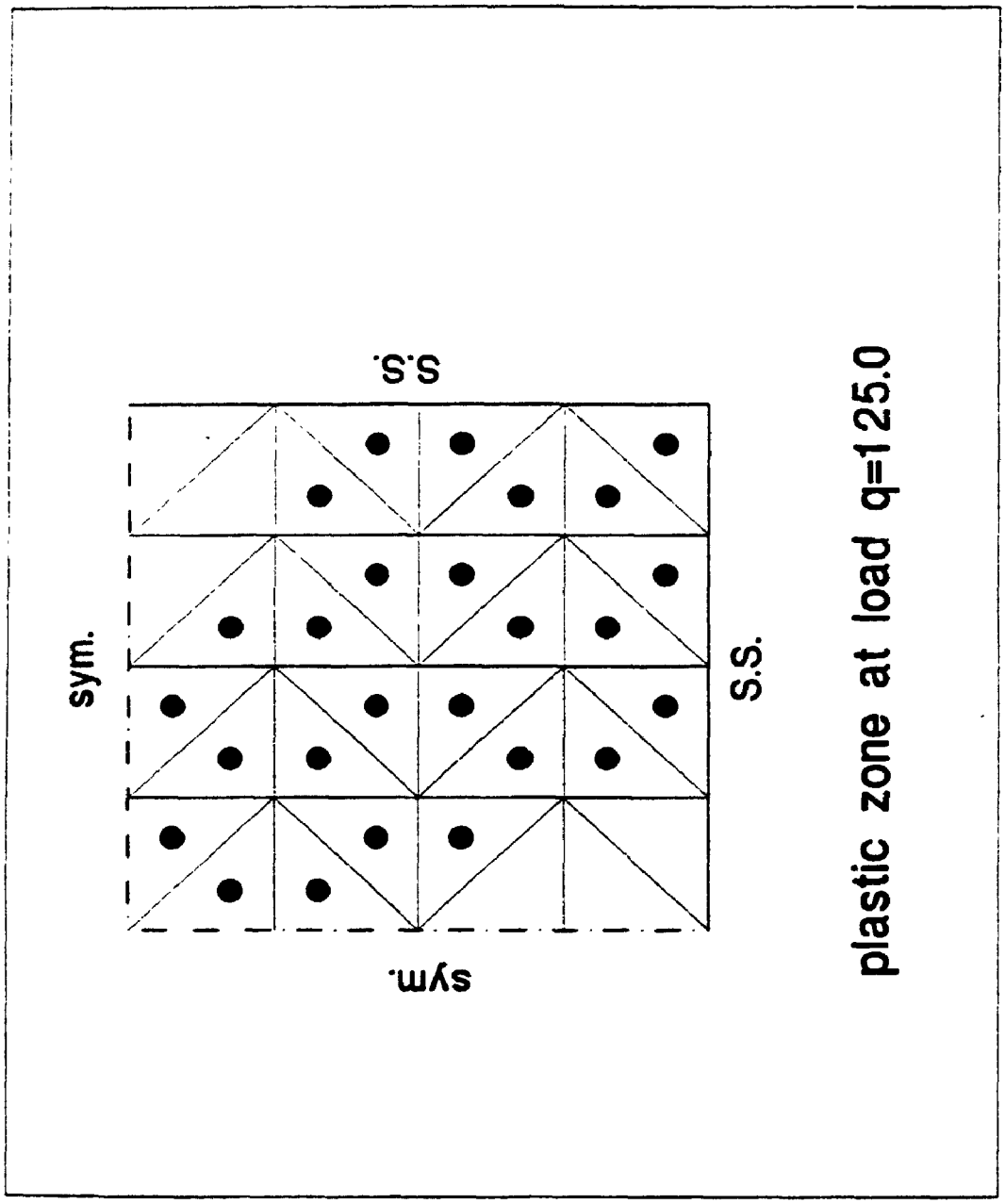

Figure 7.40 Plastic zone at load q=125.0

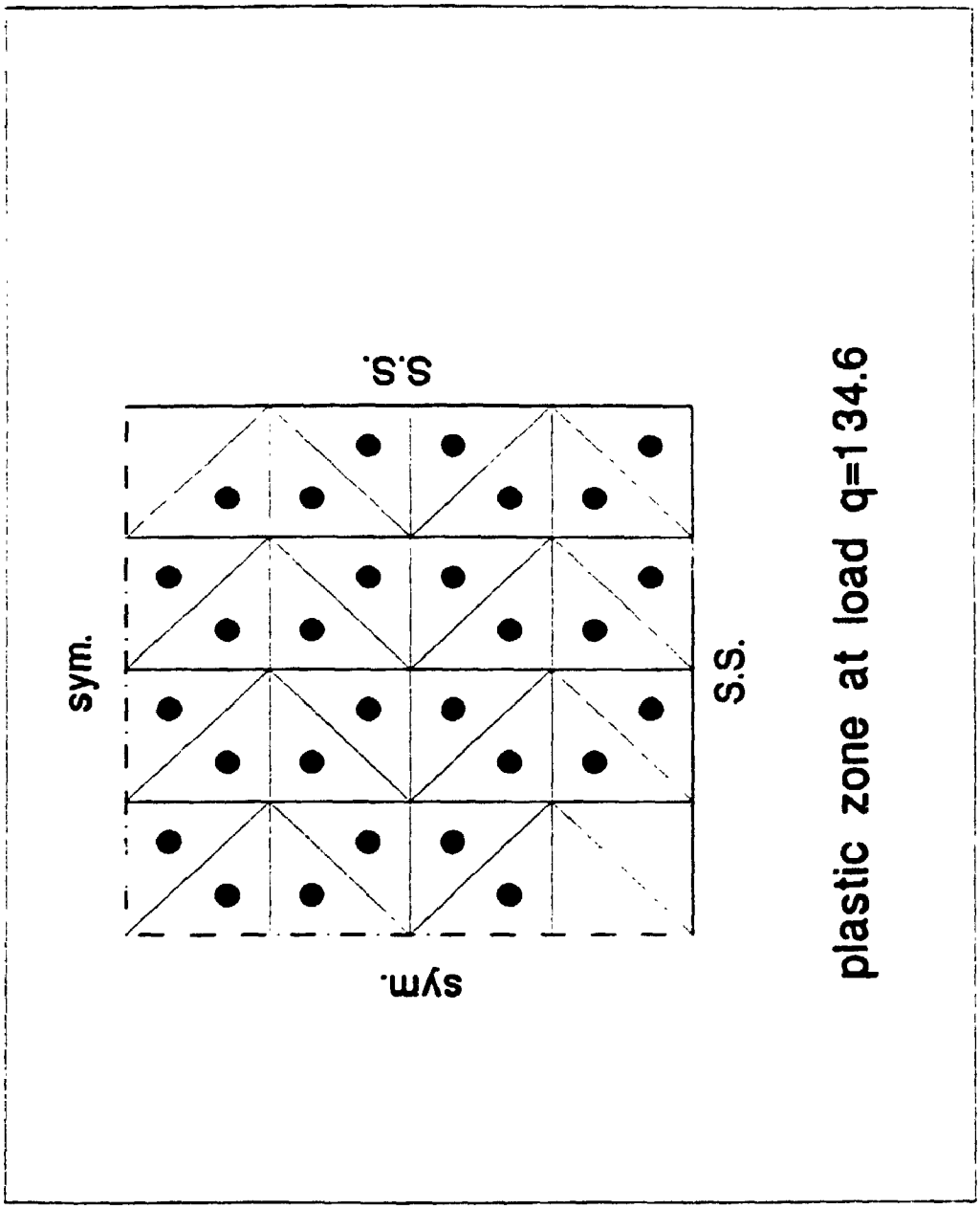

Figure 7.41 Plastic zone at load q = 134.6

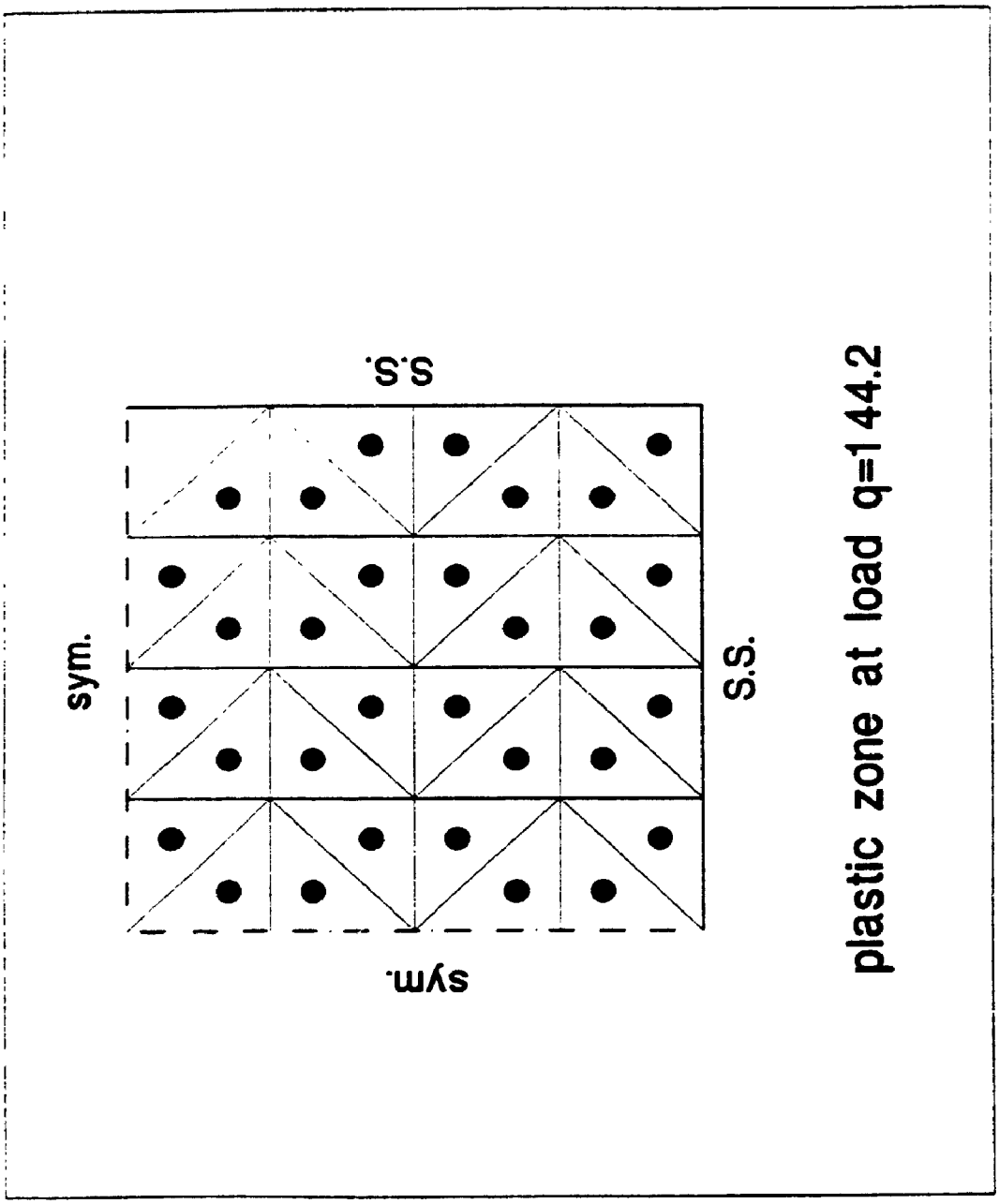

Figure 7.42 Plastic zone at load q=144.2

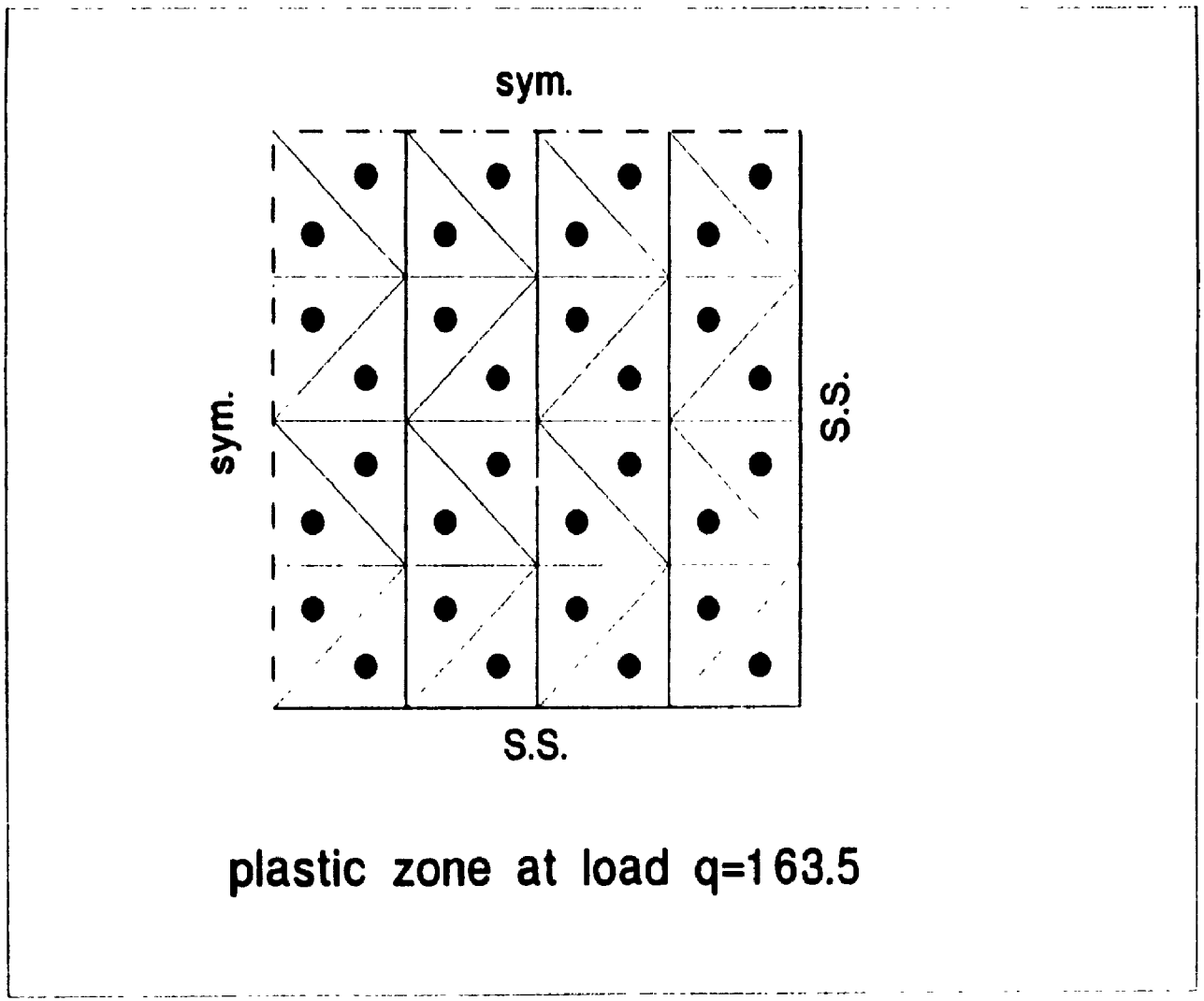

Figure 7.43 Plastic zone at load q=163.5

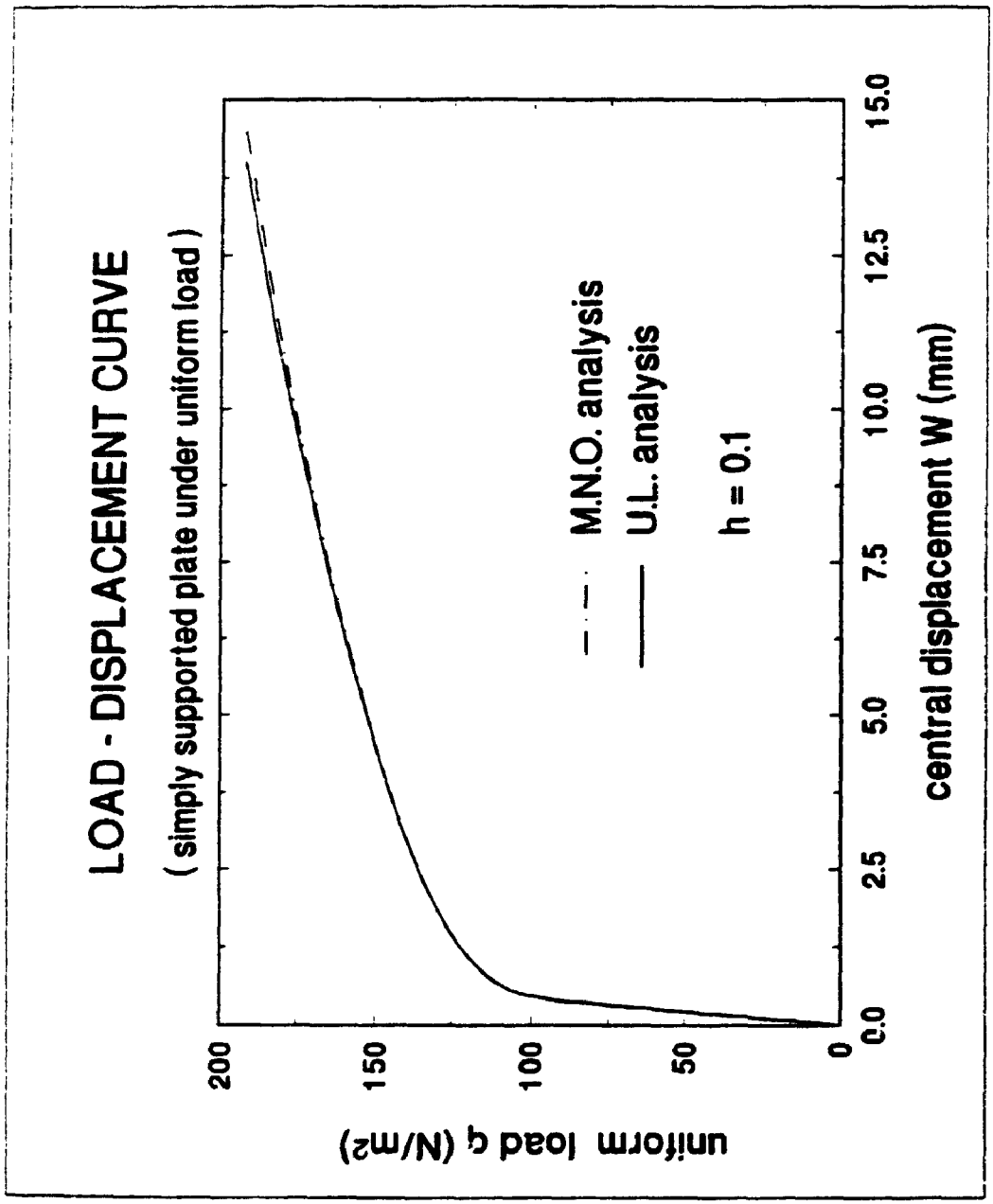

Figure 7.44 Load-displacement curve for the simply supported plate

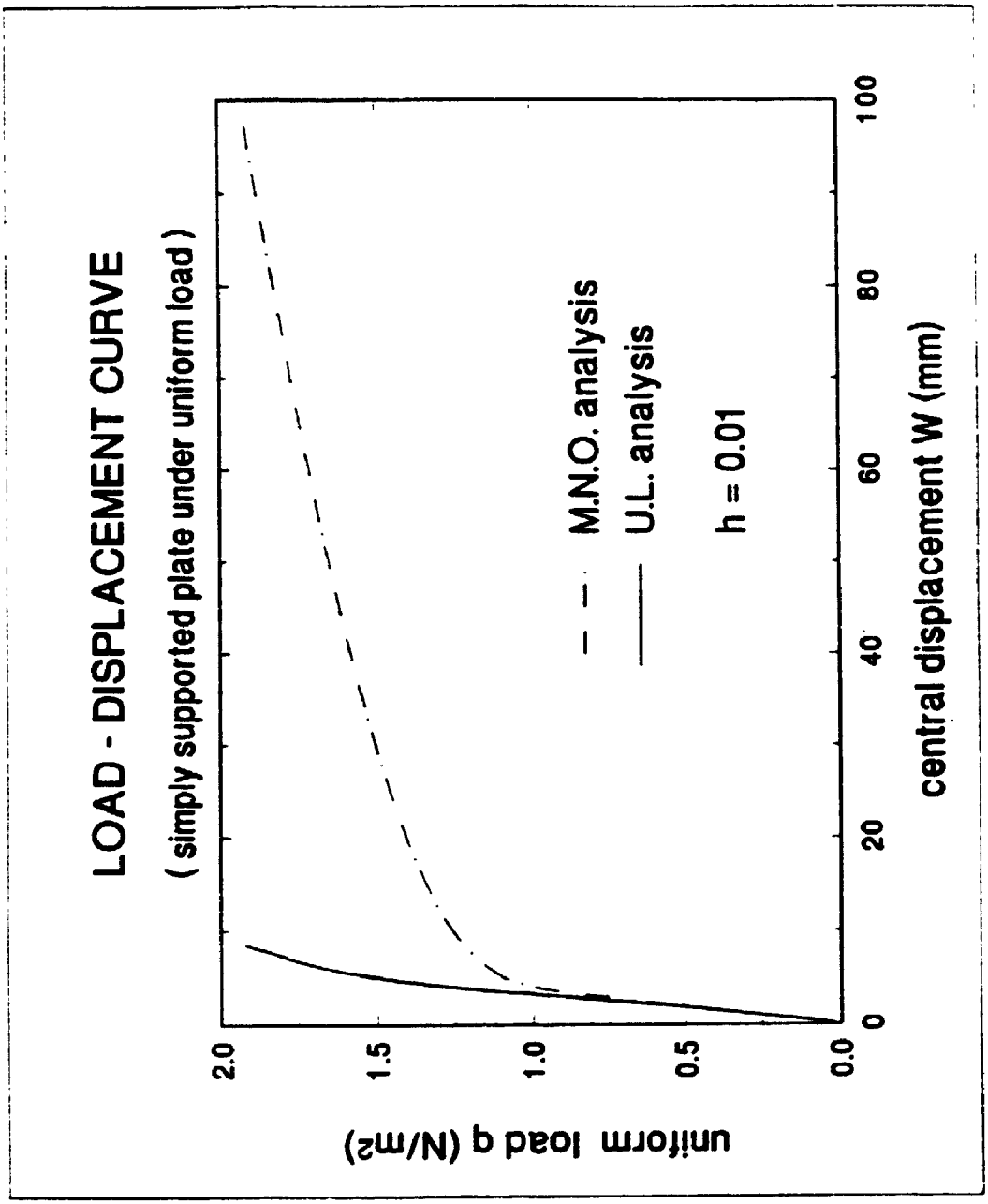

Figure 7.45 Load-displacement curve for the simply supported plate

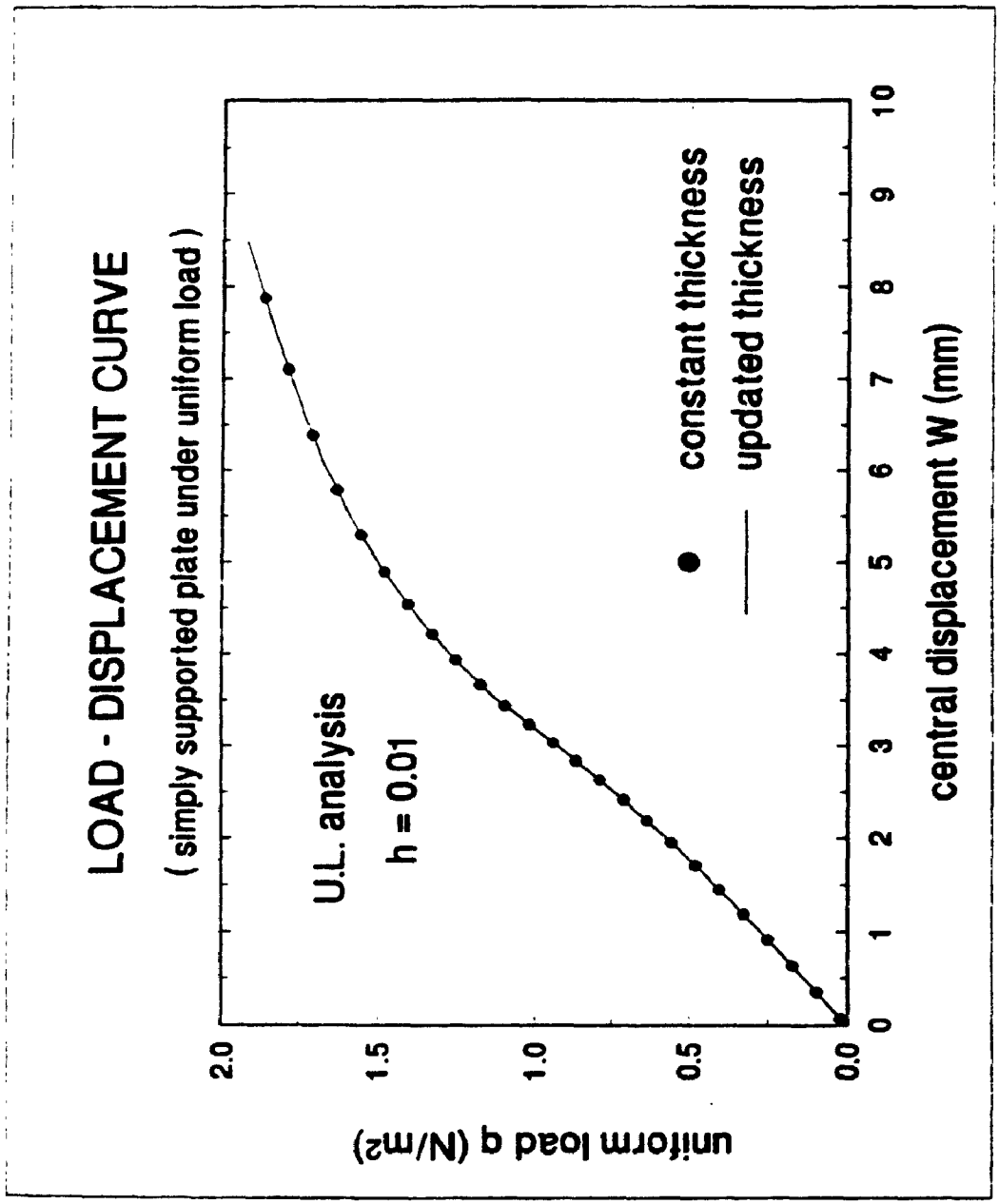

Figure 7.46 Load-displacement curve for the simply supported plate

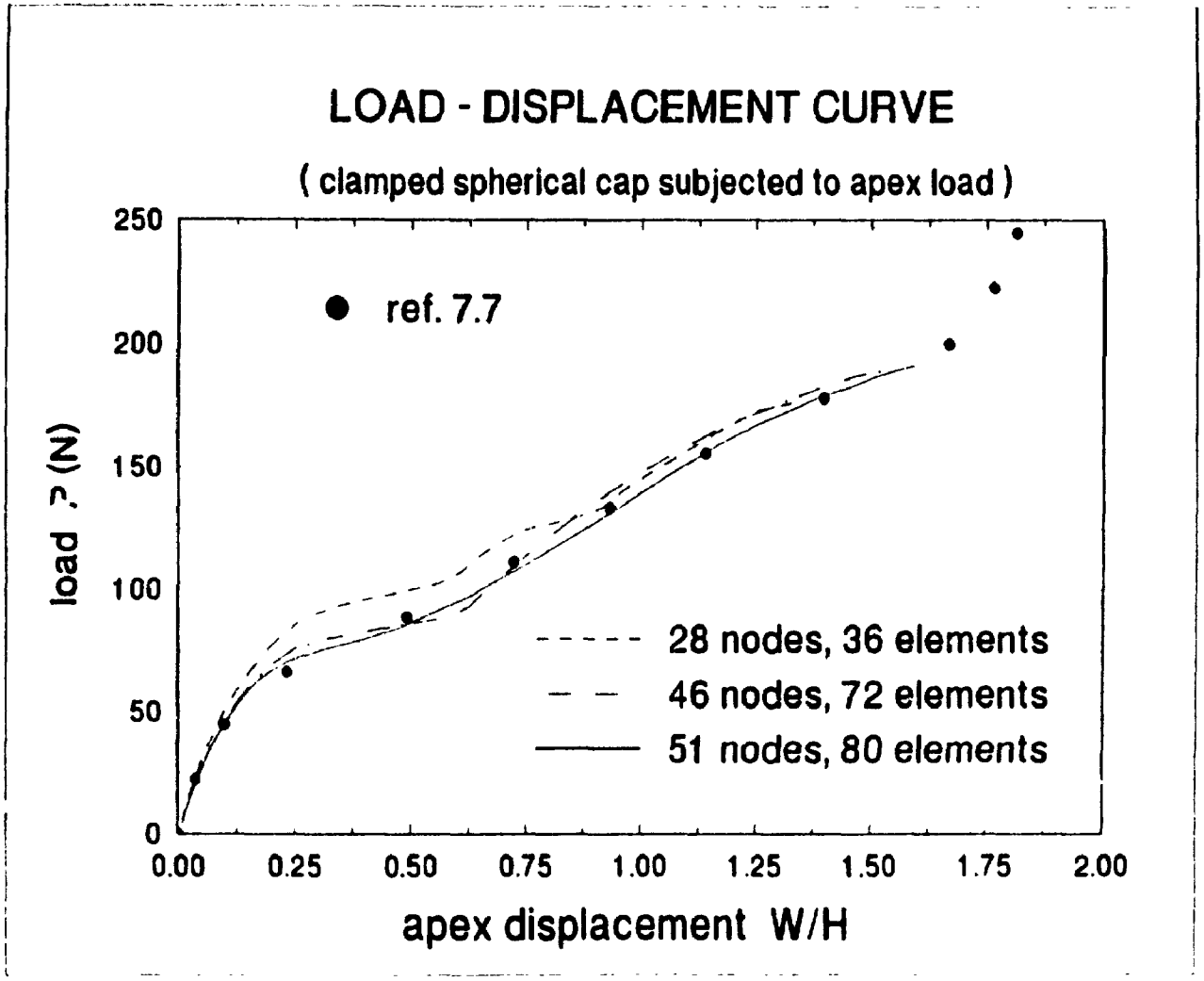

Figure 7.47 Load-displacement curve for the clamped spherical cap

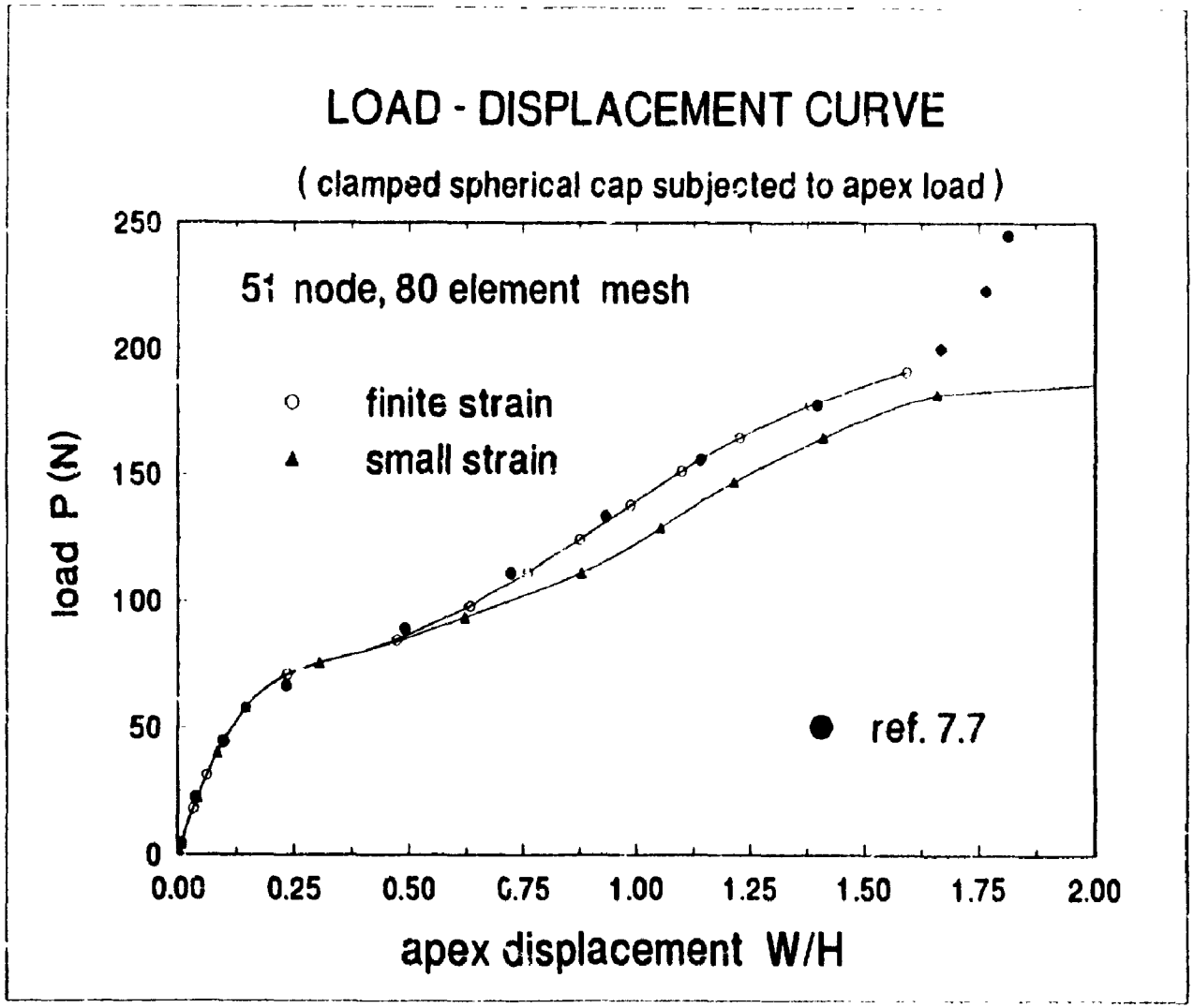

Figure 7.48 Load-displacement curve for the clamped spherical cap

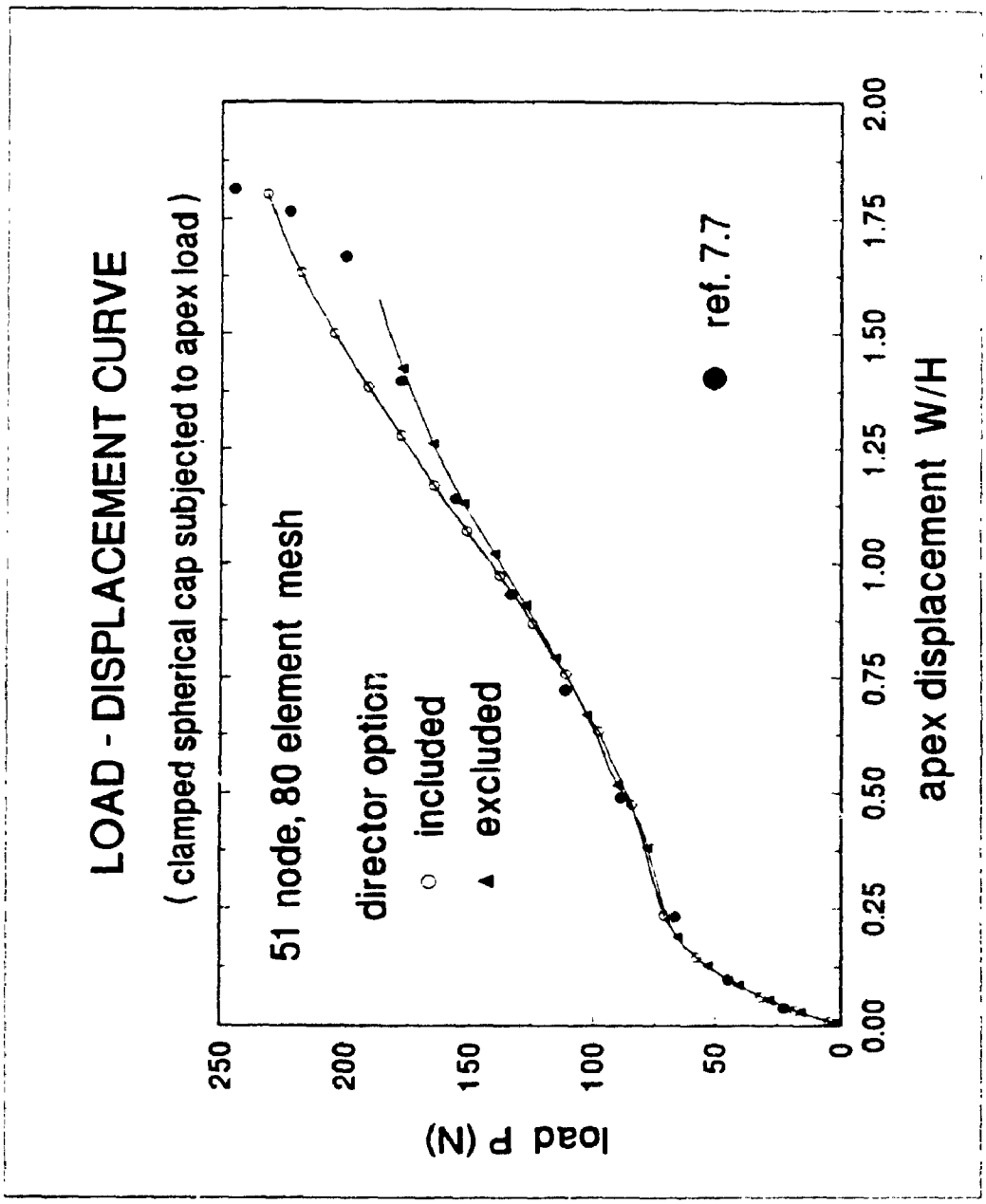

Figure 7.49 Load-displacement curve for the clamped spherical cap

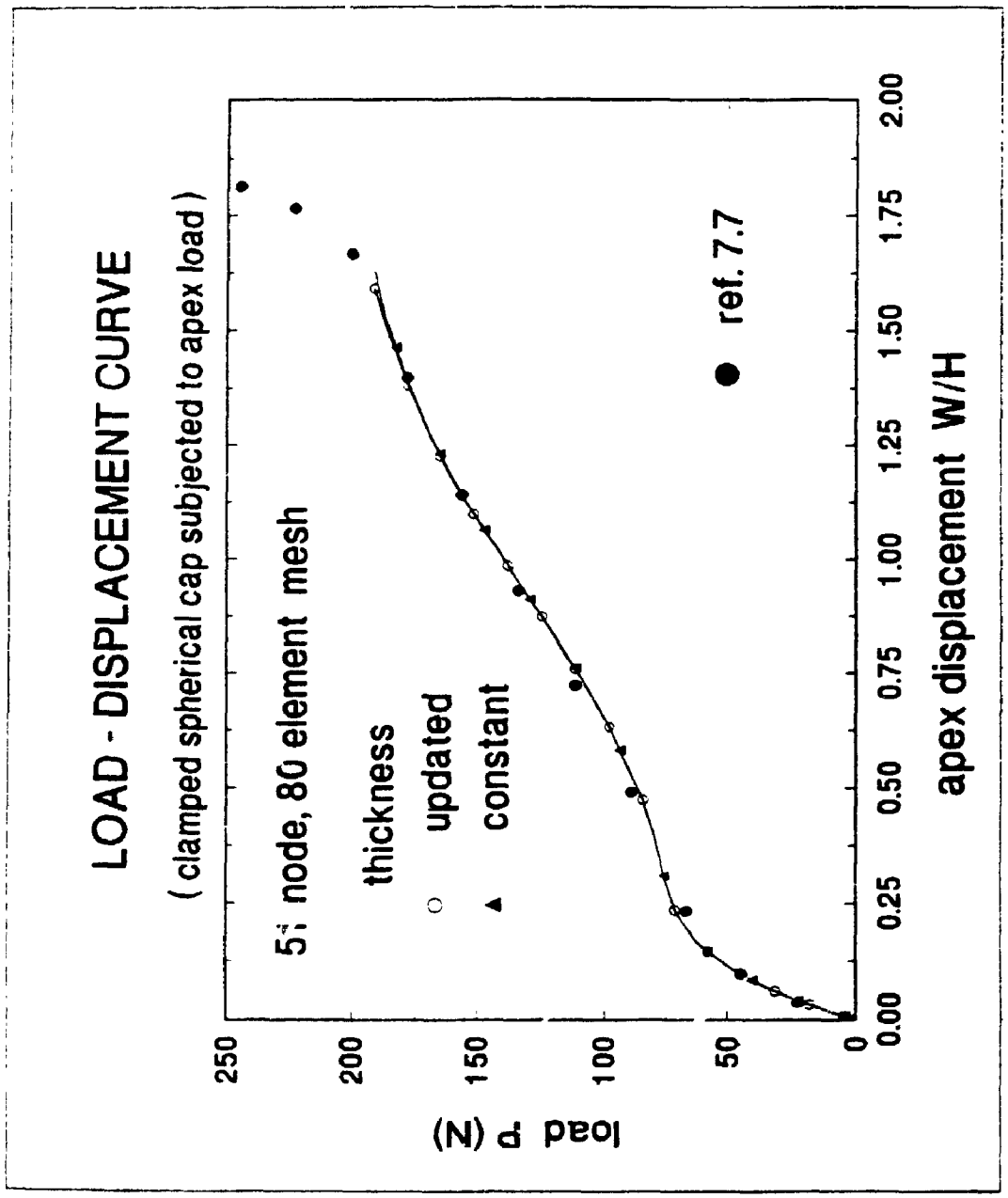

Figure 7.50 Load-displacement curve for the clamped spherical cap

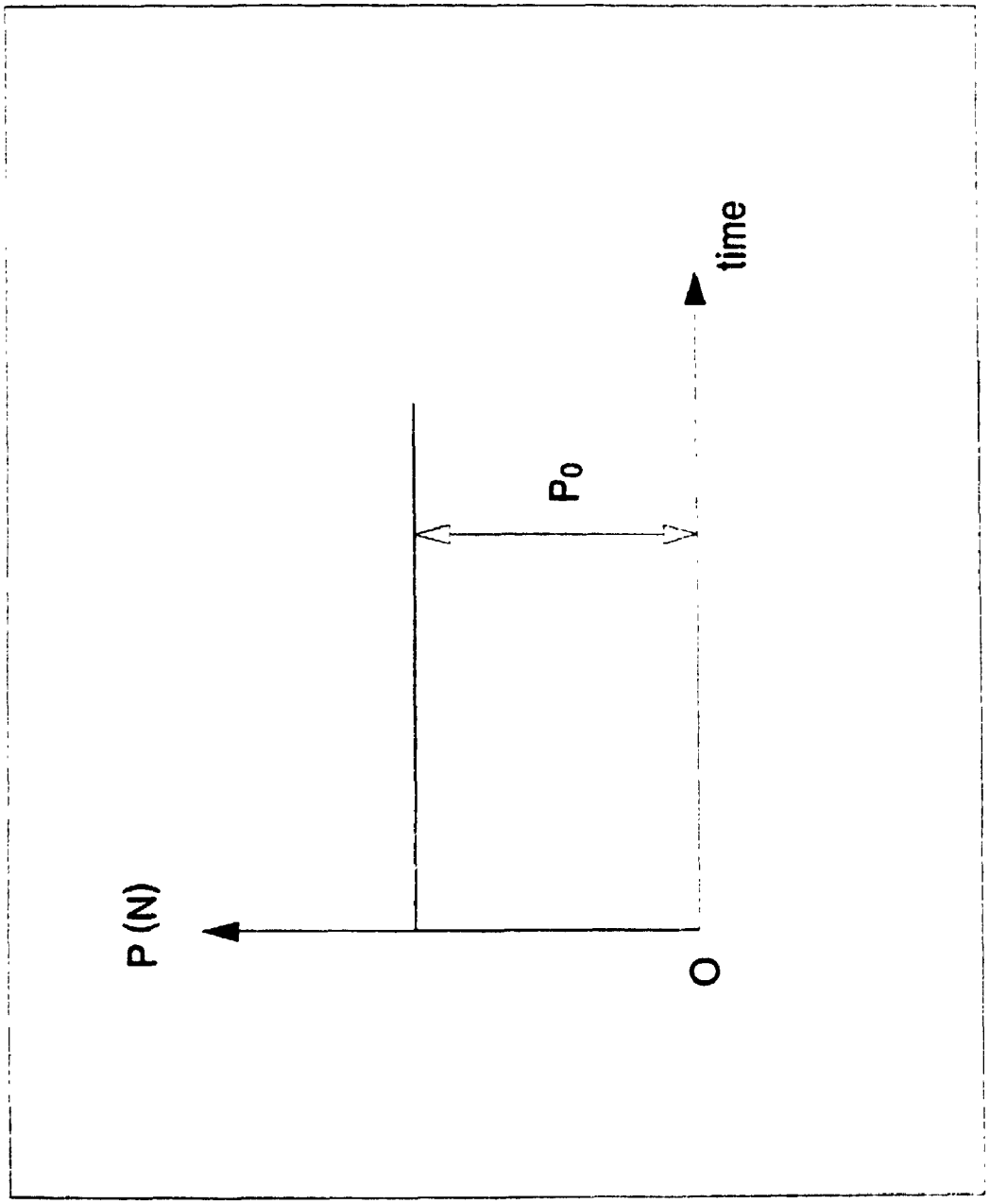

Figure 7.51 Time history of the step loading

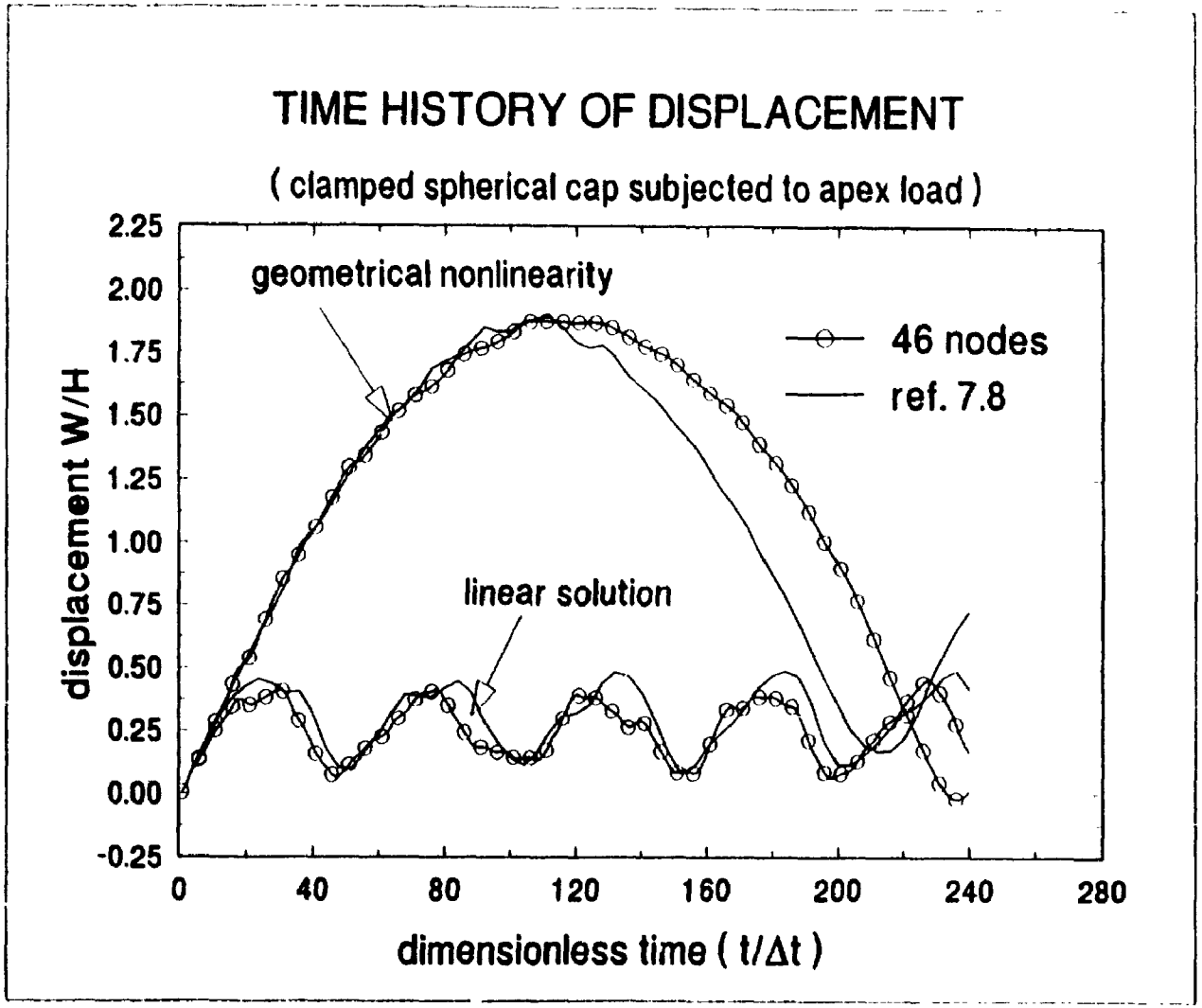

Figure 7.52 Time history of apex displacement of the clamped spherical cap

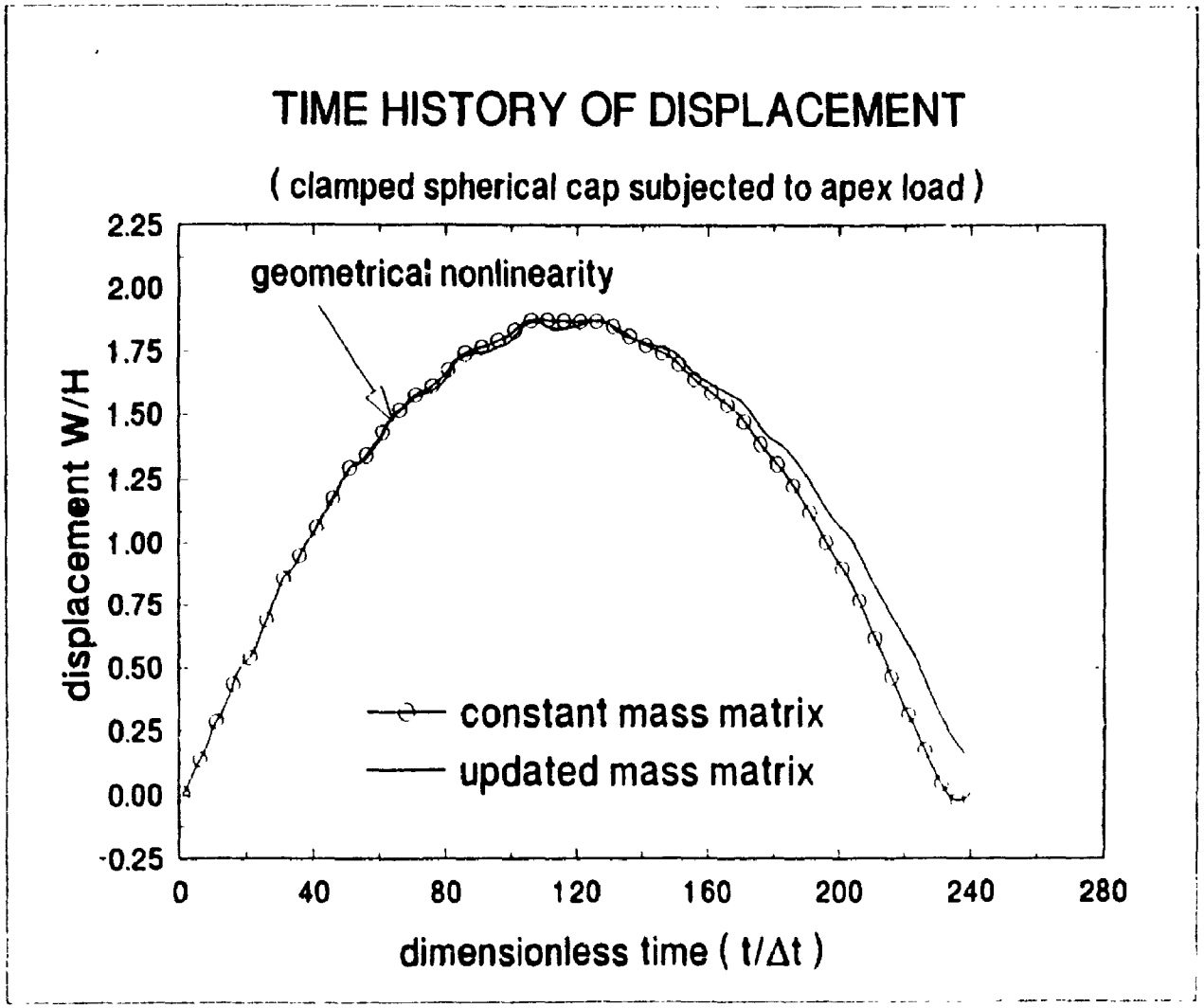

Figure 7.53 Time history of apex displacement of the clamped spherical cap

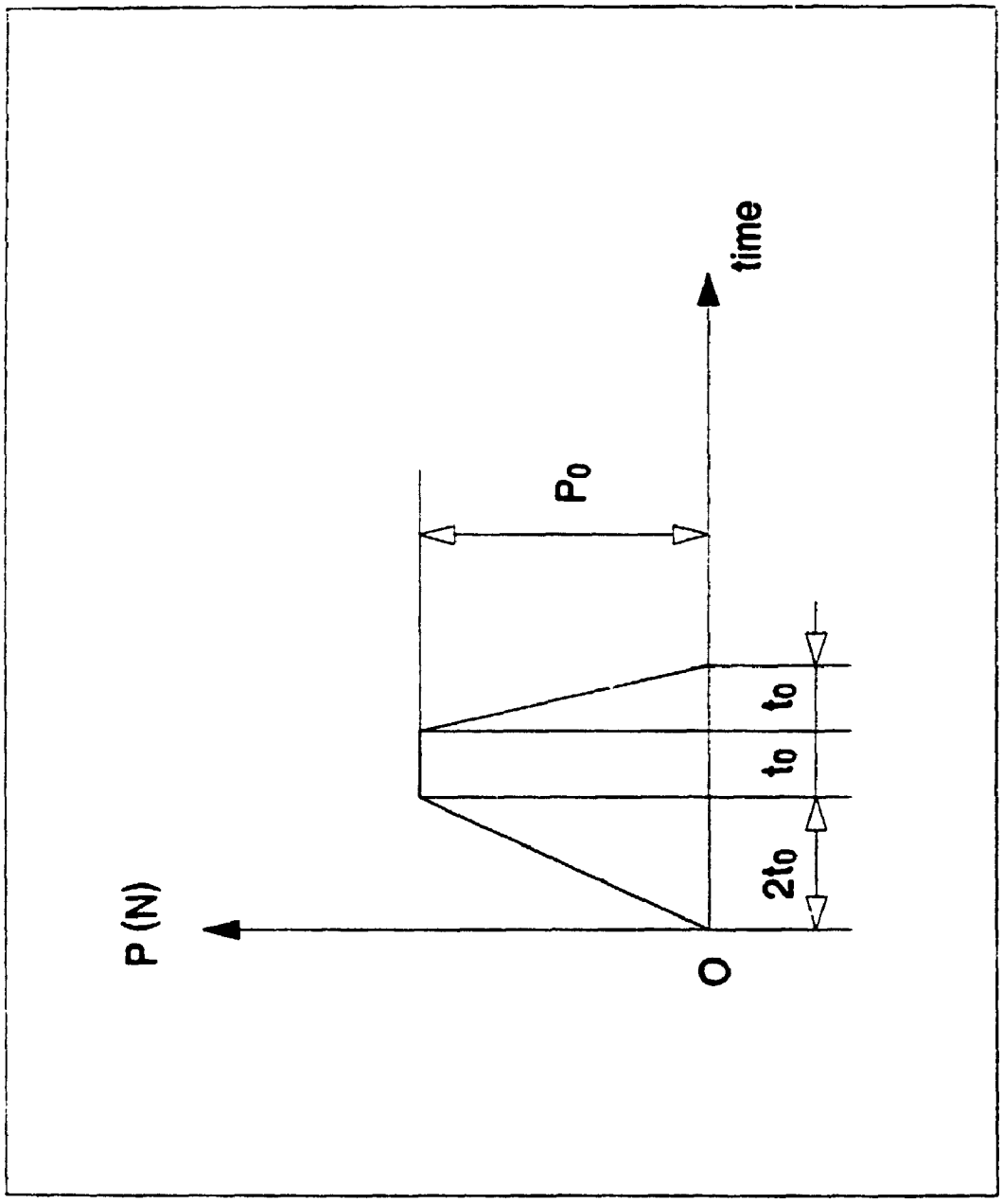

Figure 7.54 Time history of the impulse-type loading

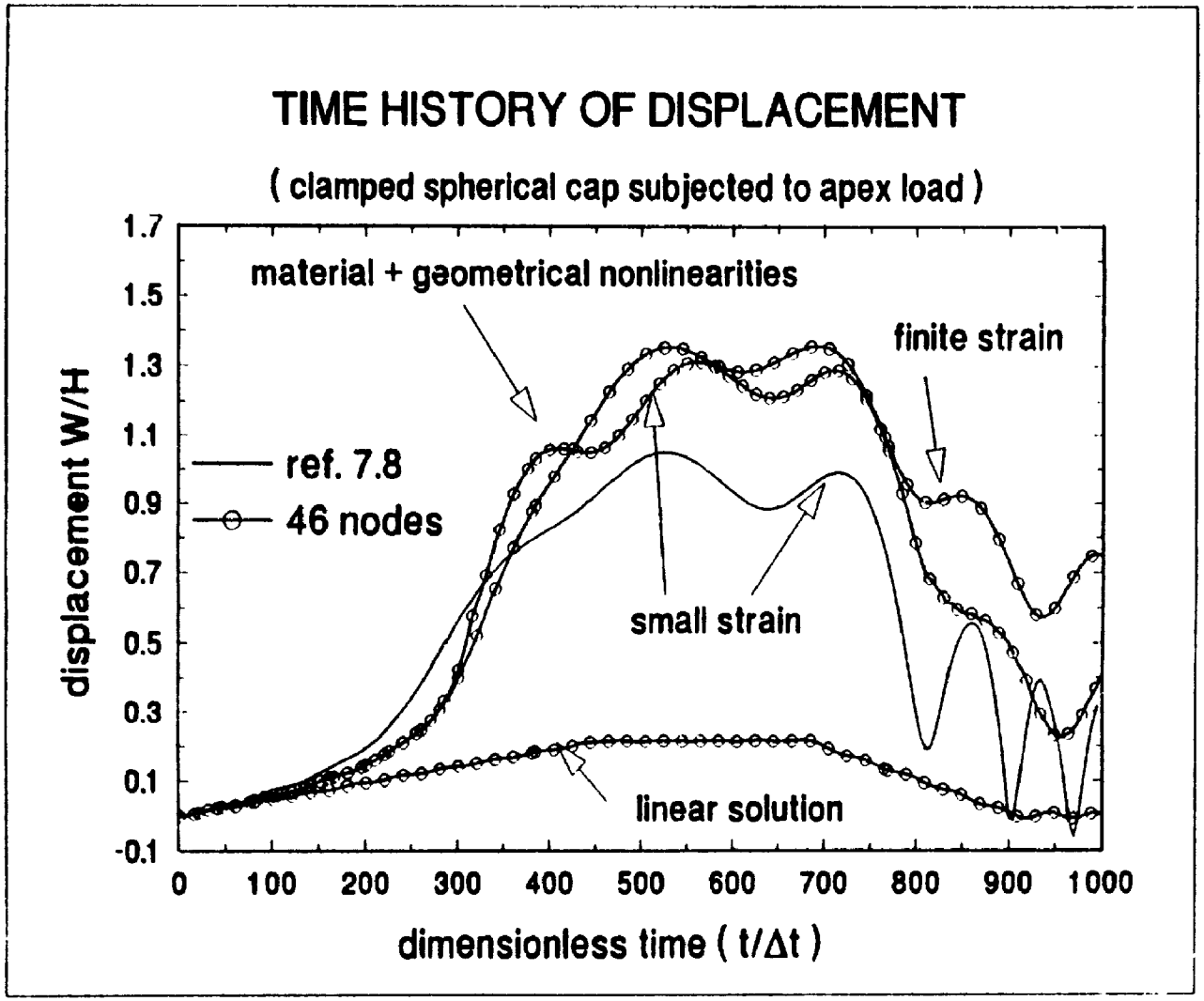

Figure 7.55 Time history of apex displacement of the clamped spherical cap

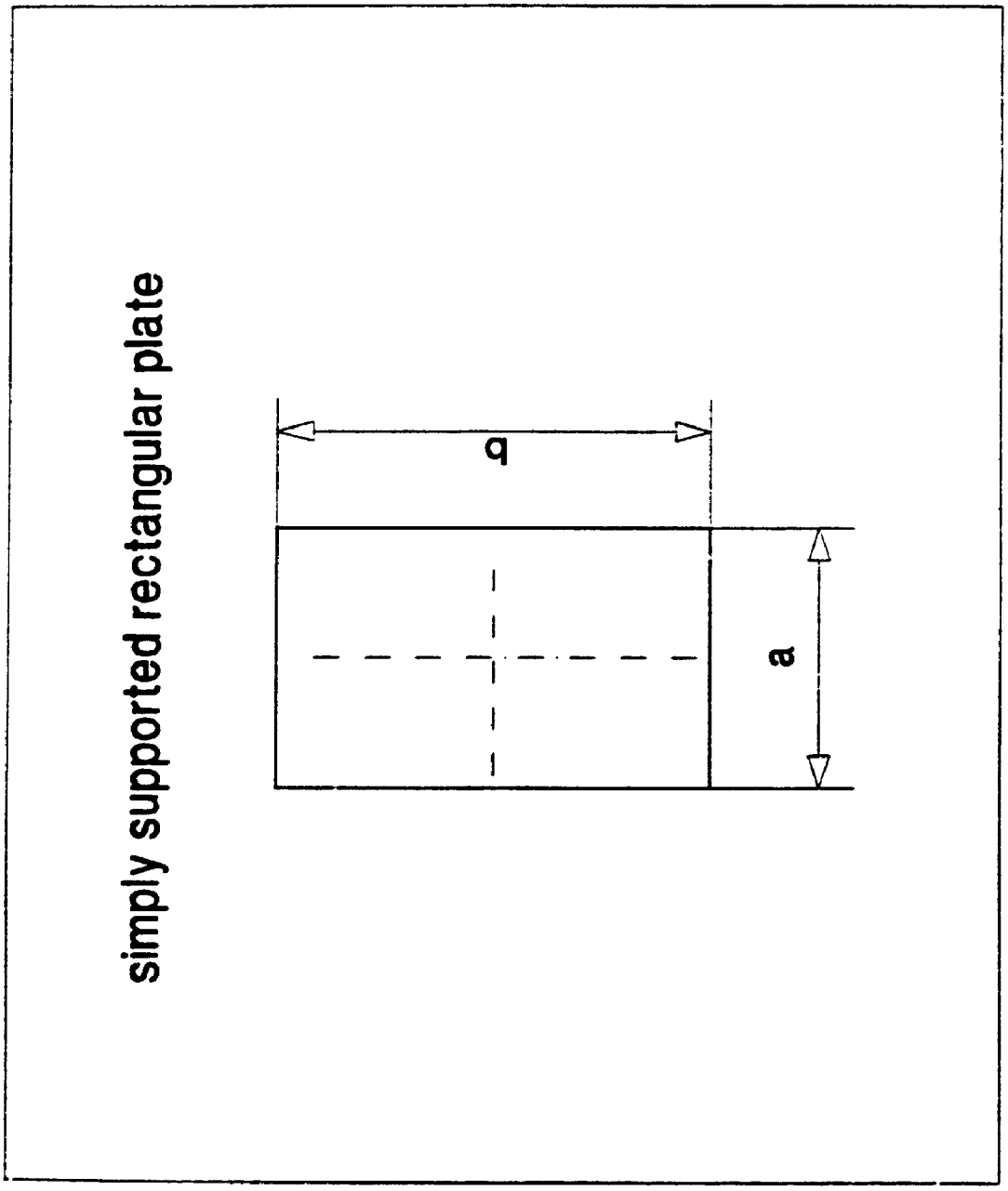

Figure 7.56 The simply supported rectangular plate

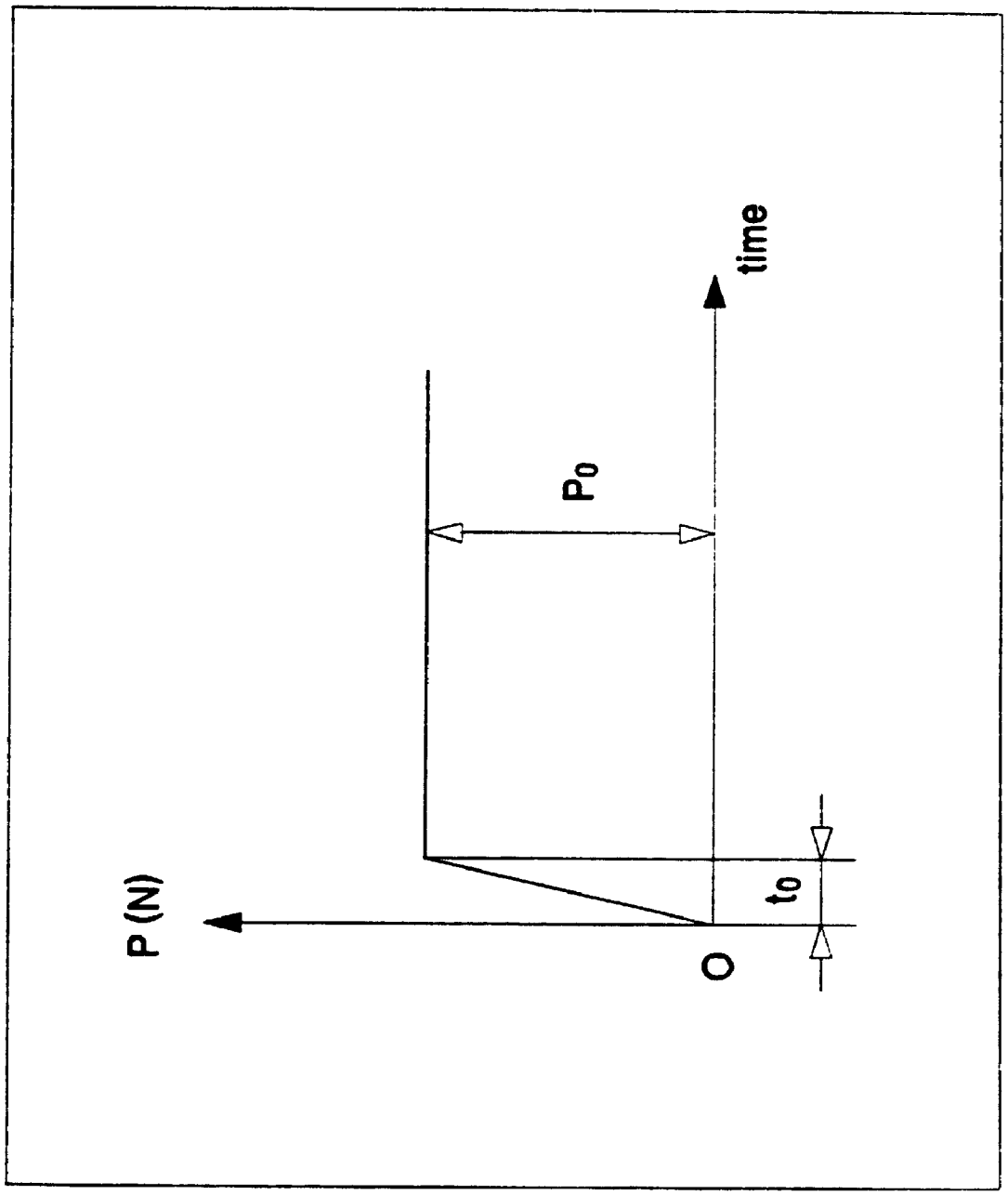

Figure 7.57 Time history of the step loading

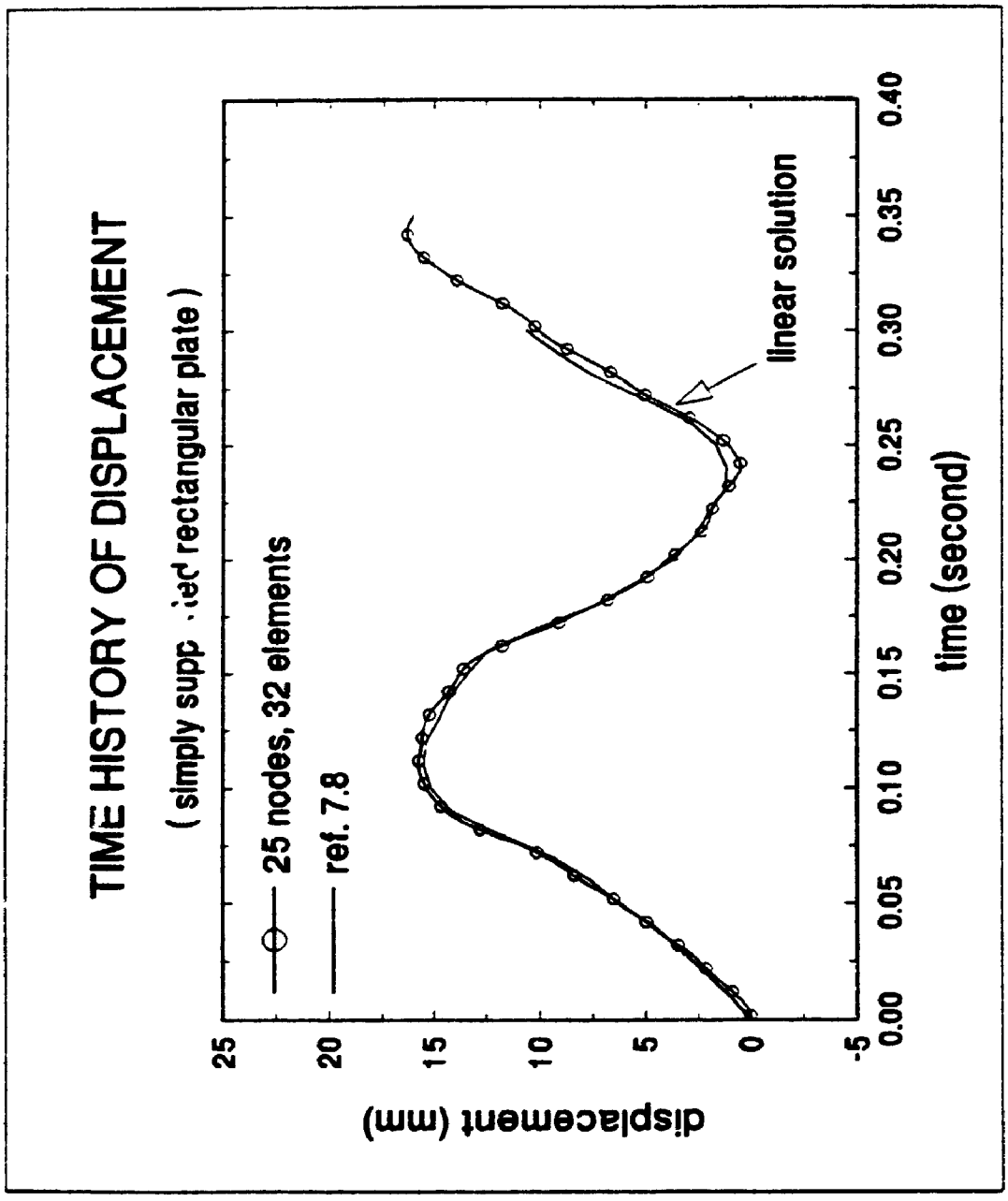

Figure 7.58 Time history of center displacement of the rectangular plate

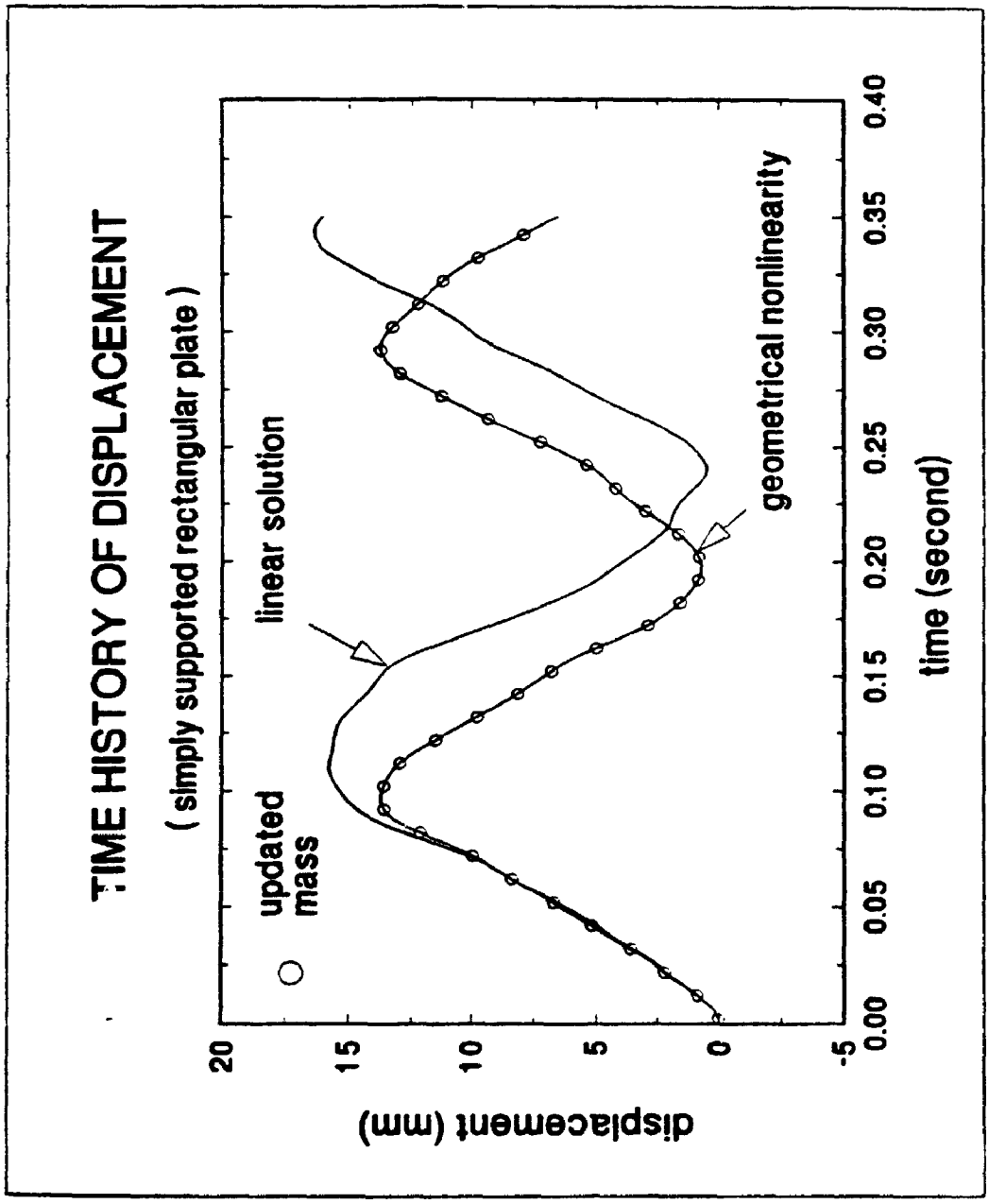

Figure 7.59 Time history of center displacement of the rectangular plate

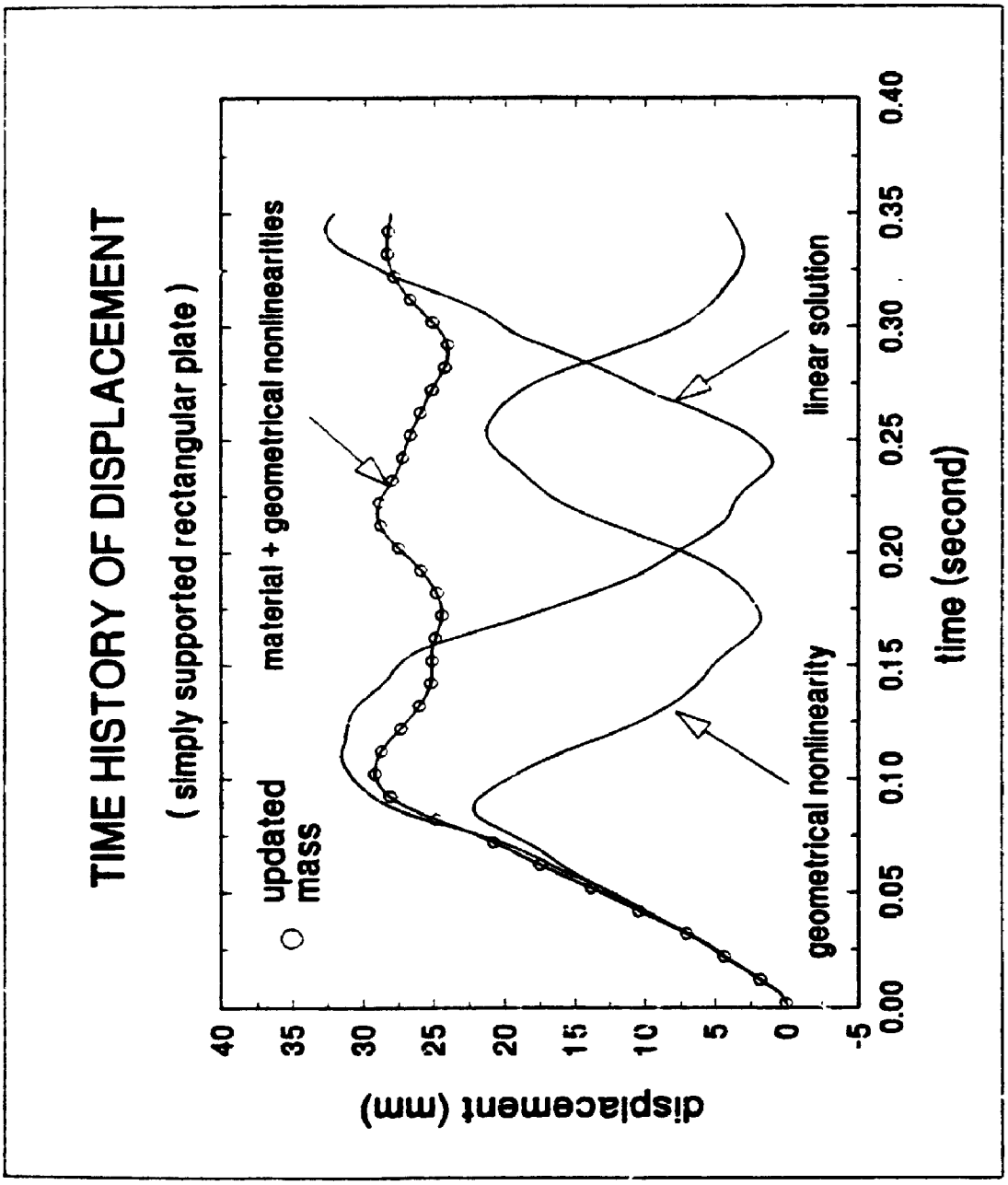

Figure 7.60 Time history of center displacement of the rectangular plate

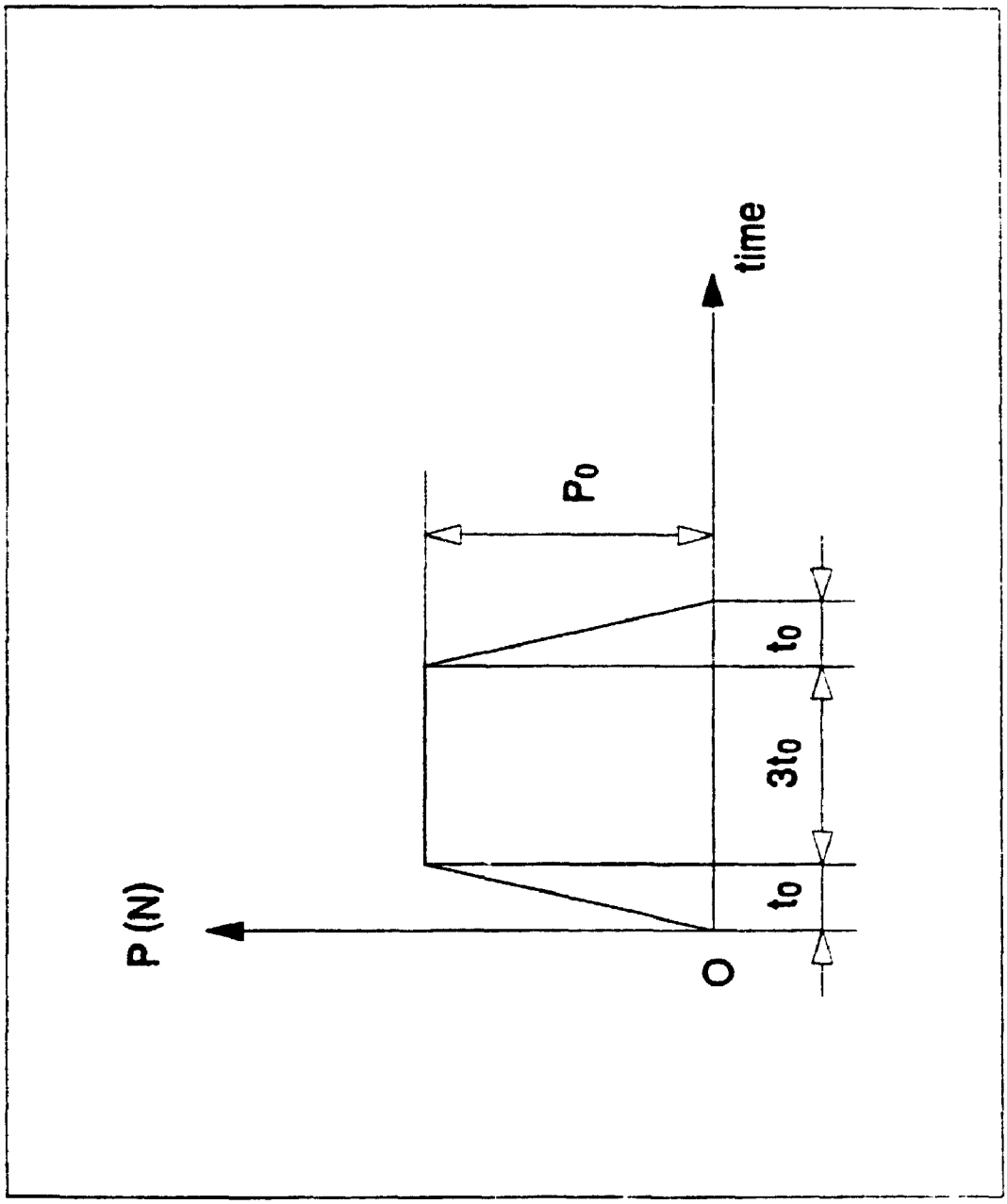

Figure 7.61 Time history of the impulse-type loading

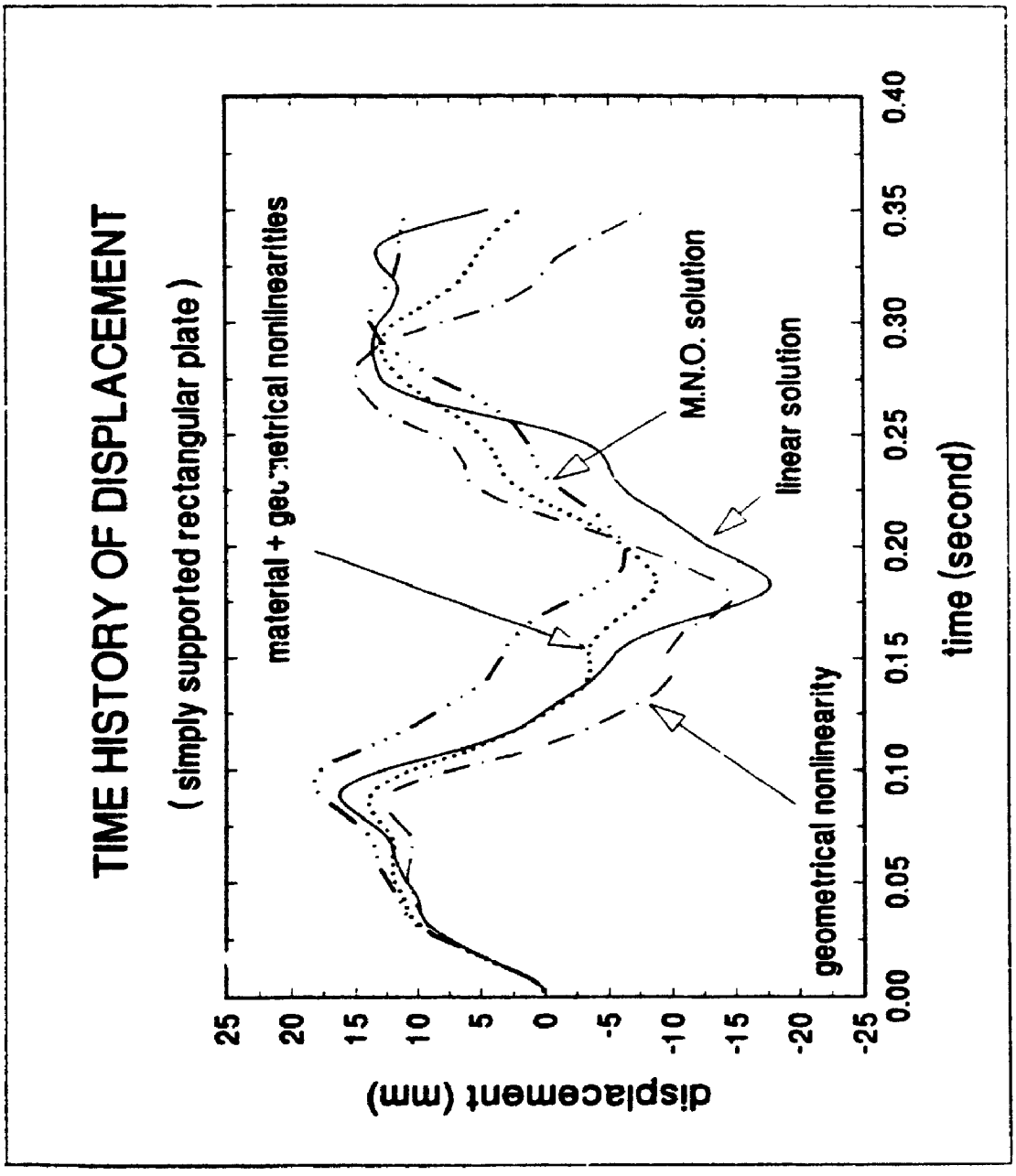

Figure 7.62 Time history of center displacement of the rectangular plate

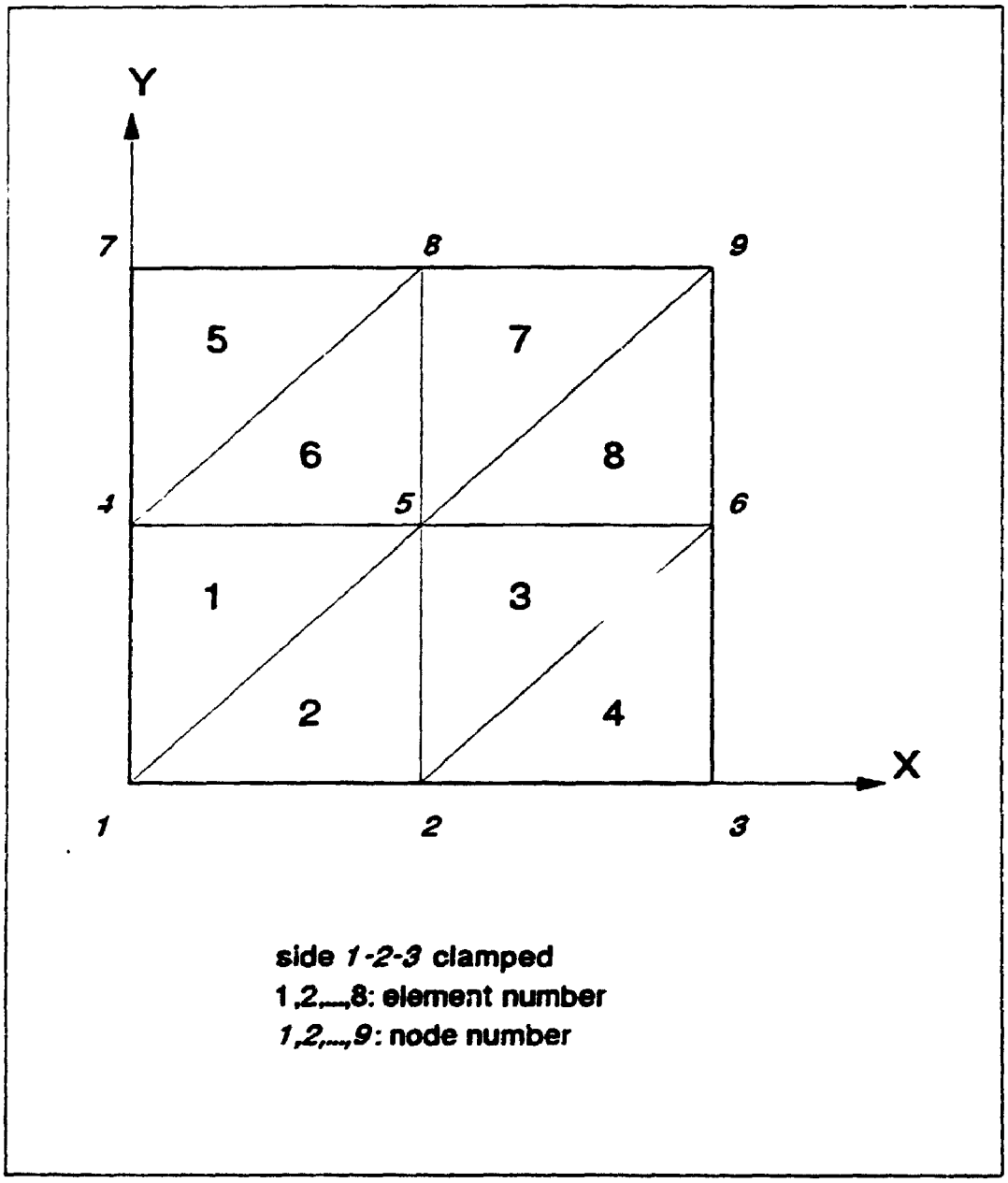

Figure 8.1 The square plate clamped at one side (full plate discretization)

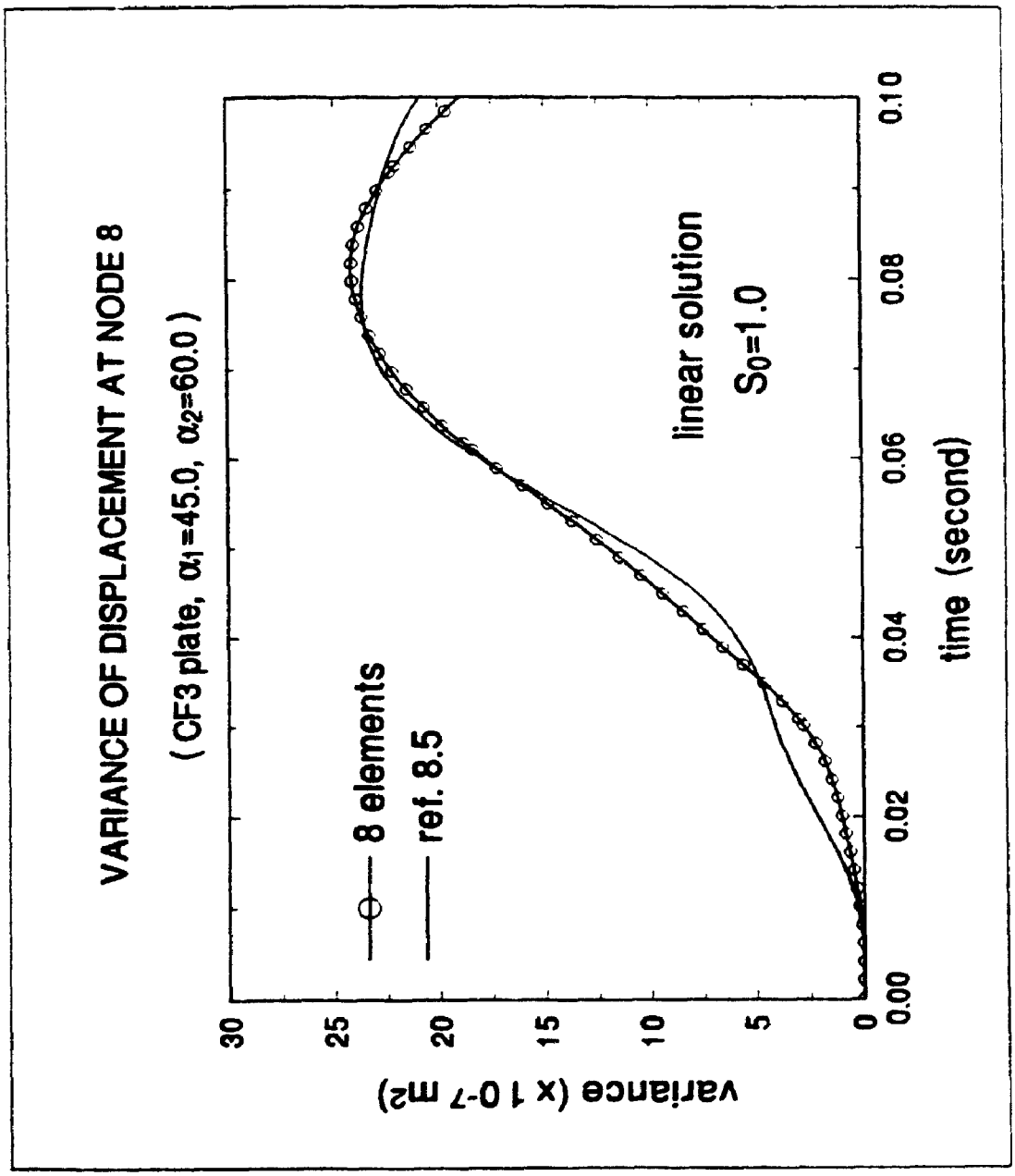

Figure 8.2 Variance of displacement at node 8

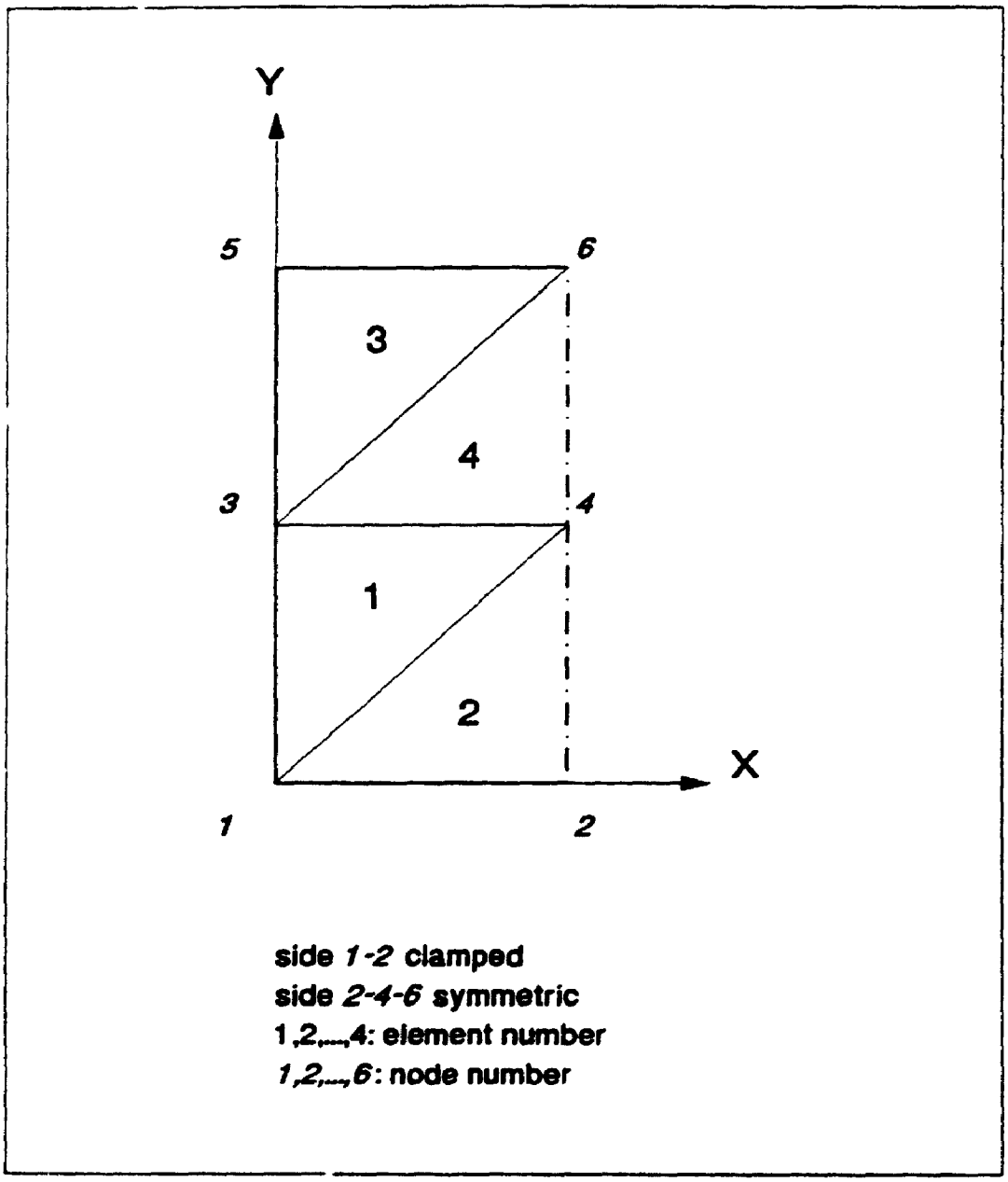

Figure 8.3 The square plate clamped at one side (half plate discretization)

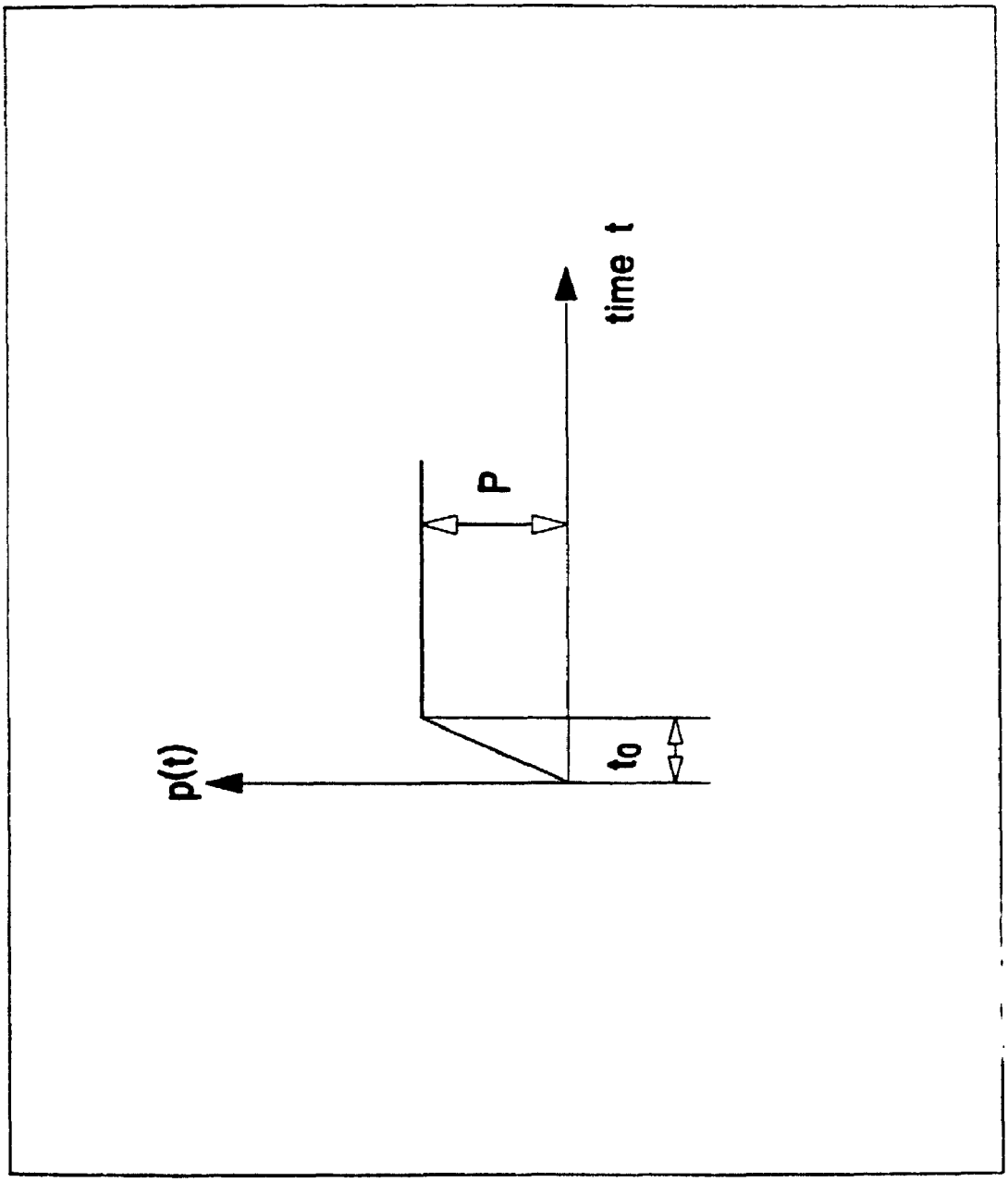

Figure 8.4 Time history of the step loading

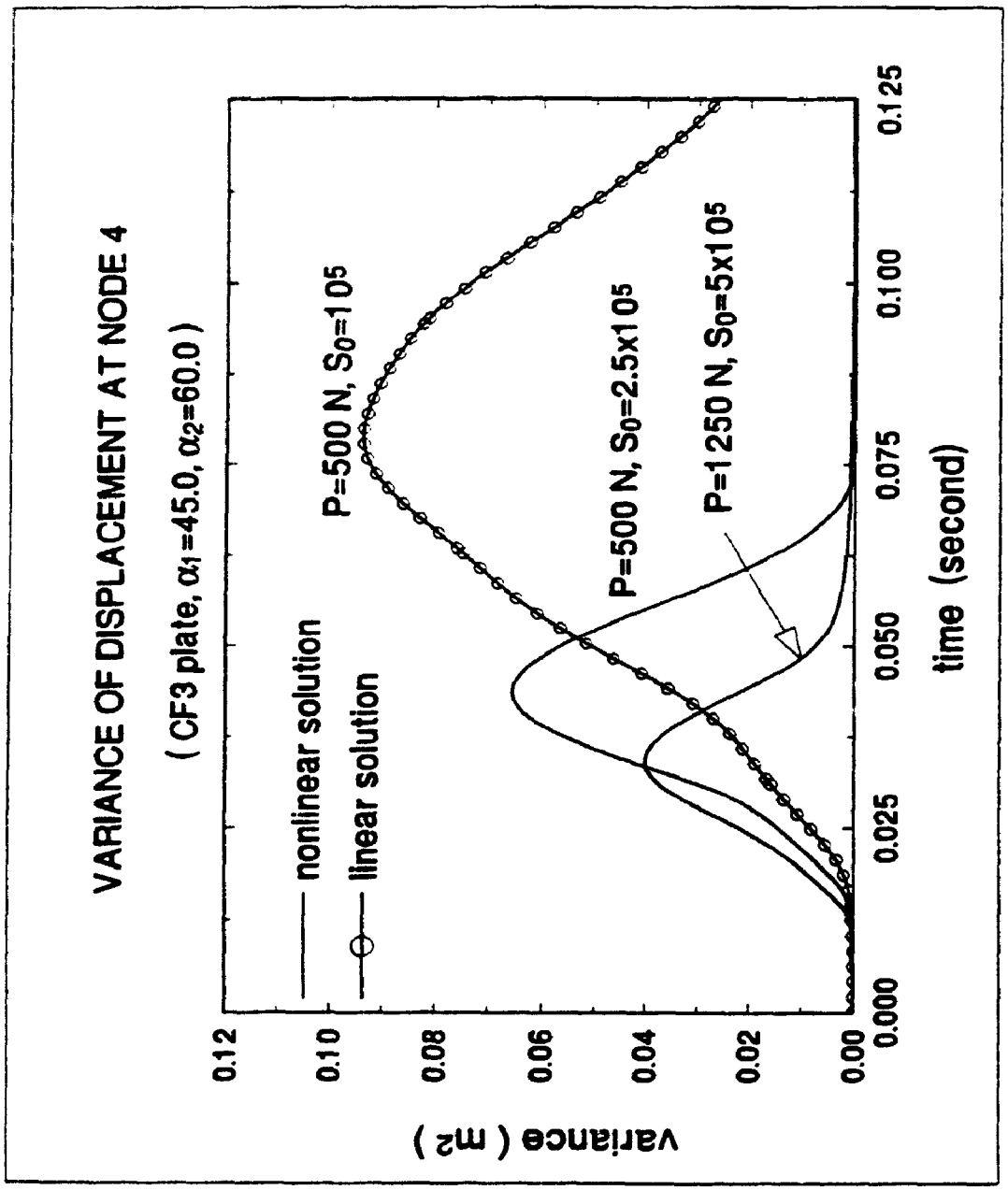

Figure 8.5 Variance of displacement at node 4

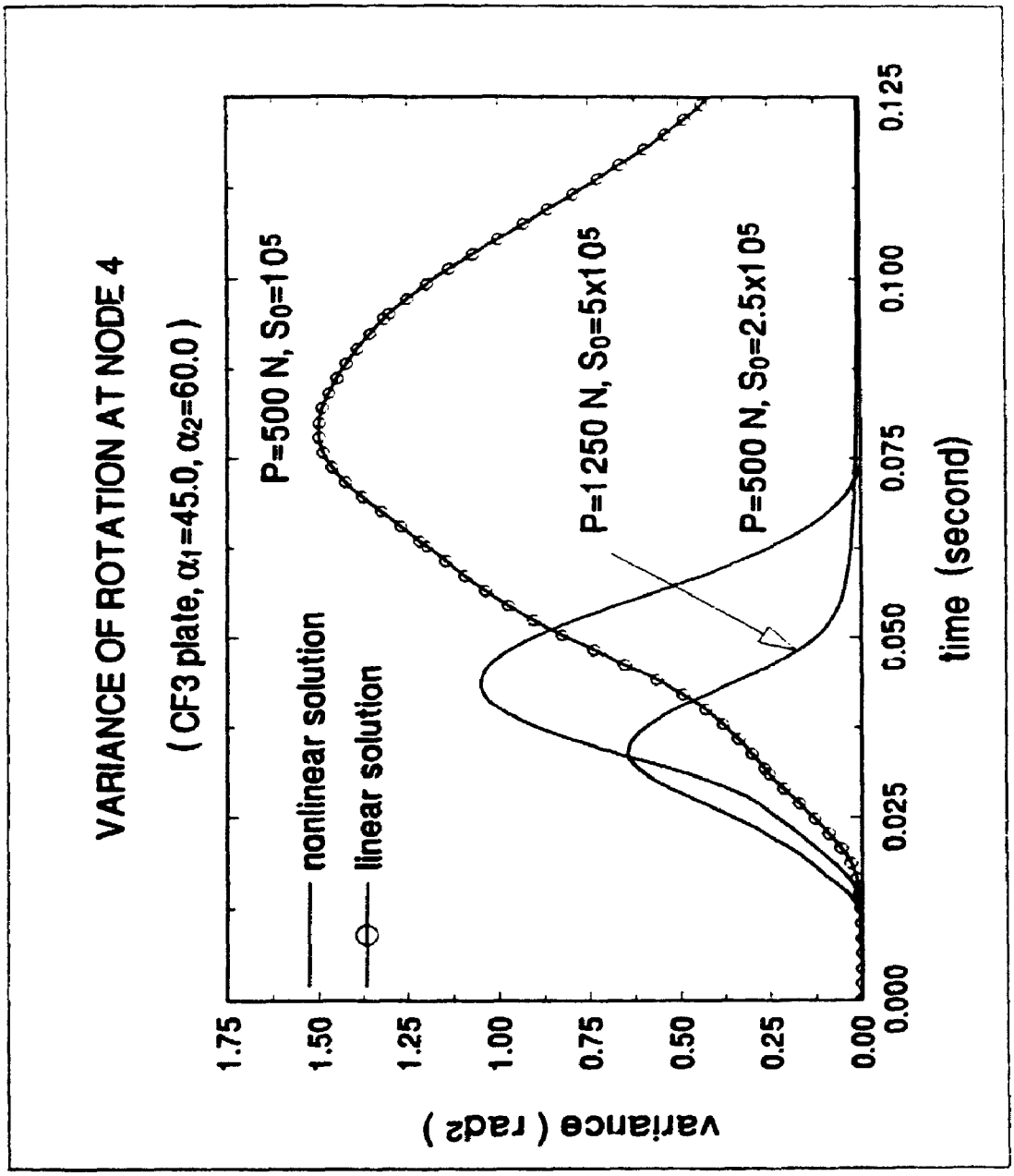

Figure 8.6 Variance of rotation at node 4

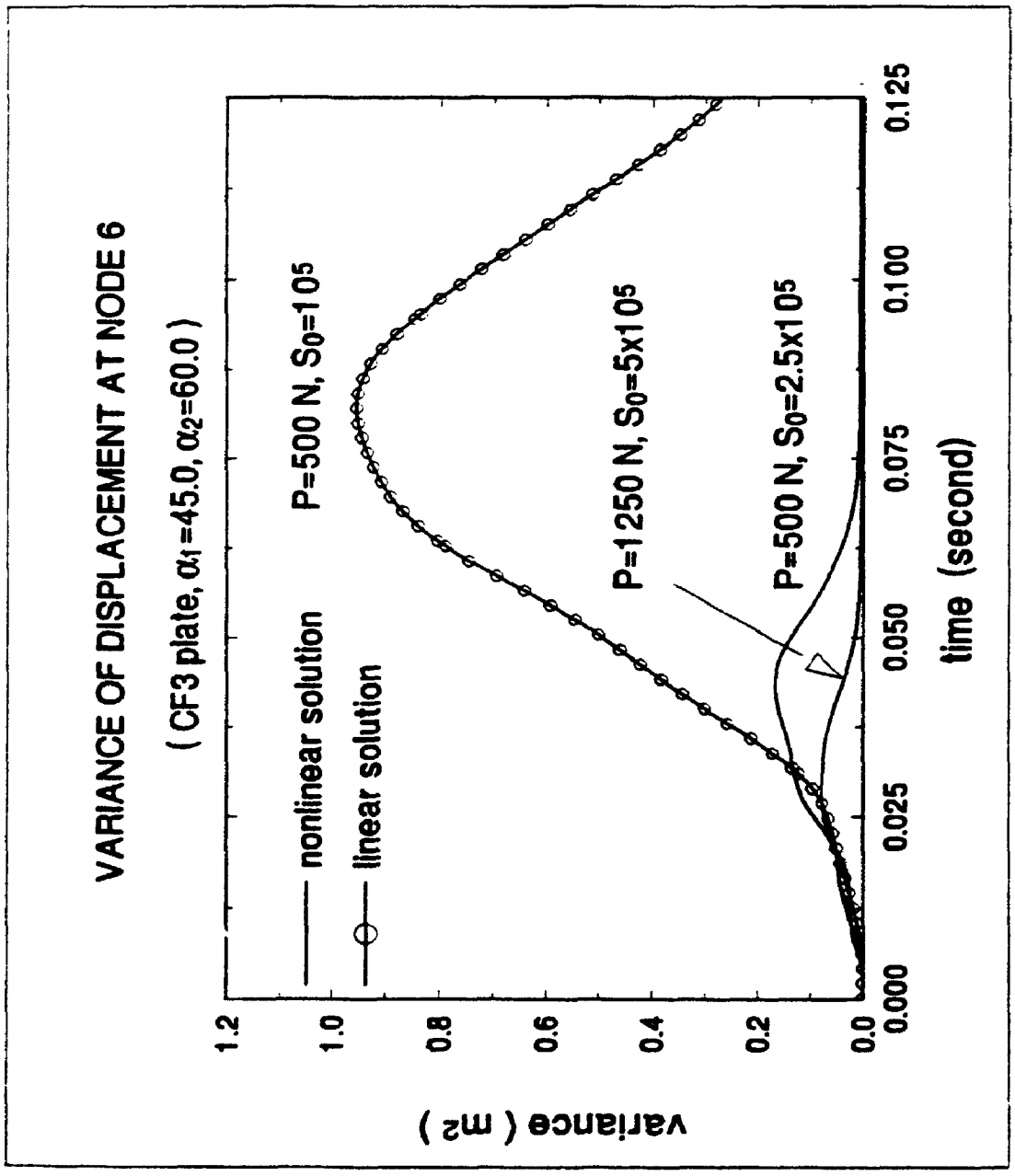

Figure 8.7 Variance of displacement at node 6

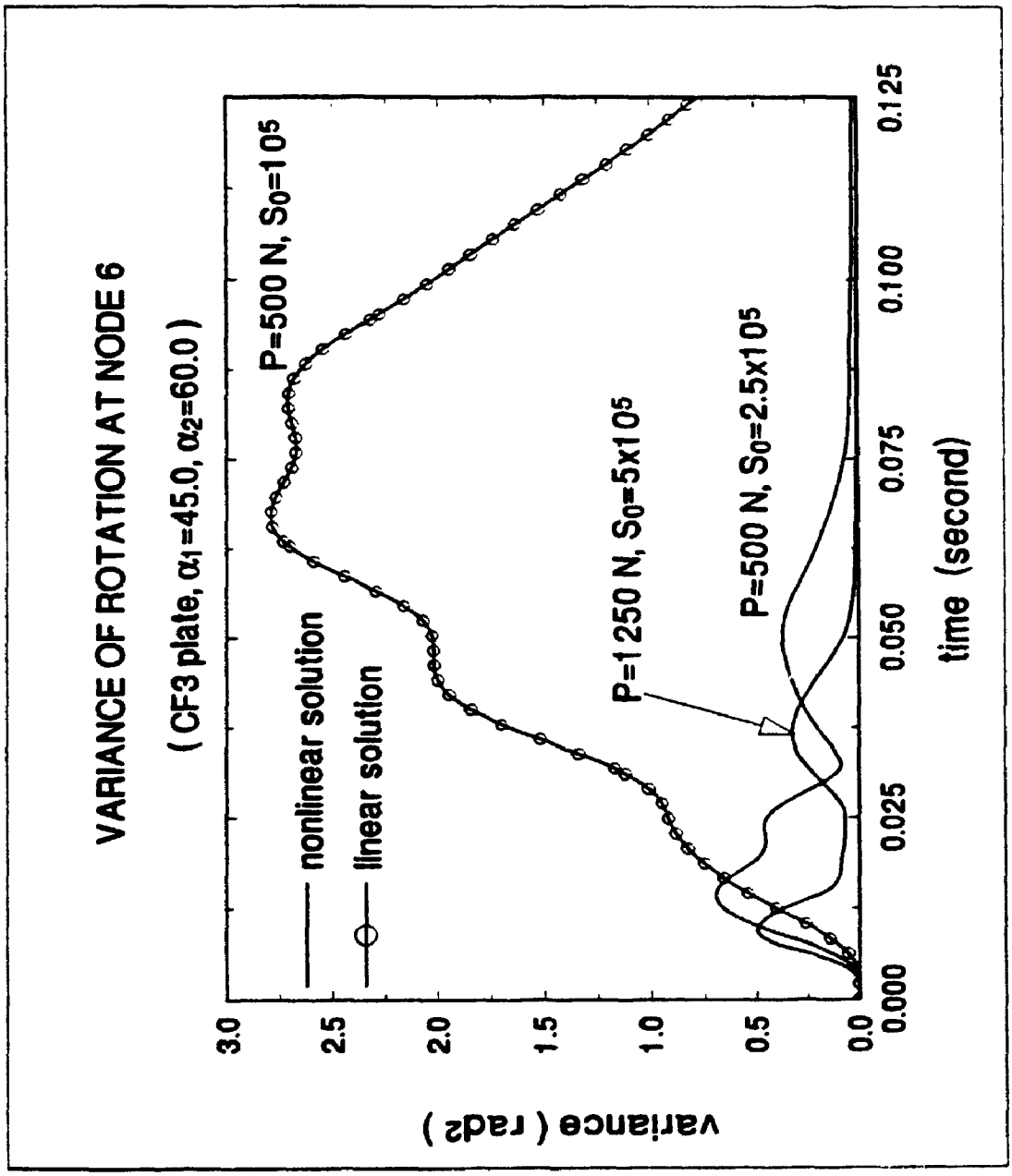

Figure 8.8 Variance of rotation at node 6

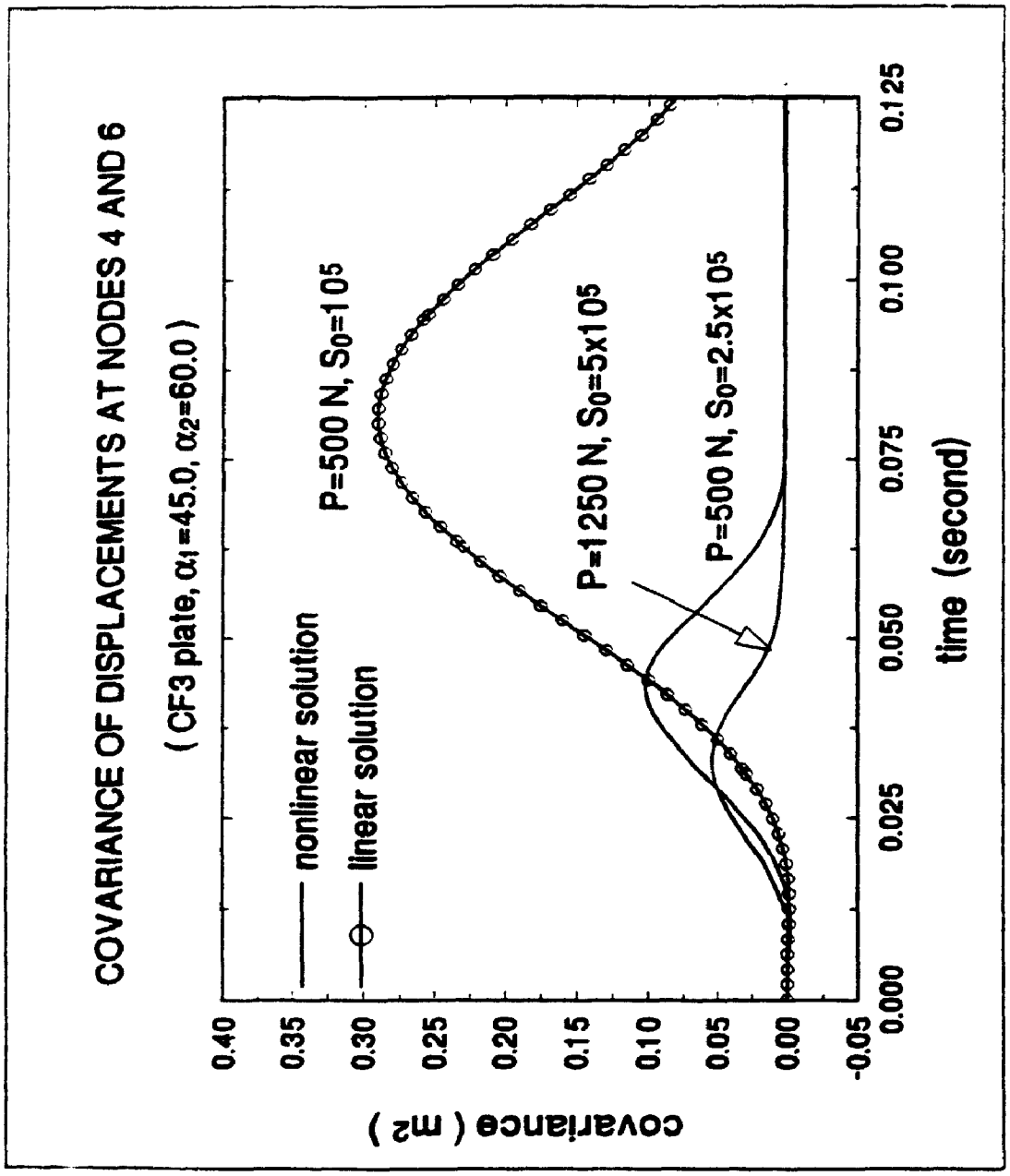

Figure 8.9 Covariance of displacements at nodes 4 and 6

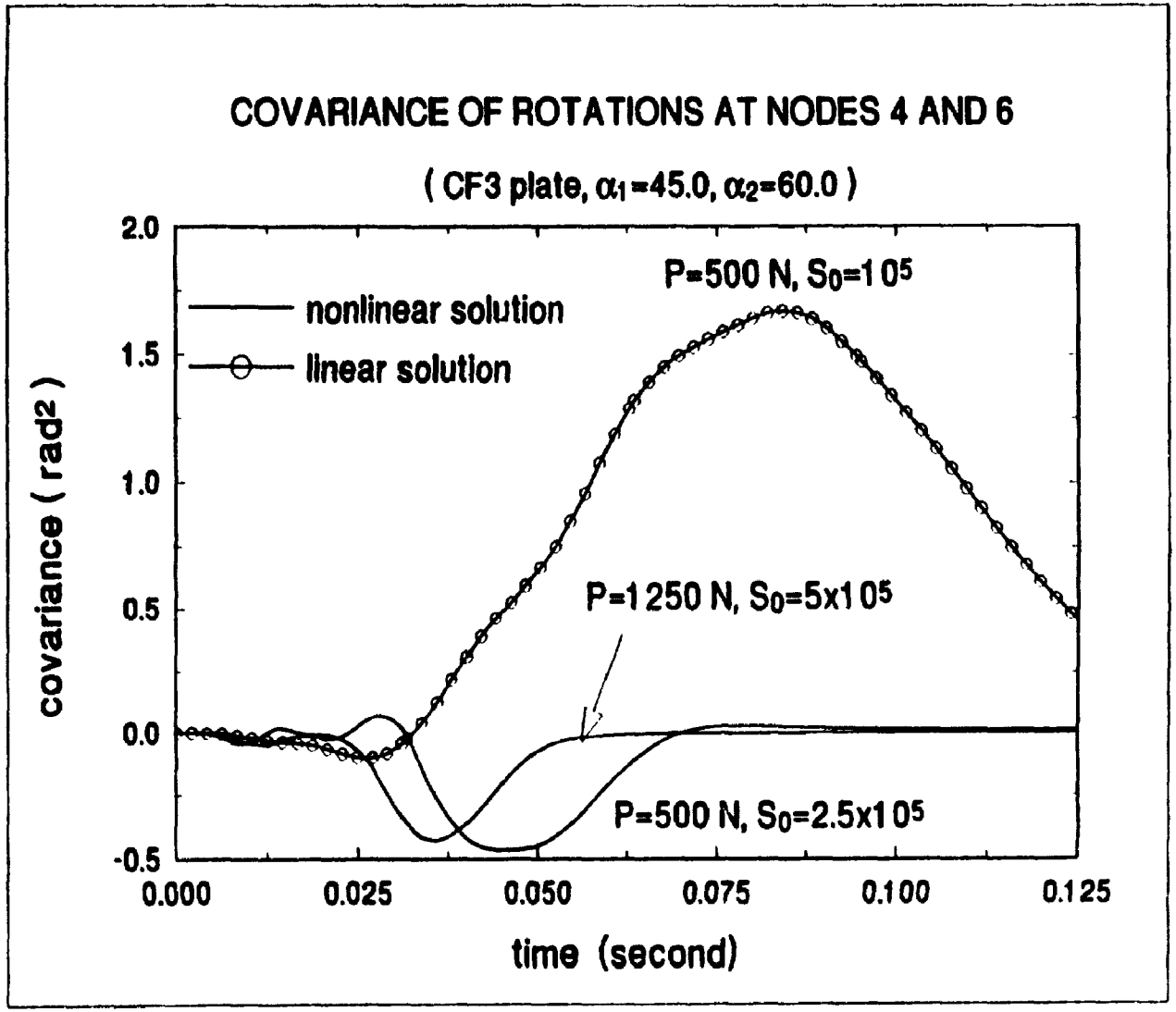

Figure 8.10 Covariance of rotations at nodes 4 and 6

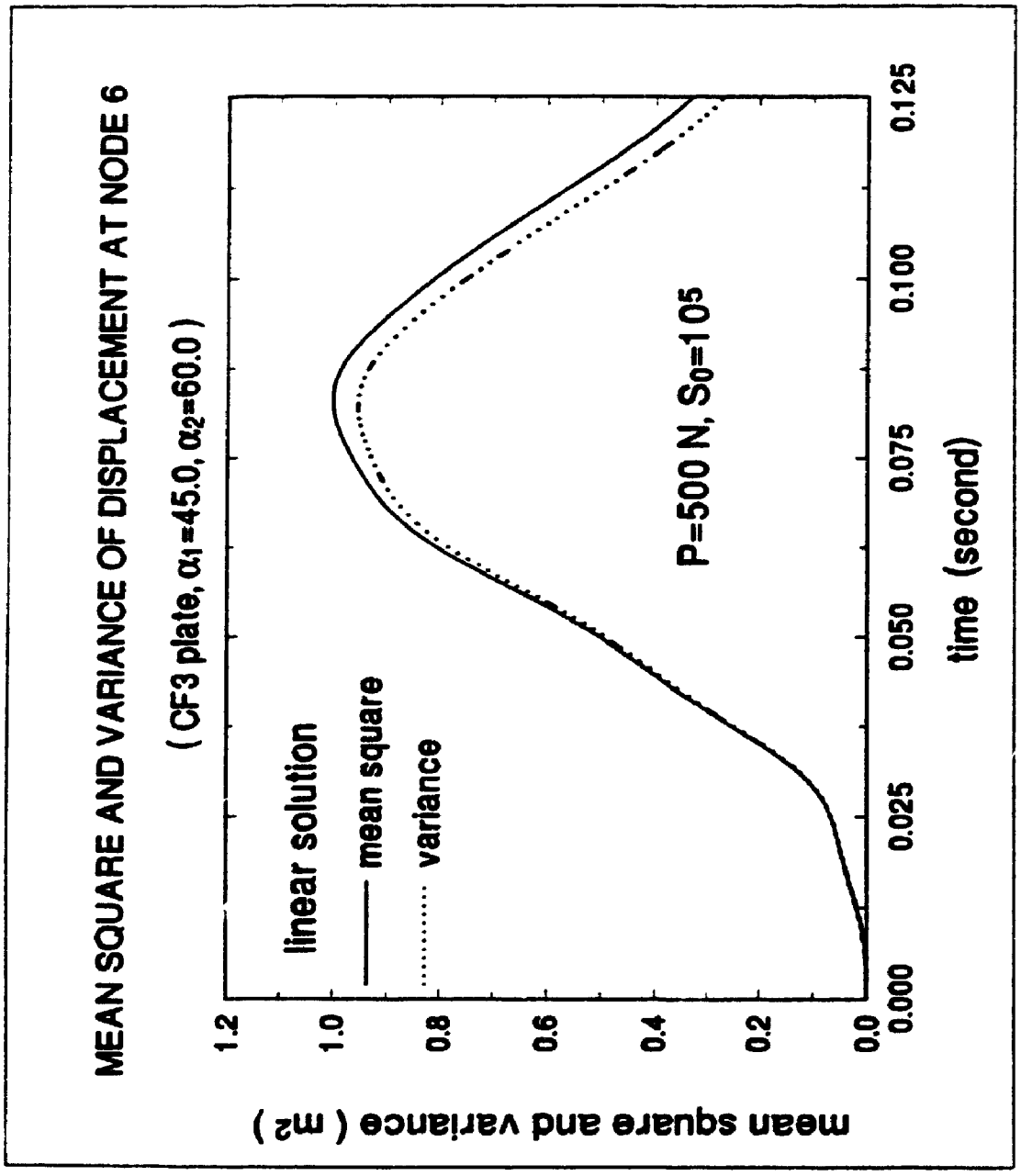

Figure 8.11 Mean square and variance of displacement at node 6

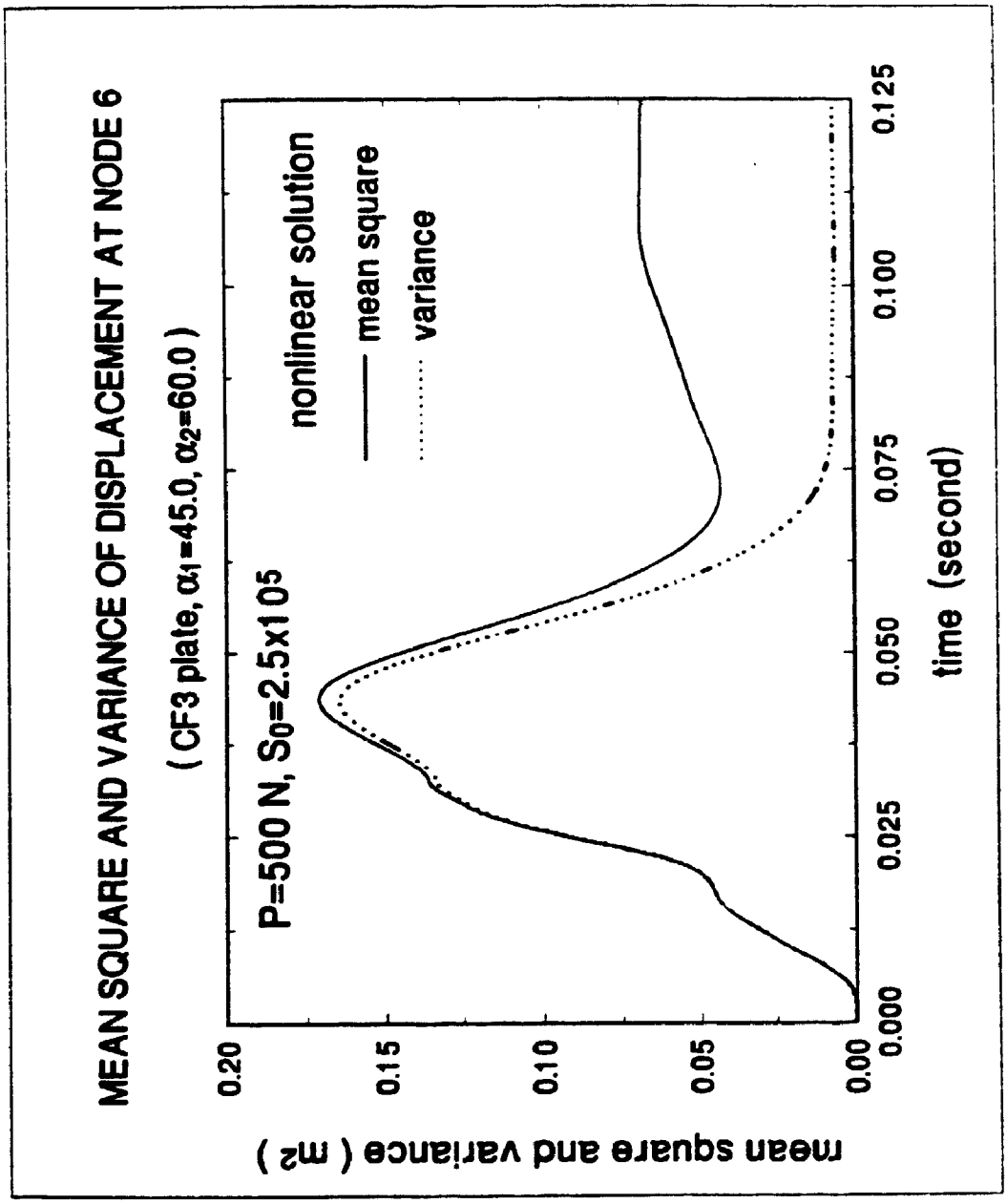

Figure 8.12 Mean square and variance of displacement at node 6

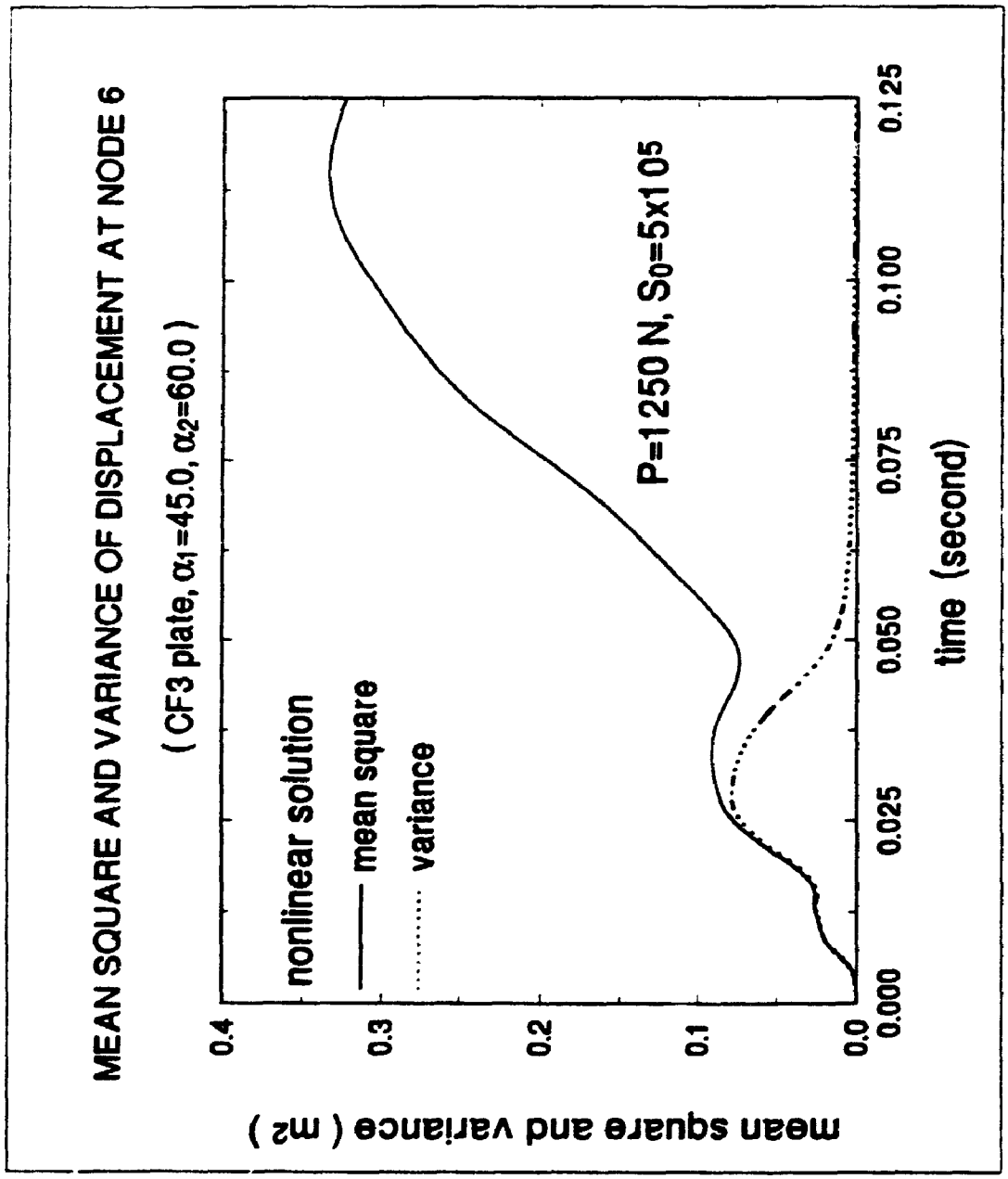

Figure 8.13 Mean square and variance of displacement at node 6

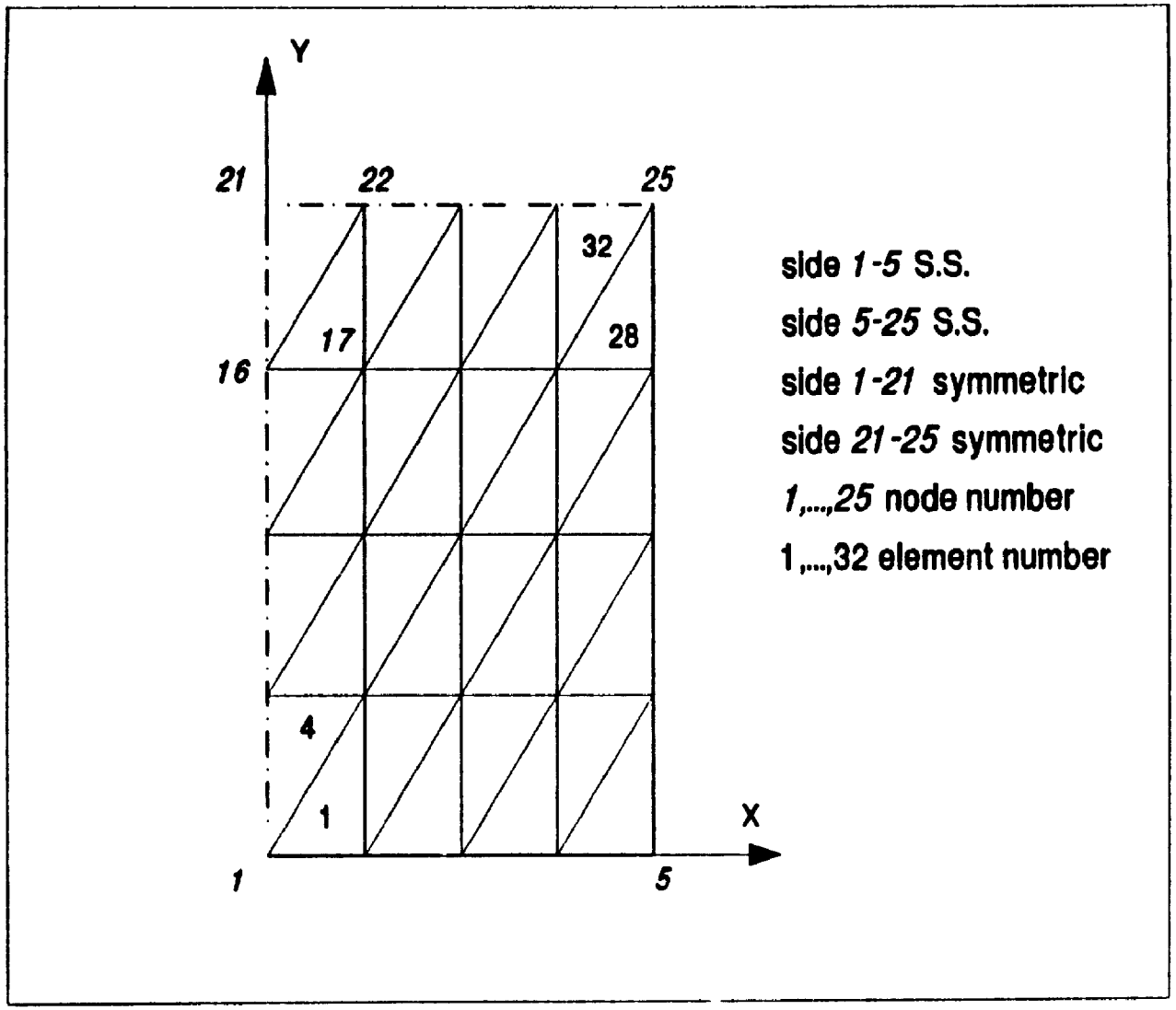

Figure 8.14 The simply supported rectangular plate (quarter plate discretization)

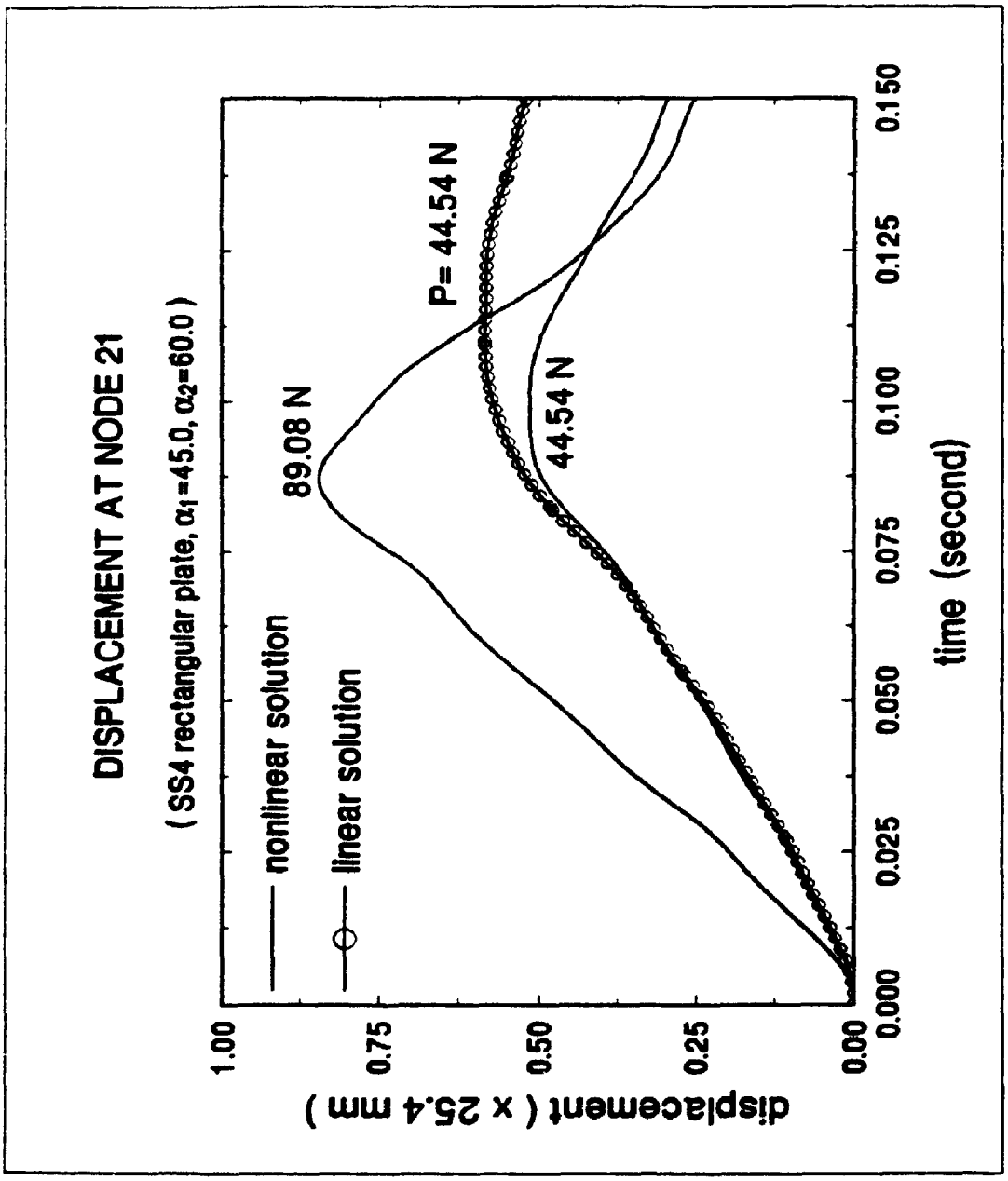

Figure 8.15 Displacement at node 21

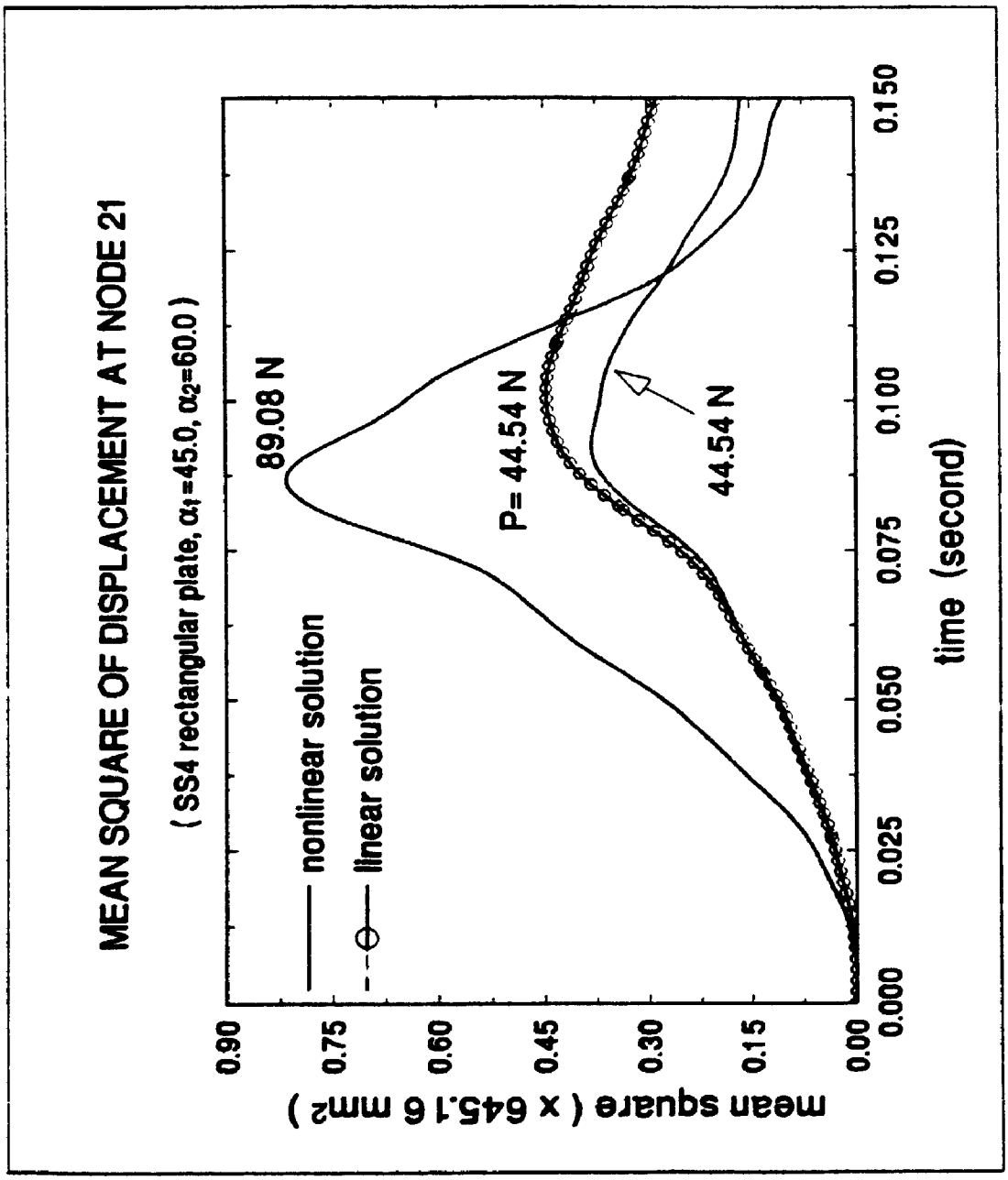

Figure 8.16 Mean square of displacement at node 21

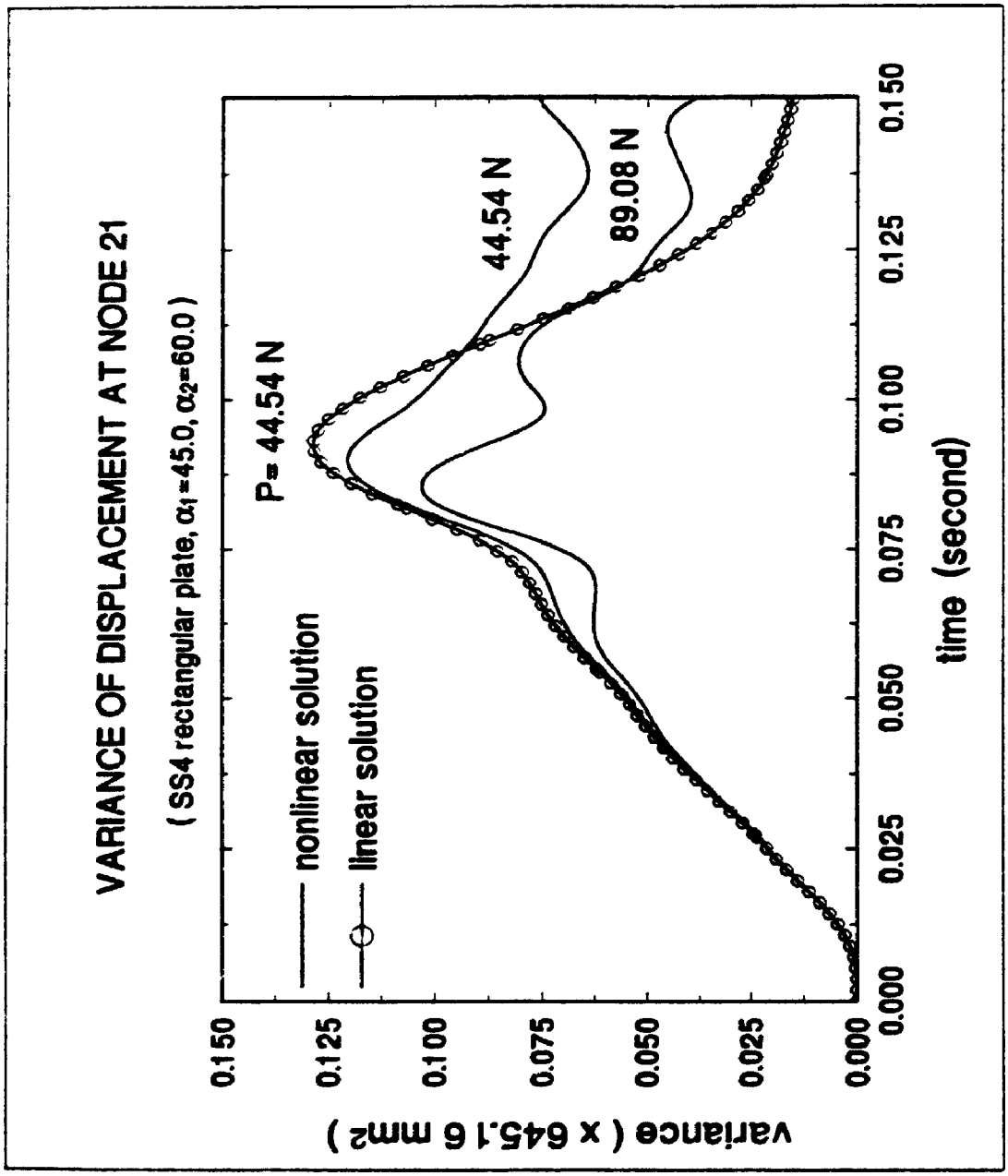

Figure 8.17 Variance of displacement at node 21

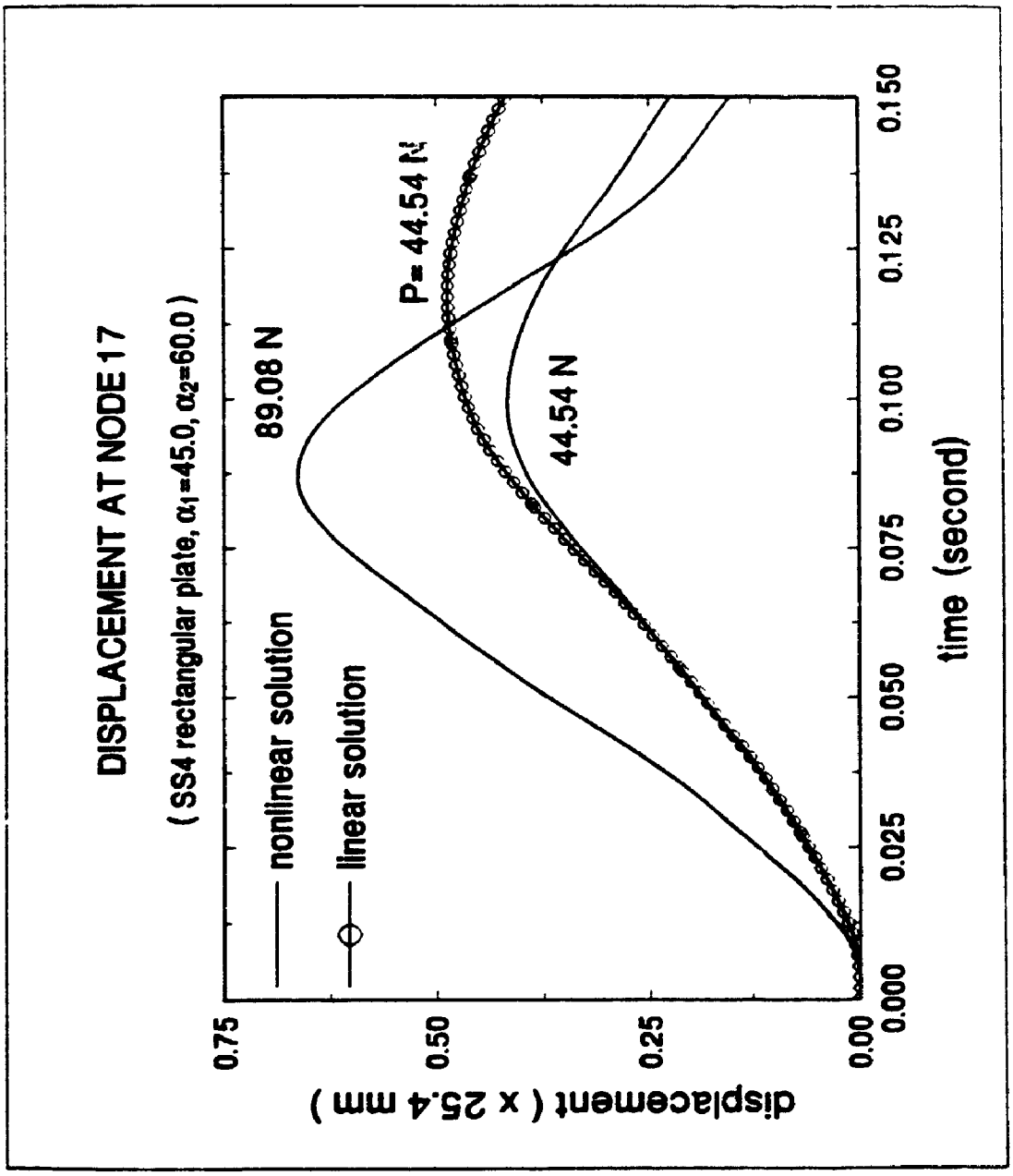

Figure 8.18 Displacement at node 17

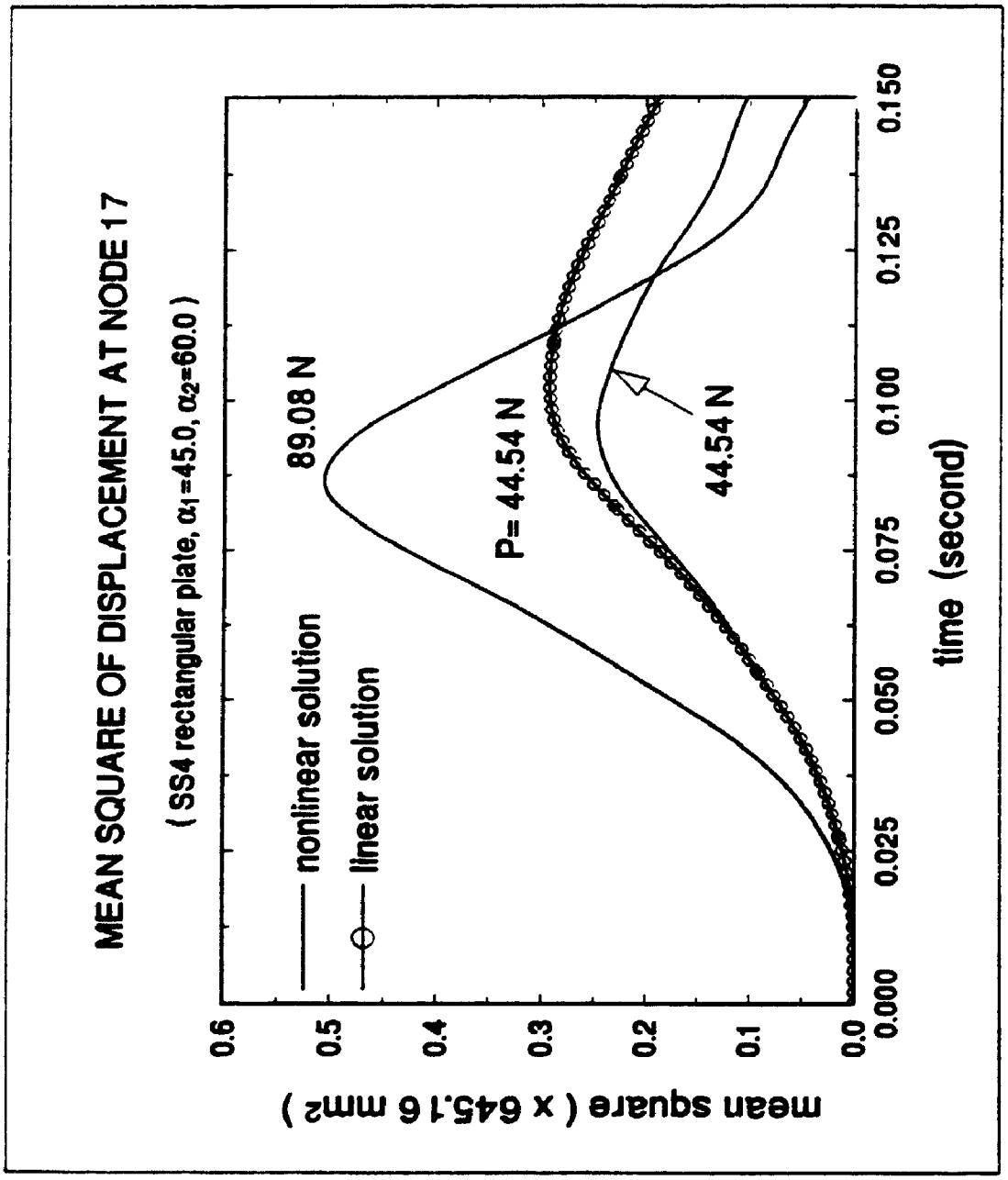

Figure 8.19 Mean square of displacement at node 17

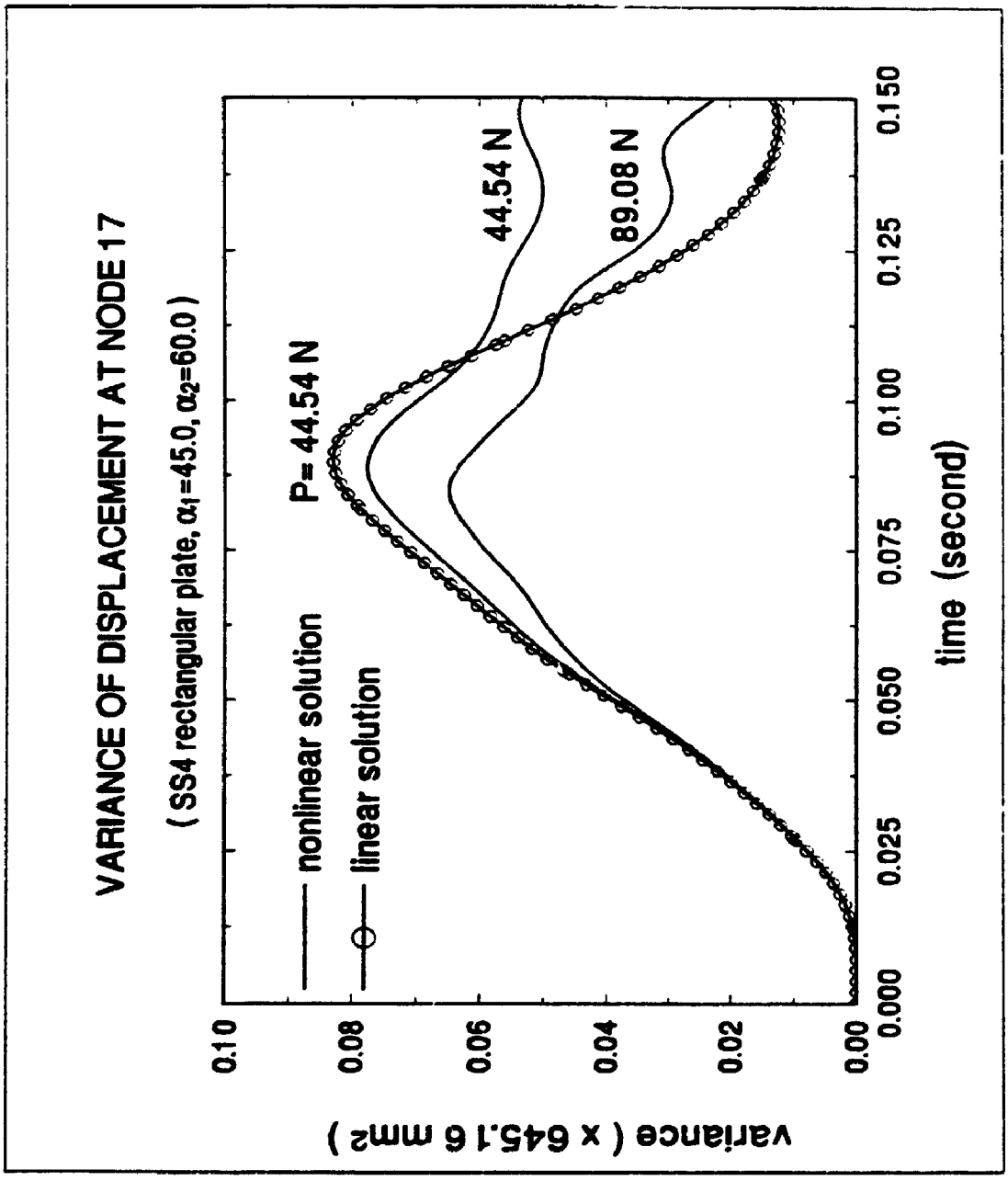

Figure 8.20 Variance of displacement at node 17

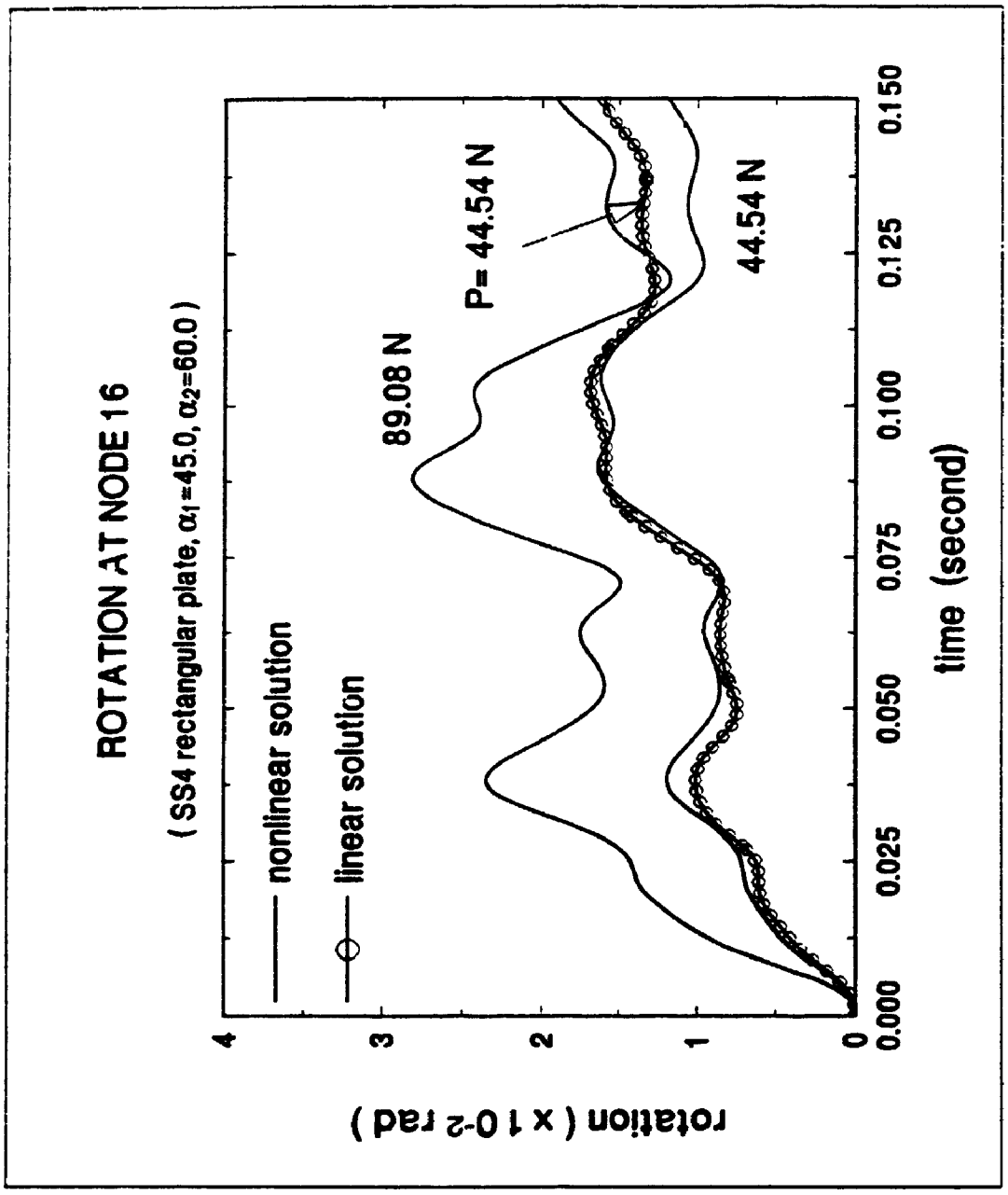

Figure 8.21 Rotation at node 16

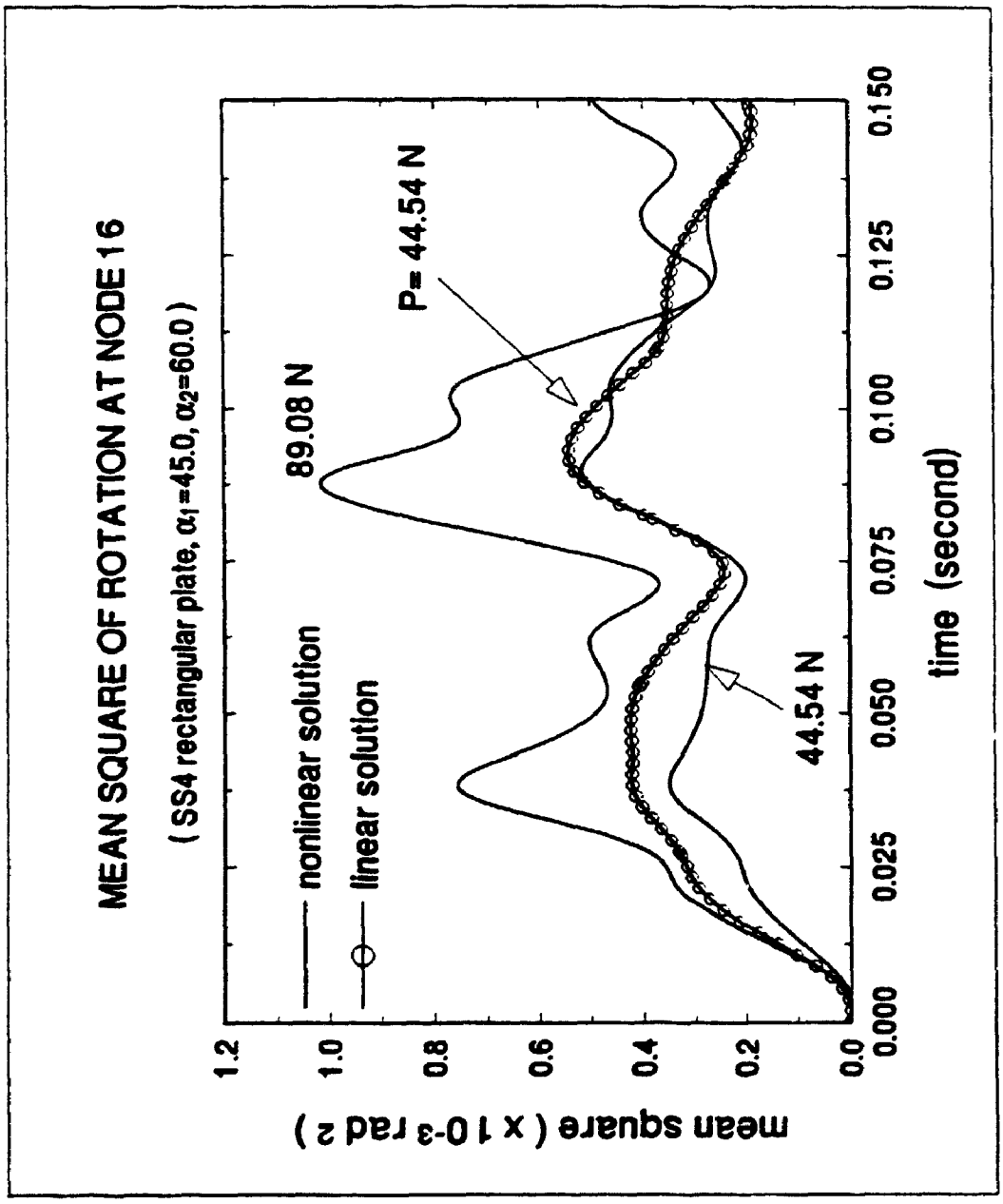

Figure 8.22 Mean square of rotation at node 16

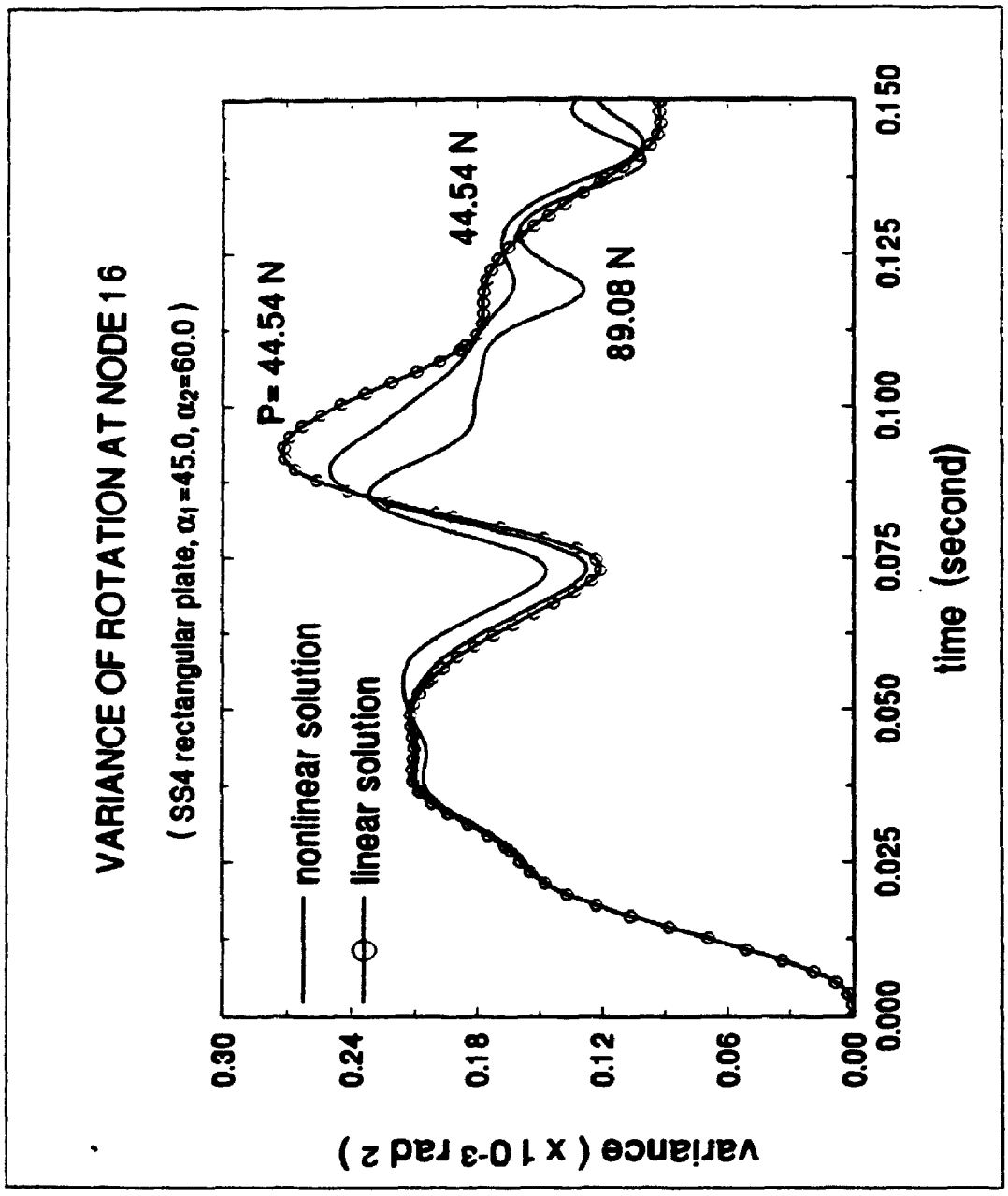

Figure 8.23 Variance of rotation at node 16

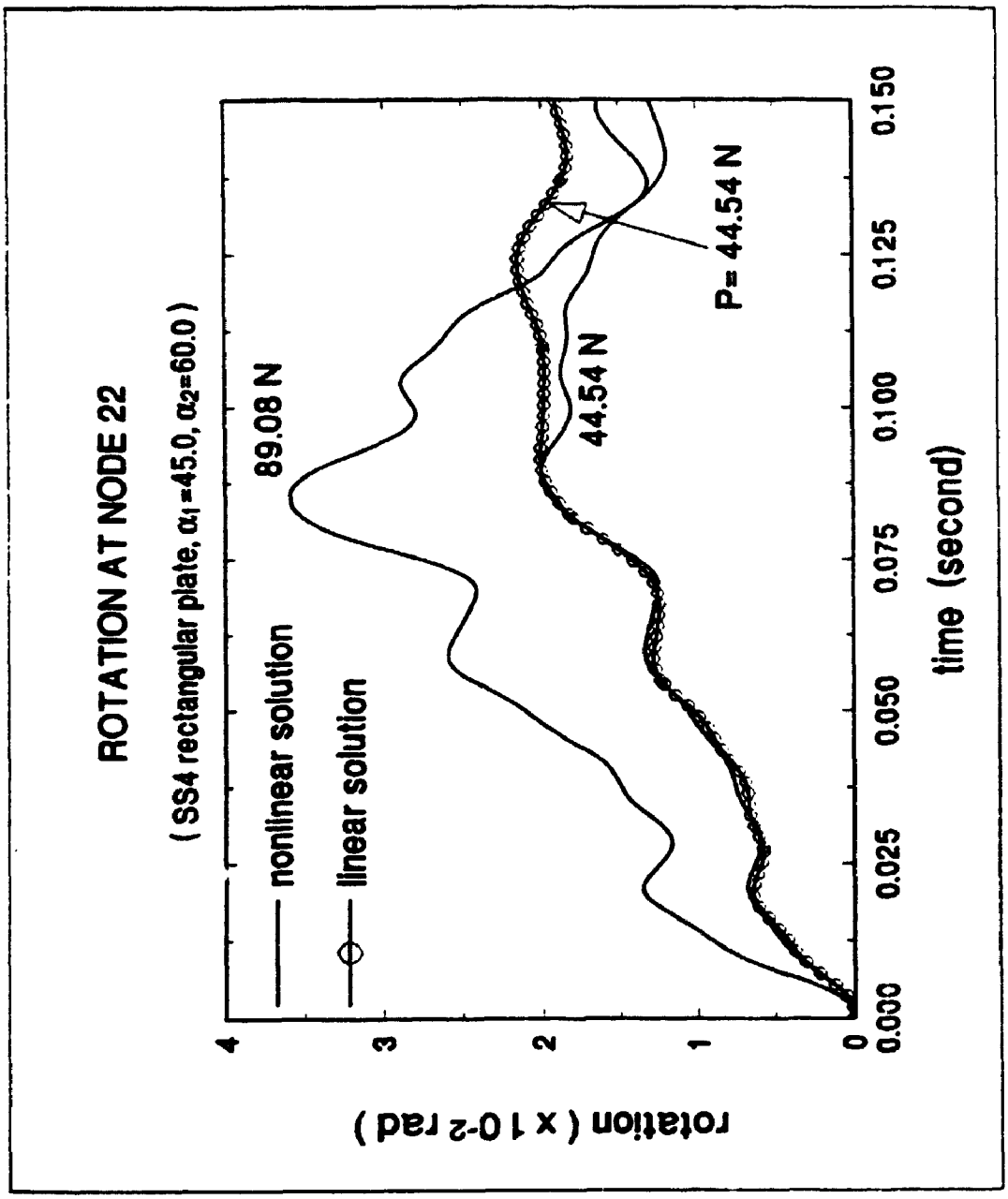

Figure 8.24 Rotation at node 22

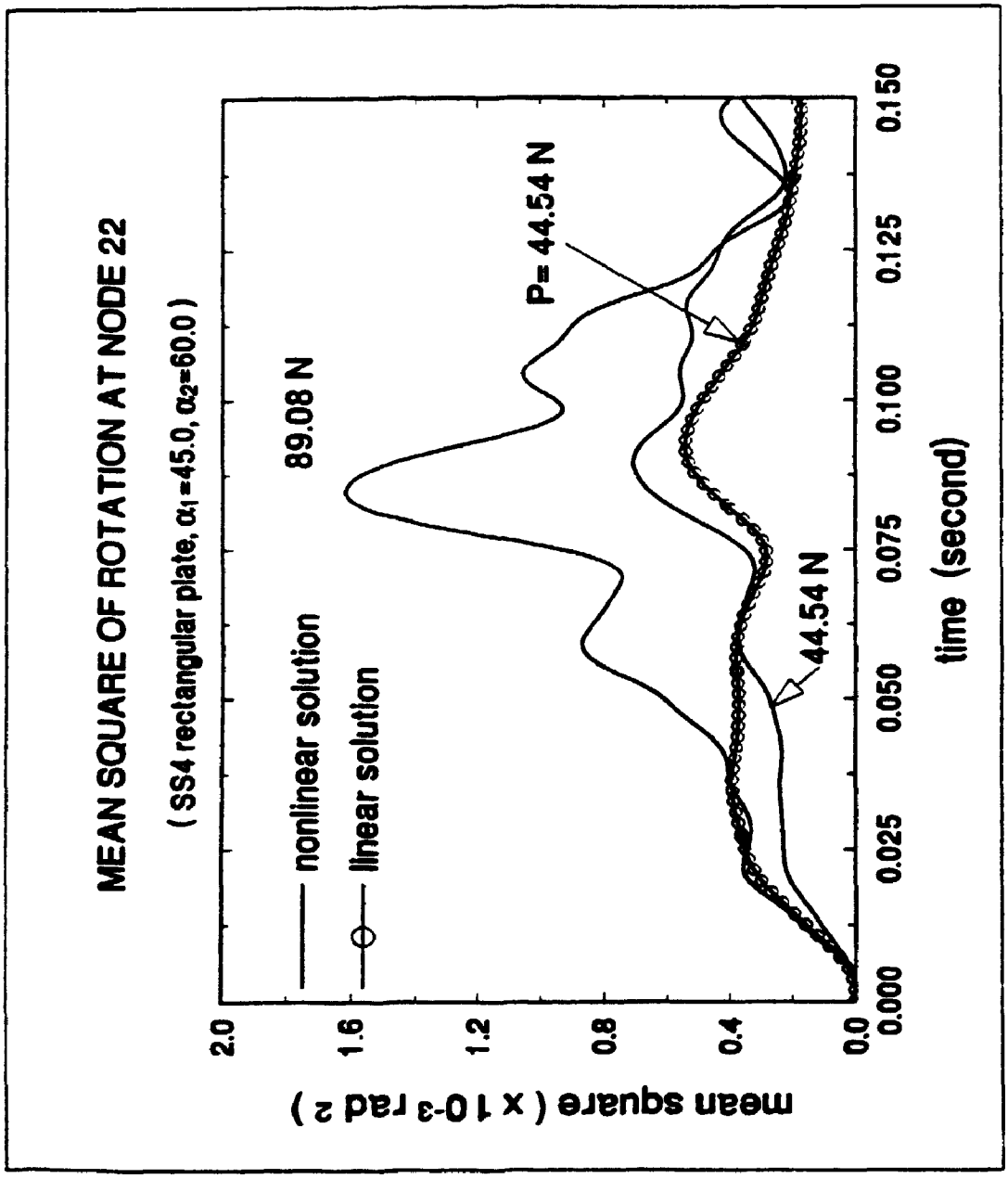

Figure 8.25 Mean square of rotation at node 22

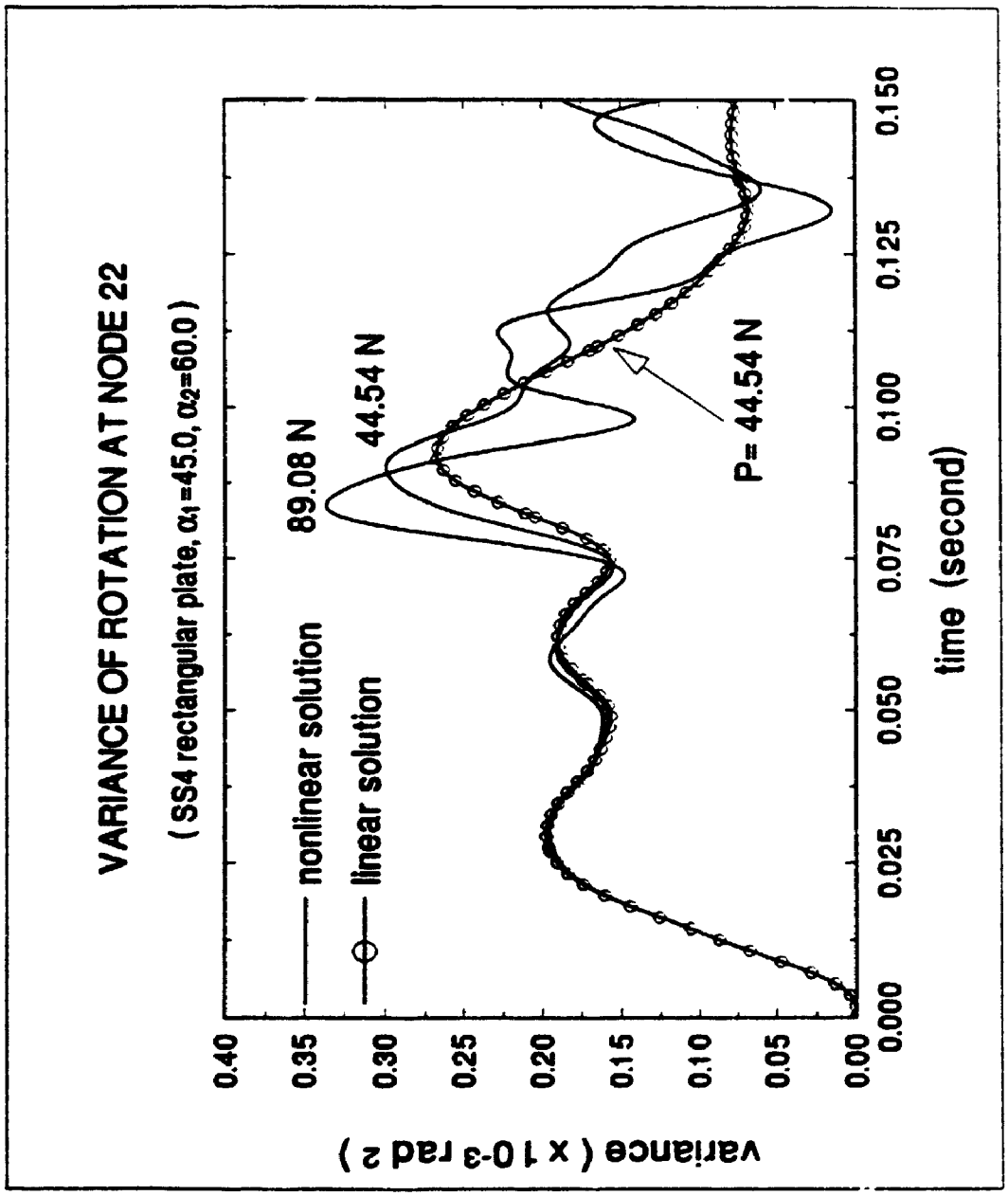

Figure 8.26 Variance of rotation at node 22

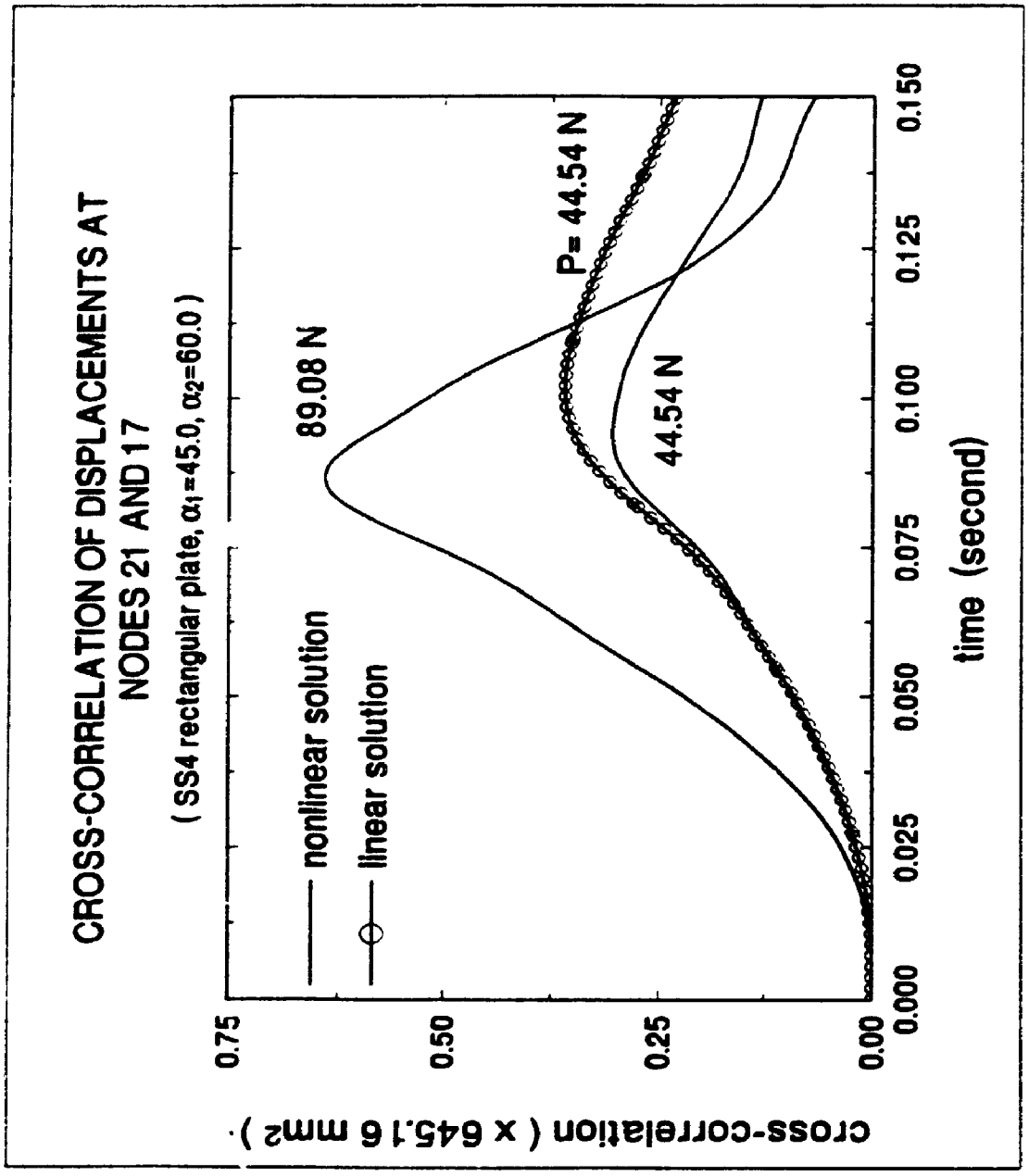

Figure 8.27 Cross-correlation of displacements at nodes 21 and 17

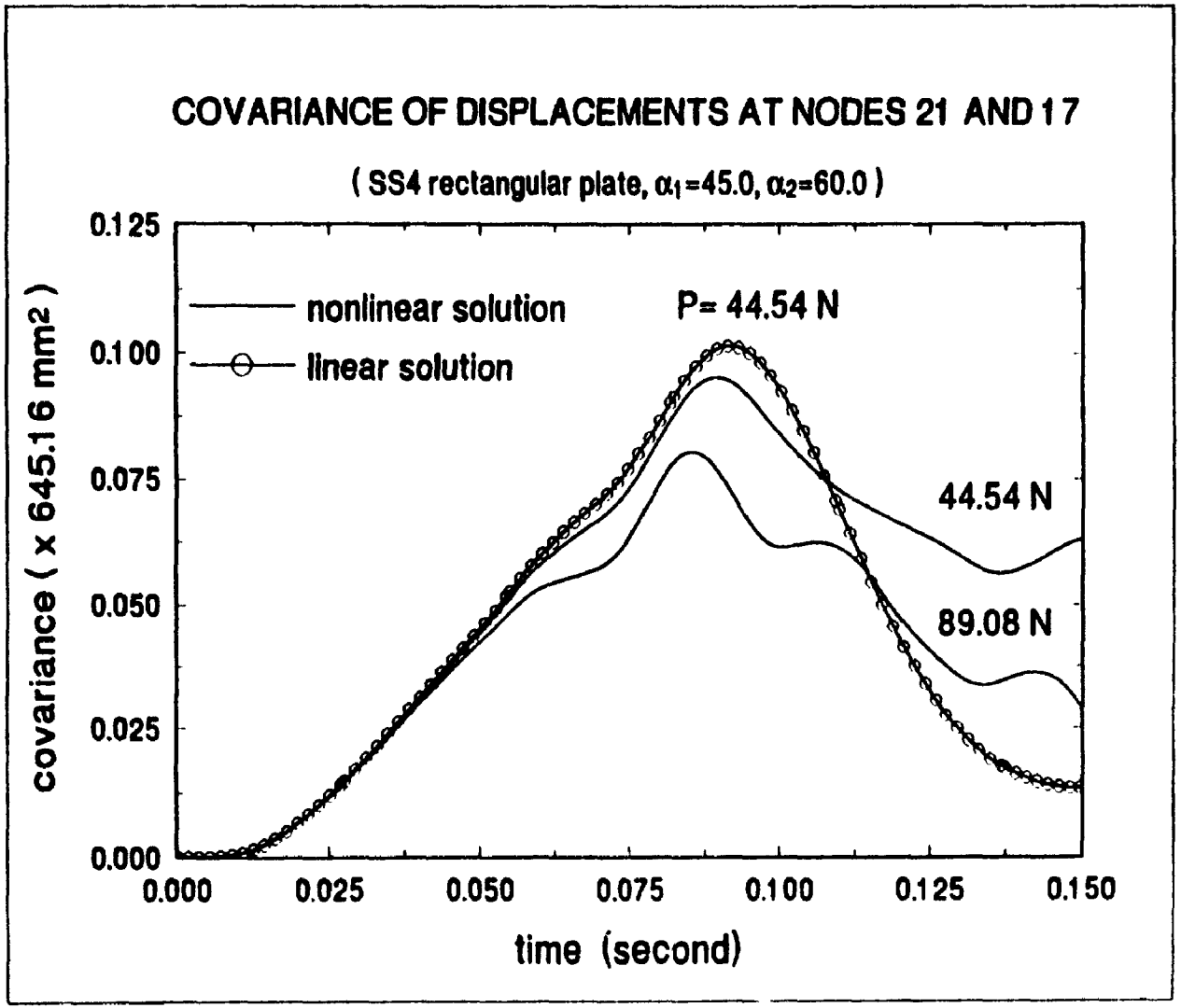

Figure 8.28 Covariance of displacements nodes 21 and 17

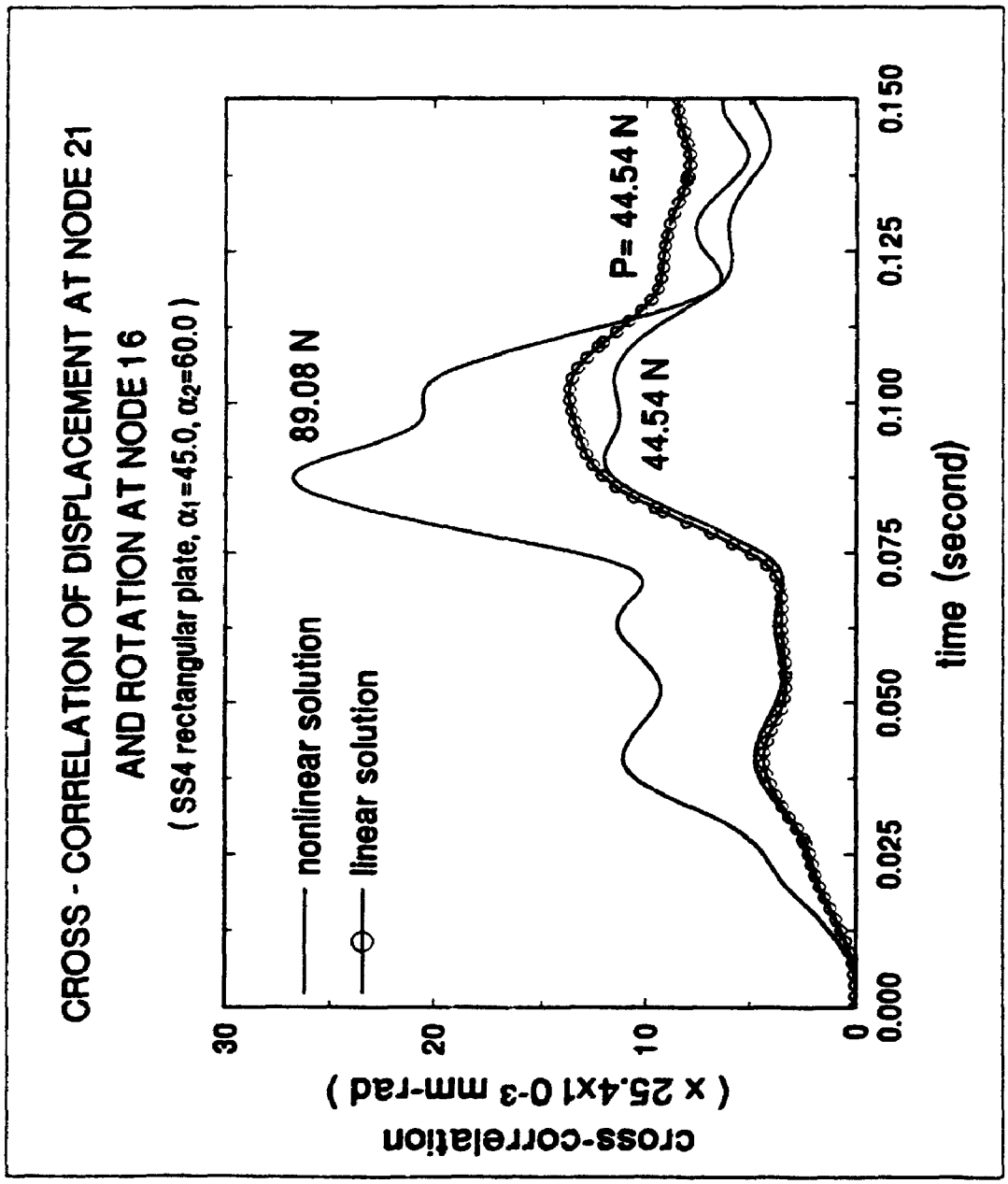

Figure 8.29 Cross-correlation of displacement at node 21 and rotation at node 16

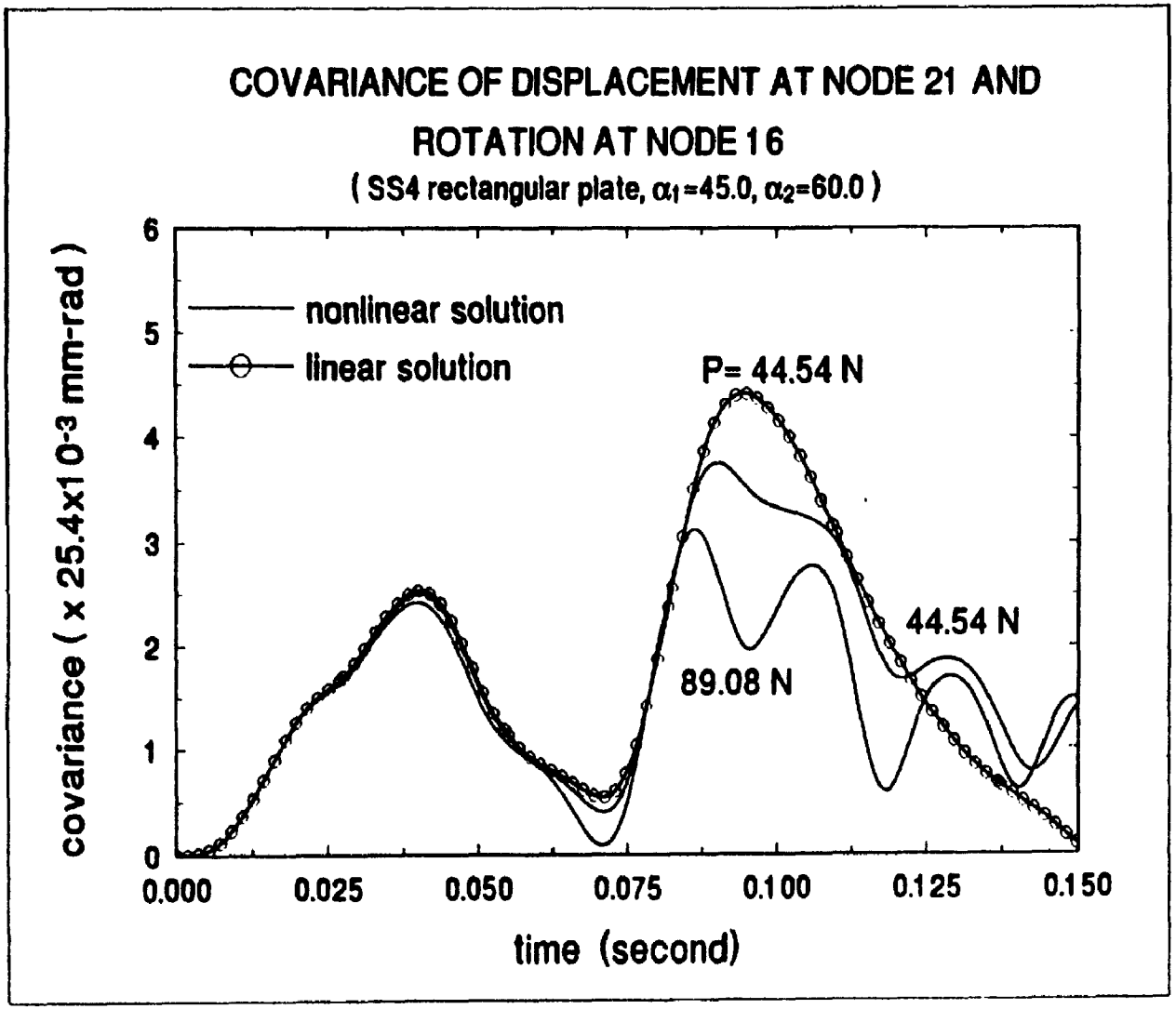

Figure 8.30 Covariance of displacement at node 21 and rotation at node 16

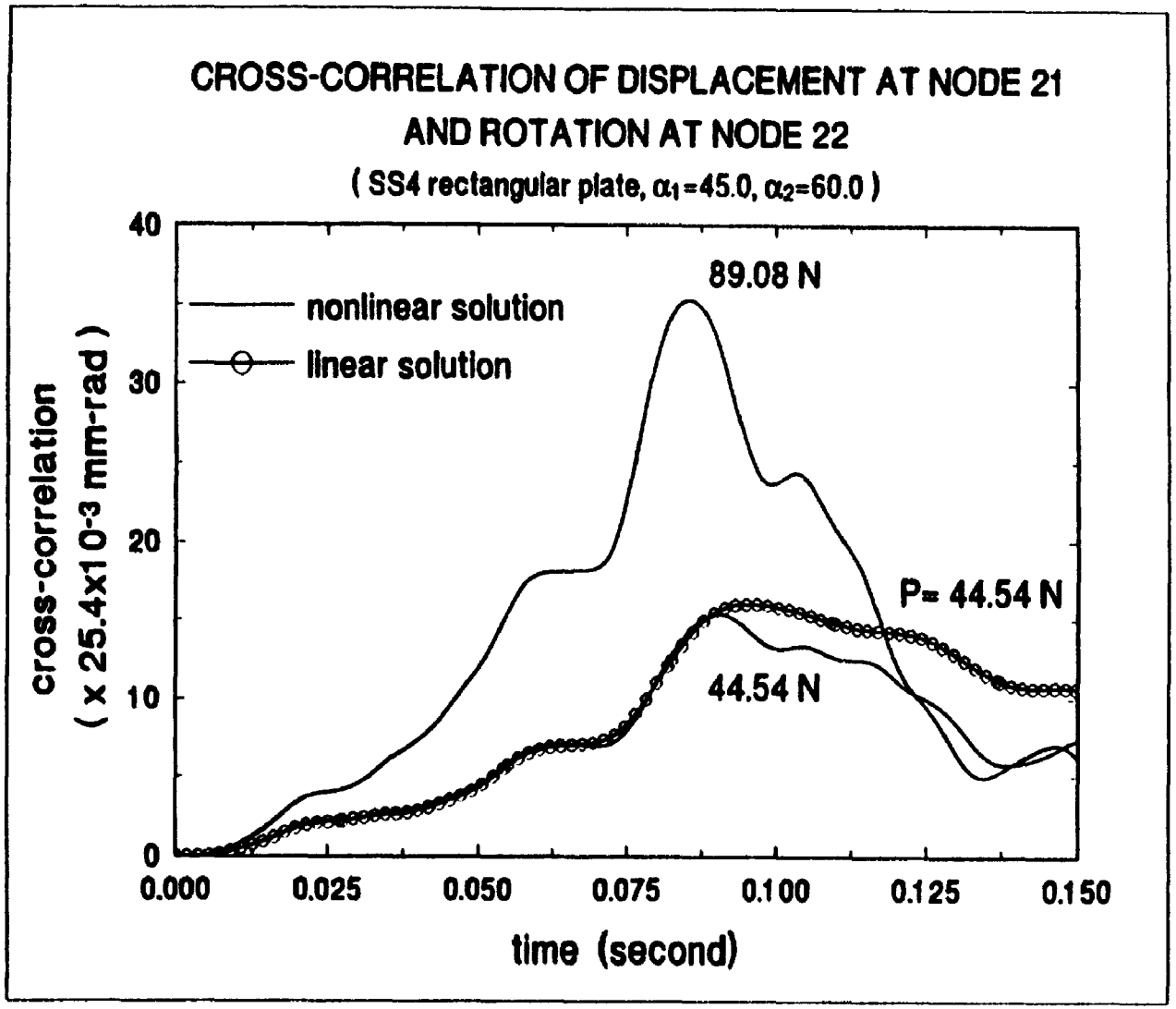

Figure 8.31 Cross-correlation of displacement at node 21 and rotation at node 22

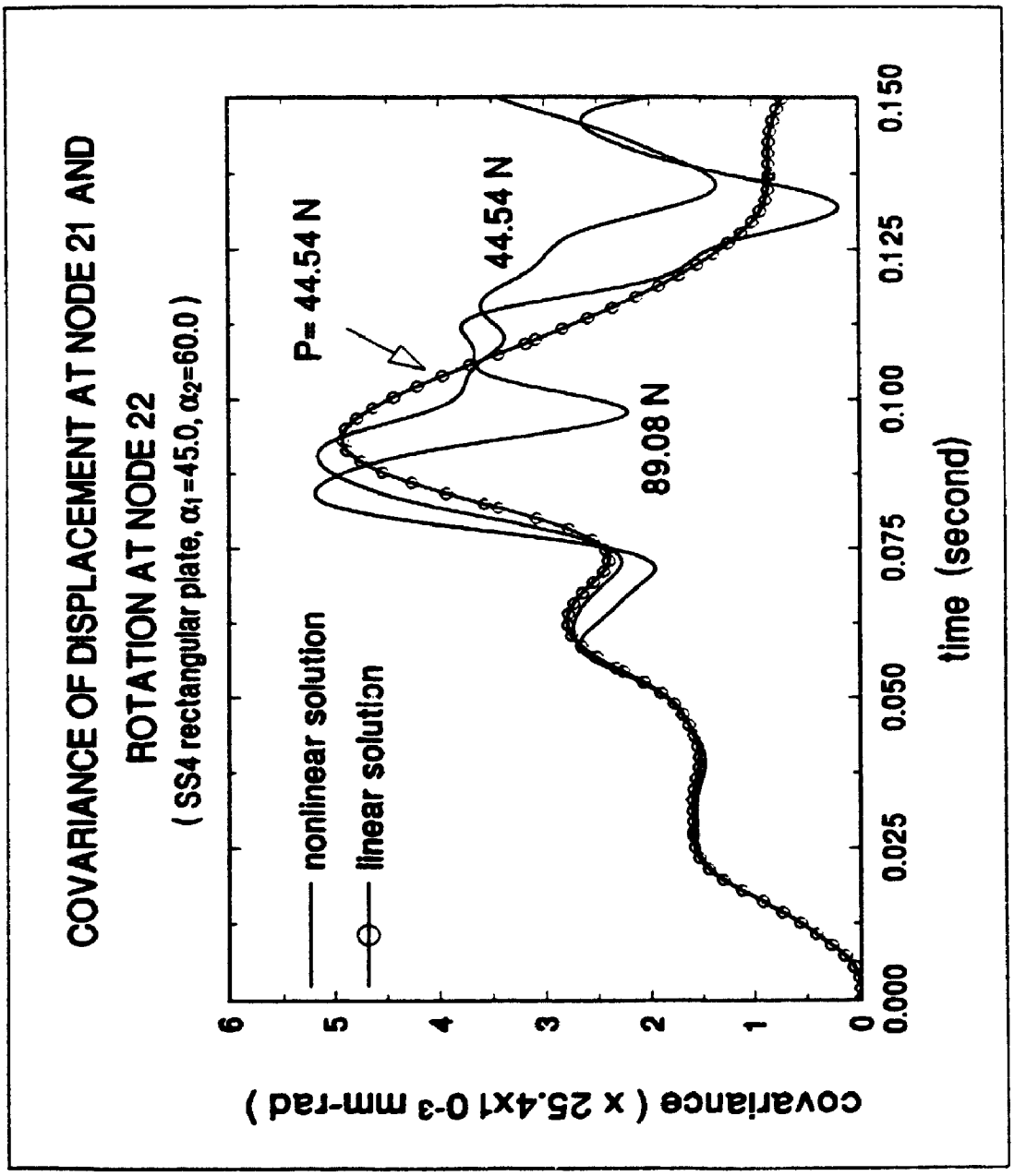

Figure 8.32 Covariance of displacement at node 21 and rotation at node 22

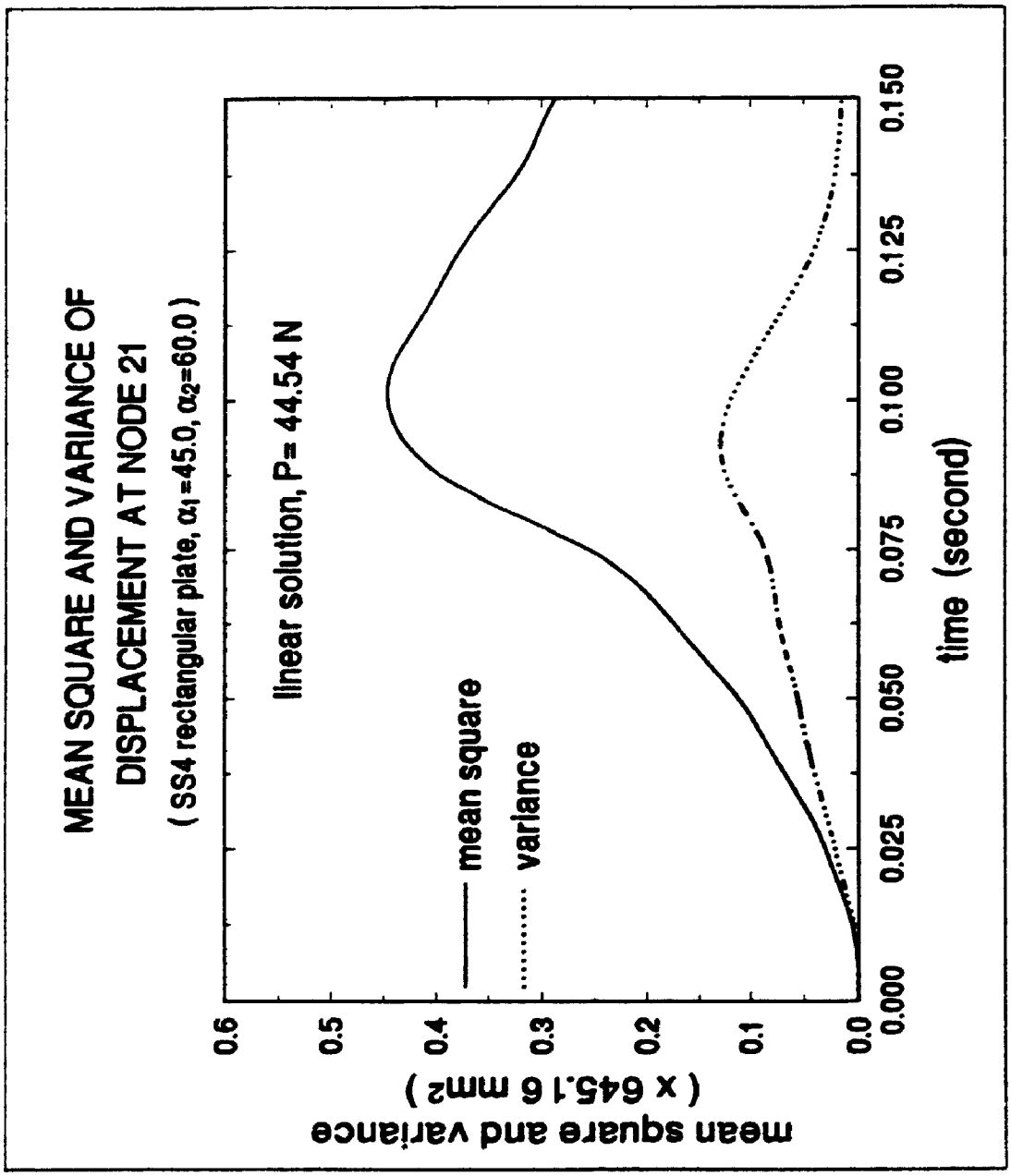

Figure 8.33 Mean square and variance of displacement at node 21

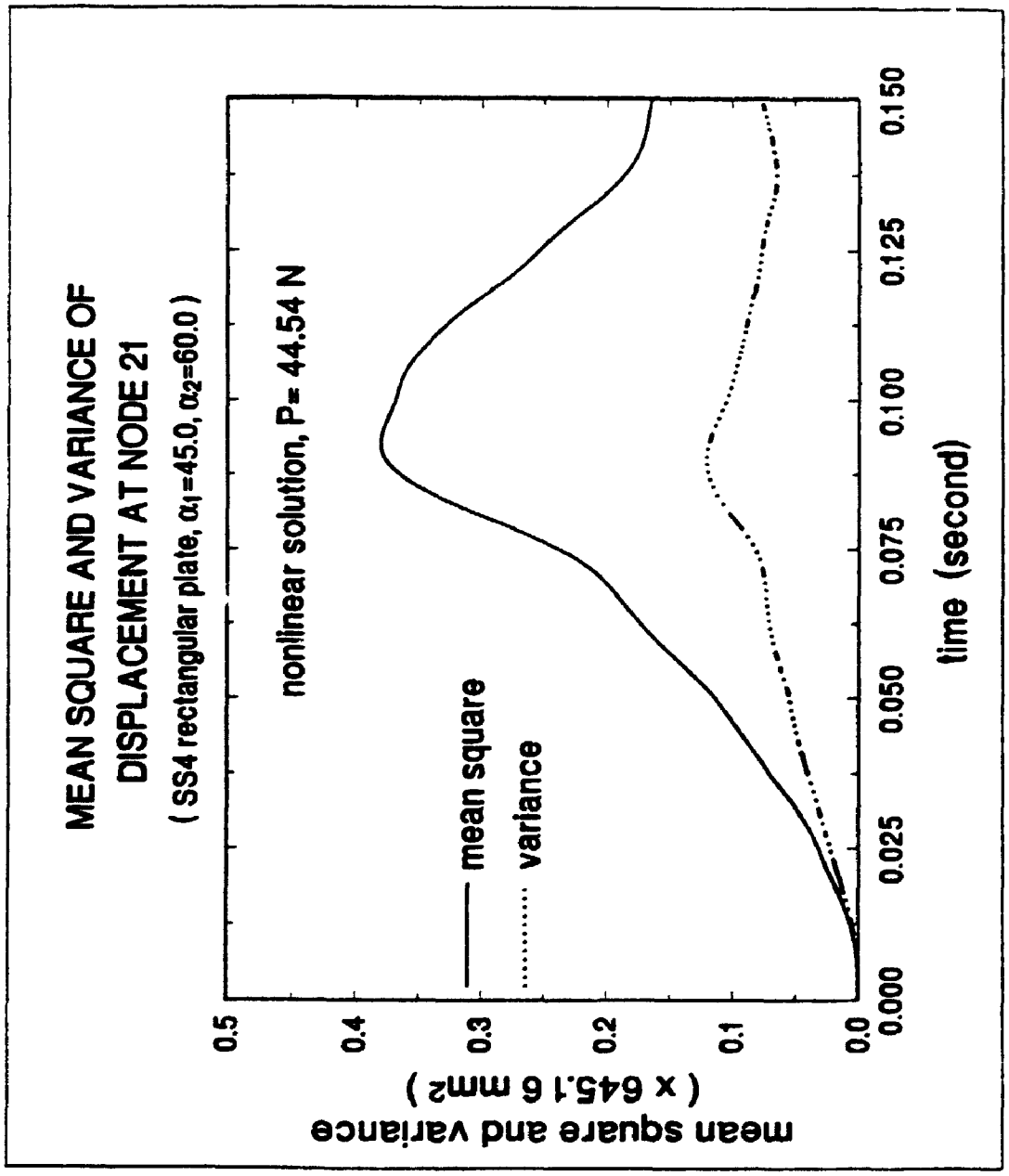

Figure 8.34 Mean square and variance of displacement at node 21

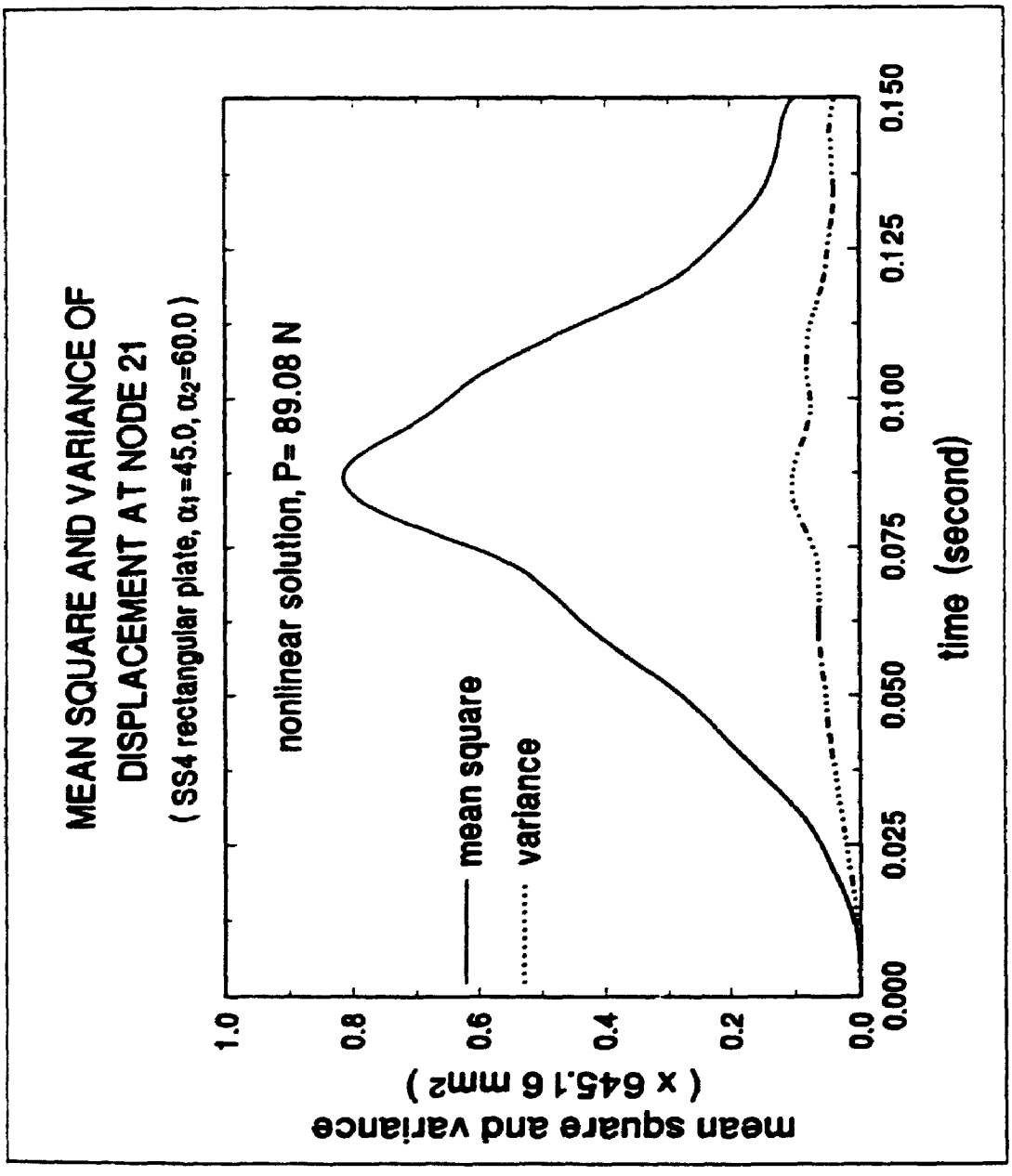

Figure 8.35 Mean square and variance of displacement at node 21

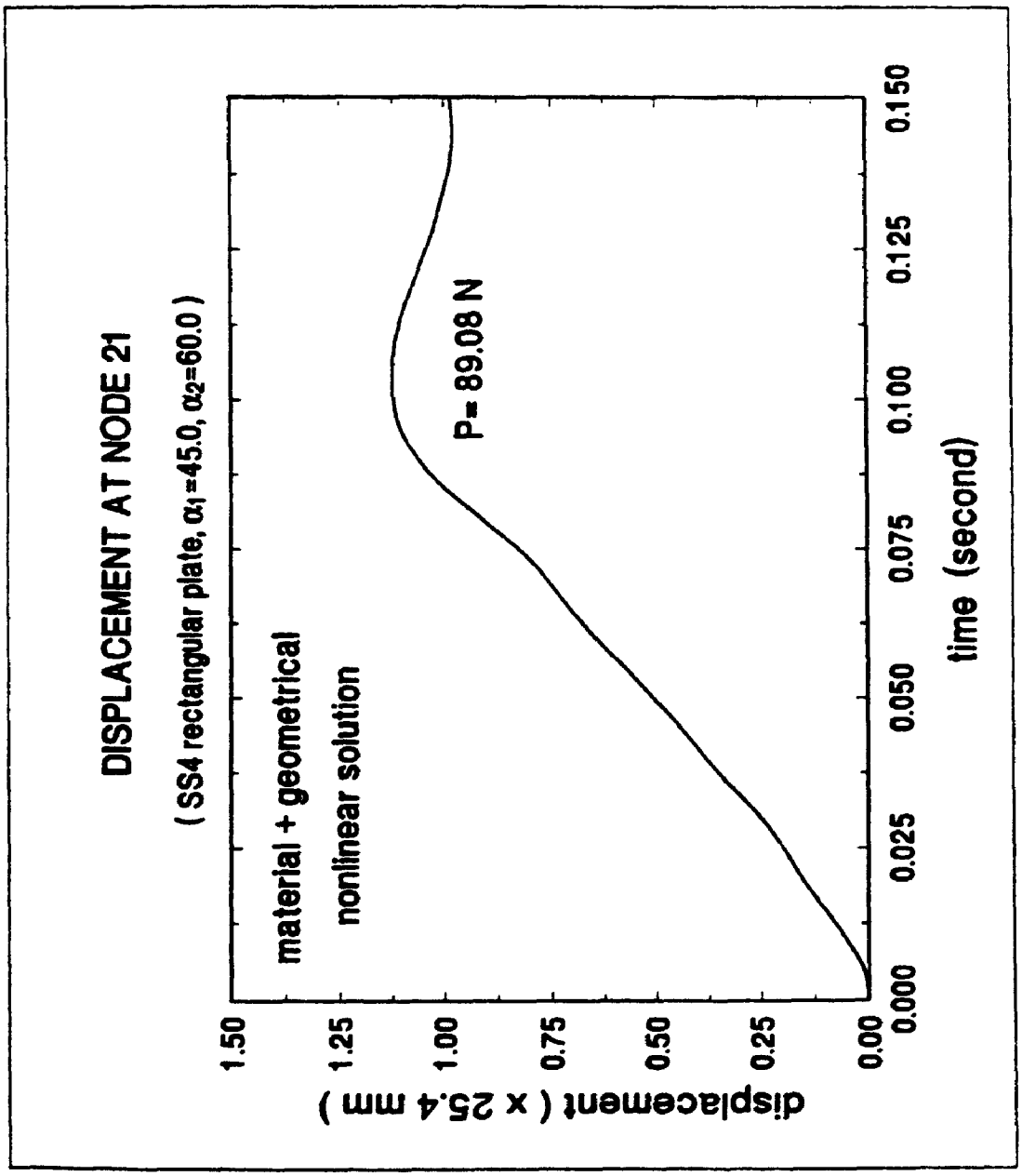

Figure 8.36 Displacement at node 21

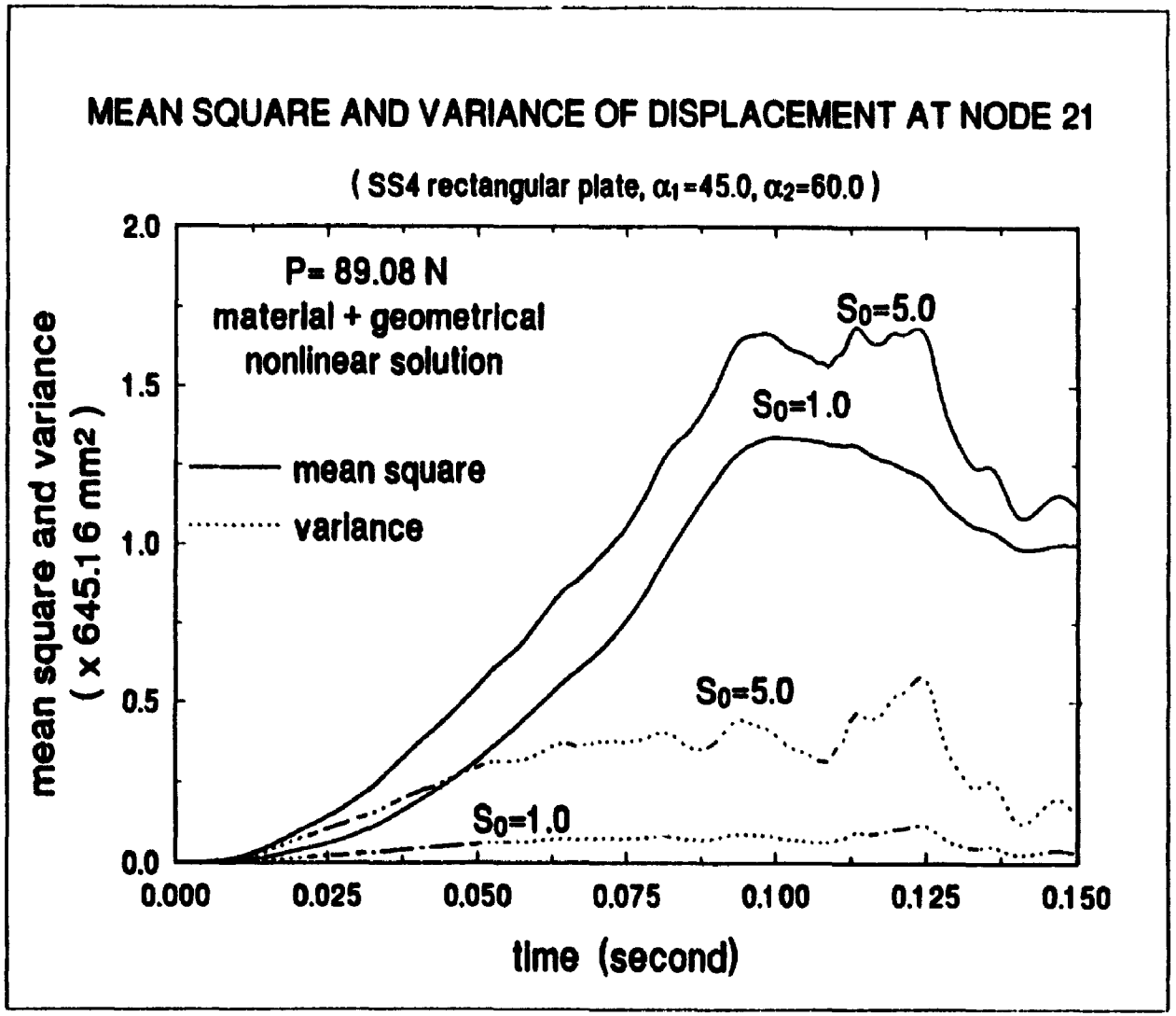

Figure 8.37 Mean square and variance of displacement at node 21

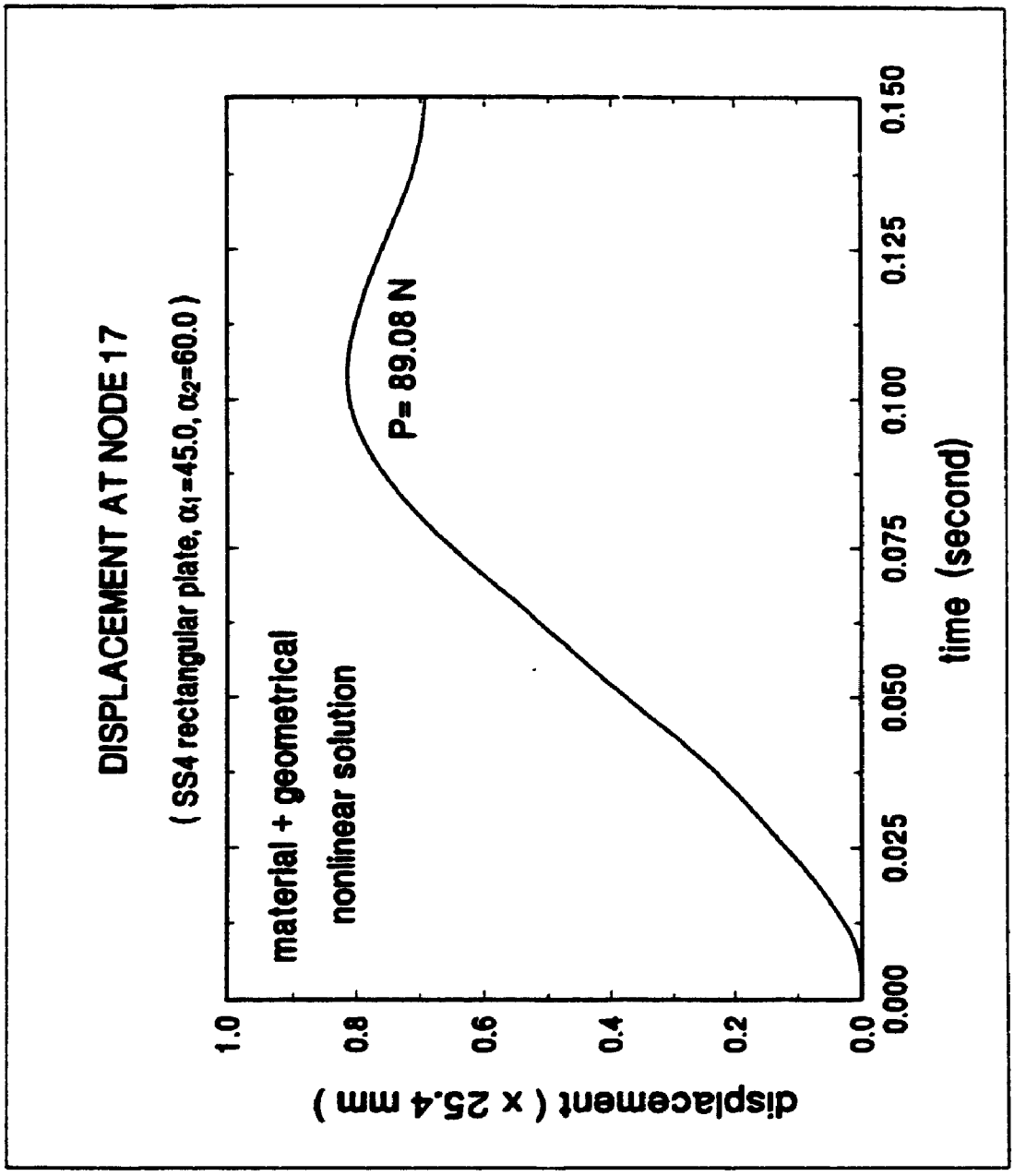

Figure 8.38 Displacement at node 17

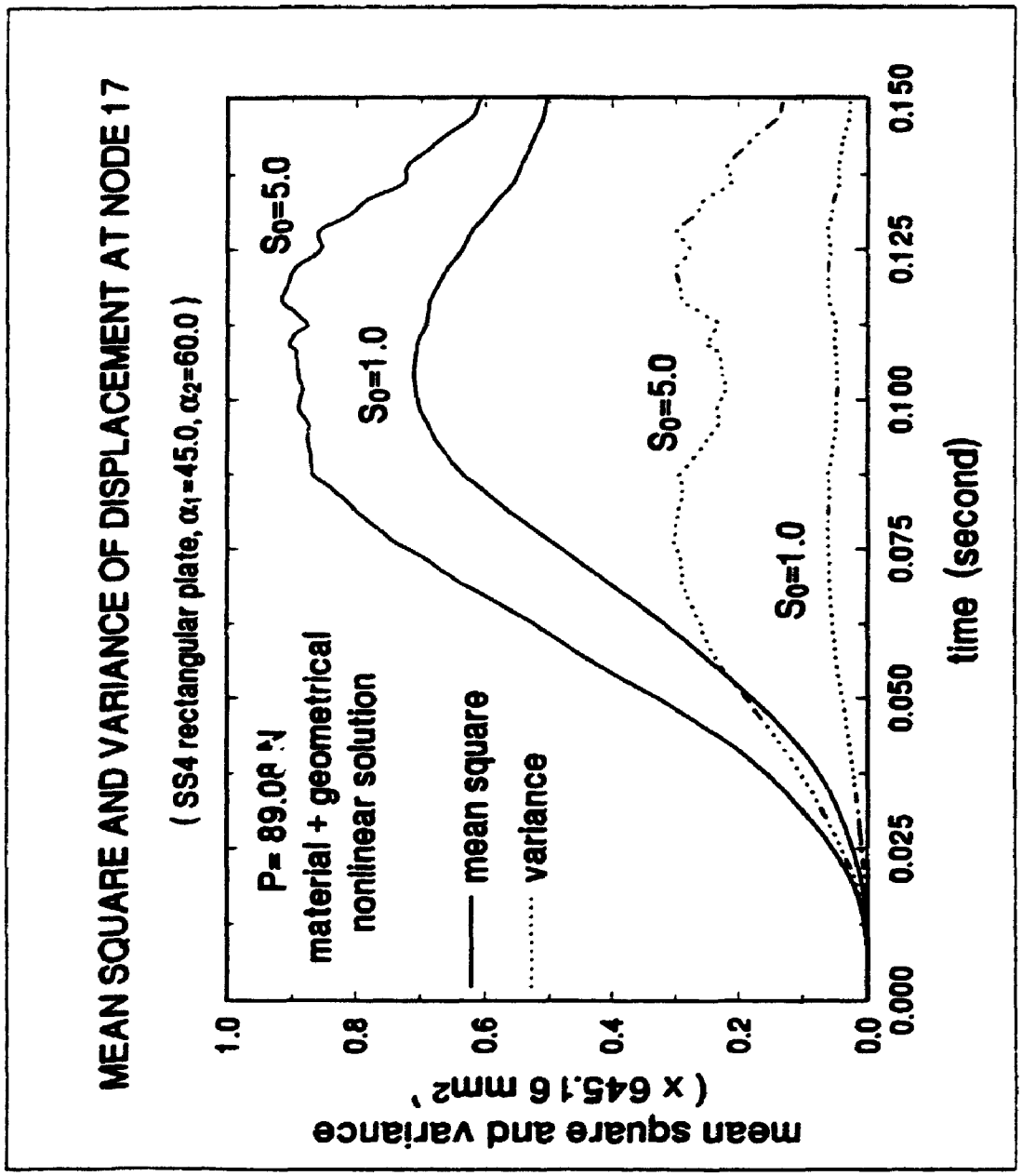

Figure 8.39 Mean square and variance of displacement at node 17

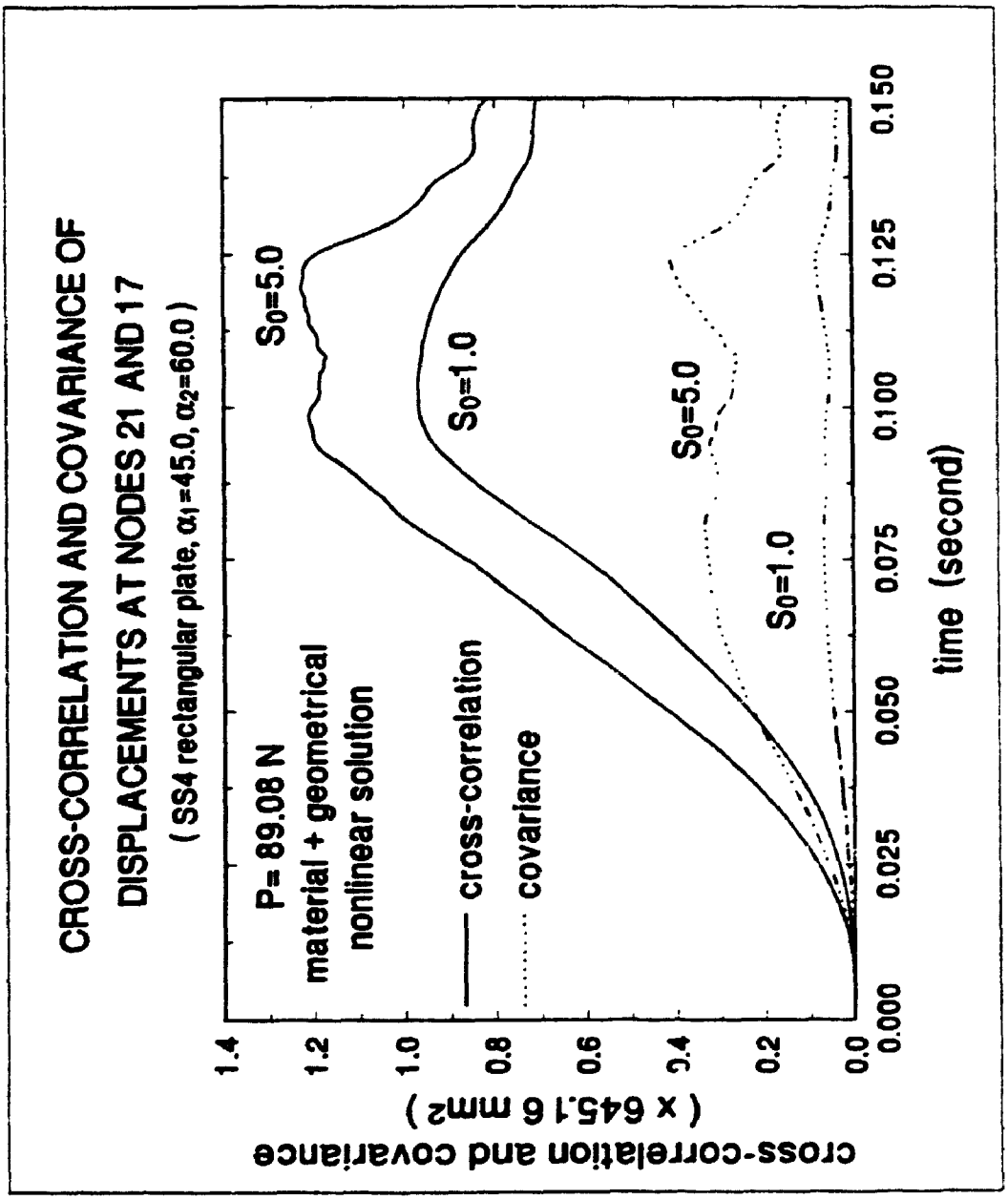

Figure 8.40 Cross-correlation and covariance of displacements at nodes 21 and 17

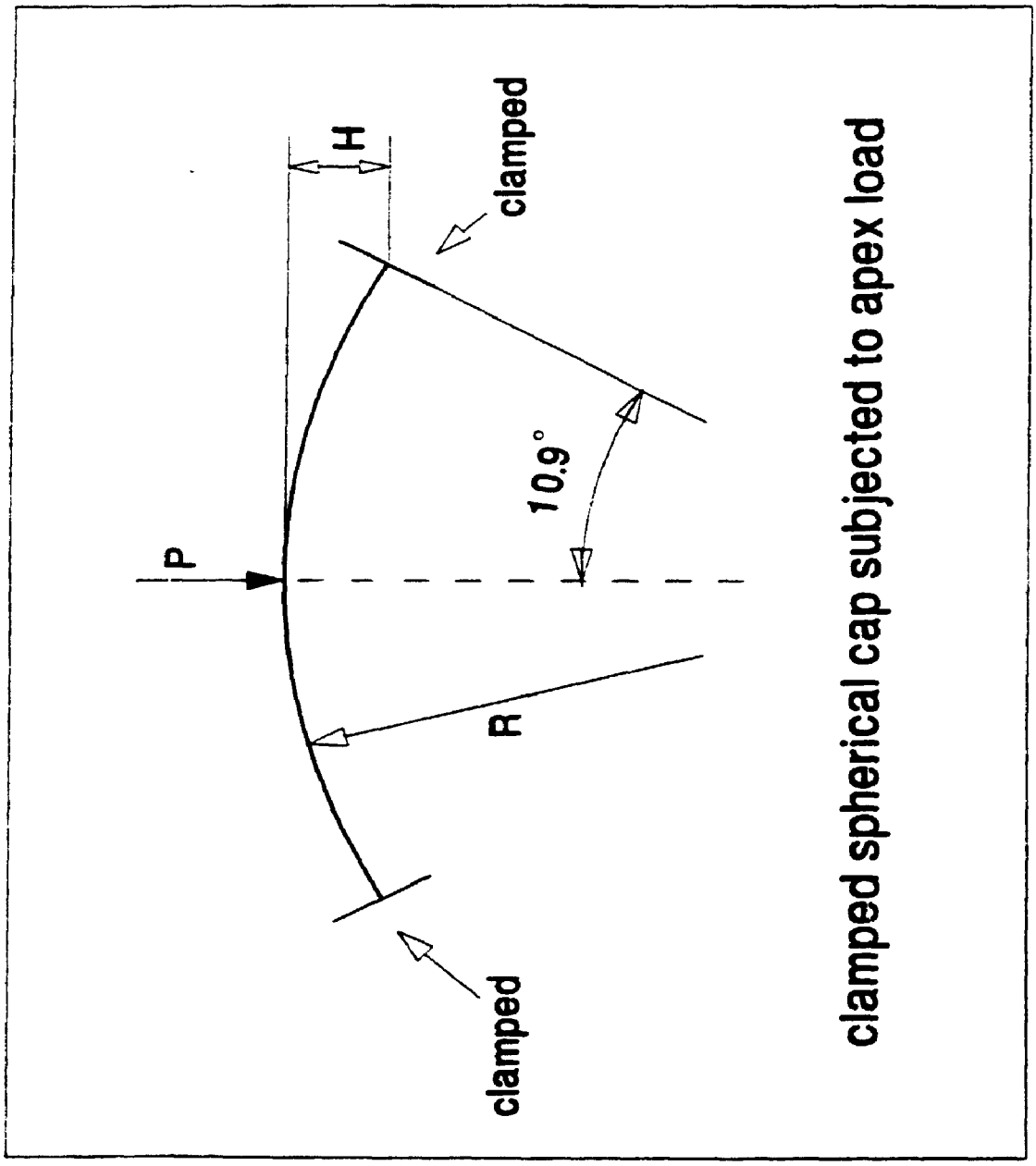

Figure 8.41 The clamped spherical cap subjected to an apex load

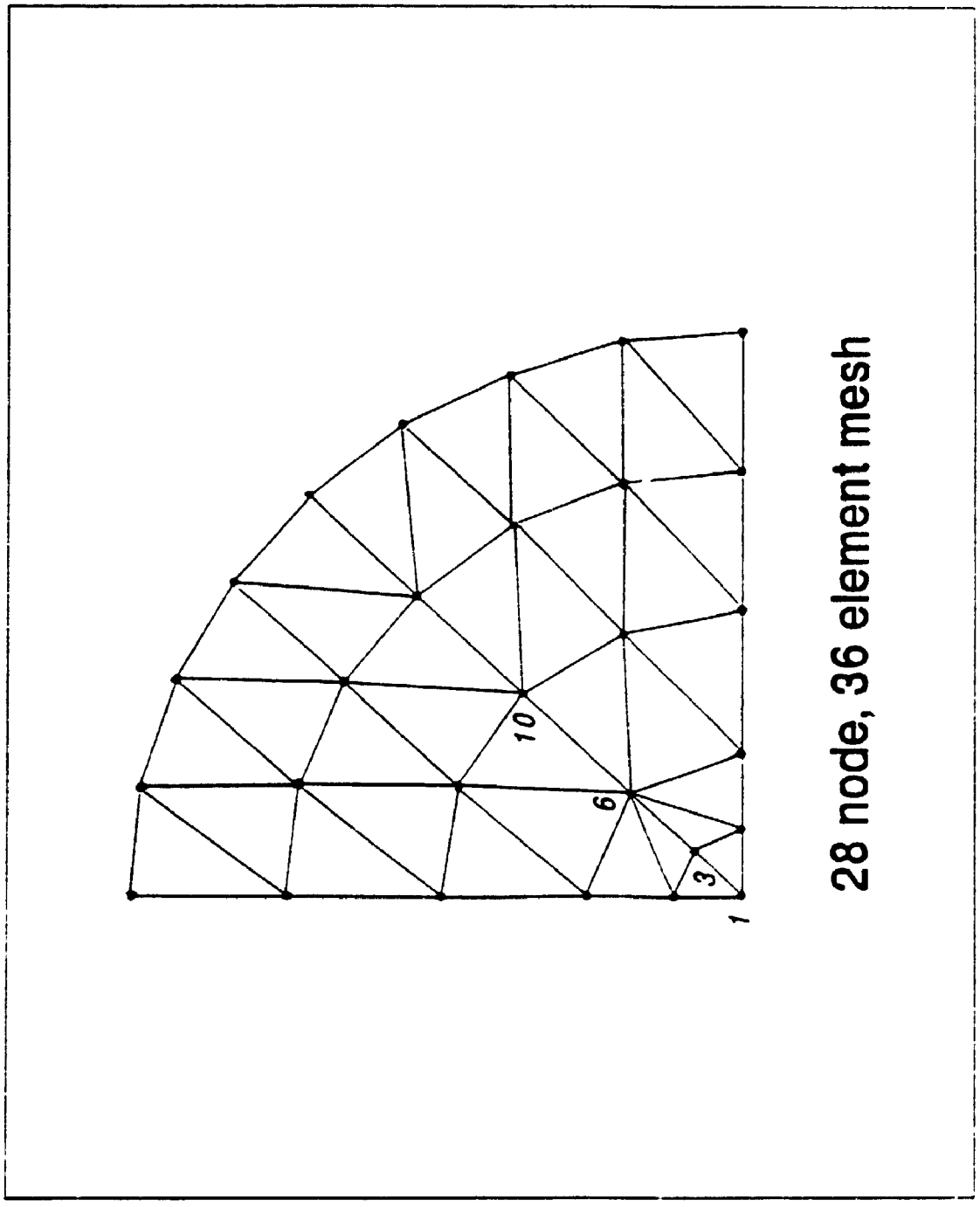

Figure 8.42 The 28 node, 36 element mesh

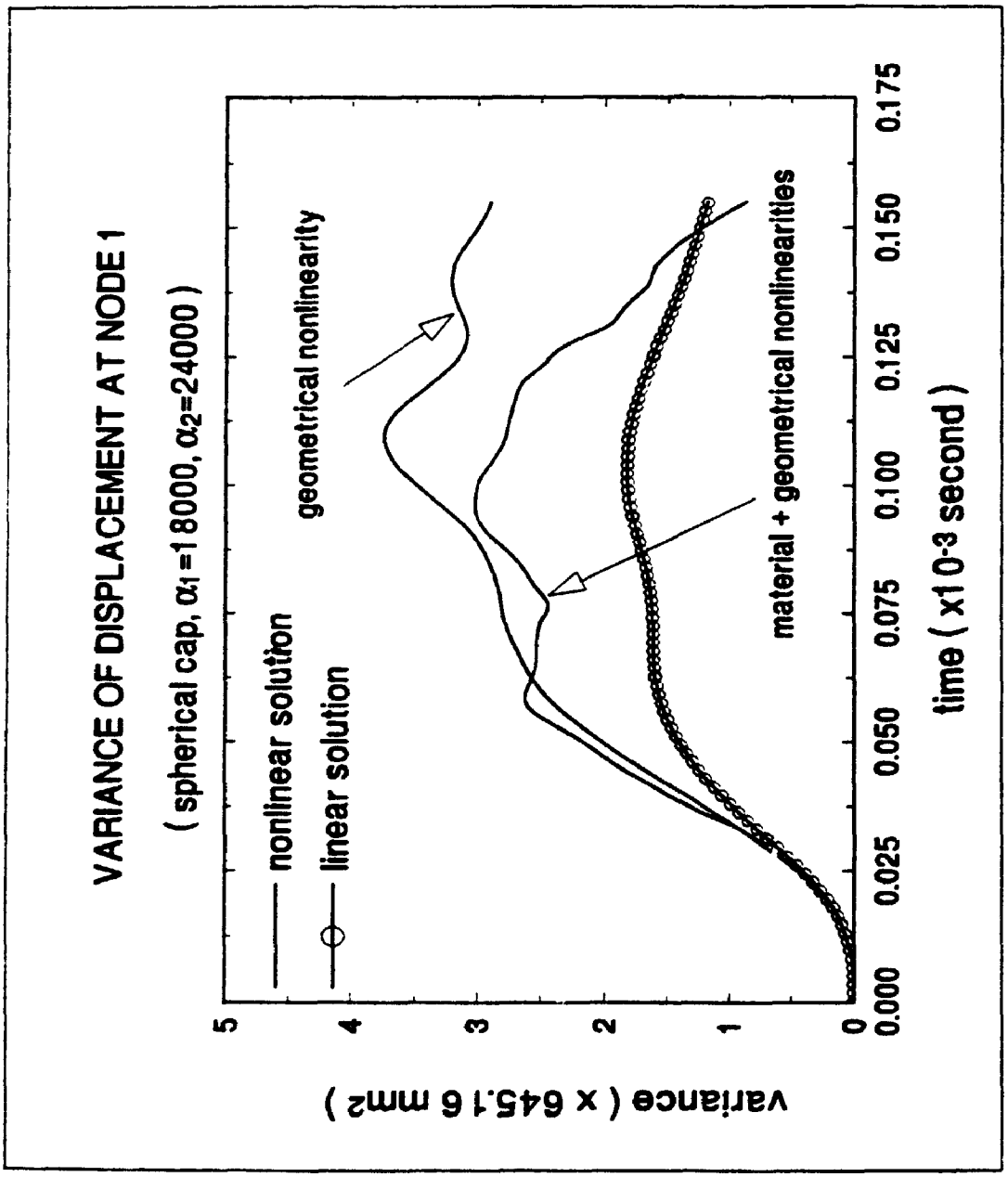

Figure 8.43 Variance of displacement at node 1

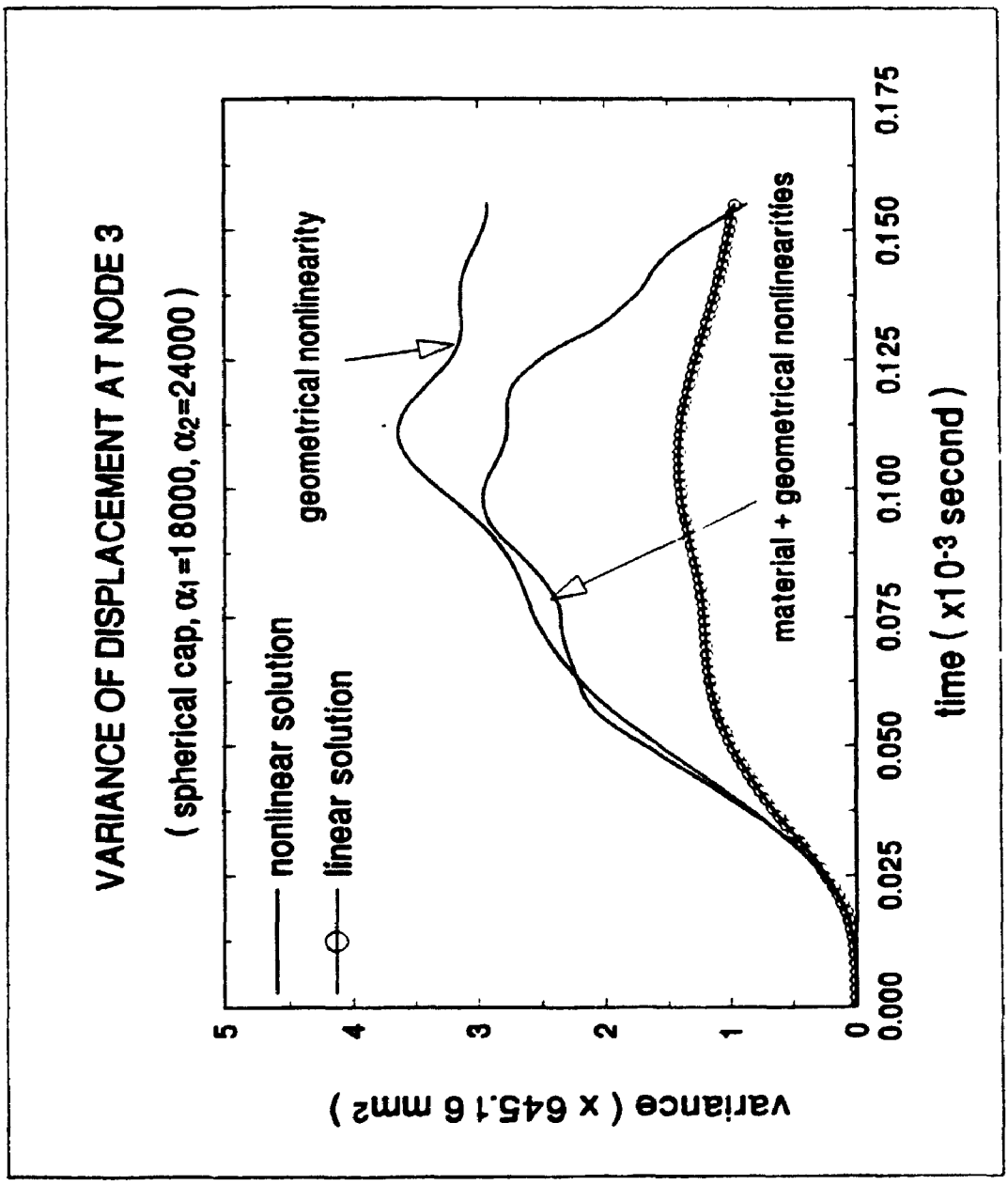

Figure 8.44 Variance of displacement at node 3

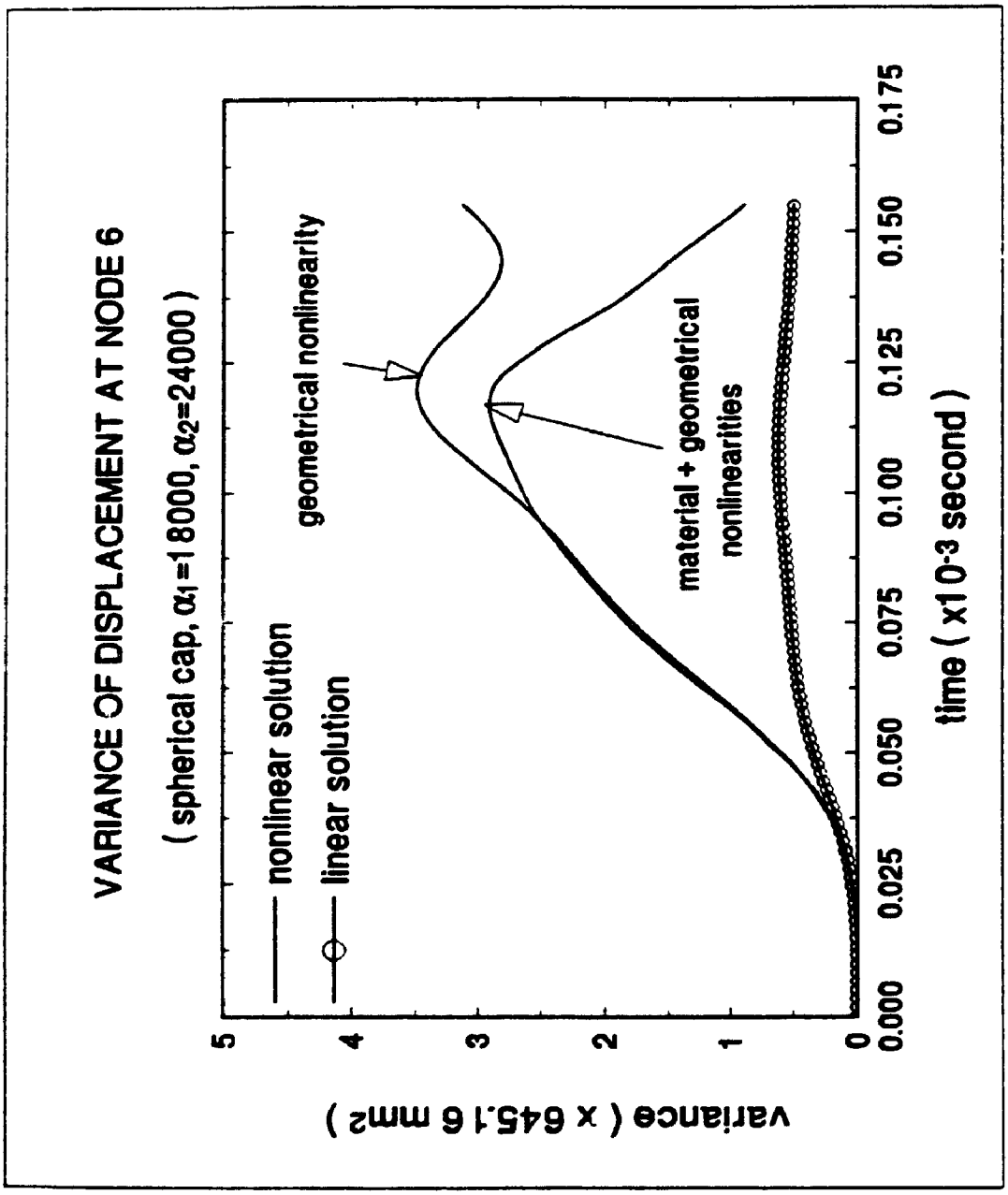

Figure 8.45 Variance of displacement at node 6

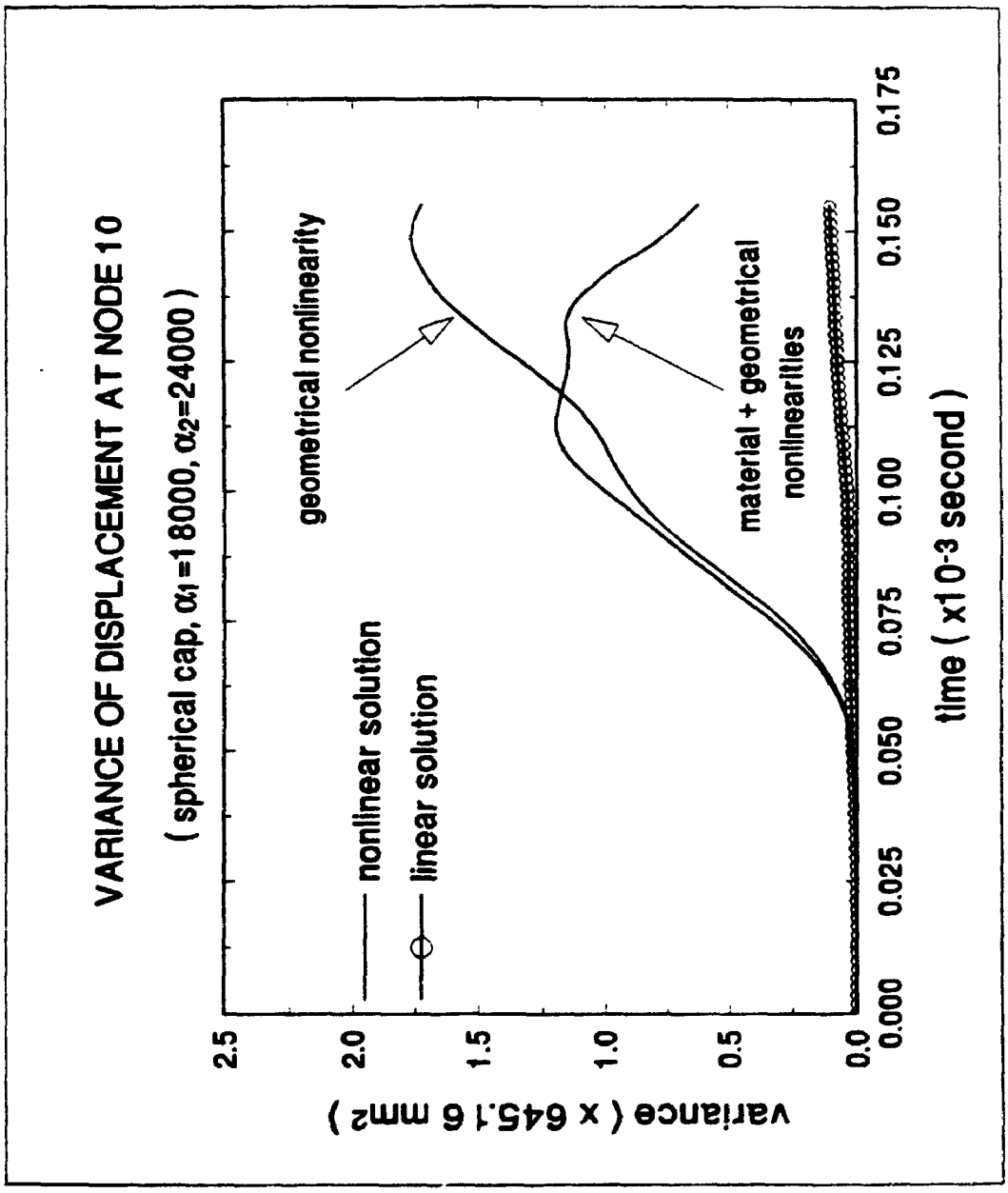

Figure 8.46 Variance of displacement at node 10

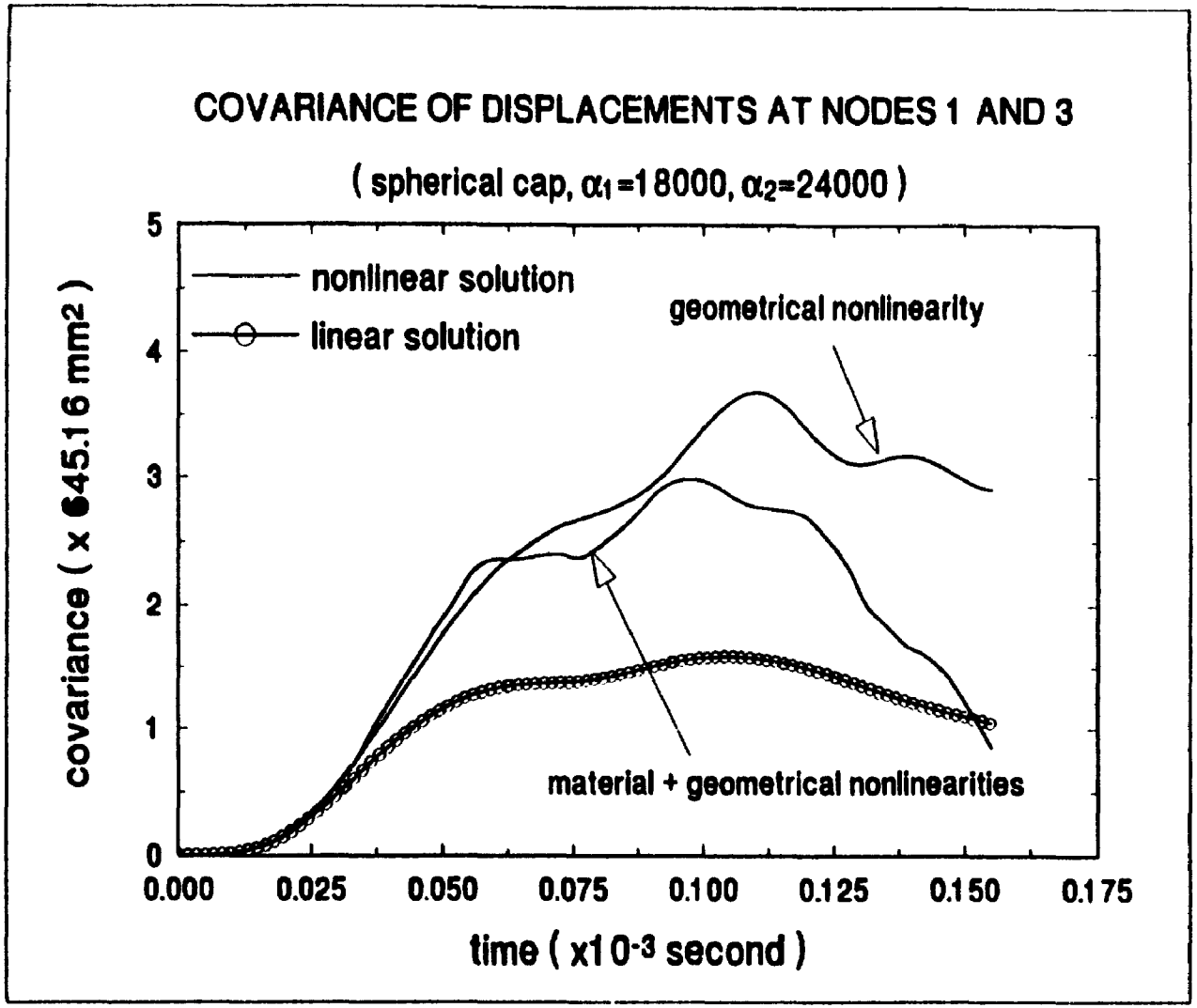

Figure 8.47 Covariance of displacements at nodes 1 and 3

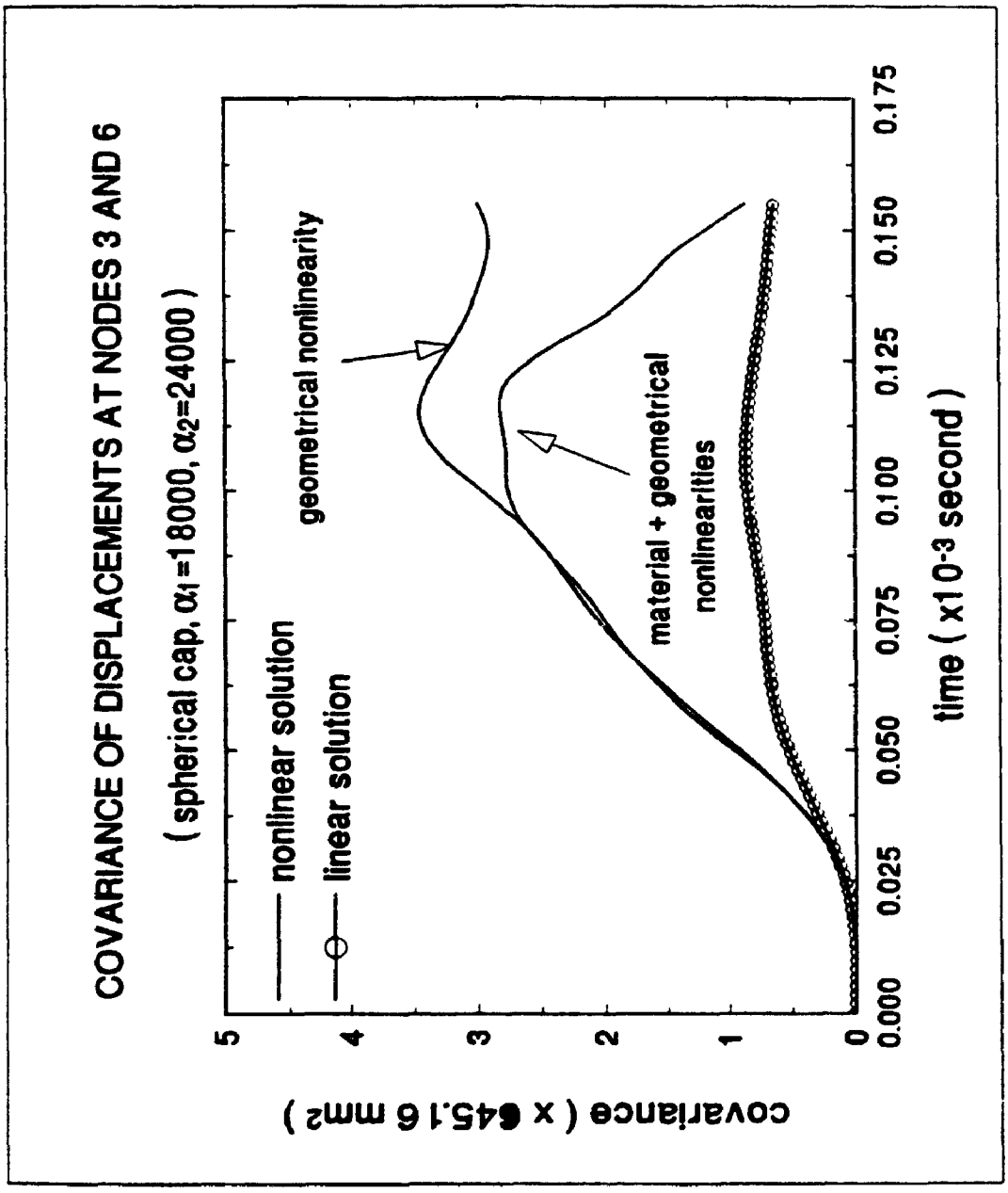

Figure 8.48 Covariance of displacements at nodes 3 and 6

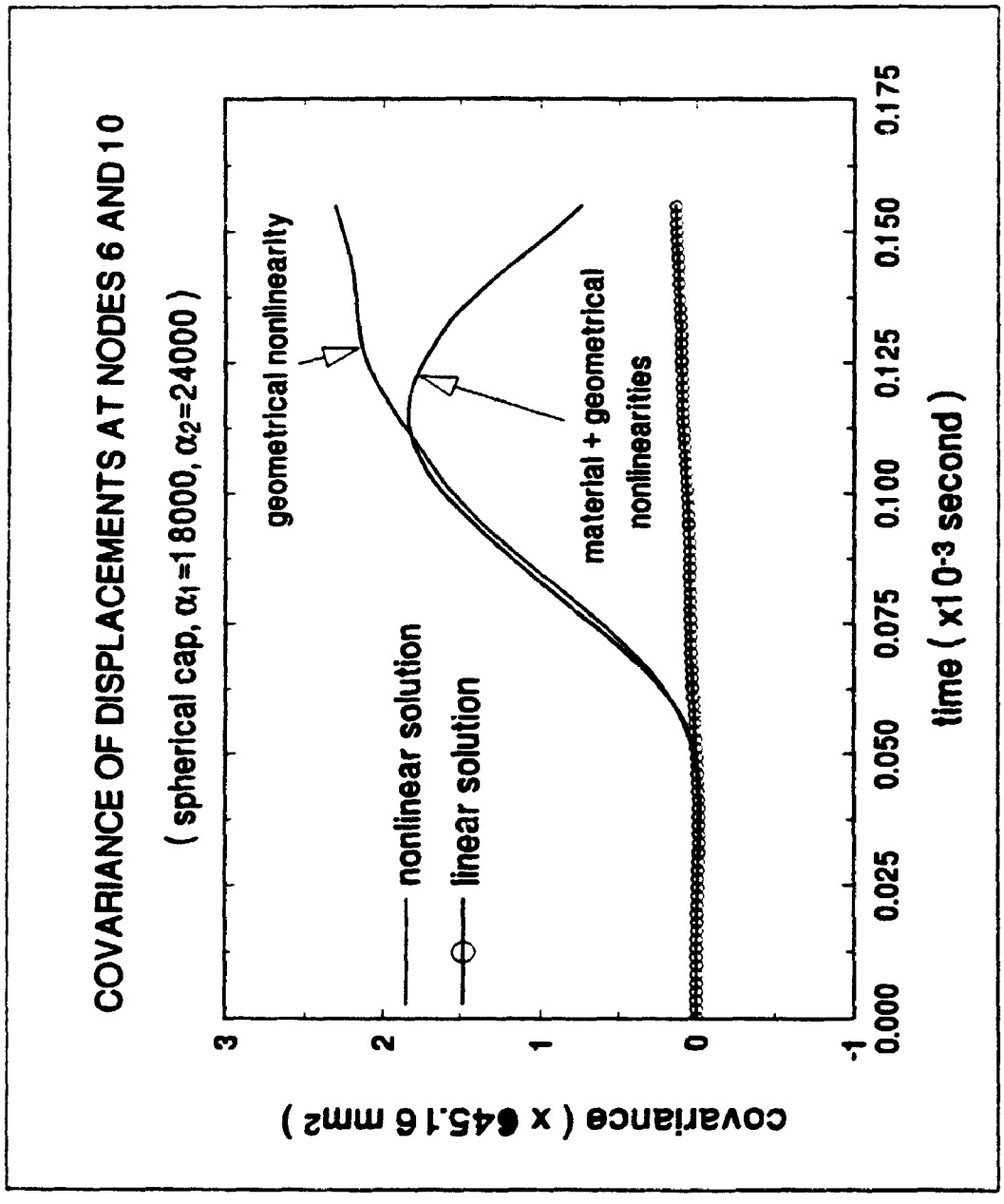

Figure 8.49 Covariance of displacements at nodes 6 and 10

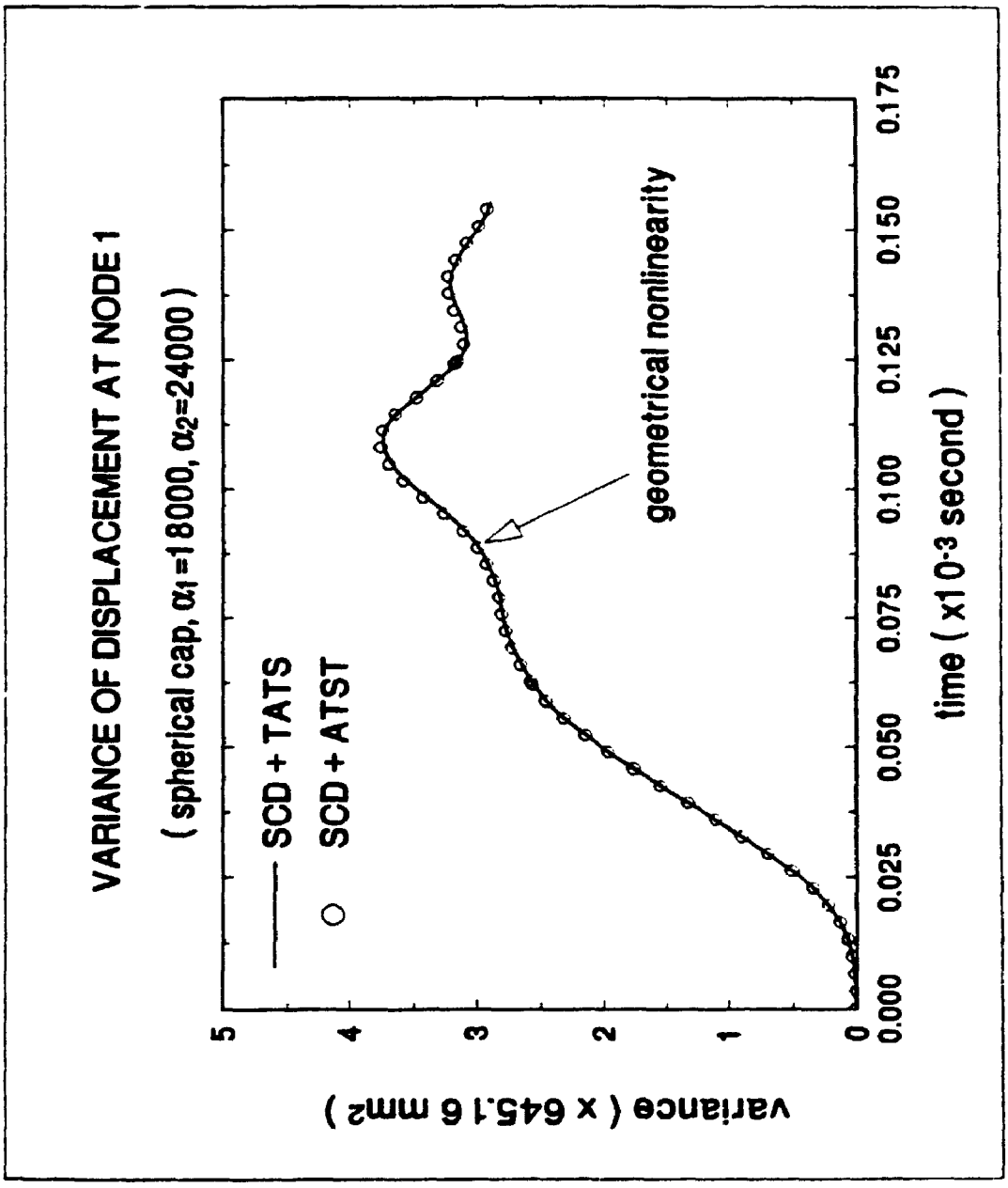

Figure 8.50 Variance of displacement at node 1

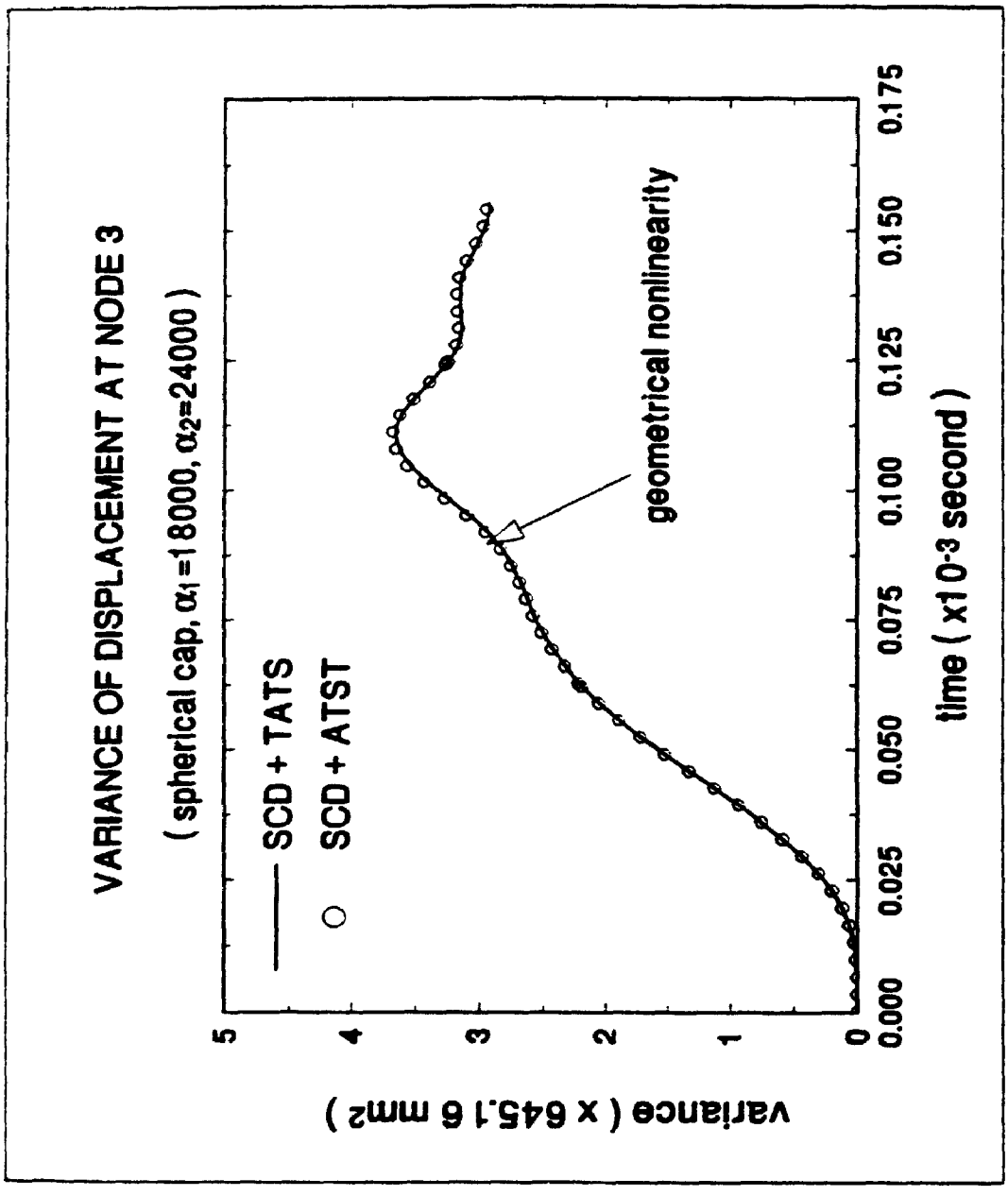

Figure 8.51 Variance of displacement at node 3

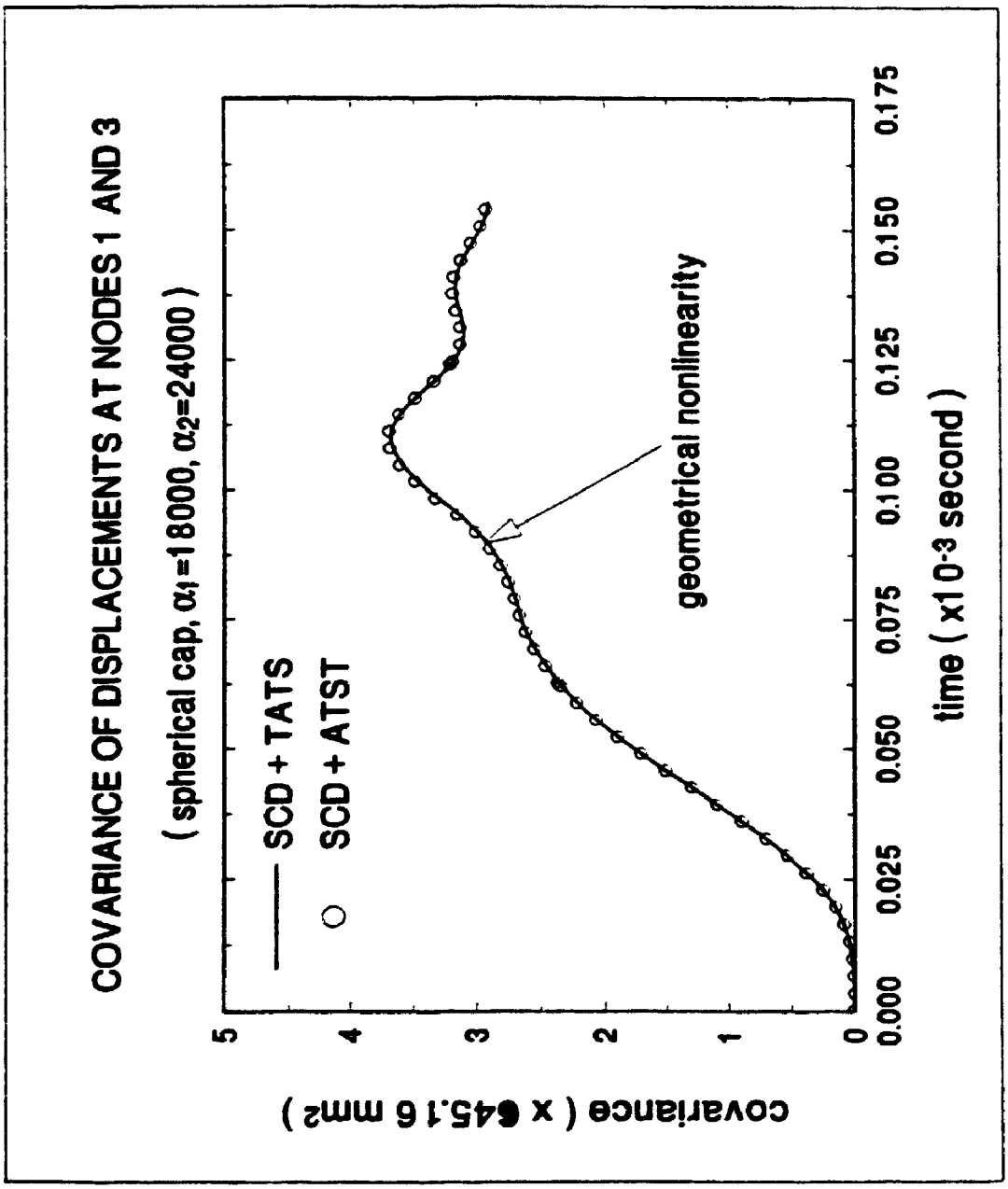

Figure 8.52 Covariance of displacements at nodes 1 and 3

APPENDIX A

MATRICES $\tilde{H}^{-1}$ AND G_e

A.1 Matrix $\tilde{H}^{-1}$

The elements of matrix $\tilde{H}^{-1}$ are, from MAPLE 4.2 output file,

$$\left[-\frac{1}{h\,A\,Ep\,(v^2-1)},\ \frac{v}{h\,A\,Ep\,(v^2-1)},\ 0,\ 0,\ 0,\ 0,\ 0,\ 0,\ 0,\ 0\right]$$

$$\left[\frac{v}{h\,A\,Ep\,(v^2-1)},\ -\frac{1}{h\,A\,Ep\,(v^2-1)},\ 0,\ 0,\ 0,\ 0,\ 0,\ 0,\ 0,\ 0\right]$$

$$\left[0,\ 0,\ \frac{1}{h\,A\,G},\ 0,\ 0,\ 0,\ 0,\ 0,\ 0,\ 0\right]$$

$$\left[0,\ 0,\ 0,\ -12\,\frac{1}{h^3\,A\,Ep\,(v^2-1)},\ 12\,\frac{v}{h^3\,A\,Ep\,(v^2-1)},\ 0,\ 0,\ 0,\ 0,\ 0\right]$$

$$\left[0,\ 0,\ 0,\ 12\,\frac{v}{h^3\,A\,Ep\,(v^2-1)},\ -12\,\frac{1}{h^3\,A\,Ep\,(v^2-1)},\ 0,\ 0,\ 0,\ 0,\ 0\right]$$

$$\left[0,\ 0,\ 0,\ 0,\ 0,\ 12\ \frac{1}{h^3\ A\ G},\ 0,\ 0,\ 0,\ 0\right]$$

$$\left[0,\ 0,\ 0,\ 0,\ 0,\ 0,\ 3\ \frac{1}{h\ A\ ks\ G\ (s3^2 + r3^2)},\ 0,\ 0,\ 0\right]$$

$$\left[0,\ 0,\ 0,\ 0,\ 0,\ 0,\ 0,\ 3\ \frac{1}{h\ A\ ks\ G\ (s3^2 + r3^2 - 2\ r3\ r2 + r2^2)},\ 0,\ 0\right]$$

$$\left[0,\ 0,\ 0,\ 0,\ 0,\ 0,\ 0,\ 0,\ 3\ \frac{1}{h\ A\ ks\ G\ r2^2},\ 0\right]$$

$$\left[0,\ 0,\ 0,\ 0,\ 0,\ 0,\ 0,\ 0,\ 0,\ \frac{1}{h\ A\ G}\right]$$

where Ep = E / (1-v^2). E, G, v, ks, A, h are Young's modulus, shear modulus, Poisson's ratio, form factor of shear, area of an element and thickness of the shell, respectively. And r2 = r_2, r3 = r_3 and s3 = s_3.

A.2 Matrices $(G_e)_m$ and $(G_e)'_m$

The non-zero elements of matrix $(G_e)'_m$ are, with [i,j] denoting the element located at i-th row and j-th column, (those of $(G_e)_m$ are obtained by setting b12, a23, b23, a31 and b31 to zero)

[1,1]

$$-\frac{A\ Ep\ h}{r2}$$

[1,2]

$$-\frac{A\ v\ Ep\ (r2 - r3)\ h}{r2\ s3}$$

[1,6]

$$-1/3\ \frac{A\ Ep\ h\ (-\ v\ r2\ b12 + s3\ a31 - v\ r3\ b31)}{r2\ s3}$$

[1,7]

$$\frac{A\ Ep\ h}{r2}$$

[1,8]

$$-\frac{A\ v\ Ep\ r3\ h}{r2\ s3}$$

[1,12]

$$-1/3\ \frac{A\ Ep\ h\ (v\ r2\ b12 + v\ r2\ b23 + s3\ a23 - v\ r3\ b23)}{r2\ s3}$$

[1,14]

$$\frac{A\ v\ Ep\ h}{s3}$$

[1,18]

$$1/3\ \frac{A\ Ep\ h\ (v\ r2\ b23 + s3\ a31 + s3\ a23 - v\ r3\ b31 - v\ r3\ b23)}{r2\ s3}$$

[2,1]

$$-\frac{A\ v\ Ep\ h}{r2}$$

[2,2]

$$-\frac{A\ Ep\ (r2 - r3)\ h}{r2\ s3}$$

[2,6]

$$-\frac{1}{3}\frac{A\ Ep\ h\ (-r2\ b12 + v\ s3\ a31 - r3\ b31)}{r2\ s3}$$

[2,7]

$$\frac{A\ v\ Ep\ h}{r2}$$

[2,8]

$$-\frac{A\ Ep\ r3\ h}{r2\ s3}$$

[2,12]

$$-\frac{1}{3}\frac{A\ Ep\ h\ (r2\ b12 + r2\ b23 + v\ s3\ a23 - r3\ b23)}{r2\ s3}$$

[2,14]

$$\frac{A\ Ep\ h}{s3}$$

[2,18]

$$\frac{1}{3}\frac{A\ Ep\ h\ (r2\ b23 + v\ s3\ a31 + v\ s3\ a23 - r3\ b31 - r3\ b23)}{r2\ s3}$$

[3,1]

$$-\frac{A\ G\ (r2 - r3)\ h}{r2\ s3}$$

[3,2]

$$-\frac{A\ G\ h}{r2}$$

[3,6]

$$\frac{1}{3}\frac{A\ G\ h\ (-s3\ b31 + r3\ a31)}{r2\ s3}$$

[3,7]

$$-\frac{A\ G\ r3\ h}{r2\ s3}$$

[3,8]

$$\frac{A\ G\ h}{r2}$$

[3,12]

$$-\frac{1}{3}\,\frac{A\,G\,h\,(r2\,a23 + s3\,b23 - r3\,a23)}{r2\,s3}$$

[3,13]

$$\frac{A\,G\,h}{s3}$$

[3,18]

$$-\frac{1}{3}\,\frac{A\,G\,h\,(-r2\,a23 - s3\,b31 - s3\,b23 + r3\,a31 + r3\,a23)}{r2\,s3}$$

where bij = b_{ij} and aij = a_{ij} (i,j = 1, 2 and 3). The remaining notations are as Appendix A.1.

A.3 Matrix $(G_e)_b$

The non-zero elements of matrix $(G_e)_b$ are,

[4,4]

$$1/12 \frac{A\ v\ Ep\ (r2 - r3)\ h^3}{r2\ s3}$$

[4,5]

$$-1/12 \frac{A\ Ep\ h^3}{r2}$$

[4,10]

$$1/12 \frac{A\ v\ Ep\ r3\ h^3}{r2\ s3}$$

[4,11]

$$1/12 \frac{A\ Ep\ h^3}{r2}$$

[4,16]

$$-1/12 \frac{A\ v\ Ep\ h^3}{s3}$$

[5,4]

$$1/12 \frac{A\ Ep\ (r2 - r3)\ h^3}{r2\ s3}$$

[5,5]

$$-1/12 \frac{A\ v\ Ep\ h^3}{r2}$$

[5,10]

$$1/12 \frac{A\ Ep\ r3\ h^3}{r2\ s3}$$

[5,11]

$$1/12 \frac{A\ v\ Ep\ h^3}{r2}$$

[5,16]

$$-\frac{1}{12}\,\frac{A\,Ep\,h^3}{s3}$$

[6,4]

$$\frac{1}{12}\,\frac{A\,G\,h^3}{r2}$$

[6,5]

$$-\frac{1}{12}\,\frac{A\,G\,(r2-r3)\,h^3}{r2\,s3}$$

[6,10]

$$-\frac{1}{12}\,\frac{A\,G\,h^3}{r2}$$

[6,11]

$$-\frac{1}{12}\,\frac{A\,G\,r3\,h^3}{r2\,s3}$$

[6,17]

$$\frac{1}{12}\,\frac{A\,G\,h^3}{s3}$$

The notations are as Appendix A.1.

A.4 Matrix $(G_e)_s$

The non-zero elements of matrix $(G_e)_s$ are,

[7,3]
1/3 A ks G h

[7,4]
1/6 A ks G h s3

[7,5]
- 1/6 A ks G h r3

[7,15]
- 1/3 A ks G h

[7,16]
1/6 A ks G h s3

[7,17]
- 1/6 A ks G h r3

[8,9]
- 1/3 A ks G h

[8,10]
- 1/6 A ks G h s3

[8,11]
- 1/6 A ks G h (r2 - r3)

[8,15]
1/3 A ks G h

[8,16]
- 1/6 A ks G h s3

[8,17]
- 1/6 A ks G h (r2 - r3)

[9,3]
- 1/3 A ks G h

[9,5]
1/6 A ks G h r2

[9,9]
1/3 A ks G h

[9,11]
1/6 A ks G h r2

The notations are as Appendix A.1.

A.5 Matrix $(G_e)_d$

The non-zero elements of matrix $(G_e)_d$ are,

[10,1]

$$1/2 \frac{A\ G\ (r3 - r2)\ h}{r2\ s3}$$

[10,2]

$$-\ 1/2 \frac{A\ G\ h}{r2}$$

[10,6]

$$1/3\ A\ G\ h$$

[10,7]

$$-\ 1/2 \frac{A\ G\ r3\ h}{r2\ s3}$$

[10,8]

$$1/2 \frac{A\ G\ h}{r2}$$

[10,12]

$$1/3\ A\ G\ h$$

[10,13]

$$1/2 \frac{A\ G\ h}{s3}$$

[10,18]

$$1/3\ A\ G\ h$$

The notations are as Appendix A.1.

APPENDIX B

MATRICES k_t^1, $(k_t^1)'$, k_t^3 AND $(k_t^3)'$

B.1 Matrices k_t^1 and $(k_t^1)'$

The non-zero elements of $(k_t^1)'$ are, (only those in the upper triangle are listed due to the symmetry of $(k_t^1)'$. The non-zero elements of k_t^1 are obtained by setting b12 = a23 = b23 = a31 = b31 = 0)

[1,1]

$$\frac{A\,(-r3+r2)^2\,h}{r2^2\,s3^2}$$

[1,2]

$$-\frac{A\,(-r3+r2)\,h}{r2^2\,s3}$$

[1,6]

$$-\frac{1}{3}\,\frac{A\,(-r3+r2)\,h\,(2\,r2\,s3+r3\,a31+s3\,b31)}{r2^2\,s3^2}$$

[1,7]

$$\frac{A\,(-r3+r2)\,r3\,h}{r2^2\,s3^2}$$

[1,8]

$$\frac{A\,(-r3+r2)\,h}{r2^2\,s3}$$

[1,12]

$$\frac{1}{3}\,\frac{A\,(-r3+r2)\,h\,(-2\,r2\,s3+r2\,a23-s3\,b23-r3\,a23)}{r2^2\,s3^2}$$

[1,13]

$$-\frac{A\,(-r3+r2)\,h}{r2\,s3^2}$$

[1,18]

$$\frac{A\,(-r3+r2)\,h\,(-r2\,a23+r3\,a31+r3\,a23-2\,r2\,s3+s3\,b31+s3\,b23)}{3\,r2^2\,s3^2}$$

[2,2]

$$\frac{A\,h}{r2^2}$$

[2,6]

$$1/3\,\frac{A\,h\,(2\,r2\,s3+r3\,a31+s3\,b31)}{r2^2\,s3}$$

[2,7]

$$-\frac{A\,r3\,h}{r2^2\,s3}$$

[2,8]

$$-\frac{A\,h}{r2^2}$$

[2,12]

$$-1/3\,\frac{A\,h\,(-2\,r2\,s3+r2\,a23-s3\,b23-r3\,a23)}{r2^2\,s3}$$

[2,13]

$$\frac{A\,h}{r2\,s3}$$

[2,18]

$$-1/3\,\frac{A\,h\,(-2\,r2\,s3-r2\,a23+r3\,a31+r3\,a23+s3\,b31+s3\,b23)}{r2^2\,s3}$$

[6,6]

$$1/18\,A\,h\,(8\,r2^2\,s3^2+8\,s3^2\,b31\,r2-3\,r3\,a31^2\,r2+3\,r2^2\,a31^2+3\,s3^2\,b12^2$$

$$+ 3\ r3^2\ a31^2 + 3\ s3^2\ b31^2 + 8\ r3\ a31\ r2\ s3 + 3\ r2\ a31\ s3\ b12$$

$$+ 6\ r3\ a31\ s3\ b31 - 3\ r2\ a31\ s3\ b31)$$

$$/\ (r2^2\ s3^2)$$

[6,7]

$$-\ 1/3\ \frac{A\ r3\ h\ (2\ r2\ s3 + r3\ a31 + s3\ b31)}{r2^2\ s3^2}$$

[6,8]

$$-\ 1/3\ \frac{A\ h\ (2\ r2\ s3 + r3\ a31 + s3\ b31)}{r2^2\ s3}$$

[6,12]

$$-1/36\ A\ h$$

$$(-\ 6\ s3^2\ b31\ b23 - 6\ r3^2\ a31\ a23 + 3\ s3\ b31\ r2\ a23 - 16\ r2^2\ s3^2$$

$$- 6\ s3\ b31\ r3\ a23 + 6\ r2\ a31\ r3\ a23 + 3\ r2\ a31\ s3\ b23$$

$$- 6\ r3\ a31\ s3\ b23 - 3\ s3\ b12\ r2\ a23 - 8\ r3\ a23\ r2\ s3 + 8\ r2^2\ a23\ s3$$

$$- 8\ s3^2\ b23\ r2 - 8\ s3^2\ b31\ r2 + 6\ s3^2\ b12^2 - 8\ r3\ a31\ r2\ s3$$

$$+ 3\ r2\ a31\ s3\ b12)$$

$$/\ (r2^2\ s3^2)$$

[6,13]

$$1/3\ \frac{A\ h\ (2\ r2\ s3 + r3\ a31 + s3\ b31)}{r2\ s3^2}$$

[6,18]

$$-1/36\ A\ h$$

$$(6\ s3^2\ b31\ b23 + 6\ r3^2\ a31\ a23 - 3\ s3\ b31\ r2\ a23 - 16\ r2^2\ s3^2$$

$$+ 6\ s3\ b31\ r3\ a23 - 6\ r2\ a31\ r3\ a23 - 3\ r2\ a31\ s3\ b23$$

$$+ 6\ r3\ a31\ s3\ b23 + 3\ s3\ b12\ r2\ a23 + 8\ r3\ a23\ r2\ s3 - 8\ r2^2\ a23\ s3$$

$$+ 8\ s3^2\ b23\ r2 - 6\ r3\ a31^2\ r2^2 + 6\ r2^2\ a31^2 + 6\ r3^2\ a31^2 + 6\ s3^2\ b31^2$$

$$+ 3\ r2\ a31\ s3\ b12 + 12\ r3\ a31\ s3\ b31 - 6\ r2\ a31\ s3\ b31)$$

$$/\ (r2^2\ s3^2)$$

[7,7]

$$\frac{A\ r3^2\ h}{r2^2\ s3^2}$$

[7,8]

$$\frac{A\ r3\ h}{r2^2\ s3}$$

[7,12]

$$1/3\ \frac{A\ r3\ h\ (-\ 2\ r2\ s3 + r2\ a23 - s3\ b23 - r3\ a23)}{r2^2\ s3^2}$$

[7,13]

$$-\ \frac{A\ r3\ h}{r2\ s3^2}$$

[7,18]

$$1/3\ \frac{A\ r3\ h\ (-\ 2\ r2\ s3 - r2\ a23 + r3\ a31 + r3\ a23 + s3\ b31 + s3\ b23)}{r2^2\ s3^2}$$

[8,8]

$$\frac{A\ h}{r2^2}$$

[8,12]

$$1/3\ \frac{A\ h\ (-\ 2\ r2\ s3 + r2\ a23 - s3\ b23 - r3\ a23)}{r2^2\ s3}$$

[8,13]

$$-\ \frac{A\ h}{r2\ s3}$$

[8,18]

$$1/3\ \frac{A\ h\ (-\ 2\ r2\ s3 - r2\ a23 + r3\ a31 + r3\ a23 + s3\ b31 + s3\ b23)}{r2^2\ s3}$$

[12,12]

1/18

$$A\,h\,\left(-3\,r3\,a23^2\,r2+3\,s3^2\,b23^2+3\,r3^2\,a23^2+6\,s3\,b23\,r3\,a23-3\,s3\,b23\,r2^2\,a23^2+3\,r2^2\,a23^2+8\,r2^2\,s3^2-3\,s3\,b12\,r2\,a23+8\,r3\,a23\,r2^2\,s3-8\,r2^2\,a23\,s3^2+8\,s3^2\,b23\,r2+3\,s3^2\,b12^2\right)/\left(r2^2\,s3^2\right)$$

[12,13]

$$-1/3\,\frac{A\,h\,(-2\,r2\,s3+r2\,a23-s3\,b23-r3\,a23)}{r2\,s3^2}$$

[12,18]

1/36

$$A\,h\,\left(6\,r3\,a23^2\,r2-6\,s3^2\,b23^2-6\,r3^2\,a23^2-12\,s3\,b23\,r3\,a23+6\,s3\,b23\,r2^2\,a23^2-6\,r2^2\,a23^2-6\,s3^2\,b31\,b23-6\,r3^2\,a31\,a23+3\,s3\,b31\,r2^2\,a23^2+16\,r2^2\,s3^2-6\,s3\,b31\,r3\,a23+6\,r2\,a31\,r3\,a23+3\,r2^2\,a31\,s3\,b23-6\,r3\,a31\,s3\,b23+3\,s3\,b12\,r2\,a23-8\,s3^2\,b31\,r2^2-8\,r3\,a31\,r2^2\,s3+3\,r2^2\,a31\,s3\,b12\right)/\left(r2^2\,s3^2\right)$$

[13,13]

$$\frac{A\,h}{s3^2}$$

[13,18]

$$-1/3\,\frac{A\,h\,(-2\,r2\,s3-r2\,a23+r3\,a31+r3\,a23+s3\,b31+s3\,b23)}{r2\,s3^2}$$

```
[18,18]

1/18

   A h

                                2                2    2          2    2
      (- 3 r3 a23  r2 + 3 s3  b23  + 3 r3  a23  + 6 s3 b23 r3 a23

                                  2    2          2                   2
        - 3 s3 b23 r2 a23 + 3 r2  a23  + 6 s3  b31 b23 + 6 r3  a31 a23

                                    2   2
        - 3 s3 b31 r2 a23 + 8 r2  s3  + 6 s3 b31 r3 a23 - 6 r2 a31 r3 a23

                                                                    2
      - 3 r2 a31 s3 b23 + 6 r3 a31 s3 b23 - 8 r3 a23 r2 s3 + 8 r2  a23 s3

                 2                2                   2          2    2          2    2
  - 8 s3  b23 r2 - 8 s3  b31 r2 - 3 r3 a31  r2 + 3 r2  a31  + 3 r3  a31

          2    2
      + 3 s3  b31  - 8 r3 a31 r2 s3 + 6 r3 a31 s3 b31 - 3 r2 a31 s3 b31)

          2   2
     / (r2  s3 )
```

The notations are as Appendices A.1 and A.2.

B.2 Matrices k_t^3 and $(k_t^3)'$

Most non-zero elements of $(k_t^3)'$ are the same as $(k_t^1)'$ except for the following listed ones (only non-zero elements in the upper triangle are listed. Those of k_t^3 are obtained by setting b12 = a23 = b23 = a31 = b31 = 0)

```
[6,6]
1/6 A h

      (2 r3 a31 r2 s3 - r2 a31 b31 s3 + 2 b31 s3^2 r2 - r3 a31^2 r2

   + 2 r3 a31 b31 s3 + r3^2 a31^2 + r2^2 a31^2 + r2 a31 b12 s3 + 2 r2^2 s3 a31

         + 2 r2 s3^2 b12 + b31^2 s3^2 + b12^2 s3^2 + 4 r2^2 s3^2 )

      / (r2^2 s3^2 )

[6,12]
-1/12 A h

      (- 2 r3^2 a31 a23 + b31 s3 r2 a23 - 2 r2 s3 r3 a23 - 2 r2 s3^2 b23

    - 2 r3 a31 b23 s3 + r2 a31 b23 s3 + 2 r2 a31 r3 a23 - 2 b31 s3 r3 a23

         - b12 s3 r2 a23 - 2 b31 s3^2 b23 + 2 r2^2 s3 a23 - 2 r3 a31 r2 s3

  - 2 b31 s3^2 r2 + r2 a31 b12 s3 + 4 r2 s3^2 b12 + 2 b12^2 s3^2 - 4 r2^2 r3^2

         )

      / (r2^2 s3^2 )
```

[6,18]

-1/12

$$A\,h\,(2\,r3^2\,a31\,a23 - b31\,s3\,r2\,a23 + 2\,r2\,s3\,r3\,a23 + 2\,r2\,s3^2\,b23 + 2\,r3\,a31\,b23\,s3 - r2\,a31\,b23\,s3 - 2\,r2\,a31\,r3\,a23 + 2\,b31\,s3\,r3\,a23 + b12\,s3\,r2\,a23 + 2\,b31\,s3^2\,b23 - 2\,r2^2\,s3\,a23 - 2\,r3\,a31\,r2\,s3 - 2\,r2\,a31\,b31\,s3 - 2\,b31\,s3^2\,r2 - 2\,r3\,a31^2\,r2 + 4\,r3\,a31\,b31\,s3 + 2\,r3^2\,a31^2 + 2\,r2^2\,a31^2 + r2\,a31\,b12\,s3 + 4\,r2^2\,s3\,a31 + 2\,b31^2\,s3^2 - 4\,r2^2\,s3^2)\,/\,(r2^2\,s3^2)$$

[12,12]

1/6

$$A\,h\,(2\,r2\,s3\,r3\,a23 + 2\,r2\,s3^2\,b23 - b12\,s3\,r2\,a23 - 4\,r2^2\,s3\,a23 + 2\,r2\,s3^2\,b12 + b12^2\,s3^2 + 4\,r2^2\,s3^2 - b23\,s3\,r2\,a23 - r3\,a23^2\,r2 + 2\,b23\,s3\,r3\,a23 + r2^2\,a23^2 + b23^2\,s3^2 + r3^2\,a23^2)\,/\,(r2^2\,s3^2)$$

```
[12,18]
1/12
   A h
                                                                    2
      (- 2 r3^2 a31 a23 + b31 s3 r2 a23 + 2 r2 s3 r3 a23 + 2 r2 s3^2 b23
     - 2 r3 a31 b23 s3 + r2 a31 b23 s3 + 2 r2 a31 r3 a23 - 2 b31 s3 r3 a23
                                    2                 2
        + b12 s3 r2 a23 - 2 b31 s3^2 b23 + 2 r2^2 s3 a23 - 2 r3 a31 r2 s3
                                  2                 2   2
        - 2 b31 s3^2 r2 + r2 a31 b12 s3 + 4 r2^2 s3^2 + 2 b23 s3 r2 a23
                                  2                 2   2         2   2
        + 2 r3 a23^2 r2 - 4 b23 s3 r3 a23 - 2 r2^2 a23^2 - 2 b23^2 s3^2
                  2   2
        - 2 r3^2 a23^2 )
          2   2
      / (r2^2 s3^2 )
[18,18]
1/6
   A h
                                                                    2
      (2 r3^2 a31 a23 - b31 s3 r2 a23 - 4 r2 s3 r3 a23 - 4 r2 s3^2 b23
     + 2 r3 a31 b23 s3 - r2 a31 b23 s3 - 2 r2 a31 r3 a23 + 2 b31 s3 r3 a23
                                    2                 2
        + 2 b31 s3^2 b23 + 2 r2^2 s3 a23 - 4 r3 a31 r2 s3 - r2 a31 b31 s3
                                  2                 2                 2   2   2   2
      - 4 b31 s3^2 r2 - r3 a31^2 r2 + 2 r3 a31 b31 s3 + r3^2 a31^2 + r2^2 a31^2
                                  2                 2   2         2   2
       + 2 r2^2 s3 a31 + b31^2 s3^2 + 4 r2^2 s3^2 - b23 s3 r2 a23 - r3 a23^2 r2
                                  2   2         2   2   2   2
        + 2 b23 s3 r3 a23 + r2^2 a23^2 + b23^2 s3^2 + r3^2 a23^2 )
          2   2
      / (r2^2 s3^2 )
```

The notations are as Appendices A.1 and A.2.

APPENDIX C

CONSISTENT MASS MATRIX

The non-zero elements of the consistent mass matrix m are, with [i,j] denoting the element located in the i-th row and j-th column of m ,

[1,1]

$$1/6\ \rho$$

[1,6]

$$1/30\ \rho\ a_{31}$$

[1,7]

$$1/12\ \rho$$

[1,12]

$$-1/60\ \rho\ a_{23}$$

[1,13]

$$1/12\ \rho$$

[1,18]

$$-1/60\ \rho\ (2\ a_{31} - a_{23})$$

[2,2]

$$1/6\ \rho$$

[2,6]

$$1/30\ \rho\ (-\ b_{12} + b_{31})$$

[2,8]

$$1/12\ \rho$$

[2,12]

$$1/60\ \rho\ (2\ b_{12} - b_{23})$$

[2,14]

$$1/12\ \rho$$

[2,18]

$$-1/60\ \rho\ (2\ b_{31} - b_{23})$$

[3,3]

$$1/6\ \rho$$

[3,4]

$$-1/30\ \rho\ a_{31}$$

[3,5]

$$-1/30\ \rho\ (-\ b_{12} + b_{31})$$

[3,9]

$$1/12\ rou$$

[3,10]

$$1/60\ rou\ a23$$

[3,11]

$$-1/60\ rou\ (2\ b12 - b23)$$

[3,15]

$$1/12\ rou$$

[3,16]

$$1/60\ rou\ (2\ a31 - a23)$$

[3,17]

$$1/60\ rou\ (2\ b31 - b23)$$

[4,4]

$$1/90\ rou\ (15\ Jh + a31^2)$$

[4,5]

$$1/180\ rou\ a31\ (2\ b31 - b12)$$

[4,9]

$$-1/60\ rou\ a31$$

[4,10]

$$-1/180\ rou\ (-15\ Jh + a31\ a23)$$

[4,11]

$$1/180\ rou\ a31\ (b12 - b23)$$

[4,15]

$$-1/30\ rou\ a31$$

[4,16]

$$-1/180\ rou\ (-15\ Jh + 2\ a31^2 - a31\ a23)$$

[4,17]

$$-1/180\ rou\ a31\ (2\ b31 - b23)$$

[5,5]

$$1/90\ rou\ (15\ Jh + b31^2 + b12^2 - b31\ b12)$$

[5,9]

$$-1/60\ rou\ (-2\ b12 + b31)$$

[5,10]

$$-1/180\ rou\ a23\ (-b12 + b31)$$

[5,11]

$$1/180\ rou\ (15\ Jh - 2\ b12^2 + b31\ b12 + b12\ b23 - b31\ b23)$$

[5,15]

$$-1/60\ rou\ (2\ b31 - b12)$$

[5,16]

$$-\frac{1}{180}\,\rho\,(2\,a31\,b31 - a31\,b12 + b12\,a23 - b31\,a23)$$

[5,17]

$$-\frac{1}{180}\,\rho\,(-15\,Jh + 2\,b31^{2} - b31\,b12 + b12\,b23 - b31\,b23)$$

[6,6]

$$\frac{1}{90}\,\rho\,(15\,Jo + a31^{2} + b31^{2} + b12^{2} - b31\,b12)$$

[6,7]

$$\frac{1}{60}\,\rho\,a31$$

[6,8]

$$\frac{1}{60}\,\rho\,(-2\,b12 + b31)$$

[6,12]

$$-\frac{1}{180}\,\rho\,(-15\,Jo + 2\,b12^{2} - b31\,b12 - b12\,b23 + a31\,a23 + b31\,b23)$$

[6,13]

$$\frac{1}{30}\,\rho\,a31$$

[6,14]

$$\frac{1}{60}\,\rho\,(2\,b31 - b12)$$

[6,18]

$$-\frac{1}{180}\,\rho\,(-15\,Jo + 2\,a31^{2} + 2\,b31^{2} - b31\,b12 + b12\,b23 - a31\,a23 - b31\,b23)$$

[7,7]

$$\frac{1}{6}\,\rho$$

[7,12]

$$-\frac{1}{30}\,\rho\,a23$$

[7,13]

$$\frac{1}{12}\,\rho$$

[7,18]

$$-\frac{1}{60}\,\rho\,(-2\,a23 + a31)$$

[8,8]

$$\frac{1}{6}\,\rho$$

[8,12]

$$\frac{1}{30}\,\rho\,(b12 - b23)$$

[8,14]

$$\frac{1}{12}\,\rho$$

[8,18]

$$-\frac{1}{60}\,\rho\,(-2\,b23 + b31)$$

[9,9]

$$\frac{1}{6}\,\rho$$

[9,10]

$$\frac{1}{30}\,\rho\,a23$$

[9,11]

$$-\frac{1}{30}\,\rho\,(b_{12}-b_{23})$$

[9,15]

$$\frac{1}{12}\,\rho$$

[9,16]

$$\frac{1}{60}\,\rho\,(-2\,a_{23}+a_{31})$$

[9,17]

$$\frac{1}{60}\,\rho\,(-2\,b_{23}+b_{31})$$

[10,10]

$$\frac{1}{90}\,\rho\,(15\,J_h+a_{23}^2)$$

[10,11]

$$-\frac{1}{180}\,\rho\,a_{23}\,(-2\,b_{23}+b_{12})$$

[10,15]

$$\frac{1}{30}\,\rho\,a_{23}$$

[10,16]

$$\frac{1}{180}\,\rho\,(15\,J_h-2\,a_{23}^2+a_{31}\,a_{23})$$

[10,17]

$$\frac{1}{180}\,\rho\,a_{23}\,(-2\,b_{23}+b_{31})$$

[11,11]

$$\frac{1}{90}\,\rho\,(15\,J_h+b_{12}^2+b_{23}^2-b_{12}\,b_{23})$$

[11,15]

$$-\frac{1}{60}\,\rho\,(-2\,b_{23}+b_{12})$$

[11,16]

$$-\frac{1}{180}\,\rho\,(2\,a_{23}\,b_{23}+a_{31}\,b_{12}-b_{12}\,a_{23}-b_{23}\,a_{31})$$

[11,17]

$$-\frac{1}{180}\,\rho\,(-15\,J_h+2\,b_{23}^2+b_{31}\,b_{12}-b_{12}\,b_{23}-b_{31}\,b_{23})$$

[12,12]

$$\frac{1}{90}\,\rho\,(15\,J_o+b_{12}^2+a_{23}^2+b_{23}^2-b_{12}\,b_{23})$$

[12,13]

$$-\frac{1}{30}\,\rho\,a_{23}$$

[12,14]

$$\frac{1}{60}\,\rho\,(-2\,b_{23}+b_{12})$$

[12,18]

$$\frac{1}{180}\,\rho\,(15\,J_o-2\,a_{23}^2-2\,b_{23}^2-b_{31}\,b_{12}+b_{12}\,b_{23}+a_{31}\,a_{23}+b_{31}\,b_{23})$$

[13,13]

$$\frac{1}{6}\,\rho$$

```
[13,18]
                              - 1/30 rou (a31 - a23)
[14,14]
                                    1/6 rou
[14,18]
                              - 1/30 rou (b31 - b23)
[15,15]
                                    1/6 rou
[15,16]
                               1/30 rou (a31 - a23)
[15,17]
                               1/30 rou (b31 - b23)
[16,16]
                        1/90 rou (15 Jh + a31^2 + a23^2 - a31 a23)
[16,17]
                  1/180 rou (2 a31 b31 + 2 a23 b23 - b23 a31 - b31 a23)
[17,17]
                        1/90 rou (15 Jh + b31^2 + b23^2 - b31 b23)
[18,18]
              1/90 rou (15 Jo + a31^2 + b31^2 + a23^2 + b23^2 - a31 a23 - b31 b23)
```

where rou = ρAh, with ρ being the mass density per unit volume, A the area of the triangular element and h the thickness of the shell. Jh = $\frac{h^2}{12}$ is the moment of inertia per unit cross-sectional area and Jo = $\frac{r_2^2+s_3^2+r_3(r_3-r_2)}{18}$ is the polar moment of inertia, per unit area of the triangular element, of the element about its centroid. aij = a_{ij} and bij = b_{ij} with i and j running from 1 to 3. Note that only those elements situated in the upper triangle are listed.

REFERENCES

1.1. G. Lame and E. Clapeyron, 'Mémoires sur l'équilibre intérieur des corps solides homogénes', *Mémoires presents a l'Academie des Sciences de l'Institut de France, second series*, **4**, (1828).

1.2. H. Aron, 'Das gleichgewicht und die bewegung einer unendich dunnen, beliebig gerkrummten, elastischen schale', *Journal fur Reine und Ange. Math.*, (1874).

1.3. A.E.H. Love, 'On the small free vibrations and deformations of thin elastic shells', *Phil. Trans. Royal Soc. (London)*, **17A**, 491 (1888).

1.4. R.H. Gallagher, *The development and evaluation of matrix methods for thin shell structural analysis*, Ph.D. thesis, State University of New York at Buffalo, (1966).

1.5. S. Utku, 'Stiffness matrices for thin triangular elements of non-zero Gaussian curvature', *AIAA J.*, **5**, 1659-1667 (1967).

1.6. S. Ahmad, B.M. Irons and O.C. Zienkiewicz, 'Curved thick shell and membran. elements with particular reference to axi-symmetric probl.r..s', in *Proc. 2nd Conf. Matrix Methods in Structural Mechanics*, Wright-Patterson A.F. Base, Ohio (1968)

1.7. A.K. Noor, 'Survey of computer programs for solution of nonlinear structural and solid mechanics problems', *Compu. Struct.*, **13**, 425-465 (1981).

1.8. T.Y. Chang and J. Padovan, 'General purpose nonlinear finite element programs', in *Structural Mechanics Software Series*, **3**, 79-101 (1980).

1.9. H. Armen and A.B. Pifko, 'Plastic analysis in general purpose programs', in *Structural Mechanics Software Series*, **3**, (1980).

1.10. C.A.Brebbia (ed.), *Finite Element Systems, A Handbook*, 3rd edn., Springer-Verlag, NY (1985).

1.11. A. Niku-Lari (ed.), *Structural Analysis Systems, Software-Hardware-Capability-Compatibility-Applications*, Vol. 1 and 2, Pergamon Press (1986).

1.12. C.W.S. To, 'The response of nonlinear structures to random excitation', *Shock Vibr. Dig.*, **16**, 13-33 (1984).

1.13. C.W.S.To, 'A stochastic version of the Newmark family of algorithms for discretized dynamic systems', *Comp. Struct.*, **44**, 667-673 (1992).

1.14. C.W.S. To, 'The Stochastic central difference method in structural dynamics', *Comp. Struct.*, **23**, 813-818 (1986).

1.15. C.W.S. To, 'Recursive expressions for random response of nonlinear systems', *Comp. Struct.*, **29**(3), 451-457 (1988).

1.16. M. Di Paola, M. Iopplo and G. Muscolino, 'Stochastic seismic analysis of multi-degree-of-freedom systems', *Eng. Struct.*, **6**, 113-118 (1984).

1.17. M. Hoshiya, K. Ishii and S. Nagata, 'Recursive co-variance of structural responses', *J. Eng. Mech.*, **110**, 1743-1755 (1984).

1.18. G.E.P. Box and G.M. Jenkins, *Time Series Analysis: Forecasting and Control*, revised edn., Holden-Day, Oakland, CA (1976).

1.19. M.B. Priestley, *Spectral Analysis and Time Series Analysis, Lecture Notes in Statistics*, Vol.21, Springer, NY (1983).

1.20. R.H. MacNeal and R.L. Harder, 'A proposed standard set of problems to test finite element accuracy', *J. Finite Elem. Anal. Des.*, **1**, 3-20 (1985).

2.1. C.W.S. To, 'The Stochastic central difference method in structural dynamics', *Comp. Struct.*, **23**, 813-818 (1986).

2.2. C.W.S. To, 'Direct integration operators and their stability for random responses of multi-degree-of-freedom systems', *Comp. Struct.*, **30**(4), 865-874 (1988).

2.3. C.W.S. To, 'Recursive expressions for random response of nonlinear systems', *Comp. Struct.*, **29**(3), 451-457 (1988).

2.4. C.W.S. To, 'Parametric effects on time step of the stochastic central difference method', *J. Sound Vibr.*, **137**(3), 509-515 (1990).

2.5. C.W.S. To, 'Random response of multi-degree-of-freedom systems with geometrical nonlinearities by the stochastic central difference method', submitted to *J. Nonlinear Dyn.*, (1992).

2.6. C.W.S. To, 'Time-dependent variance and covariance of responses of structures to non-stationary random excitations', *J. Sound Vibr.*, **93**(1), 135-156 (1984).

2.7. R.D. Cook, D.S. Malkus and M.E.Plesha, *Concepts and Applications of Finite Element Analysis*. 3rd edn., John Wiley & Sons, Inc., NY (1989).

2.8. R.W. Clough and J. Penzien, *Dynamics of Structures*. McGraw-Hill Book Co., NY (1975).

2.9. G.B. Warburton, *The Dynamical Behaviour of Structures*. 2nd edn., Pergamon Press, Oxford (1976).

2.10. B. Wang, *Non-Stationary Random Responses of Plates with Geometric Non-Linearity*. M.E.Sc. thesis, The University of Western Ontario, Canada (1991).

2.11. F. Ma, Private communication (1992).

2.12. K.Kimura and M.Sakata, 'Nonstationary response analysis of a nonsymmetric nonlinear multi-degree-of-freedom system to nonwhite random excitation', *JSME International Journal*, **31**(4), 690-697 (1988).

2.13. C.W.S.To and S.W.Zhang, 'On techniques for digital simulation of random response of nonlinear oscillators', *J. Sound Vibr.*, **131**(1), 168-173 (1989).

2.14. C.W.S.To, 'A stochastic version of the Newmark family of algorithms for discretized dynamic systems', *Comp. Struct.*, **44**, 667-673 (1992).

2.15. K.J. Bathe and E.L. Wilson, 'Stability and accuracy analysis of direct integration methods', *Earthquake Engrg. Struct. Dynamics*, **1**, 283-291 (1973).

3.1. O.C. Zienkiewicz, C.J. Parikh and I.P. King, 'Arch dam analysis by a linear finite element shell solution program', in *Proc. Symposium on Arch Dams*, I.C.C., London, 19-22 (1968).

3.2. R.W. Clough and C.P. Johnson, 'A finite element approximation for the analysis of thin shell', *Int. J. Solids Struct.*, **4**, 43-60 (1968).

3.3. J.H. Argyris, P.C. Dunne, G.A. Malejannakis and E. Schelke, 'A simple triangular facet shell element with application to linear and nonlinear equilibrium and elastic stability problems', *Comp. Methods Appl. Mech. Eng.*, **10**, 371-403 (1977); **11**, 97-131 (1977).

3.4. J.L. Batoz, K.J. Bathe and L.W. Ho, 'A study of three-node triangular plate bending elements', *Int. j. numer. methods eng.*, **15**, 1771-1812 (1980).

3.5. J.L. Batoz, 'An explicit formulation for an efficient triangular plate-bending element', *Int. j. numer. methods eng.*, **18**, 1077-1089 (1982).

3.6. K.J. Bathe and L.W. Ho, 'A simple and effective element for analysis of general shell structures', *Comp. Struct.*, **13**, 673-681 (1981).

3.7. J.L. Batoz and G. Dhatt, 'Development of two simple shell elements', *AIAA J.*, **10**, 237-248 (1972).

3.8. H.T.Y. Yang, S. Saigal and D.G. Liaw, 'Advances of thin shell finite elements and some applications, Version I', *Comp. Struct.*, **35**, 481-504 (1990)

3.9. O.C. Zienkiewicz, R.L. Taylor and J.M. Too, 'Reduced integration technique in general analysis of plates and shells', *Int. j. numer. methods eng.*, **3**, 275-290 (1971).

3.10. D.G. Kang, 'Present finite element technology from a hybrid formulation perspective', *Comp. Struct.*, **35**, 321-329 (1990).

3.11. H. Stolarski and T. Belystchko, 'Membrane locking and reduced integration for curved elements", *J. Appl. Mech. ASME*, **49**, 172-176 (1982).

3.12. H. Parisch, 'A critical survey of the 9-node degenerated shell element with special emphasis on thin shell element application and reduced integration', *Comp. Methods Appl. Mech. Eng.*, **20**, 323-350 (1979).

3.13. H.C. Huang and E. Hinton, 'A new nine node degenerated shell element with enhanced membrane and shear interpolation', *Int. j. numer. methods eng.*, **22**, 73-92 (1986).

3.14. H. Stolarski and T. Belystchko, 'Shear and membrane locking in curved C^0 elements', *Comp. Methods Appl. Mech. Eng.*, **41**, 279-296 (1983).

3.15. N. Carpenter, H. Stolarski and T. Belystchko, 'A flat triangular shell element with improved membrane interpolation', *Commun. appl. numer. methods*, **1**, 161-168 (1985).

3.16. D.J. Allman, 'A compatible triangular element including vertex rotations for plane elasticity analysis', *Comp. Struct.*, **19**, 1-8 (1984).

3.17. D.J. Allman, 'The constant strain triangle with drilling rotations: A simple prospect for shell analysis', in J.R. Whiteman (ed.). *Proceedings The Mathematics of Finite Elements and Applications*, Academic Press, New York, 230-236 (1987).

3.18. D.J. Allman, 'Evaluation of the constant strain triangle with drilling rotations', *Int. j. numer. methods eng.*, **26**, 2645-2655 (1988).

3.19. R.B. Cook, D.S. Malkus and M.E. Plesha, *Concepts and Applications of Finite Element Analysis*, John Wiley & Sons, New York, 1989.

3.20. N. Carpenter, H. Stolarski and T. Belystchko, 'Improvements in 3-node triangular shell elements', *Int. j. numer. methods eng.*, **23**, 1643-1667 (1986).

3.21. M.L. Liu and C.W.S. To, 'Hybrid strain based three-node flat triangular shell elements, Part II: Numerical studies', *Int. j. numer. methods eng.* (submitted 1993).

3.22. R.H. MacNeal and R.L. Harder, 'A proposed standard set of problems to test finite element accuracy', *J. Finite Elem. Anal. Des.*, **1**, 3-20 (1985).

3.23. D.G. Ashwell and A.B. Sabir, 'A new cylindrical shell finite element based on simple independent strain functions', *Int. J. Mech. Sci.*, **14**, 171-183 (1972).

3.24. O.C. Zienkiewicz and R.L. Taylor, *The Finite Element Method, Vol.2*, McGraw-Hill, New York, 1991.

3.25. A.F. Saleeb, T.Y. Chang and S. Yingyuengyong, 'A mixed formulation of C^0-linear triangular plate/shell element, the role of edge shear constraints', *Int. j. numer. methods eng.*, **26**, 1101-1128 (1988).

3.26. A.F. Saleeb, T.Y. Chang and W. Graf, 'A quadrilateral shell element using a mixed formulation', *Comp. Struct.*, **26**, 787-803 (1987).

3.27. MAPLE Reference Manual, Symbolic Computation Group, Department of Computer Science, University of Waterloo, Canada, Fifth Edition (1988).

3.28. J. Fish and T. Belytschko, 'Stabilized rapidly convergent 18-degrees-of-freedom Flat shell triangular element', *Int. j. numer. methods eng.*, **33**, 149-162 (1992).

3.29. A.K. Noor and S.J. Hartley, 'Nonlinear shell analysis via mixed isoparametric elements', *Comp. Struct.*, **7**, 615-626 (1977).

3.30. W. Kanok-Nukulchai, 'A simple and efficient finite element for general shell analysis', *Int. j. numer. methods eng.*, **14**, 179-200 (1979).

3.31. E. Reissner, 'A note on variational principles in elasticity', *Int. J. Solids Struct.*, **1**, 93-95 (1965).

3.32. T.J.R. Hughes and F. Brezzi, 'On drilling degrees of freedom', *Comp. Methods Appl. Mech. Eng.*, **72**, 105-121 (1989).

3.33. A. Ibrahimbegovic, R.L. Taylor and E.L. Wilson, 'A robust quadrilateral membrane finite element with drilling degrees of freedom', *Int. j. numer. methods eng.*, **30**, 445-456 (1990).

3.34. T.J.R. Hughes, F. Brezzi, A. Masud and I. Harari, 'Finite element with drilling degrees of freedom: Theory and numerical evaluation', *preprint*, 1989.

4.1. R.H. MacNeal and R.L. Harder, 'A proposed standard set of problems to test finite element accuracy', *J. Finite Elem. Anal. Des.*, **1**, 3-20 (1985).

4.2. C.W.S. To and M.L. Liu, 'Hybrid strain based three-node flat triangular shell elements, Part I: Formulation and element stiffness matrices', submitted to *Int. j. numer. methods eng.*, 1993.

4.3. N. Carpenter, T. Belystchko and H. Stolarski, 'Locking and shear factors in C^0 bending elements', *Comp. Struct.*, **22**, 39-52 (1986).

4.4. D.J. Allman, 'A compatible triangular element including vertex rotations for plane elasticity analysis', *Comp. Struct.*, **19**, 1-8 (1984).

4.5. D.J. Allman, 'The constant strain triangle with drilling rotations: A simple prospect for shell analysis', in J.R. Whiteman (ed.). *Proceedings The Mathematics of Finite Elements and Applications*, Academic Press, New York, 230-236 (1987).

4.6. D.J. Allman, 'Evaluation of the constant strain triangle with drilling rotations', *Int. j. numer. methods eng.*, **26**, 2645-2655 (1988).

4.7. H. Stolarski and T. Belystchko, 'Shear and membrane locking in curved C^0 elements', *Comp. Methods Appl. Mech. Eng.*, **41**, 279-296 (1983).

4.8. M.L. Liu and C.W.S. To, 'Hybrid strain based three-node flat triangular shell elements, Part III: Nonlinear theory and incremental formulation', to be submitted to *Int. j. numer. methods eng.*

4.9. C.W.S. To and M.L. Liu, 'Hybrid strain based three-node flat triangular shell elements, Part IV: Numerical investigation of nonlinear problems', to be submitted to *Int. j. numer. methods eng.*

4.10. A.F. Saleeb, T.Y. Chang and S. Yingyuengyong, 'A mixed formulation of C^0-linear triangular plate/shell element, the role of edge shear constraints', *Int. j. numer. methods eng.*, **26**, 1101-1128 (1988).

4.11. S. Timoshenko and S. Woinowsky-Krieger, *Theory of Plates and Shells*, 2nd ed., McGraw-Hill, New York, 1956.

4.12. O.C. Zienkiewicz, R.L. Taylor, P. Papadopoulos and E. Onate, 'Plate bending elements with discrete constraints: New triangular elements', *Comp. Struct.*, **35**, 505-522 (1990).

4.13. N. Carpenter, H. Stolarski and T. Belystchko, 'A flat triangular shell element with improved membrane interpolation', *Commun. appl. numer. methods*, **1**, 161-168 (1985).

4.14. N. Carpenter, H. Stolarski and T. Belystchko, 'Improvements in 3-node triangular shell elements', *Int. j. numer. methods eng.*, **23**, 1643-1667 (1986).

4.15. J. Fish and T. Belytschko, 'Stabilized rapidly convergent 18-degrees-of-freedom Flat shell triangular element', *Int. j. numer. methods eng.*, **33**, 149-162 (1992).

4.16. A.F. Saleeb, T.Y. Chang and W. Graf, 'A quadrilateral shell element using a mixed formulation', *Comp. Struct.*, **26**, 787-803 (1987).

4.17. W. Kanok-Nukulchai, 'A simple and efficient finite element for general shell analysis', *Int. j. numer. methods eng.*, **14**, 179-200 (1979).

4.18. Z.E. Mazurkiewicz and R.T. Nagorski, *Shells of Revolution*, Elsevier Science Publishing Co. Inc., New York, 1991.

4.19. M.D. Olson and T.W. Bearden, 'A simple flat triangular shell element revisited', *Int. j. numer. methods eng.*, **14**, 51-68 (1979).

5.1. D.J. Gorman, *Free Vibration Analysis of Rectangular Plates*, Elsevier North Holland, Inc. (1982).

5.2. A.W. Leissa, *Vibration of Plates*, Washington, D.C.: US Government Printing Office, (1969).

5.3. A.W. Leissa, 'Recent studies in plate vibrations, 1973-1976: Classical theory', *Shock Vibr. Dig.*, **9**(10), 13-24 (1977).

5.4. A.W. Leissa, 'Plate vibration research, 1976-1980: Classical theory', *Shock Vibr. Dig.*, **13**(9), 11-22 (1987).

5.5. A.W. Leissa, J.C. MacBain and R.E. Kielb, 'Vibrations of twisted cantilevered plates, Summary of previous and current studies', *J. Sound Vibr.*, **96**(2), 159-173 (1984).

5.6. A.W. Leissa, 'Recent studies in plate vibrations, 1981-1985: Part I, Classical theory', *Shock Vibr. Dig.*, **19**(2), 11-18 (1987).

5.7. A.W. Leissa, 'Recent studies in plate vibrations, 1981-1985: Part II, Complicating effects', *Shock Vibr. Dig.*, **19**(3), 10-24 (1987).

5.8. M.S. Qatu, 'Review of shallow shell vibration research', *Shock Vibr. Dig.*, **24**(9), 3-15 (1992).

5.9. A.W. Leissa, *Vibration of Shells*, Washington, D.C.: US Government Printing Office. (1973).

5.10. F.E. Eastep and F.G. Hemmig, 'Natural frequencies of circular plates with partially free, partially clamped edges', *J. Sound Vibr.*, **84**(3), 359-370 (1982).

5.11. I.M. Basci, T.G. Toridis and K. Khozeimeh, 'Improved method of static and free vibration analysis of thin rectangular plates', *Comp. Struct.*, **16**(1-4), 433-440 (1983).

5.12. M. Swaminadham, J. Danielski and O. Mahrenholtz, 'Free vibration analysis of annular sector plates by holographic experiments', *J. Sound Vibr.*, **95**(3), 333-340 (1984).

5.13. P. Priolo and C. Sitzia, 'Efficiency of annular finite elements for flexural vibrations of thick disks', *J. Sound Vibr.*, **92**(1), 21-31 (1984).

5.14. N. Ganesan and K.R. Sivadas, 'Free vibration of cantilever circular cylindrical Shells with Variable Thickness', *Comp. Struct.*, **34**(4), 669-677 (1990).

5.15. C.T.F. Ross, 'Finite element for the vibration of cones and cylinders', *Int. j numer. methods eng.*, **9**(4), 833-845 (1975).

5.16. D.R. Navaratra, 'Natural vibrations of deep spherical shells', *AIAA J.*, **4**(11), 2056-2058 (1966).

5.17. C.W. Bert, 'Research on dynamic behaviour of composite and sandwich plates---V: Part I', *Shock Vibr. Dig.*, **23**(6), (1991).

5.18. P.A.A. Laura, M.J. Maurizi and R.E. Rossi, 'A survey of studies dealing with Timoshenko beams', *Shock Vibr. Dig.*, **22**(11), 3-10 (1990).

5.19. P.A.A. Laura and M.J. Maurizi, 'Recent research on vibrations of arch-type structures', *Shock Vibr. Dig.*, **19**(1), 6-9 (1987).

5.20. A. Mukherjee and M. Mukhopadhyay, 'A review of dynamic behaviour of stiffened plates', *Shock Vibr. Dig.*, **18**(6), 3-8 (1986).

5.21. M. Mukhopadhyay and A. Mukherjee, 'Recent advances on the dynamic behaviour of stiffened plates', *Shock Vibr. Dig.*, **21**(4), 6-9 (1989).

5.22. M. Mukhopadhyay and G. Sinha, 'A review of dynamic behaviour of stiffened shells', *Shock Vibr. Dig.*, **24**(8), (1992).

5.23. O.C. Zienkiewicz and R.L. Taylor, *The Finite Element Method, I and II*, 4th edn. McGraw-Hill, N.Y. (1991).

5.24. R. Dungar, R.T. Severn and P.R. Taylor, 'Vibration of plate and shell structures using triangular finite elements', *J. Strain Analysis*, **2**(1), 73-83 (1967).

5.25. C.W.S. To and M.L. Liu, 'Hybrid strain based three-node flat triangular shell elements, Part I: Formulation and element stiffness matrices', submitted to *Int. j. numer. methods eng.*, (1993).

5.26. M.L. Liu and C.W.S. To, 'Hybrid strain based three-node flat triangular shell elements, Part II: Numerical studies', submitted to *Int. j. numer. methods eng.*, (1993).

5.27. Symbolic Computation Group, *MAPLE Reference Manual* (5th ed.), Department of Computer Science, University of Waterloo, Canada (1988).

5.28. R.H. MacNeal, 'A simple quadrilateral shell element', *Comp. Struct.*, **8**, 175-183 (1978).

5.29. R.H. MacNeal (ed.), *The NASTRAN Theoretical Manual* (1972).

5.30. A. Tessler and T.J.R. Hughes, 'A three-node Mindlin plate element with improved transverse shear', *Comp. Methods Appl. Mech. Eng.*, **50**, 71-101 (1985).

5.31. T.C. Huang, 'The effect of rotary inertia and of shear deformation on the frequency and normal mode equations of uniform beams with simple end conditions', *J. Appl. Mech.*, **28**, 579-583 (1961).

6.1. J.A. Stricklin, W.E. Haisler, H.R. MacDougall and F.J. Stebbins, 'Nonlinear analysis of shells of revolution by the matrix displacement method', *AIAA J.*, **6**, 2306-2312 (1968).

6.2. S. Yagmai, *Incremental Analysis of Large Deformations in Mechanics of Solids with Applications to Axisymmetric Shells of Revolution*, Ph.D. Thesis, Department of Civil Engineering, University of California at Berkeley, Berkeley, Ca., Report No. SESM 68-17 (1968).

6.3. L.A. Schmidt, F.K. Bcgner and R.L. Fox, 'Finite deflection structural analysis using plate and shell discrete elements', *AIAA J.*, **6**, 781-791 (1968).

6.4. C. Brebbia and J. Connor, 'Geometrically nonlinear finite element analysis', *J. Eng. Mech.*, **95**, 463-483 (1969).

6.5. G.S. Dhatt, 'Instability of thin shells by the finite element method', in *IASS Symp. Folded Plates and Prismatic Struct.*, Vienna, 1970.

6.6. G. Thomas and R.H. Gallagher, *A triangular thin shell element: Nonlinear analysis*, Department of Structural Mechanics, Cornell University, Ithaca, N.Y., Report No. NASA CR-2483 (1975).

6.7. R.D. Wood, *The Application of Finite Element Methods to Geometrically Nonlinear Structural Analysis*, Ph.D. Thesis, University of Wales, Swansea, U.K. (1973).

6.8. C. Tahiani and L. Lachance, 'Linear and non-linear analysis of thin shallow shells by mixed finite elements', *Comp. Struct.*, **5**, 167-177 (1975).

6.9. A.K. Noor and S.J. Hartley, 'Nonlinear shell analysis via mixed isoparametric elements', *Comp. Struct.*, **7**, 615-626 (1977).

6.10. G. Horrigmoe, 'Hybrid stress finite element model for non-linear shell problems', *Int. j. numer. methods eng.*, **12**, 1819-1839 (1978).

6.11. P.L. Boland and T.H.H. Pian, 'Large deflection analysis of thin elastic structures by the assumed stress hybrid finite element method', *Comp. Struct.*, **7**, 1-12 (1977).

6.12. K.J. Bathe and S. Bolourchi, 'Large displacement analysis of three-dimensional beam structures', *Int. j. numer. methods eng.*, **14**, 861-886 (1979).

6.13. K.J. Bathe and L.W. Ho, 'A simple and effective element for analysis of general shell structures', *Comp. Struct.*, **13**, 673-681 (1981).

6.14. K.J. Bathe and S. Bolourchi, 'A geometric and material nonlinear plate and shell element', *Comp. Struct.*, **11**, 23-48 (1980).

6.15. K.J. Bathe, E.L. Wilson and R.H. Iding, *NONSAP, A Structural Analysis Program for Static and Dynamic Response of Nonlinear Systems*, Report No. SESM 74-3, Structural Engineering Laboratory, University of California, Berkeley, California (1974).

6.16. T.J.R. Hughes and W.K. Liu, 'Nonlinear finite element analysis of shells, Part I: Three dimensional shells', *Comp. Methods Appl. Mech. Eng.*, **26**, 331-362 (1981).

6.17. T.J.R. Hughes and E. Carnoy, 'Nonlinear finite element shell formulation accounting for large membrane strains', *Comp. Methods Appl. Mech. Eng.*, **39**, 69-82 (1983).

6.18. H. Javaherian and P.J. Dowling, 'Large deflection elastoplastic analysis of thin shells', *Eng. Struct.*, **7**, 154-163 (1985).

6.19. R.A.F. Martins and D.R.J. Owen, 'Elastoplastic and geometrically nonlinear thin shell analysis by the semiloof element", *Comp. Struct.*, **13**, 505-513 (1981).

6.20. H. Parisch, 'Large displacements of shells including material nonlinearities', *Comp. Methods Appl. Mech. Eng.*, **27**, 183-214 (1984).

6.21. P.M. Pinsky and J. Jang, 'An elastoplastic shell element based on assumed covariant strain interpolations', *J. Eng. Mech.*, **114**, 1045-1062 (1988).

6.22. A.F. Saleeb, T.Y. Chang, W. Graf and S. Yingyeunyong, 'A hybrid/mixed model for non-linear shell analysis and its applications to large rotation problems', *Int. j. numer. methods eng.*, **29**, 407-446 (1990).

6.23. K.J. Bathe, *Finite Element Procedures in Engineering Analysis*, Prentice-Hall, New York (1982).

6.24. H. Horrigmoe and P.G. Bergan, 'Incremental variational principles and finite element models for nonlinear problems', *Comp. Methods Appl. Mech. Eng.*, **7**, 201-217 (1976).

6.25. S.N. Atluri, 'On the hybrid stress finite element method for incremental analysis of large deflection problems', *Int. J. Solids Struct.*, **9**, 1177-1191 (1973).

6.26. M.S. Gadala, M.A. Dokainish and G.AE. Oravas, 'Formulation methods of geometric and material nonlinearity problems', *Int. j. numer. methods eng.*, **20**, 887-914 (1984).

6.27. M.S. Gadala, and G.AE. Oravas, 'Numerical solutions of nonlinear problems of continua--I: Survey of formulation methods and solution techniques', *Comp. Struct.*, **19**, 865-877 (1984).

6.28. J.T. Oden, *Finite Elements of Nonlinear Continua*, McGraw-Hill Book Co., New York, (1972).

6.29. C.W.S. To and M.L. Liu, 'Hybrid strain based three-node flat triangular shell elements, Part I: Formulation and element stiffness matrices', submitted to *Int. j. numer. methods eng.*, 1993.

6.30. T. Belytschko, 'Nonlinear analysis descriptions and numerical stability', in *Shock and Vibration Computer Programs, Reviews and Summaries* (eds. W. Pilkey and B. Pilkey), U.S. Department of Defense, 1975, pp.537-562.

6.31. T. Belytschko and B.J. Hsieh, 'Nonlinear transient finite element analysis with convected coordinates', *Int. j. numer. methods eng.*, **7**, 255-271 (1973).

6.32. T. Belytschko, L. Schwer and M.J. Klein, 'Large displacement, transient analysis of space frames', *Int. j. numer. methods eng.*, **11**, 65-84 (1977).

6.33. M. Kleiber, *Incremental Finite Element Modelling in Nonlinear Solid Mechanics*, Ellis Horwood Ltd., (1989).

6.34. J.H. Chiou, J.D. Lee and A.G. Erdman, 'Development of a three-dimensional finite element program for large strain elastic-plastic solids', *Comp. Struct.*, **36**, 631-645 (1990).

6.35. S.N. Atluri, 'Alternate stress and conjugate strain measures, and mixed variational formulations involving rigid rotations, for computational analysis of finitely deformed solids with applications to plates and shells, I: Theory', *Comp. Struct.*, **18**, 93-116 (1984).

6.36. S. Nemat-Nasser, 'Continuum bases for consistent numerical formulations of finite strains in elastic and inelastic structures', in *Finite Element Analysis of Transient Nonlinear Structural Behaviour* (ed. T. Belytschko, J.R. Osias and P.V. Marcal), ASME, New York, 1975, pp.85-98.

6.37. S. Nemat-Nasser, 'Decomposition of strain measures and their rates in finite deformation elastoplasticity", *Int. J. Solids Struct.*, **15**, 155-166 (1979).

6.38. S. Nemat-Nasser, 'On finite deformation elasto-plasticity', *Int. J. Solids Struct.*, **18**, 857-872 (1982).

6.39. V.A. Lubarda and E.H. Lee, 'A correct definition of elastic and plastic deformation and its computational significance', *J. Appl. Mech.*, **48**, 35-40 (1981).

6.40. E.H. Lee, 'Elastic plastic deformation at finite strains', *J. Appl. Mech.*, **36**, 1-6 (1969).

6.41. E.H. Lee and R.M. McMeeking, 'Concerning elastic and plastic components of deformation', *Int. J. Solids Struct.*, **16**, 715-721 (1980).

6.42. E.H. Lee, 'Some comments on elasto-plastic analysis', *Int. J. Solids Struct.*, **17**, 859-872 (1981).

6.43. E.H. Lee, 'Finite deformation effects in plasticity analysis', in *Numerical Methods in Industrial Forming Processes* (eds. J.F.T. Pittman, O.C. Zienkiewicz, R.D. Wood and J.M. Alexander), Pineridge Press, Swansea, 1982, pp.39-50.

6.44. E.H. Lee, 'The structure of the elastic-plastic constitutive relations for finite deformation', in *Constitutive Equations: Macro and Computational Aspects* (ed. K.J. William), ASME, New York, 1984, pp.103-110.

6.45. A.E. Green and P.M. Naghdi, P.M., 'Some remarks on elastic-plastic deformation at finite strain", *Int. J. Eng. Sci.*, **9**, 1219-1229 (1971).

6.46. J.H. Chiou, J.D. Lee and A.G. Erdman, 'Comparison between two theories of plasticity', *Comp. Struct.*, **24**, 23-37 (1986).

6.47. J.D. Lee, 'Finite element procedures for large strain elastic-plastic theories', *Comp. Struct.*, **28**, 395-406 (1988).

6.48. J.C. Simo, 'A framework for finite strain elasto-plasticity based on maximum plastic dissipation and the multiplicative decomposition: Part I, Continuum formulation', *Comp. Methods Appl. Mech. Eng.*, **66**, 199-219 (1988).

6.49. J.C. Simo, 'A framework for finite strain elasto-plasticity based on maximum plastic dissipation and the multiplicative decomposition, Part II: Computational aspects', *Comp. Methods Appl. Mech. Eng.*, **68**, 1-31 (1988).

6.50. R.M. McMeeking and J.R. Rice, 'Finite element formulations for problems of large elastic-plastic deformation', *Int. J. Solids Struct.*, **11**, 601-616 (1975).

6.51. J.W. Hutchinson, 'Elastic-plastic behaviour of polycrystalline metals and composites', *Proc. Roy. Society of London*, **A319**, 247-272 (1970).

6.52. N. Stander, A. Matzenmiller and E. Ramm, 'An assessment of assumed strain methods in finite rotation shell analysis', *Eng. Comput.*, **6**, 58-66 (1989).

6.53. G. Wempner, 'Finite elements, finite rotations and small strains of flexible shells', *Int. J. Solids Struct.*, **5**, 117-153 (1969).

6.54. K.M. Hsiao, 'Nonlinear analysis of general shell structures by flat triangular shell element', *Comp. Struct.*, **25**, 665-675 (1987).

6.55. K.M. Hsiao and H.C. Hung, 'Large deflection analysis of shell structure by using corotational total Lagrangian formulation', *Comp. Methods Appl. Mech. Eng.*, **73**, 209-225 (1989).

6.56. K.S. Surana, 'Geometrically nonlinear formulation for curved shell elements', *Int. j. numer. methods eng.*, **19**, 581-615 (1983).

6.57. J. Oliver and E. Onate, 'A total Lagrangian formulation for the geometrically nonlinear analysis of structures using finite elements, Part I, Two-dimensional problems: Shell and plate structures', *Int. j. numer. methods eng.*, **20**, 2253-2281 (1984).

6.58. J.C. Simo, 'A finite strain beam formulation. The three-dimensional dynamic problem. Part I", *Comp. Methods Appl. Mech. Eng.*, **49**, 55-70 (1985).

6.59. J.C. Simo and L. Vu-Quoc, 'A three-dimensional finite strain rod model, Part II: Computational aspects', *Comp. Methods Appl. Mech. Eng.*, **58**, 79-116 (1986).

6.60. C.W.S. To and M.L. Liu, 'Hybrid strain based three-node flat triangular shell elements, Part IV: Computed results of nonlinear problems', submitted to *Int. j. numer. methods eng.*, 1993.

6.61. J.C. Simo and L. Vu-Quoc, 'On the dynamics in space of rods undergoing large motions. A geometrically exact approach', *Comp. Methods Appl. Mech. Eng.*, **66**, 125-161 (1988).

6.62. J.C. Simo and D.D. Fox, 'On a stress resultant geometrically exact shell model. Part I: Formulation and optimal parametrization', *Comp. Methods Appl. Mech. Eng.*, **72**, 267-304 (1989).

6.63. J.C. Simo, D.D. Fox and M.S. Rifai, 'On a stress resultant geometrically exact shell model. Part II: The linear theory; Computational aspects', *Comp. Methods Appl. Mech. Eng.*, **73**, 53-92 (1989).

6.64. J.C. Simo, D.D. Fox and M.S. Rifai, 'On a stress resultant geometrically exact shell model. Part III: Computational aspects of the nonlinear theory', *Comp. Methods Appl. Mech. Eng.*, **79**, 21-70 (1990).

6.65. J.C. Simo, M.S. Rifai and D.D. Fox, 'On a stress resultant geometrically exact shell model. Part IV: Variable thickness shells with through-the-thickness stretching', *Comp. Methods Appl. Mech. Eng.*, **81**, 91-126 (1990).

6.66. J.C. Simo and J.G. Kennedy, 'On a stress resultant geometrically exact shell model. Part V: Nonlinear plasticity; Formulation and integration algorithms', *Comp. Methods Appl. Mech. Eng.*, **96**, 133-171 (1992).

6.67. J.C. Simo, M.S. Rifai and D.D. Fox, 'On a stress resultant geometrically exact shell model. Part VI: Conserving algorithms for nonlinear dynamics', *Int. j. numer. methods eng.*, **34**, 117-164 (1992).

6.68. N. Buechter and E. Ramm, 'Shell theory versus degeneration--A comparison in large rotation finite element analysis', *Int. j. numer. methods eng.*, **34**, 39-59 (1992).

6.69. C. Sansour and H. Bufler, 'An exact finite rotation shell theory, its mixed variational formulation and its finite element implementation', *Int. j. numer. methods eng.*, **34**, 73-115 (1992).

6.70. Y. Basar, 'A consistent theory of geometrically nonlinear shells with an independent rotation vector', *Int. J. Solids Struct.*, **23**, 1401-1415 (1987).

6.71. Y. Basar and Y. Ding, 'Finite rotation elements for the nonlinear analysis of thin shell structures', *Int. J. Solids Struct.*, **26**, 83-97 (1990).

6.72. Y. Basar and Y. Ding, 'Finite rotation shell elements for the analysis of finite rotation shell problems", *Int. j. numer. methods eng.*, **34**, 165-169 (1992).

6.73. J.H. Argyris, 'An excursion into large rotations', *Comp. Methods Appl. Mech. Eng.*, **32**, 85-155 (1982).

6.74. E. Ramm, 'A plate/shell element for large deflections and rotations', in *Formulations and Computational Algorithms in Finite Element Analysis* (eds. K.J. Bathe, J.T. Oden and W. Wunderlich), M.I.T. Press, Cambridge, Ma., 1976, pp.255-291.

6.75. J.H. Argyris, H. Balmer, J. St. Dolysinis, P.C. Dunne, M. Haase, M. Kleiber, G.A. Malejannakis, H.P. Mlejnek, M. Muller and D.W. Scharpf, 'Finite element method, the natural approach', *Comp. Methods. Appl. Mech. Eng.*, **17/18**, 1-106 (1979).

6.76. J.F. Besseling, 'Derivatives of deformation parameter for bar elements and their use in buckling and postbuckling analysis', *Comp. Methods Appl. Mech. Eng.*, **12**, 97-124 (1977).

6.77. R.H. MacNeal, 'A simple quadrilateral shell element', *Comp. Struct.*, **8**, 175-183 (1978).

6.78. *The NASTRAN Theoretical Manual* (ed. R.H. MacNeal), 1972

6.79. M.L.Liu and C.W.S. To, 'Vibration analysis of structures by hybrid strain based three-node flat triangular shell elements', to be submitted to *J. Sound Vibr.*, 1993.

6.80. M.A. Dokainish and K. Subbaraj, 'A survey of direct time-integration methods in computational structural dynamics--I. Explicit methods', *Comp. Struct.*, **32**, 1371-1386 (1989).

6.81. K. Subbaraj and M.A. Dokainish, 'A survey of direct time-integration methods in computational structural dynamics--II. Implicit methods', *Comp. Struct.*, **32**, 1387-1401 (1989).

6.82. C.W.S. To, 'Direct integration operators and their stability for random response of multi-degree-of-freedom systems', *Comp. Struct.*, **30**, 865-874 (1988).

6.83. C.W.S. To, 'The stochastic central difference method in structural dynamics', *Comp. Struct.*, **23**, 813-816 (1986).

6.84. C.W.S. To, 'Random responses of multi-degree-of-freedom systems by the stochastic central difference method', In *Proc. Int. Conf. on Computational Mechanics*, Tokyo, Japan, 25-29 May, 1986, pp. XI.181-186.

6.85. C.W.S. To, 'A stochastic version of the Newmark family of algorithms for discretized dynamic systems', *Comp. Struct.*, **44**, 667-673 (1992).

6.86. C.W.S. To, 'Recursive expressions for random response of nonlinear systems', *Comp. Struct.*, **29**, 451-457 (1988).

6.87. C.W.S. To, 'Random response of a Duffing oscillator by the stochastic central difference method', *J. Sound Vibr.*, **124**, 427-433 (1988).

6.88. C.W.S. Tc, 'Parametric effects on time step size of the stochastic central difference method", *J. Sound Vibr.*, **137**, 509-515 (1990).

6.89. C.W.S. To and M.L. Liu, 'Random responses of discretized beam and plate by the stochastic central difference method with time co-ordinate transformation', submitted to *Comp. Struct.*, 1992.

6.90. M.L. Liu and C.W.S. To, 'Adaptive time schemes for non-stationary random responses of nonlinear multi-degrees-of-freedom systems', submitted to *Comp. Struct.*, 1992

6.91. M.L. Liu and C.W.S. To, 'Hybrid strain based three-node flat triangular shell elements, Part II: Numerical studies', submitted to *Int. j. numer. methods eng.*, 1993.

6.92. M. Robinson, 'A comparison of yield surfaces for thin shells', *Int. J. Mech. Sci.*, **13**, 345-354 (1971).

6.93. D.J. Allman, 'A compatible triangular element including vertex rotations for plane elasticity analysis', *Comp. Struct.*, **19**, 1-8 (1984).

6.94. A. Tessler and T.J.R. Hughes, 'A three-node Mindlin plate element with improved transverse shear', *Comp. Methods Appl. Mech. Eng.*, **50**, 71-101 (1985).

6.95. J.W. Hutchinson, 'Finite strain analysis of elasto-plastic solids and structures', in *Numerical Solution of Nonlinear Structural Problems* (ed. R.F. Hartung), ASME, Detroit, 1975, pp.17-29.

6.96. J.C. Nagtegaal and J.E. de Jong, 'Some computational aspects of elastic-plastic large strain analysis', *Int. j. numer. methods eng.*, **17**, 15-41 (1981).

6.97. T.J.R. Hughes and J. Winget, 'Finite rotation effects in numerical integration of rate type constitutive equations arising in large deformation analysis', *Int. j. numer. methods eng.*, **15**, 1862-1867 (1980).

6.98. A. Needleman, 'A numerical study of necking in circular cylindrical bars', *J. Mech. Phys. Solids*, **20**, 111-127 (1972).

6.99. D.R.J. Owen and E. Hinton, *Finite Elements in Plasticity: Theory and Practice*, Pineridge Press, Swansea, U.K. (1980).

6.100. A.A. Ilyushin, *Plasticity* (in Russian), Gostekhizdat, Moscow (1948).

6.101. G.S. Shapiro, 'On yield surfaces for ideally plastic shells', in *Problems of Continuum Mechanics*, SIAM, Philadelphia, Pa., 1961, pp.414-418.

6.102. D.D. Fox and J.C. Simo, 'A drill rotation formulation for geometrically exact shells', *Comp. Methods Appl. Mech. Eng.*, **98**, 329-343 (1992).

6.103. J.C. Simo, D.D. Fox and T.J.R. Hughes, 'Formulations of finite elasticity with independent rotations', *Comp. Methods Appl. Mech. Eng.*, **95**, 277-288 (1992).

6.104. M.L. Liu and C.W.S. To, 'Hybrid strain based three-node flat triangular shell elements, Part V: Nonlinear theories', report No. NDRL TR-9401, The Department of Mechanical Engineering, The University of Western Ontario, Feb., 1994.

7.1. A.F. Saleeb, T.Y. Chang, W. Graf and S. Yingyeunyong, 'A hybrid/mixed model for non-linear shell analysis and its applications to large rotation problems', *Int. j. numer. methods eng.*, **29**, 407-446 (1990).

7.2. J.C. Simo, D.D. Fox and M.S. Rifai, 'On a stress resultant geometrically exact shell model. Part III: Computational aspects of the nonlinear theory', *Comp. Methods Appl. Mech. Eng.*, **79**, 21-70 (1990).

7.3. T.J.R. Hughes and W.K. Liu, 'Nonlinear finite element analysis of shells, Part I: Three dimensional shells', *Comp. Methods Appl. Mech. Eng.*, **26**, 331-362 (1981).

7.4. K.K. Chen, 'Evaluation of a finite element for binder warp calculation', *General Motors Research Publication GMR-5209*, (1985).

7.5. K.J. Bathe and S. Bolourchi, 'A geometric and material nonlinear plate and shell element', *Comp. Struct.*, **11**, 23-48 (1980).

7.6. H. Parisch, 'Large displacements of shells including material nonlinearities', *Comp. Methods Appl. Mech. Eng.*, **27**, 183-214 (1984).

7.7. J. Oliver and E. Onate, 'A total Lagrangian formulation for the geometrically nonlinear analysis of structures using finite elements, Part I, Two-dimensional problems: Shell and plate structures', *Int. j. numer. methods eng.*, **20**, 2253-2281 (1984).

7.8. K.J. Bathe, E.L. Wilson and R.H. Iding, *NONSAP, A Structural Analysis Program for Static and Dynamic Response of Nonlinear Systems*, Report No.

SESM 74-3, Structural Engineering Laboratory, University of California, Berkeley, California (1974).

7.9. K.J. Bathe, *Finite Element Procedures in Engineering Analysis*, Prentice-Hall, New York (1982).

7.10. W. Johnson and P.B. Mellor, *Engineering Plasticity*, Ellis Horwood Ltd., Chichester, U.K. (1983).

7.11. J.A. Stricklin, W.E. Haisler, H.R. MacDougall and F.J. Stebbins, 'Nonlinear analysis of shells of revolution by the matrix displacement method', *AIAA J.*, **6**, 2306-2312 (1968).

7.12. G.S. Dhatt, 'Instability of thin shells by the finite element method', in *IASS Symp. Folded plates and Prismatic Struct.*, Vienna (1970).

8.1 C.W.S. To, 'Recursive expressions for random response of nonlinear systems', *Comp. Struct.*, **29**(3), 451-457 (1988).

8.2 C.W.S. To, 'Parametric effects on the time step size of the stochastic central difference method', *J. Sound Vibr.*, **137**(3), 509-515 (1990).

8.3 K.J. Bathe and E.L. Wilson, 'Stability and accuracy analysis of direct integration methods', *Earthquake Eng. Struct. Dynamics*, **1**, 283-291 (1973).

8.4 C.W.S. To, 'A stochastic version of the Newmark family of algorithms for discretized dynamic systems', *Comp. Struct.*, **44**(3), 667-673 (1992).

8.5 B. Wang, *Nonstationary Random Responses of Plates with Geometric Nonlinearity*, M.E.Sc. thesis, The University of Western Ontario, London, Ontario, Canada (1990).